Radionuclides in the Environment

Published on January 1, 1970 on http://pubs.acs.org | doi: 10.1021/ba-1970-0093.fw001

Radionuclides in the Environment

A symposium sponsored by
the Division of Nuclear
Chemistry and Technology
at the 155th Meeting of
the American Chemical
Society, San Francisco,
Calif., April 1-3, 1968.

E. C. Freiling,
Symposium Chairman

ADVANCES IN CHEMISTRY SERIES 93

AMERICAN CHEMICAL SOCIETY
WASHINGTON, D. C. 1970

Coden: ADCSHA

Library of Congress Catalog Card 74-112987

PRINTED IN THE UNITED STATES OF AMERICA

Advances in Chemistry Series

Robert F. Gould, *Editor*

AMERICAN CHEMICAL SOCIETY PUBLICATIONS

FOREWORD

ADVANCES IN CHEMISTRY SERIES was founded in 1949 by the American Chemical Society as an outlet for symposia and collections of data in special areas of topical interest that could not be accommodated in the Society's journals. It provides a medium for symposia that would otherwise be fragmented, their papers distributed among several journals or not published at all. Papers are refereed critically according to ACS editorial standards and receive the careful attention and processing characteristic of ACS publications. Papers published in ADVANCES IN CHEMISTRY SERIES are original contributions not published elsewhere in whole or major part and include reports of research as well as reviews since symposia may embrace both types of presentation.

PREFACE

To get things done in this world, we need men of action and common sense; to see that more good is done than harm, we need men of reflection and uncommon sense. Both types play their role in maintaining the balance between the extremes of recklessness and stagnation. These days both types could hardly avoid being aware of the difficulties and unforeseen consequences resulting from our unprecedented technical achievements. The problems of environmental pollution have attracted attention and concern at all levels of responsibility and from all fields of competence.

Radionuclides constitute a special kind of environmental pollution. Their artificial production rate has increased exponentially since the development of the first nuclear reactor. They have brought us blessings in the form of power, of new research tools, and of new knowledge; they have brought us problems in the form of the release of hazardous radionuclides and of the management of large quantities of radioactive waste.

The responsibility for overseeing the development of nuclear power and the acquisition and utilization of nuclear resources is important, difficult, and expensive. At the June 1967 meeting of the American Nuclear Society in San Diego, it was noted that it costs as much money to prove the safety of a Snap device as it does to develop it. Obviously, decision makers are conscientiously exercising their responsibility. As scientists we are in the fortunate position of giving advice without having to make decisions. However, we still have responsibilities and difficulties—only of a different kind. As scientists our job is:

(1) To foresee hazards and to forewarn decision makers

(2) To provide the most reliable information possible in the most economical manner possible

(3) To help maintain perspective.

To maintain perspective, we must consider artificial radioactivity in comparison with the natural radioactivity with which man has learned to live, and some with which he hasn't (such as the radon and thoron daughters of uranium). To provide good information efficiently we who are working on various aspects of this problem need to trade ideas and criticisms and techniques of sampling, analysis, data reduction, and interpretation.

We undertake our responsibility out of scientific self interest and out of concern for the technical progress of our nation and the benefit of

mankind. It is to our advantage as scientists to have the maximum freedom for the use of radioactive tracers consistent with regard for the common safety. It will benefit our nation to be able to exploit the peaceful application of nuclear explosives under the same constraints. The prudent utilization of nuclear energy offers many potentials for developing underprivileged nations.

The task of providing input for the man who must calculate the risk has problems of its own which discourage the fainthearted. A nuclear detonation, a runaway reactor, a radioisotopic power source that is entering the atmosphere—these are examples of highly irreversible processes occurring under unfamiliar conditions of temperature, pressure, cooling rate, and admixture of new material into the system. Nuclear detonations, which have been primarily responsible for the uncontrolled release of radioactivity into the environment, are characterized by fractionation processes that send one fission product aloft on small particles and bring another to the ground on large particles and require almost individual consideration of every nuclide.

Encouragement can be taken in the simplification offered by the limited number of fundamental processes that unify this diversity: the process that governs the uptake of radon or thoron on dust particles in a uranium mine is the same process that governs the uptake of fission product molybdenum oxide on a coral particle. Fission-product condensation onto a particle is essentially the same movie as the one for fission product escape from a reactor particle, but run backward. The same ion-exchange processes are considered in waste disposal, in the leaching of fallout particles in the gut, in ground-water contamination from Plowshare events, and in the release of radionuclides to the ocean. The aerosols that would result from a re-entering isotopic power source are not greatly different from those produced by a nuclear detonation in air. The atmospheric transport of these and naturally occurring aerosols bearing cosmic-ray induced nuclides are governed by the same laws.

These are some examples of the similarities which can be exploited when we learn more about what our fellow man is doing. The exchange of such information was the primary purpose of this symposium, and wherever possible, the authors point out the relation of their work to current investigations in other phases of this general subject.

San Francisco, Calif.
June 1969

E. C. FREILING

1

Mass-Transfer Mechanisms in Source-Term Definition

E. C. FREILING[1]

Naval Radiological Defense Laboratory, San Francisco, Calif. 94135

This paper deals mainly with the condensation of trace concentrations of radioactive vapor onto spherical particles of a substrate. For this situation the relation between the engineering approach, the molecular approach, and the fluid-dynamic approach are illustrated for several different cases of rate limitation. From these considerations criteria are derived for the use of basic physical and chemical parameters to predict the rate-controlling step or steps. Finally, the effect of changing temperature is considered and the groundwork is thereby laid for a kinetic approach to predicting fallout formation. The relation of these approaches to the escape of fission products from reactor fuel and to the deposition of radon and thoron daughters on dust particles in a uranium mine is indicated.

This chapter introduces and supplies the background for the papers of the session on mass transfer. Mass-transfer considerations are fundamental to source-term definition and to a basic understanding of radionuclide fractionation processes. However, they are unfamiliar to many radiochemists and environmental scientists, who may constitute most of the readers of this volume. They represent primarily an engineering approach, whose suitability seems too obvious to belabor.

We are basically interested in heterogeneous, high temperature kinetics. At high temperatures, the chemical reactions occur as fast as the reactants can get together, like ionic solution reactions. Hence, we are concerned mainly with how fast the species can get from one part of the system to another. These transport processes are the bottlenecks

[1] Present address: U. S. Naval Weapons Laboratory, FCA, Dahlgren, Va. 22448.

that regulate the behavior of the system. We can approach them from many viewpoints:

(1) Kinetic theory of gases (collision model or Monte Carlo approach)

(2) Chemical engineering principles and boundary-layer theory

(3) Reaction kinetics and statistical mechanics

(4) Thermal analogs (continuum theory)

We will touch on all of these. The last is of interest because so many of the problems worked out by thermophysicists can be applied to chemical problems by a few simple changes in notation.

Because the subject is vast, the presentation is limited to a discussion of the uptake of a tracer from the vapor phase by spherical particles. This is the viewpoint of one concerned with fallout formation. The reverse process—escape from spherical particles—is the viewpoint of one concerned with reactor fuels. For the idealized case the treatment is exactly the same for the two situations. The fact that we deal with trace quantities and concentration means that we can neglect changes in the particle properties as the reaction proceeds and that we need not be concerned with surface nucleation.

Mention of fallout formation brings us to the second purpose of this chapter. Both developers and users of fallout-formation models have long recognized the need for a kinetic approach to predict fallout formation. Yet, despite the availability of the highly developed kinetic theory of gases and of a wealth of material on the engineering approach to mass, heat, and momentum transfer, the development of such an approach has been slow to materialize. The principal barrier has been ignorance of the relative importance of the fundamental processes involved in radionuclide condensation at high temperature—namely:

(1) Diffusion of fission-product species through the gas phase

(2) Reflection or condensation of these species at the surfaces of particles

(3) Diffusion of condensed species within particles

(4) Re-evaporation of condensed species.

Recent work at NRDL (*1*) has established the rate-controlling steps for several cases of interest, and the time is now ripe to lay the foundation for a realistic approach to fallout formation.

Of course, the first question is, "where must the system go?" This is formally answered by chemical thermodynamics in terms of equilibrium-distribution coefficients or Henry's Law constants. For our purposes these are well described from the elementary viewpoint by MacDougall (*8*) and from the viewpoint of practical application by Norman (*9*).

The next question is, "How does it get there?"

Background

Table I presents six basic equations in a general way. Those on the left apply to transfer within a phase A, and those on the right to transfer across a phase boundary AB. The top row expresses the mutual definition of force F, proportionality constant K, and potential ϕ. The second row expresses the phenomenological proportionality between flux J and force F. The bottom row states the conservation constraints. The left equation says merely that in a given volume the difference between the accumulation rate and the emanation rate must be attributed to a source S. As stated, these equations apply to any conserved quantity which is diffusing, either within a phase under the influence of a potential gradient or across a phase under the influence of a potential difference.

Before particularizing, we can consider a number of simplifications. In the steady-state condition, all time derivatives are zero. At equilibrium, in addition to zero time derivatives, all potential differences and potential gradients are zero. If the system is sourceless and sinkless, $S = 0$. By Green's theorem

$$-\int_{\text{surface}} J_n^{A}\, d\sigma^{A} = -\int_{\text{volume}} \nabla \cdot \mathbf{J}^{A}\, d\tau^{A} = \int_{\text{volume}} K^{A}\, \nabla^2 \phi^{A}\, d\tau^{A} \qquad (1)$$

where $d\tau$ is an increment of volume, and this is frequently a more useful form of the emanation rate.

Table I. Basic Equations[a]

Within Phase A		*Across Boundary AB*
	Force	
$\mathbf{F}^{A} = -K_F^{A} \operatorname{grad} \phi^{A}$		$F_n^{A,B} = -K_F^{AB}\ (\phi^{A;B} - \phi^{B;A})$
	Flux	
$\mathbf{J}^{A} = K_J^{A}\, \mathbf{F}^{A}$		$J_n^{A;B} = K_J^{AB}\, F_n^{A,B}$
	Conservation	
$-\int J_n^{A}\, d\sigma^{A} + S^{A} = \dfrac{\partial Q^{A}}{\partial t}$		$-J_n^{A;B} = J_n^{B;A}$
Surface Emanation Rate +	Source Strength =	Accumulation Rate

[a] Definitions:
$F_n^{A,B} = -F_n^{B,A}$ = force in direction from A to B.
$\phi^{A;B}$ = potential in phase A at boundary AB.
Q = quantity, $d\sigma$ = surface element.
n = normal to surface from bulk.

If we apply these equations to the condensation of a fission product in a cooling nuclear fireball, we must deal with sources from radioactive growth, sinks from radioactive decay, and dynamic conditions of temperature drop. In the simple case of radioactive decay

$$S = -\lambda Q \tag{2}$$

where λ is the radioactive decay constant. To simplify the remaining discussion, we treat only cases where λ is very small and S may be neglected. We then consider first isothermal deposition and discuss later the effects of temperature change.

To apply these equations to fission-product diffusion, we then make the analogy

$$\phi{:}a = K{:}D = (Q/\tau){:}C \tag{3}$$

where a is the thermodynamic activity, D is the diffusion constant, and C is the concentration. The same equations are applied to thermal diffusion by the analogy

$$\phi{:}T = K{:}K_T = (Q/\tau){:}\rho cT \tag{4}$$

where T is the temperature, K_T is the thermal conductivity, ρ is the density, and c is the volume specific heat. The former analogy leads to Fick's Laws and the latter to Fourier's. I have chosen the thermodynamic activity rather than the concentration as the potential because it has all the advantages of concentration but the added advantage of making a better analogy to T.

Table II presents some consequences of these analogies for a vapor phase and a condensed phase together with the thermal analogs. Here n_i is the concentration of the vapor in molecules per unit volume, N_i is the mole fraction in the condensed phase, $\mathbf{V}^C$ is the molar volume of the substrate, p_i is the partial pressure, and γ_i is the rational activity coefficient.

Mass Transfer

From the viewpoint of the chemical engineer, the application of the fundamentals just discussed takes the form of mass-transfer theory, and the constants K_J are called mass-transfer coefficients. However, some care must be exercised in determining the potential difference between two phases. One cannot simply take the difference between the thermodynamic activities in two phases without ensuring that they are adjusted to the same reference state. The point is illustrated with a brief consideration of the boundary-layer model.

Frequently one must account for relative motion between the particle and the vapor. Figure 1 illustrates schematically the boundary-layer

Table II. Equations for a Vapor Phase and a Condensed Phase[a]

Vapor	*Condensed*	*Thermal Analog*
$C_i^V = n_i^V$	$C_i^C = \frac{N_i^C}{V^C}$	$C_T = \rho c T$
$\phi_i^V = p_i = n_i RT$	$\phi_i^C = a_i^C = \gamma_i^C N_i^C$	$\phi_T = T$
$\left(\frac{\phi}{C}\right)_i^V = RT$	$\left(\frac{\phi}{C}\right)_i^C = \gamma_i^C V^C$	$\left(\frac{\phi}{C}\right)_T = \frac{1}{\rho c}$
$(K_{F\cdot J}^V)_i = D_i^V$	$(K_{F\cdot J}^C)_i = D_i^C$	$(K_{F\cdot J})_T = K$
Diffusion Constants		Thermal Conductivity

[a] Definitions:
ρ = density.
c = specific heat.
$K_{F\cdot J}^A \equiv K_F^A K_J^A$.
ρc = volume specific heat.
V = molar volume.

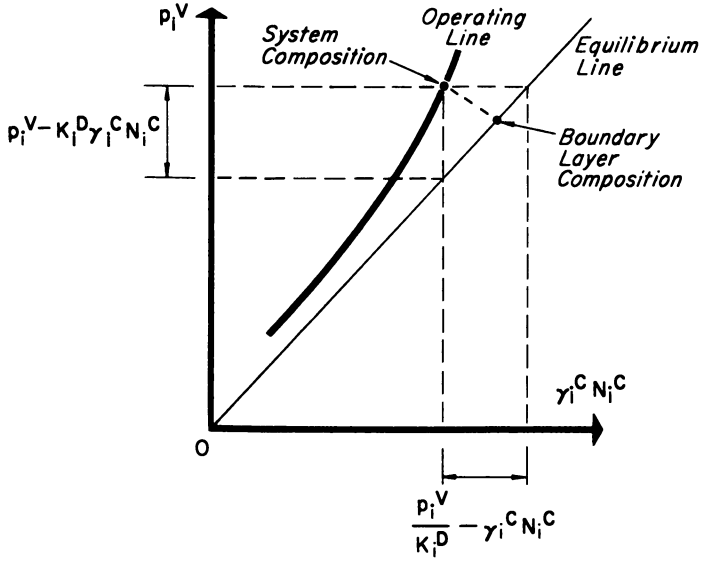

Figure 1. Boundary-layer model

model for applying the previous fundamentals to this problem. One takes the stagnant boundary layer L as being a part of the vapor phase which is next to the condensate and which has some small fictitious width, which is a function of the relative velocity. This layer is assumed to be in equilibrium—*i.e.*, in this layer the partial pressure of the condensing

species is related to its surface concentration by an equilibrium relationship.

Across the boundary LV, the flux is proportional to the difference in potential; the same is true for boundary LC. Since the two fluxes are equal, there is no accumulation of fission product in the layer.

We can use the equilibrium condition in the layer to eliminate the L terms for either of two expressions. The over-all result is:

$$J_n^{V;C} = K_i^{V:C}\,(p_i^V - K_i^D\,\gamma_i^C\,N_i^C) = K_i^{C:V}\left(\frac{p_i^V}{K_i^D} - \gamma_i^C\,N_i^C\right) \qquad (5)$$

The first equality takes the vapor phase as a reference and uses the distribution coefficient K_i^D to adjust the activity in the condensed phase. The second equality takes the condensed phase as reference and uses K_i^D to adjust the activity in the vapor phase. Obviously

$$K_i^{C:V} = K_i^D\,K_i^{V:C} \qquad (6)$$

Further clarification is obtained from Figure 2 where the relations are depicted by a composition diagram where the vapor phase composition is the ordinate and the condensed phase composition is the abscissa. A straight line with a slope equal to the equilibrium distribution constant K_i^D is the locus of all equilibrium compositions. The curved line represents a set of nonequilibrium conditions for condensation out of the vapor phase. The departure from equilibrium can be projected on either axis, and the lengths of the projections correspond to the two expressions for potential difference shown above. Refs. 2 and 10 treat the boundary layer in detail.

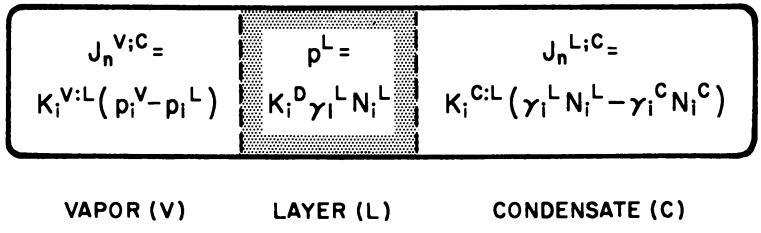

Figure 2. Phase compositions

Kinetic Theory

To bridge the gap between molecular processes and empirical coefficients and between laboratory determinations of input data and an engineering approach to predictions, we want to develop the above fundamental equations in terms of the kinetic theory of gases and reaction rate theory. There are three principal candidates for the rate-controlling

step in the condensation mechanism: diffusion through the vapor, condensation at the particle surface, and diffusion in the particle. For all three cases we can write

$$J_n^{V;C} = K_{F\cdot J}^{V:C} (p_i^V - K_i^D \gamma_i^C N_i^C) \quad (7)$$

Vapor-Diffusion Control. If deposition is governed by the rate of diffusion through the vapor, Maxwell's equation gives

$$K_{F\cdot J}^{V:C} = D^V/\mathbf{R}\,kT \text{ [cm.}^{-2}\text{ sec.}^{-1}\text{ atm.}^{-1}\text{]} \quad (8)$$

where **R** is the radius of the particle, and k is the Boltzmann constant. The particle is at uniform concentration, but the vapor is relatively depleted near the particle surface. The situation occurs when there is a strong interaction between the condensing molecule and the substrate, so that the condensation coefficient is at or near unity. If there is no re-evaporation, the second term in the transport equation can be neglected. Lassen, Rau, and Weicksel have shown that the deposition onto dust particles of the daughter products of radioactive rare gases in a uranium mine (radon and thoron) follows such an equation (*7*, *11*). If re-evaporation occurs, the second term grows from zero to its equilibrium value. Lai and Freiling (*6*) have estimated recently D^V for vaporized fission products and fission-product oxides over the temperature range 500°–2500°K. They found that they vary from 0.093 cm.^{2} sec.$^{-1}$ for Cs_2 at 500°K. to 4.8 cm.^{2} sec.$^{-1}$ for As and Se at 2500°C.

Section 9.7 of Ref. 3 gives other equations which are adaptable to this situation.

Surface Control. This situation is characterized by a large activation barrier for condensation. Concentration gradients in both the vapor and condensed phase are lacking. The condensation coefficient α is the dominant quantity. The system can be treated by a well-stirred phase model which leads to a simple exponential decay of the departure of the system from equilibrium (*see* pp. 18, 19 of Ref. 4).

$$K_{F\cdot J}^{V:C} = \alpha(2\pi mkT)^{-1/2} \quad (9)$$

Particle-Diffusion Control. Here the activation barriers are most pronounced in the condensate, and so is the concentration gradient. Equilibrium pertains at the surface, but the mass-transfer coefficient varies with time. Pressure in the vapor phase is constant.

$$K_{F\cdot J}^{V:C} \propto Dt^{-1/2} \quad (10)$$

Diffusion profiles can be obtained from sections 9.3 (I and IV), 9.6, and 13.9 (I) of Ref. 3.

Mixed Forms of Control and Thermal Analogs. Since nature does not always provide simple situations with a single controlling process, it is necessary to consider cases where more than one process significantly impedes the rate of deposition. By understanding complex cases, we will be able to develop criteria for predicting what processes will be controlling in any given situation. Attempts to consider the simultaneous operation of all three processes have led to intractable equations. We therefore consider two mixed cases and develop prediction criteria from these.

VAPOR-DIFFUSION CONTROL *vs.* SURFACE CONTROL. The general equation (*4*) is shown in Scheme A. For particles greater than a mean free path L (as are all particles we are interested in here), the Fuchs general equation simplifies to the form shown in the middle of the figure. Here v is the mean speed. This equation will take different forms, depending on the magnitude of $\alpha Rv/4D$ with respect to unity. One form gives the equation for vapor-diffusion control, and the other form gives the equation for surface control.

Therefore, we have a limited criterion for predicting control if we know the values of α, R, v, and D.

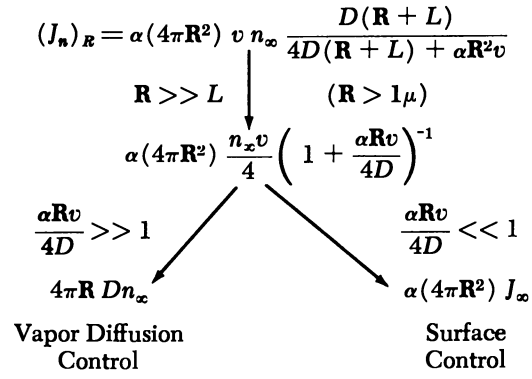

Definition: $J_\infty = n_\infty v/4$

Scheme A. Vapor-Diffusion Control vs. *Surface Control*

COLLISION MODEL. Figure 3 shows an instructive, efficient, and convenient method for treating the case of mixed surface and particle-diffusion control. It is instructive because it is easy to visualize. It is efficient because although it is a molecular approach, it does not require Monte Carlo calculations, which are expensive and should be avoided whenever possible. It is convenient because it leads to a set of differential equations

that have been solved by thermophysicists, and the method is described in several standard works.

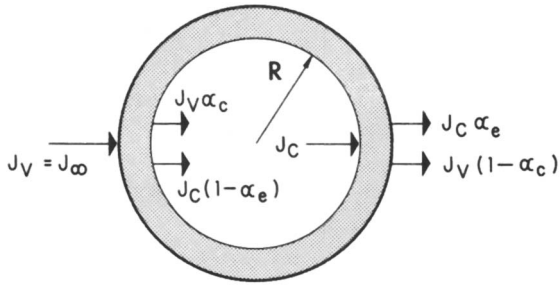

Figure 3. Collision model (boundary layer in particle)

We visualize a particle of radius **R** with an infinitestimally thin surface layer. The flux J_V from the vapor is constant, but only a fraction α_c of it is transmitted through the surface. The remainder $J_V\ (1 - \alpha_c)$ is reflected. On the inner side, the surface is hit by a flux J_C of which a fraction α_e escapes.

The net inward flux densities at the inner and outer surfaces are equal. At the inner surface this is proportional to the activity gradient, and at the outer surface it is proportional to the potential difference. In the latter case we call the proportionality constant H. Hence, we have

$$J_n^{V;C} = J_V\,\alpha_c - J_C\,\alpha_e = D_i^C \frac{\partial(\gamma_i^C N_i^C)}{\partial r} \tag{11}$$

where r is the distance from the center of the particle and

$$-J_n^{C;V} = J_n^{V;C} = H\left(\frac{p_i^V}{K_i^D} - \gamma_i^C N_i^C\right) \tag{12}$$

Now as $t \to 0$, $N_i^C \to 0$, $J_C \to 0$ so the net inward flux becomes

$$J_n^{V;C} = J_\infty\,\alpha_c = \left(\frac{\alpha_c p_i^V}{\sqrt{2\pi m_i kT}}\right) \tag{13}$$

and

$$H = \frac{K_i^D\,\alpha_c}{\sqrt{2\pi m_i kT}} \tag{14}$$

H is therefore proportional to both the distribution coefficient and the condensation coefficient.

The equations for the diffusion profile can be obtained from the heat-conduction equations of Carslaw and Jaeger [Ref. 3, Eq. 9.4 (*10*)] by using the substitutions we have indicated. The subject is discussed from a different approach by Adams, Quan, and Balkwell (*1*). The profiles can then be integrated over the volume of the sphere to obtain the uptake as a function of time.

Fundamental Criteria for Predicting Control. We are now in a position to establish criteria for predicting the control of condensation by using fundamental physicochemical parameters. As we have seen from the application of the kinetic theory of gases, the choice between vapor-diffusion control and surface control is governed by the magnitude of the quantity $\mathbf{R}v\alpha/4D_V$ compared with unity. Furthermore, the choice between vapor-diffusion control and particle-diffusion control is based upon the relative magnitudes of D_V and D_PK^D—*i.e.*, by the relative rates of diffusion when corrected to the same standard state. As a means of intercomparing all three, we define the following three resistivities.

Resistivity to transport through the vapor:

$$k_V = 1/D_V \tag{15}$$

Resistivity to transport through the particle:

$$k_P = 1/D_PK^D \tag{16}$$

Resistivity to transport across the surface:

$$k_S = 4/\alpha\mathbf{R}v = n/\alpha\mathbf{R}J_n \tag{17}$$

The relative magnitudes of these resistivities will then be measures of the corresponding degrees of control. For ease of presenting the data we can further define degrees of control d by

$$d_i = k_i/\sum_j k_j \tag{18}$$

$$\sum_i d_i = 1 \tag{19}$$

This will allow use of the familiar Gibbs triangular coordinates for displaying data.

When there is a strong interaction between the vapor species and the substrate, α can be assumed to be unity. For weak interactions the theory of absolute reaction rates may provide order-of-magnitude estimates. For many cases, this would probably be sufficient.

Changing Temperatures

Temperature Effects. Since the temperature is not constant, we must first consider the effect of temperature on the position of equilib-

rium. The answer is provided by well-understood relations between the equilibrium distribution coefficient and the partial molar heat contents. If instead, Henry's Law is invoked, some new terms are added, one involving the coefficient of thermal expansion.

Anisothermal Homogeneous Diffusion. Using the reasonable simplifications that the flow of heat is much faster than the transport of matter and that thermal kinetic effects can be neglected, we can dispense with the effect of changing temperature on diffusion within a phase simply by using a reduced time $\tau \equiv tD/\mathbf{R}^2$. Use of a reduced radius $\rho \equiv r/\mathbf{R}$ and a new potential $\mu \equiv \phi r$ puts the equation in the form $\frac{\partial^2 \mu}{\partial \rho^2} = \frac{\partial \mu}{\partial t}$. The temperature affects both the diffusivity and the potential, but since the diffusivity is buried in the reduced time, this is automatically under control as long as we remember that reduced time at any instant will be different in different phases. Use of the concentration for a potential completes the calculation. Ref. 2 (Section 18.4) gives a more rigorous treatment.

Anisothermal Transport Across a Phase Boundary. Once we know the effect of temperature on equilibrium position, we need know only its effects on diffusivities and the condensation coefficient to complete our task. The Stephan-Maxwell equation states that diffusivity in the vapor increases with the square root of the absolute temperature. In the condensed phase the temperature effect is expressed by an Arrhenius-type equation.

The condensation coefficient is the principal remaining unknown. Much theoretical and experimental work remains to be done before we will have a usable knowledge and understanding of the condensation coefficient.

Conclusions

This chapter has outlined the basic ingredients of a scheme for predicting from fundamental quantities the rate of uptake of fission products by spherical particles under dynamic conditions of temperature and pressure. A subsequent paper by Adams, Quan, and Balkwell (*1*) will present laboratory verification that the approach is on sound ground for isothermal conditions. Additional work is desirable to test the validity of the anisothermal approach to various cooling rates over large temperature extremes.

Besides the particle radius, the fundamental quantities indicated above are D_V, D_P, K^D, v, and α. v can be calculated from kinetic theory (*5*), Lai and Freiling have calculated D_V (*6*), and Norman has estimated D_P and K^D (*9*, *12*). Only the problem of estimating α remains.

Literature Cited

(1) Adams, C. F., Quan, J. T., Balkwell, W. R., ADVAN. CHEM. SER. **93**, 35 (1969).
(2) Bird, R. B., Stewart, W. E., Lightfoot, E. N., "Transport Phenomena," Wiley, New York, 1960.
(3) Carslaw, H. S., Jaeger, J. C., "Conduction of Heat in Solids," Clarendon Press, Oxford, 1959.
(4) Freiling, E. C., Crocker, G. R., Adams, C. E., "Radioactive Fallout from Nuclear Weapons Tests," pp. 16-18, U. S. Atomic Energy Commission, Division of Technical Information, November 1965.
(5) Kennard, E. H., "Kinetic Theory of Gases," McGraw-Hill, New York, 1938.
(6) Lai, J. R., Freiling, E. C., Naval Radiological Defense Laboratory, *Tech. Rept.* **TR-69-45** (June 10, 1969).
(7) Lassen, L., Rau, G., Weicksel, H., *Z. Physik.* **160**, 504 (1960); **161**, 339 (1961); **163**, 363 (1961).
(8) MacDougall, F. H., "Thermodynamics and Chemistry," Chap. XIII, Wiley, New York, 1939.
(9) Norman, J. H., General Atomic, **GA-7058** (1966).
(10) Schlichting, H., "Boundary-Layer Theory," McGraw-Hill, New York, 1955.
(11) U. S. At. Energy Comm. Rept. UR-tr-647, University of Rochester, June 8, 1964.
(12) Winchell, P., Norman, J. H., General Atomic, **GA-8182** (1967).

RECEIVED December 9, 1968. Research sponsored by the U. S. Atomic Energy Commission under Contract AT(49-7)-163.

Spheres: Diffusion-Controlled Fission Product Release and Absorption

J. H. NORMAN, P. WINCHELL, J. M. DIXON, B. W. ROOS, and R. F. KORTS

Gulf General Atomic Inc., San Diego, Calif. 92112

Concern about fission-product release from coated reactor fuel particles and fission-product sorption by fallout particles has provided stimulus to understand diffusion. In a fallout program mathematics of diffusion with simple boundary conditions have been used as a basis for (1) an experimental method of determining diffusion coefficients of volatile solutes and (2) a calculational method for estimating diffusion profiles with time dependent sources and time dependent diffusion coefficients. The latter method has been used to estimate the distribution of fission products in fallout. In a fission-product release program, a numerical model which calculates diffusion profiles in multicoated spherical particles has been programmed, and a parametric study based on coating and kernel properties has provided an understanding of fission product release.

The use of simple mathematical models has been found valuable in the description of diffusion controlled processes. This paper (1) reviews and updates the vaporization technique for determining diffusion coefficients in molten silicates (*11*, *12*); (2) expands upon a calculational method for describing fractionation of isotopes during fallout formation (*8*, *11*) and presents results of employing this method to describe Small Boy fallout; and (3) describes the results of a calculational technique used to estimate the loss of fission products from spherical coated fuel particles for nuclear reactors.

The Vaporization Technique of Measuring Diffusion Coefficients

Important parameters in describing the absorption of fission products by particulate matter during the cooling of a cloud from a near-surface

nuclear detonation are the diffusion coefficients of the fission products in the particles. Diffusion coefficients of fission products that are volatile below 2000°K. are particularly important. As a portion of a program aimed at describing the fractionation of fission products during fallout formation, the diffusion coefficients of the more volatile fission products in silicate samples have been determined.

Diffusion from spherical silicate samples can be studied readily by observing the loss of volatile components of the silicate as a function of time. Where the sphere is initially uniform in composition and subsequent vaporization allows one to assume a zero surface concentration of the vaporizing component thereafter, the solution to the differential equations and boundary conditions governing concentration-independent diffusion is given by

$$\overline{C}(t)/C_0 = \frac{6}{\pi^2} \sum_{n=1}^{\infty} (1/n^2) \exp\left(-\frac{n^2\pi^2 Dt}{R^2}\right) \tag{1a}$$

$$= 1 + \frac{3Dt}{R^2} - 6\left(\frac{Dt}{R^2}\right)^{1/2}\left(\pi^{-1/2} + 2\sum_{n=1}^{\infty} \text{ierfc}\,\frac{nR}{(Dt)^{1/2}}\right) \tag{1b}$$

where $\overline{C}(t)$ is the average concentration of the diffusion species in the sample at time t, D is the species diffusion coefficient, R is the radius of the sample sphere, and C_0 is the initial uniform concentration of this species (*1*). Equation 1a has been found especially valuable for calculations involving large diffusional losses, and Equation 1b works well for small losses. In Equation 1a this is particularly true for $\overline{C}(t)/C_0 \leqslant 0.2$, since for this condition n can be taken as unity. For $\overline{C}(t)/C_0 \geqslant 0.8$, the ierfc term in Equation 1b can be eliminated.

Of course, Equations 1a and 1b can be reversed to consider fractional uptakes in an atmosphere that at equilibrium would lead to a concentration C_0 throughout the particle. This amounts to only a change in initial conditions, and the fractional uptakes are given by $F = 1 - \overline{C}(t)/C_0$. This form of Equations 1a and 1b is more useful in calculations of fission product fractionation during fallout formation as discussed later.

We consider now Equation 1a where $\overline{C}(t_1)/C_0 \leqslant 0.2$. The continuation of an experiment to t_2, following an interruption at t_1 is governed by

$$\overline{C}(t_2)/\overline{C}(t_1) = \exp\left(-\frac{\pi^2 D(t_2 - t_1)}{R^2}\right) \tag{2}$$

By determining average concentrations before and after an experiment, the diffusion coefficient can be determined from the average concentrations, the sphere radius, and the duration of the experiment $(t_2 - t_1)$.

Additionally, in Equation 1 the Dt term can be replaced by $\int_c d(Dt)$, such that in using Equation 2 the previous thermal history is unimportant if D is only a function of T. Thus, using a single sample and evaluating $\overline{C}(t_n)$ at different times and temperatures after the condition $\overline{C}(t_{n-1})/C_0 \leqslant 0.2$ is attained, the diffusion coefficient of a volatile species can be experimentally determined as a function of temperature.

Examples of the application of this method are given in Ref. 12. An extension of this method directly to fission products formed *in situ* in silicate particles is presented here. Also in this study an attempt was made to improve the geometrical match between the mathematical model and the actual silicate sample.

For this study about 1% UO_2, 93% enriched, was dissolved in a glass of composition of the $CaSiO_3$–$CaAl_2Si_2O_8$–SiO_2 eutectic. The UO_2 did not dissolve readily in the absence of oxygen but did dissolve readily in air. Because of a bubbling problem, this yellow glass was degassed in vacuum for several days at ~1400°C. The glass became nearly colorless (light green) without significant loss of U, suggesting the reduction of U back to the 4+ state. This glass was crushed, and larger chunks were melted in vacuum into a 70° conical depression in a 1-mil platinum ribbon to just overflowing. Since the glass–platinum contact angle is ~35°, the geometrical form of the silicate sample is that of a cone whose apex corresponds to the center of a sphere defined by the outer surface of the glass. If the platinum depression acts as a perfect diffusion barrier for the species to be studied, the sample form as described allows the application of Equations 1 and 2 to the studies of vaporization of the diffusing species from the spherical surface.

After forming these silicate cones—*i.e.*, equivalent spheres, they were freed from the platinum ribbon forms and subjected to a thermal neutron flux in a Gulf General Atomic TRIGA reactor. The cones containing the fission products were allowed to "cool" for about a week. At this time after fission, ^{132}I, ^{131}I, ^{132}Te, ^{133}Xe, ^{99}Mo, and ^{99}Tc are all near their maximum contributions to the total activity. Diffusion coefficient measurements of some of these species were made by resetting the cones in conical depressions in new platinum ribbons made with the same punch and die and then heating the ribbons resistively in about 1 torr of air instead of a vacuum, which greatly lessened bubble formation, to reestablish the glass–platinum bond. The diffusion experiments in this atmosphere were begun by initially diffusing out, in general, at least 50% of a volatile fission product. At only about 50% diffused out, a bias of about +20% might be expected in the measured diffusion coefficient using Equation 2. This bias is well within our precision, and thus was not recognizable. Diffusion experiments with larger losses make up the

major portion of the data. Sensitivity requirements necessitated using the higher working limits. Also, 50% diffused out is sufficient to obliterate recoil profiles. Temperatures on the side of the Pt cone were measured with an attached thermocouple, and they compared well with optically measured Pt ribbon temperatures that were corrected for Pt emissivities.

The diffusion coefficients for ^{131}I, ^{133}Xe, and ^{132}Te are given as a function of the temperature in Figures 1, 2, and 3, respectively. These data are summarized in Table I according to an Arrhenius form of the temperature dependence of the diffusion coefficients where

$$D/D_0 = e^{-\Delta H^*/RT} \quad (3)$$

The diffusion coefficients for iodine are close to those measured previously in the same glass (*12*) at the experimental temperatures. However, the activation energies of these two measurements differ. The experiments differ to some degree in that iodine and other fission products were made from dissolved UO_2 in this experiment, while iodine only was made from TeO_2 under a neutron flux in the previous experiment. The latter mode of formation should lead to a greater excess of oxygen in the glass.

The xenon measurements are believed to be unique. Some experimental difficulties were apparent in these measurements. In some experi-

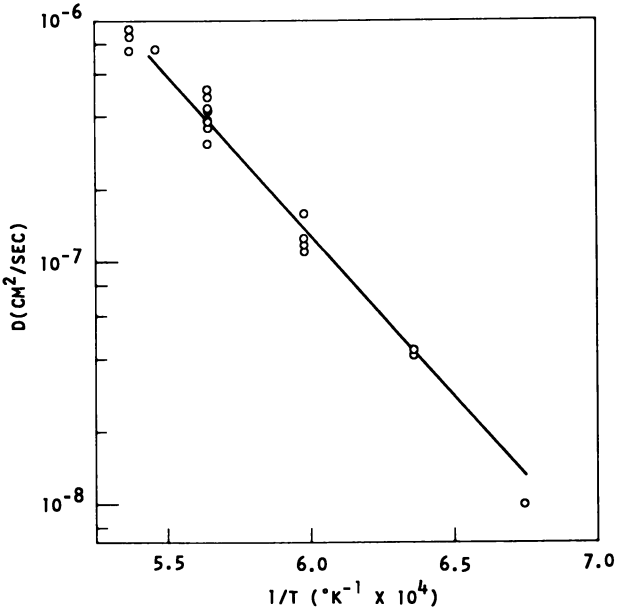

Figure 1. Iodine-131 diffusion in $CaSiO_3$–$CaAl_2Si_2O_8$–SiO_2 eutectic

ments Xe appeared to be trapped in bubbles in the glass. This was manifest in an apparently increasing diffusion coefficient as more and more Xe was released.

The tellurium measurements exhibit less accuracy than the Xe and I measurements. This was resolved as a counting problem. The data are, however, in good agreement with those reported previously (*12*).

Measurements of the diffusion of other elements at this time after fission is very difficult. Signal-to-noise ratios and radioactive decay problems make the study of ^{99}Mo and ^{99}Tc very difficult. Other isotopes present in the sample do not exhibit sufficient volatility to be studied

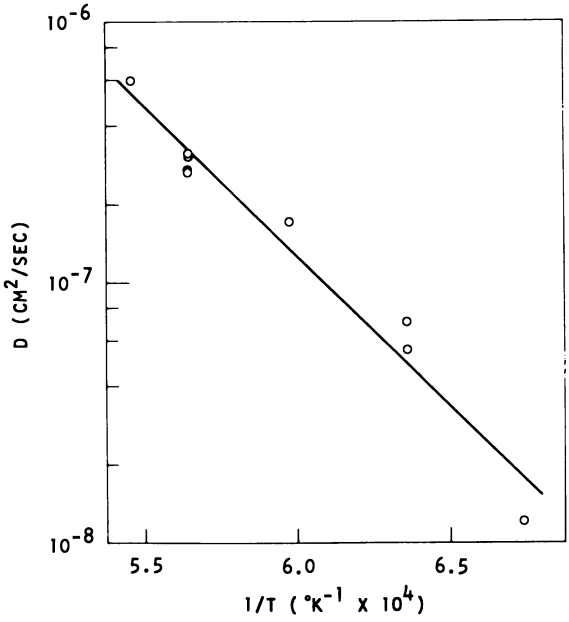

Figure 2. Xenon-133 diffusion in $CaSiO_3$–$CaAl_2Si_2O_8$–SiO_2 eutectic

with this technique. Other techniques such as the often-employed plane source technique (*12*) can be applied in the determination of diffusion coefficients of these isotopes.

Calculation of Isotope Fractionation During Fallout Formation

Fractionation of fission products during fallout formation was recognized by Freiling (*4*) in early studies of fallout particles. He also recognized that this phenomenon involved the volatility of the fission products. In an attempt to describe fractionation quantitatively, Miller (*9*) devised

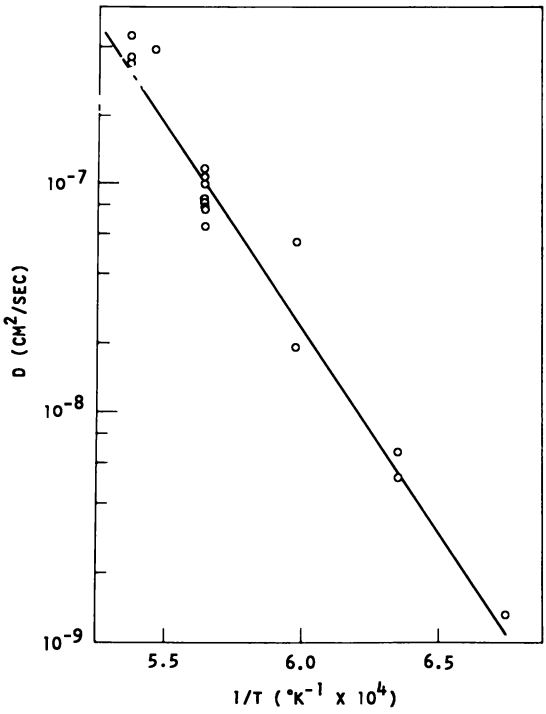

Figure 3. Tellurium-132 diffusion in $CaSiO_3$–$CaAl_2Si_2O_8$–SiO_2 eutectic

Table I. Diffusion Coefficients as a Function of a Pre-exponential Term and an Activation Energy

	$log_{10}D_0$		ΔH^*, *kcal./mole*	
	This Study	Ref. 12	This Study	Ref. 12
I	1.3	7.3	63	103
Xe	0.0	—	53	—
Te	3.1	3.3	82	71

a model whereby fission products were absorbed according to available equilibrium thermodynamics above a certain temperature and were only adsorbed at lower temperatures. This model proved reasonably successful and was apparently phenomenologically satisfactory when used for relatively nonviscous fallout matrices that crystallize on cooling. Silicates generally do not fit in this condition, and a calculational scheme that involves diffusivities would seem to be more appropriate.

A temperature-stepping diffusion-controlled fission product absorption model, where equilibrium is taken to occur at the surface of the

fallout particles and the penetration of the sorbed fission products from the surface of the particles is taken as diffusion controlled, has been constructed (*8*). The method is based on Equations 1a and 1b, diffusivities (*12*), and equilibrium thermodynamics as Henry's law constants (*10*), as available. Its basic equation is a mass balancing equation between condensed and gaseous fission products. This involves summed equations of the form of Equations 1a and 1b for the time–temperature stepping system. The nuclear cloud is taken as being a uniform distribution of fission products and particles of various sizes. At time t_1 after burst, one can consider the quantity of a particular fission product absorbed:

$$C_1 \sum_{n=1}^{N} \left(\frac{\overline{C}_{1,1n}}{C_1}\right) W_n = Y_1 - \frac{C_1 H_1 V_1 M}{RT_1} \tag{4}$$

where C_1 is the surface concentration of the fission product, $\overline{C}_{1,1n}$ is the average concentration of the fission product diffused into particles of effective radius r_n during time Δt_1 at temperature T_1, W_n is the total weight of the particles in the nth size fraction, Y_1 is the fission product yield at time t_1, H_1 is Henry's law constant at T_1, V_1 is the volume of the nuclear cloud at t_1, M is the fission product molecular weight, and R is the gas constant. The only unknown in this equation is the surface concentration. The values for $(\overline{C}_{1,1n}/C_1)$ are obtained from Equation 1 and the diffusion coefficient for the fission product at T_1. In a second time step, the yield and the concentrations are decayed or augmented, if important, to describe the appropriate nuclear processes. The diffusion problem (evaluating $\overline{C}_{1,2n}/C_1$) established for Δt_1 is augmented by solving Equation 1 for $D_1\Delta t_1 + D_2\Delta t_2$ instead of just $D_1\Delta t_1$. If no radioactive decay has been important as far as quantities and distribution of the fission product in question are concerned, a second mass balance equation,

$$C_2 \sum_{n=1}^{N} \left(\frac{\overline{C}_{2,2n}}{C_2}\right) W_n + C_1 \sum_{n=1}^{N} \left(\frac{C_{1,2n}}{C_1}\right) W_n = Y_2 - \frac{(C_2 + C_1)\, H_2 V_2 M}{RT_2}, \tag{5}$$

is solved as if the fission product diffusing from C_2 during the second time period, Δt_2, were different from that diffusing from C_1. If radioactive disintegration has affected the mass balance, it is taken into account. Subsequently, more time steps are taken. If sufficient time steps of short enough duration are taken, this calculational process approaches an exact solution to the problem. This calculational scheme has been described more fully by Korts and Norman (*8*). They also

describe a method for calculating fission product profiles in particles at a desired time after burst.

As a description of the calculational method, a 100-KT near-surface burst over $CaSiO_3$–$CaAl_2Si_2O_8$–SiO_2 eutectic was simulated. The particle size distribution is given in Table II.

The refractory nuclide chain, 95, and the volatile chain, 137, were investigated. If the fission product absorption process began at 2700°K. and proceeded using 200°K. steps to 900°K., the radial distributions of the fission products in these chains at the final temperatures can be obtained. Calculations show little variation in concentration of any of

Table II. Selected Particle Size Distribution

Designation	*Particle Radius, cm.*	*Weight Percent of Particle Fraction*
T	0.00030	0.38
S	0.0030	28.92
M	0.0154	60.2
L	0.13	10.5

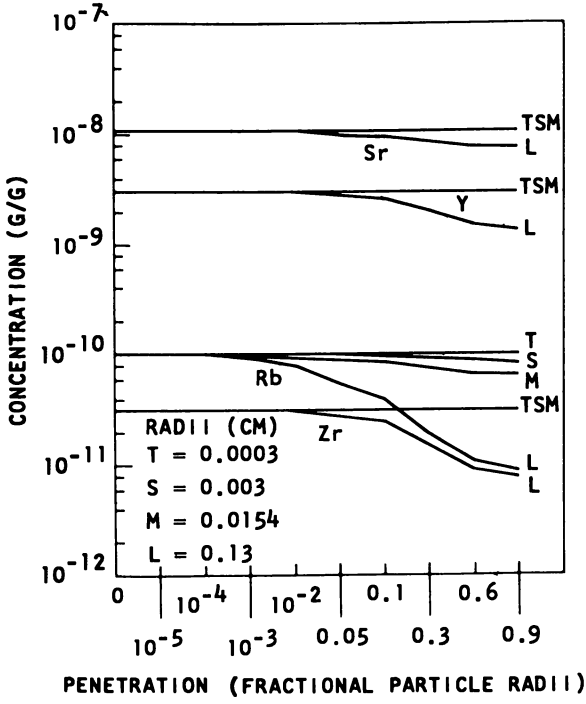

Figure 4. Nuclide 95-chain profiles at 900°K. from 100-kiloton event

the members of the 95 chain (Figure 4). The exceptions are rubidium, which has an intermediate volatility, and all elements in the large particles where the time provided at the highest temperatures was insufficient to come close to equilibrium concentrations. However, the volatile chain, 137, shows large concentration gradients with radial position. Tellurium-137 (Figure 5) can be shown to be surface oriented. Important amounts of Te are still found in the gas phase at 900°K. It should be noted that the larger the particle, the more depleted are the centers of the particles. Figure 6 shows that ^{137}I somewhat reflects the ^{137}Te curves.

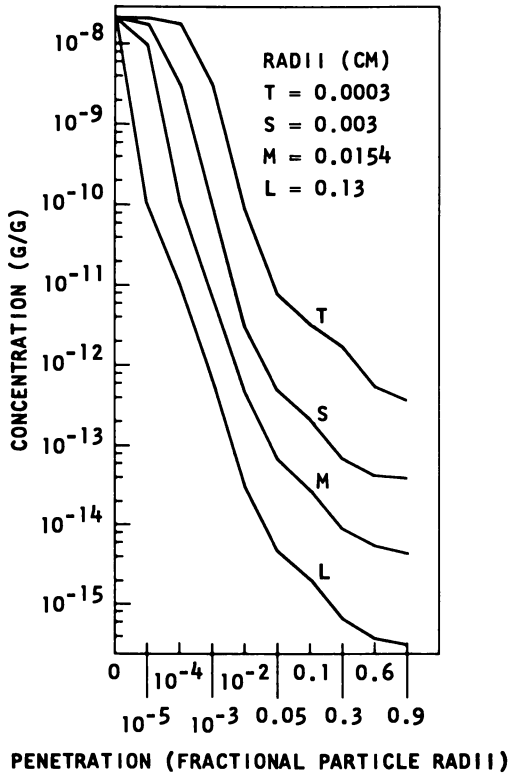

Figure 5. Tellurium-137 profile at 900°K. from 100-kiloton event

In the time scale covered by the calculation, the ^{137}I in the particles results from *in situ* decay of ^{137}Te. The low surface concentration is associated with the high volatility of iodine in an oxidizing atmosphere. In this same figure the ^{137}Xe curves reflect their parent ^{137}I curves to some extent. The surface concentration of this element probably does not represent a true vapor pressure equilibrium but just the thermody-

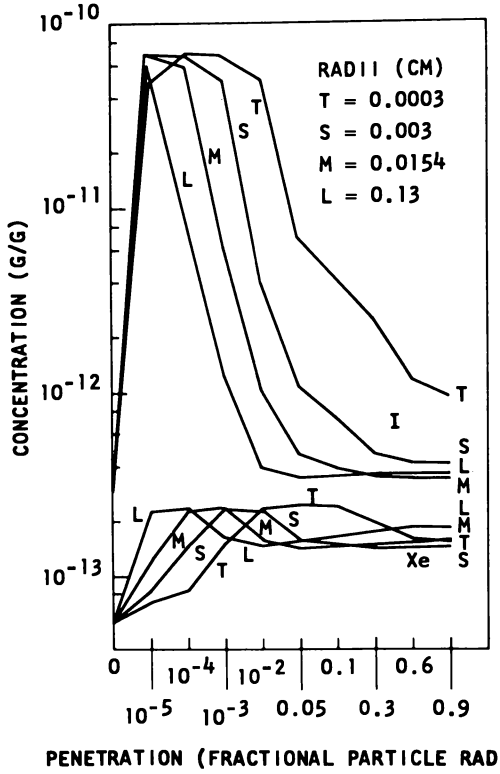

Figure 6. Iodine-137 and xenon-137 profiles at 900°K. from 100-kiloton event

namic estimation system used to obtain the employed Henry's law constants (*10*). The ^{137}Cs profiles in Figure 7 result mainly from absorption from the gas phase of decaying ^{137}Xe.

In parametric studies using this method, calculation of fission product distribution among the various particle size groups was found to be insensitive to size of the detonation and the quantity of soil picked up. It is, of course, somewhat sensitive to the thermodynamic and kinetic values used, but most of all, it is sensitive to the particle size distribution itself. This result is of considerable interest.

This calculational scheme has been applied to the Small Boy detonation. The test was made to compare fractionation data from this well-studied event (*2*) with calculated values. Using 25 particle size fractions that approximate the fallout from the event and the time–temperature history given in Table III, which was derived from generalized time–temperature event histories, the fission product contents of the nuclide chains 80 through 150 in the particle size fractions were calcu-

lated. This was done under the assumption that the Henry's law constants and the diffusion coefficients for various fissions products in the $CaSiO_3$–$CaAl_2Si_2O_8$–SiO_2 eutectic were applicable to Small Boy fallout. In a cursory consideration of this question, the assumption seemed reasonable.

The results of these calculations for some of the more important nuclides are presented in Figures 8 and 9. Figure 8 presents fractionation ratios, $r_{i,95}$, $(C_i/Y_i/C_{95}/Y_{95})$, (at appropriate times after burst) for moderately large particles as related to fractionation slopes as reported by Crocker, Kawahara, and Freiling (2) for Small Boy. The fractionation plots from which these slopes are obtained are log-log plots of the fractionation ratio for a given isotope *vs.* 95 against 89 *vs.* 95. This figure shows a high correlation between the calculated fractionation ratio and the experimental fractionation slopes. Figure 9 compares calculated and experimental fractionation slopes. While some of the calculated fractionation slope plots were not linear, a best slope was chosen.

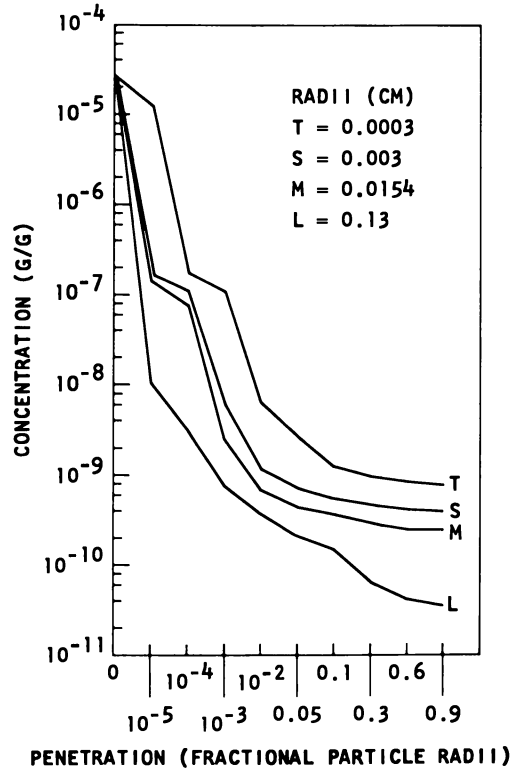

Figure 7. Cesium-137 profile at 900°K. from 100-kiloton event

Here also, there is excellent correlation between calculated and experimental values.

A more significant test is the comparison of calculated and experimental fractionation ratios with particle sizes. Crocker, Kawahara, and Freiling (*2*) have presented Small Boy experimental ^{89}Sr fractionation ratios *vs.* particle sizes. Figure 10 is a reproduction of their plot with

Table III. Small Boy Time–Temperature History

Time, sec.	*Temperature, °K.*
0.6	4000
0.85	3600
1.2	3200
1.6	2900
2.3	2600
3.0	2400
3.6	2200
4.1	2000
4.7	1800
5.3	1600
6.1	1400
7.0	1200
8.2	1000
9.8	800

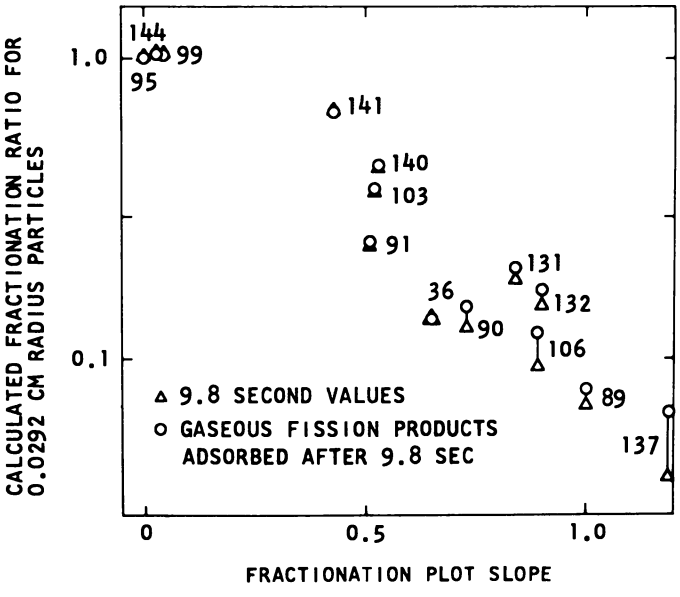

Figure 8. Correlation of experimental and calculated fractionation for Small Boy

the calculated Small Boy values superimposed. While the calculated fractionation ratios (solid circles for adsorption after 9.8 sec. and triangles for the 9.8-sec. data) appear to be somewhat higher for small particles and lower for large particles, there is considerable similarity between the calculated and observed values. There is a trend in the experimental values for the fractionation ratio to become invariant as the particles increase in size. This might be explained by these particles' not absorbing as much zirconium as the calculational model would indicate. Indeed, such a situation does not seem unreasonable. Large particles could deplete neighboring gas fields of zirconium and, thus, not load to the same degree that a small particle in a similar gas field would. A similar problem is noted in our calculational method where large par-

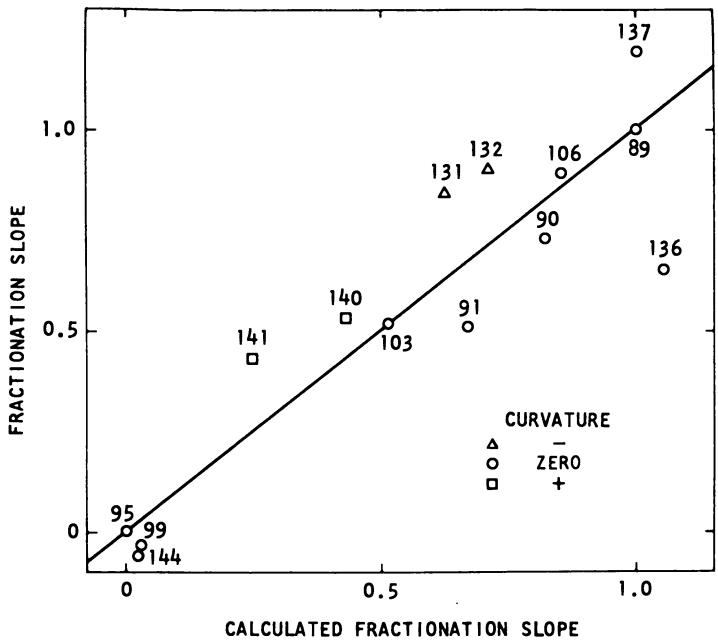

Figure 9. Correlation of experimental and calculated fractionation slopes for Small Boy

ticles do not load strictly on a volume basis. However, this effect is the result of insufficient time for a particle to diffuse sufficiently, for example, zirconium to an essentially uniform concentration. This problem may occur in the real case and contribute to some "fractionation" of zirconium in large particles.

Predictions of the USNRDL radial distribution model (*5*) have been added to Figure 10 by Freiling (*6*) to compare this model with the

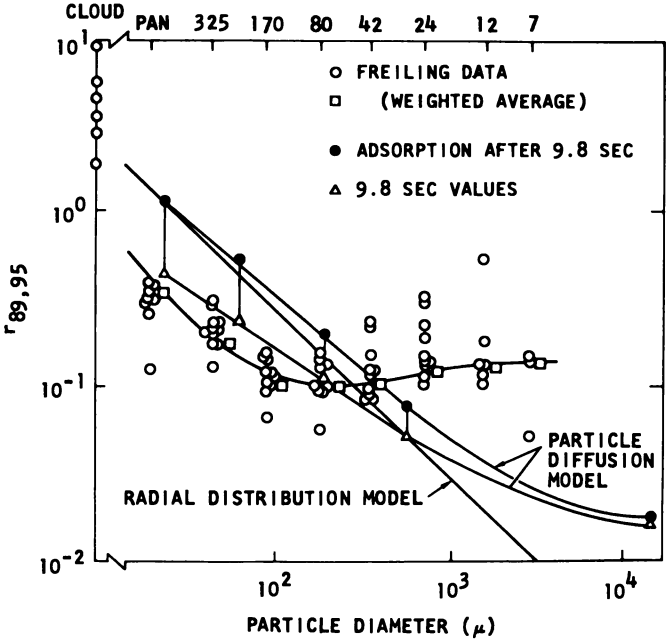

Figure 10. Correlation of experimental and calculated fractional ratios of 85 to 89 with fallout particle size for Small Boy

diffusion controlled absorption model. Freiling has also added cloud fractionation ratios as if they pertained to 1-μ particles. The diffusion controlled model appears to provide a somewhat better fit to the data than the radial distribution model. Figure 10 suggests that the diffusion model represents an appreciable advance over the radial distribution model in predicting fission product distribution in fallout.

These results are the basis for optimism concerning the calculated distribution of fission products in fallout using the described method. A further test will be the application of the DELFIC particle distribution calculational system (3) using the calculated particle fission product inventories and comparing calculated and experimental radiation fields.

Fission Product Release from Coated Particles

An important parameter in the evaluation of the safety of a reactor system is the release of fission products from the fuel. The fuel in the high-temperature gas-cooled reactor (HTGR) consists of spherical particles (U, ThC_2) that are coated with a material presenting a diffusion

barrier to the fission products. Estimation of the release of fission products from these particles during reactor operation has been attempted using a high-speed computer program called SLIDER (7).

SLIDER is a Fortran IV computer program for investigating the diffusion of a single fission-product isotope in a multilayered spherical fuel particle. This code enables one to compute, on the basis of Fick's law of diffusion, the transient and steady-state fission product concentrations and releases in multilayered spherical geometry.

It is assumed that the spherical fuel particle consists of Q component layers, each consisting of a different material. The diffusion coefficient D of the species in a particular layer is assumed to be independent of concentration and positional coordinates but may depend on the time.

Assuming that the particle concentration $C(r, t)$ of a fission product is a function of time and the radial coordinate only, the continuity equation takes the form

$$\frac{\partial C(r,t)}{\partial t} = -\frac{1}{r^2}\frac{\partial}{\partial r}\left(r^2 J(r,t)\right) - \lambda C(r,t) + S(r,t) \tag{6}$$

where $J(r, t)$ denotes the radial component of the particle current, $S(r, t)$ is the source, and λ denotes the decay constant. According to Fick's law, the following relation exists between the particle current $J(r, t)$ and the concentration:

$$J(r,t) = -D(t)\frac{\partial C(r,t)}{\partial r} \tag{7}$$

Hence, assuming that the diffusion coefficient of the species considered is constant over a particular layer, one may write, in spherical coordinates, the following diffusion equation for that layer:

$$\frac{\partial C(r,t)}{\partial t} = D(t)\frac{1}{r^2}\frac{\partial}{\partial r}\left(r^2\frac{\partial C}{\partial r}\right) - \lambda C(r,t) + S(r,t) \tag{8}$$

At an interface, $r = a_p$, between the layers $a_{p-1} < r < a_p$ and $a_p < r < a_{p+1}$, we impose the solubility condition that the concentration $C^-(a_p, t)$ just to the left of the interface is a fraction of the concentration $C^+(a_p, t)$ just to the right of the interface,

$$C^-(a_p,t) = \Phi(p)C^+(a_p,t) \tag{9}$$

We require furthermore that the particle currents are continuous at an interface point,

$$J^-(a_p,t) = J^+(a_p,t) \tag{10}$$

or

$$D(p,t)\frac{\partial C(a_p,t)}{\partial r}\bigg|^- = D(p+1,t)\frac{\partial C(a_p,t)}{\partial r}\bigg|^+ \tag{11}$$

where $D(p, t)$ is the diffusion coefficient in the layer $a_{p-1} < r < a_p$. The boundary conditions imposed on the concentration at the center of the sphere and on its outer surface are

$$\lim_{r \to 0} r\,C(r, t) = 0 \tag{12}$$

and

$$C(r = b, t) = 0 \tag{13}$$

where $r = b$ denotes the outer surface of the sphere. Thus, we assume that once a fission product reaches the outer boundary of the fuel particle it disappears immediately—*i.e.*, there is no holdup of fission products in the fuel compact. With respect to the initial condition, we require that the fission product concentration at time $t = 0$ is a known function of the radial coordinate,

$$C(r, t = 0) = f(r) \tag{14}$$

To evaluate fission product release in a reactor, it is necessary to supply the appropriate particle geometry, diffusion coefficients, and distribution coefficients. This is a formidable task. To approach this problem, postirradiation fission product release has been studied as a function of temperature. The results of these studies are complex and require considerable interpretation. The SLIDER code without a source term has proved to be of considerable value in this interpretation. Parametric studies have been made of the integrated release of fission products, initially wholly in the fueled region, as a function of the diffusion coefficients and the distribution coefficients. These studies have led to observations of critical features in describing integrated fission product releases. From experimental values associated with these critical features, it is possible to evaluate at least partially diffusion coefficients and distribution coefficients. These experimental values may then be put back into SLIDER with appropriate birth and decay rates to evaluate in-reactor particle fission product releases. Figure 11 is a representation of SLIDER simulation of a simplified postirradiation fission product release experiment. Calculations have been made with the following pertinent input data:

(1) A 0.01-cm. radius kernel initially uniformly loaded with a stable fission product.

(2) A coating 0.007-cm. thick initially free of this fission product.

(3) Diffusion coefficients of 1.4×10^{-12} cm.^{2}/sec. and 4.8×10^{-9} cm.^{2}/sec. in the kernel and coating, respectively; a distribution coefficient of unity; and a perfect sink outside the coating.

It has been found convenient to express the integrated release as a function of the square root of time, as in Figure 11. The critical features

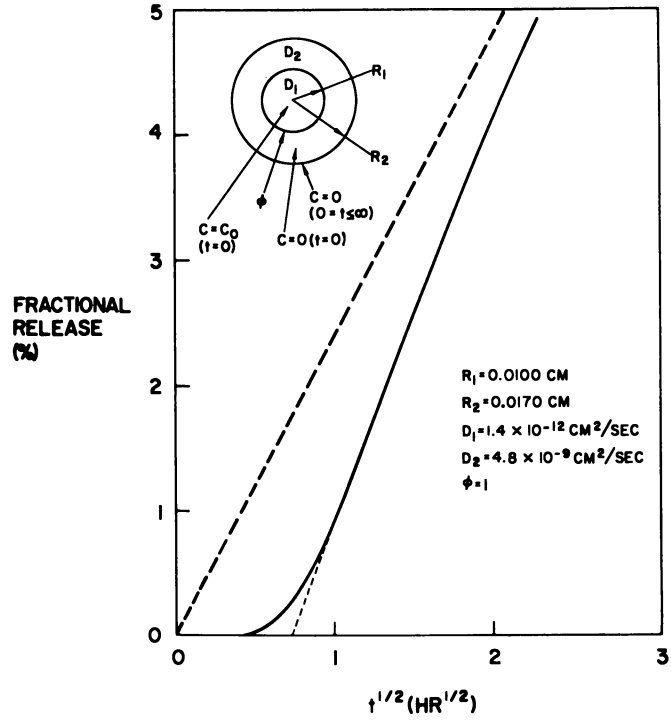

Figure 11. Calculated fractional release from a two-zone particle

apparent in this curve are a delayed initial release and a later release which, with increasing time, approaches the release this kernel would have shown if it had not been coated. This assymptote is represented by the dotted line passing through the origin. In this particular system, the quantity of fission product in the coating is approximated by the difference between the two curves—*i.e.*, the release from the fueled kernel is hardly altered by the coating and the release from the particle soon becomes rate-limited by the release from the kernel. If the particle release curve is extrapolated linearly from the straight portion of the release curve to a zero release point on the time axis, one obtains $t_d^{1/2}$ where t_d can be called a delay time for release. A delay time for release from a membrane of thickness l, where the membrane is initially free of a diffusing species and has a constant source on one side and a perfect sink on the other, can be given by

$$6Dt_d = l^2 \tag{15}$$

This particular formula predicts the delayed release of the coated particle reasonably well. In this case, the delay time predicted by the formula

was somewhat longer than the extrapolated value. The main reason for this deviation appears to be that the kernel source is far from constant. If it were constant, the release curve would exhibit a much higher slope, and the calculated release curve would thus extrapolate to a longer delay time.

The calculated releases shown in Figure 12 were obtained in parametric variations of the values used in deriving Figure 11. These curves illustrate changing (1) the diffusion coefficient in the coating ($D_2 \times 2$), characterized by an appropriate change in $t_d^{1/2}$ ($\times 2^{-1/2}$) and a faster approach to the bare kernel release line; (2) the diffusion coefficient in the kernel ($D_1 \times 2$), characterized by an approach to a steeper bare kernel release with an unchanged delay time; and (3) the distribution coefficient ϕ($\phi = 1, 10^2, 10^{-2}$). Where the distribution coefficient has been changed to provide a greater driving force for transfer of fission product from the fueled region to the coating ($\phi = 10^{-2}$) the fission

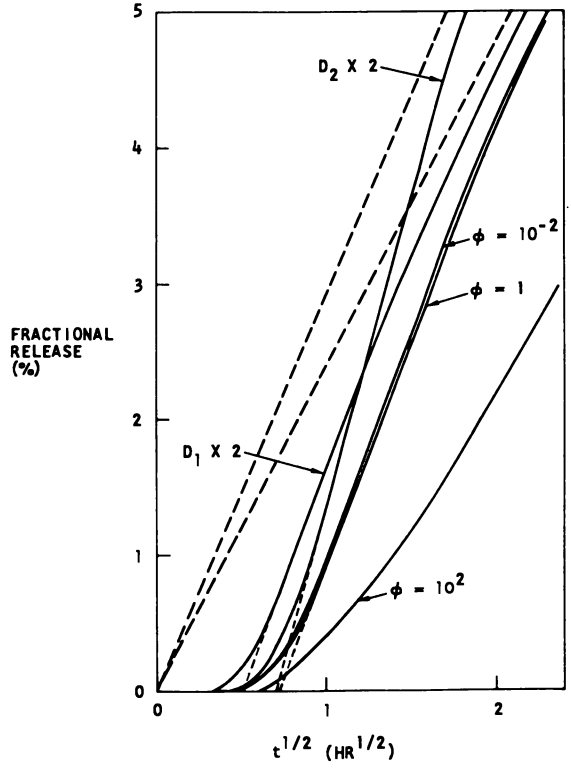

Figure 12. Calculated fractional releases from a two-zone particle (with parametric variations of values for Fig. 11)

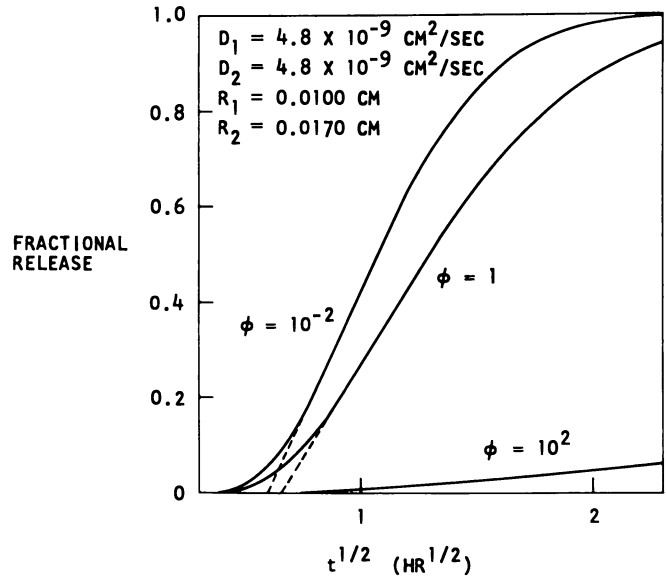

Figure 13. Calculated fractional releases with equivalent diffusion coefficients in the two zones

product release curve is almost identical to the one for unit ϕ, which has been repeated in this figure ($\phi = 1$). Where the driving force has been decreased, the release curve shows quite a different character. The release is decreased considerably and the nearly linear character of releases *vs.* $t^{1/2}$ following the delay time is not apparent. This suggests transfer from kernel control of release to coating control. Apparently, this change has greatly lengthened the time period during which the release can be considered to be characterized by membrane diffusion.

Release behaviors in the region of parameters described by these figures are useful in determining experimental values of these parameters. In particular, the diffusion coefficient in the coating can be approximated from delay times and coating thicknesses, and the diffusion coefficient in the kernel can be derived from later behavior. Distribution coefficients may be revealed in some cases by permeabilities and diffusion coefficients.

A study was also made of release with equal diffusion coefficients in the coating and the kernel. The description of delay time is much the same as in the previous case. Figure 13 illustrates this similarity in delay time, as well as later release behavior. In this case also, the $t^{1/2}$ plot shows a long linear region. The reason is probably that depletion effects are reasonably followed by this function and not that there is kernel

control. This release has a much greater tendency to be coating controlled. Since kernel control does not occur until very late times, if at all, a kernel diffusion coefficient is generally not well defined by the releases. However, the effect of the distribution coefficient as described in this figure is generally important, and release data can be used to evaluate this quantity within the ranges of the illustrated parametric changes.

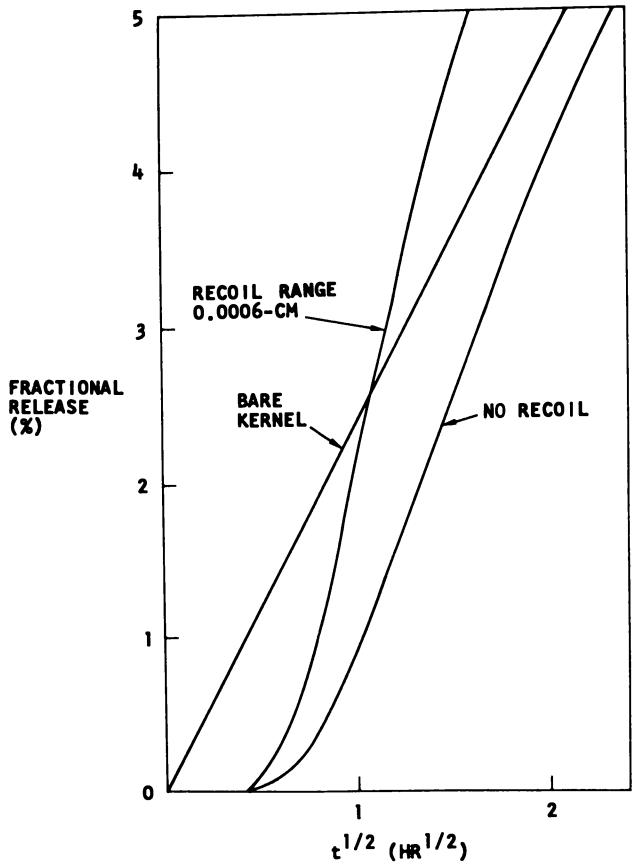

Figure 14. Effect of fission product recoil on release (parameter same as Fig. 11 except for thin high-diffusivity coating between kernel and outside coat)

An attempt to investigate more realistic fuel particles and fission product loadings has been made. A recoiled fission product-absorbing buffer carbon layer has been included in the particle, and fractional releases with recoil into this layer have been considered. Another factor

that may be important is the dependence of the diffusion coefficient on radiation flux. A future study of this effect is planned.

Calculations for Figure 14 illustrate a recoil source with the same parameters as those used in the study depicted by Figure 11, except that a buffer carbon layer 0.0006 cm. thick with a diffusion coefficient of 10^{-6} cm.^{2}/sec. was placed between the coating and the kernel. Distribution coefficients were taken as unity. A recoil range of 0.0006 cm. was assumed in both the kernel and coating materials. Results of this calculation differ considerably from those for experiments with no recoil. These differences are consistent with ~4.5% release from the kernel during irradiation. After release of this quantity of fission product from the particle, the releases begin to approach those of the bare kernel. The recoil effects were unimportant after releases of 7 to 8%.

An attempt has been made to describe distribution coefficient (ϕ) control of release of fission products from a particle for the purpose of understanding retentivity of fueled particles. A ϕ control layer can be added to a particle between the fuel and the outer coating. This layer with, for instance, even a somewhat larger diffusion coefficient than the normal coating layer may have the property of either strongly rejecting or strongly absorbing a particular fission product and thus limiting the release of this fission product. In the case of large ϕ (at the inner boundary), the layer can act as a permeation barrier to the fission product. In the case of small ϕ, the layer may act as a sink, thus greatly reducing the concentration of fission product available to be diffused through an outer coating. One advantage the highly absorptive layer may have over the rejecting layer is that it would function independently of the continuity of this layer. It may be more difficult, however, to find an appropriate material for this layer. When selecting the fuel material itself, this absorptive effect might be considered.

Conclusions

The concepts presented in this paper emphasize the importance of diffusional phenomena during fallout formation and HTGR fission product retention. While other phenomena may be of considerable importance, these studies present a worthwhile position from which to view these processes. The advances resulting from those conceptual points of view have been considerable and it is believed are far from exhausted.

Literature Cited

(1) Crank, J., "The Mathematics of Diffusion," Oxford University Press, London, 1956.

(2) Crocker, G. R., Kawahara, F. K., Freiling, E. C., "Radioactive Fallout from Nuclear Weapons Tests," A. W. Klement, Jr., Ed., p. 72, USAEC, Oak Ridge, Tenn., Nov. 1965.
(3) Department of Defense Land Fallout Prediction System, Defense Atomic Support Agency *Rept.* **DASA-1800** (1966).
(4) Freiling, E. C., U. S. Naval Radiological Defense Laboratory *Rept.* **USNRDL-TR-385** (Oct. 1959).
(5) Freiling, E. C., U. S. Naval Radiological Defense Laboratory *Rept.* **USNRDL-TR-680** (Sept. 1963).
(6) Freiling, E. C., U. S. Naval Radiological Defense Laboratory, private communication (Dec. 1967).
(7) Jadhav, K. B., Roos, B. W., Gulf General Atomic *Rept.* **GA-8566,** to be published.
(8) Korts, R. F., Norman, J. H., U. S. Naval Radiological Defense Laboratory *Rept.* **GA-7598,** General Dynamics, General Atomic Division (Jan. 1967).
(9) Miller, C. F., "Fallout and Radiological Countermeasures," Stanford Research Institute, Office of Civil Defense Report, Jan. 1963.
(10) Norman, J. H., U. S. Naval Radiological Defense Laboratory *Rept.* **GA-7058,** General Dynamics, General Atomic Division (Nov. 1966).
(11) Norman, J. H., Winchell, P., Staley, H. G., Tagami, M., Hiatt, M. A., *Proc. Symp. Thermodynamics Nucl. Materials Emphasis Solution Systems, Vienna, Austria, 1967,* IAEA, Vienna, 209 (1967).
(12) Winchell, P., Norman, J. H., *Proc. Intern. Symp. High-Temperature Technol., 3rd, Asilomar, Calif., 1967.*

RECEIVED June 24, 1968. Work supported by the U. S. Atomic Energy Commission under Contract AT(04-3)-167, Project Agreement 17, and the Office of Civil Defense, U. S. Naval Radiological Defense Laboratory, under Contract N00228-68-C-2376.

High Temperature Measurements of the Rates of Uptake of Molybdenum Oxide, Tellurium Oxide, and Rubidium Oxide Vapors by Selected Oxide Substrates

CHARLES E. ADAMS,[1] JACK T. QUAN, and WILLIAM R. BALKWELL
U. S. Naval Radiological Defense Laboratory, San Francisco, Calif. 94135

The rates of uptake of molybdenum, tellurium, and rubidium oxide vapors by substrates of calcium ferrite and a clay loam have been measured in air over a temperature range of 900° to 1500°C. and a partial pressure range of about 10^{-7} to 10^{-4} atm. The measured rates of uptake of molybdenum and tellurium oxide vapors by molten calcium ferrite and of rubidium oxide vapor by both molten clay loam and calcium ferrite were controlled by the rates of diffusion of the oxide vapors through the air. The measured rates of uptake of molybdenum and tellurium oxide vapors by molten clay loam were controlled by a combination of a slow surface reaction and slow diffusion of the condensate into the substrate.

During the formation of radioactive fallout particles, one of the most important processes is the uptake, in the cooling nuclear fireball, of the vaporized radioactive fission products by particles of molten soil or other environmental materials. Owing to the differences in the chemical nature of the various radioactive elements, their rates of uptake vary, depending upon temperature, pressure, and substrate and vapor-phase composition. These varying rates of uptake, combined with different residence times of the substrate particles in the fireball, result in radiochemical fractionation of the fallout. This fractionation has a considerable effect on the final partition of radioactivity, exposure rate, and radionuclides between the ground surface and the atmosphere.

[1] Present address: U. S. Naval Ordnance Laboratory, White Oak, Silver Spring, Md. 20901.

There are little data available which can be used to predict the rates of uptake of the different vaporized radioactive elements or oxides. Since such data are important to the application of any fallout prediction model based on kinetics, a program has been started at this laboratory to measure the rates of uptake of a selected group of fission-product oxides under conditions approximating those found in the cooling fireball. The data from these measurements will be useful, not only as input to fallout models, but also for discovering the mechanisms which govern the rates of uptake.

Caution must be used in applying the findings of this report to the actual uptake processes occurring in the nuclear fireball. There the situation is much more complicated. Not only are there rapid changes of temperature and pressure and violent turbulence, but the radioactive elements themselves constitute a small fraction of the total vaporized material. It is difficult to estimate how these factors would affect the uptake rates.

This paper presents the more important data and conclusions from three reports which describe the uptake behavior of the vaporized oxides of molybdenum, tellurium, and rubidium by molten and solid substrates at high temperatures (*1, 2, 3*). These oxides were used as the vapor species because of their relatively high volatility and because of their importance as radioactive constituents, or the precursors of important constituents, of radioactive fallout particles.

Two substrate materials were used for most of the measurements. They were chosen as representative of two types of environmental material found in actual fallout. The first was a clay loam occurring in the Berkeley Hills, Calif. This is a more-or-less typical example of a silicate soil found in extensive areas in the temperate zones. The second material used was a calcium ferrite. This material has been observed in fallout resulting from nuclear explosions at the Pacific Proving Grounds where large amounts of calcium oxide, derived from the coral sand, and iron oxide, derived from towers, barges, or other structures, have been fused together.

Experimental

Apparatus. The apparatus consisted of a vertical tube furnace 74 cm. high and 2.2 cm. i.d. (Figure 1). The furnace tube was made from dense, gas-tight, high purity alumina (McDanel Co.). The upper third of the furnace was a high temperature zone wound with 17 gage Pt–20% Rh resistance wire, and the lower two-thirds was a low-temperature zone wound with 17 gage Kanthal A-1. The two heating sections were connected to different voltage sources, and their temperatures could be varied independently.

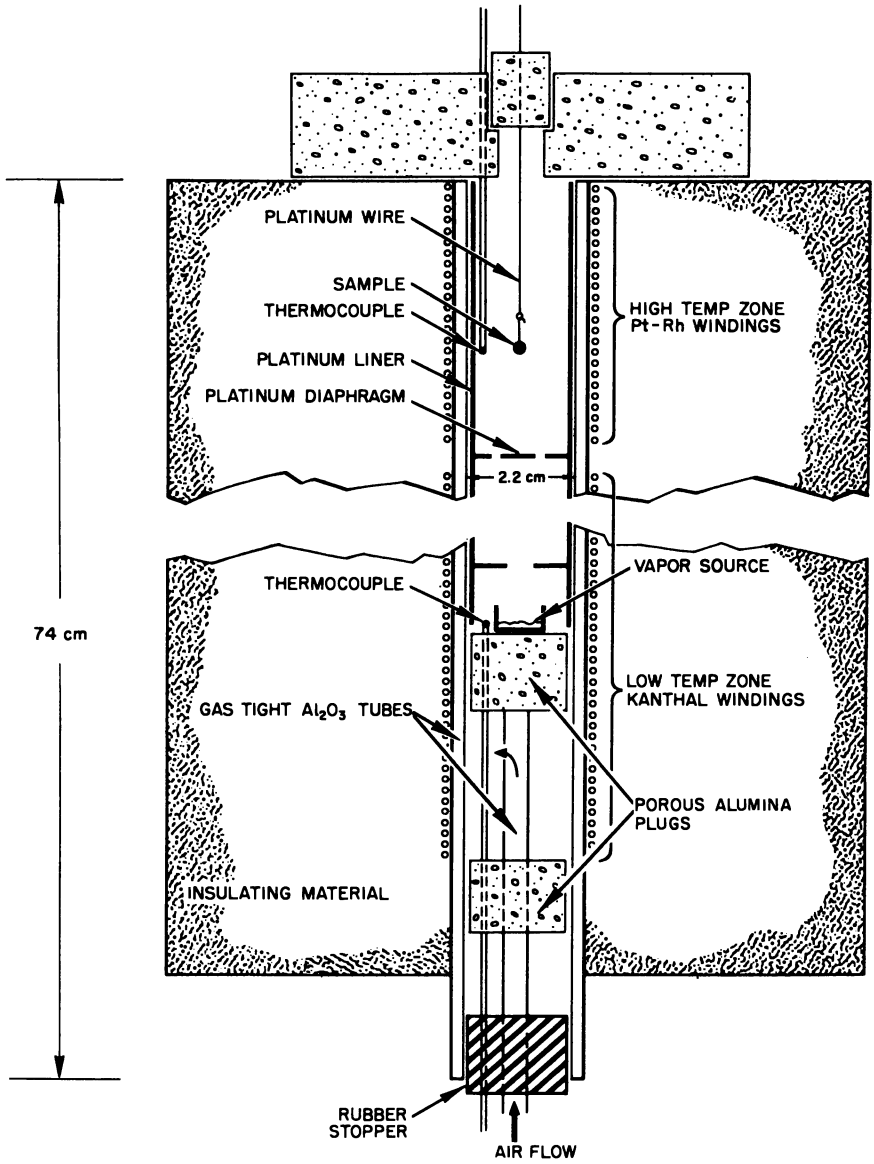

Figure 1. Two-temperature furnace

The radioactive oxides which served as the vapor sources were contained in a small platinum crucible. This crucible was placed on top of an assembly of two porous alumina plugs, mounted in tandem on a small, gas-tight alumina tube. The whole assembly could be inserted through the bottom opening of the furnace tube into the low temperature zone.

A dry air stream was introduced into the furnace *via* a hole in the small alumina tube just below the top alumina plug. The air flowed up and around the top alumina plug where it mixed with the radioactive oxide vapor, and the air-radioactive oxide vapor mixture flowed up through the high temperature zone and left through the top of the furnace.

The substrate samples were inserted into the high temperature zone through a hole in the top of the furnace lid. These samples consisted of beads fused onto small platinum wire loops which were suspended from a long platinum wire holder cemented into an alumina plug.

Furnace temperatures were measured by two Pt–10% Rh thermocouples. One was mounted next to the suspended substrate samples and the other next to the vapor source. The rate of flow of the dry air through the furnace was determined by measuring the air pressure upstream from a capillary restriction in the air line. The pressure was measured by an oil manometer which had been calibrated against known flow rates of air through the capillary restriction.

The interior of the furnace was lined with platinum foil to limit any reaction of the oxide vapors with the alumina furnace walls. Three perforated platinum foil diaphragms were placed at intervals inside the furnace to act as heat shields and to ensure thorough mixing of the oxide vapor–air mixtures.

Preparation of Materials and Samples. The source of the molybdenum oxide vapor was MoO_3 containing ^{99}Mo tracer. The ^{99}Mo was supplied as ammonium molybdate in NH_4OH solution (Nuclear Science and Engineering Co.). The solution was evaporated to dryness in a platinum crucible, and the ammonium molybdate was heated in air at about 500°C. for several hours to decom ose it to MoO_3.

The source for the tellurium oxide vapor was TeO_2 containing ^{127m}Te tracer. The ^{127m}Te was supplied as H_2TeO_3 in HCl solution (New England Nuclear Corp.). A small amount of Na_2TeO_4 carrier was added to the solution and dissolved with complete exchange with the ^{127m}Te tracer. The tellurium was precipitated subsequently as telluric acid, H_2TeO_4, which was then converted to TeO_2 by heating at 500°C. for 24 hours.

The source for the rubidium oxide vapor was a rubidium titanate mixture prepared by fusing Rb_2CO_3 and TiO_2 to give a low melting eutectic composition of 34 mole % Rb_2O and 66 mole % TiO_2. Radioactive ^{86}Rb tracer, supplied as RbCl (Oak Ridge National Laboratory) was exchanged with the Rb_2CO_3 in solution.

The clay loam used for the substrate samples was prepared by being sieved to remove the larger pebbles and pieces of organic matter. The material passing the sieve was dried and ground and melted in a nickel crucible at about 1300°–1400°C. for about an hour. Upon cooling, the melt formed a black glass, which was broken up and ground to a powder in a steel mortar. To form the spherical substrate samples, this powder was melted onto the platinum wire loops with a gas–oxygen torch. Analysis of the nonvolatile constituents of the clay loam is shown at the top of p. 39.

The calcium ferrite samples were prepared by weighing out the appropriate amounts of Reagent grade Fe_2O_3 and CaO powders so that the final composition of the mixture would be 80% Fe_2O_3 and 20% CaO

Oxide	*Weight %*
SiO_2	67.5
Al_2O_3	15.9
Fe_2O_3	7.3
CaO	2.7
MgO	2.7
Na_2O	2.3
K_2O	1.6
	100.0

by weight. The dry powders were mixed thoroughly in a mortar and the mixture was fused directly onto the platinum wire loops.

Procedure. In preparation for a series of experimental runs, the top and bottom sections of the furnace were brought to their proper operating temperatures, the air flow was started, and a standby source of radioactive oxide vapor was inserted into the lower section of the furnace. After about a 24-hour equilibration period, the standby oxide source was replaced with the regular source which had just been weighed.

During the actual experimental runs, the substrate samples were preheated in a gas flame and then inserted into the top of the furnace for varying times, usually 2–20 minutes depending upon the rate of uptake of radioactive vapor. The samples were then withdrawn, counted, and their counting rates were compared with that of a standard to determine the amount of radioactive oxide uptake. After counting, the substrate samples were reinserted into the furnace, and the procedure was repeated. The total accumulated time in the furnace for each sample was usually about 30–60 minutes.

At the end of each day's runs, the regular radioactive vapor source was removed from the furnace and was replaced by the standby source. The regular source was then reweighed, and the amount of radioactive oxide vapor which had evaporated was determined. This weight, combined with the known volume of air passed through the furnace, gave the vapor concentration of the radioactive oxide in the furnace.

Some checks on the experimental techniques were made. There was uncertainty as to whether or not the vapor concentrations in the furnace might not be changed by repeated opening of the furnace lid for the inserting and removing the samples. To test this effect, two identical samples of clay loam were prepared and were exposed to molybdenum oxide vapor in the furnace. One sample was inserted into the furnace and left for 60 minutes and then withdrawn and counted. The other sample was inserted and withdrawn 12 times. Each interval in the furnace was 5 minutes, and the sample was counted after a total accumulated time in the furnace of 60 minutes. It was found that the sample which had been left in the furnace for the one 60-minute interval had taken up 7% less MoO_3 than the sample which had been exposed for 12 five-minute intervals. This discrepancy is considerably smaller than the over-all accuracy of the measurements, and therefore no correction was applied to the data.

A check was also made on the effect of varying the flow rate of the carrier gas (air). The flow rate used in most of the experiments was 70

ml./min. (measured at 25°C.). Two experimental runs were made under identical conditions except that in one run the flow rate was 70 ml./min. and in the second it was increased three-fold to 210 ml./min. After the change in partial pressure of the oxide vapor by the increased volume in air was taken into account, there was no significant change in the vapor uptake rate by substrates of either clay loam or calcium ferrite.

Errors. The precision of the experimentally measured quantities probably exceeds the over-all accuracy of the experiment by an order of magnitude. That is, measurements such as the source weight losses, volumes of carrier air, and the weights and diameters of the substrate samples could all be determined to within about ±5%. However, the largest uncertainty was in determining the radioactive oxide vapor concentration at the substrate sample position in the furnace. At the low partial pressures of the oxide vapors, absorption or reaction with the walls of the furnace could be important. In addition, in cases where the amounts of uptake of oxide vapor by the substrate samples were low, the counting rates were low enough to cause appreciable errors. In view of these uncertainties, it is estimated that the reproducibility is good to within ±50% for the measurements with molybdenum oxide vapor and to within a factor of about 2 for the measurements with tellurium and rubidium oxides. The over-all accuracy of the measurements are probably good to within a factor of about 2 for the molybdenum and a factor of about 4 to 5 for the tellurium and rubidium oxide measurements.

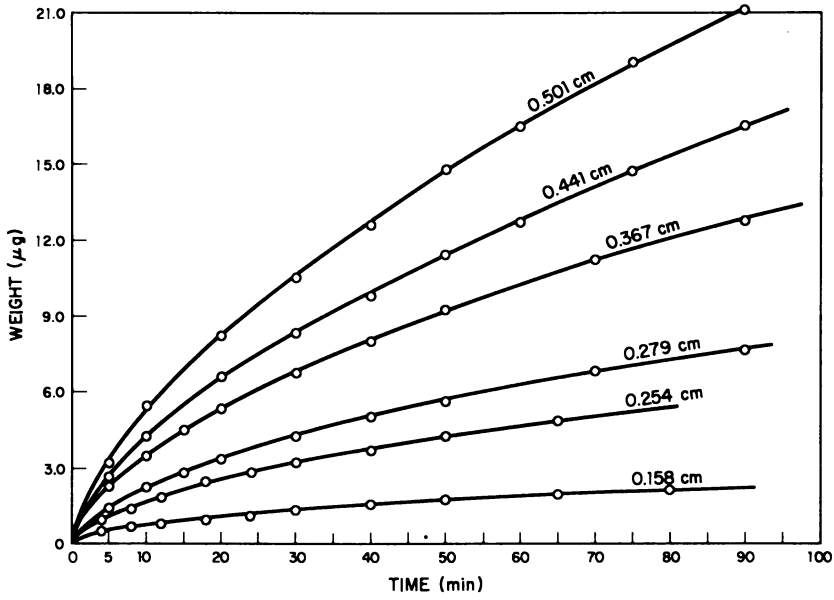

Figure 2. Uptake of MoO_3 by clay loam as a function of particle diameter and time

T = 1400°C., MoO_3 vapor concentration = 6.3 μgrams/liter

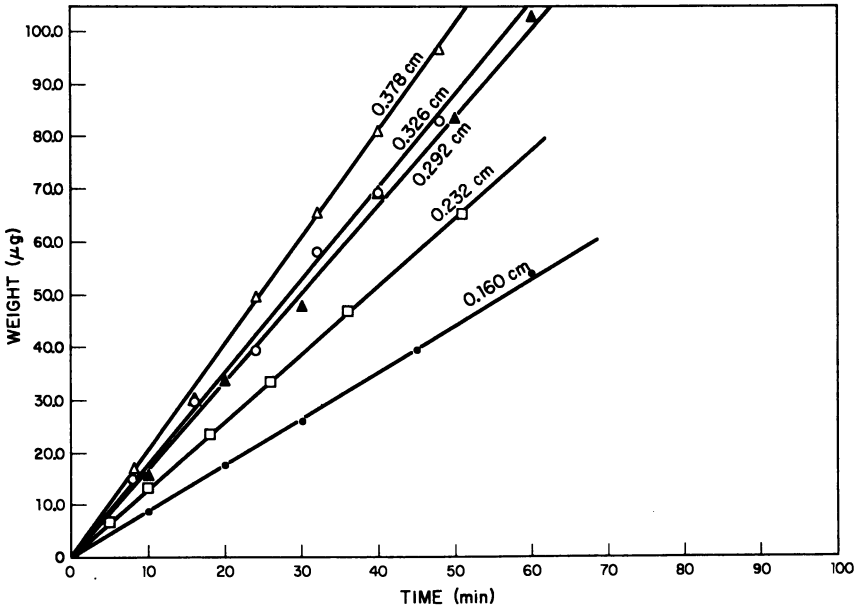

Figure 3. Uptake of MoO_3 by calcium ferrite as a function of particle diameter and time

T = 1400°C., MoO_3 vapor concentration = 7.5 μgrams/liter

Results

Most of the experimental data can be grouped into three parts:

(1) The uptake of the radioactive oxide vapors as a function of particle size at constant temperature and oxide partial pressure.

(2) The uptake of oxide vapor as a function of oxide partial pressure at constant particle size and temperature.

(3) The uptake of oxide vapor as a function of temperature at constant particle size and oxide partial pressure.

Figures 2 and 3 show the uptake of molybdenum oxide vapor by various sized particles of clay loam and calcium ferrite at 1400°C. Over the temperature and oxide partial pressure ranges used in these experiments, molybdenum oxide vapor consists of a mixture of MoO_3, Mo_2O_6, and Mo_3O_9 molecules whose proportions are temperature and pressure dependent. Data which can be used to calculate these ratios are available from a report of a mass-spectrometric study of the sublimation of MoO_2 by Burns *et al.* (*6*). Usually, for convenience, the total vapor concentration (μgram/liter) of all the polymers of MoO_3 vapor were used in this report in place of partial pressures. In some situations it was necessary to compute the partial pressure of each polymeric species.

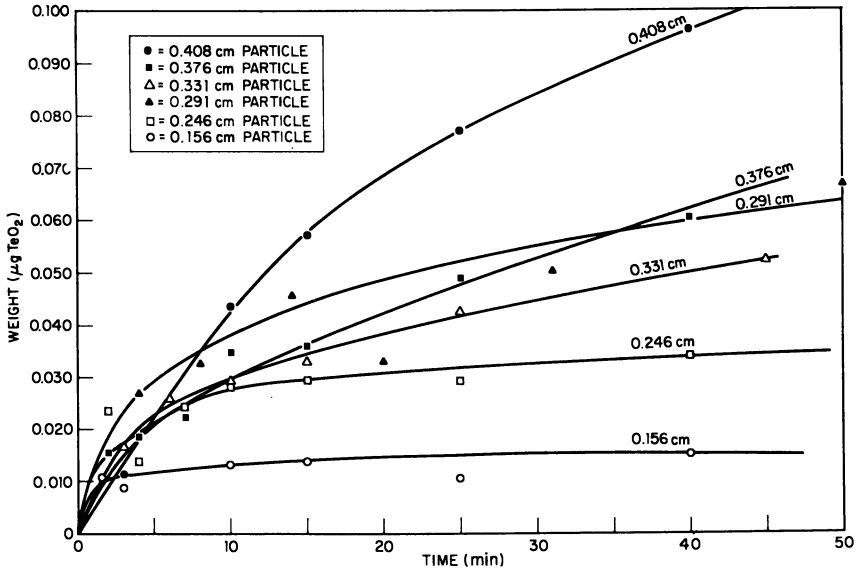

Figure 4. Uptake of TeO_2 by clay loam as a function of particle diameter and time

T = 1400°C., TeO_2 partial pressure = 9.2×10^{-6} atm.

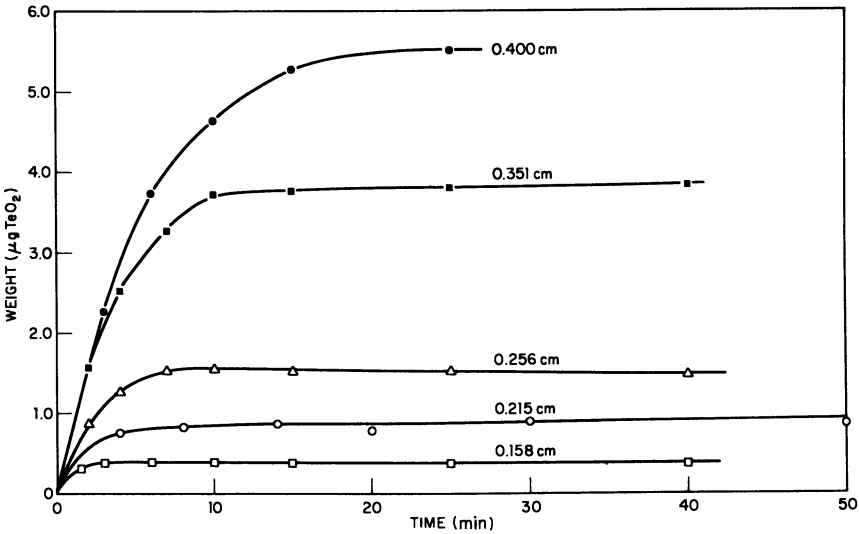

Figure 5. Uptake of TeO_2 by calcium ferrite as a function of particle diameter and time

T = 1400°C., TeO_2 partial pressure = 9.2×10^{-6} atm.

Figures 4 and 5 show the uptake of tellurium oxide vapor by various sized particles of clay loam and calcium ferrite at 1400°C. Over the temperature and pressure ranges used here, TeO_2 is the predominant vapor species (*4*).

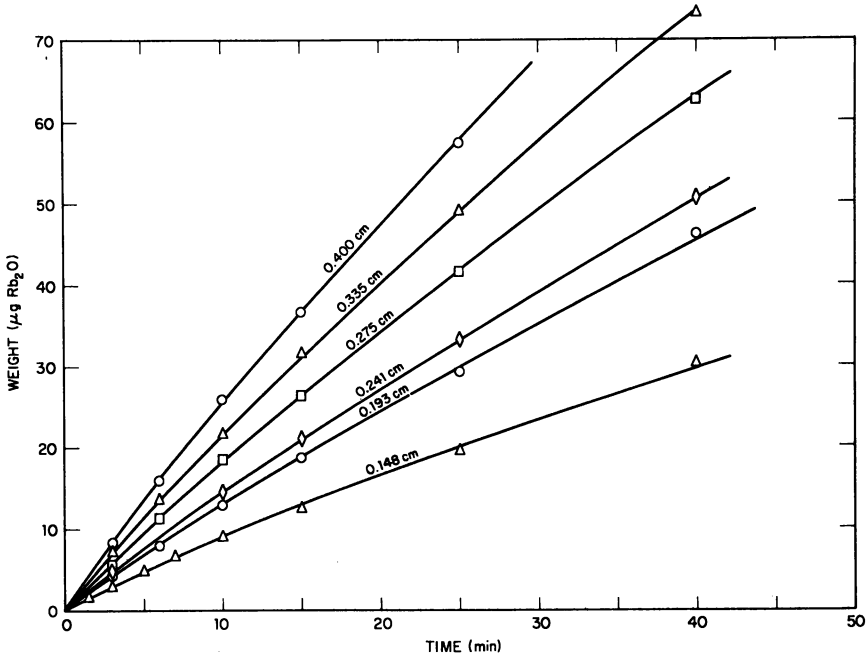

Figure 6. Uptake of RbO by clay loam (uptake weight calculated in terms of the condensed species, Rb_2O) as a function of particle diameter and time

T = 1400°C., RbO partial pressure = 1.5 × 10^{-5} atm.

Figures 6 and 7 show the uptake of rubidium oxide vapor by various sized particles of clay loam and calcium ferrite at 1400°C. There is uncertainty as to the molecular species found in rubidium oxide vapor under the experimental conditions. Data furnished by Bedford and Jackson indicate that the vapor should consist of a mixture of RbO and Rb molecules with RbO predominating (*4*). Experimental work by Norman and Staley indicate that the vapor should consist predominately of Rb with minor amounts of Rb_2O molecules (*13*). To calculate vapor pressures it was assumed that the vapor consisted only of RbO. Since the molecular weight of Rb is only 16% less than that of RbO, no large error is introduced by this assumption even if the vapor consists of Rb molecules.

Figures 8, 10, and 12 show the initial rates (at $t = 0$) of uptake of the molybdenum, tellurium, and rubidium oxide vapors by samples of

clay loam and calcium ferrite at 1400°C. and at constant particle size but with varying partial pressures. Figures 9, 11, and 13 show the initial rates at constant partial pressure and constant particle size but at varying temperatures. In some cases rates at other than $t = 0$ have also been plotted, but, in general, the initial rates have been emphasized since

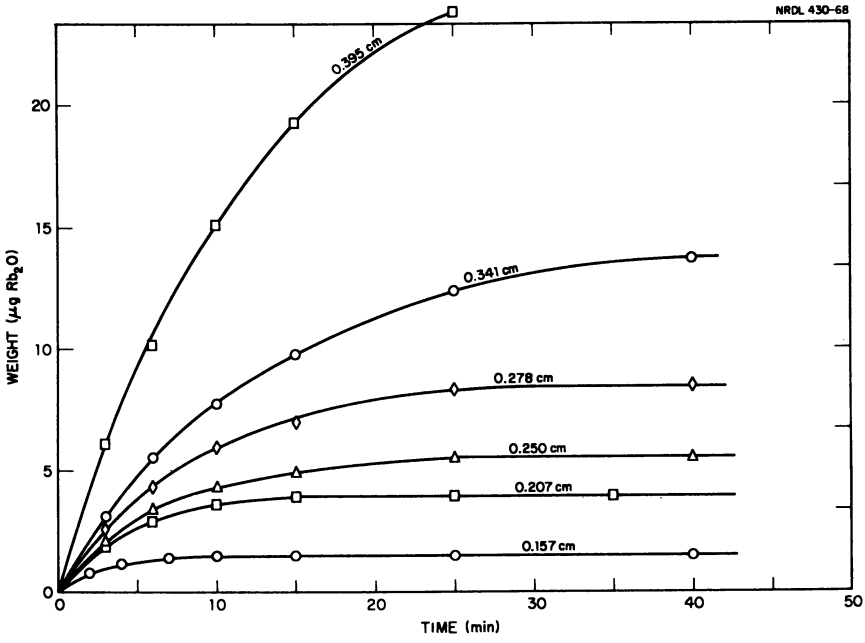

Figure 7. Uptake of RbO (calculated as Rb_2O) by calcium ferrite as a function of particle diameter and time

T = 1400°C., RbO partial pressure = 1.5 × 10^{-5} atm.

they are independent of the time of exposure of the samples and since they can be used to determine the mechanisms which govern the rate of vapor uptake.

A series of runs was made in which the uptakes of the radioactive oxide vapors by samples of single, unmelted oxides were measured. This was done to obtain some information on the relative reactivity of the oxide vapors with various simple oxides. The partial pressures of the oxide vapor and the sample temperature (1400°C.) were held constant. All oxide samples used had melting points in excess of 1400°C. The samples were prepared by pressing the powdered oxides (Reagent grade) into pellets 0.62 cm. in diameter and about 0.05 to 0.08 cm. thick. The

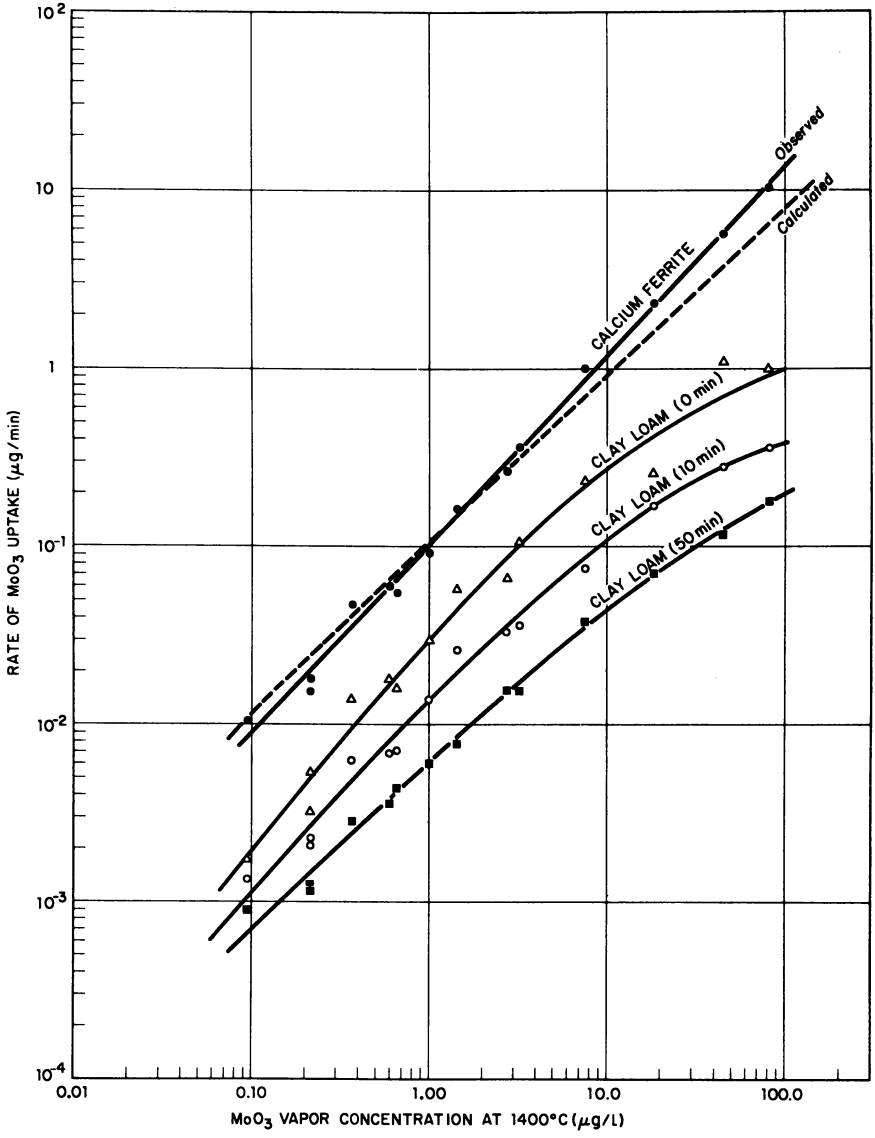

Figure 8. Rates of uptake of MoO_3 at 1400°C. as a function of MoO_3 vapor concentration

Total partial pressure range (sum of the partial pressures of all three MoO_3 vapor polymers) covered in these measurements is from about 9×10^{-8} to 4×10^{-5} atm. Average particle diameters were 0.22 ± 0.02 cm. Rates of uptake on the clay loam particles are shown at 0, 10, and 50 minutes. Dashed line indicates the rate of uptake calculated by Maxwell's equation

pellets were backed with platinum foil so that only one face was exposed to the oxide vapors. The results of these measurements are shown in Figures 14, 15, and 16.

These results are not precise: some of the pellets tended to crumble or shrink in the furnace so that the surface areas exposed were irregular. Also, the rates of the oxide vapor reactions are affected by the rates of diffusion of the condensed vapor oxides into the solid oxide substrates and by the particle size and microscopic surface structures of the substrate oxides.

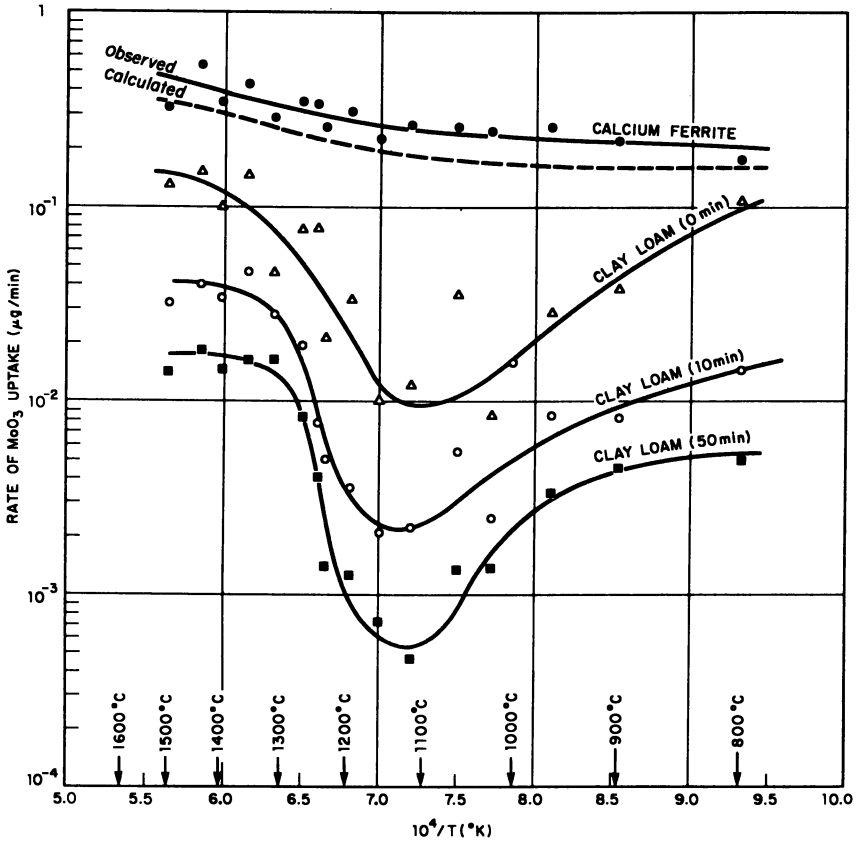

Figure 9. Rates of uptake of MoO_3 as a function of temperature

Because the ratios of the three gaseous polymers of MoO_3 changed as the temperature varied, it was impossible to keep the total MoO_3 partial pressure constant. It varied from 2.6×10^{-6} atm. at 1500°C. to 1.0×10^{-6} atm. at 800°C. Average particle diameters were 0.22 ± 0.02 cm. Rates of uptake on the clay loam samples are shown at 0, 10, and 50 minutes. Dashed line indicates the rate of uptake calculated by Maxwell's equation

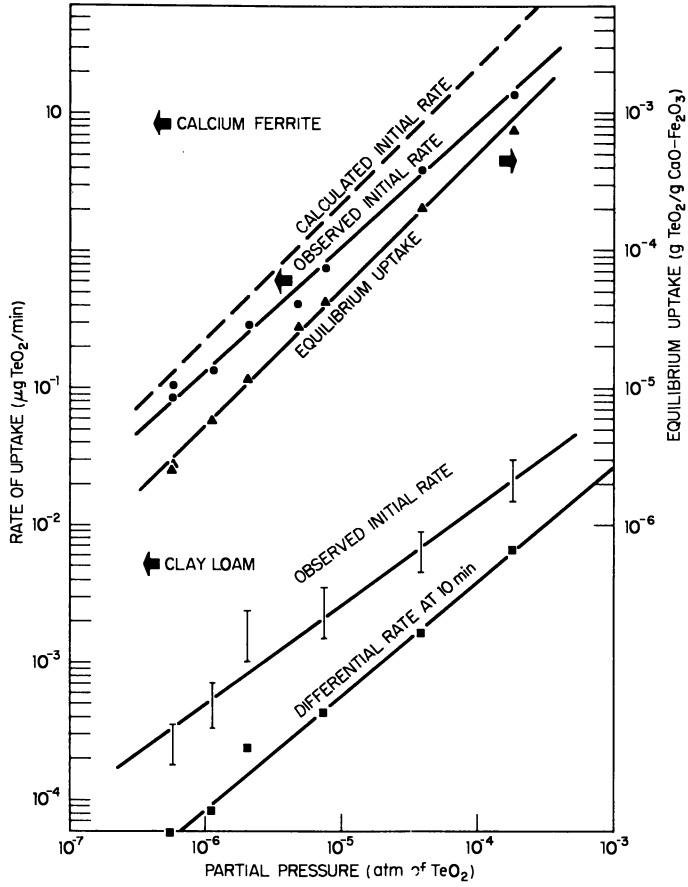

Figure 10. Rates of uptake of TeO_2 at 1400°C. as a function of TeO_2 partial pressure

The degree of uncertainty in the rate of uptake by the clay loam samples is indicated by the vertical lines. Average particle diameters were 0.30 ± 0.01 cm. Also plotted is the equilibrium uptake of TeO_2 in the calcium ferrite melts as a function of TeO_2 partial pressure

Discussion

Theoretical Introduction. There are three basic steps in the uptake of the radioactive oxide vapors by the substrate particles, and any one of these might be slow enough compared with the others to be the rate-determining step. These three steps are:

(1) The diffusion of the oxide vapor molecules through the air to the surface of the particle.

(2) The reaction and condensation of the oxide vapor molecules at the surface of the particle.

(3) The diffusion of the products of condensation of the oxide vapor into the interior of the particle.

If one assumes that the diffusion of the oxide vapor molecules through the air is the rate-determining step, this process can be described

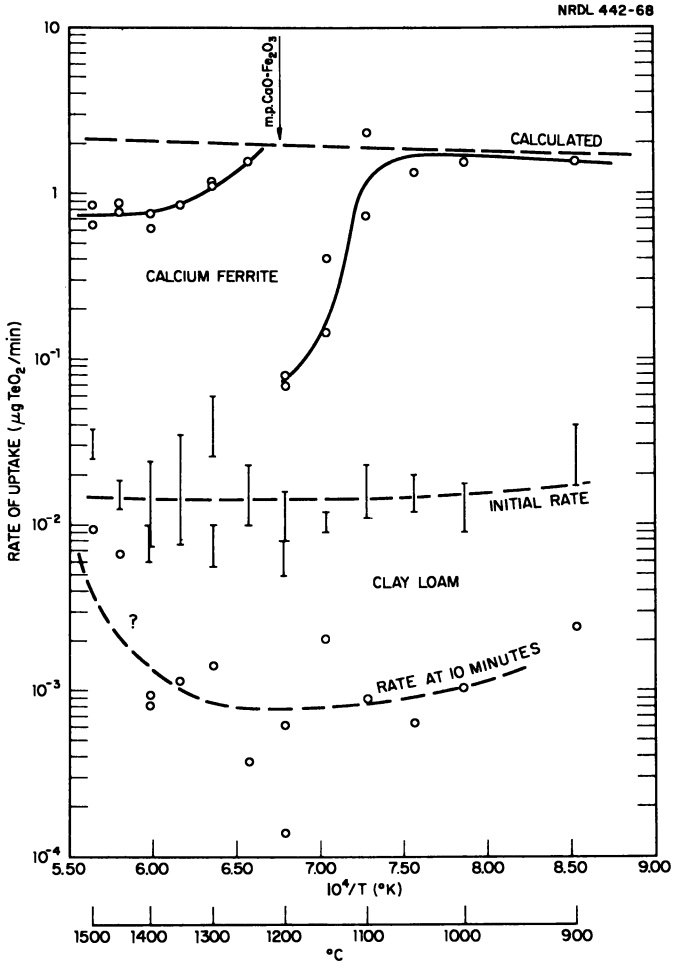

Figure 11. Rates of uptake of TeO_2 as a function of temperature

TeO_2 partial pressure was 9.2 × 10^{-6} atm. Average diameter of the calcium ferrite particles was 0.30 ± 0.01 cm., and average diameter of the clay loam particles was 0.34 ± 0.01 cm.

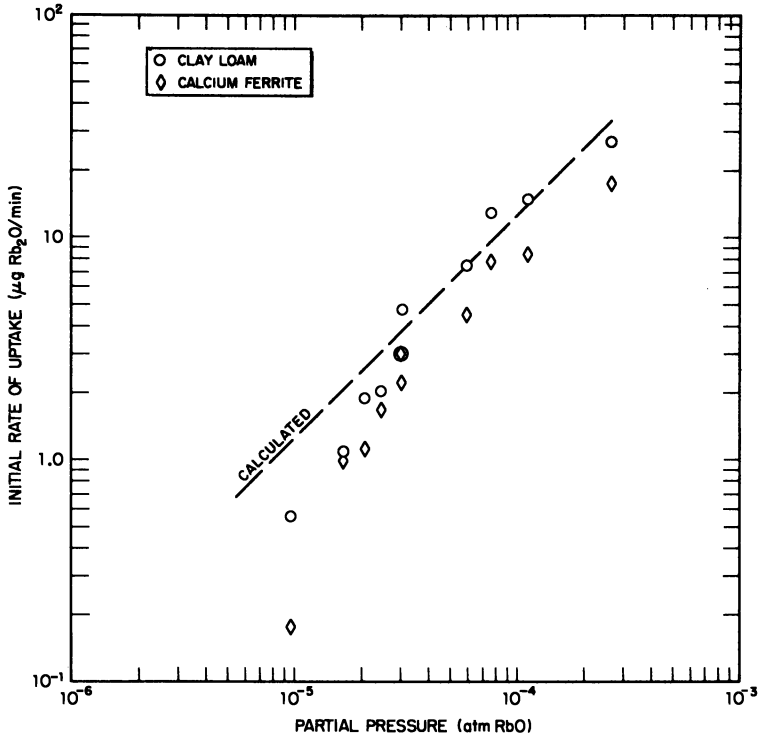

Figure 12. Initial rates of uptake of RbO (calculated as Rb_2O) at 1400°C. as a function of RbO partial pressure

Average particle diameters were 0.34 ± 0.01 cm.

by Maxwell's equation (8):

$$I = \frac{2\pi d D_{12} M (P_\infty - P_o)}{RT}$$

where I is the rate of impingement of the vapor species, of molecular weight M upon a particle of diameter d, D_{12} is the interdiffusion constant of the vapor species in the gaseous medium, P_∞ is the partial pressure of the vapor at a large distance from the particle, and P_o is the partial pressure at the surface of the particle. Maxwell's equation is based on the case of evaporation (or condensation) of a vapor from (or onto) a spherical drop which is motionless relative to an infinite, uniform medium. For evaporation, it is assumed that the vapor concentration at the surface is equal to its equilibrium concentration. For condensation the pressure term (P_∞) refers to the vapor partial pressure at a distance from the drop. It is further assumed that the radius of the drop is significantly greater than the mean free path of the vapor molecule and that the vapor

obeys the ideal gas law. If vapor diffusion is the rate-determining step, Maxwell's equation shows that with constant temperature and pressure the rate of uptake of the oxide vapor will be proportional to the diameter of the particle, and therefore the total amount taken up will be proportional to the product of the particle diameter and time.

If the rate-determining step is the reaction or the condensation of the oxide vapor at the surface of the particle, the rate will be proportional to the surface area of the particle or to the diameter squared. The total amount taken up will be proportional to the product of the diameter squared and time.

If the diffusion of the condensed oxide vapor into the particle is slow compared with the other two steps and if condensation is reversible, the outer surface layer of the particle reaches equilibrium, or pseudo-equilibrium, with the oxide vapor, and further uptake is governed by

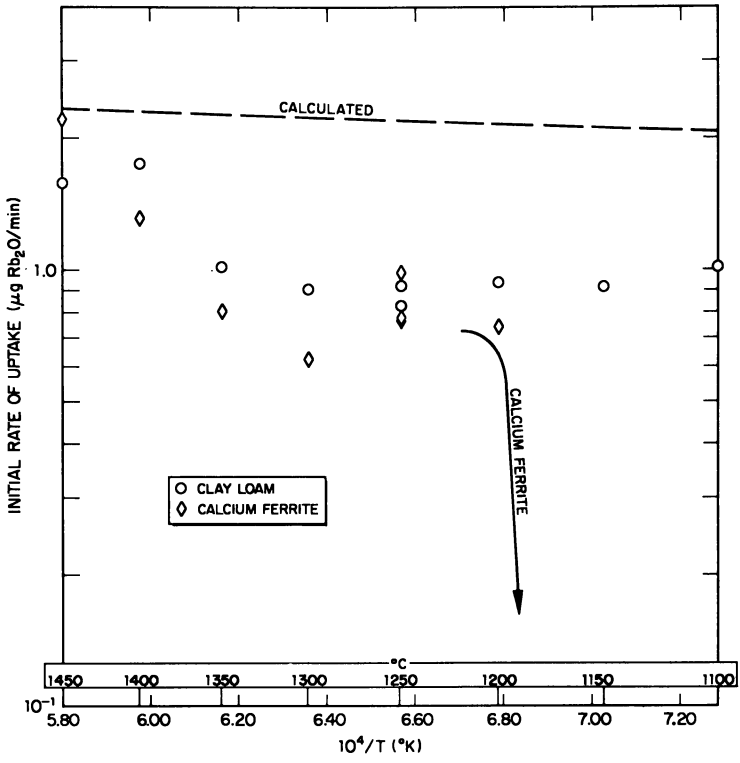

Figure 13. Initial rates of uptake of RbO (calculated as Rb_2O) as a function of temperature

RbO partial pressure was 1.8 × 10^{-5} atm. Average particle diameters were 0.34 ± 0.01 cm.

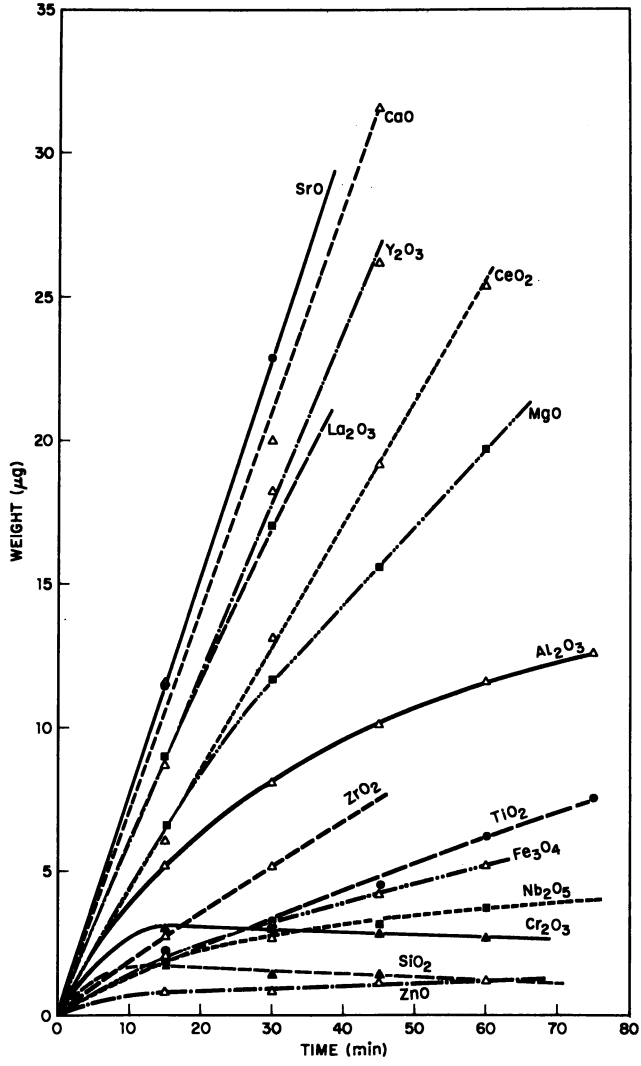

Figure 14. Uptake of MoO_3 by solid oxide pellets 0.62 cm. in diameter

T = 1400°C., MoO_3 vapor concentration = 3.8 μgrams/liter. Total MoO_3 partial pressure = 2.8 × 10^{-6} atm.

the rate at which the condensed oxide diffuses away from the surface zone into the particle. As a model for this process one can envisage a spherical particle of the substrate material surrounded by a solution containing the condensed oxide vapor at a constant concentration. A graphical solution of the mathematical relations for this type of diffusion

is given by Crank (7). At early times in the diffusion process,

$$\frac{M_t}{M_\infty} \sim \left[\frac{Dt}{d^2}\right]^{1/2}$$

where $\frac{M_t}{M_\infty}$ is the ratio of the amount of material diffusing into a particle of diameter d at time t to the total amount which diffuses into the particle

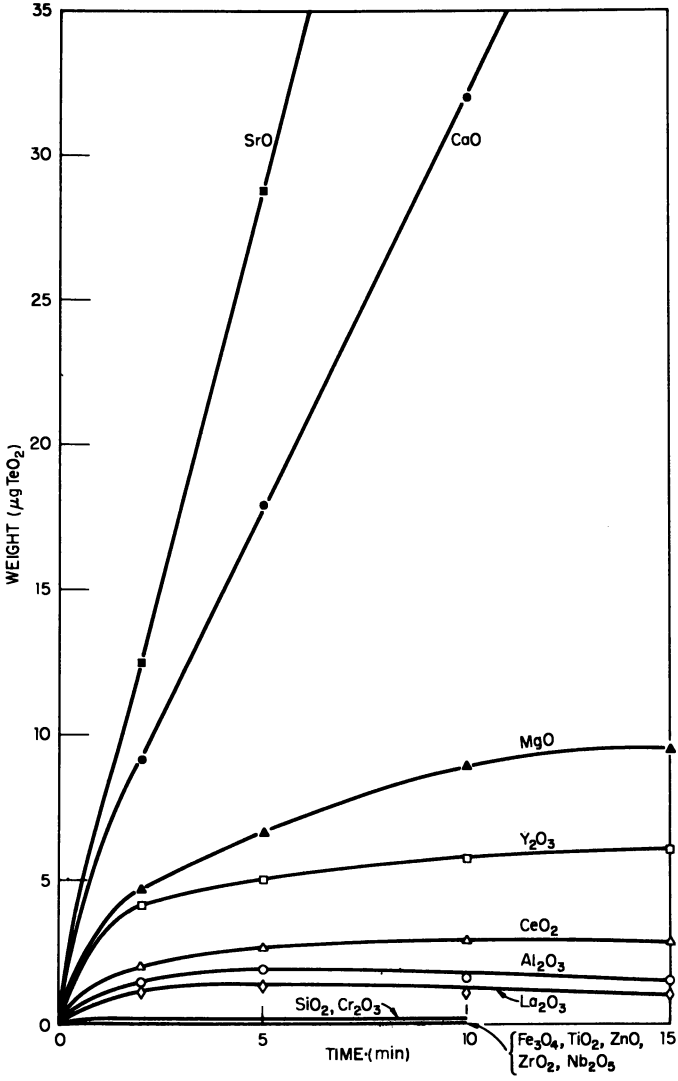

Figure 15. Uptake of TeO_2 by solid oxide pellets 0.62 cm. in diameter

T = 1400°C., TeO_2 partial pressure = 3.5 × 10^{-5} atm.

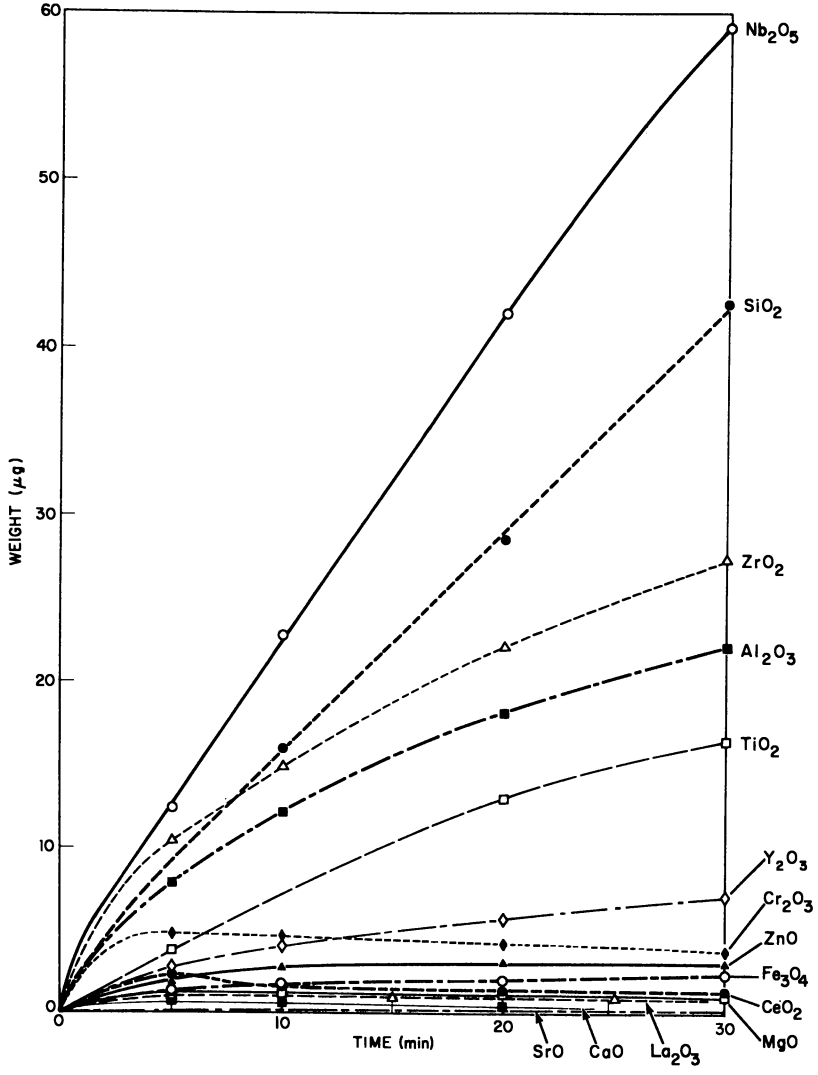

Figure 16. Uptake of RbO (calculated as Rb_2O) by solid oxide pellets 0.62 cm. in diameter

T = 1400°C., RbO partial pressure = 1.5 × 10^{-5} atm.

at infinite time. D is the diffusion constant of the diffusing material in the particle. M_∞ is proportional to the volume of the particle, or to d^3, so that at constant temperature,

$$M_t \sim d^2 t^{1/2} \text{ (for } M_t < 0.2\, M_\infty)$$

Therefore, if diffusion of the condensed oxide vapor into the particle is rate determining, the total amount of oxide vapor taken up will be

proportional to the diameter squared of the particle multiplied by the square root of time. The rate of uptake will be proportional to the diameter squared divided by the square root of time.

These relationships are summarized in Table I and are true only for relatively small time intervals during which the composition of the particles does not change appreciably.

Table I. Rate of Uptake in a Rate-Controlling Process

Rate-Controlling Process	*Rate of Uptake is Proportional to:*	*Amount of Uptake is Proportional to:*
Diffusion of oxide vapor through air	d	dt
Reaction or condensation rate at surface of the particle	d^2	d^2t
Diffusion of the condensed oxide vapor into particle	$\frac{d^2}{\sqrt{t}}$	$d^2\sqrt{t}$

Identification of the Rate-Determining Steps in the Uptake Processes. Examination of the uptake data for various sized substrate particles (Figures 2–7) shows that in two cases—the uptake of molybdenum oxide vapor by calcium ferrite and of rubidium oxide vapor by the clay loam—the amount of uptake is nearly proportional to time. This suggests that the rate-determining step is either the diffusion of the oxide vapor through the air or the rate of reaction or condensation at the surfaces of the particles (*see* Table I). To distinguish between these possibilities, plots of the amount of uptake at constant time and plots of the initial rates of uptake were made *vs.* particle diameter and diameter squared. In all cases the plots of the data *vs.* diameter were linear and those *vs.* diameter squared were not. Therefore, the rate-determining step in these cases is apparently the diffusion of the molybdenum and rubidium oxide vapors through the air.

For the uptake of molybdenum oxide vapor by the clay loam particles, the uptake of rubidium oxide vapor by the calcium ferrite, and the uptake of the tellurium oxide by both the clay loam and the calcium ferrite, the uptake *vs.* time plots are curved, and it is not immediately obvious what the rate-determining steps are. Plots of amounts of uptake at constant time and initial rates of uptake *vs.* particle diameters and diameters squared were therefore made.

These plots show that for the uptake of both tellurium and rubidium oxide vapors by the calcium ferrite particles the rate-determining step is also the diffusion of the oxide vapor molecules through the air. The curvature of the plots showing amounts of uptake *vs.* time is caused by

the limited solubility of the TeO_2 and the Rb_2O in the calcium ferrite so that the final equilibrium uptake is attained after just a few minutes' exposure of the substrate particles in the furnace. Radioautographs of hemisections of calcium ferrite particles which have been exposed to tellurium and rubidium oxide vapors for varying times show that mixing of the condensed oxides throughout the particles is rapid. This is probably caused by convection currents within the very fluid calcium ferrite melts. The low viscosity of the calcium ferrite above its sharply defined melting point (~1205°C.) contrasts with the high viscosity of the siliceous clay loam melts at 1400°C.

Plots of amounts of uptake and initial rates of uptake *vs.* particle diameters and diameters squared for the cases of molybdenum and tellurium oxide uptake by the clay loam particles were inconclusive in identifying the rate-controlling step. In most graphs, the data plotted against neither the diameter nor the diameter squared gave a straight line. This behavior, and the fact that the initial rates of uptake were quite low compared with the cases where the rate was controlled by the diffusion of the vapor molecules through the air, suggested that the rate was controlled by both a slow reaction of the oxide vapor at the surfaces of the particles and a slow rate of diffusion of the condensed vapors into the particles.

Calculation of a Theoretical Rate of Uptake Where Diffusion Through the Air is Rate Determining. Assuming that diffusion of the oxide vapors through the air is rate controlling, it should be possible to use Maxwell's equation to calculate the rate of uptake of the oxide vapors under varying conditions of pressure and temperature. The use of Maxwell's equation requires knowledge of the interdiffusion constant (D_{12}) of the oxide vapor in air. The interdiffusion constants of the vapor species studied here are not known, but they may be estimated by the Stefan-Maxwell equation (*14*):

$$D_{12} = \frac{1}{\pi \sigma^2_{12} (n_1 + n_2)} \left[\frac{2kT}{\pi \mu}\right]^{1/2}$$

where σ_{12} is the mean collision diameter of the oxide vapor and air molecules; μ is the reduced molecular mass, $\frac{m_1 + m_2}{m_1 m_2}$; and n_1 and n_2 are the numbers of molecules of each species per cm.[3]

The collision diameters of the oxide vapor molecules must be estimated. For many common vapor molecules, the collision diameters are roughly twice the average geometrical diameters as determined by molecular or atomic radii. By use of estimated molybdenum–oxygen bond distances and a proposed configuration of the Mo_3O_9 vapor molecule (*5*),

the geometric diameters of each of the three molybdenum oxide vapor species were estimated, and these values were doubled to give a crude approximation of the collision diameters (MoO_3, 8.4×10^{-8} cm.; Mo_2O_6, 10.6×10^{-8} cm.; Mo_3O_9, 12.2×10^{-8} cm.). By using these collision diameters and that of air (3.7×10^{-8} cm.), the interdiffusion constants for each molybdenum oxide vapor species were calculated for the various temperatures used in these experiments.

Maxwell's equation also requires the partial pressure of the diffusing species (P_∞). These were calculated for each of the three vapor polymers using the measured total molybdenum oxide vapor concentration and the polymeric vapor equilibrium data (*6*).

Finally, the flux of each molybdenum oxide polymer striking the substrate particles was calculated over the range of pressures and temperatures covered by the experimental measurements, and the sum gave the net rate of molybdenum oxide uptake. Since Maxwell's equation assumes stationary air relative to the particle, a small correction, about +15%, was applied to the net flux to accommodate the increased rate of condensation owing to the flow of carrier air up the furnace tube (*9*). These corrected rates of uptake have been plotted as dashed lines in Figures 8 and 9.

In a similar fashion the net rates of uptake of tellurium and rubidium oxide vapors have been calculated. By extrapolating known bond distances of SO_2 and SeO_2 vapor molecules (*10*), the average geometric diameter of the TeO_2 vapor molecule was estimated, and this was doubled to give a rough estimate of the collision diameter (7×10^{-8} cm.). Similarly, by using the monovalent ionic radii of Rb^+ and O^-, the collision diameter of the RbO vapor molecule was estimated (9×10^{-8} cm.). The calculated rates of uptake of TeO_2 as functions of pressure and temperature are shown as the dashed lines in Figures 10 and 11 and those of RbO in Figures 12 and 13. If the rubidium oxide vapor consisted of Rb molecules instead of RbO, the calculated uptake rate would be about the same because the diameters and molecular weights of these two molecules are similar.

Figures 8 and 9 show that the calculated rates of uptake of molybdenum oxide vapor by the calcium ferrite particles are close to the experimentally measured rates over large ranges of pressure and temperature. The correspondence between the observed and calculated rates helps substantiate the conclusion that the rate-determining step is indeed the diffusion of the molybdenum oxide vapor through the air.

The calculated rate of TeO_2 uptake agrees well over a large pressure range with the measured initial rate on the calcium ferrite particles (Figure 10). The agreement is not as good for the temperature variation runs (Figure 11). Below 1100°C. and from somewhat above the melting

point of the calcium ferrite (~1205°C.) the agreement is good. At higher temperatures the measured rate is only about one-half to one-third the calculated rate, and just below the melting point of the calcium ferrite there is a large decrease in the rate. The cause of this decrease is unknown.

The calculated curve is based on the assumption that the term P_o in Maxwell's equation is zero. This is probably an acceptable approximation when the condensation coefficient of the vapor is unity. If the condensation coefficient is smaller than unity, P_o will have a finite value, and the flux, I, will be smaller.

Figure 12 shows that the measured initial rates of uptake of RbO vapor by both the clay loam and the calcium ferrite particles are close to the calculated rate over a large pressure range. In the temperature variation runs, the observed uptake rates are close to the calculated rate at high temperatures but drop to about one-half the calculated rate at lower temperatures. Below the melting point of the calcium ferrite, the amount of RbO uptake drops markedly.

Test of the Uptake Model Based on the Assumption That Diffusion within the Particle is Rate Controlling. As discussed earlier, the plots of molybdenum and tellurium oxide vapor uptake data *vs.* diameters and diameters squared of the clay loam particles gave inconclusive evidence as to whether the rate-controlling step was a slow rate of reaction at the surfaces of the particles or a slow rate of diffusion of the condensed vapor into the particles.

It was felt that the inclusions within the clay loam particles of the platinum wire loops might be distorting the uptake data. To eliminate this possibility, a sample of clay loam was formed into a hemisphere ($r = 0.150$ cm.) by melting the clay loam onto a small, flat disc of platinum foil which had been welded at right angles onto the straight end of a platinum wire hook. The hook was hung in the furnace with the pendant, hemispherical drop of clay loam facing down. The uptake of molybdenum oxide vapor by this sample was measured at intervals over several hours until it was saturated with molybdenum oxide. At a temperature of 1400°C. and a molybdenum oxide vapor concentration of 22.4 μgrams/liter, the equilibrium uptake was 3.81×10^{-3} gram MoO_3/gram clay loam. The molybdenum oxide uptake as a function of time is shown in Figure 17.

These data were used to check the hypothesis that diffusion of the condensed molybdenum oxide within the clay loam particles is the rate-controlling step. As described earlier in this chapter, Crank (7) has given a graphical solution for the integrated diffusion equation for a sphere in a well-stirred solution. From the experimental measurements on the molybdenum oxide uptake by the hemisphere, all terms in the

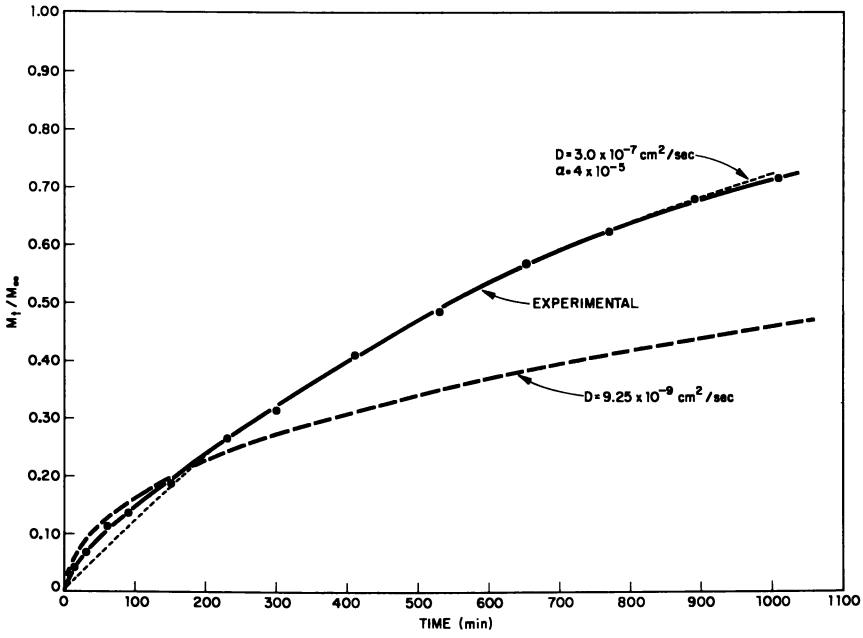

Figure 17. Uptake of MoO_3 by hemisphere of clay loam (diameter = 0.30 cm.)

T = 1400°C., MoO_3 vapor concentration = 22.4 μgrams/liter (total MoO_3 partial pressure = 1.3 × 10^{-5} atm.). The large dashed line indicates the uptake of MoO_3 as calculated by use of the simple diffusion model (D = 9.25 × 10^{-9} cm.²/sec.). Small dashed line indicates the uptake of MoO_3 as calculated by the complex model combining a slow surface reaction with diffusion within the particle (α = 4 × 10^{-5}, D = 3.0 × 10^{-7} cm.²/sec.)

solution are known except the diffusion constant (D) of the MoO_3 in the clay loam at 1400°C. By successive approximations a value of D was found such that when used in the diffusion equation the calculated uptake of molybdenum oxide by the hemisphere equaled the measured uptake at the point where the uptake was 20% of the final equilibrium uptake ($M_t/M_\infty = 0.20$). Using this value of D, the predicted uptake of molybdenum oxide by the clay loam hemisphere was calculated as a function of time. This uptake was plotted as the large dashed curve in Figure 17.

The calculated and experimental curves deviate considerably in shape, and it seems that the simple diffusion model is not adequate to describe the kinetics of the uptake process in this case. Also the value of D (9.25 × 10^{-9} cm.²/sec.) required to make the two curves coincide at early times seems to be much smaller than expected. The only data available on the diffusion of molybdenum oxide in liquid silicates is from a report by Norman *et al.* (*11*), who measured the diffusion constant of

MoO_3 in a calcium aluminum silicate melt (CaO, 23%; Al_2O_3, 15%; and SiO_2, 62% by weight). At 1400°C. they report a diffusion constant of 3.0×10^{-7} cm.^{2}/sec. which exceeds the value of D used here by a factor of about 31.

The diffusion constant of MoO_3 in the calcium aluminum silicate (CAS) melt may differ appreciably from that in the clay loam melt. However, Norman *et al.* have also compared the diffusivities of cesium in CAS and in a melt of soil from the Nevada Test Site and found that the difference in diffusivities in the two matrices was smaller than the experimental uncertainties (*12*). They concluded that the CAS melt was a fair model of the Nevada soil with respect to the diffusion of most radionuclides of interest in fallout.

Test of Uptake Model Based on a Slow Surface Reaction Combined with Diffusion within the Particle. Since the simple diffusion model is inadequate to describe the uptake behavior of the molybdenum and tellurium oxide vapors by the clay loam particles, a more complex model is required, in which the effects of a slow surface reaction and of diffusion of the condensed vapor into the particle are combined. Consider the condensation of a vapor at the surface of a substrate (of any geometry) and the passage by diffusion of the condensed vapor through a thin surface layer into the body of the substrate. The change in concentration of solute per unit volume in the surface layer caused by vapor condensation is:

$$\frac{dC}{dt} = \frac{1}{x}(M_c - M_e) \tag{1}$$

where M_c is the amount of vapor condensing and M_e is the amount of vapor evaporating per unit area per unit time, and x is the thickness of the surface layer.

$$M_c = \alpha F \tag{2}$$

where α is the condensation coefficient of the vapor and F is the flux of vapor striking the substrate surface (α is assumed constant for dilute solutions).

At equilibrium, $M_e = M_c$, and at any intermediate time,

$$M_e = M_c \frac{C}{C_\infty} = \alpha F \frac{C}{C_\infty} \tag{3}$$

where C_∞ is the final equilibrium concentration of condensed vapor in the substrate.

Combining Equations 1, 2, and 3:

$$\frac{dC}{dt} = \frac{\alpha F}{x}\left[\frac{C_\infty - C}{C_\infty}\right] \tag{4}$$

The loss of condensed solute from the surface layer by diffusion into the interior can be expressed by

$$\frac{dC}{dt} = \frac{D}{x}\frac{dC}{dx} \tag{5}$$

where D is the diffusion constant of the condensed vapor in the substrate, and dC/dx is the concentration gradient of the condensed vapor in the substrate.

If a steady state is assumed where the amount of condensate accumulating in the surface layer is small compared with the amount passing through, the amount entering the surface layer by condensation (Equation 4) will be equal to the amount lost by diffusion (Equation 5).

$$D\frac{dC}{dx} + \frac{\alpha F}{C_\infty}(C - C_\infty) = 0 \tag{6}$$

where $\alpha F/C_\infty$ is a constant.

Crank (7) solves this equation for evaporation (or condensation) of a diffusing substance across the surface of a sphere. Using this solution the uptake of molybdenum oxide by the clay loam sphere can be calculated as a function of time if the terms D, F, α, and C_∞ are known.

F (2.1×10^{-4} gram/cm.^{2} sec.) was calculated from the partial pressures of the three polymers of molybdenum oxide vapor, and C_∞ (6.8×10^{-3} gram/cm.^{3}) was measured experimentally. For purposes of calculation D was assumed to be 3.0×10^{-7} cm.^{2}/sec. (Norman's value of D for MoO_3 diffusing in the CAS melt at 1400°C.). Successive estimates of α were tried until a good fit between the calculated and the experimental curves was obtained. The best over-all fit between the two curves was obtained with $\alpha = 4 \times 10^{-5}$ (*see* Figure 17). This value is an effective condensation coefficient for all three polymers of molybdenum oxide vapor.

Except for an initial period where the experimentally measured uptake rate is about twice the calculated rate, the shapes of the two curves correspond quite well. This supports the hypothesis that the uptake rate, where the vapor condensation coefficient is small, is determined by the combined effect of a slow rate of surface reaction and slow diffusion of the condensate into the interior of the substrate.

An attempt was made to apply Equation 6 to the uptake data of tellurium oxide vapor by the clay loam and the CAS melts. The uptake of TeO_2 by a particle of each substrate material was followed until equilibrium was reached (about 50–70 hours). The temperature was 1410°C., the TeO_2 partial pressure was 1.1×10^{-5} atm., and the final equilibrium concentrations were 3.7×10^{-5} gram TeO_2/gram clay loam and 1.8×10^{-5} gram TeO_2/gram CAS. These data and Norman's value of

1.07×10^{-6} cm.^{2}/sec. for the diffusion constant of TeO_2 in CAS were used in Equation 6, and successive values of α were tried until the best fits between the calculated and measured uptake curves were obtained. A fair correspondence between the curves for the CAS was obtained with $\alpha = 2 \times 10^{-7}$. Although the over-all correspondence was fair, there was considerable deviation at early times, and the initial rate determined experimentally exceeded the calculated initial rate by an order of magnitude.

The correspondence between the calculated and measured curves in the case of TeO_2 uptake by the clay loam was poor. Figure 4 shows that there is a tendency for the rate of uptake to be large at first and then to decrease abruptly, and in some cases reach a pseudo-equilibrium. This produces a rather pronounced bend in the experimental curves which is not present in the calculated curve. It appears that there was relatively rapid condensation of the TeO_2 onto available sites at or near the surface, and that after these have been saturated, the uptake process decreases markedly.

Conclusions

Analysis of the uptake data has shown that for molybdenum and tellurium oxide vapors condensing onto substrates of molten calcium ferrite and for rubidium oxide vapor condensing onto substrates of both clay loam and calcium ferrite, the initial rate of uptake is determined by the rate at which the vapors (at low partial pressures) diffuse through the air to the surfaces of the substrate particles. In these cases the approximate initial rates of uptake can be calculated by first estimating a collision diameter for the vapor molecules, then calculating the interdiffusion constant using Stefan-Maxwell's equation, and finally calculating the uptake rate using Maxwell's equation.

Where the condensation coefficient of the vapor is quite small, as for molybdenum and tellurium oxides condensing on the clay loam particles, the initial rate seems to be determined by the combined effect of a slow reaction and slow diffusion of the condensed vapor into the substrate. An equation has been derived which relates the amount of vapor uptake to the condensation coefficient of the vapor onto the substrate material, the equilibrium uptake of the vapor by the substrate material, and the diffusion constant of the condensed vapor in the substrate material. This equation has yet to be tested extensively in other systems, but it does describe successfully the uptake behavior of molybdenum oxide vapor by the clay loam particles.

During this investigation some aspects of the behavior of the systems were observed which have not yet been explained adequately. For

example, the occurrence of minima in the curves showing the initial rates of uptake *vs.* temperature for the molybdenum and tellurium oxide vapors on the clay loam and calcium ferrite particles, respectively. Also, it is surprising that the high rate of uptake of the molybdenum and tellurium oxide vapors on calcium ferrite and the rubidium oxide vapor on clay loam do not decrease greatly at temperatures below the melting points of the substrates. Where the rate of diffusion in the solid state is so much slower than in the liquid, it might be expected that the rate-controlling mechanism would change to one governed by the slow diffusion rate, and the uptake rate would show a corresponding decrease.

Literature Cited

(1) Adams, C. E., Balkwell, W. R., Quan, J. T., U. S. Naval Radiological Defense Laboratory, **USNRDL-TR-67-98** (June 13, 1967).
(2) Adams, C. E., Balkwell, W. R., Quan, J. T., U. S. Naval Radiological Defense Laboratory, **USNRDL-TR-67-134** (September 26, 1967).
(3) Adams, C. E., Quan, J. T., Balkwell, W. R., **NRDL-TR-68-100** (July 16, 1968).
(4) Bedford, R. G., Jackson, D. D., Lawrence Radiation Laboratory, **UCRL-12314** (Jan. 20, 1965).
(5) Berkowitz, J., Inghram, M. G., Chupka, W. A., *J. Chem. Phys.* **26,** 842 (1957).
(6) Burns, R. P., DeMaria, G., Drowart, J., Grimley, R. T., *J. Chem. Phys.* **32,** 1363 (1960).
(7) Crank, J., "The Mathematics of Diffusion," pp. 88-91, Oxford University Press, London, 1956.
(8) Fuchs, N. A., "Evaporation and Droplet Growth in Gaseous Media," p. 1, Pergamon, New York, 1959.
(9) Green, H. L., Lane, W. R., "Particulate Clouds: Dusts, Smokes and Mists," 2nd ed., p. 97, Van Nostrand, Princeton, 1964.
(10) Kleinberg, J., Argersinger, W. J., Griswold, E., "Inorganic Chemistry," p. 443, Heath, Boston, 1960.
(11) Norman, J. H. *et al.*, General Atomic Division, General Dynamics Corp., *OCD Rept.* **GA-6094** (Jan. 29, 1965).
(12) Norman, J. H., Winchell, P., Staley, H. G., Gulf General Atomic Inc., *USNRDL Rept.* **GA-8472,** 21 (Jan. 31, 1968).
(13) Norman, J. H., Staley, H. G., Gulf General Atomic Inc., *Rept.* **GA-7247** (June 30, 1966).
(14) Purnell, H., "Gas Chromatography," pp. 47-49, Wiley, New York, 1962.

Received December 9, 1968. Research sponsored by the U. S. Atomic Energy Commission Contract AT(49-7)-163 and by the Defense Atomic Support Agency.

The Retention of Iodine by Pyrolytic Carbon-Coated Nuclear Fuel Particles

SIDNEY LANGER, C. C. ADAMS, E. E. ANDERSON, J. N. GRAVES, and T. YAMAGUCHI

Gulf General Atomic Incorporated, San Diego, Calif. 92112

The retention of fission product iodine and xenon by unirradiated and irradiated pyrolytic-carbon-coated (Th,U)C_2 fuel particles has been studied in annealing experiments and has been compared with similar studies of the release (or retention) of barium and strontium. The objective was to study the effects of irradiation on the retention of the two types of fission products and to determine the mechanism of release which could account for the observed behaviors. In both unirradiated and irradiated particles, iodine and xenon were found to be retained highly by the impervious isotropic pyrolytic coating which was unaffected by the irradiation. In contrast, the fuel kernel which controls the release of the metallic species is damaged severely by the irradiation, resulting in a marked decrease in its ability to retain the metals.

The retention of iodine, the noble gases, and metallic fission products by pyrolytic carbon-coated nuclear fuel particles is of interest to reactor programs using particulate fuels. This paper reports primarily on the retention of fission product iodine and xenon but also on the release of barium and strontium, by pyrolytic carbon-coated (Th,U)C_2 fuel particles considered for use in high temperature gas-cooled reactors (HTGRs). Emphasis is placed on the markedly different retentions of the gases and the metals by the coated particles, and reasons for the different behaviors are suggested. However, this paper is appropriate to this volume only in a negative sense since the results of this study emphasize the excellent retention characteristics of pyrolytic carbon coatings for iodine and the fission gases.

The use of coated particles as fuels in HTGRs has been discussed by Jaye and Goeddel (*5*), while an extensive survey of coated fuels is given in Ref. 2. The particle preparation, coating, and irradiation performance have been reviewed by Goeddel and Siltanen (*4*), who also provide an extensive bibliography of studies on particulate fuels. Studies of the release of fission gases from pyrolytic carbon-coated fuel particles have been reported in a series of papers by Reagan *et al.* (*10, 11, 12*).

In the present work, the releases of iodine and xenon from both unirradiated fuel particles and particles irradiated to high burnup ($\leqslant$ 24% FIMA) were studied in annealing experiments at 1100° and 1300°C. to determine the effects of irradiation on the release. [FIMA = fissions per initial metal (U + Th) atom. The fuel particles in power reactor concepts utilizing particulate nuclear fuels generally operate in the range 900°–1300°C. with a maximum "hot spot" temperature of 1400°C.] These data are compared with the results of similar studies on the nuclides ^{140}Ba and ^{91}Sr. In addition, a material balance was obtained between the amounts of xenon detected by release measurements and the inventory retained in the particles after the high temperature anneals.

Experimental

The fuel particles used in these studies were typical pyrolytic carbon-coated thorium–uranium dicarbide, $(Th,U)C_2$, microspheres. The kernels, $\sim$ 200μ in diameter, were prepared from ThO_2, UO_2, and C and converted to the carbide at temperatures below 2200°C., followed by a spheroidization above the melting point, 2450°–2500°C. The bare kernels were coated with a 30–50μ layer of low density ($\sim$ 1.0 gram/cm.^{3}) "buffer" pyrolytic carbon, followed by a 40–70μ layer of high density ($\sim$ 2.1 grams/cm.^{3}) isotropic pyrolytic carbon in a fluidized bed. The particle preparatory work has been described previously (*2, 4*). Coatings of the type described [known as BISO coatings, the name given to Gulf General Atomic particles having buffer and pyrolytic (isotropic) carbon coatings] have been shown to have excellent retention characteristics for the noble fission gases and iodine. Typical photomicrographs of unirradiated and irradiated BISO coated particles are shown in Figure 1 (*8*). The fuel kernel, the buffer layer, and the outer isotropic pyrolytic carbon layer are all clearly visible. The clearly evident damage to the kernel caused by irradiation is in contrast to the undamaged appearance of the coating. These physically observable effects are responsible for the changes in retention properties reported in this paper.

In these studies, samples of approximately 20 irradiated or 5000 unirradiated particles were leached with hot 13*M* HNO_3 for about 1 hour to remove surface contamination (uranium) and then activated at ambient temperatures in the TRIGA reactor to produce inventories of the

short lived nuclides ^{135}Xe (9.1 hours), ^{133}I (21 hours), ^{140}Ba (12.8 days), and ^{91}Sr (9.7 hours). [In this paper the term activated is used to describe short, low level irradiations ($\sim 10^{13}$ fissions) sufficient to produce adequate inventories of the nuclides being studied but contributing insignificantly to the burnup of the uranium. "Irradiated" particles, on the other hand, have undergone long term irradiations sufficient to have "burned up" to $\sim 24\%$ of the initial metal (U + Th) atoms. This burnup level is approximately equivalent to 240,000 MWD/ton of heavy metal.] Each sample was permitted to decay for about 24 hours to reduce the activity of very short lived fission products and to permit most of the ^{135}I to decay to ^{135}Xe. In contrast, approximately half of the ^{133}I was still present at the start of the anneal. The particles were loaded into a graphite crucible and transferred to a graphite-tube King furnace (*6*) for the annealing studies. The samples were annealed for about 15 hours at 1100° and 1300°C., during which time the ^{135}Xe (daughter of ^{135}I) released by the sample was purged from the furnace with helium and collected in a liquid nitrogen-cooled charcoal trap; the ^{133}I was caught on a copper-plated stainless steel cold finger. The releases were determined by counting the trap and the material leached from the cold finger. [The annealing periods were determined by the times required to release easily measurable amounts of the nuclides at low temperatures and major fractions of the nuclides at high temperatures.]

The anneals were interrupted at 1-, 5-, and 8-hour intervals to transfer the particles to fresh graphite crucibles (and to change cold fingers).

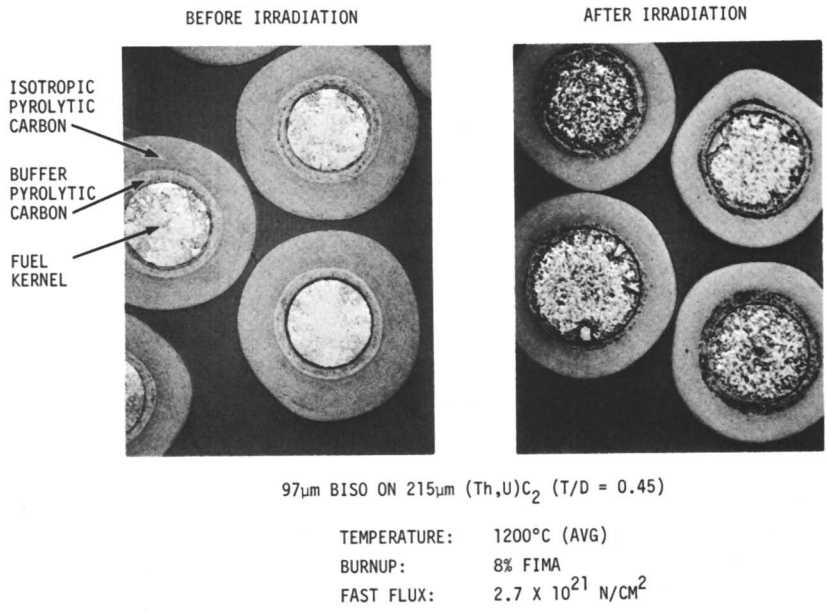

Figure 1. Photomicrographs of typical BISO coated fuel particles before and after irradiation (60×)

Table I. Fractional Release from

Sample No.	*Burnup, % FIMA*	*Annealing*	
		Temp., °C.	*Time, hrs.*
3023-77E	0	1100	15
	8.5	1100	1.5
		1100	4.6
		1100	8.0
		1100	15.0
	0	1300	15
	8.5	1300	2.0
		1300	5.2
		1300	8.0
		1300	14.9
2824-9E	0	1100	15
	24	1100	1
		1100	5
		1100	15
		1600	2.5
	0	1300	15
	24	1300	1
		1300	5
		1300	15
		1600	2.5

[a] Typical values for similar fuel particles.

This procedure made it possible to measure concomitantly the releases of ^{140}Ba and ^{91}Sr from the particles since at the temperatures of the anneals these nuclides are highly retained as sorbed species by the graphite crucibles (*13*). The release of the metallic nuclides is determined by gamma counting the empty crucibles.

In addition to studying the release from unirradiated particles, two samples of particles that had been irradiated previously were also studied to determine the effect of burnup (if any) on the release. One sample [Sample No. 3023–77E (*see* Table I)] had undergone 8.5% FIMA burnup at 1200°C., while the other sample [Sample No. 2824–9E (*see* Table I)] had sustained 24% FIMA burnup at 1230°C. in the Engineering Test Reactor (ETR). Both samples had "cooled" for a sufficient time to ensure that the inventories of the nuclides being studied had decayed to very low levels. Activation of these samples in the TRIGA reactor produced fresh inventories of the ^{135}Xe, ^{133}I, ^{140}Ba, and ^{91}Sr. These inventories (before the samples were annealed) could be calculated for the unirradiated samples from the ^{140}La activity and for the irradiated samples from the residual fissionable atom concentration (after the ETR irradiation), the effective cross sections and fission yields, and the TRIGA power level during activation.

Pyrolytic Carbon-Coated Fuel Particles

Fractional Release			
^{135}Xe	^{133}I	^{140}Ba	^{91}Sr
$<10^{-5}$	$<10^{-4}$	$(5 \times 10^{-4})^a$	$(<1.0 \times 10^{-3})^a$
—	—	—	2.6×10^{-3}
—	—	—	4.4×10^{-2}
—	—	—	5.3×10^{-2}
$<1.7 \times 10^{-5}$	$<3.2 \times 10^{-4}$	$<9.0 \times 10^{-4}$	7.5×10^{-2}
$<10^{-5}$	$<10^{-4}$	—	—
—	—	6.0×10^{-3}	2.4×10^{-1}
—	—	3.4×10^{-2}	2.8×10^{-1}
—	—	8.0×10^{-2}	3.5×10^{-1}
$<4.4 \times 10^{-5}$	$<7.5 \times 10^{-4}$	1.5×10^{-1}	3.9×10^{-1}
$<10^{-5}$	$<10^{-4}$	$(5 \times 10^{-4})^a$	$(<1.0 \times 10^{-3})^a$
—	—	$<2.0 \times 10^{-3}$	4.0×10^{-3}
—	—	1.7×10^{-2}	3.0×10^{-1}
—	—	5.8×10^{-2}	4.3×10^{-1}
$<6.2 \times 10^{-5}$	$<1.4 \times 10^{-3}$	2.6×10^{-1}	9.4×10^{-1}
$<10^{-5}$	$<10^{-4}$	—	—
—	—	1.6×10^{-1}	5.6×10^{-1}
—	—	5.6×10^{-1}	8.1×10^{-1}
—	—	7.2×10^{-1}	9.8×10^{-1}
$<5.6 \times 10^{-5}$	$<5.8 \times 10^{-4}$	—	~ 1.0

The releases of the metallic nuclides ^{140}Ba and ^{91}Sr were known to be of the order of 10^{-1} fraction in 15 hours at about 1400°C. for unirradiated particles (*3*), and therefore no measurements of barium and strontium releases were made on the unirradiated particles. For the irradiated material, the releases of these metallic species were high and readily detectable; however, in none of the samples, either irradiated or unirradiated, was the release of ^{133}I or ^{135}Xe detectable after 15 hours at temperature, and thus only an upper limit could be set for the release. To aid in estimating the upper limit of gaseous release for the highly irradiated sample (24% FIMA), the temperature of the furnace was increased to 1600°C. for 2.5 hours to enhance the release.

Results

The results of the release measurements are given in Table I as a function of temperature and annealing time. For the unirradiated samples, typical release data for the metallic nuclides are included for comparison. The data clearly show that the releases of iodine and xenon have been unaffected by irradiation. The releases of barium and strontium, on the other hand, have been enhanced by a factor of about five at 8.5% FIMA and 10 at 24% FIMA. These data are interpreted in the

following section in terms of a diffusion model for the release of fission products from coated spherical fuel particles.

To obtain a material balance for the iodine (—*i.e.*, to ensure that the balance of the iodine was actually retained in the microspheres), the particles were burned at 1000°C. in a 10% oxygen/90% argon atmosphere one day after the completion of the annealing experiments. By this time, most of the ^{133}I (21 hours) had decayed to ^{133}Xe. The gases released in the burning operation were collected in a liquid nitrogen-cooled charcoal trap that was gamma counted to determine the ^{133}Xe content. The retention of ^{133}I by the 24% FIMA particles that were annealed at 1100°C. was 94%; ^{133}I retention by those annealed at 1300°C. was 95%. Since release from intact particles at ambient temperatures, both during and after the irradiation, does not occur, these percentage values are equivalent to 100% retention within the uncertainty of the measurements.

Release data for the 8.5% FIMA particles indicated lower fractional releases of metallic nuclides than for the 24% FIMA particles. In addition, the low releases of iodine and xenon were supported by direct gamma spectroscopy on one sample of the annealed particles (8.5% FIMA, 1300°C. anneal), which showed virtually quantitative retention of ^{133}I. Direct gamma counting was not possible for the higher burnup particles because of the high level of background activity. Finally, oxidative destruction of the 8.5% FIMA particles and analysis of the effluent traps for ^{133}Xe confirmed essentially 100% retention of ^{133}I and ^{133}Xe.

Discussion

Postactivation annealing fission product release data can be analyzed on the basis of a model that assumes the release to be a diffusion-controlled process from a spherical particle. The release is limited by diffusion either in the kernel or in the coating. This model is discussed by Norman and Winchell (*9*) in another chapter in this volume.

Numerous studies by other workers (*1, 10*) have shown that the releases of iodine and the noble-gas fission products from pyrolytic carbon-coated fuel particles are controlled by diffusion of these nuclides through grain boundaries, cracks, and defects in the isotropic pyrolytic carbon coating. When coatings are intact, however, the release of these fission product nuclides is low. However, the pyrolytic carbon coating constitutes only a delaying barrier to the metallic nuclides barium and strontium through which they diffuse with diffusion coefficients of the order of 10^{-9} cm.^{2}/sec. (at $\sim$ 1400°C.). The steady-state release of these metallic nuclides is controlled instead by diffusion out of the fuel kernel,

where the diffusion coefficient D is probably $< 10^{-14}$ cm.^{2}/sec. at 1400°C. The diffusion coefficient is related to the reduced diffusivity D' by the equation $D' = D/r^2$, where r is the effective radius of the releasing grain. Extensive data supporting this mechanism of fission product release will be published elsewhere (7). [The steady-state release from the fuel particle, which is controlled by the kernel in a postactivation experiment, should not be confused with the release of those nuclides to the coolant in a reactor, which is probably controlled by the process of diffusion through a thick web of graphite.]

Since the diffusion-controlled mechanisms discussed above satisfactorily explain postactivation annealing fission product release data, it is of interest to examine the effects of irradiation in terms of these mechanisms. The releases of the metallic species, which are controlled by the fuel kernel, are increased by irradiation, indicating that damage to the kernel has resulted from the irradiation (perhaps by a decrease in the effective radius of the releasing grain). The coating of the fuel particle, on the other hand, is not damaged by irradiation and continues to constitute an effective barrier to the release of iodine and xenon. This interpretation, while perhaps somewhat simplified, is supported by the appearance of highly irradiated fuel particles, which show extensive porosity of the fuel kernel while the coating appears to be unchanged (*see* Figure 1).

Conclusions

Postactivation annealing fission product release measurements have shown that the excellent retention of iodine and noble fission gases by pyrolytic carbon-coated fuel particles is unaffected by irradiation up to 24% FIMA. These data are interpreted as indicating that the pyrolytic carbon coatings remain undamaged by these high levels of irradiation.

Similar measurements on the alkaline earth fission products have shown increased releases that may depend functionally on the level of irradiation. The increased releases may be interpreted as indicating that damage to the fuel kernel has occurred since the kernel has been shown to control the steady-state release of these metals.

Acknowledgments

The authors thank C. S. Luby of the Metallurgy Department of Gulf General Atomic Incorporated for supplying the photomicrographs in Figure 1.

Literature Cited

(1) Bromley, J., *J. Brit. Nucl. Energy Soc.* **3** (4), 99 (1964).
(2) European Atomic Energy Community (Euratom), *Proc. Conf. Fuel Cycles—High Temp. Gas-Cooled Reactors, Brussels* (June 10-11, 1965).
(3) Fort St. Vrain Nuclear Generating Station, Preliminary Safety Analysis Report, Public Service Company, Denver, Colo. (Sept. 1966).
(4) Goeddel, W. V., Siltanen, J. N., *Ann. Rev. Nucl. Sci.* **17**, 189 (1967).
(5) Jaye, S., Goeddel, W. V., *Nucl. Eng. Design* **7**, 283 (1968).
(6) King, A. S., *Astrophys. J.* **28**, 335 (1908).
(7) Langer, S., Adams, C. C., Graves, J. N., to be submitted to *Nucl. Sci. Eng.*
(8) Luby, C. S., *Nucl. Appl.* **3**, 728 (1967).
(9) Norman, J. H., Winchell, P., Roos, B. W., ADVAN. CHEM. SER. **93**, 13 (1969).
(10) Reagan, P. E., Carlsen, F. L., Carroll, R. M., *Nucl. Sci. Eng.* **18**, 301 (1964).
(11) Reagan, P. E., Morgan, J. G., Sisman, O., *Nucl. Sci. Eng.* **23**, 215 (1965).
(12) Reagan, P. E., Beatty, R. L., Long, Jr., E. L., *Nucl. Sci. Eng.* **28**, 34 (1967).
(13) Zumwalt, L. R., Anderson, E. E., Gethard, P. E., "Materials and Fuels for High Temperature Nuclear Energy Applications," Chap. 9, MIT Press, Cambridge, 1964.

RECEIVED June 21, 1968. Work supported by the U. S. Atomic Energy Commission under Contract AT(04-3)-633.

The Transport of Fission-Product Cesium from Sodium

I. N. TANG, A. W. CASTLEMAN, JR., and H. R. MUNKELWITZ

Brookhaven National Laboratory, Upton, N. Y. 11973

The vaporization of fission-product cesium from liquid sodium into flowing inert gases was investigated at 730°K. The cesium release rate was found to depend on both the liquid depth of sodium and the molecular weight of the inert carrier gases. A general release equation is developed by considering diffusion in both the liquid and gas phases. This equation is shown to represent the experimental results very well. The limiting case of maximum extent of release, expressed in terms of fractional fission-product vaporization as a function of the fraction of sodium vaporized, can often be calculated from thermodynamic considerations.

The possibility of the distribution of radioactive fission products in the environment is of major concern when making safety analyses of nuclear reactors. To predict the fission-product transport rates and the extents of vaporization, an understanding of the fundamental release mechanism is imperative. For instance, recent studies have led to an identification of mass-transfer processes controlling the release of fission-product iodine from molten uranium (*12*) and from solid hyperstoichiometric uranium monocarbide (*2*). The results from these studies make it possible to calculate the time dependence of iodine release from the respective systems.

In considering the operational safety and accident analyses of sodium-cooled fast reactors, similar information on the release of fission products from sodium is needed. Although the extent of vaporization can often be calculated from thermodynamic considerations (*3, 4*), appropriate transport models are required to describe the rate phenomena. In this chapter the results of an analytical and experimental investigation of cesium transport from sodium into flowing inert gases are presented. The limiting case of maximum release is also considered.

Analytical Studies

Transport Model. A general release equation is developed by considering diffusion in both the liquid and gaseous phases. Figure 1 is a sketch of a vessel containing liquid sodium, blanketed by a flowing inert gas and maintained at constant temperature. The assumed cesium concentration profiles for both phases are shown in the sketch. Fick's law of diffusion may be applied to the liquid phase:

$$\frac{\partial C}{\partial t} = D\frac{\partial^2 C}{\partial y^2} \tag{1}$$

If we consider cases where only a small fraction of sodium is vaporized during the time period of interest, the boundary conditions (BC) become

$$\text{BC I.} \quad t = 0, C = C_o \text{ at } 0 < y < l$$

$$\text{BC II.} \quad t > 0, -D\frac{\partial C}{\partial y} = 0 \text{ at } y = 0$$

$$\text{BC III.} \quad t > 0, -D\frac{\partial C}{\partial y} = J_l \text{ at } y = l$$

A stagnant gas layer, through which cesium diffuses, is assumed to exist between the liquid–gas interface and the top edge of the vessel. In addition, a linear concentration gradient within the stagnant gas and a negligible cesium partial pressure at the edge of the vessel are also assumed. Thus, the mass flux in the gas phase may be represented by the following equation:

$$J_g = -\frac{D_{v2}}{RT}\frac{\partial p}{\partial y} \tag{2}$$

Integrating between l and $l + b$ in the direction of diffusion leads to

$$J_g = (D_{v2}/bRT)p_i \tag{3}$$

The equilibrium partial pressure at the interface may be expressed in terms of vapor pressure, activity coefficient, and mole fraction at the liquid surface:

$$p_i = p_2{}^o\gamma_2 x_i \tag{4}$$

Since in practical cases the concentration of fission-product cesium in the sodium coolant is usually very dilute, the molar density of the mixture is essentially that of pure sodium, ρ. It follows that

$$x_i \cong C_i/\rho \tag{5}$$

Substituting Equations 4 and 5 into 3, we obtain

$$J_g = \alpha C_i \tag{6}$$

where

$$\alpha = (D_{v2}/b)\,(p_2{}^o\gamma_2/\rho RT) = \text{constant} \tag{7}$$

Applying the condition of mass flux continuity at the interface—*i.e.*, $J_g = J_l$ at $y = l$—we can rewrite BC III into the following form:

$$\text{BC IIIa.} \quad -D\frac{\partial C}{\partial y} = \alpha C_i \text{ at } y = l$$

The solution to Equation 1 with the given boundary conditions was first obtained by Newman (*9*) and later summarized by Crank (*7*). The final expression, in terms of fractional release, takes the following form:

$$f_2 = 1 - \frac{C}{C_o} = 1 - \sum_{n=1}^{\infty} \frac{2L^2 \exp\,(-\beta_n{}^2 Dt/l^2)}{\beta_n{}^2(\beta_n{}^2 + L^2 + L)} \tag{8}$$

where β_n's are the positive roots of

$$\beta \tan \beta = L \tag{9}$$

and

$$L = l\alpha/D \tag{10}$$

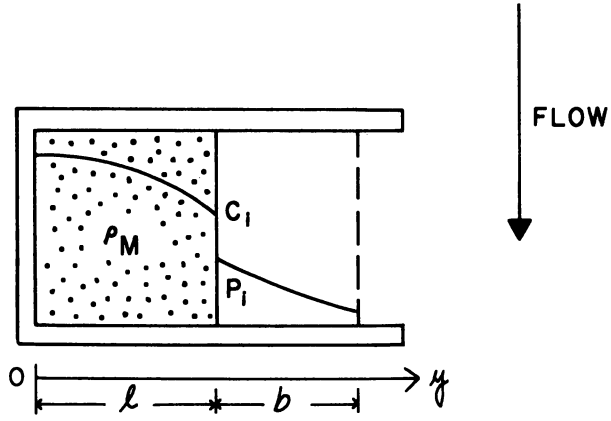

Figure 1. Sketch of vaporization cell showing boundary conditions and hypothetical concentration profiles

The fractional cesium release during any given time period may be calculated, provided that all of the constants in Equation 8 are known. Unfortunately, however, liquid-phase diffusivities can be estimated only to within an order of magnitude. An alternative approach, therefore, is to evaluate the constants D and α from two sets of experimental release data and to use these values to predict the fractional release for other conditions.

Maximum Release. The analytical model described above assumes that the liquid phase is completely stagnant. While this may be true in an ideal laboratory experiment where a small sample can be kept isothermal at a specified temperature, in large scale systems where nonisothermal conditions exist, both natural convection and molecular diffusion will contribute to mass transfer. This combined effect, which is often very difficult to assess quantitatively, will result in an increase in fission-product release rate. Therefore, in making reactor safety analyses, it is desirable to be able to estimate the maximum release under all possible conditions.

In considering the case of maximum release, it is apparent that complete mixing in the liquid phase will lead to a greater release rate than that expected in cases where diffusion operates in two phases. Therefore, consider the case where both the solvent (Na) and the solute (volatile fission product) diffuse through a gas layer of constant thickness. It follows from the solution to Fick's law with appropriate boundary conditions that

$$\ln(1 - f_1) = -\frac{D_{v1}p_1^{\circ}}{RTb_1\rho}\frac{t}{l} \tag{11}$$

and

$$\ln(1 - f_2) = -\frac{D_{v2}p_2^{\circ}\gamma_2}{RTb_2\rho}\frac{t}{l} \tag{12}$$

It can be shown from the Chilton-Colburn analogy (*6*) that under identical flow conditions the ratio of b_1 to b_2 is equal to the 1/3 power of the ratio of the respective diffusivities. Substituting and combining Equations 11 and 12 leads to

$$\frac{\ln(1 - f_2)}{\ln(1 - f_1)}(p_2^{\circ}\gamma_2/p_1^{\circ})(D_{v2}/D_{v1})^{2/3} = A\phi$$

or

$$f_2 = 1 - (1 - f_1)^{A\phi} \tag{13}$$

where

$$A = p_2^{\circ}\gamma_2/p_1^{\circ} \tag{14}$$

$$\phi = (D_{v2}/D_{v1})^{2/3} \tag{14a}$$

Equation 13 reduces to the Rayeigh equation (*3*) when the ratio of the gas-phase diffusivities, ϕ, is unity. Since gas-phase diffusivity is inversely proportional to the square root of the reduced mass, in the case of fission product–sodium systems where sodium has the smallest molecular weight, the above diffusivity ratio is less than unity. Therefore, the Rayleigh equation, which was derived on the basis of equilibrium vaporization, in fact represents an upper limit for the fractional fission-

product release as a function of the fraction of sodium vaporized. The latter quantity may often be estimated by making a heat balance for the system under consideration.

Experimental

Apparatus. A schematic of the apparatus is shown in Figure 2. The main section of the apparatus is a 60-mm. quartz tube with ground joints fused onto both ends. This tube is positioned vertically inside a Marshall 2000-watt tubular resistance furnace. The quartz tube is lined with a length of type 321 seamless stainless steel tubing, 1.5 inches diameter by 0.016 inch wall thickness, to protect the quartz from attack by the alkali metal vapors at high temperatures. The resistance furnace, which is 3 ft. long, has three separately controlled heating zones and is operated with a flat axial temperature profile. A 7/16-inch i.d. nickel crucible with a 1/4-inch diameter by 3/4 inch deep well at the bottom is tightly fitted on the sealed end of a stainless steel tube. A chromel–alumel thermocouple is positioned inside this tube with the beaded end extended into the crucible well. This is used to measure the crucible temperature during an experiment. Before a run, the crucible containing the sample can be withdrawn into a spool-piece located directly below a 5/8-inch

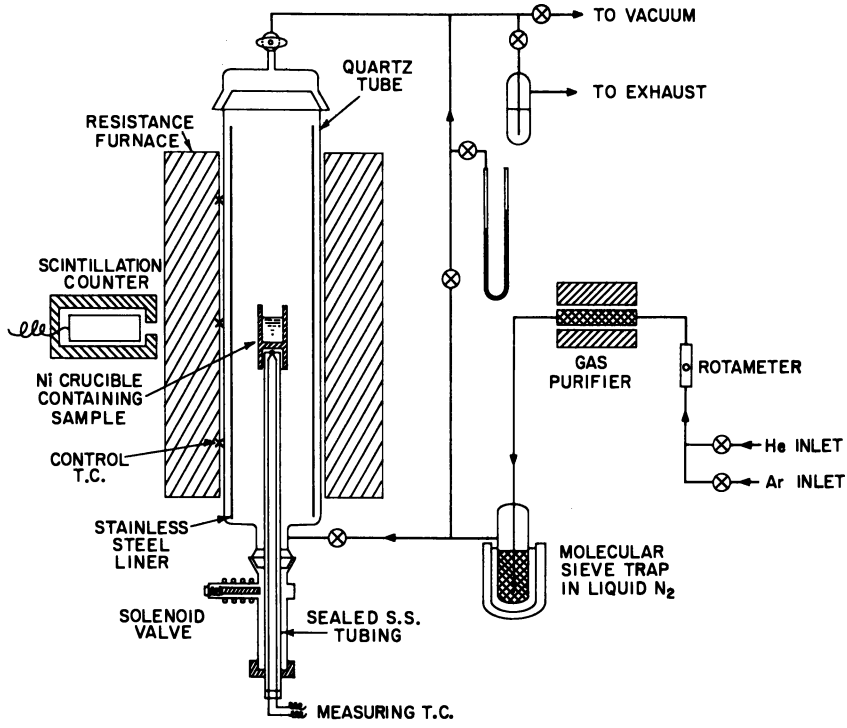

Figure 2. Schematic of the vaporization apparatus

Veeco model SV62 vacuum solenoid valve. This enables the sample to be kept under an inert atmosphere during transfer from a dry box to the apparatus and during the time the apparatus is being evacuated. A scintillation counter, connected to a rate meter and a programmed printer, is sighted on the sample to monitor continuously the ^{137}Cs radioactivity during a run. The remaining part of the apparatus consists of a high vacuum system and a gas purification train also shown in the schematic in Figure 2.

Procedure. Prior to an experiment, an aqueous solution of carrier-free ^{137}Cs chloride is evaporated to dryness inside the crucible. This crucible then is brought inside a dry box, loaded with a weighed piece of purified sodium ($<$ 10 p.p.m. oxygen), mounted on the supporting stainless steel tube, and withdrawn into the spool-piece below the solenoid valve. After removal from the dry box, the solenoid valve is attached to the quartz tube by way of the lower ball joint and then sealed in place. The furnace is brought to a temperature of 730° ± 5°K. while the system is being pumped down to a vacuum of at least 5×10^{-5} torr. After the evacuation, the apparatus is filled with an inert gas, and a predetermined flow rate is set. The solenoid valve is opened, and the crucible is raised into the lower section of the furnace for sample equilibration at a temperature of 150° to 200°C. This equilibration period is usually continued overnight to ensure complete dissolution and conversion of cesium chloride to metallic cesium, thereby forming a homogeneous cesium–sodium solution. (In one run where the cesium–sodium alloy was formed before transfer into the crucible, the equilibration procedure was eliminated.) The experiment is started after the crucible is raised further into the middle section of the furnace. At this time the scintillation counter is sighted directly on the sample by a quick scanning procedure.

Results and Discussion

Vaporization of Pure Sodium. Several vaporization experiments using pure sodium tagged with ^{22}Na were made to check the assumption that a stagnant gas layer exists above the liquid surface up to the edge of the crucible. In this case the following equation (*11*), which takes into consideration a changing liquid level during vaporization, is applicable:

$$b_t^2 - b_o^2 = 2t(D_{v1}/RT\rho)(p_1^o/P_{BM}) \qquad (15)$$

Here P_{BM}, the logarithmic mean pressure of the stagnant gas, may be taken as the total pressure of the system since the vapor pressure of sodium is negligible (p_1^o = 1.60 mm. Hg at 730°K.).

Figure 3 shows the result from a typical experiment carried out with a helium flow of 300 cc./min., an initial liquid depth of 1.25 cm., and an initial gas-phase diffusion path, b_o, of 1.29 cm. Although Equation 15 is quadratic, the initial part of the release curve may be approximated by a straight line, as shown in Figure 3. This arises from the fact that only a small change in gas-film thickness took place initially.

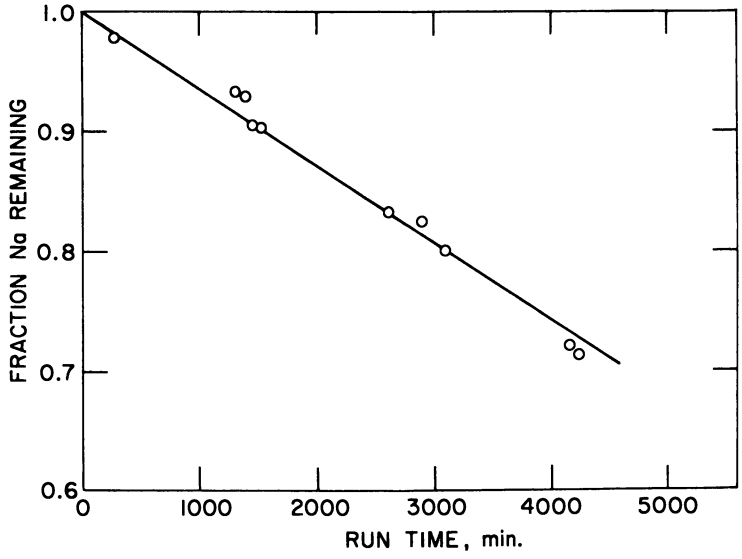

Figure 3. Vaporization of sodium into flowing helium at 730°K.

The gas-phase diffusivity of sodium in helium D_{v1} may then be evaluated from the experimental data by using Equation 15. A value of 1.96 cm.²/sec. was obtained, which compares favorably with 2.11 cm.²/sec. estimated from an equation given by Hirschfelder, Curtiss, and Bird (8), using Lennard-Jones parameters given by Chapman (5). The close agreement obtained here seems to justify the assumption of a stagnant gas layer through which both sodium and cesium diffuse.

Effect of Carrier-Gas Molecular Weight. Studies were also undertaken to determine whether the release phenomenon was controlled by diffusion in the liquid phase, in the gaseous phase, or in both phases. This was accomplished by fixing all the variables except the molecular weight of the carrier gas. The results, shown in Figure 4, were obtained from two sets of experiments employing helium and argon, respectively. If liquid-phase diffusion were predominant, the two sets of release data should have grouped together, thereby showing no dependence on the molecular weight of the carrier gas. On the other hand, taking the results in argon as a basis, the release in helium should follow the dashed line if only a gas-phase resistance were operational. According to Equation 12, the two release curves should be separated from each other by a constant value equal to the ratio of the cesium diffusivity in helium to that in argon—namely,

$$\frac{\ln(1-f)_{He}}{\ln(1-f)_{Ar}} = \frac{(D_{v2})_{He}}{(D_{v2})_{Ar}} = \frac{1.53}{0.43} = 3.56$$

Here the diffusivities were estimated by the method described previously in the text.

The fact that the two release curves show some separation but not enough to account solely for gas-phase diffusion, indicates that the release is actually governed by mass transfer resistances in both phases. This is in qualitative agreement with the transport model presented above. The quantitative agreement will be demonstrated in the next section.

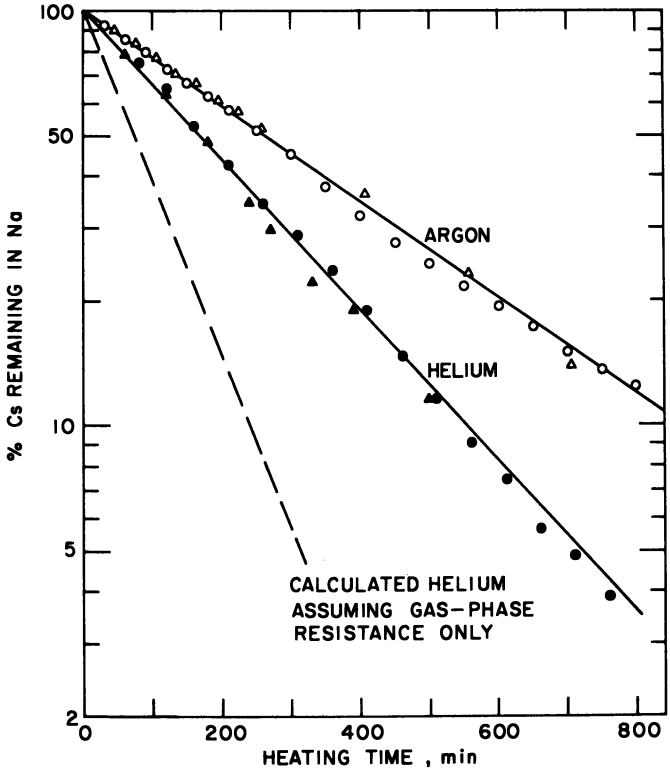

Figure 4. Effect of carrier-gas molecular weight on cesium vaporization rate. The geometric parameters in these experiments are: l = *1.2 cm.*, b = *0.8 cm.*

Comparison of Release Data with Proposed Model. A summary of the cesium release data obtained with helium as carrier gas is shown in Figure 5, where the percentage of cesium remaining is plotted *vs.* heating time on semilogarithmic coordinates. In all of the experiments the flow rate was maintained at 300 cc./min. and the temperature at 730° ± 5°K. The geometric parameters are indicated on each curve. Since only about 5% of the sodium was vaporized in each experiment, the assumption of a stationary liquid-phase boundary is justified.

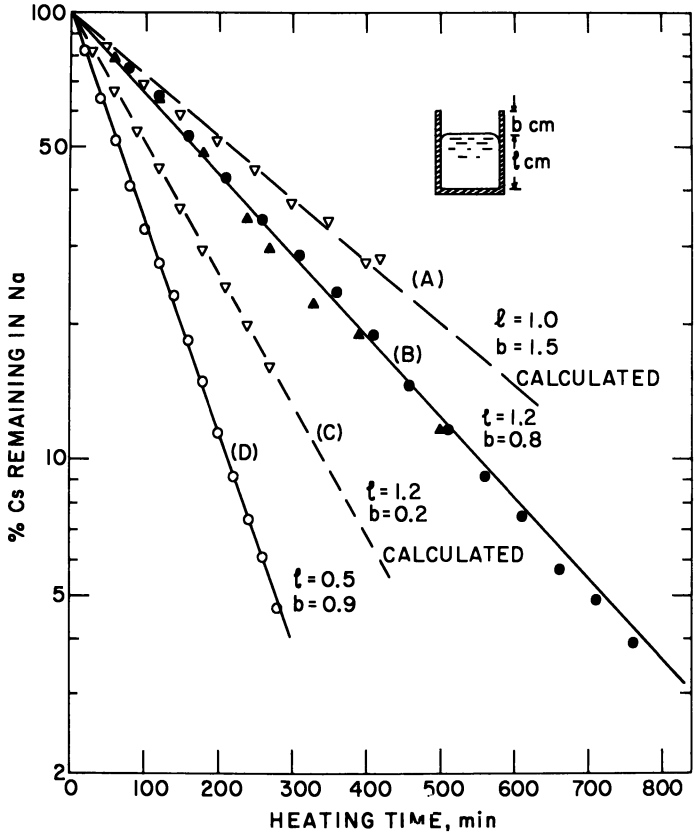

Figure 5. Summary of the results from cesium vaporization experiments carried out at 730°K. in flowing helium

The constants D and α were evaluated from two sets of the experimental release data using Equation 8. Although Equation 8 is in the form of an infinite series, numerical evaluation readily shows that the first term predominates even for very short times. This is also obvious from the plot in Figure 5 where it can be seen that a straight line may be drawn through the points starting from $t \cong 0$. Thus, the slopes of the lines taken after a reasonably short time will yield the exponential power, $-\beta^2 Dt/l^2$, where β is the first positive root of Equation 9.

The two lines B and D, plotted in Figure 5, were used to evaluate the constants. The ratio of the two slopes gives a value of 1.419 for β_B/β_D. It follows, by combining Equations 7 and 10 and taking the ratio of the resulting equation for the two experiments, that

$$L_B/L_D = (l_B/l_D)(b_D/b_B) = 2.76$$

The values of the L's and β's are obtained by trial-and-error used in

conjunction with the tabulated roots (*1*) for Equation 9. Once the L's and β's are known, it is simple to calculate the diffusivity, D, and the α's from the slopes of the lines and Equation 10. The diffusivity evaluated by this method is 8.1×10^{-5} cm.^{2}/sec. A number of correlation methods are available for estimating diffusivities in liquid metals (*9*). Using the various methods, the estimated cesium diffusivity in liquid sodium at 730°K. ranges from 7 to 11 $\times$ 10^{-5} cm.^{2}/sec. It is evident that the procedure used to evaluate D from the experimental data does not simply result in the evaluation of an adjustable parameter but gives a reasonable estimation of the liquid-phase diffusivity.

Using the estimated α's, D, and Equation 8, we computed the fractional cesium release as a function of time for two other cases with liquid depths of 1.0 and 1.2 cm. and gas depths of 1.5 and 0.2 cm., respectively. The predicted releases are shown by dashed lines A and C. Experiments were then carried out employing these geometric parameters. The experimental results (open triangles) agree very well with the theoretical lines.

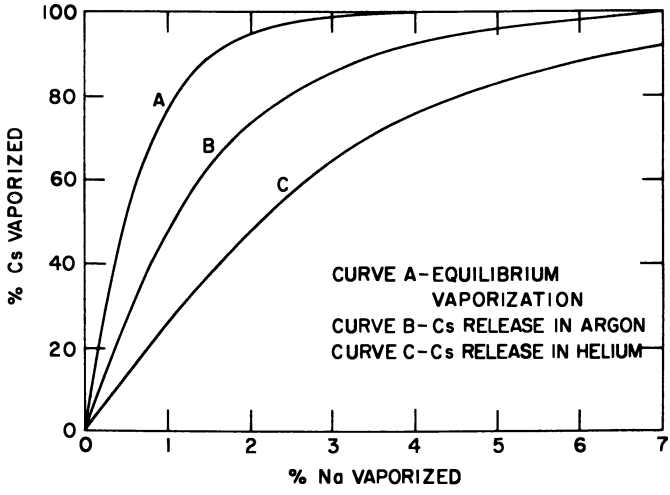

Figure 6. Comparison of equilibrium and nonequilibrium vaporization

Equilibrium Vaporization. The cesium release results presented in this chapter may also be used to demonstrate our earlier conclusion that equilbirium vaporization represents the upper limit for the fractional fission-product release as a function of sodium vaporization. Figure 6 shows three cesium release curves. Curve A was calculated from the Rayleigh Equation in conjunction with the partial molar excess free energy of mixing of infinitely dilute cesium–sodium solutions reported

earlier (3), while Curves B and C were converted from the release data given in Figure 4. The equilibrium vaporization represented by Curve A is a limiting case for maximum cesium release.

Nomenclature

A = vaporization parameter defined by Equation 14
b = gas-layer thickness
C = liquid-phase molar concentration of cesium
D = liquid-phase diffusivity of cesium
D_v = gas-phase diffusivity
f = fractional release
J = mass flux
L = a dimensionless parameter defined by Equation 10
l = liquid depth
P = total gas pressure
p = partial pressure
p_o = vapor pressure
R = gas-law constant
T = absolute temperature
t = release time
x = mole fraction
y = diffusion distance

Subscripts

1 = sodium
2 = cesium
g = gas-phase
l = liquid-phase
i = gas-liquid interface
o = initial

Greek Letters

α = a parameter defined by Equation 7
β_n = roots of Equation 9
γ = activity coefficient of cesium in sodium at infinite dilution
ρ = molar density of sodium
ϕ = gas-phase diffusivity ratio defined by Equation 14a

Literature Cited

(1) Carslaw, H. S., Jaeger, J. C., "Conduction of Heat in Solids," p. 491, 2nd ed., Oxford, 1959.
(2) Castleman, Jr., A. W., Munkelwitz, H. R., *Trans. Am. Nucl. Soc.* **11**, 155 (1968).
(3) Castleman, Jr., A. W., Tang, I. N., Mackay, R. A., "Alkali Metal Coolants," pp. 729-741, IAEA, Vienna, 1967.
(4) Castleman, Jr., A. W., Tang, I. N., *Trans. Am. Nucl. Soc.* **10**, 494 (1967).
(5) Chapman, T. W., *A.I.Ch.E. J.* **12**, 395 (1966).
(6) Chilton, T. H., Colburn, A. P., *Ind. Eng. Chem.* **26**, 1183 (1934).
(7) Crank, J., "The Mathematics of Diffusion," p. 56, Oxford, 1964.

(8) Hirschfelder, J. O., Curtiss, C. F., Bird, R. B., "Molecular Theory of Gases and Liquids," p. 539, Wiley, New York, 1964.
(9) Newman, A. B., *Trans. A.I.Ch.E.* **27**, 203 (1931).
(10) Pasternak, A. D., Olander, D. R., *A.I.Ch.E. J.* **13**, 1052 (1967).
(11) Sherwood, T. K., Pigford, R. L., "Absorption and Extraction," p. 17, McGraw-Hill, New York, 1962.
(12) Tang, I. N., Castleman, Jr., A. W., *Trans. Am. Nucl. Soc.* **10**, 720 (1967).

RECEIVED December 6, 1968. Work performed under the auspices of the U. S. Atomic Energy Commission.

Radioactive Fallout in Astronomical Settings

Plutonium-244 in the Early Environment of the Solar System

P. K. KURODA

University of Arkansas, Fayetteville, Ark. 72701

The half-life of ^{244}Pu (8.2×10^7 years) is short compared with the age of the earth (4.5×10^9 years), and hence this nuclide is now extinct. However, the time interval (Ξ) between the element synthesis in stars and formation of the solar system may have been comparable with the half-life of ^{244}Pu. It has been found recently in this laboratory that various meteorites contain excess amounts of heavy xenon isotopes, which appear to be the spontaneous fission decay products of ^{244}Pu. The value of Ξ calculated from the experimental data range between 1 to 3 $\times$ 10^8 years. The process of formation of the solar system from the debris of supernova is somewhat analogous to the formation of fallout particles from a nuclear explosion.

In 1952 Harold C. Urey (*19*) made the following statement:

Dr. Edward Teller remarked recently that the origin of the earth was somewhat like the explosion of the atomic bomb: the physical effects are often temporary, but the chemical effects, such as radioactive and non-radioactive elements, remain. It is possible by a study of these substances to learn much about the bomb, and also about the origin of the earth.

We have attempted to follow Urey's suggestion and maintained two research projects side by side in our laboratories during the past decade: (a) studies on the debris from the nuclear weapons tests, and (b) studies on the origin of the earth and the solar system.

In pursuing a research problem as complex as this, it was felt desirable to have encouragement from a leading astronomer. The statements by Öpik (*13*) in "The Oscillating Universe" seem to fulfill this requirement. He compares the formation of new stars to meteorological phenomena—a cycle like that of precipitation and evaporation of water on

earth. According to Öpik (*13*), the "clouds" (the nebula) produce brilliant "raindrops" (new born stars), which emerge from a cosmic "rainstorm" (supernova explosion).

Expanding the ideas expressed by these investigators, we attempt in this report to find an analogy between the processes of formation and transport of "hot" single particles from nuclear weapons and the formation of the solar system from the debris of supernova explosions.

Radioactive Fallout in Geophysical Settings

The energy release from an atom bomb equivalent to 20,000 tons of TNT is roughly 8×10^{20} ergs (*7*). The fireball cools rapidly, and according to Freiling *et al.* (*6*), the cooling rate is about 10°K./sec. at 1000°K. Thus, the time interval between the nuclear explosion and condensation of the single fallout particles is somewhat less than one minute. Some of the fission product decay chains have gaseous and volatile members, whose half-lives lie in the range of seconds to minutes. For example:

3.2-min. ^{89}Kr → 15.4-min. ^{89}Rb → 50.4-day ^{89}Sr →

10-sec. ^{91}Kr → 72-sec. ^{91}Rb → 9.7-hr. ^{91}Sr → 58-day ^{91}Y →

16-sec. ^{140}Xe → 66-sec. ^{140}Cs → 12.8-day ^{140}Ba →

In a decay chain such as

$$A \xrightarrow{\beta^-} B \xrightarrow{\beta^-} C \xrightarrow{\beta^-}$$

where A is a gaseous precursor, B is a volatile nuclide such as an alkali metal, and C is a fairly long lived nonvolatile nuclide, the nuclide C will become depleted in single particles if the half-lives of A and B are comparable with the time interval (Ξ) between nuclear detonation and formation of the single particles. Thus, the following relationship should hold:

$$C = C^* + A.\, e^{-\lambda_A \Xi} + B.\, e^{-\lambda_B \Xi} + A \frac{\lambda_A}{\lambda_B - \lambda_A} (e^{-\lambda_A \Xi} - e^{-\lambda_B \Xi}) \qquad (1)$$

where C is the number of atoms of C that should have been present in the particle, C^* is the number of atoms of C found in the particle, A and B are the number of atoms of A and B produced directly from the fissioning nuclide (independent yields expressed in terms of number of atoms), and λ_A and λ_B are the decay constants of A and B, respectively (*4*).

Figure 1 shows some of the single fallout particles collected after the Chinese nuclear explosion on May 14, 1965 (*14*). Figure 2 shows the mass–yield distribution of the fission products in some of the single fallout particles (*5*). The values of Ξ calculated in this manner range from 30–50 sec., as shown in Table I (*4*).

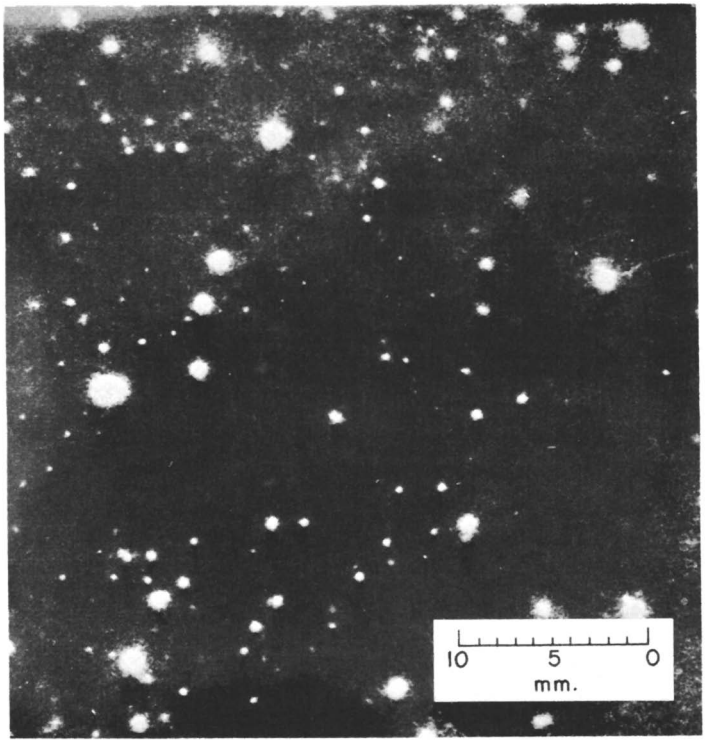

Science

Figure 1. Autoradiograph of single fallout particles collected after the Chinese nuclear explosion, May 14, 1965 (14)
(Copyright 1966 by the American Association for the Advancement of Science)

The eastward movement of the nuclear debris injected into the atmosphere at Lop Nor (90°E and 40°N) can be computed as shown in Figure 3 (*10*). Whenever the fresh nuclear debris completes one cycle around the earth, there is usually a sudden increase in the concentrations of short lived isotopes such as 33-day ^{141}Ce, 50.4-day ^{89}Sr, 65-day ^{95}Zr, as well as the number of single fallout particles in the unit volume of air, as shown in Figures 4 and 5 (*1, 16, 17*).

Radioactive Fallout in Astronomical Settings

In studying astrochemical phnomena, we must depend on the meteorite samples until the samples of moon and other planetary objects become available to us. The time and distance factors involved are enormously large. According to Öpik (*13*), we consider the following sequence of events. Roughly 4.5 billion years ago a supernova explodes at a place within a radius of some 100 light years from the relative location where the solar system is situated now in our galaxy. The fresh

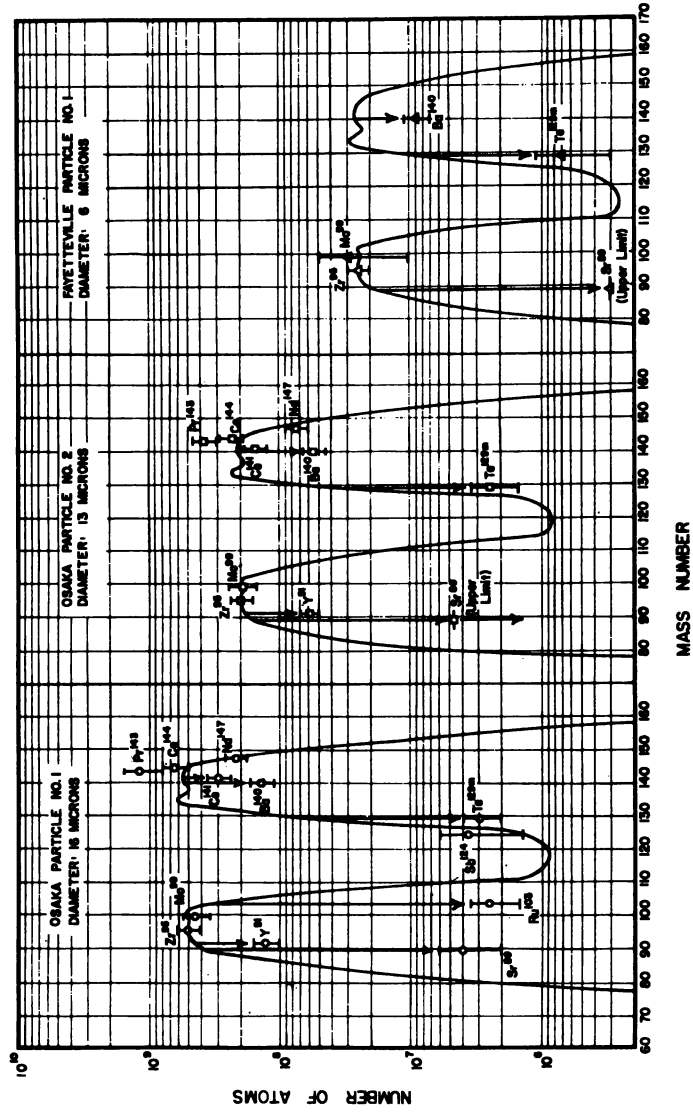

Journal of Geophysical Research

Figure 2. Mass–yield distribution of the fission products in single fallout particles collected at Osaka, Japan and Fayetteville, Ark. after the May 9, 1966 Chinese nuclear explosion (4)

The curves show the general shape of the ^{235}U fission mass–yield curve. The yields at masses 89, 91, and 140 are down because of their gaseous and volatile precursors (see text). The yields at masses 103 and 129 are also low owing to the volatile properties of the elements Ru and Te

debris from the supernova expands at an initial velocity of 1000 miles/sec., collecting interstellar dust and increasing its mass. The explosion of supernova will be visible from nearby stars situated a few thousand light years away, just as the explosion of a supernova in the constellation Taurus was visible on July 4, 1054 A.D. to the Chinese astronomers. Since the distance scale is so large, the 1054 supernova explosion is still visible today as the famous Crab Nebula, 914 years after the explosion. The diameter of the Crab Nebula is now 7 light years, and the "fresh" debris are still expanding at a velocity of some 800 miles/sec.

Table I. Time Interval (Ξ) Between Nuclear Detonation and Formation of Single Fallout Particles

	Ξ, *Seconds*		
Nuclides Used for Calculation	*Osaka Particle 1, 16-μ Diameter*	*Osaka Particle 2, 13-μ Diameter*	*Fayetteville Particle 1, 6-μ Diameter*
$^{140}Ba/^{95}Zr$	36	38	51
$^{91}Y/^{95}Zr$	34	42	N.D.
$^{141}Ce/^{95}Zr$	20	43	N.D.

The "shock wave" of fresh debris from a supernova explosion travels a great distance. For example, it has been calculated that the Crab Nebula will attain a diameter of 70 light years 23,000 years from now; 140 light years in 260,000 years; 210 light years in 1.3 million years; and 280 light years in 4 million years. After that the expanding shell will begin to dissipate because the velocity of expansion drops to about 1–2 miles/sec. (3,600–7,200 miles/hr.), which is the velocity of the molecules of interstellar gas.

An object which is about 300 light years in diameter and which closely resembles the terminal stage of a supernova explosion is visible today in the constellation Orion (the Orion Halo). A number of very bright young stars are located within the Orion Halo, and their ages are estimated to be less than 5–10 million years; obviously their formation was triggered by the "shock wave" of the supernova explosion.

If the sun and the solar system originated under the astronomical conditions described above, the materials used for the solar system must have contained some fresh "debris" from the supernova. Burbidge *et al.* (2) reported in 1956 that the chemical elements heavier than uranium can be synthesized under conditions such as those existing in supernova. Type I supernovae, during their explosion, release 10^{49}–10^{50} ergs of energy. A most remarkable property of the Type I supernova is that their light curve falls off exponentially, decreasing to half its value in 55 ± 1 days; this agrees surprisingly well with the spontaneous fission half-life of ^{254}Cf.

The half-life of ^{254}Cf is unfortunately too short for "tracer" studies of the condensation process of the solar system if we recall that the materials thrown out of the supernova must travel a great astronomical distance and the time period involved is of the order of magnitude of 5 to 10 million years between the supernova explosion and formation of the sun and the solar system.

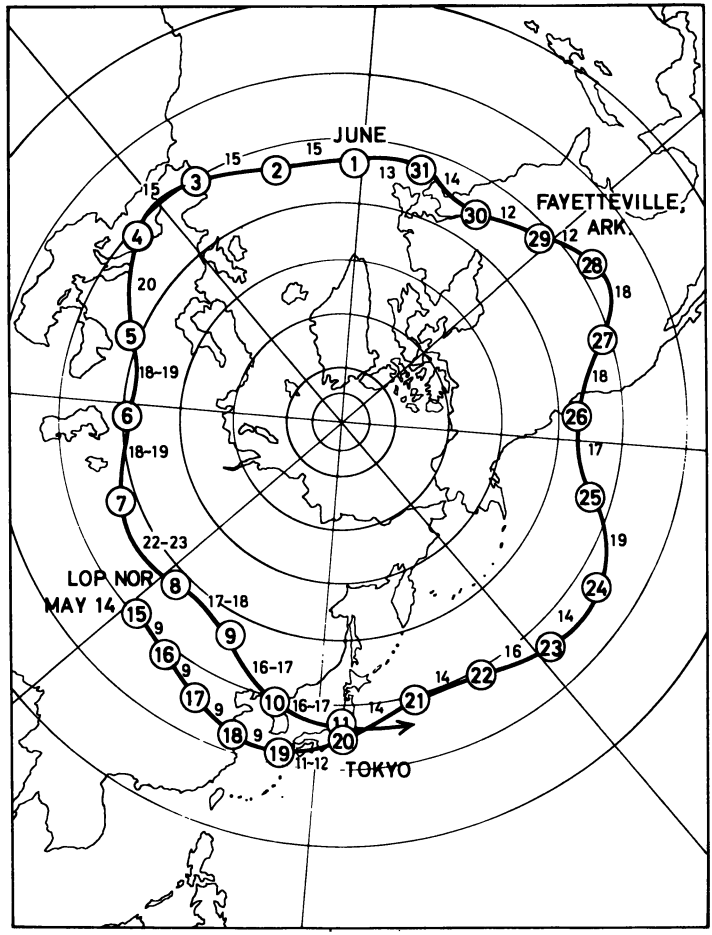

Figure 3. Air trajectory in the Northern Hemisphere during May and June 1965 (10). This figure indicates the air movement at the height of 5650 meters in the troposphere, which is known to give a representative over-all average value of the tropospheric air movement. Circled numbers show dates; numbers between circles show average wind velocities in meters/sec. The fresh debris from the Chinese nuclear explosion of May 14, 1965 travelled eastward and circled the earth

According to Wood (*20*) and Goldstein and Short (*8*) most of the meteorites seem to have cooled at a rate of 1°–10°C./million years in the temperature range between 300° and 700°C. This suggests that the

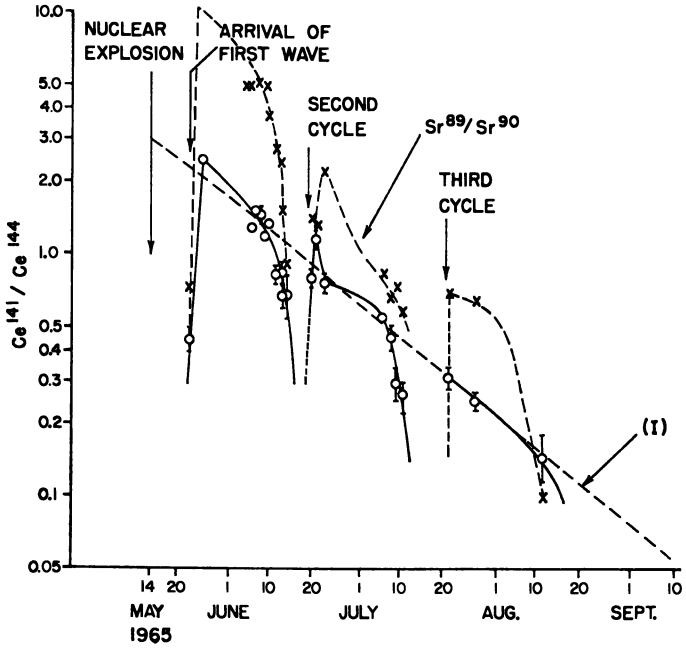

Figure 4. Variation of the $^{141}Ce/^{144}Ce$ and $^{89}Sr/^{90}Sr$ ratios in rain at Fayetteville, Ark., after the nuclear explosion of May 14, 1965 (17).

O: $^{141}Ce/^{144}Ce$ ratio in rain.
X: $^{89}Sr/^{90}Sr$ ratio in rain.

Curve I (which is approximately linear) is given by the equation

$$^{141}Ce/^{144}Ce = \frac{4.6\, e^{-0.0189t}}{\exp(0.0176t) + 0.52}$$

where t = 0 on May 14, 1965 (the date of nuclear explosion). The above empirical equation can be derived theoretically, and the deviation of the experimentally observed Ce isotope ratio data from Curve I illustrates the extent to which the tropospheric atmosphere is not instantly and uniformly mixed; this enables us to follow the eastward movement of the nuclear debris around the world

planetary condensation and cooling process was slow and lasted perhaps several hundred million years. Thus, in studying the condensation process of the solar system using meteorites we must search for a suitable

"tracer," whose half-life is about 100 million years. Such an isotope is found in the decay chain of one of the isotopes of Cf:

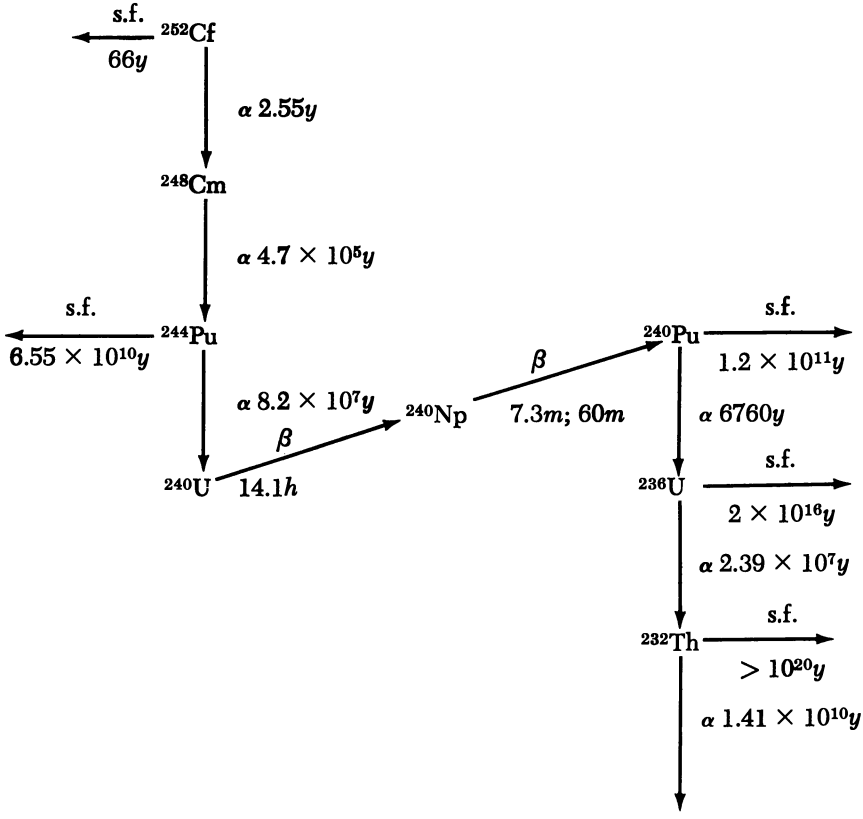

^{244}Pu was discovered in the debris of the Bikini test in 1952, and its decay constants have been redetermined by Fields *et al.* to be as follows: α-decay $(8.18 \pm 0.26) \times 10^{7}y$, spontaneous fission decay $(6.55 \pm 0.32) \times 10^{10}y$ (5).

^{244}Pu may be considered as an ideal "tracer" nuclide for these studies because of its decay characteristics. Its existence or absence in the early solar system can be considered as a crucial test for or against the theories of the synthesis of chemical elements in stars.

The α-decay products of ^{244}Pu are difficult to identify because they all decay to the long lived ^{232}Th. Fortunately, however, the spontaneous fission decay rate of ^{244}Pu is not too slow. Thus, ^{244}Pu produces a reasonably large quantity of stable xenon isotopes such as ^{131}Xe, ^{132}Xe, ^{134}Xe, and ^{136}Xe. Since the abundance of xenon in the earth or in meteorites is extremely low, the production of fissiogenic xenon by ^{244}Pu may produce

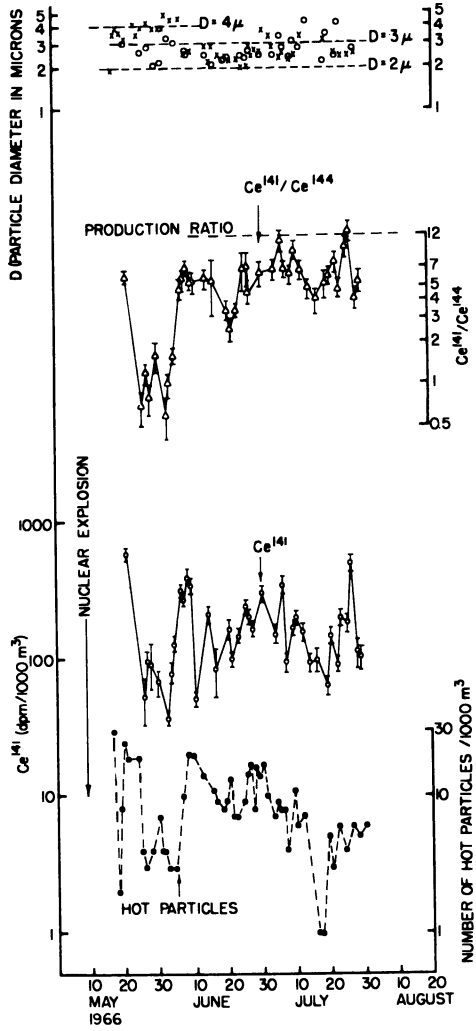

Figure 5. Variation of the number of single fallout particles, ^{141}Ce and $^{141}Ce/^{144}Ce$ ratio in the ground-level air at Fayetteville, Ark. (1)

Radioactivities have been extrapolated back to the time of the bomb explosion (May 9, 1966). Top: Calculated mean diameters of particles. An apparent over-all average diameter (D) *of the particles in the daily air filter samples was calculated by the method first proposed by Baugh* et al. (1). *O: from ^{141}Ce data, X: from ^{95}Zr data. Values of* D *calculated from the ^{141}Ce and ^{95}Zr data do not agree well, owing to the effect of atmospheric fractionation of nuclear debris, but they range between* ca. 2 *and 4μ. The $^{141}Ce/^{144}Ce$ production ratio in the induced fission of ^{235}U by fission spectrum neutrons shown here was calculated from the fission yields given by Zysin* (21)

the so-called xenon isotope "anomalies" either in terrestrial or meteoritic xenon (*9*).

These anomalies are interpreted as being caused by the decay of ^{129}I and ^{244}Pu in the early history of the solar system (*9, 15, 18*).

$$^{129}I \xrightarrow[1.7 \times 10^7 y]{\beta^-} {}^{129}Xe \text{ (stable)}$$

$$^{244}Pu \begin{cases} \xrightarrow[8.2 \times 10^7 y]{\alpha} \text{to } ^{232}Th \\ \xrightarrow[6.55 \times 10^{10} y]{\text{spontaneous fission}} {}^{131\text{-}136}Xe \end{cases}$$

Just as earlier we were able to observe mass–yield distributions of the fission products from the fissionable nuclide used in the Chinese nuclear device, it is possible to "see" part of the mass–yield curve from the fission of ^{244}Pu, which was synthesized originally in a supernova. Figure 6 shows the mass–yield distribution of the excess fissiogenic xenon observed in the meteorite Pasamonte (*15*).

The quantities of excess fissiogenic xenon actually found in the meterorites agree with the calculated value, based on astronomical models described by Öpik (*13*).

According to Öpik (*13*), the supernova explosion sweeps up and compresses into an expanding shell a mass of interstellar gas of the order of 15,000 solar masses, 1000 times greater than the original mass of the supernova. This means that the fresh debris from a supernova is diluted 1000 times by old debris.

If the $^{244}Pu/^{238}U$ ratio in the fresh supernova debris is P and that in the interstellar matter (old debris) is Q, the initial $^{244}Pu/^{238}U$ ratio (α) in the mixture of matter from which the solar system was formed is

$$\alpha = (^{244}Pu/^{238}U)_o = \frac{(P) + (1000)\ (Q)}{1001} \tag{2}$$

Q has been calculated to be 0.0235 (*12*) according to the continuous nucleosynthesis model. Then we have

$$\alpha = 0.025 \tag{3}$$

Similarly, the initial $^{129}I/^{127}I$ ratio (β) in the mixture of matter from which the solar system was formed is

$$\beta = 0.004 \tag{4}$$

The isotopic compositions of xenon extracted from about a dozen achondrites and several chondrites recently have been determined care-

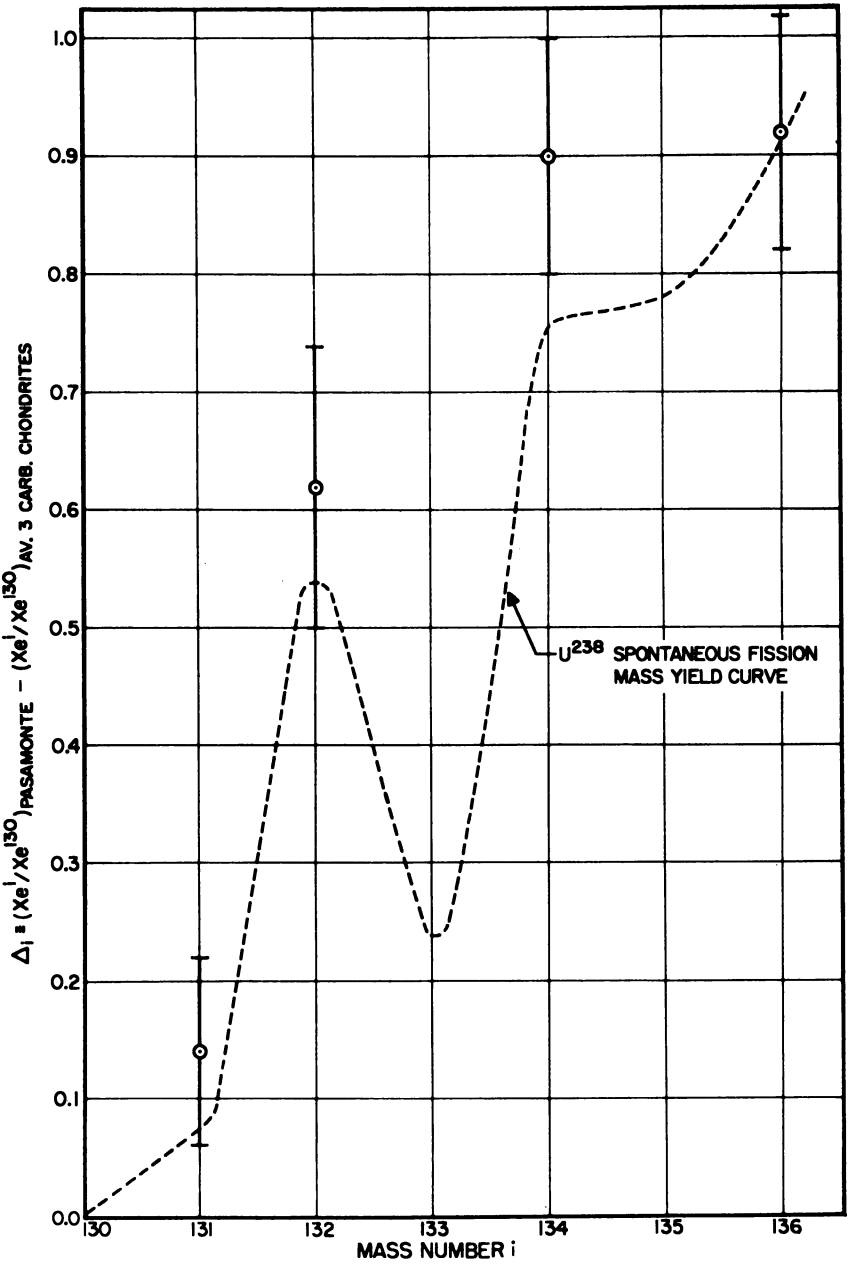

Figure 6. Mass-yield distribution of the fissiogenic xenon isotopes in the meteorite Pasamonte (15).

fully in this laboratory (*11*). All of these meteorite samples contain excess ^{129}Xe and ^{136}Xe. The abundances of I and U in these meteorites have also been determined (*3*). If the excess $^{129}Xe(^{129r}Xe)$ and the excess $^{136}Xe(^{136f}Xe)$ found in the meteorites are the decay products of the extinct nuclides ^{129}I and ^{244}Pu, the ratios $^{129r}/I$ and $^{136f}Xe/U$ should be a function of the time interval (Ξ) between the supernova explosion and "formation" of the meteorites.

The values of α and β can be expressed in terms of ^{129r}Xe and ^{136f}Xe and the amounts of U and I found in the meteorites today. Thus

$$(^{136f}Xe/U)_{obs} = \alpha' \cdot e^{-\lambda_{244}\Xi} \tag{5}$$

and

$$(^{129r}Xe/I)_{obs} = \beta' \cdot e^{-\lambda_{129}\Xi} \tag{6}$$

where

$$\alpha' = 3.4 \times 10^{-4} \text{ cc. STP } ^{136f}Xe/\text{gram U} \tag{7}$$

and

$$\beta' = 7.1 \times 10^{-1} \text{ cc. STP } ^{129r}Xe/\text{gram I} \tag{8}$$

The spontaneous fission of ^{238}U contributes to the production of ^{136f}Xe in the meteorites. This contribution is small, however, and amounts to

$$(^{136f}Xe/U)_{238} = 3.1 \times 10^{-6} \text{ cc. STP/gram U} \tag{9}$$

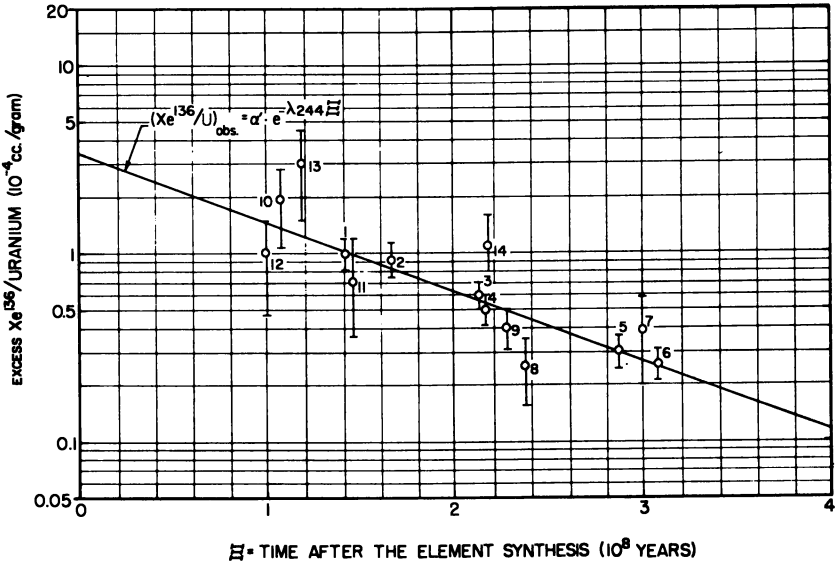

Figure 7. Decay of ^{244}Pu in the early solar system. The meteorite samples used are: (1) Bruderheim, (2) Pena Blanca Springs, (3) Juvinas, (4) Sioux County, (5) Pasamonte, (6) Stannern, (7) Mount Padbury, (8) Nakhla, (9) Lafayette, (10) Richardson, (11) Fayetteville, (12) Abee, (13) Pantar, (14) Petersburg

Some of the experimental results obtained so far are plotted in Figure 7. In preparing this plot, the values of Ξ were calculated first from $(^{129r}Xe/I)_{obs}$ using Equation 6, and the values of $(^{136f}Xe/U)_{obs}$ were then plotted against the values of Ξ.

Figure 7 shows that the experimental data are in reasonably good agreement with Equation 5. The result seems to indicate that the "formation" of the meteorites took place during the time period between 100 to 300 million years after the last supernova explosion.

Table II. Comparison of an Atom Bomb and a Supernova Explosion

	Geophysical Fallout	*Astronomical Fallout*
Bomb	20-kiloton device	supernova
Energy release, ergs	8×10^{20}	up to 10^{50}
"Tracers"	3.2-min. ^{89}Kr 16-sec. ^{140}Xe, etc.	$8.2 \times 10^{7}y$ ^{244}Pu $1.7 \times 10^{7}y$ ^{129}I
Time interval, Ξ	10–60 sec.	$1–3 \times 10^{8}$ years
Velocity of the debris	about 10^{1}–10^{2} miles/hour	10^{3} miles/sec.
Distance covered by debris	circle the earth in few weeks	expand to 300 light years diameter in 5–10 million years
Radius of particles	up to about 17μ	typical meteorite parent body of the size of few 100 km.
Mass–yield curve	entire mass range visible	mass 131–136 region only
Cooling rate	10°K./sec. at 1000°K.	meteorite parent bodies seem to have cooled 5–9°C. per million years

Summary

Table II summarizes some of the features of the radioactive fallout processes in geophysical and astronomical settings. It seems that similarities do exist between the processes of formation of single particles from nuclear explosions and formation of the solar system from the debris of supernova explosion. We may be able to learn much more about the origin of the earth, by further investigating the process of radioactive fallout from the nuclear weapons tests.

Literature Cited

(1) Baugh, J. O., Yoshikawa, K., Kuroda, P. K., *Science* **155**, 1405 (1967).
(2) Burbidge, G. R., Hoyle, F., Burbidge, E. M., Christy, R. F., Fowler, W. A., *Phys. Rev.* **103**, 1145 (1956).
(3) Clark, R. S., Rowe, M. W., Ganapathy, R., Kuroda, P. K., *Geochim. Cosmochim. Acta* **31**, 1605 (1967).
(4) Clark, R. S., Yoshikawa, K., Rao, M. N., Palmer, B. D., Thein, M., Kuroda, P. K., *J. Geophys. Res.* **72**, 1793 (1967).
(5) Fields, P. R., Friedman, A. M., Milsted, J., Lerner, J., Stevens, C. M., Metta, D., Sabine, W. K., *Nature* **212**, 131 (1966).
(6) Freiling, E. C., Crocker, G. R., Adams, C. E., "Radioactive Fallout from Nuclear Weapons Tests," A. W. Klement, Jr., Ed., p. 15, U. S. Atomic Energy Commission, Nov. 1965.
(7) Friedlander, G., Kennedy, J. W., Miller, J. M., "Nuclear and Radiochemistry," p. 493, Wiley, New York, 1964.
(8) Goldstein, J. I., Short, J. M., *Geochim. Cosmochim. Acta* **31**, 1733 (1967).
(9) Kuroda, P. K., *Nature* **187**, 36 (1960).
(10) Kuroda, P. K., Miyake, Y., Nemoto, J., *Science* **150**, 1289 (1965).
(11) Kuroda, P. K., Rowe, M. W., Clark, R. S., Ganapathy, R., *Nature* **212**, 241 (1966).
(12) Kuroda, P. K., "Radioactive Dating and Methods of Low-Level Counting," p. 259, International Atomic Energy Agency, Vienna, 1967.
(13) Öpik, E. J., "The Oscillating Universe," pp. 96–101, Mentor Book, The New American Library of World Literature, Inc., New York, 1960.
(14) Rao, M. N., Yoshikawa, K., Sabu, D. D., Clark, R. S., Kuroda, P. K., *Science* **153**, 633 (1966).
(15) Rowe, M. W., Kuroda, P. K., *J. Geophys. Res.* **70**, 709 (1965).
(16) Thein, M., Johnson, H., Kuroda, P. K., *J. Geophys. Res.* **73**, 3129 (1968).
(17) Thein, M., Kuroda, P. K., *J. Geophys. Res.* **72**, 1673 (1967).
(18) Reynolds, J. H., *Phys. Rev. Letters* **4**, 8(1960).
(19) Urey, H. C., "The Planets: Their Origin and Development," p. ix, Yale University Press, New Haven, 1952.
(20) Wood, J. A., *Icarus* **6**, 1 (1967).
(21) Zysin, Y. A., "Fission Product Yields and Their Mass Distribution," p. 63, Consultants Bureau, New York, 1964.

RECEIVED June 4, 1968. Work supported by the U. S. Atomic Energy Commission and the National Science Foundation.

7

Leaching of Radionuclides at Sedan Crater

JOHN J. KORANDA, JOHN R. MARTIN, and ROBERT W. WIKKERINK

Bio-Medical Division, Lawrence Radiation Laboratory, University of California, Livermore, Calif. 94550

The distribution of tritium and long-lived gamma radioactivity was studied in crater ejecta from the Sedan detonation (July 1962). Tritium concentrations were determined in soil water extracted from crater ejecta samples collected from the surface to 6 feet, and at distances of 3000 feet from the crater from 1966–1968. Tritium distribution was very obviously modified by postshot environmental effects, especially rainfall leaching. Tritium maximum concentrations were found below the strata in which they were deposited. Gamma radionuclides exhibited limited movement in the crater ejecta strata or in preshot soil covered by Sedan ejecta. A subtle leaching of ^{137}Cs was demonstrated by considering the $^{137}Cs/^{54}Mn$ ratios in the ejecta strata.

The Sedan thermonuclear detonation in July 1962 created the largest man-made crater ever produced by a single explosive. Approximately 7.6 million tons of earth were moved by this detonation to produce a crater with a radius of 608 feet and a depth of 323 feet (*9*). Fifty-eight percent of the crater mass or 4.8 million tons of desert alluvium were ejected from the crater during the detonation and distributed somewhat symmetrically around the ground zero point to a distance of 6000–7000 feet (*1*).

The ejecta or earth materials deposited on the desert surface around the crater consisted of large rock missiles on long trajectories, alluvium lifted and ejected in mass (bulk ejecta), and materials which remained airborne for longer times (missile ejecta). Fine particles remaining in the cloud were transported greater distances from the crater and constitute close-in and long range fallout.

Sedan ejecta was laid down as a relatively simple substratum composed of bulk ejected materials covered by a surface layer of missile ejecta which fell at later times. At the edge of the crater, a "hinge"

effect occurred, and a large portion of the ejecta forming the apparent crater lip is actually overturned alluvium, which was covered by missile ejecta (*9*).

The radioactive products of the Sedan detonation were present in the fireball and mixed into the mass of earth moved by the detonation. As the fireball cooled, condensation occurred, and radioactivity in various forms was scavenged by earth materials entering the cloud. Apparently a large fraction of the residual tritium from the explosive was present in the cloud as tritiated steam. This tritiated water was entrained by the ejecta as it fell onto the surrounding land surface, and the resulting postshot substratum thus contained a most significant and mobile tracer. Other radionuclides scavenged by the ejected earth mass constitute another type of tracer for Sedan ejecta.

Field study of Sedan ejecta began in 1965 with the major interest being the fate of residual tritium in the ecological system that has evolved in the Sedan postshot environment. Biological and physical aspects of the movement of radionuclides in this natural laboratory were therefore embraced in the scope of this research. Some of the results of these radiobiological and radioecological studies are reported elsewhere (*5, 6, 7, 8*). This study is concerned with the movement of radionuclides which were deposited in the bulk and missile ejecta in the vicinity of the crater.

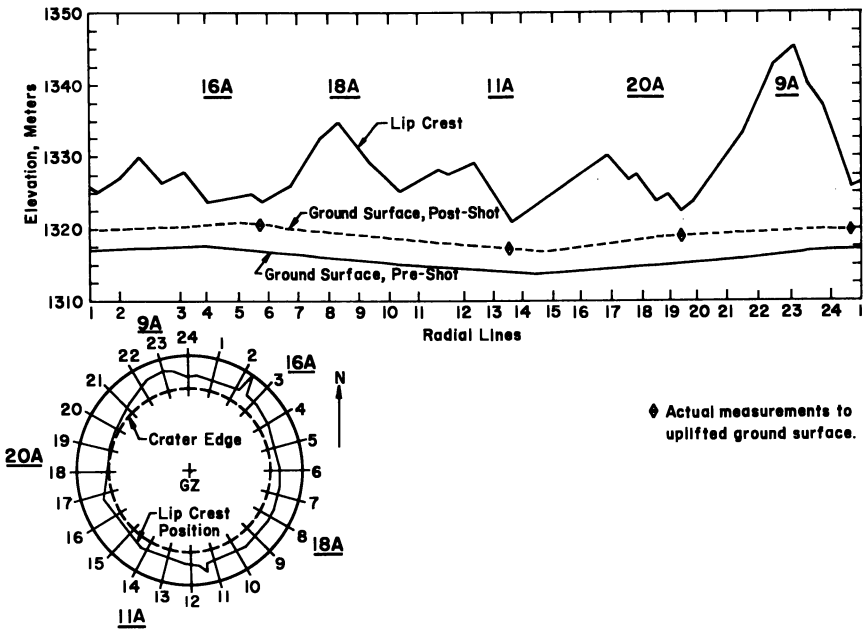

Figure 1. Sedan crater lip profile and sample stations

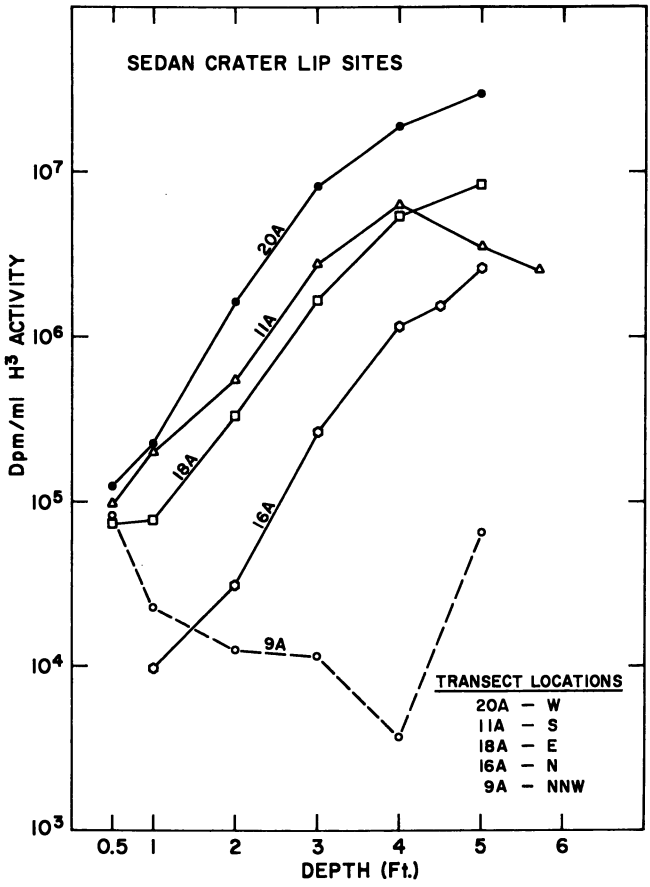

Figure 2. Concentrations of tritium in soil water in Sedan crater lip ejecta (five sites)

Methods

Samples of Sedan ejecta were collected around the crater lip and along several transects of the ejecta field. A 10-inch diameter hole is dug with a conventional posthole auger at each sampling station. Discrete samples are taken at depths of 6 inches, 1 foot and at 1-foot intervals below that to a depth of 5 or 6 feet. The sample is passed through a 2-mm. sieve and collected into 1-quart wide-mouthed Mason jars. Samples are shipped to the Lawrence Radiation Laboratory (Livermore, Calif.), where aliquots are taken from the jars and lyophilized on a large vacuum manifold. Individual glass traps are utilized on the manifold and extracted water from each ejecta sample is collected separately. The extracted water is assayed for tritium with a model 3375 Packard liquid

scintillation spectrometer. Details of the analytical techniques and data reduction for liquid scintillation data and gamma spectra are given by Clegg *et al.* (*2*). Gamma pulse height spectra are obtained with an 18 cm.^{3} lithium-drifted germanium solid-state detector with a high degree of Compton suppression and a 2048 channel pulse-height analyzer. Construction and operational details of this solid-state gamma spectrometer system are given by P. Phelps (*10*).

Discussion

At any time postshot, the distribution of radionuclides in the ejecta of a nuclear crater will be determined by the depositional pattern created at shot time, and by the subsequent movement of those radionuclides by

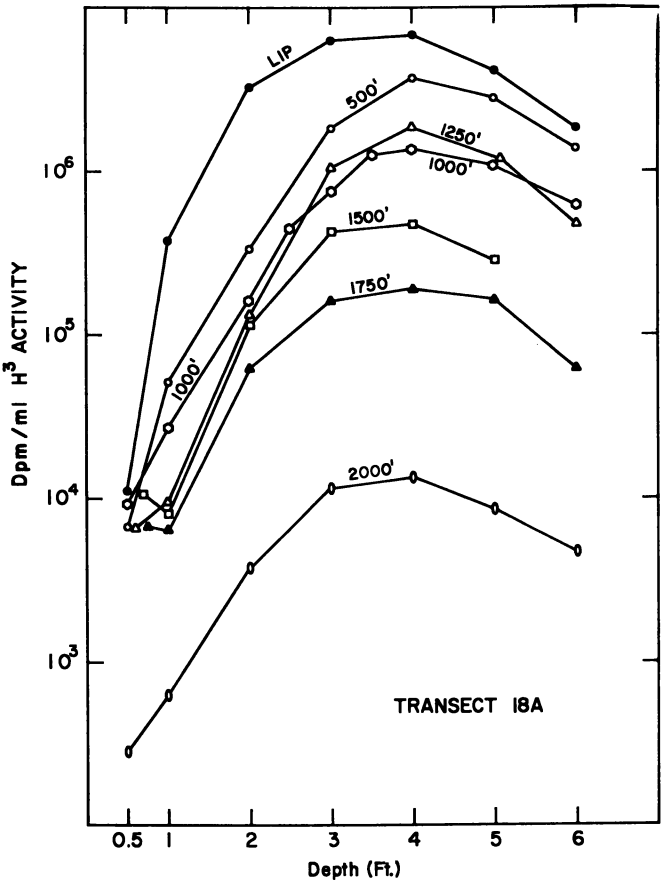

Figure 3. Concentrations of tritium in soil water in Sedan ejecta, 18A transect, crater lip to 2000 ft.

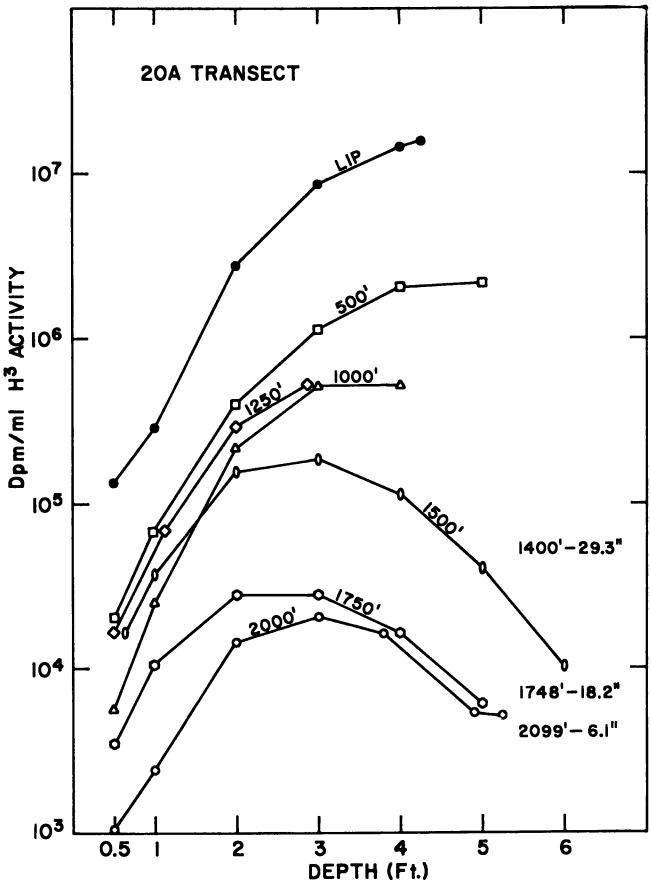

Figure 4. Concentrations of tritium in soil water in Sedan ejecta, 20A transect, crater lip to 2000 ft.

environmental influences. Within the complex of radionuclides present in nuclear crater ejecta, the movement of specific radionuclides will depend upon their physical and chemical state or manner of deposition on the particulate matrix. One of the major environmental factors which will influence the movement of radionuclides in nuclear crater ejecta is the rate and distribution of rainfall. In this research the current distribution of tritium and certain gamma-emitting radionuclides was determined from soil samples collected in the vicinity of Sedan crater.

A major problem encountered in field studies of nuclear craters at long periods after shot time lies in separating the depositional variations from those which have taken place since shot time. The ability to separate depositional variations from those caused by environmental influences will depend upon an adequate documentation of the spatial and

temporal variations in the concentrations of radionuclides through a time period which spans several seasonal cycles.

The mass distribution of Sedan ejecta around the crater has been described by Carlson and Roberts (*1*). A cross section of the crater lip and close-in ejecta by Richards (*11*) shows that the depth of ejecta on the crater lip is from 2 to 5 feet, and data from Carlson and Roberts (*1*) indicate that the ejecta depth decreases to less than 1 inch beyond 5600 feet from ground zero. The Sedan ejecta field consists of two main zones distributed around the crater. The inner zone which extends from the crater lip to approximately 2100 feet from ground zero is composed of bulk ejecta covered by a deposit of missile ejecta which varies from 1 to 15 cm. in depth. Carlson and Roberts (*1*) define bulk ejecta as that ma-

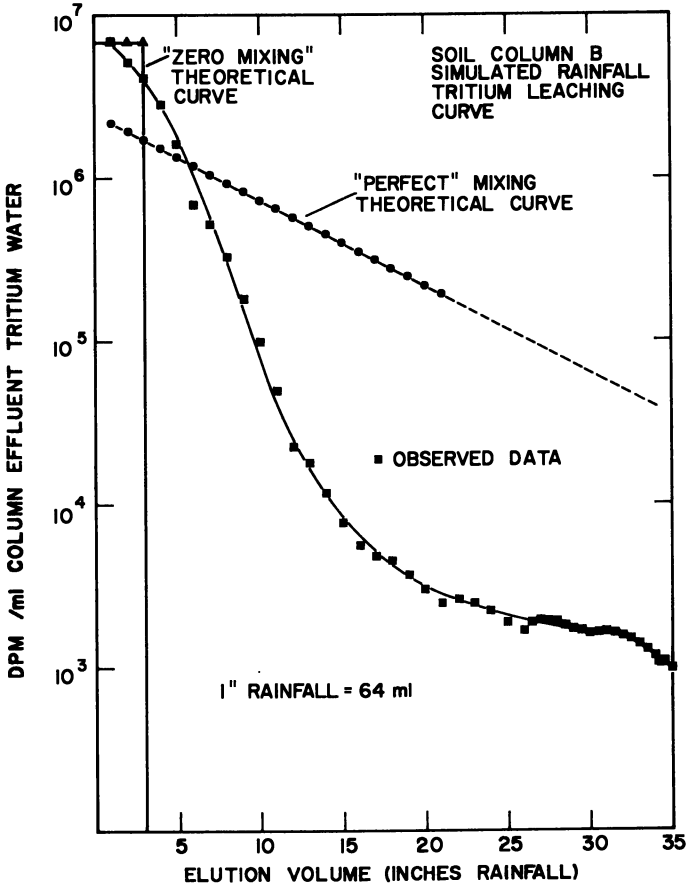

Figure 5. Simulated rainfall leaching of tritium from soil column of Sedan ejecta

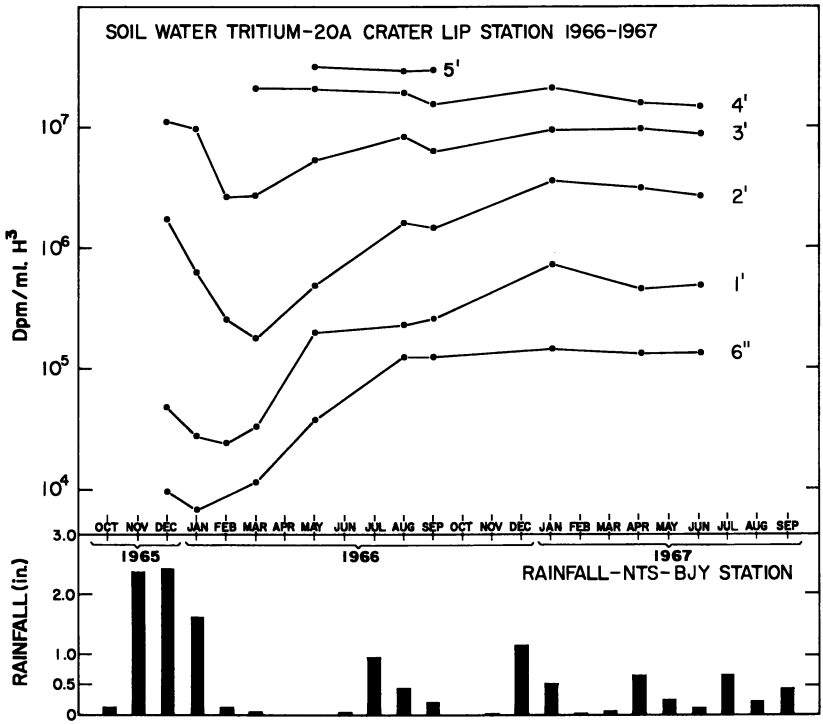

Figure 6. Soil water tritium, 20A crater lip station 1966–1967

terial which was moved essentially in mass and was relatively unaffected by the atmosphere as it moved at low velocities or even with fluid flow dynamics to the point of deposition. Missile ejecta is composed of base surge materials, debris on high angle trajectories, and fused material similar to primary fallout (*1*).

The outer zone of the ejecta field is covered only by missile ejecta, and at the outermost limits of this zone, at approximately 7000 feet from ground zero, it is primarily composed of fine base surge deposits. Aeolian erosion has largely removed fine base surge materials at distances beyond 4000 feet from ground zero.

The Sedan ejecta distribution is characterized by both areal and vertical or depth variations. The presence of fused materials of high specific activity almost exclusively in the missile ejecta suggests that gamma radioactivity may be localized in surface layer of ejecta. Some variations in the distribution of ejecta around the crater are correlated with events that took place during venting and subsequent breakup of the lofted earth mound as the crater was forming. Our data indicate that most of the long lived gamma radioactivity in the Sedan ejecta field is found in the missile ejecta layer. Residual tritium on the other hand, has

responded very obviously to environmental influences, and its present distribution in the Sedan ejecta is considerably different from that which pertained at shot time.

Interpretation of Analytical Results—Tritium. The locations of transects in the Sedan ejecta field at which samples were collected are shown in Figure 1. The distribution of tritium with depth at five sites on Sedan crater lip is shown on Figure 2. Except for the 9A area, the various sectors of the crater lip have very similar tritium depth profiles. The 9A area is a unique sector of the crater lip. A large mass of earth lifted by the detonation fell back to the crater in the 9A area earlier than the rest of the crater ejecta. Part of this material slumped into the crater, and the rest remained on the crater lip forming a prominence on the crater profile. Missile ejecta is thinner on this high point, and open-field radiation levels are lower. Tritium concentrations in the ejecta or slumped material at 9A are lower than in the rest of the crater lip mass.

A steep gradient of tritium concentration occurs with depth in the Sedan ejecta on the crater lip, where the deepest stratum of ejecta was

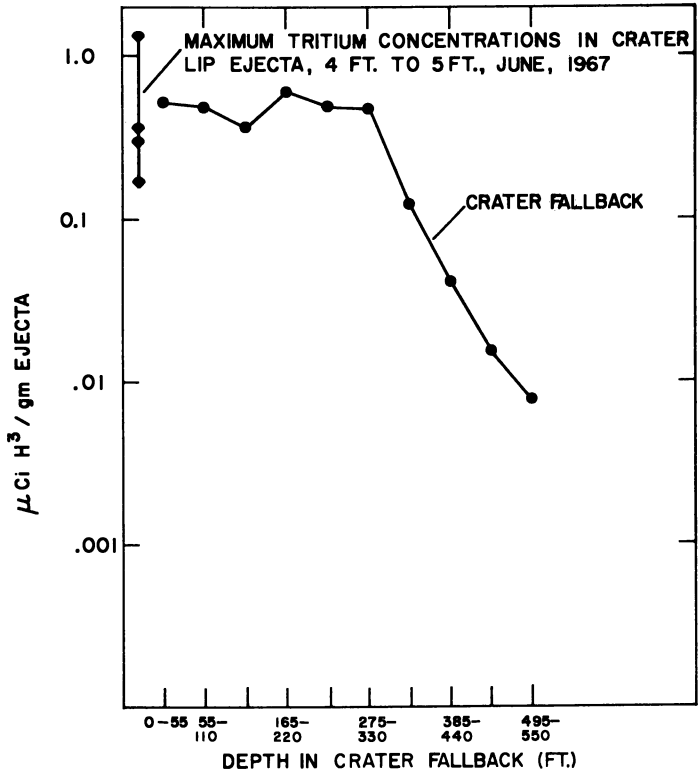

Figure 7. Concentrations of tritium in Sedan crater fallback

deposited, and at the more distant stations, where ejecta deposition was thin. The initial distribution of tritium in the ejecta layers immediately after the shot was not determined.

If one assumes, however, that tritium is scavenged in a similar manner as other radioactivity, then immediately following the detonation most of the tritium observed in the present ejecta profiles would have been in the missile ejecta stratum. This supposition is supported by the consistent pattern of tritium distribution with depth on the crater lip and at more distant stations where ejecta was deposited as a thin layer on undisturbed soil materials.

Table I. Integrated Tritium Inventory at a Single Crater Lip Site Sedan Crater[a]

20A Sedan Crater Lip Date	*Integrated Tritium Inventory 0–6 ft. Depth Ci./ft.²*
May 1966	0.1083
August 1966	0.0985
September 1966	0.0826
January 1967	0.0897
April 1967	0.0769
June 1967	0.0594
April 1968	0.0458
July 1968	0.0377
November 1968	0.0202

[a] Mean residence time = 20.7 ± 2.4 months.
Residence half time = 14.3 ± 1.7 months.

Figure 3 shows the pattern of tritium distribution on the 18A (southeastern) transect. The concentrations of tritium increase sharply with depth at all stations on the transect, and the peak tritium concentration occurs at a depth of 3 to 5 feet at all stations *regardless of ejecta depth.* In another transect of the ejecta field on the west side of the crater at 20A, shown in Figure 4, the tritium depth profiles show a similar pattern, and maximum tritium concentrations occur in the same zone, 2–5 feet. At a distance of 2000 feet from the crater lip, the depth of ejecta was 2–3 inches. The maximum concentration of tritium in soil water was at 3 feet at that site.

The only source for the tritium found below the ejecta layer (2–3 inches) in the undisturbed soil below was the missile ejecta. It is our opinion that all of the tritium profiles shown in Figures 3 and 4, including that of the crater lip, were produced by rainfall leaching. We believe the source layer for tritium was in the missile ejecta layer immediately after the detonation and that most of the tritium in the bulk layer has

been eluted there since shot time by rainfall. The distribution of tritium in the Sedan ejecta field therefore has been altered significantly by post-shot environmental effects.

Laboratory studies of tritium leaching from Sedan ejecta have shown that a front of almost undiluted soil water is "pushed" from a soil column when the column is leached with successive aliquots of water. A sample of ejecta was obtained from the maximum tritium zone at 4 feet on Sedan crater lip. This material was placed in four long glass columns, 72 mm. in diameter and 30 cm. long. Separate aliquots of water (equal to 1 inch of rainfall) were poured on the top of the soil columns each day. The column was allowed to drain, and each aliquot of leachate was collected daily and assayed for tritium. Figure 5 shows the elution of tritium from one of the large columns of Sedan ejecta. Each data point in Figure 5 represents the concentration of tritium in the daily collection of leachate.

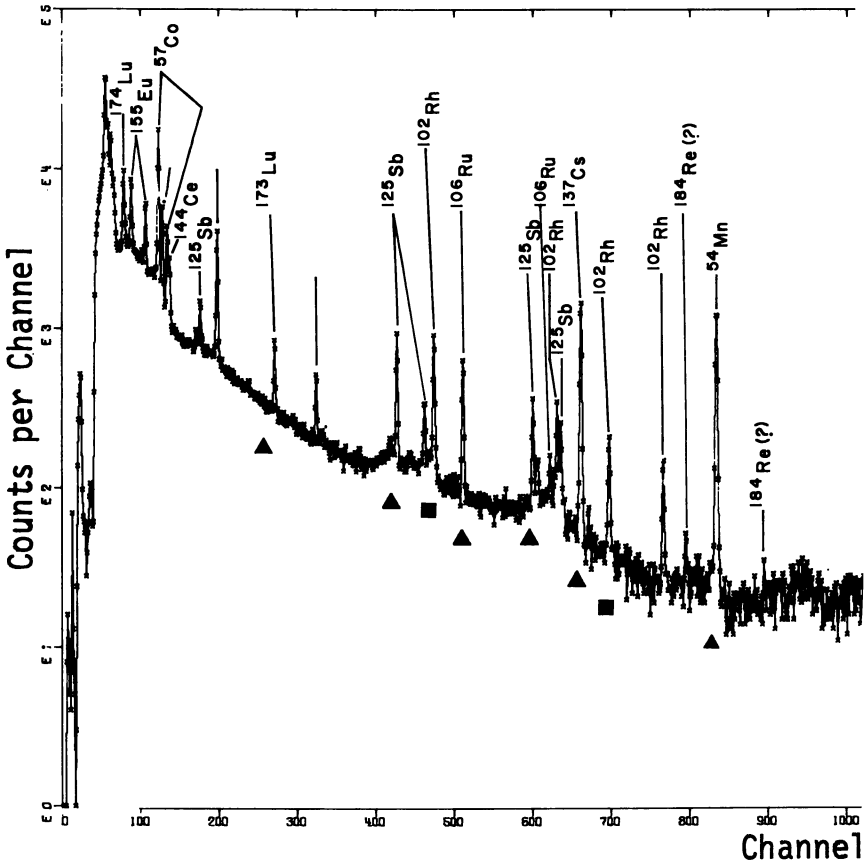

Figure 8. Gamma spectrum

Four replicate columns were run, and all produced the same type of elution curve. Lyophilized samples of another aliquot of the same soil used in the columns yielded soil water with a tritium concentration the same as that in the first aliquot drawn from the column. The first aliquot was equivalent to 1 inch of rain on the column and represents about one-third of the free water in the original soil material in the column. Zimmerman (*13*) reported a similar phenomenon when he used tritiated water to trace pulses of rainwater in soil systems. He found a relatively discrete front associated with the tritium injection after rainfall had occurred and eluted the tritium pulse into the soil profile. The frontal movement of high specific activity tritiated water from the surface layers in ejecta strata Sedan accounts for the peak tritium concentrations observed at depths just below the maximum penetration of rainfall.

To illustrate the soil water movements that take place in the Sedan ejecta, the tritium depth profile data for the 20A crater lip station for an

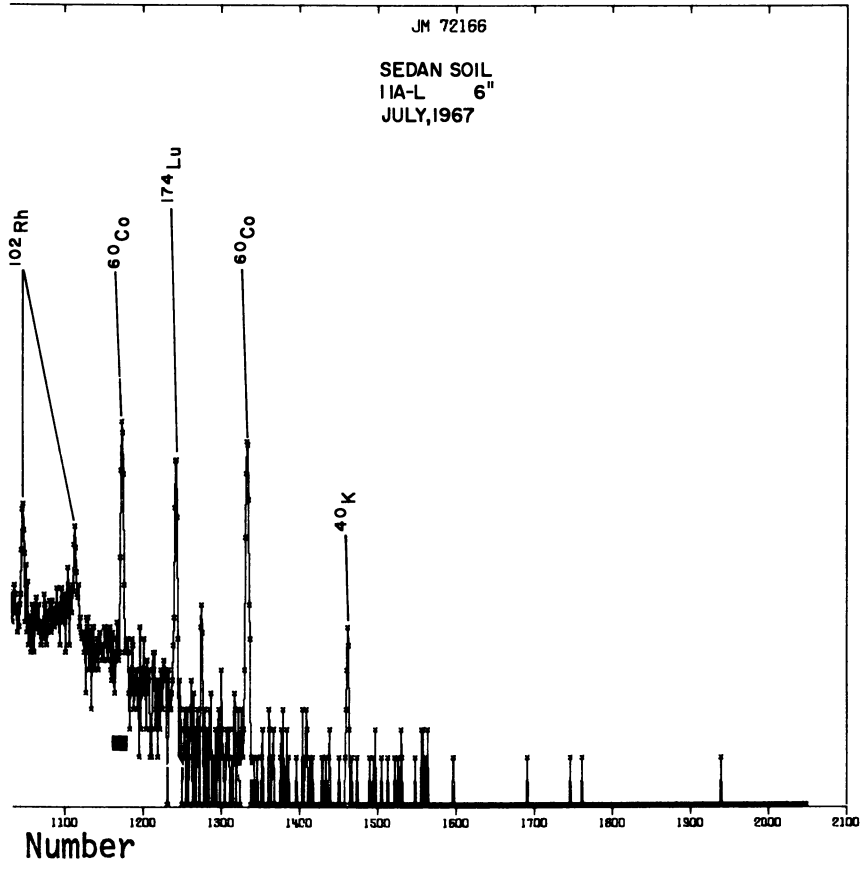

of Sedan crater lip ejecta

18-month period have been compiled and are shown in Figure 6. This period fortuitously included a winter of unusually high rainfall (over 10 inches). Obvious dilution effects are seen to a depth of 3 feet during this period. Rickard and Murdock (*12*) demonstrated that the average rainfall of 3.1 inches/year penetrated to a depth of 24 inches in Northern Yucca Flat where Sedan crater is located. The normal average rainfall which occurred in the winter of 1966–1967 did not produce the perturbations in the tritium concentration profile that were observed in the previous winter of high rainfall.

Fallback presents a different condition from the bulk ejecta because it is that portion of the ejecta which falls through the fireball or cloud as it drops back into the crater. The tritium distribution in fallback in

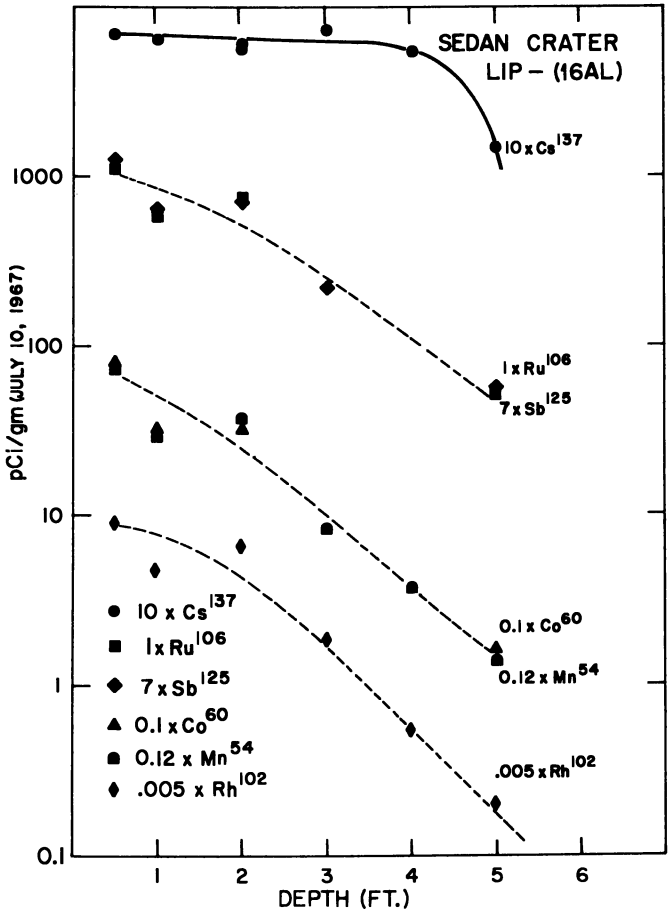

Figure 9. Gamma-emitting radionuclide depth profiles at Sedan crater lip, 16A site

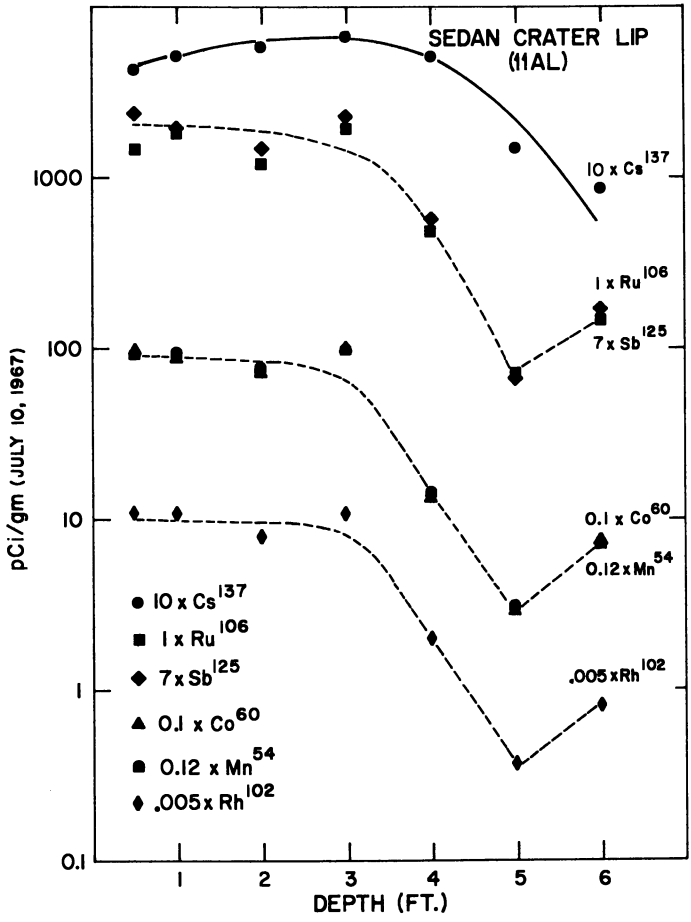

Figure 10. Gamma-emitting radionuclide depth profiles at Sedan crater lip, 11A site

Sedan crater as determined by Hansen (*4*) is quite uniform to the depth of explosive emplacement or over 300 feet. The maximum concentrations of tritium in soil water observed on the crater lip at 4 to 5 feet in our samples are in the same range as those reported by Hansen (*4*) in crater fallback. Figure 7 shows the vertical distribution of tritium in soil water extracted from Sedan crater fallback, according to Hansen (*4*), and the maximum concentrations found at our four crater lip sites.

In the more than 5 years since the detonation there has been a net loss of tritium from the Sedan postshot environment. The integrated values for the 20A transect provide some indication of the rate of loss, but a detailed analysis of tritium losses will be made in a future report. Table I shows the depth-integrated tritium value in curies per square

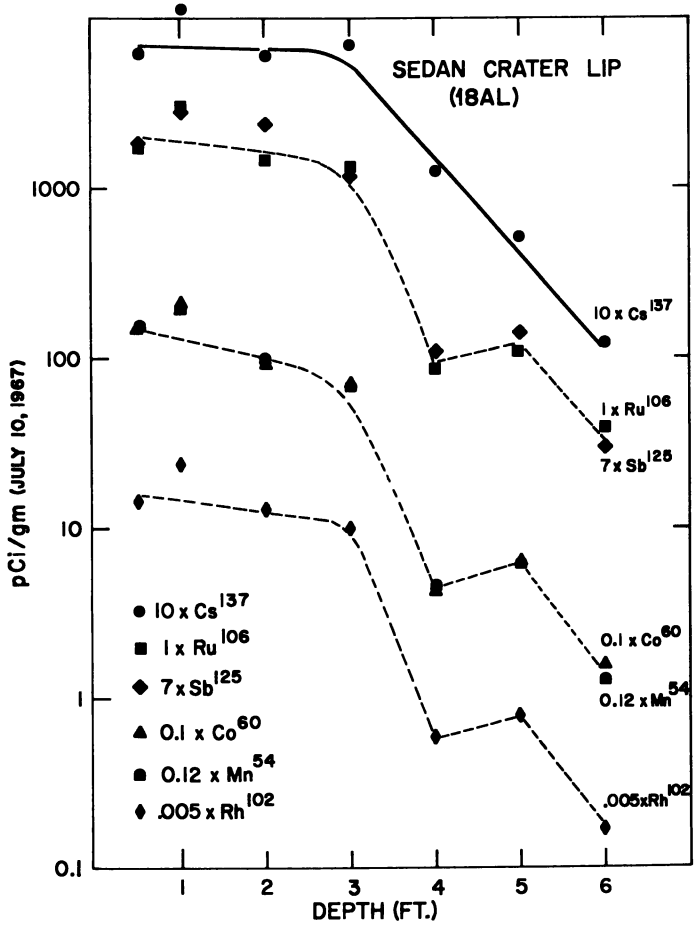

Figure 11. Gamma-emitting radionuclide depth profiles at Sedan crater lip, 18A site

foot for the 20A crater lip site during the time period covered in Figure 6. The integrated tritium value was obtained by integrating the plot of tritium concentration in Ci per gram *vs.* depth from the surface to a 6-foot depth and multiplying this value by the density. The integrated tritium value is therefore a site inventory of tritium, and when this measurement is made at several points in time, it is possible to determine the rate of loss in the zone being measured. The mean residence time for tritium in the 0–6-foot zone at 20A crater lip is 20.7 ± 2.4 months.

Tritium Distribution. The present distribution of tritium in the Sedan ejecta field has therefore been produced by rainfall and attendant environmental factors of the desert ecosystem. The initial distribution of tritium was primarily in the missile ejecta layer which had the greatest

exposure and opportunity to scavenge radioactivity from the cloud which rose through these airborne materials. Missile ejecta undoubtedly scavenged tritiated water vapor or steam relatively effectively because the fraction of total residual tritium retained in the ejecta mass is large. Bulk ejecta which remains essentially intact during its deposition apparently has limited contact with the fireball and the cloud of radioactive particles and gases as they rise and cool. Deep fallback tritium concentrations probably represent the initial concentration of tritium in missile ejecta.

Other Radionuclides (Gamma Radionuclides). The distribution of other radionuclides in the Sedan ejecta field provides another means of determining the effects of the environment during the postshot period in translocating radionuclides into the subejecta soil system. Presumably, most or all of these radionuclides would be less mobile than tritium because of their physicochemical state in the nuclear ejecta. If the same elution that has produced the leached tritium profile has also mobilized gamma radionuclides, then tritium and gamma profiles will be similar. If not, the distribution of gamma radionuclides will define the initial depositional pattern of radioactivity in the Sedan ejecta. It is also pos-

Table II. Radionuclides in Sedan Ejecta (20A—1500 feet from Crater Lip)
pCi/Gram (July 19, 1967)

	Depth, ft.			
Radionuclide	*0.5*	*1*	*2*	*3–6*
^{137}Cs	251 ± 3	238 ± 3	3.6 ± .5	⩽ .4
^{54}Mn	214 ± 9	136 ± 3	1.8 ± .6	⩽ .8
^{173}Lu	72 ± 9	55 ± 7	2.2 ± 1.4	⩽1.6
^{106}Ru	591 ± 29	—	26 ± 4	⩽2.7
^{125}Sb	102 ± 7	107 ± 6	2.3 ± .9	⩽ .9
^{102}Rh	745 ± 12	—	12 ± 2	⩽2
^{60}Co	297 ± 5	—	3.6 ± 1	⩽1.3

Ejecta Depth
15.3 cm.

Table III. Ratios of ^{137}Cs and ^{54}Mn at 20A—1500 feet from Sedan Crater

	pCi/gram (July 19, 1967)		*pCi/gram at* T_0		*Ratio*
	^{137}Cs	^{54}Mn	^{137}Cs	^{54}Mn	*Cs/Mn*
6 in.	251 ± 3	214 ± 9	283 ± 3	1.26×10^4	.022
1 ft.	230 ± 3	136 ± 3	258 ± 3	8.02×10^3	.032
2 ft.	3.6 ± .5	1.8 ± .6	4.0 ± .6	1.06×10^3	.037
3 ft.	N.D.[a]	N.D.	N.D.	N.D.	

[a] N.D. = not detectable.

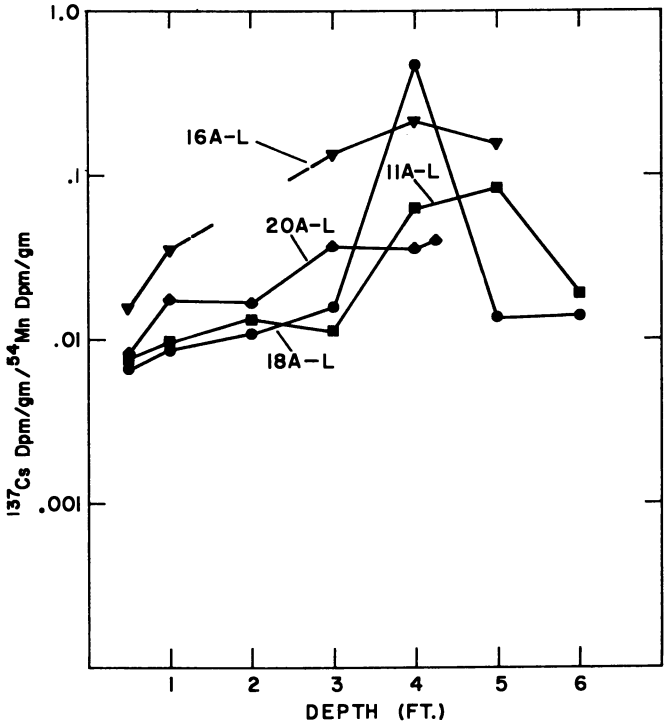

Figure 12. $^{137}Cs/^{54}Mn$ ratios in Sedan crater lip ejecta

sible that some radionuclides could be leached from the ejecta while others would remain in the materials in which they were deposited. For example, radionuclides that had been adsorbed or scavenged onto the surfaces of particles will be more mobile than those that are present in the ejecta as condensed globules of the refractory metals.

The gamma radionuclides present in Sedan ejecta are shown in Figure 8, which is a 2048 channel pulse-height spectrum of a 300-gram sample collected at the crater lip. The specific activity of seven radionuclides of those shown in Figure 8 have been determined for each depth interval sample. The radionuclide concentration profiles are shown in Figures 9, 10, and 11. A steep concentration gradient occurs for each radionuclide with the concentrations at 5 feet being one to two orders of magnitude less than at the surface. The ^{137}Cs appears to have a slightly different depth distribution than the other radionuclides in the profile.

The ejecta layer was a shallow surface stratum at distances between 1000 and 3000 feet from the crater lip. The radionuclide depth profiles at 1500 feet were studied in detail to determine whether or not any radionuclide had been leached from the surface stratum of radioactivity. At

1500 feet from the crater lip on 20A transect, the ejecta depth was 15.3 cm. or slightly over 6 inches.

The specific activity of individual radionuclides in the Sedan ejecta field at 20A—1500 feet, corrected for decay to sampling time, is given in Table II. It is apparent that some gamma activity had been leached to the two-foot depth. Below this depth all gamma radioactivity was less than detectable limits. The ratio of ^{137}Cs to ^{54}Mn indicates an enrichment of ^{137}Cs over ^{54}Mn with depth in this profile. This increase is caused by preferential leaching of ^{137}Cs from the source layer by rain water. ^{137}Cs is scavenged onto the surfaces of particles in the ejecta and is more water soluble, while ^{54}Mn is present in the ejecta as refractory oxides and hydroxides of low solubility. The data for ^{137}Cs and ^{54}Mn corrected for decay to shot time (T_o) are given in Table III.

^{137}Cs occurs in crater ejecta and fallout debris as a surface-adsorbed, soluble radionuclide, owing to its gaseous precursor. The behavior of

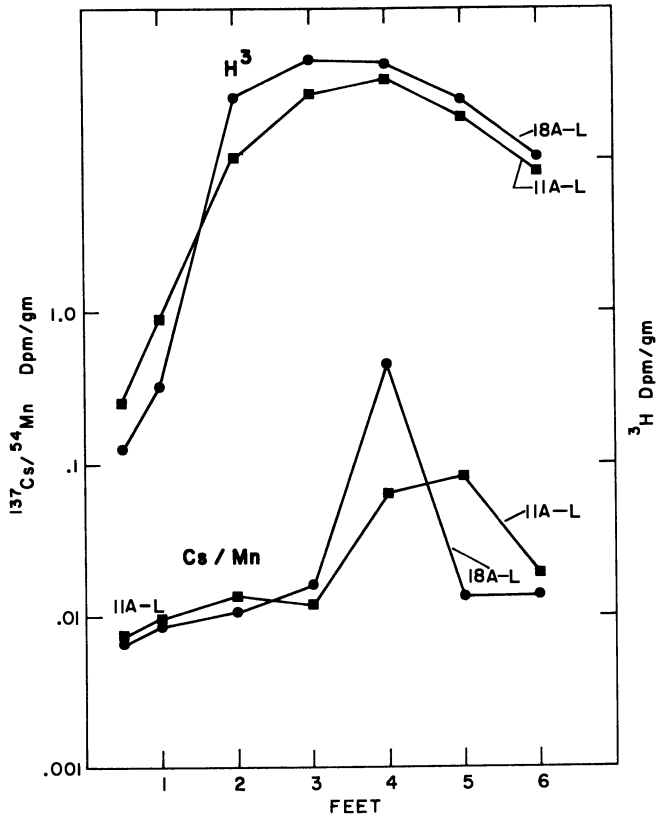

Figure 13. $^{137}Cs/^{54}Mn$ ratios and tritium depth profiles at two crater lip sites

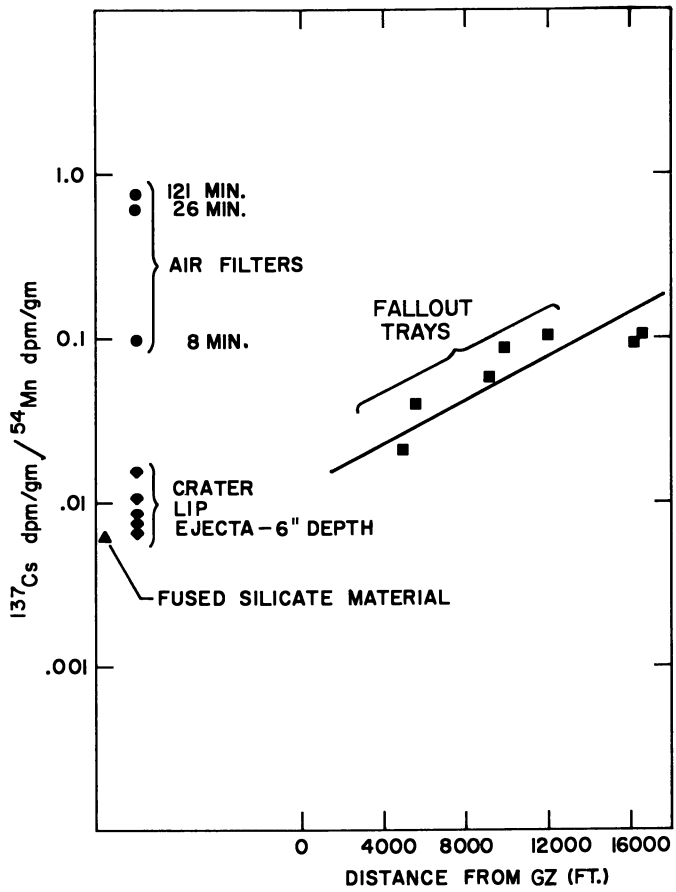

Figure 14. $^{137}Cs/^{54}Mn$ ratios in fallout tray samples, air filters, and crater ejecta

fallout ^{137}Cs in the world biosphere attests to its high availability from nuclear debris. Gustafson and Miller (*3*) reviewed the movement and biological significance of fallout ^{137}Cs in the biosphere and noted that its appearance in plant materials was primarily by foliar absorption, which implies high solubility in water of the original fallout particle or its surface-adsorbed constituents.

If the Cs/Mn ratios are calculated for the depth profiles at the crater lip stations, as was done for the 20A—1500 foot station, a similar condition is seen. Figure 12 shows the Cs/Mn ratios for ejecta samples collected at several crater lip stations. An increase in ^{137}Cs concentration relative to ^{54}Mn with depth is seen at each crater station. Increases in the ratio with depth represent enrichment of Cs with respect to Mn by rainfall leaching. Cs/Mn ratios of 0.01 to 0.02 are characteristic of the

surface ejecta between the crater lip and 2000 feet from ground zero, at the limits of bulk ejecta deposition.

Figure 13 shows a comparison of the tritium depth profiles with Cs/Mn ratios for two crater lip sites. A maximum Cs/Mn ratio occurs at approximately 4 feet where peak tritium specific activity is also found. The use of the Cs/Mn ratio has therefore demonstrated the similarity of mechanisms for cesium and tritium movement in the postshot environment.

A gradient of Cs/Mn ratios with distance from the crater beyond 1500 feet is present owing to the fractionation of those radionuclides during the detonation, and subsequent deposition of ejecta and fallout. Figure 14 shows Cs/Mn ratios for 6-inch depth ejecta samples collected at Sedan crater from the lip to 3000 feet from ground zero. Any increase in Cs/Mn ratios observed at sites distant from the crater lip must be evaluated in view of the fractionation that is evident in the ejecta with respect to these two radionuclides. The Cs/Mn ratio at crater lip sites and those out to 1500 feet are all close to 0.01–0.02. A sample of fused silicate material, which represents a class of ejecta extremely depleted in volatile radionuclides, had a low Cs–Mn ratio of 0.006.

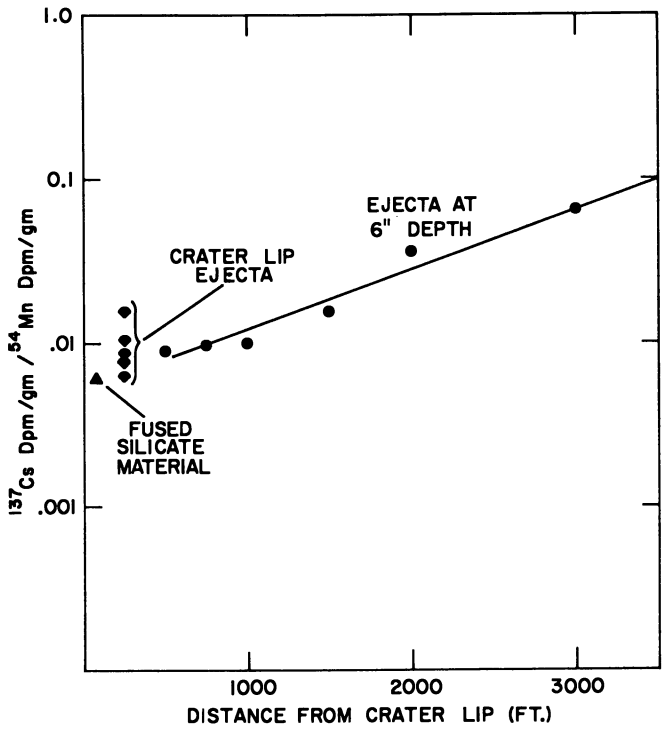

Figure 15. $^{137}Cs/^{54}Mn$ *ratios in Sedan ejecta*

The same increase in ^{137}Cs relative to ^{54}Mn with distance from ground zero is also detected in more distant samples collected at shot time. Figure 15 shows the Cs/Mn ratios for fallout tray samples collected from 5100 to 16,500 feet from ground zero. Air filter sample data and crater lip ejecta samples are also shown for comparison. All data are corrected to T_0 or shot time.

The greatest Cs/Mn ratio observed in the fallout tray samples was 0.1 at 16,500 feet or 10 times that seen in the crater lip ejecta. Air filter samples, on the other hand, exhibited the expected enrichment in the volatile fission product, ^{137}Cs, relative to the highly refractory ^{54}Mn. The relationships of crater ejecta and fallout materials to volatile and refractory nuclear detonation products, shown in Figures 14 and 15, conform to the generally accepted theories on the contrasting behavior of these two radionuclides.

The reason for discussing the data shown in Figures 14 and 15 is to demonstrate that the Cs/Mn ratios cited previously as evidence of vertical translocation or leaching of ^{137}Cs, are not found in the unmodified ejecta or fallout and that the enriched $^{137}Cs/^{54}Mn$ ratios cited are significant when compared with those obtained by the analysis of other sample materials representing Sedan debris.

Summary

The distribution of radionuclides in Sedan crater ejecta has been determined on a vertical and horizontal basis at selected sites in the area covered by ejecta. The present distribution of residual tritium represents a highly modified pattern caused by rainfall leaching. Maximum tritium concentrations are found at essentially the same depth in a transect of the ejecta field where the ejecta depth is decreasing. The source of tritium in the Sedan crater ejecta is identified as the missile ejecta layer which had greater exposure to detonation products than bulk ejecta.

Gamma radioactivity is localized in the surface or missile ejecta layer even on the crater lip where the total ejecta depth is 2 to 5 feet. Whenever ejecta was deposited in a shallow layer on the undisturbed soil surface, only a small amount of gamma radioactivity has been leached. It has been demonstrated, however, that a subtle preferential movement of ^{137}Cs has taken place in the ejecta, at both the crater lip and more distant sites, by a consideration of the $^{137}Cs/^{54}Mn$ ratios in those ejecta materials.

A similarity in the leaching behavior of ^{137}Cs, a volatile fission product, and residual tritium, a gaseous detonation product which probably behaves in its own unique manner, has been demonstrated.

Literature Cited

(1) Carlson, R. H., Roberts, W. A., *Boeing Co. Rept.* **PNE-217F** (1963).
(2) Clegg, B. R., Hamby, K. O., Martin, J. R., "Abstracts of Papers," 155th Meeting, ACS, April 1968, O 068.
(3) Gustafson, P. F., Miller, J. E., *HASL Fallout Program, Quart. Summ. Rept.* **184** (January 1968).
(4) Hansen, S. M., *Lawrence Radiation Lab. Rept.* **UCRL-50213** (1966).
(5) Hatch, F. T., Moore, J. L., Koranda, J. J., *Lawrence Radiation Lab. Rept.* **UCRL-70318,** *Abstr.* (1967).
(6) Koranda, J. J., *Lawrence Radiation Lab. Rept.* **UCRL-70292** (1967).
(7) Koranda, J. J., Martin, J. R., Wikkerink, R. W., *Lawrence Radiation Lab. Rept.* **UCRL-50360** (1967).
(8) Koranda, J. J., Gunnink, R., *Lawrence Radiation Lab. Rept.* **UCRL-70165** (1966).
(9) Nordyke, M. D., Williamson, M. M., *Lawrence Radiation Lab., U. S. Army Corps Engrs. Rept.* **PNE-242F** (1965).
(10) Phelps, P., Hamby, K. O., Potter, G. D., Shore, B., ADVAN. CHEM. SER. **93,** 202 (1969).
(11) Richards, W. D., *Lawrence Radiation Lab. Rept.* **PNE-240F** (1964).
(12) Rickard, W. H., Murdock, J. R., *Ecology* **44,** 821 (1963).
(13) Zimmerman, U., Münnich, K. O., Roether, W., *Geophys. Monograph Ser.* 11 (1967).

RECEIVED December 13, 1968. Work performed under the auspices of the U. S. Atomic Energy Commission.

8

Plutonium in the Water Environment

I. Characteristics of Aqueous Plutonium

JULIAN B. ANDELMAN and THOMAS C. ROZZELL

Graduate School of Public Health, University of Pittsburgh, Pittsburgh, Pa. 15213

In the pH range of natural waters colloidal plutonium(IV) hydroxide forms from polymeric hydrolysis products and ages slowly. At least over a period of several days an increase in particle sizes is observed. At pH 7 such solutions aged for a few months showed a significant increase in size of the colloidal plutonium as the ionic strength increased from 0.002 to 0.1. The centrifugability of the colloid, aged for three and seven days at pH 7, decreased for plutonium concentrations less than 10^{-7}M. The addition of macroscopic grains of crystalline silica affected the colloidal plutonium size distribution as did the variation in pH over the range of 5 to 8. The addition of 10^{-2}M bicarbonate ions at pH 7 also influenced the distribution but less systematically.

Although the levels of plutonium in environmental waters are generally low, there is the possibility of plutonium contamination from weapons testing, nuclear reactor operations, laundry and decontamination wastes, fuel reprocessing, and accidental release during transportation. It has been estimated that by 1980 the United States will be producing 15,000–20,000 kg. of plutonium per year (*12*). Its growing use will increase the probability of environmental contamination.

In an analysis of the hazards of the alpha emitters from reactor operations it has been pointed out (*25*) that the most significant and hazardous species are plutonium, americium, curium, and neptunium. Plutonium is as hazardous as such fission products as ruthenium-106, cesium-137, cerium-144, and promethium-147, depending on the kind of fuel, the power of the reactor, the storage time of the waste, and whether it is released to the atmosphere or to water. If strontium-90 is removed

from the wastes, plutonium is likely to become the most hazardous radionuclide. Without such removal plutonium still becomes relatively more hazardous with increased storage times because of the short half-life of strontium-90.

The presence of small quantities of plutonium in the environment, far removed from test areas in both time and distance, has been demonstrated in several instances. Magno, Kauffman, and Shleien (*24*) found that deposition of ^{239}Pu in Winchester, Mass. arising from rainfall during the period May 1965–May 1966 ranged from 0.86 to 8.8 pCi/sq. meter. Plutonium-239 in surface sea water in 1964 was as high as 30 pCi/liter ($2 \times 10^{-13}M$), as reported by Pillai, Smith, and Folsom (*30*). Wood and Burden (*42*) found that ^{239}Pu accumulated along with other naturally occurring and fission isotopes on a water filter sand bed. They reported a value of 123 pCi/gram on coated sand. Olafson and Larson (*28*) estimate that the general environmental contamination with ^{239}Pu is approximately an order of magnitude less than the strontium-90 level or approximately 1 mCi per sq. mile.

When plutonium and other radionuclides are released to surface or ground waters, they may be concentrated by and in plants and on silt, sediments, and suspended materials in the water. The concentration of plutonium and other radionuclides on sediments or in aquatic organisms frequently exceeds their concentration in the surrounding water, often by several orders of magnitude (*33*). It is this concentration process which poses one of the greatest problems in the management of low level radioactive wastes. The radionuclides, having been so concentrated, may be released suddenly at some future time in quantities far exceeding their maximum permissible concentrations.

It has been well established that plutonium hydrolysis products exhibit colloidal behavior (*6, 22, 27, 31*) and may sorb onto minerals and other surfaces as radiocolloids. It is often difficult to determine whether a radiocolloid is a true colloid or a pseudocolloid formed by sorption of the radioactive species onto other colloidal impurities in the solution (*35*). In some instances both types are present in the same solution (*14*).

Rhodes (*31*) has studied the sorption of plutonium by a subsurface soil in the vicinity of the Hanford plant. Christenson *et al.* (*3*) studied the sorption of plutonium by a core of soil turf taken from the Los Alamos area. Jacobson and Overstreet (*13*) found that although the plutonium may in most instances be held tightly by soil components, between 19 and 94% of it was taken up by barley plants grown in a bentonite suspension on which plutonium was sorbed. The sorption of plutonium on quartz and glass was studied by Samartseva (*32*) and King (*15*). The former found that in the concentration range of 10^{-8} to $10^{-10}M$, plutonium had a sorption peak around pH 2.8–3.6, with decreasing but significant

amounts being sorbed in the pH range 4–11. King found that the sorption increased as the hydrogen ion concentration decreased.

In the present paper the chemistry of plutonium is reviewed, with particular reference to the ambient conditions likely to be encountered in natural waters. In addition, experimental work is presented concerning the effects of such variables as pH, plutonium concentration, ionic strength, and the presence of complexing agents on the particle size distributions of aqueous plutonium. In subsequent papers it will be shown that these variables, as they influence the particle size distribution of the aqueous plutonium, greatly affect its interaction with mineral surfaces. The orientation of these studies is the understanding of the likely behavior and fate of plutonium in environmental waters, particularly as related to its interaction with suspended and bottom sediments.

Chemical and Physical Properties of Plutonium in Aqueous Solution

Plutonium-239 exists in aqueous solutions in five possible oxidation states, Pu(III), Pu(IV), Pu(V), Pu(VI), and as recently reported, Pu(VII) (*38*). The latter apparently occurs only in very basic aqueous solutions. Pu(II) oxidizes readily in aqueous solution.

Trivalent plutonium, Pu(III), appears in many compounds. It also occurs as the Pu^{3+} ion which is relatively stable in solutions of medium acidity (*40*). It has been shown (*11*) that acid solution hydrolysis of Pu^{3+} is negligible. At a pH of about 7 the first small quantities of the hydrolysis product $Pu(OH)^{2+}$ appear.

Pentavalent plutonium, Pu(V), is believed to exist only as the oxyion PuO_2^+ in aqueous solutions. Generally Pu(V) quickly disproportionates to form Pu(VI) and Pu(IV) in solutions of moderate acidity (*40*).

Hexavalent plutonium, Pu(VI), is relatively stable in aqueous solution and exists as the oxyion plutonyl, PuO_2^{2+} (*40*). The chemical properties of Pu(VI) compounds are somewhat similar to those of U(VI).

The tetravalent state, Pu(IV), may be maintained as the sole oxidation state by holding the nitrate ion concentration high and the pH low. Tetravalent plutonium is known to exist in many compounds and in solutions of about 0.5*M* hydrogen ion concentration or greater it exists predominantly as unhydrolyzed Pu^{4+}, or some complex thereof, depending on the anions present (*10*). In media containing sufficiently non-complexing ions, and whose hydrogen ion concentration is 1*N*, Pu(IV) is believed to exist as the hydrated form, $Pu(H_2O)_x^{4+}$ (*23*). Near pH 1 Pu^{4+} begins to hydrolyze appreciably (*18*, *22*).

Kraus (*18*) has recognized three types of hydrolysis products of Pu(IV), U(IV), Th(IV), and Am(IV). These are: (1) simple monomeric hydrolysis products, (2) low molecular weight hydrolytic polymers

in equilibrium with each other and with M^{4+}, and (3) high molecular weight colloidal polymeric products (probably more than one type) not in equilibrium with the monomer. Lindenbaum and Westfall (*22*) as well as Kraus have shown that once hydrolysis takes place, the reaction reverses only at a very low rate, even in the presence of high hydrogen ion concentration or with solubilizing complexing agents such as citrate.

Even though the solubility product of $Pu(OH)_4$ is 1×10^{-56}, some Pu^{4+} must remain in solution as the equilibrium is established. The monomeric $Pu(OH)_4$ and the very low molecular weight polymeric species are able to pass through an ultrafilter, and Lindenbaum and Westfall (*22*) found that as much as 5% of the hydrolysis species remained ultrafilterable after 72 hours at pH 11. These unfilterable species may be either true radiocolloids or pseudocolloids. The latter likely occur as a result of minute impurities in the solutions which act as nuclei on which the polymeric or ionic species adsorb (*14*). However, this point has been the subject of extensive debate (*36, 37, 39*), and opinions vary as to whether pseudocolloids form in this manner, or in fact whether there are such species at all. In general the term "colloidal plutonium" will be used throughout this paper to indicate all of the insoluble plutonium hydrolysis products and polymeric species of colloidal size.

The plutonium colloid can be formed under a variety of conditions, forming especially at high plutonium concentrations and at hydrogen ion concentrations less than 0.5*M*. If an acid solution of plutonium is diluted with water, polymerization occurs owing to the existence of transient regions of high pH, even though the final acidity may be high enough to prevent formation of the polymer. On the basis of solubility product calculations at different pH's, and at different plutonium concentrations Davydov (*7*) concluded that the composition of the particles formed in the polymerization process depends upon the concentration of the OH^- ions present and the concentration of the plutonium. Carniglia (*2*), investigating the adsorption of colloidal Pu(IV) by glass, concluded that colloidal Pu(IV) is positively charged. It has also been reported (*10*) that the Pu(IV) charge varies with pH.

Colloidal plutonium particles vary in weight and size, the molecular weight being estimated variously as high as 10^{10} with a minimum of approximately 4000 (*27*). However, no definitive measure has been made and, if attempted, would have little significance because of the extreme inhomogeniety and variability of the colloid system. Lutz and co-workers (*23*) estimated that the colloidal particles, containing a number of polymers, have from 10^6–10^{10} atoms of plutonium. Ockenden and Welch (*27*) estimated that there are 4.2×10^5 atoms based on diffusion data and 2×10^7 atoms when ultracentrifugation was used. Costanzo and Biggers (*5*) concluded that the plutonium polymer is not a well

defined chemical species but rather an aggregate of micelles of different sizes. It has been found that heating plutonium(IV) solutions causes a considerable increase in particle size (*2*). Evidence has also been obtained for an increase in particle size with increasing pH (*31*).

The depolymerization of the plutonium polymers is a very slow reaction at room temperatures and moderate acid concentrations. It is only upon heating or by the use of very concentrated acid that the depolymerization rate can be made appreciable. Kraus (*16*) has compared, in two nitric acid media, 6*M* and 10*M*, the depolymerization of already formed polymers—one at room temperature and the other at 95°C. for one hour. The values for the half time of the reactions ranged from 29 minutes for the non-heated, 10*M* HNO_3 solution to 730 minutes for the heated, 6*M* HNO_3 solution. Lindenbaum and Westfall (*22*) found that at pH 7.8, a region of environmental interest, the rate of depolymerization was only about 0.04% per hour and at pH 4.0 increased to only 0.18% per hour.

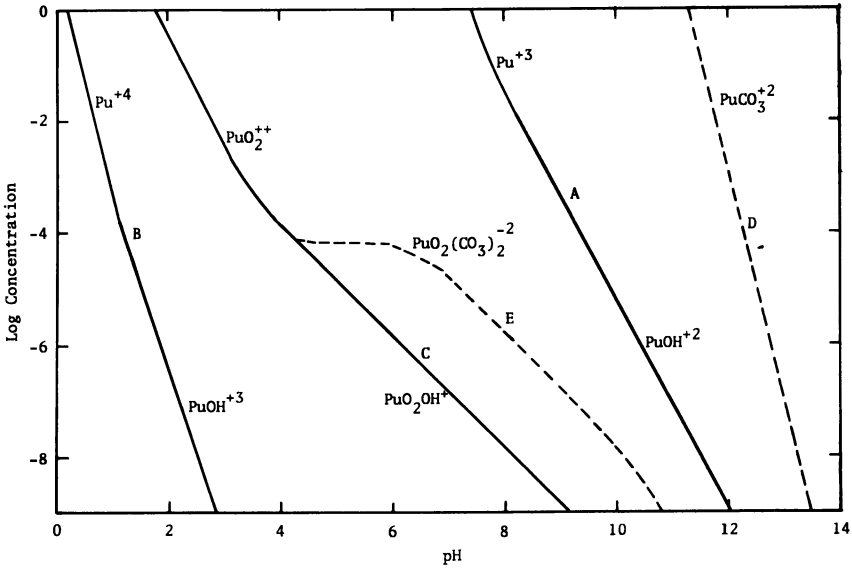

Figure 1. Solubilities of Pu in various oxidation states in equilibrium with the respective solid hydroxides. (——) In the absence of added carbonate. (– – –) In the presence of 10^{-3}M stoichiometric carbonate (see text). Curves: A: PU(III), B: Pu(IV), C: Pu(VI), D: Pu(IV) with added carbonate, E: Pu(VI) with added carbonate. The predominant species are indicated for each oxidation state— i.e., *$Pu(OH)^{3+}$ for Pu(IV) in the pH range 1–3*

To understand the nature of the plutonium species likely to be present in natural waters, it is useful to compare graphically the solubilities

Table I. Selected Equilibrium Constants for Aqueous Plutonium Reactions[a]

	Log K
$Pu(OH)_3(s) \rightarrow Pu^{3+} + 3\ OH^-$	−19.7
$Pu(OH)_4(s) \rightarrow Pu^{4+} + 4\ OH^-$	−55.2
$PuO_2(OH)_2(s) \rightarrow PuO_2^{2+} + 2\ OH^-$	−24.5
$Pu^{3+} + H_2O \rightarrow PuOH^{2+} + H^+$	− 7.2
$Pu^{4+} + H_2O \rightarrow PuOH^{3+} + H^+$	− 1.3
$PuO_2^{2+} + H_2O \rightarrow PuO_2OH^+ + H^+$	− 3.3
$Pu^{4+} + CO_3^{2-} \rightarrow PuCO_3^{2+}$	+47
$PuO_2^{2+} + 2\ CO_3^{2-} \rightarrow PuO_2(CO_3)_2^{2-}$	+15

[a] Generally at 25°C. but at varying ionic strengths; data taken from Coleman (*4*).

of its various oxidation states, particularly considering the effect of carbonate ions which are important species in natural waters and good complexing agents for plutonium. In Figure 1 the solubilities of the tri-, tetra- and hexavalent forms of plutonium are plotted, taking into account the monohydroxy hydrolysis species and carbonate complexes. Each of these species is in equilibrium with its respective hydroxide solid, no consideration being given to redox equilibria. In constructing this solubility diagram the data used for the solubility products, hydrolysis reactions, and carbonate complex formation constants are given in Table I. For each oxidation state in equilibrium with its respective solid hydroxide the solubility decreases with increasing pH. However, as indicated in Figure 1, as the pH increases and hydrolysis products form, the latter become the predominant species in solution, and the solubility is higher than would be expected in their absence. Curves D and E of Figure 1 indicate that added carbonate significantly increases the solubilities of Pu(VI) and Pu(IV) owing to the formation of carbonate complexes. These curves were calculated for an ambient stoichiometric carbonate concentration of $10^{-3}M$, a typical value for natural fresh waters. Stoichiometric carbonate includes H_2CO_3, HCO_3^-, and CO_3^{2-}.

Table II. Standard Reduction Potentials (at 25°C.) for Various Plutonium Hydroxides in Equilibrium with $Pu(OH)_4$ (*21*)

Reaction	E°, *volts*	Eh
$PuO_2(OH)_2 + 2H^+ + 2e \rightleftharpoons Pu(OH)_4$	+0.51	0.51–0.059 pH
$PuO_2(OH) + H^+ + H_2O + e^- \rightleftharpoons Pu(OH)_4$	+0.76	0.76–0.059 pH
$Pu(OH)_4 + H^+ + e^- \rightleftharpoons Pu(OH)_3 + H_2O$	−0.95	−0.95–0.059 pH

Although Figure 1 is useful in visualizing the relative solubilities of various oxidation states as affected by pH and carbonate, it is incomplete in that it does not consider the redox potential of the solution and the

redox equilibria among the various plutonium oxidation states. The most stable form of insoluble plutonium hydroxide in the pH range of natural waters is the tetravalent oxidation state (*10, 22, 23*). Table II shows the standard reduction potentials, $E°$, and the expression for the redox potentials, *Eh*, at which the solid hydroxides of the tri-, penta-, and hexavalent states are each in equilibrium with that of the tetravalent state.

For the reduction of $PuO_2(OH)_2$ to $Pu(OH)_4$, if *Eh* of the solution is less than +0.51 minus 0.059 pH, the $Pu(OH)_4$, is the stable species. $Pu(OH)_3$ cannot exist as a solid form in equilibrium with water because if *Eh* becomes less than zero minus 0.059 pH, water would be reduced to hydrogen. The pentavalent hydroxide form, $PuO_2(OH)$, is unstable in both acidic and basic aqueous solutions (*21*) and converts to either the hexavalent or the tetra or trivalent forms because of its $E°$. Thus, if *Eh* is greater than 0.51 — 0.059 pH, $PuO_2(OH)_2$ will be the stable form, while below this *Eh* $Pu(OH)_4$ will be, these being the only stable plutonium hydroxides likely to be found in equilibrium with water. The question remains as to the likely *Eh* to be encountered in natural waters or even under laboratory conditions. Baas Becking, Kaplan, and Moore (*1*) have collected many reports of *Eh* values in natural waters. In an

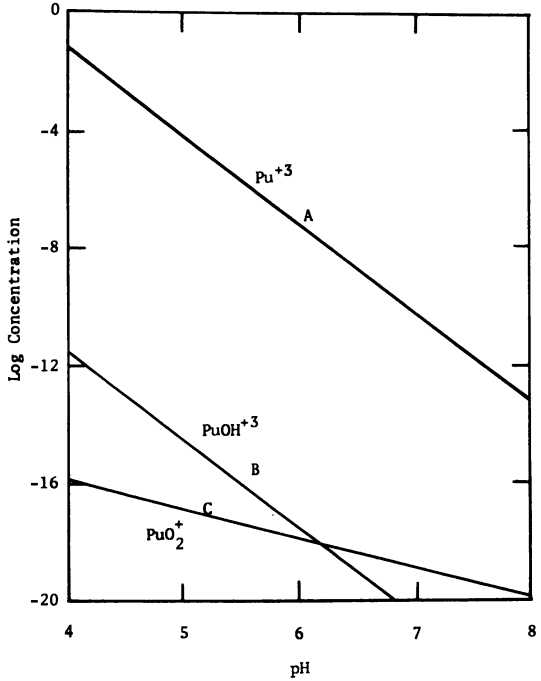

Figure 2. Soluble Pu in equilibrium with $Pu(OH)_4(s)$ at 25°C. Eh = *0.4–0.059 pH*

extension of their data, Garrels and Christ (*8*) indicate that the majority of streams, and other waters in contact with the atmosphere, have *Eh* values between approximately 0.4 and 0.8 minus 0.059 pH.

If all plutonium oxidation states are potentially present in an aqueous solution, the predominant species of soluble plutonium in equilibrium with the stable $Pu(OH)_4$, will be determined by the redox potential of the solution. If it is assumed that the *Eh* for an aqueous system varies with pH according to $Eh = 0.42 - 0.059$ pH, it is possible to construct a log *C vs.* pH diagram and determine the concentrations of the soluble plutonium species in equilibrium with $Pu(OH)_4$. This is done in Figure 2 from pH 4 to 8, a region of environmental interest, using the *Eh* values and solubility product and hydrolysis constants in Table I; it is assumed that no carbonate is present. In this range of pH Figure 2 indicates that Pu^{3+} is the most soluble species expected to be in equilibrium with solid $Pu(OH)_4$. The Pu(IV) hydrolysis product, $PuOH^{3+}$, and PuO_2^+ have equilibrium concentrations which are considerably less than Pu^{3+}, while PuO_2^{2+} and its monohydroxy hydrolysis product have even lower solubilities and are not included in the figure.

However, these solubility relationships will change with *Eh*—*e.g.*, as *Eh* becomes more positive, the Pu^{3+} line will be lower, while those for $Pu(OH)^{3+}$ and PuO_2^+ will be raised. Also the presence of carbonate will raise the solubility line for Pu(IV) significantly. Nevertheless, in the neutral region of pH Figure 2 indicates that at the *Eh* used here, a typical environmental value, the solubility of plutonium in equilibrium with solid $Pu(OH)_4$ is quite low.

Ockenden and Welch (*27*) measured the distribution of valence states in equilibrium with ionic Pu(IV) in 0.1*M* nitric acid. They found that, starting with a solution containing only the ionic form of Pu(IV), the colloid is formed very quickly with the disproportionation 3Pu(IV) = 2Pu(III) + Pu(VI) competing. After several hours approximately 55% was insoluble colloidal Pu(IV), 25% was Pu(III), about 15% was Pu(VI), and the remainder was still ionic Pu(IV).

Experimental

The 1-mCi plutonium(IV) stock solution (in 5.1 ml. of 2.6*N* HNO_3) was obtained from The Radiochemical Center, Amersham, England, which furnished the mass analysis of the plutonium: 99% ^{239}Pu, 1% ^{240}Pu, <0.01% ^{241}Pu, <0.01% ^{241}Am, <0.0025% ^{238}Pu. To obtain the appropriate ambient solution plutonium concentration, pH, and ionic strength, aliquots of this stock solution were diluted typically with doubly distilled and demineralized water, then titrated to a given pH, and buffer and salt solutions were added. Except when studying the effects of aging, the solution was then agitated with a magnetic stirrer for one to two hours before centrifugability studies. Borosilicate vessels and

other glassware were generally used. The typical pH 7 solution studied contained 0.001*M* phosphate buffer, $10^{-7}M$ Pu and had an ionic strength of 0.1. All experiments were performed at 24°–26°C.

Occasionally, granular silica (supplied either by the Ottawa Silica Co. or Fisher Scientific Co.) was added to the plutonium solution for various periods before centrifugation to determine its effect on the colloidal system. The silica was first dry sieved, washed thoroughly, then oven dried at 120°C.; the particle sizes ranged from 280 to 390μ. Other chemicals used were reagent grade.

The plutonium solution concentration was determined by alpha counting 0.5-ml. aliquots evaporated to dryness on planchets. Gas flow internal proportional counting was used with 90% argon–10% methane gas and Nuclear Measurement Corp. counters.

The effect of solution composition on plutonium particle size or its distribution was determined by two centrifugation techniques. In the first, the percent of plutonium centrifugable was determined for a given time and speed of centrifuging (*e.g.*, 5 minutes at 19,000 r.p.m. or 31,000 *g*), using a Sorvall Model RC2-B high speed centrifuge with a 34° rotor, No. SS-34. The solution was sampled at 1.5 cm. below its surface. The second method, by which plutonium particle size distributions were determined, utilized a Sorvall Model GLC-1 centrifuge with a horizontal bucket rotor, No. HL-4. Using 3-ml. centrifuge tubes, four aliquots of a given plutonium colloidal solution were centrifuged for 5 minutes at speeds of 200, 400, 1000, and 3000 r.p.m., respectively. Before inserting the plutonium solutions, silica sand was placed in the bottom of the tube to a height of 1 cm., creating a false bottom. After centrifugation the entire volume above the sand (approximately 1 ml.) was removed and alpha counted, the false bottom serving to prevent resuspension of centrifuged plutonium. The size distribution was then calculated by the method of Menis, House, and Boyd (*26*), which corrects for some removal of particles smaller than the limiting diameter species, all of which is centrifuged from that portion of the solution above the upper surface of the false bottom at the given speed and time. With the assumption of spherical plutonium hydroxide colloidal species with a density of 14.0 (that of PuO_2), the method included the equivalent spherical diameter range of 0.076–1.13μ. Although the assumptions of geometry and density are questionable, the method is still useful as a comparative one.

To study the effect of ionic strength on plutonium particle size distributions, three pH-7 solutions were prepared, and the ionic strengths were adjusted to 0.002, 0.01, and 0.1. The latter two had $NaClO_4$ added, and this was the major source of the ionic strength. The solutions of lowest ionic strength did not receive any $NaClO_4$, and the principal species came from the sodium hydroxide and monopotassium phosphate. After aging for a few months, the solutions were centrifuged, and the particle size distributions were determined. The results are shown in Figure 3. In this figure and subsequent plots of particle size distributions the abscissa is a probability scale. It is clear that there is a general shift to larger size particles with increasing ionic strength.

Further evidence of the effect of ionic strength on the plutonium colloidal system is shown in Figure 4, in which the size distribution of a 43-day old solution with an ionic strength of 0.002 is compared with a

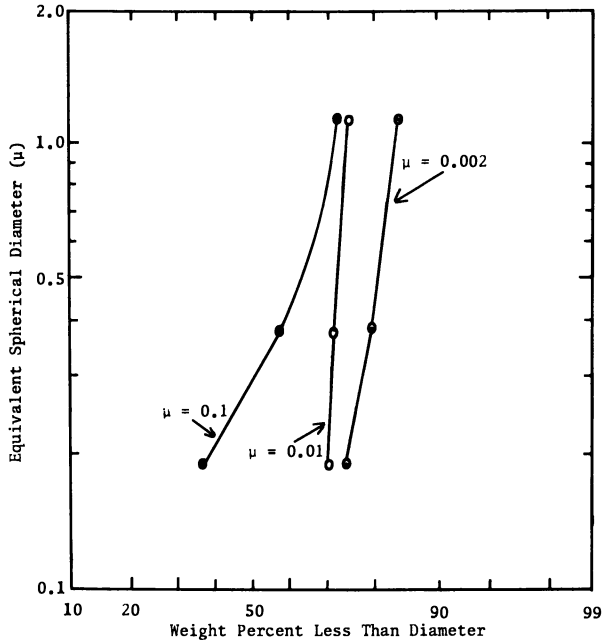

Figure 3. Pu(IV) particle size distributions in solutions of different ionic strengths at pH 7

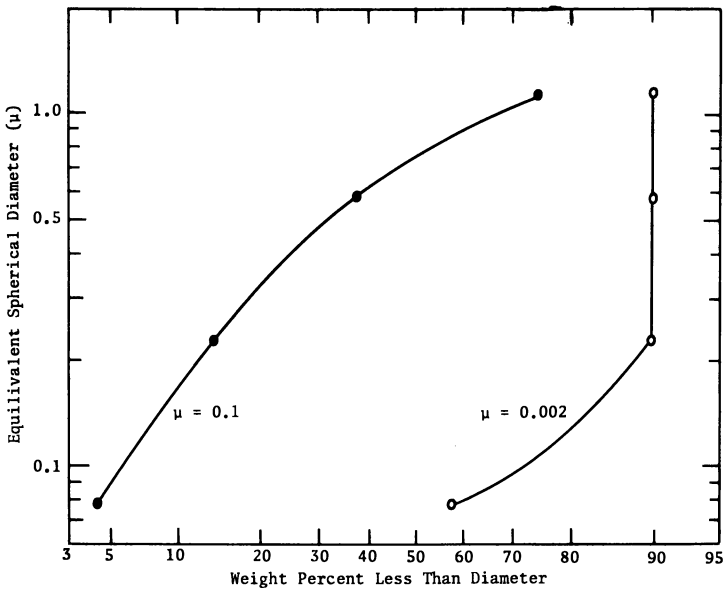

Figure 4. Comparison of Pu(IV) particle size distributions in aged pH 7 solutions prior to and 5 days after raising the ionic strength

portion of the same solution five days after the ionic strength was raised to 0.1 by adding $NaClO_4$. As a control, the distribution of the original solution was determined again and had not changed. The increase in the percentages of large and intermediate sizes is quite marked, indicating that the addition of the $NaClO_4$ promoted the growth of the plutonium particles.

To study the effects of aging and radionuclide concentration on the particle sizes of the colloid, plutonium solutions, initially ranging in concentration from approximately 2×10^{-6} to $2 \times 10^{-8}M$, were aged up to 7 days at pH 7 and $\mu = 0.1$. Prior to aging and after 3 and 7 days, each solution was centrifuged for 5 minutes at 50 *g*; the results are given in Figure 5. Although there were very few differences initially in centrifugability at the various plutonium concentrations and this centrifugability was relatively low, with aging the colloids grew significantly larger, also showing some variation with plutonium concentration. To determine the effect of added silica, 4 grams of the latter were added to each of several 80-ml. fresh and aged plutonium solutions, all of which were then aged for 18 days before measuring the centrifugability. These results are also given in Figure 5. Note that when silica surfaces are exposed to the colloidal plutonium, significant quantities of the latter may sorb onto the former, and this phenomenon occurred here. The data summarized in Figure 5 generally indicate that aging, ambient plutonium concentration, and the presence of silica surfaces all affect the radiocolloidal size distribution.

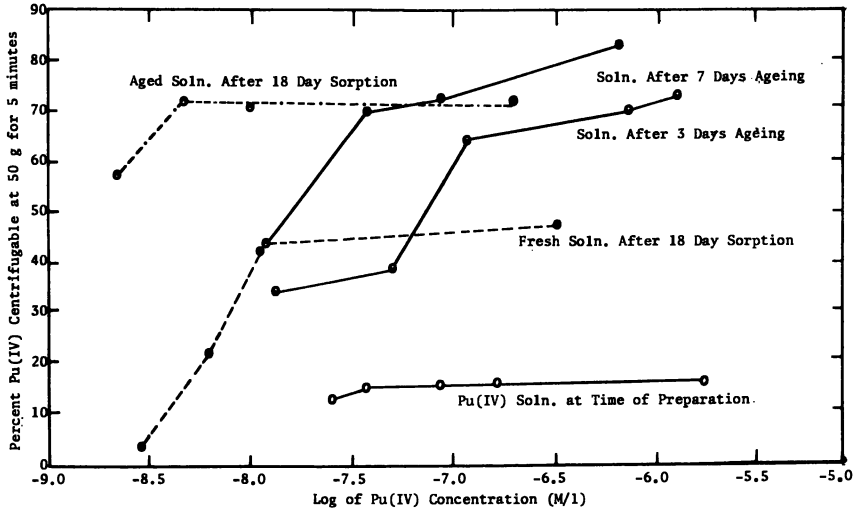

Figure 5. Percent Pu(IV) centrifugable at different times as a function of concentration at pH 7

To determine the effect of varying pH in the region of environmental interest on the plutonium size distribution, the latter was measured for plutonium solutions at an ionic strength of 0.01 pH of 5.4, 6.2, 6.9, and 8.2, shortly after pH adjustment, and also following 12 days of aging.

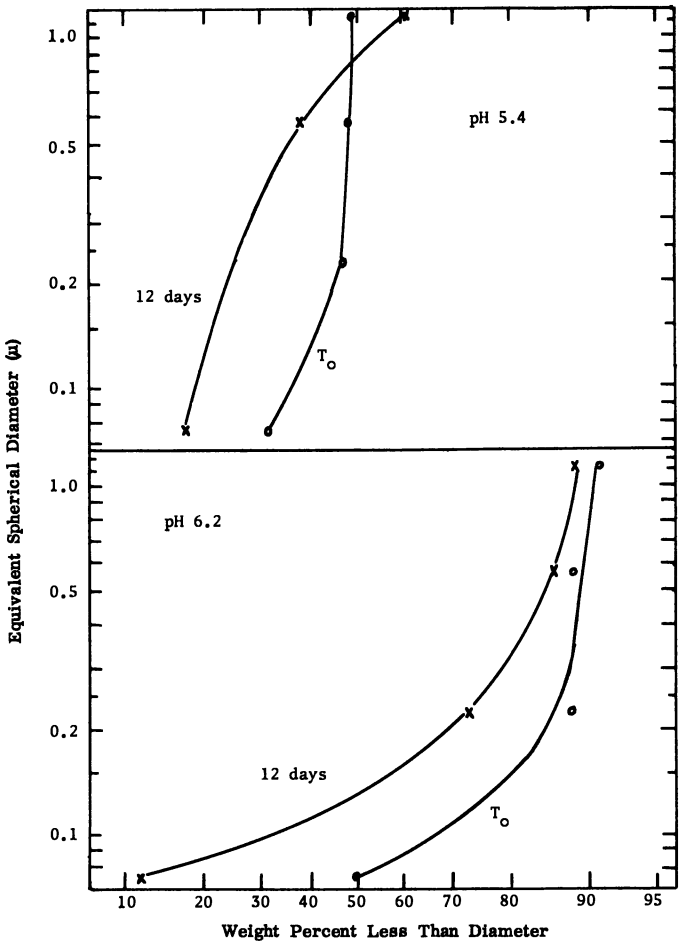

Figure 6. Pu(IV) size distributions for fresh and 12-day aged solutions at pH 5.4 and 6.2 at $\mu = 0.01$

The distributions are shown in Figure 6 for pH 5.4 and 6.2, and Figure 7 for 6.9 and 8.2. Although at each pH there was an increase in colloid size with aging, after 12 days the distributions at pH 5.4 and 8.2 contained significantly more of the larger particles than did those at pH 6.2 and 6.9.

To determine if bicarbonate has similar effects on the nature of the radiocolloid, the plutonium size distributions were studied at pH 7 as a function of bicarbonate concentration, using bicarbonate only from atmospheric CO_2 and in solutions with $[CHO_3^-]$ equal to $10^{-2}M$. The latter were prepared by adding $NaHCO_3$. Two different ionic strengths were used to distinguish between the effects of added bicarbonate and ionic strength. The distributions of identical solutions which were shaken in flasks with and without granular silica were determined initially and

after 13 days. The distribution curves for the low ($\mu = 0.012$) and high ($\mu = 0.112$) ionic strength solutions are shown in Figures 8 and 9, respectively. As previously, there was a general increase in the particle size distributions with aging and increased ionic strength. At the lower ionic strength (Figure 8) the higher bicarbonate concentration had a greater effect on the distribution of the larger sized particles than on that of the smaller ones. At the higher ionic strength the effect was less systematic but nonetheless large. At both ionic strengths the distributions were affected more markedly by bicarbonate initially, as compared with 13 days subsequently. As previously, the presence of silica significantly shifted the plutonium ambient particle size distribution, the shift being in opposite directions, however, at low and high ionic strengths.

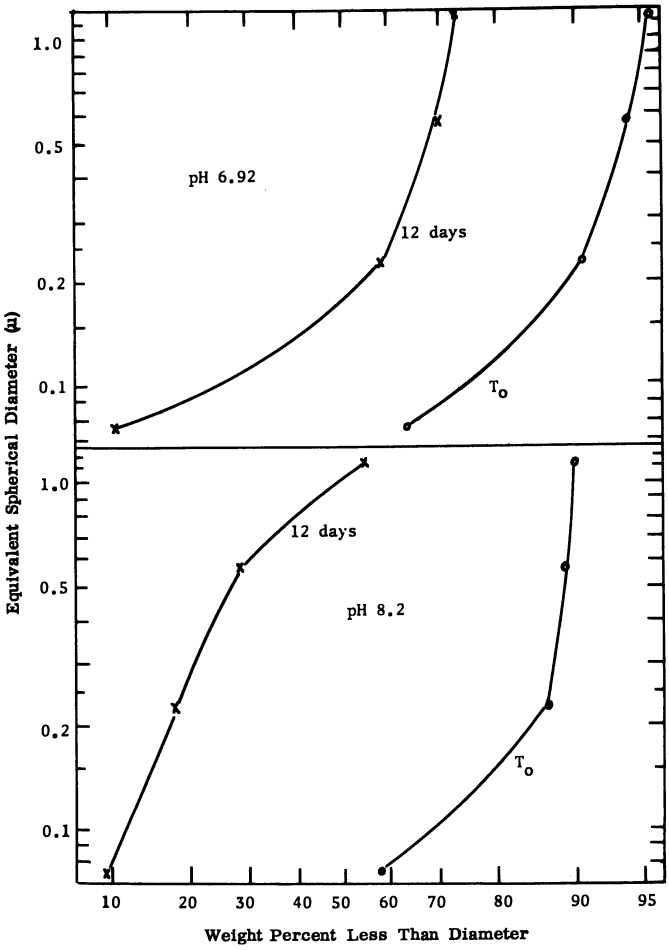

Figure 7. Pu(IV) size distributions for fresh and 12-day aged solutions at pH 6.9 and 8.2 at $\mu = 0.01$

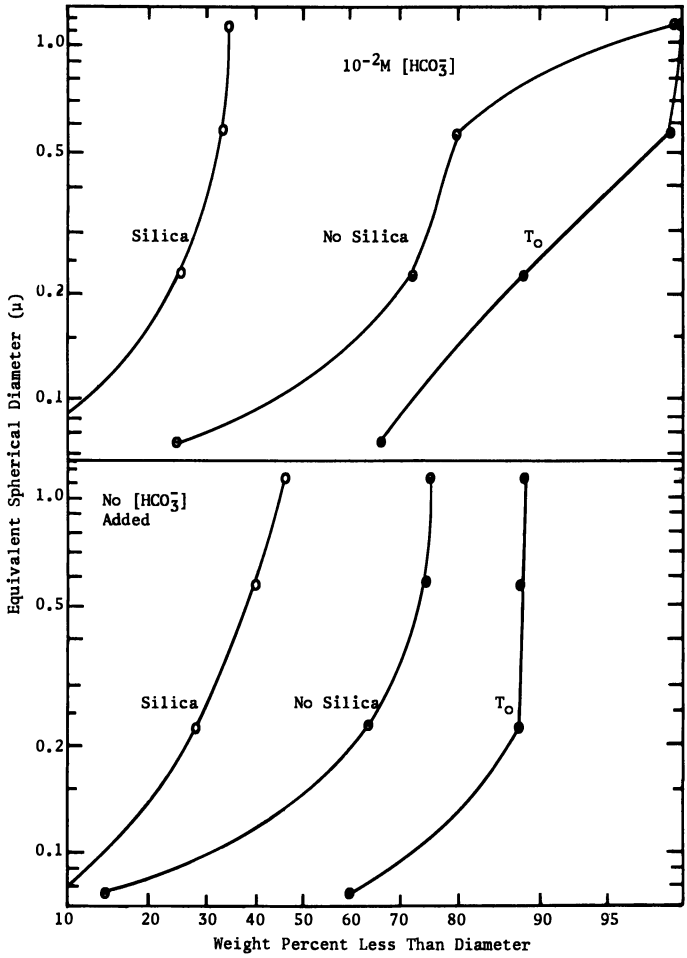

Figure 8. Effect of bicarbonate on Pu(IV) size distribution at pH 7 and ionic strength 0.012

Discussion

The centrifugability studies made on aging solutions in the absence of silica indicate, as shown in Figure 5, that the plutonium hydrolysis products undergo slow coagulation as the suspension ages. On the basis of Smoluchowski's theory of slow coagulation, as discussed by Kruyt (*19*), the fresh solutions have a large percentage of "primary," uncoagulated particles which with time coagulate to form larger species, with a steady-state distribution of sizes finally being attained and the total number of particles ultimately being smaller than that initially present.

The coagulation of the plutonium, while characteristically slow, may also be classified as limited. The particle size distributions indicate that, even after considerable aging, there remain particles in a large range of sizes, though considerably fewer of the small particles. Kruyt (*19*) has explained limited coagulation on the basis of a decrease in rate because the repulsive forces between large particles are greater than those between small primary particles. However, Gillespie (*9*) believes that deflocculation occurs in competition with flocculation, limiting the extent of coagulation and establishing an equilibrium distribution among the different sizes.

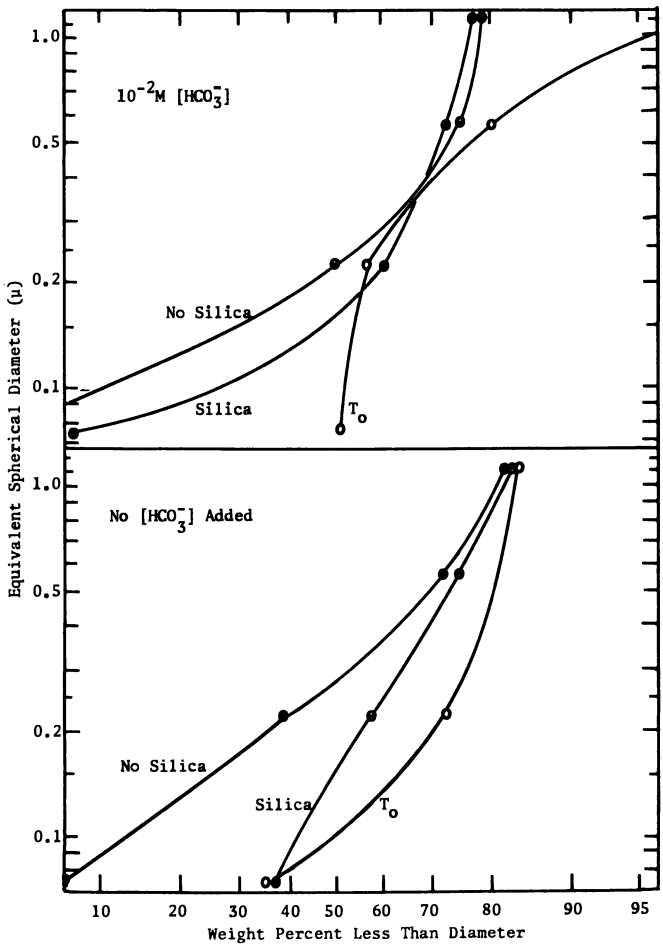

Figure 9. Effect of bicarbonate on Pu(IV) size distribution at pH 7 and ionic strength 0.112

The study of the percent plutonium centrifugable as a function of concentration, as shown in Figure 5, clearly indicates that not only does the percentage of larger particles increase with time but also with concentration, at least for the aged solutions. However, it it possible that the smaller concentrations of colloids simply coagulate at a slower rate. The aged solutions which had sorbed onto silica for 18 days, also shown in Figure 5, measured quite constant centrifugabilities, about the same as those of the more concentrated 7-day aged solution, in agreement with this hypothesis. In any event, at some point in decreasing the plutonium concentration its centrifugability must also decrease, especially as the solubility limit is approached.

When the ionic strength of the plutonium solutions was increased by the addition of sodium perchlorate, as would be expected with colloid systems (*34*), there was an increase in the degree of aggregation and formation of large particles, as shown in Figure 3. If the colloid suspension is relatively stable, as was the 43-day old solution shown in Figure 4, electrolyte addition causes the immediate onset of aggregation, leading to a substantially higher percentage of large particles. Van Olphen (*41*) points out that this arises from a compression of the electrical double layer, which leads to a reduction in the range of the repulsive forces between two approaching colloidal particles.

The bicarbonate ion, HCO_3^-, is a prevalent species in natural waters, ranging in concentrations up to 0.8×10^{-3}. As was indicated previously, carbonate ions have the ability to form complexes with plutonium. Starik (*39*) mentions that, in an investigation of the adsorption of uranium, there was a decrease in the adsorption after reaching a maximum, which was explained by the formation of negative carbonate complexes. Kurbatov and co-workers (*20*) found that increasing the bicarbonate ion concentration in a UX_1 (thorium) solution decreased the amount of thorium which formed a colloid and became filterable. This again was believed to be caused by the formation of a soluble complex with the bicarbonate.

As shown in Figures 8 and 9, the addition of 0.01*M* bicarbonate at pH 7 had a greater effect initially on the particle size distribution, as compared with the solutions aged for 13 days. At $\mu = 0.112$ the effect was uniform in the direction of larger particle formation, while at $\mu = 0.012$ only particles of equivalent spherical diameters in the range of 0.2 to 1.0μ were lost in favor of larger particles. The formation of carbonate complexes in solution reduces the net positive charge of the ionic plutonium and would be expected to do the same with a positively charged colloidal plutonium hydroxide if carbonate surface complexes were formed. The reduced surface charge would reduce the mutual electrostatic repulsion of the coagulating species, and thereby facilitate the formation of larger colloids. Parks (*29*) has indicated that the isoelectric

pH of solid metal hydroxides frequently is equal to that of the soluble species of the corresponding metal ion, the complex and hydrolysis products of the soluble metal being duplicated at the metal hydroxide surface.

It should be noted, however, that there is still some question as to the sign of the charge of the plutonium hydroxide colloid at pH 7. Although Grebenshchikova and Davydov (*10*) have shown by electromigration studies of $2 \times 10^{-5}M$ plutonium(IV) that below a pH of 7.5 to 8 the colloid is positively charged, while above this pH it is negative, in a later study Davydov (*6*) indicated that at lower plutonium concentrations—*e.g.*, $7 \times 10^{-7}M$, the isoelectric pH is as low as 3.2. He explains this is caused by the formation of pseudocolloids at the lower concentrations by sorption of the plutonium onto negatively charged colloidal contaminants. However, the general existence of this pseudocolloid is disputed by Starik *et al.* (*39*), who consider it an artifact in Davydov's work, owing to the formation of silica acid colloids from the glass containers. If such a phenomenon were important in the present work, it could not be considered an artifact; father it would be comparable with the pseudocolloidal plutonium systems likely to be found in natural waters, which contain significant quantities of colloidal silica and other negatively charged colloidal minerals.

Although the general effect of the addition of bicarbonate was to increase the size of the colloidal species, Lindenbaum and Westfall obtained the opposite effect with citrate addition over the pH range 4–11, as measured by the percent of plutonium(IV) that was ultrafilterable (*22*). However, their plutonium concentrations were $2 \times 10^{-5}M$, and the solutions probably contained true colloids, rather than pseudocolloids, if one accepts Davydov's analysis. Lindenbaum and Westfall concluded that the mechanism of the citrate action was the complexation of plutonium, thereby preventing the formation of hydrolytic polymers. It should be noted, however, that even with a citrate–plutonium molar ratio of 1800 ($3.4 \times 10^{-4}M$ citrate), about 10% of the plutonium still could not pass through the ultrafilter for solutions aged up to four days (*22*).

In considering the effects of bicarbonate on the colloidal size distributions, it was also observed that the addition of silica affected the latter slightly at an ionic strength of 0.112, but increased the size of the colloid significantly at an ionic strength of 0.012, as shown in Figure 8. Although in subsequent papers the interactions of the plutonium with the silica surfaces will be considered in detail, note that the plutonium sorption onto the silica is much higher at the higher ionic strength, and that the distribution of sizes of the sorbed plutonium is quite different from that in the ambient solution. For the present discussion, however, it is sufficient to note that the presence of the silica may affect the plutonium colloid size distribution markedly.

The aging phenomenon, resulting in larger plutonium colloids, was also observed for solutions whose pH were varied from 5.4 to 8.2, as shown in Figures 6 and 7. The distributions at the three higher pH are initially all quite similar and generally smaller than that at pH 5.4. However, after 12 days of aging, only the distributions for the highest and lowest pH's, namely 5.4 and 8.2, are very similar and represent significantly greater quantities of the larger particles than do those at pH 6.2 and 6.9, which are also quite similar. Finally it should be noted that for these 12-day aged solutions at all values of pH the relative amounts of small particles, those less than 0.074μ equivalent spherical diameter, are all nearly equal at 10–15% of the total plutonium.

In contrast to these varying distributions, Lindenbaum and Westfall (*22*) obtained reasonably constant percentages of ultrafilterable plutonium over this same region of pH—*i.e.*, about 10% one hour after pH adjustment in the absence of citrate and 90% after four days in the presence of citrate (these percentages referring to that which passes through the ultrafilter). This consistency in ultrafilterability with pH is in agreement with the reasonably constant percentage of particles found below 0.074μ for the 12-day aged solutions reported here. Similar constancy was shown by Grebenshchikova and Davydov (*10*) over this same range of pH with about 6% ultrafilterable plutonium (less than 1–3 mμ particles) and 10% not centrifugable (less than 30–40 mμ particles). Samartseva (*32*) obtained similar and constant results with ultrafiltration, but obtained variations with pH by centrifugation, without stating the experimental conditions for the latter. Nevertheless, at pH 4.4, 6.8, 7.2, 7.4, 7.7, and 8.0 the percentage of plutonium(IV) centrifuged from solution was 51, 70, 70, 65, 5, and approximately zero, respectively. This is essentially opposite to the results reported here in Figures 6 and 7. Near the isoelectric pH or point of zero charge of the colloidal plutonium, one would expect a region of stability with small primary colloidal particles (*19*), which could be near the pH region of 6.2 and 6.9 (*10*) but could also be significantly lower (*6*). However, the growth to larger colloids at pH 5.4 and 8.2 is difficult to interpret in these solutions of constant ionic strength. A possible explanation of a tendency to form larger colloids with increasing pH is the presence of multicharged negative phosphate species, which could affect the coagulating process by reducing the electric double layer if the colloidal plutonium hydroxide were in fact positively charged throughout this range of pH; with increasing pH the average charge on the phosphate species increases as well.

Although it is important to understand the mechanisms in the formation of the distribution of sizes among the colloidal plutonium hydroxide particles, the distributions themselves will influence the behavior

and fate of this material in environmental waters. The ability of plutonium to settle out from or be carried by a flowing stream, and the interaction of the various sized colloidal particles with other bottom or suspended colloidal minerals and biota, will both be affected by aging, changes in pH, fluctuations in ionic strength as encountered in tidal estuaries, and variations in bicarbonate and other natural complexing agents. To understand or predict the nature of these processes or interactions, it will be useful, if not necessary, to ascertain the kinds of and distribution of sizes among the colloidal plutonium species because such particles are the dominant plutonium species likely to be encountered in a natural water contaminated with plutonium.

Literature Cited

(1) Baas Becking, L. G. M., Kaplan, I. R., Moore, O., *J. Geol.* **68,** 243 (1960).
(2) Carniglia, S. C., *U. S. At. Energy Comm.* **CN-2330** (Nov. 1944).
(3) Christenson, C. W., Fowler, E. B., Johnson, G. L., Rex, E. H., Virgil, F. A., *Sew. Ind. Wastes* **30,** 1478 (1958).
(4) Coleman, G. H., *Natl. Acad. Sci. Natl. Res. Council, Publ.* **3058** (1965).
(5) Costanzo, D. A., Biggers, R. E., *U. S. At. Energy Comm.* **ORNL-TM-585** (1963).
(6) Davydov, Yu. P., *Radiokhimiya* **9,** 94 (1967).
(7) *Ibid.*, p. 52.
(8) Garrels, R. M., Christ, C. L., "Solutions, Minerals and Equilibria," Harper and Row, New York, 1965.
(9) Gillespie, Thomas, *J. Colloid Sci.* **15,** 313 (1960).
(10) Grebenschchikova, V. I., Davydov, Y. P., *Radiokhimiya* **7,** 191 (1965).
(11) Hindman, J. C., *Natl. Nuclear Energy Ser.* **14B,** Paper 4.4 (1954).
(12) International Atomic Energy Agency, *IAEA Tech. Rept.* **49** (1965).
(13) Jacobson, L., Overstreet, R., *Soil Sci.* **65,** 129 (1948).
(14) Kepak, F., Kanka, J., *Intern. J. Appl. Radiation Isotopes* **18,** 673 (1967).
(15) King, E. L., *U. S. At. Energy Comm.* **MDDC-393** (1946).
(16) Kraus, K. A., *U. S. At. Energy Comm.* **CN-3399** (1945).
(17) Kraus, K. A., *Intern. Conf. Peaceful Uses Atomic Energy, 1st,* **7,** 245 (1956).
(18) Kraus, K. A., *Natl. Nuclear Energy Ser.* **14B,** Paper 3.16 (1954).
(19) Kruyt, H. R., "Colloidal Science," Vol. 1, Elsevier Publishing Co., New York, 1952.
(20) Kurbatov, M. H., Webster, H. B., Kurbatov, J. D., *J. Phys. Colloid Chem.* **54,** 1239 (1950).
(21) Latimer, W. M., "Oxidation Potentials," 2nd ed., Prentice-Hall, Englewood Cliffs, N. J., 1952.
(22) Lindenbaum, A., Westfall, W., *Intern. J. Appl. Rad. Isotopes* **16,** 545 (1965).
(23) Lutz, M., Metivier, H., Langlois, Y., *Rapport* **CEA-R-3092** (1956).
(24) Magno, P. J., Kauffman, P. E., Shleien, B., *Health Phys.* **13,** 1325 (1967).
(25) McKay, H. A. C., "Atomic Energy Waste," E. Glueckauf, Ed., Interscience, New York, 1961.
(26) Menis, O., House, H. P., Boyd, C. M., *U. S. At. Energy Comm.* **ORNL-2345** (1957).
(27) Ockenden, D. W., Welch, G. A., *J. Chem. Soc.* **653,** 3358 (1956).
(28) Olafson, J. H., Larson, K. H., *Proc. Nat. Symp. Radioecology, 1st, Colorado State Univ.* (1961).

(29) Parks, George A., *Chem. Rev.* **65,** 177 (1965).
(30) Pillai, K. C., Smith, R. C., Folsom, T. R., *Nature* **203,** 568 (1964).
(31) Rhodes, D. W., *Soil Sci.* **84,** 465 (1957).
(32) Samartseva, A. G., *Radiokhimiya* **4,** 647 (1962).
(33) Sayre, W. W., Guy, H. P., Chamberlain, A. R., *U. S. Geol. Survey, Profess. Paper* **433-A** (1963).
(34) Schenkel, J. H., Kitchener, J. A., *Trans. Faraday Soc.* **56,** 161 (1960).
(35) Schubert, J., Conn, E. E., *Nucleonics* **4,** 2 (1949).
(36) Schweitzer, G. K., Jackson, W. M., *J. Am. Chem. Soc.* **76,** 941 (1954).
(37) Sinitsyna, G. S. *et al., Radiokhimiya* **9,** 397 (1967).
(38) Spitsyn, V. I. *et al., J. Inorg. Nucl. Chem.* **31,** 2733 (1969).
(39) Starik, I. E. *et al., Radiokhimiya* **9,** 105 (1967).
(40) Taube, M., "Plutonium," The Macmillan Co., New York, 1964.
(41) Van Olphen, H., "An Introduction to Clay Colloid Chemistry," Interscience, New York, 1963.
(42) Wood, R., Burden, B. A., *Nature* **213,** 637 (1967).

RECEIVED January 10, 1969. Work supported by the National Center for Radiological Health, U. S. Public Health Service, Research Grant No. RH 00322-03. A portion of this work is abstracted from the Sc.D. dissertation of T. C. Rozzell, Graduate School of Public Health, University of Pittsburgh, October 1968.

9

Transport Patterns and Residence Times for Atmospheric Trace Constituents *vs.* Altitude

E. A. MARTELL

National Center for Atmospheric Research, Boulder, Colo. 80302

Mechanisms and rates of transport of nuclear test debris in the upper and lower atmosphere are considered. For the lower thermosphere vertical eddy diffusion coefficients of 3–6 × 10^6 $cm.^2$ $sec.^{-1}$ are estimated from twilight lithium enhancement observations. Radiochemical evidence for samples from 23 to 37 km. altitude at 31°N indicate poleward mean motion in this layer. Large increases in stratospheric debris in the southern hemisphere in 1963 and 1964 are attributed to debris from Soviet tests, transported via *the mesosphere and the Antarctic stratosphere. Most of the carbon-14 remains behind in the Arctic stratosphere.* $^{210}Bi/^{210}Pb$ *ratios indicate aerosol residence times of only a few days at tropospheric levels and only several weeks in the lower stratosphere. Implications for the inventory and distribution of radioactive fallout are discussed.*

Our incomplete understanding of the numerous processes which control the redistribution of atmospheric trace constituents limits our ability to predict radioactive fallout, to assess the atmospheric burden of nuclear bomb debris, to evaluate the influx of extraterrestrial dust, and to solve related problems. At each level of the atmosphere there are various processes which compete in their influence on particle transport, including molecular diffusion, ion migration, gravitational sedimentation, turbulent or eddy mixing, atmospheric mean motions, particle coagulation, precipitation scavenging, etc. At the outset of atmospheric fallout research little was known about the circulation processes that govern fallout transport in the upper atmosphere. Recent studies (*2, 5, 9, 21, 26*) of the distribution of bomb products and natural radioactivity have contributed

to our understanding of stratospheric transport processes. It is now well known that the upper atmosphere is not a simple well-mixed reservoir, but a highly complex system in which the patterns and rates for the redistribution of constituents vary markedly with altitude, latitude, season, and year.

This chapter reviews and clarifies some of the main features in the pattern and rate of transport of nuclear bomb debris from the upper atmosphere down to the surface of the earth. The atmospheric nonmenclature used is that based on the thermal structure of the atmosphere and recommended by the International Union of Geodesy and Geophysics at Helsinki in 1960, shown in Figure 1. Starting with the lower thermosphere, the important mechanisms of vertical transport are discussed

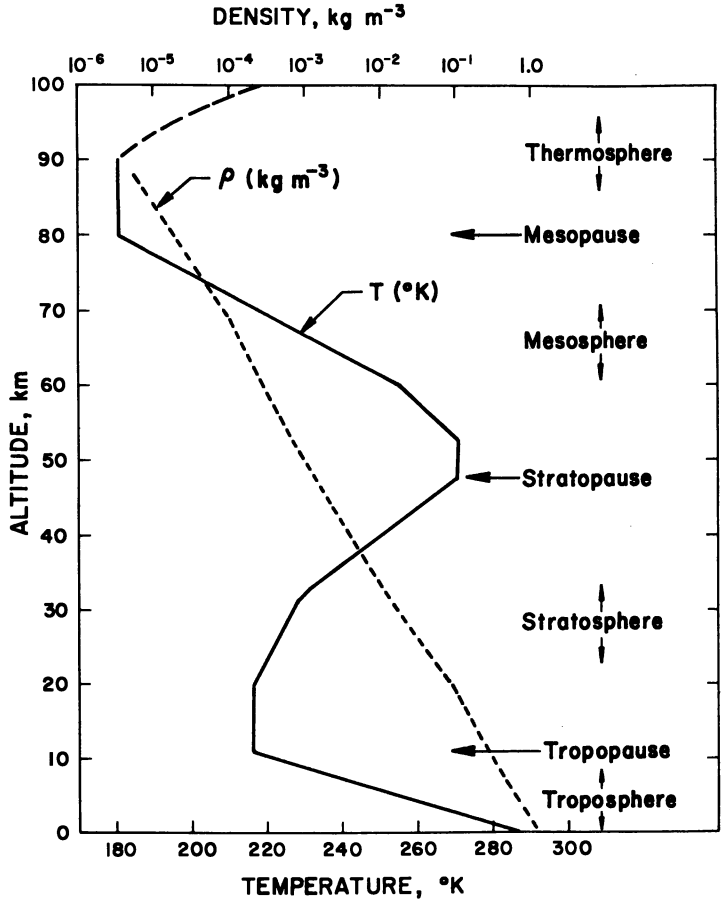

Figure 1. Temperature and density profile according to the U. S. Standard Atmosphere (1962) and the IUGG nomenclature (1960)

together with an indication of the significant seasonal and latitudinal variations in the pattern of downward mixing. Where possible, the mean residence time of trace constituents in each atmospheric layer or region is indicated.

Atmospheric residence times and apparent ages are convenient concepts used by geochemists to characterize the stability of an air parcel or the average lifetime of aerosols or trace gases within an air parcel. The half-residence time for an air parcel which is well mixed with respect to a given tracer is the time required to reduce the tracer concentration to one-half its initial value by mixing with tracer-free surrounding air. The mean or average residence time, τ_R, equals the half-residence time divided by ln 2. Relationships for estimating apparent ages from the observed concentration of one or more radioactive cosmic ray spallation products are given by Bhandari *et al.* (*2*) and Lal and Peters (*26*). The estimation of residence times and aerosol ages from radon daughter product concentrations is discussed later in this paper.

Descent in the Thermosphere

The thermosphere is the thin outer layer of our atmosphere extending from the mesopause near 80 km. altitude out to the exosphere, some several thousand km. altitude, where the mean free path is sufficiently long to allow escape of atomic hydrogen and helium and atmospheric capture of coronal gas constituents. In the lower thermosphere, heated by solar ultraviolet and x-radiation, the temperature increases rapidly with altitude, with temperatures above 400 km. varying between about 700° and 2100°K., depending on solar activity.

Nuclear debris injected into the thermosphere by high altitude nuclear explosions will be transported rapidly downward by several mechanisms. Ions and charged particles in the high mesosphere will spiral rapidly downward along magnetic field lines toward both conjugate points at high latitudes, penetrating to levels well below 400 km. where they are neutralized. Except for the lightest atoms, neutral constituents will descend quickly by gravitational sedimentation and molecular diffusion down to the turbopause, near 120 km. altitude. Below the turbopause transport by eddy diffusion controls the vertical redistribution of atoms and molecules.

Above 120 km. the atmosphere is essentially in diffusive equilibrium (*34*). For the altitude interval between 80 and 120 km. Colegrove *et al.* (*6*) estimated an average vertical eddy diffusion coefficient of 4×10^6 cm.^{2} sec.$^{-1}$ by a careful evaluation of the O/O_2 concentration ratio profile over this altitude interval. Using their eddy diffusion coefficient and following the procedure of Kellogg (*22*) it is estimated that molecular

debris, dispersed in a layer at 120 km. altitude, would require about 23 days for essentially complete mixing down to 80 km. It is shown below that atomic lithium from high altitude thermonuclear explosions may have mixed downward from 120 km. to the mesopause in about 16 days. These observations suggest an average vertical eddy diffusion coefficient of about 6×10^6 cm.^{2} sec.$^{-1}$ for the lower thermosphere, in good agreement with the value of Colegrove *et al.* (*6*).

Banister and Davis (*1*) have studied the descent of large neutral molecules and small particles through a stagnant exponential atmosphere under the influence of molecular diffusion and gravitational sedimentation over the interval 100–50 km. altitude. Mange (*27*) gives a comprehensive discussion of the processes governing the vertical redistribution of ions and neutral atoms over the altitude interval from the turbopause to 200 km. In this layer there is appreciable holdup of bomb tritium, lithium, and carbon-14 owing to diffusion of their ions and neutral atoms upward above the turbopause, the level at which vertical transport by eddy diffusion and molecular diffusion are equally effective.

Twilight Lithium Anomalies

The observation of enhanced atomic lithium in the twilight emission spectra following high altitude thermonuclear explosions (*11, 16, 38*) provides indirect evidence of the debris cloud heights and their early vertical redistribution in the atmosphere. Sullivan *et al.* (*38*) indicate that the maximum in the vertical distribution of atomic lithium in twilight occurs near the mesopause at about 80 km. altitude. Lithium is almost fully dissociated at higher altitudes and is combined chemically at lower levels. The two major enhancements of lithium abundance followed the Teak thermonuclear rocket shot of Aug. 1, 1958 and either the Bluegill or Kingfish rocket shots of Oct. 26 and Nov. 1, 1962. The lithium emission observations for these two occasions are presented in Figure 2. Teak was a megaton yield shot detonated at 77 km. altitude over Johnston Island (39) for which the radioactive cloud was observable by line-of-sight from Honolulu (*31*). Kingfish and Bluegill were submegaton yield devices, each detonated at an altitude of tens of km. over Johnston Island (39). For these shots also the rising fireball and outgrowth cloud was observed from the Hawaiian chain. Since the ground level distance between Johnston Island and Honolulu is about 1340 km., those portions of the Teak, Bluegill, and Kingfish clouds, which were visible above the horizon from Honolulu, exceeded 155 km. altitude. In contrast to the large lithium enhancements of August 1958 and November 1962 (Figure 2) the 1.4-megaton yield Starfish explosion at 400 km. above Johnston Island on July 9, 1962 produced only very small enhancements of brief

duration (*10, 38*), presumably caused by the holdup of lithium, mainly as ions, above the turbopause.

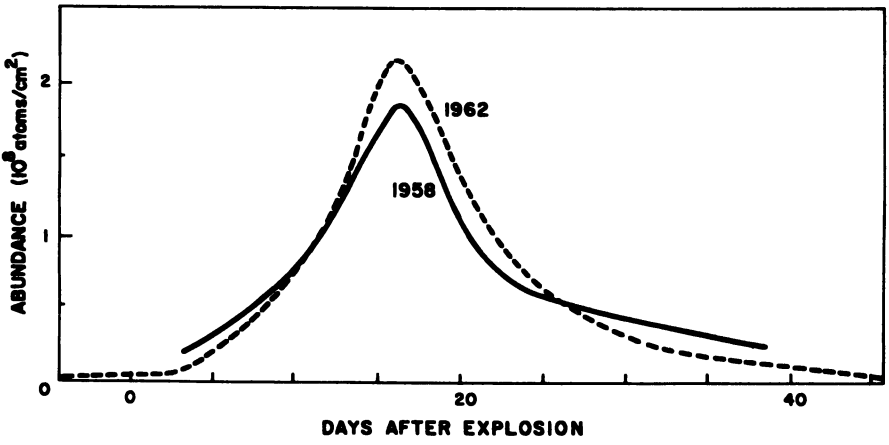

Figure 2. Variations in twilight lithium abundance at 80 km. altitude following the Teak and Starfish rocket explosions (16)

The redistribution of lithium released by the Teak, Bluegill, and Kingfish shots provides a convenient tracer for estimating an upper limit for the vertical eddy diffusion coefficient in the lower thermosphere. It is assumed that the debris had an initial concentration distribution which increased with altitude in the lower thermosphere up to the turbopause and above. Because atomic lithium is much lighter than air, both neutral and ionized lithium will be transported upward by molecular diffusion above the turbopause and downward by eddy diffusion at lower levels. On this basis, the time of occurrence of the maximum in the bomb lithium enhancements—about 16 days following the thermonuclear explosions (Figure 2)—is the time necessary for essentially complete mixing from the vicinity of the turbopause down to the mesopause. Following Kellogg (*22*), the corresponding vertical eddy diffusion coefficient, D_E, can be estimated by the relation:

$$\tau_{DE} = \frac{L^2}{2D_E} = 16 \text{ days}$$

where D_E is the eddy diffusion coefficient, τ_{DE} is the diffusion time, and L is the height of the turbulent layer, in this case the mesopause–turbopause interval. Assuming turbopause heights of 120 or 110 km. the corresponding vertical eddy diffusion coefficients are $\sim 6 \times 10^6$ or $\sim 3 \times 10^6$ cm.^{2} sec.$^{-1}$, respectively. Because horizontal transport by mean motions and eddy diffusion in the lower thermosphere is relatively rapid

(*6, 12, 14*) compared with rates of vertical mixing, the large distances between Johnston Island and the latitudes of twilight lithium observations may not affect these estimates. Such rapid horizontal transport also suggests that debris injected into the lower thermosphere is mixed well throughout the lower thermosphere within about 16 days. A uniform layer spread globally throughout the lower thermosphere with an abundance of $\sim 2 \times 10^8$ lithium atoms per cm.^{2} (Figure 2) corresponds to only 11 kg. of lithium if ionized lithium is inappreciable, as proposed by Sullivan and Hunter (*38*). This is only a small fraction of the total release of lithium that might be expected for thermonuclear devices of megaton yield, lending support for the initial vertical distribution and subsequent pattern of redistribution suggested above. It also is possible that the atomic lithium layer is present only at high latitudes. Alternatively, depending on the actual height distribution of sources, horizontal transport near 80 km. altitude may explain observations (*12*).

Assuming that the lower thermosphere is well mixed and that all of the lithium is uncombined at the mesopause level, the exponential decay in lithium concentration after 16 days (Figure 2) indicates a mean residence time of about 8 days for the lower thermosphere owing to eddy diffusion downward into the upper mesosphere. The corresponding vertical eddy diffusion coefficient over the interval one scale height below the mesopause ($\sim$ 7.2 km.) is $\sim 4 \times 10^5$ cm.^{2} sec.$^{-1}$, which is about one-fourth of the upper limit estimated for this interval based on heat transport considerations (*18*). However, if the lithium is partially combined chemically at the mesopause, the fraction combined should be larger at the higher concentrations. This would indicate a somewhat shorter eddy diffusion time and a correspondingly larger vertical eddy diffusion coefficient.

Transport in the Mesosphere

Bomb products, rocket reentry burnup products, meteoritic dust, and other trace constituents will be redistributed rapidly within the mesosphere by large scale circulation, by eddy diffusion and, for particles of significant size, by gravitational sedimentation as well (*1*). Murgatroyd and Singleton (*32*) discuss the circulation of the mesosphere and indicate a meridional pattern, with ascent over the summer pole, descent over the winter pole, and a well defined flow from the summer hemisphere to the winter hemisphere above 50 km., with speeds of the order of meters sec.$^{-1}$ horizontally and cm. sec.$^{-1}$ vertically.

The pattern of eddy mixing in the mesosphere apparently may be highly nonisotropic, similar to that indicated for the lower thermosphere. The upper limit of vertical eddy diffusion coefficients for the mesosphere

based on thermal constraints (*18*) range from about 2×10^6 cm.^{2} sec.$^{-1}$ at the mesopause to 2×10^5 cm.^{2} sec.$^{-1}$ at the stratopause. Results from rocket vapor trail observations (*22*) indicate much larger eddy diffusion coefficients of about 2×10^7 cm.^{2} sec.$^{-1}$ and 1×10^7 cm.^{2} sec.$^{-1}$ at corresponding levels, presumably because these observations apply to horizontal eddy transport. Taking the average vertical eddy diffusion coefficient to be about 8×10^5 cm.^{2} sec.$^{-1}$, essentially complete vertical mixing of a cloud source within the mesosphere would require from 12 days to 1.5 months, depending on its initial distribution with altitude. Similarly, meridional eddy mixing will spread the source 100–200 km. per month. Vertical and meridional mean motions, poorly known at these levels, will accelerate the mixing and complicate the redistribution pattern.

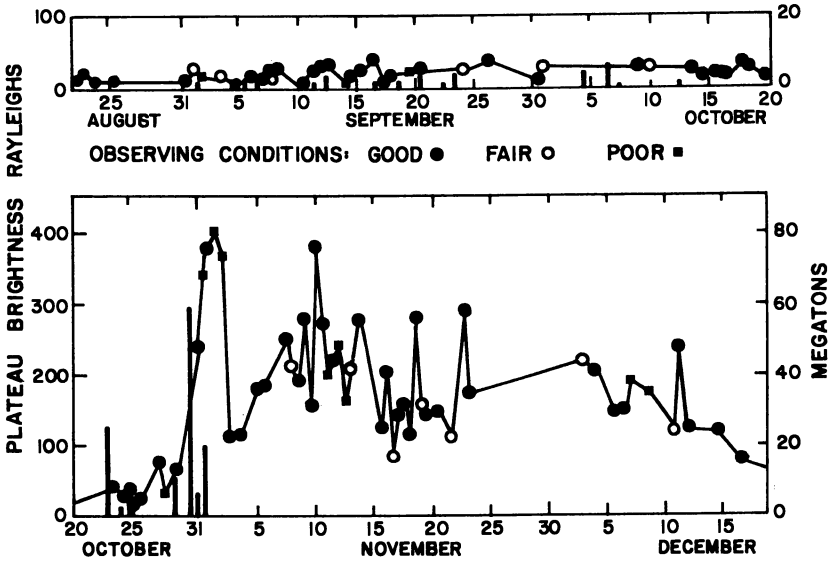

Figure 3. Twilight lithium enhancements at Saskatoon during the Soviet thermonuclear tests of Sept. 1–Nov. 4, 1961 (37)

With this in mind, it is of interest to examine the twilight lithium observations at Saskatoon during the latter half of 1961 (Figure 3). It is likely that the 25-megaton Soviet test of Oct. 23, 1961 and the 55–60-megaton Soviet test of Oct 30, 1961 contributed to the lithium enhancements in this period. These two thermonuclear tests were air shots at an altitude of about 12,000 feet over Novaya Zemlya, 75°N (*39*). The fairly regular decrease in the lithium concentration with time after one month (Figure 3) can be interpreted to signify that vertical mixing within the turbulent layer, between 55 and 80 km. altitude, is essentially com-

plete by that time, consistent with vertical diffusion rates estimated above. Additionally, zonal winds in the mesosphere, with speeds of several tens of meters sec.$^{-1}$, should have extended the cloud into a continuous toroidal distribution well within one month. The decrease with time thereafter, with an apparent mean residence time of about 25 days (Figure 3) can be ascribed mainly to meridional redistribution within the turbulent layer and to chemical reactions of atomic lithium. As the northern hemisphere summer approaches, meridional winds above 50 km. should reverse direction (*32*) and carry the thermonuclear debris rapidly into the southern hemisphere.

It is possible to estimate roughly the mesosphere budget of bomb lithium in molecular form during early December 1961. It is assumed that the cloud was well mixed vertically in the mesosphere by that time. The initial cloud width, roughly twice the cloud altitude (*13*) would have expanded meridionally owing to eddy mixing and mean motions to perhaps 600 km. or more by early December. The resulting toroidal cloud near 75°N would be roughly 6×10^{16} cm.^{2} in area. According to Sullivan *et al.* (*37*) a zenith plateau brightness of 200 Rayleighs (Figure 3) corresponds to 12.4×10^6 lithium atoms per cm.^{2} column above about 80 km. Assuming the same mixing ratio for the mesosphere, the toroidal cloud contained only about 4 kg. of lithium, a very small fraction of the total lithium released by the 25 and 60 megaton explosions. This result is no index of the actual total of bomb lithium and other bomb products injected into the mesosphere by these two nuclear explosions. Most of the bomb lithium could have been combined chemically and incorporated into bomb debris particles during cloud rise through the upper stratosphere and throughout November in the mesosphere.

Stratospheric Transport

The pattern and rate of exchange of stratospheric air with the mesosphere, with the troposphere, and between hemispheres is still poorly known. Within the stratosphere a complex pattern of eddy mixing and mean motions governs the redistribution of trace constituents. In the lower stratosphere the adsorption or attachment of trace constituents to natural sulfate particles influences their subsequent transport. Some main features in stratospheric transport processes based on tracer studies are reviewed here.

The rhodium-102 and cadmium-109 high altitude tracer experiments provide the best information on the pattern and time-scale of downward mixing from the mesosphere to the lower stratosphere and troposphere (*20, 21*). The ^{102}Rh tracer injected into the lower thermosphere on Aug. 11, 1958, mixed down into the lower stratosphere selectively at high lati-

tudes and attained the maximum observed concentration level at 20 km. altitude in February 1960 in the Arctic stratosphere. Similar concentrations were observed at the highest latitudes of sampling in the southern hemisphere stratosphere a few months later. On the basis of the foregoing discussion of transport in the lower thermosphere and mesosphere, the ^{102}Rh tracer must have been well-mixed globally down to the stratopause within about two months. The ^{102}Rh measurements (*20, 21*) show that this tracer mixed down into the lower Arctic stratosphere continuously between October 1959 and February 1960 and perhaps some six months later into the lower Antarctic stratosphere. On the basis of these observations it may be surmised that vertical mixing in the polar stratosphere proceeds mainly within the polar vortex which forms in the high latitude stratosphere in the late fall, expands equatorwards in winter, and breaks up in early spring. The ^{102}Rh tracer required two such periods for descent from the stratopause to 20 km. altitude, a mean descent rate of some 2 to 3 km. per month in the vortex region. The ^{102}Rh tracer required an additional year to attain its maximum concentration in the troposphere. Thus, the ^{102}Rh observations make it clear that the over-all atmospheric mean residence time for trace constituents in the mesosphere is nearly three years or longer.

The results from measurements of radioisotopes in air filter samples collected by balloon provide evidence of the pattern of meridional mixing at stratospheric levels up to 35 km. Recently, it was pointed out (*29*) that throughout the winter and spring following the massive October 1958 Soviet nuclear tests, Soviet debris was not detected in balloon samples collected above 23 km. at 31° and 45°N latitude, indicating little or no equatorwards transport from high latitudes at these stratospheric levels. An examination of the radiochemical data for balloon samples collected following the high yield Soviet thermonuclear tests from Sept. 1 to Nov. 4, 1961 again shows a large contribution of Soviet debris below 23 km. and very little at higher levels. Substantial increases in the concentration of long lived fission products at 31°N above 23 km. occurred only in late 1962, following the U.S. atmospheric tests at Christmas Island between April 25 and July 11, 1962.

The massive Soviet tests of late 1961 included a reported 14 high-yield atmospheric shots which ranged from about 1–60 megatons in yield. These tests, between Sept. 10 and Nov. 4, at Novaya Zemlya, 75°N, injected debris over the full range of altitudes from the tropopause to the stratopause and above. The debris was redistributed further vertically within the Arctic stratosphere by eddy mixing and mean motions. Undoubtedly these tests provided an essentially continuous vertical distribution of debris at high concentrations throughout the polar stratosphere near 75°N. The absence of significant contribution from this

source in balloon samples above 23 km. clearly indicates negligible equatorwards transport from high latitudes at these stratospheric levels. This is consistent with the observed downward transport of the high altitude ^{102}Rh and ^{109}Cd tracers only at high latitudes in the stratosphere. It is also in accord with the observation (*29*) that the large increases in radioactivity of balloon samples above 23 km. at the end of 1958 involved equatorial test debris rather than debris from the tests at Novaya Zemlya in October 1958. This evidence suggests that above 23 km. altitude there is a poleward flow at least sufficient to counterbalance any equatorwards transport by eddy mixing from higher latitudes. Below 23 km., rapid meridional eddy mixing obscures the pattern of slow mean motions. However, in this layer, very little Soviet test debris mixes south of 30°N, indicating that poleward flow must oppose equatorwards eddy mixing in the lower tropical stratosphere. Thus, the radioactive tracer observations are not inconsistent with slow meridional circulations of the pattern proposed by Brewer (*4*) and by Murgatroyd and Singleton. Gravitational settling and the complex pattern of eddy mixing also exert important influence on the redistribution of stratospheric aerosols. Additionally, mean motions which accompany stratospheric wind reversals further affect the distribution of trace constituents (*29, 40*). Thus the interpretation of apparent ages from radioactive aerosol ratios and concentrations is complicated by the several processes involved.

As Martell has pointed out (*30*), in the region of the stratospheric large particle layer near 18–20 km. altitude, radioactive aerosol particles become attached to natural sulfate particles in the size range of about 0.1–0.4 μmeter radius. Subsequent upward transport of the radioactive aerosols is opposed by gravitational sedimentation. This combination of processes affords an explanation for the observed accumulation of ^{210}Pb near 20 km. in the tropical stratosphere (*2*). At higher latitudes where slow mean motions are directed poleward and downward, no such accumulation is possible.

The pattern of eddy mixing in the stratosphere is highly variable. Newell (*33*) has shown that, except near the equator, the meridional and vertical components of eddy mixing exhibit large seasonal, latitudinal, and even yearly variations. Maximum vertical and meridional eddy mixing rates occur at the higher latitudes in winter and appear to correlate with the polar vortex distribution. Additionally, on the basis of the global fallout distribution of radioactive ^{185}W from equatorial tests, it was pointed out (*29*) that the coefficient of meridional eddy mixing must increase markedly with latitude at low latitudes in the tropical stratosphere. This pattern of eddy mixing coupled with slow mean motions upward and poleward in the tropical stratosphere can

explain why most of the ^{185}W debris injected near 20 km. altitude at 11°N was confined to the northern hemisphere.

With these circulation features in mind, the apparent stratospheric residence times deduced from the tungsten tracer data (*9*), the cosmic ray spallation product distribution (*2*), and the ^{90}Sr concentration variations displayed by recent balloon samples (*23*) can be placed in better perspective.

The short apparent residence time for the ^{185}W tracer in the tropical stratosphere during the first few months following the HARDTACK tests (*9*) can be explained in part by mean motion upward. This redistribution continued until upward transport and gravitational settling were in balance. Additionally, the observed persistence of the maximum in the ^{185}W concentration distribution in the tropical stratosphere (*9*) does not rule out slow mean motion poleward. The combined influence of slow outflow to higher latitudes and meridional eddy mixing with eddy diffusion coefficients which increase with latitude can explain the observed slow migration of the center of concentration from the point of injection at 11°N to a point near the equator where the meridional component of transport is a minimum.

The seasonal and annual changes in the ^{90}Sr content of samples collected using balloon-borne air filters are shown in Figure 4. Krey's interpretation of the observed seasonal variations in terms of vertical mean motions (*23*) depends on the apparent marked decrease in ^{90}Sr concentration with altitude. However, it is likely that the sampler efficiency decreases with radioactive aerosol particle size which has been shown to decrease with altitude (*30*). Thus the actual ^{90}Sr gradient may be less steep or even reversed. On the basis that the debris is continuously transported poleward from equatorial sources, the observed seasonal variations, Figure 4, can be interpreted in a different manner, independent of the vertical distribution. The rapid decrease each winter and the smaller increase each summer and fall (Figure 4) can be explained on the basis of little change in meridional transport rate with season between the equatorial source region and ballooning latitudes and large seasonal changes in the rate of poleward transport towards higher latitudes, in keeping with the reported pattern of eddy mixing (*33*).

The apparent mean residence time of about 11 to 12 months, indicated by the average annual decrease in ^{90}Sr concentration (Figure 4), is only an index of the annual change in ^{90}Sr concentration in the equatorial source region and does not correspond to the residence time of the debris in the stratosphere as a whole, despite published suggestions to this effect. In view of the general pattern of slow mean motion and eddy mixing described above, it is becoming evident that the residence

time of debris injected into the stratosphere increases with altitude, decreases with increasing latitude at a given altitude, and varies somewhat with season and year of injection. A mean residence time of roughly 1 year appears reasonable for about 18–20 km. altitude, near the sulfate particle layer, as indicated by the tropospheric ^{102}Rh tracer data (*20*). Similarly the June 17, 1967 Chinese thermonuclear shot of several megatons yield, which injected most of its debris at or just above 19 km. altitude at middle latitudes (*24*), resulted in no detectable fallout in the troposphere for the first few months thereafter. Most of the fallout from this shot, following the pattern observed for ^{102}Rh (*20*), should appear at tropospheric levels in the spring of 1968. The range of mean stratospheric residence times for debris injected to altitudes between 20 km. and the stratopause might be expected to vary between about

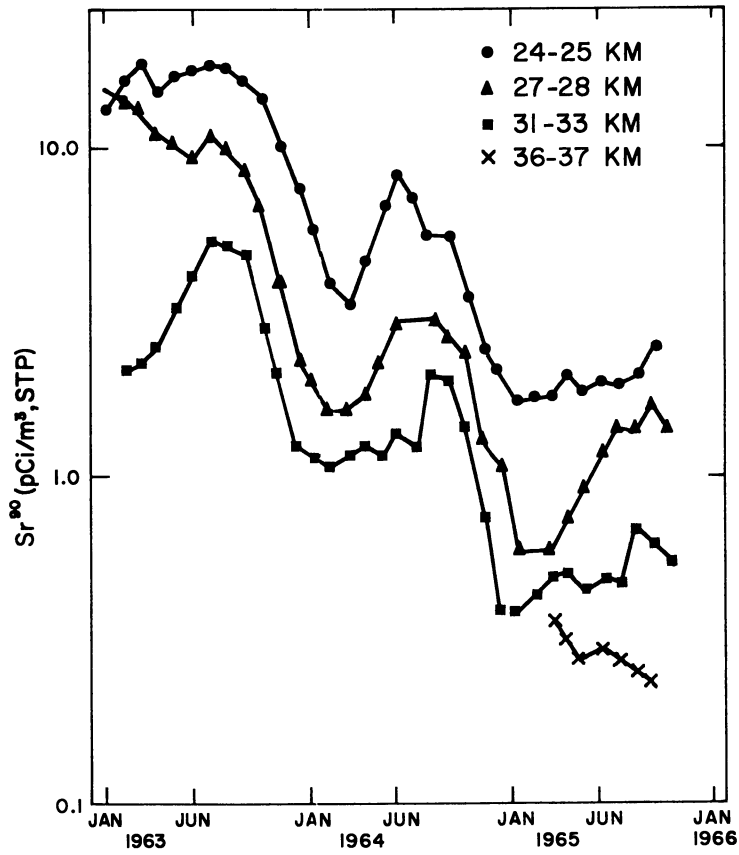

Figure 4. ^{90}Sr concentration vs. time for air filter samples collected by balloon over San Angelo, Tex., 31°N (24)

1 year at 20 km. to at least 3 years at the stratopause, in view of the results of the ^{102}Rh tracer experiment (*20, 21*).

In the lowest layer of the stratosphere the residence times for aerosol constituents increase with height above the tropopause, from several weeks near the tropopause (*see below*) to about 1 year near 18 to 20 km. altitude. Evidence that the residence time is only several weeks at lower levels of the northern polar stratosphere is given by the rapid rate of decrease in fallout concentration in this region each year following the breakup of the polar vortex and the reestablishment of the summer easterly wind regime [*see,* for example, Hvinden *et al.* (*17*)]. The decrease can be attributed to a diminished transport downward from above after the breakup of the polar vortex and to a continuing rapid exchange of lower stratospheric air with tropospheric air. The relatively long apparent ages of 8–10 months for the stratospheric zone, 30°–70° latitude and 12–18 km. altitude based on cosmic ray spallation product concentrations and ratios (*2*) can be explained by the influence of downward transport. Because both the spallation product production rate and aerosol residence times increase markedly with altitude in this region, the apparent ages estimated from the cosmic ray spallation product data are too long owing to the influence of vertical advection.

Tropospheric Aerosol Ages

The apparent ages or atmospheric residence times for troposphere aerosols and trace constituents have been variously estimated by measurements of radon daughter products, cosmic ray spallation products, and radioactive bomb products in air and precipitation (*3, 5, 15, 25, 28, 35, 37*). The results from these several methods are highly variable and unsatisfactory. Ratios of ^{210}Pb and radon or its short lived daughters vary widely and are unsuitable for aerosol age determinations for a number of reasons discussed by Junge (*19*). The mean residence time of about 32 days based on tropospheric fallout concentration changes (*37*) is unsatisfactory because of unknowns about the atmospheric distribution of the source during the period of observation. $^{210}Po/^{210}Pb$ ratios (*5, 28, 35*) indicate relatively high apparent ages for tropospheric aerosols, suggesting that ^{210}Po in air may not all be caused by the decay of radon in the atmosphere. Cosmic ray spallation product concentration and ratio data also yield high age values because both the spallation production rate and aerosol residence times increase with altitude. Even a small admixture of air from higher levels affects the results obtained by this method.

In an attempt to obtain improved information on the residence times of aerosols at various levels of the troposphere and lower stratosphere,

the author and an associate have initiated recently the measurement of ^{210}Pb, ^{210}Bi, ^{210}Po, and ^{90}Sr in large air filter samples. Samples are collected on efficient polystyrene microfiber filters, in surface air, by NCAR aircraft up to 30,000 feet altitude, and by U.S. Air Weather Service RB-57F aircraft up to about 65,000 feet. Within 1–3 days following sample collection the 5.0-day half-life ^{210}Bi is separated, and the measured activity is corrected for decay following chemical separation and for growth from mid-sampling time. Subsequently ^{210}Pb and ^{90}Sr disintegration rates are determined by β^- assay of their daughter products and the ^{210}Po activity is determined by α-spectroscopy, using ^{208}Po or ^{209}Po for chemical yield determination.

Table I. ^{210}Pb, ^{210}Bi, and ^{90}Sr Radioactivities and Apparent Ages of Aerosols Over Colorado Near 39°N (36)

Date, 1967	*Altitude km.*	*Activity Concentrations,[a] dpm/100 meters*			*Residence Time, τ_R[b] days*
		^{210}Pb	*^{210}Bi*	*^{90}Sr*	
3/21	Surface	2.42 ± 0.14	0.83 ± 0.02	1.64 ± 0.06	3.8
3/22	Surface	1.98 ± 0.02	0.87 ± 0.04	1.80 ± 0.03	5.2
3/13	3.0	4.7 ± 0.9	⩽2.2	3.5 ± 0.3	<6.3
3/21	4.7	2.07 ± 0.08	0.83 ± 0.04	1.87 ± 0.07	4.8
3/13	6.1	⩽4.0	2.6 ± 0.3	3.5 ± 0.3	>13
3/21	7.6	5.75 ± 0.16	1.06 ± 0.05	0.89 ± 0.10	1.6
3/13	8.8	⩽5.4	2.4 ± 0.6	11.8 ± 1.0	>5.7
3/13	11.0	2.9 ± 1.0	2.3 ± 0.2	5.2 ± 0.3	(37)
3/13	13.4	1.80 ± 0.05	1.35 ± 0.06	15.6 ± 0.5	22
3/13	15.8	1.3 ± 0.3	0.90 ± 0.07	81.4 ± 1.0	(16)
3/13	18.3	1.3 ± 0.5	1.06 ± 0.15	155 ± 3	(31)

[a] Corrected to mid-period of sampling. Errors indicated are one standard deviation. Volumes are in meters^3, STP.
[b] $\tau_R/(\tau_R + \tau_B) = N_B\lambda_B/N_A\lambda_A$.

Some preliminary results of this work are presented in Table I. The apparent age of each sample is estimated from the $^{210}Bi/^{210}Pb$ activity ratio, assuming steady-state conditions in the atmosphere. With this assumption, the activity of a radioactive daughter product, B, is related to that of its parent, A, by the relation:

$$N_A\lambda_A = N_B\,(\lambda_B + \lambda_R)$$

where λ_R is the exponential removal rate by both precipitation scavenging and particle sedimentation. The apparent age of the aerosols, τ_R is the reciprocal of λ_R. Thus the activity of each radioactive daughter, B, is related to its immediate parent, A, by the relation:

$$N_B\lambda_B = N_A\lambda_A\,\tau_R/(\tau_R + \tau_B)$$

Similarly, $N_C\lambda_C$, that portion of the observed ^{210}Po radioactivity which accumulated in the aerosol by decay from its parent activity, is related to ^{210}Pb activity by the relation:

$$N_C\lambda_C = N_A\lambda_A \tau_R^2/(\tau_B + \tau_R)(\tau_C + \tau_R)$$

Any excess ^{210}Po radioactivity comes from other sources. Because of its volatility ^{210}Po may be introduced directly into the atmosphere as a pollutant by burning coal and by various industrial activities, with possible contribution from the biosphere as well.

The results, Table I, show a number of features which indicate the usefulness of $^{210}Bi/^{210}Pb$ ratio data. The ^{210}Pb concentration gradient shows little change with altitude in the troposphere, presumably because the known marked decrease in the parent radon concentration with altitude over continental area does not apply to its long-lived daughters. The daughter products are redistributed by convective and vertical eddy mixing processes throughout their period of atmospheric residence. Aerosol residence times of only a few days or less are observed in surface air and at cloud levels. Results in parentheses, Table I, for samples collected near and above the tropopause are inconclusive because of small sample size and large errors in ^{210}Pb determination.

By comparison, $^{210}Po/^{210}Pb$ activity ratios of 0.085 to 0.23, measured in samples collected between 3.0 and 8.5 km. altitude over Colorado, correspond to aerosol ages between 3 and 10 weeks. These high values suggest that much of the atmospheric ^{210}Po may be biological or industrial in origin. Therefore, $^{210}Po/^{210}Pb$ ratio data appear to be unsatisfactory for aerosol age determination. However, if the concentration distribution of unsupported ^{210}Po in the upper troposphere can be assessed by precise $^{210}Pb/^{210}Bi/^{210}Po$ ratio measurements, then $^{210}Po/^{210}Pb$ ratios may be useful for estimating the ages of aerosols at stratospheric levels.

Comparison of ^{90}Sr and ^{210}Pb concentrations (Table I) indicates that stratospheric ^{210}Pb for which the ^{210}Bi daughter should be in secular equilibrium did not contribute significantly to the ^{210}Pb and ^{210}Bi activities of the samples collected at tropospheric levels. However, ^{210}Po from stratospheric levels contributes to a limited extent to the ^{210}Po activity of tropospheric aerosols. Additionally, if an aerosol sample were collected at tropospheric levels in an air parcel of high potential vorticity (7), the stratospheric contribution to the ^{210}Pb, ^{210}Bi, and ^{210}Po in the sample may be substantial.

It is concluded tentatively from these preliminary $^{210}Bi/^{210}Pb$ ratio data that tropospheric aerosols have a much shorter atmospheric residence time than is generally appreciated. If so, both natural aerosols and radioactive fallout observed at tropospheric levels will not be well mixed zonally but for the most part will be deposited within a few

thousand miles downwind of their sources or zones of entry. Thus, if there are important longitudinal variations in the pattern of stratosphere–troposphere exchange, significant longitudinal variations in the pattern of deposited fallout are to be expected. This would make the fallout inventory far more difficult to assess. The situation can be even more complex in view of possible large variations in aerosol residence times or deposition rates with climate. Thus, deposition rates may vary widely in different geographical areas and vary further with season in each area.

Discussion and Conclusions

It was pointed out above that the ^{185}W tracer observations, the excess ^{210}Pb in the tropical stratosphere, and the radiochemical evidence from fallout samples collected by balloon can be reconciled with the slow mean motion of air upward across the equatorial tropopause and within the tropical stratosphere and outward toward higher latitudes at stratospheric levels up to about 35 km. Above 23 km. altitude, such mean motions poleward can explain the lack of significant equatorwards transport of fallout debris from Novaya Zemlya. In the stratosphere, below 23 km., meridional eddy mixing obscures the pattern of slow mean motions. However, even in this layer, little Soviet test debris mixes south of about 30°N, suggesting that poleward mean motions restrict equatorwards transport by eddy mixing within the lower stratosphere between the equator and 30°N.

The tungsten tracer observations and the excess ^{210}Pb in the tropical atmosphere are explained by the competing influence of sedimentation, slow mean motions, and eddy mixing. Radioactive aerosols in the lower stratosphere become attached to the natural sulfate particles which are of sufficient size and density to oppose upward transport to levels much above 20–25 km. (*30*). The coefficient of meridional eddy mixing appears to increase with latitude near the equator (*29*), with little seasonal change (*33*). At higher latitudes the rate of poleward transport exhibits large seasonal variations, with a maximum in winter (*33*).

This pattern of stratospheric circulation and mixing leads to the conclusion that there is little exchange between hemispheres at stratospheric levels. If so, the explanation of Feely *et al.* (*8*) for the large influx of Soviet test debris in the southern stratosphere in 1963, Figure 5, must be incorrect. Alternatively, it is suggested that the interhemisphere exchange took place in the mesosphere. The late 1961 Soviet tests injected nuclear debris into the mesosphere, as evidenced by the twilight lithium enhancements (Figure 3). In the next few months, mesosphere winds and eddy diffusion should have redistributed this high altitude debris throughout the turbulent layer all the way to the Antarctic. Dur-

ing the southern hemisphere winters of 1962 and 1963, some of the debris mixed down through the Antarctic stratosphere. Equatorwards transport in the lower southern stratosphere during the period May–October 1963 can account for the observed large increase in ^{90}Sr (Figure 5). The time delay and period of arrival in the southern stratosphere parallels that observed for the high altitude ^{102}Rh tracer (*21*).

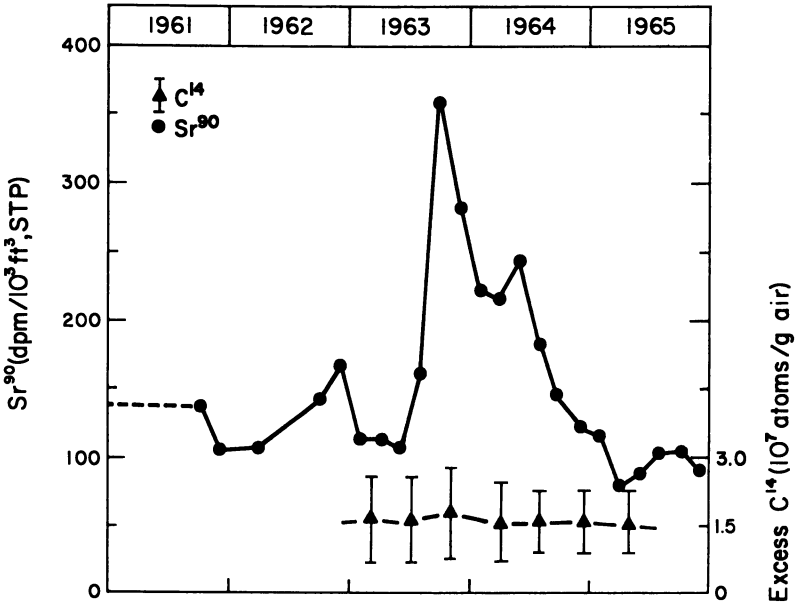

Figure 5. ^{90}Sr and ^{14}C excess (above natural ^{14}C level) at 35°–40°S near 20 km. altitude (8)

A rough upper limit for the amount of Soviet debris injected into the mesosphere can be determined by comparing the increase in ^{90}Sr near 20 km. during 1963 (Figure 5) with the ^{102}Rh concentration in this region 2 years after 3 MCi of ^{102}Rh were injected into and above the mesosphere. On this basis some 10–20 megatons of fission debris may have reached the mesosphere from the 1961 Soviet Tests. Assuming only 5 megatons of fission for the low fission yield 55–60 megaton shot and a fusion-to-fission ratio of about 2 for the other Soviet shots (*39*), it is estimated that some 15 megatons of fission debris and 75 megatons of fusion debris may have been involved. Thus it appears that a major portion of the debris clouds from the two largest 1961 Soviet shots may have reached the mesosphere.

The absence of a corresponding increase in the carbon-14 content of the southern stratosphere during 1963 and 1964 (*8*, Figure 5) can be

explained on the following basis. Under the influence of residual radiation heating, portions of stabilized thermonuclear clouds with the highest concentrations of radioactivity could have risen into the mesosphere from their initial heights in the Arctic stratosphere. Because carbon-14 is made by escape neutrons throughout a large air volume outside the fireball at detonation altitude, most of it was left behind at lower levels of the stratosphere. Thus, fission products, induced activities, and tritium but correspondingly little carbon-14 would be transported to the southern hemisphere *via* the mesosphere. The absence of an increase in carbon-14 in the southern stratosphere during 1963 and 1964 (Figure 5), thus reinforces strongly the conclusion that the large increase in fission products and induced radioactivities can be attributed to Soviet test debris transported *via* the mesosphere.

On the basis of the foregoing, it appears that past assessments of the atmospheric inventory of bomb debris have been seriously underestimated. The important omission was lack of information on the debris content of the Arctic stratosphere and of both the mesosphere and the Antarctic stratosphere as well. A decrease in the efficiency of balloon-borne samplers with increasing altitude is another possible source of error. Additionally, mean motions in the tropical stratosphere may carry fine particles and gaseous products of equatorial tests upward out of reach above balloon sampling levels. Also, transport of fallout down across the tropopause may be selective with longitude. If so, short residence times of only a few days for tropospheric aerosols, indicated by the $^{210}Bi/^{210}Pb$ ratio data over Colorado (Table I) would deposit the fallout selectively with longitude. This result would complicate the estimation of the inventory of deposited fallout but might help to explain the imbalance of fallout over continents and oceans.

The atmospheric residence time for a trace constituent injected into various regions of the atmosphere is the integrated time spent by the average particle along the path it follows through the atmosphere. Because the patterns and rates of transport shift with altitude, latitude, season, and year, observations in one tracer study are unlikely to apply in the same region and season in another year, unless the meteorological environment also is similar. Thus, for example, the observed persistence of the HARDTACK tungsten-185 tracer in the tropical stratosphere, may apply only during a period of tropical easterlies. The rate of poleward redistribution of a tracer in the tropical stratosphere undoubtedly would be very rapid in one of those infrequent periods when the polar vortex extends into the equatorial source region. With these reservations it can be stated that stratospheric residence times vary from about several weeks near the tropopause to about one year near 20 km. and to several years in the high stratosphere. Trace constituents in the mesosphere

have a combined residence time in the mesosphere and polar stratosphere of at least three years. In the troposphere, aerosol constituents exhibit a short and highly variable residence time, averaging only a few days at cloud levels and below if the results for the Colorado profile (Table I) are at all representative.

Evidence is cited (*17*) indicating only several weeks residence time for the lower polar stratosphere over a several months period following the breakup of the polar vortex. The $^{210}Bi/^{210}Pb$ ratio at 13.4 km. (Table I) indicates a similarly short residence time for the lower stratosphere in late winter. These observations suggest a continuous rapid exchange of air between the lower polar stratosphere and the troposphere. On this basis it can be concluded that the large seasonal variations in tropospheric fallout and tropospheric ozone are explained by seasonal variations in vertical exchange within the stratosphere.

Acknowledgments

The generous support of the U.S. Air Force Air Weather Service and the National Center for Atmospheric Research Aircraft Facility for aircraft sampling support is gratefully acknowledged. The author is especially indebted to S. E. Poet who carried out the laboratory measurements and assisted in the sampling operations that provided the data in Table I.

Literature Cited

(1) Banister, J. R., Davis, H. L., *Phys. Fluids* **5**, 136 (1962).
(2) Bhandari, N., Lal, D., Rama, *Tellus* **XVIII** 2, 391 (1966).
(3) Blifford, I. H., Lockhart, L. B., Rosenstock, H. B., *J. Geophys. Res.* **57**, 499 (1952).
(4) Brewer, A. W., *Quart. J. Roy. Meteorol. Soc.* **75**, 351 (1949).
(5) Burton, W. M., Stewart, N. G., *Nature* **186**, 584 (1960).
(6) Colegrove, F. D., Hanson, W. B., Johnson, F. S., *J. Geophys. Res.* **70**, 4931 (1965).
(7) Danielsen, E. F., *Mineral Ind., Penn State Univ.* **33** (March 1964).
(8) Feely, H. W., Seitz, H., Lagomarsino, R. J., Biscaye, P. E., *Tellus* **XVIII** 316 (1966).
(9) Feely, H. W., Spar, J., *Defense At. Support Agency Rept.* **DASA 1222** (Dec. 31, 1960).
(10) Gadsden, M., *Ann. Geophys.* **18**, 392 (1962).
(11) Gadsden, M., Salmon, K., *J. Atmospheric Terrest. Phys.* **22**, 75 (1961).
(12) Gault, W. A., Rundle, H. N., *Can. J. Phys.* **44**, 1099 (1966).
(13) Glasstone, S., Ed., "The Effects of Nuclear Weapons," U. S. Government Printing Office, Washington, D. C., 1962.
(14) Greenhow, J. S., Lovell, A. C. B., "Physics of the Upper Atmosphere," J. A. Ratcliffe, Ed., Chap. 11, Academic Press, 1960.
(15) Haxel, O., Schumann, G., *Z. Physik* **142** 127 (1955).
(16) Hunten, D. M., *Science* **145**, 26 (1964).
(17) Hvinden, T., Hveding, D., Lillegraven, A., Small, S. H., *Nature* **185**, 805 (1960).

(18) Johnson, F. S., Wilkins, E. M., *J. Geophys. Res.* **70,** 1281, 4063 (1965).
(19) Junge, C. E., "Air Chemistry and Radioactivity," Academic Press, New York, 1963.
(20) Kalkstein, M. I., *J. Geophys. Res.* **68,** 3835 (1963).
(21) Kalkstein, M. I., *Science* **137,** 645 (1962).
(22) Kellogg, W. W., *Space Sci. Rev.* **3,** 275 (1964).
(23) Krey, P. W., *J. Geophys. Res.* **72,** 2987 (1967).
(24) Krey, P. W., *U. S. At. Energy Comm. Health Safety Lab. Rept.* **HASL-183,** U. S. Department of Commerce, Clearinghouse, Springfield, Va. (October 1, 1967).
(25) Lal, D., *Indian J. Meteorol. Geophys.* **10,** 147 (1959).
(26) Lal, D., Peters, B., *Progr. Elemen. Particle Cosmic Ray Phys.* **6,** 3 (1962).
(27) Mange, P., *Ann. Geophys.* **17,** 277 (1961).
(28) Marenco, A., Fontan, J., Blanc, D., Lacombe, J. P., Hugnet, R., *Geofis. Meteorol.* **XVI,** 31 (1967).
(29) Martell, E. A., *J. Atmospheric Sci.* **25,** 113 (1968).
(30) Martell, E. A., *Tellus* **XVIII,** 486 (1966).
(31) Matsushita, S., *J. Geophys. Res.* **64,** 1149 (1959).
(32) Murgatroyd, R. J., Singleton, F., *Quart. J. Roy. Meteorol. Soc.* **87,** 125 (1961).
(33) Newell, R. E., Wallace, J. M., Mahoney, J. R., *Tellus* **XVIII,** 363 (1966).
(34) Nicolet, M., Mange, P., *J. Geophys. Res.* **59,** 15 (1954).
(35) Peirson, D. H., Dambray, R. S., Spicer, G. S., *Tellus* **XVIII,** 427 (1966).
(36) Poet, S. E., Martell, E. A., unpublished data.
(37) Stewart, N. G., Crooks, R. N., Fisher, E. M. R., *At. Energy Res. Estab. Rept. A.E.R.E.* **HP/R 1701** (June 1955).
(38) Sullivan, H. M., Hunten, D. M., *Can. J. Phys.* **42,** 937 (1964).
(39) *U. S. At. Energy Comm., Health Safety Lab. Rept.* **HASL-142,** U. S. Department of Commerce, Clearinghouse, Springfield, Va. (January 1, 1964).
(40) Wallace, J. M., *Quart. J. Roy. Meteorol. Soc.* **93,** 176 (1967).

RECEIVED June 6, 1968. Sponsored by the National Science Foundation.

10

The Measurement and Behavior of Airborne Radionuclides Since 1962

C. W. THOMAS, J. A. YOUNG, N. A. WOGMAN, and R. W. PERKINS

Battelle Memorial Institute, Pacific Northwest Laboratory,
Richland, Wash. 99352

The atmospheric concentration of natural and bomb-produced radionuclides has been measured at ground level for several years at three locations throughout the world. The manner in which the concentration decreased suggested a half-residence time for stratospheric aerosols of 11.8 months at 46°N latitude. The annual spring concentration maximum occurred one to four months earlier at 71°N than at 46°N. Cosmogenic ^{7}Be attained a maximum concentration before the bomb-produced radionuclides at 71°N and later than the bomb-produced isotopes at 46°N. The rate of increase toward the annual peak concentration for most radionuclides could be approximated by an exponential in which the concentration doubled every 60 days; likewise, the rate of decrease from the maximum concentration could be approximated by an exponential with a half-time of about 40 days for most radionuclides except ^{7}Be at 46°N, which shows a half-time of about 60 days.

The atmosphere contains many radionuclides which result from nuclear weapons testing and from natural processes. The nuclear weapons-produced radionuclides include both fission products and activation products from the construction materials of the device. The natural radionuclides include the decay products of radon and thoron, the natural radionuclides in the airborne dust, and the cosmic-ray-produced radionuclides which result from spallation reactions in the atmosphere. Through the determination of the absolute and relative concentrations of this wide spectrum of radionuclides, it should be possible to define the rates of both the long term stratospheric processes and the shorter term tropospheric processes. At the beginning of 1962 a ground-level

air sampling program was initiated at Richland, Wash., using highly developed instrumental analysis which has allowed the behavior of some 20 airborne radionuclides to be followed. More recently, sampling stations have been set up at Point Barrow, Alaska, and Rio de Janeiro, Brazil. Measurements at these locations are helping to define the temporal and spatial distribution of airborne radionuclides and providing information for estimating surface deposition.

Sampling and Instrumental Techniques

The ground-level air sampling was performed by filtering air through 5-μ pore size membrane filter papers at flow rates of 400–700 cu. ft./min. These membrane filters are essentially 100% efficient for the atmospheric aerosols on which airborne radionuclides are attached (*8*). The air is drawn through four 1-sq. ft. membrane filters which are mounted on the vertical sides of a cube-shaped air sampler (*10*). The air pumps

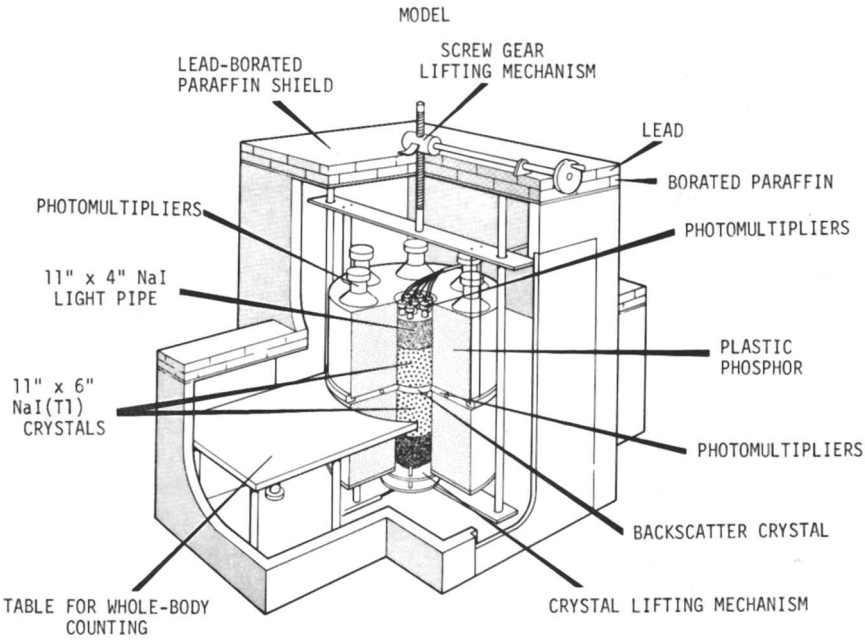

Figure 1. Large crystal multidimensional γ-ray spectrometer system

were all positive displacement units with direct shaft linkage to their electric motors. Filters were changed semimonthly, depending on the sampling station, and pressed into a standard counting geometry of 1.25-cm. thick $\times$ 5-cm. diameter.

All of the radionuclide measurements were performed by direct instrumental analysis of the air filters. Most of the measurements were

made with a multidimensional γ-ray spectrometer. The sample was counted between two 11-inch diameter by 6-inch thick NaI(Tl) detectors, while a third detector, a large plastic phosphor, served as the anticoincidence shield (*15*). This detector assembly, shown in Figure 1, measures both the single and coincidence γ-rays emitted from the sample and stores the events in a 4096-word computer memory at locations which uniquely define the energies of the γ-rays. Large volume coaxial Ge(Li) diodes (2) with resolutions of 2.9 kev. (FWHM) or better at the 1332 kev. γ-ray of ^{60}Co were also used to measure certain radionuclides which were not resolved by the NaI(Tl) system. Recently the anticoincidence shielded Ge(Li) diode shown in Figure 2 has been used for the fallout studies and has provided a new dimension in selectivity for the measurement of radionuclides in fresh fallout (*3*). It combines a reasonably high sensitivity with a peak-to-Compton edge ratio for ^{137}Cs of about 240 to 1.

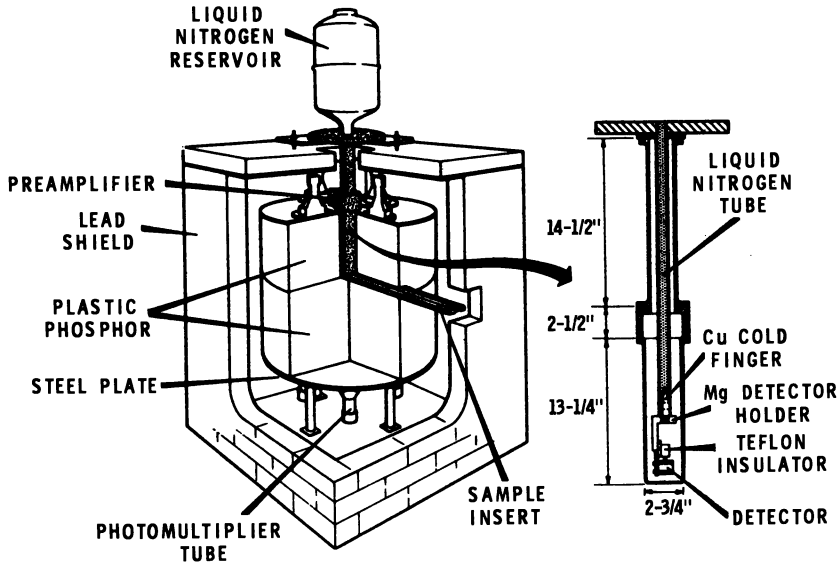

Figure 2. Anticoincidence spectrometer system

Ground-Level Radionuclide Measurements

High volume air sampling stations are presently in operation at Point Barrow, Alaska (71°N), Richland, Wash. (46°N), and Rio de Janeiro, Brazil (23°S). The air sampling rates at Alaska and at Rio de Janeiro are 400 cfm, while a 700-cfm sampling rate is employed at Richland, Wash. The observed radionuclide concentrations in ground level air at the three sampling locations are summarized in Figures 3 through 6. The measurements at Richland (*13*) cover the six-year period from early 1962 to 1968 and provide excellent definition of the seasonal variations. The Alaskan measurements provide similar definition over

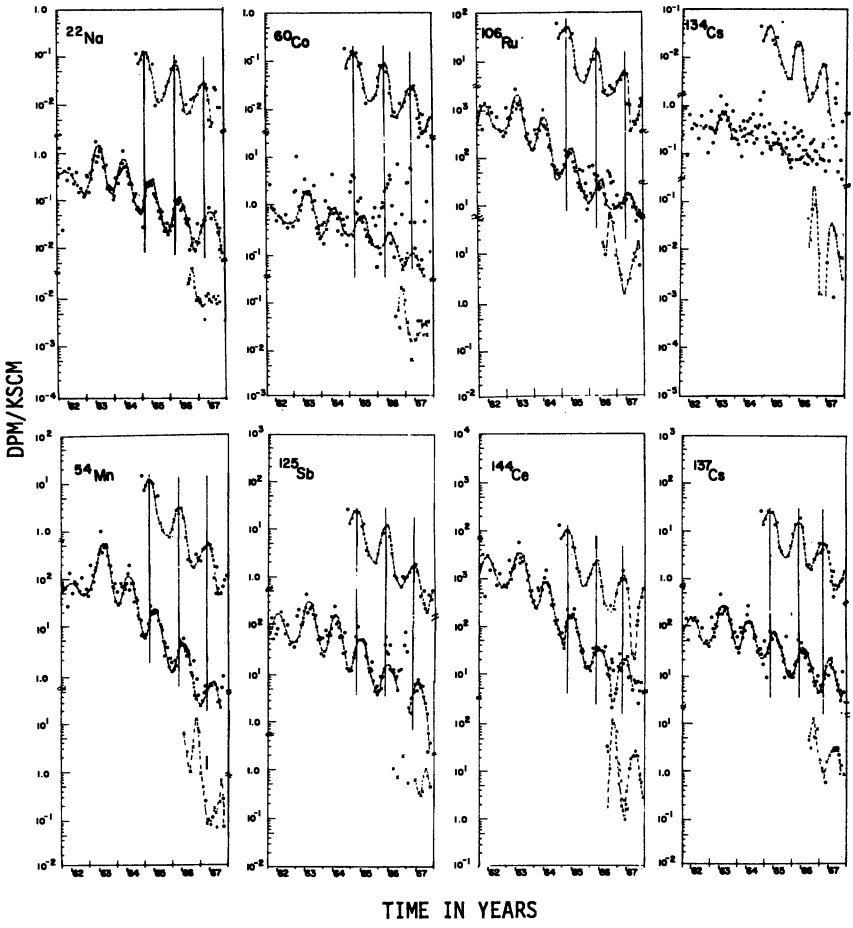

Figure 3. Ground level air concentration of radionuclides that show prominent seasonal variations

Top curve: 71°N latitude
Middle: 46°N latitude
Bottom: 23°S latitude

a shorter period. The Brazil measurements reflected the southern hemisphere nuclear testing and did not provide good definition of the normal seasonal variations in the ground-level air concentrations.

The seasonal concentration variations at Richland and Point Barrow were used to classify the radionuclides somewhat arbitrarily into four groups. The first group consists of the relatively long lived bomb-produced radionuclides ^{54}Mn, ^{60}Co, ^{106}Ru, ^{110}Ag, ^{125}Sb, ^{134}Cs, ^{137}Cs, and ^{144}Ce (Figure 3). They were inserted into the atmosphere mainly during the 1961–1962 nuclear test series and show prominent seasonal concen-

tration variations with maximum concentrations occurring in the spring and minimum concentrations occurring in the fall. Their concentrations have decreased at a very nearly exponential rate during the last five years because of radioactive decay, vertical and meridional mixing in the atmosphere, and wet and dry deposition at the earth's surface. These radionuclides were mainly of stratospheric origin. Because relatively

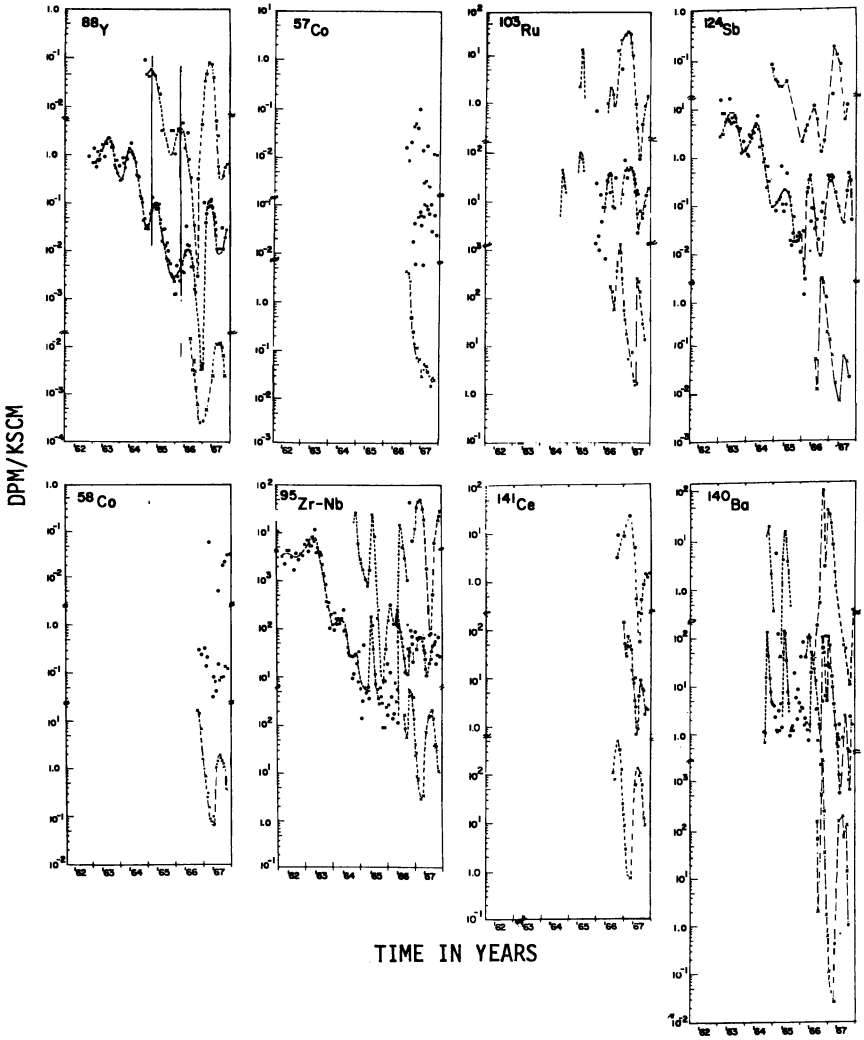

Figure 4. Ground level air concentration of radionuclides whose concentration has been effected by seasonal variations and recent nuclear weapons testing

Top curve: 71°N latitude
Middle: 46°N latitude
Bottom: 23°S latitude

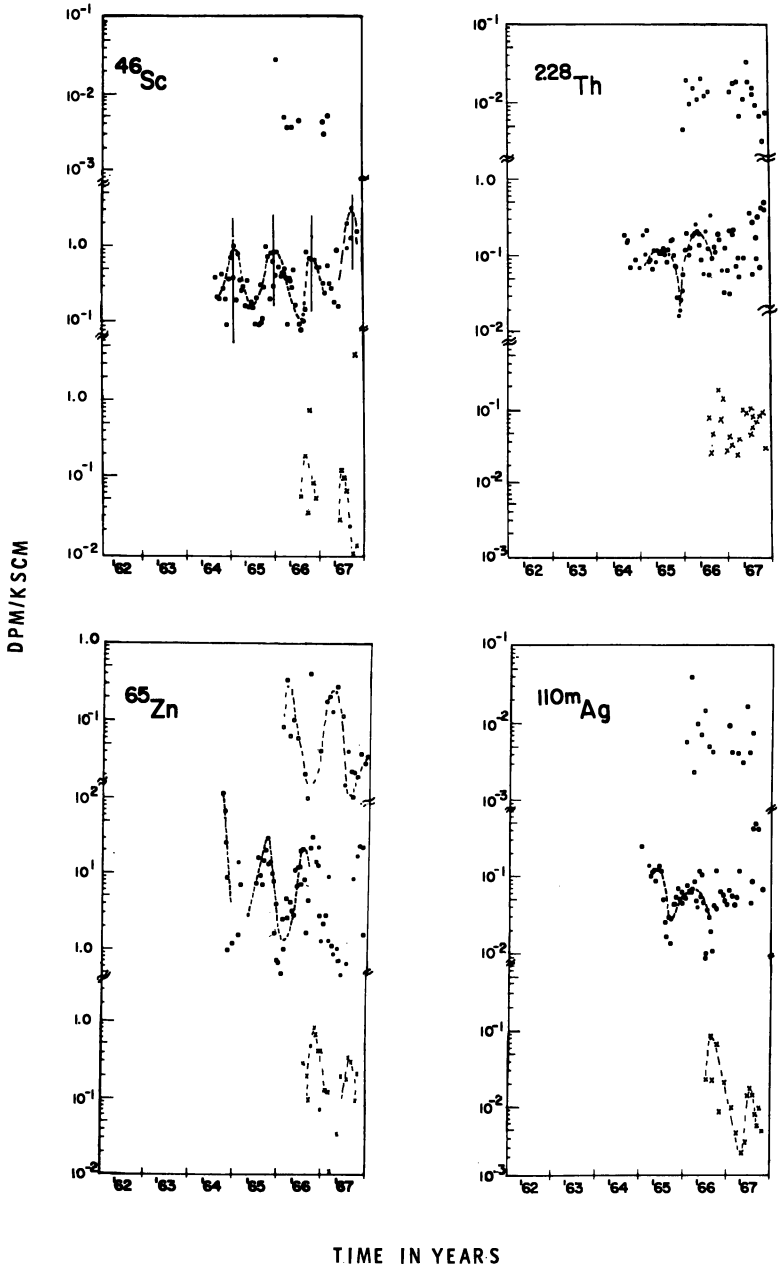

Figure 5. Ground level air concentration of radionuclides at Richland, Wash. that show unusual variation during the year

Top curve: 71°N latitude
Middle: 46°N latitude
Bottom: 23°S latitude

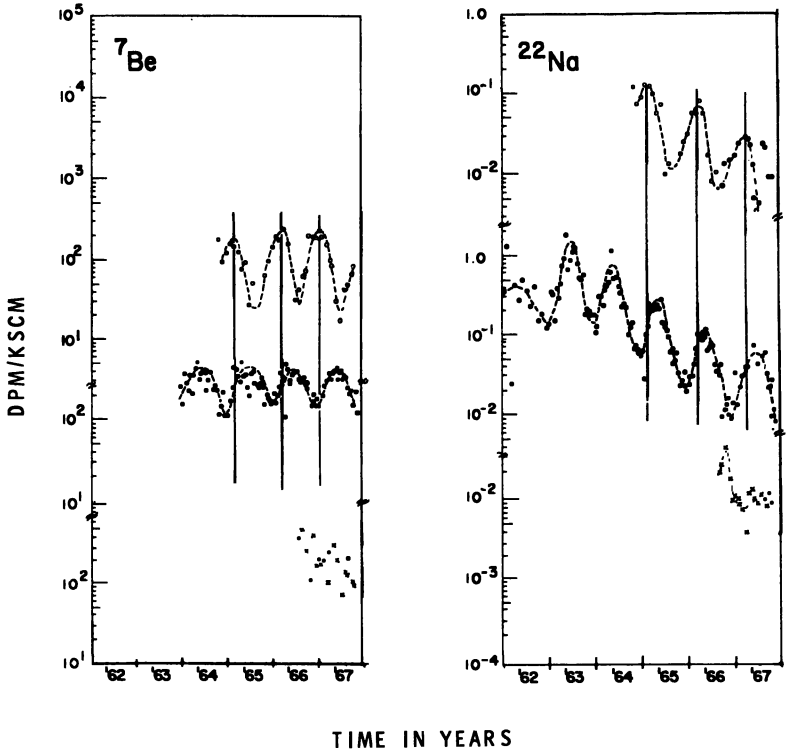

Figure 6. Ground level air concentration of radionuclides produced by cosmic rays

Top curve: 71°N latitude
Middle: 46°N latitude
Bottom: 23°S latitude

small amounts of these radionuclides have been inserted into the stratosphere since the 1961–1962 nuclear tests, this rate of decrease provides a measure of the stratospheric half-residence time. If best-fit lines are drawn through the apexes of the last five annual maxima in the ground-level air concentrations of the above radionuclides, as is done in Figure 7 for ^{137}Cs, and corrections are made for radionuclide decay, an average stratospheric half-residence time of 11.8 months is obtained. If the same method is used for the air concentrations at 71°N, a slightly longer half-residence time of 13 months is obtained. Because of the short observation period at 71°N (three years), the difference between the two residence times may not be statistically significant. These residence half-times can be compared with the integrated stratospheric residence half-time of about 11 months for ^{90}Sr (*11*) and the residence half-time of 11.1 months for ^{137}Cs (*1*). Since the residence time varies with latitude

and altitude in the stratosphere, as well as seasons of the years, the above residence times apply specifically to debris injected for the latitude pattern of the 1961–1962 test series. Radionuclides injected at a different latitude and/or altitude would be expected to show a somewhat different residence half-time.

The second group of radionuclides consists of the shorter lived nuclear weapons-produced radionuclides whose concentrations since 1964 have been affected dramatically by recent nuclear testing (Figure 4). This group includes ^{57}Co, ^{58}Co, ^{88}Y, ^{95}Zr-^{95}Nb, ^{103}Ru, ^{124}Sb, ^{140}Ba, and ^{141}Ce. Yttrium-88, antimony-124, and (zirconium-niobium)-95 showed

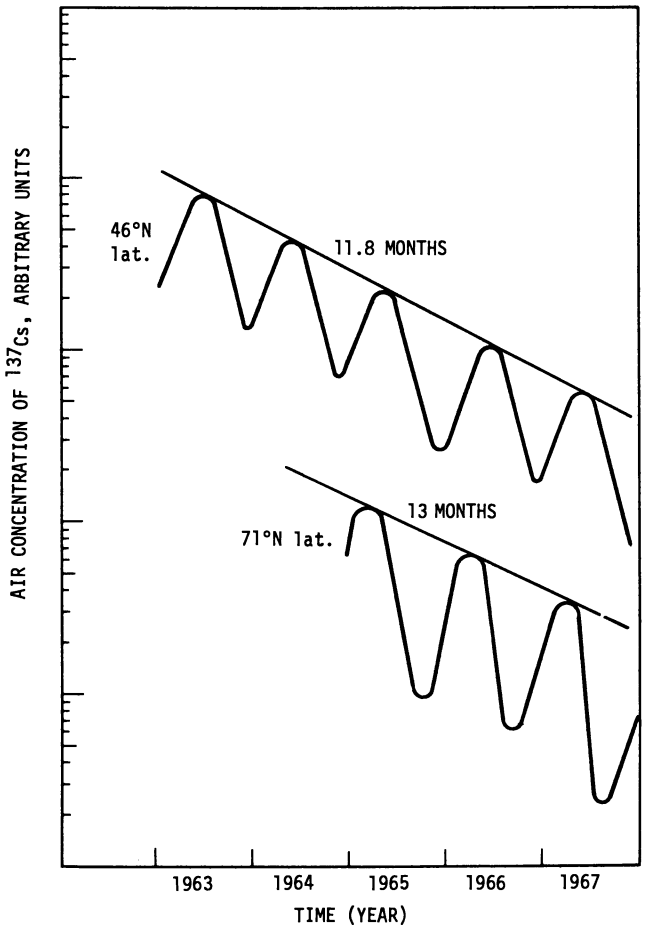

Figure 7. Stratospheric residence half-time for ^{137}Cs determined by measuring ground level air samples at 46°N and 71°N latitude

normal seasonal concentration variations during this time, and their concentrations mainly reflect short term processes.

The radionuclides ^{46}Sc, ^{65}Zn, and ^{228}Th form a third group (Figure 5). The source of ^{228}Th is dust picked up by the wind from the earth's surface. Thorium-228 concentrations varied erratically and showed no consistent seasonal variation. Scandium-46 and zinc-65 concentrations varied with the season at Richland, but the maximum concentrations occurred in the fall or winter. It is suspected that most of the ^{46}Sc and ^{65}Zn in ground-level air at the Richland sampling site came from the effluent water from the Hanford reactors. It has been shown that a fraction of the effluent water radionuclides become airborne at the effluent water basins which are located only 25 to 35 miles from the air-sampling location (*14*). The higher concentrations in the fall and winter at Richland may result either from changes in the wind velocity and/or direction or to decreased vertical mixing in the winter owing to the greater stability of the winter air. Scandium-46 and zinc-65 concentrations at Point Barrow and Rio de Janeiro were considerably lower and generally exhibited the normal seasonal variations; however, the ^{46}Sc concentrations at Point Barrow were often too low to be measured.

The fourth group consists of the cosmic-ray-produced radionuclides ^{7}Be and ^{22}Na (Figure 6). Beryllium-7 and sodium-22 are produced continuously in the atmosphere by cosmic rays. Their production rates vary considerably with latitude and altitude but remain relatively constant with time. Lal (*5*) has shown that their production rates per gram of air increase approximately exponentially with increasing altitude, increasing by almost three orders of magnitude between ground level and about 70,000 ft. at 46°N. Above 70,000 ft. the production rate at 46°N decreases slowly with increasing altitude. About 70% of the ^{7}Be is produced in the stratosphere, while only 30% is produced in the troposphere. The half lives of ^{7}Be (53 days) and ^{22}Na (2.6 years) are long enough so that a significant fraction of the ^{7}Be and ^{22}Na measured in the troposphere could be of stratospheric origin. The seasonal variations in the ^{7}Be and ^{22}Na concentrations were very similar to those of the bomb-produced radionuclides (Figure 6). Since ^{7}Be was apparently not produced in significant amounts by nuclear testing and any which was produced would have decayed rapidly ($T_{1/2}$ for ^{7}Be is 53 days), the average ^{7}Be concentration did not change from year to year. On the other hand, large amounts of ^{22}Na were inserted into the stratosphere during the 1961–1962 test period (*9*). Since then the ground-level atmospheric concentrations at Richland and Point Barrow have been decreasing nearly exponentially. At the present time, there is relatively little bomb-produced ^{22}Na left in the stratosphere. If no further ^{22}Na is inserted into the atmosphere by nuclear testing, average yearly ^{22}Na concentrations

will remain constant in the future at a level determined by the rate of production by cosmic rays.

The ground-level air concentrations of ^{7}Be and ^{137}Cs at 46°N and 71°N are shown in Figure 8. The ^{137}Cs concentration variations are typical of relatively long lived nuclear weapons-produced radionuclides and illustrate the variation in the concentrations of these radionuclides with latitude and time. It is evident that the concentrations and seasonal concentration variations were substantially different at the two latitudes. There also were differences in the seasonal variations between ^{7}Be and the bomb-produced radionuclides. Based on the idealized curves drawn

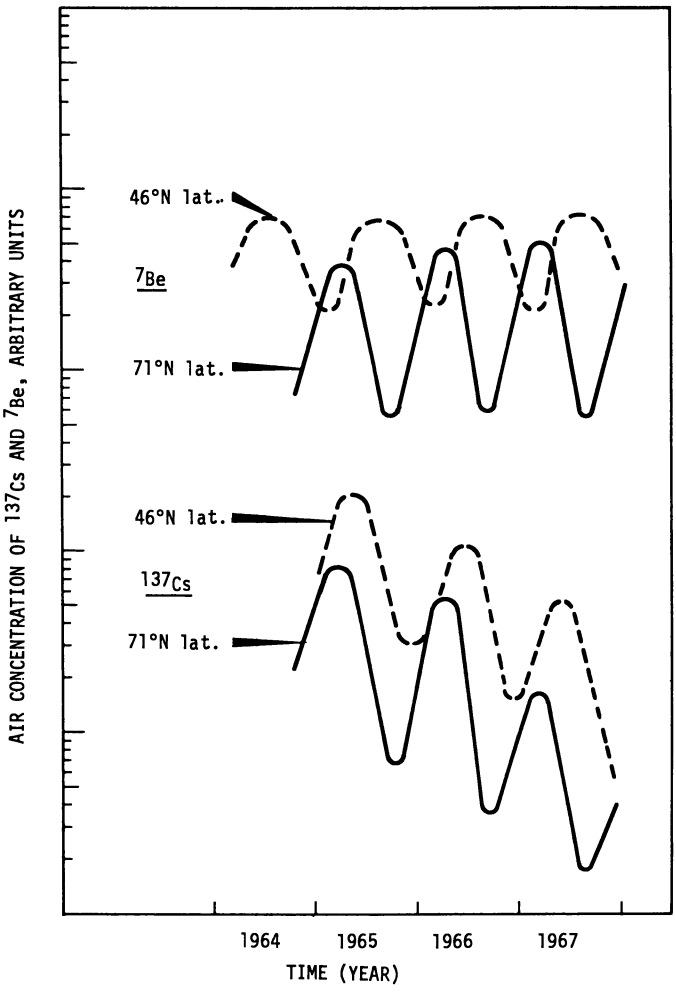

Figure 8. Seasonal variation in the ground level air concentration at 46°N latitude and 71°N latitude for ^{7}Be and ^{137}Cs

through the data points, the maximum concentrations of both ^{7}Be and ^{137}Cs occurred one to four months earlier at 71°N than at 46°N. The maximum concentrations were normally about twice as high at 46°N as at 71°N. The seasonal variations (peak to trough concentrations) were greater at 71°N than at 46°N; at 71°N the maximum concentrations were only about four times as high as the minimum concentrations. The peak to trough variations of ^{137}Cs at 46°N were significantly greater than the ^{7}Be variations at this latitude and just slightly less than ^{137}Cs variations at 71°N.

The rate at which the concentration approached a maximum each year was about the same for all radionuclides at 46°N and 71°N. This rate could be approximated from the idealized curves by an exponential with the concentrations doubling about every 60 days, as is shown in Figure 9 for ^{7}Be. The rate at which the concentrations decreased after the maximum had been reached was also the same for all of the radionuclides at 71°N and for the bomb-produced radionuclides at 46°N. This rate of decrease was approximately exponential with a half-life of about 40 days. The rate of decrease of ^{7}Be at 46°N was appreciably slower with a half-time of about 60 days.

Discussion

The differences in radionuclide concentrations between Richland and Point Barrow do not necessarily reflect accurately the average global meridional differences between 46°N and 71°N. The concentrations at any station are affected by local conditions such as rainfall rate and air stability. Several other investigators have measured ground-level atmospheric ^{7}Be concentrations between 42°N and 51°N (*4, 6, 7, 12*) and ^{137}Cs concentrations between 51°N and 60°N (*1*). These measurements show the same general seasonal variations as those at Richland. The spring peaks and fall and winter minimums occur at about the same times. The ^{7}Be concentrations at these mid-latitudes show smaller seasonal variations and a slower and later decrease in ^{7}Be concentration in the fall and winter than do the ^{7}Be measurements at Point Barrow. At Argonne, Ill. (42°N) (*4*), as at Richland, the ^{7}Be fall concentration decrease was smaller and slower than the ^{137}Cs concentration decrease. However, the ^{7}Be concentrations reported by the Argonne investigators were generally lower than those measured at Richland. This may be caused by either the low rainfall rate at Richland (3 to 8 inches per year) or to vertical mixing resulting from the presence of the Cascade Mountains upwind from Richland.

The seasonal variations in the ground-level air concentrations of nuclear weapons-produced and cosmic-ray-produced radionuclides are

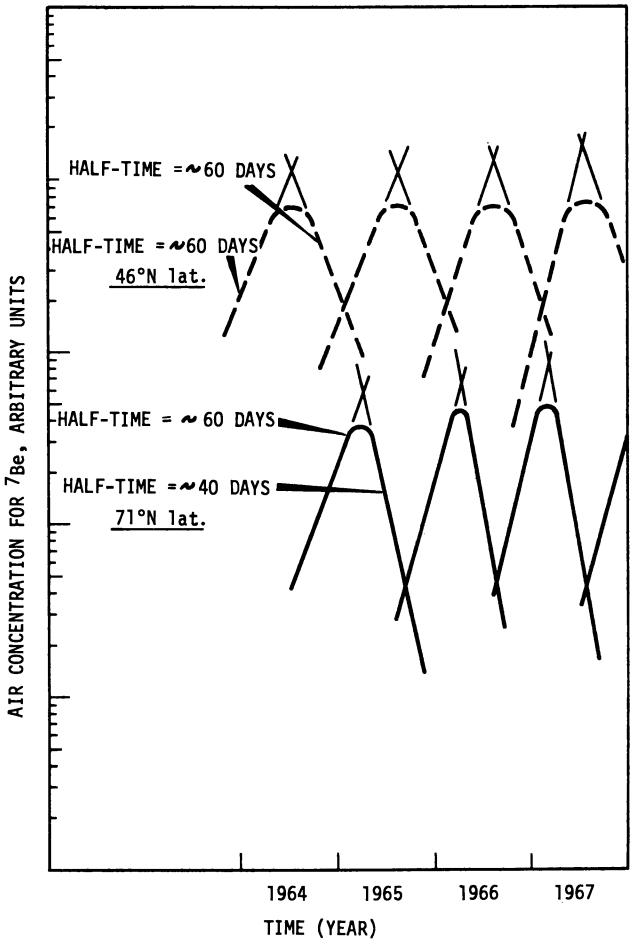

Figure 9. Comparison of the rise and decay rates of the seasonal peak for ^{7}Be

Top curve: 46°N latitude
Bottom curve: 71°N latitude

the result of seasonal variations in the rate of transfer of radionuclides from the stratosphere into the troposphere, seasonal variations in the rate of tropospheric mixing, and seasonal variations in the rate of deposition at the earth's surface. It is generally believed that radionuclides are transferred into the troposphere from the stratosphere mostly in the region of the tropopause discontinuity at mid-latitudes. The increase in the concentration of radionuclides in ground-level air in the spring at mid-latitudes results from an increase in the rate of transfer of radionuclides from the stratosphere into the troposphere at that latitude. How-

ever, if the transfer of radionuclides through the tropopause is negligible at high latitudes, the seasonal concentration variations may still be explained in the following manner. In the winter the rate of transfer of radionuclides through the tropopause gap is low, and the rate of meridional mixing in the tropopause is at a maximum; therefore, the concentrations at 46°N and 71°N tend to become equal at this time. In the spring the rate of transfer of radionuclides through the tropopause gap into the troposphere increases so that the concentrations increase at 46°N. As a result of meridional mixing between 46°N and 71°N, the concentrations also increase at 71°N; however, the rate of meridional mixing decreases with time in the spring. This tends to decrease the rate of transfer of radionuclides from mid-latitudes to high and low latitudes. When the rate of transfer to high latitudes becomes smaller than the rate of deposition at the earth's surface at high latitudes, the concentrations at high latitudes begin to decrease, even though the concentrations at mid-latitudes are still increasing owing to the transfer of radionuclides through the tropopause gap. In the summer meridional mixing is at a minimum, and concentrations fall to very low values at 71°N. At mid-latitudes, however, the lack of meridional mixing keeps the concentrations high, even though transfer through the tropopause gap is decreasing. In the fall the rate of meridional mixing in the troposphere increases. Since the concentrations are higher at 46°N than at 71°N at this time, increased meridional mixing results in a considerable transfer of radionuclides from mid-latitudes to high latitudes, causing the concentrations at high latitudes to increase and concentrations at mid-latitudes to decrease. The decrease at mid-latitudes is caused also by increased mixing with low latitudes and by the fact that the transfer of radionuclides through the tropopause gap is at a minimum at this time.

The differences between the seasonal concentration variations of ^{7}Be and ^{137}Cs at 46°N probably result mainly from the continuous production of ^{7}Be in the troposphere. Tropospheric ^{7}Be production at mid-latitudes would decrease the seasonal concentration variation and the rate of concentration decrease by holding the ^{7}Be concentrations up in the fall and winter. Tropospheric production at low latitudes would also slow the concentration decrease at 46°N in the fall and winter by lowering the meridional concentration gradient and thereby lowering the rate of transfer of ^{7}Be from mid- to low-latitudes. The smaller seasonal variation of ^{7}Be than of ^{137}Cs may also arise from a smaller seasonal variation in the rate of transfer of ^{7}Be through the tropopause gap. The spring increase in the rate of radionuclide transfer through the tropopause gap results from an increase in radionuclide concentrations in the lower polar stratosphere in the winter. This is caused by an increased rate of transfer of radionuclides down from the higher stratosphere in the winter. The

relatively short 53-day half-life of ^{7}Be and its continuous production by cosmic rays would tend to decrease the magnitude of the concentration change which would be produced by vertical mixing. In 1967 the ^{7}Be concentration at 40,000 ft. at 46°N varied less with season than did the ^{137}Cs concentration.

Summary and Conclusions

Studies of airborne radioactivity at different latitudes since 1962 have shown that considerable information can be learned about tropospheric and stratospheric mixing processes from ground-level air measurements. The concentrations of some 20 radionuclides have been measured for a period of six years at Richland, Wash. and shorter periods at Point Barrow, Alaska, and Rio de Janeiro, Brazil. The long lived fission products show a different annual deposition rate than the natural cosmic-ray-produced ^{7}Be. From these measurements, an apparent stratospheric half-residence time of 11.8 months at 46°N and of 13 months at 71°N was observed. In addition, these data have shown that the annual peak in the ground-level air concentration occurs one to four months earlier at 71°N than at 46°N. Also, cosmic-ray-produced ^{7}Be attains a maximum before the bomb-produced radionuclides at 71°N and later than the bomb-produced isotopes at 46°N. The radionuclide concentrations in ground-level air are about twice as high at 46°N as at 71°N. The rate of increase toward the annual peak concentration for all radionuclides at both 46°N and at 71°N can be approximated by an exponential in which the concentration doubles about every 60 days. Likewise, rate of decrease can be approximated by an exponential with a half-time of about 40 days for all radionuclides at both latitudes with the exception of ^{7}Be at 46°N. Beryllium-7 shows an exponential decrease with a half-time of about 60 days. The earlier spring maximum radionuclide concentration at 71°N than at 46°N may be simply caused by stratospheric input at that latitude. However, this early spring maximum concentration could also be explained on the basis of rapid tropospheric meridional transport during the winter of air from the mid-latitudes.

Literature Cited

(1) Cambray, R. S., Fisher, E. M. R., Brooks, W. L., Peirson, D. H., *AERE-R* **5575**, 4-41 (1967).
(2) Cooper, J. A., Wogman, N. A., Palmer, H. E., Perkins, R. W., *Health Phys.* **15**, 419 (1968).
(3) Cooper, J. A., Wogman, N. A., Perkins, R. W., *IEEE Trans. Nucl. Sci.* **15**, 407 (1968).
(4) Gustafson, P. F., Kerrigan, M. A., Brar, S. S., *Nature* **191**, 454 (1961).
(5) Lal, D., Malhotra, P. K., Peters, B., *J. Atmospheric Terrest. Phys.* **12**, 306 (1958).

(6) Parker, R. P., *Nature* **193,** 967 (1962).
(7) Peirson, D. H., *J. Geophys. Res.* **68,** 3831 (1963).
(8) Perkins, R. W., Thomas, C. W., Nielsen, J. M., *Proc. Conf. Radioactive Fallout Nucl. Weapons Tests, 2nd, Germantown, Md.,* **CONF-765,** 198 (1965).
(9) Perkins, R. W., Nielsen, J. M., *Health Phys.* **11,** 1297 (1965).
(10) Rieck, H. G., *Ann. Rept. 1966 USAEC Div. Biol. Med., Vol. II: Phys. Sci., Pt. 2, Radiological Sci.* **BNWL-481 2,** 26 (1967).
(11) Seitz, H., Davidson, B., Friend, J. P., Feely, H. W., *NYO* **3654-4,** 39 (1968).
(12) Shumann, G., Stoeppler, M., *J. Geophys. Res.* **68,** 3827 (1963).
(13) Thomas, C. W., Wogman, N. A., *Ann. Rept. 1966 USAEC Div. Biol. Med., Vol. II: Phys. Sci., Pt. 2, Radiological Sci.* **BNWL-481 2,** 4-17 (1967).
(14) Thomas, C. W., Perkins, R. W., *Proc. IAEA Symp. Assessment Airborne Radioactivity, Vienna, Paper SM-95/47 (1967).*
(15) Wogman, N. A., Robertson, D. E., Perkins, R. W., *Ann. Rept. 1966 USAEC Div. Biol. Med., Vol. II: Phys. Sci., Pt. 2, Radiological Sci.* **BNWL 481 2,** 43 (1967).
(16) Young, J. A., unpublished data.

RECEIVED August 1, 1968. Work performed under U. S. Atomic Energy Commission Contract AT(45-1)-1830.

An Internal Gas Proportional Counter for Measuring Low Level Environmental Radionuclides

W. R. SCHELL[1]

Teledyne Isotopes, Palo Alto, Calif.

A membrane proportional counter has been constructed and tested for analyzing radioactive gases at low backgrounds and high pressures. The detector design is similar to the Oeschger type detector but differs in its ability to count all the sample gas. A simple pressure controller permits both sides of the sealed membrane to be filled at the same time with sample and background gas. Wall effects using 3.5 and 7.7 mg./cm.^{2} between chambers have been measured. Carbon-14, tritium, and argon-37 have been counted at pressures from 1 to 10 atm. at environmental levels. Proportional spectra of background tritium, argon-37, and krypton-83m are presented. Background reduction by 36% was achieved using 2 inch × 4 inch paraffin blocks and cadmium sheet around the detector. The minimum detectable limit for tritium using a 2σ standard deviation of background and a 1000-minute counting time at 800 cm. Hg pressure is ±2 TU. The limit of counting sensitivity for carbon-14 dating equivalent to a sample age greater than 60,000 years.

Gas counting technology has been advancing rapidly during the past 10 years. The development of solid state electronic amplifiers and counters has reduced the noise and temperature drift problems which existed a few years ago. High voltage d.c. power supplies are now sufficiently stable and transient noise free to be used in place of the large battery packs. These electronic components are available commercially from nuclear electronics manufacturers. Thus, since the electronic stability has increased, more accurate analysis of environmental radioactive

[1] Present address: International Atomic Energy Agency, Kärtnerring 11, A-1010, Vienna 1, Austria.

gases is now possible using improved detectors. This chapter describes a gas detector which has proved to be a high sensitivity, low background counter for measuring environmental gases.

For low level analysis of radioactivity, background radiation must be suppressed. This is usually done using an anticoincidence guard ring surrounding the sample counter. When a radiation (γ-ray; cosmic particle, etc.) is recorded simultaneously in the two chambers, the sample counter is blocked electronically, and no pulse is registered. This technique effectively reduces the background of a counting system, providing low background radioactive counter materials are used and guarding geometry is optimized. Background can be reduced further by massive shielding and by placing paraffin with cadmium or boron around the detector. Massive shielding, 8 inches of steel or the equivalent thickness of lead, attenuates the environmental γ-radiation and cosmic particles. The paraffin with cadmium or boron reduces the neutron component. Oeschger (*17*) enumerates the various components contributing to background in an internal gas counter as:

(1) Ionizing particles not detected by the anticoincidence arrangement.
(2) α And β contamination of the counter wall.
(3) Compton, photo, and pair electrons produced by gamma particles in the counter wall and in the gas.
(4) Neutron induced events.

These contributions to the background have been analyzed by Oeschger (*17*) using a unique detector design developed first by Moljk *et al.* (*16*) and Houtermans and Oeschger (*12*). Cameron (*2*) has reviewed low background counting systems using conventional and Oeschger type detectors for tritium and carbon-14 measurements. He discusses the criteria desirable for low background counting as well as sample preparation methods used in laboratories throughout the world.

Device Design

Curran and Oeschger Counters. Curran and Oeschger counters are designed to eliminate wall effects and to provide more efficient anticoincidence shielding against external radiation. These counters use an aluminized polystyrene foil cylinder inside a larger steel cylinder. In the annulus between the steel wall and the foil, a ring of center wires is strung. The wires are anodes for the anticoincidence counters, with a center wire inside the aluminized polystyrene foil serving as the anode for the inner counter. The polystyrene foil has holes to allow equal pressure on both sides of the membrane. The sample acts as counting gas for both the anticoincidence counter and the inner counter. Pulses

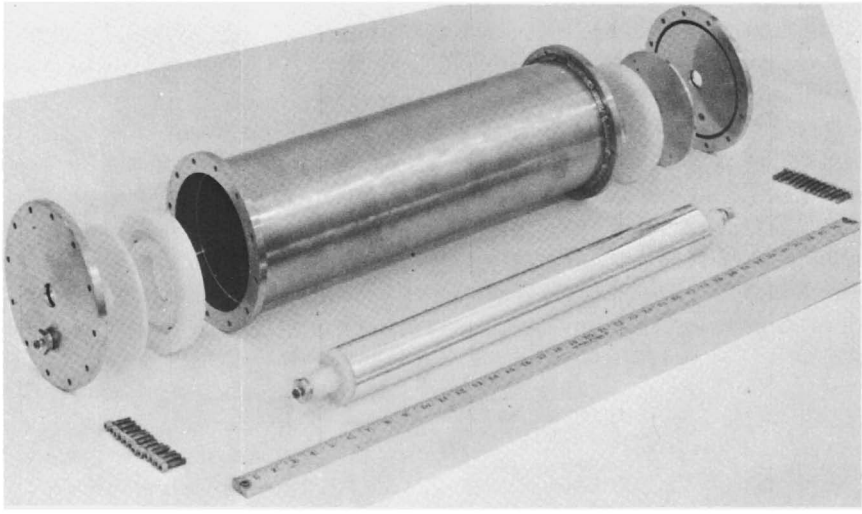

Figure 1. Membrane detector

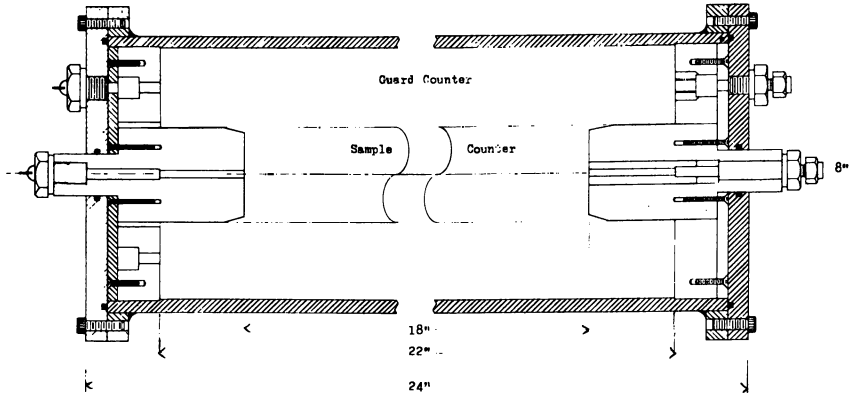

Figure 2. Construction detail of membrane detector

from the anticoincidence ring are proportional pulses so that differences in the detection efficiencies of the Geiger and proportional regions, as found in counters of conventional design, are eliminated.

Modified Design. The modified detector design at the University of Washington (UW) and Isotopes, Inc. (II) has the same counter configuration as the Curran and Oeschger counters but confines the sample to the inner detector volume. Charalambus and Goebel (*3*) have used the principle of confining the sample to the inner chamber and obtained excellent low background counting characteristics. Their filling system is a manual operation using mercury safety valves to ensure minimum pressure differential. The detector consists of a thin-walled inner counter,

of about 1-liter volume, inside a larger counter of 9 liters which acts as the anticoincidence shield (Figures 1 and 2) (*7, 18*). The anodes of both chambers are 0.001-inch diameter stainless steel wire.

The inner counter cylinder, made of metallized Mylar foil, is leak-tight relative to the outer counter. By means of two solenoid valves actuated by a differential mercury manometer, the outer and inner counters can be filled separately with a pressure differential on the partitioning foil of less than 0.5 cm. Hg. This pressure controller minimizes the danger of rupturing the partition. Two control circuit diagrams are shown in Figure 3. Figure 3A shows the mercury "U" tube with electrical

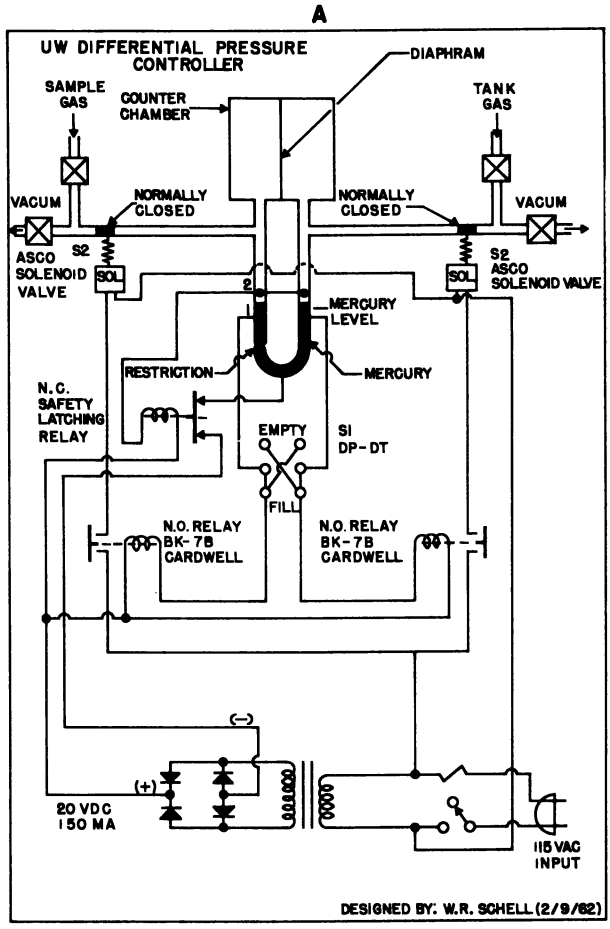

Figure 3. Circuit diagrams

A: Electrical switch

contacts imbedded in the glass for controlling the pressures on the two sides of the membrane. Figure 3B shows the controlling mechanism using a light source and photoresistant diodes. In operation, mercury conducts electricity or breaks the light path, which then triggers the controlling solenoids. The controller operates from vacuum to pressures greater than 11 atm. The entire sample to be measured is introduced into the inner counter, while inert background gas is fed into the outer counter. The foil remains expanded owing to a slight pressure differential, which ensures a constant volume of gas in the inner counter. This counter configuration permits about a 30% increase in sample counting efficiency

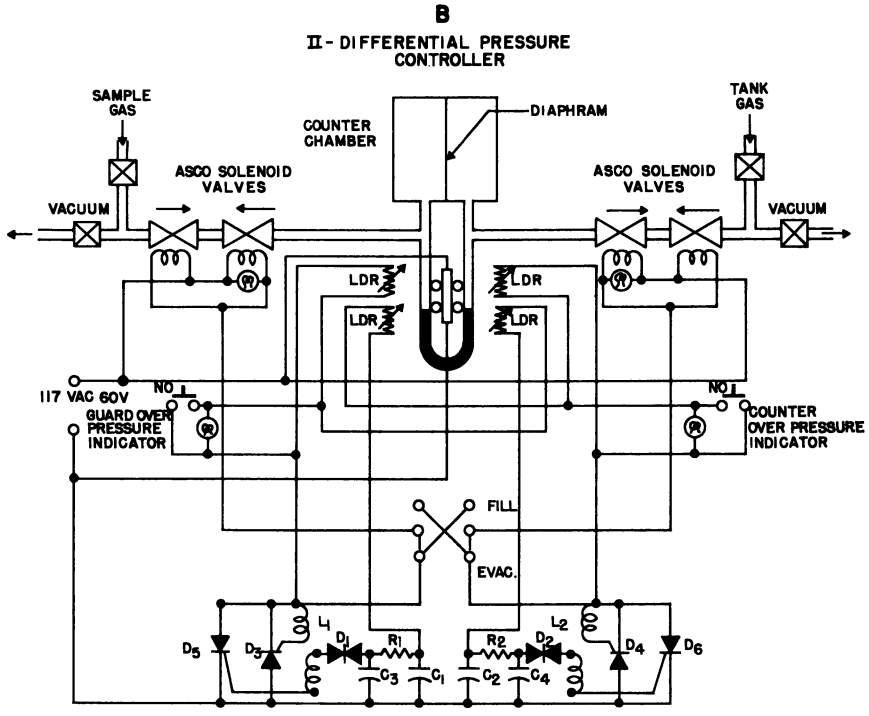

D_1-D_2	MT-32	LDR-C_1	4 each
D_3-D_6	2N4154	R -R	15K $\frac{1}{2}$ W
L_1-L_2	Sprague 11Z12	Panel Lights	45M- 33K
C_1-C_2	0.1 f	Activator Lights	Syn #61
C_3-C_4	0.05 f		

of pressure control

B: Photoresistant diode switch

because the sample gas does not act as its own anticoincidence filling gas, as in the Oeschger type counters.

Metallic parts of the detector are made of commercial high purity nickel. This metal was easier to procure than the more commonly used O.F.H.C. copper. The results have fully justified this choice, as the outer counter has low alpha activity of 5 alpha pulses/hr./100 cm.^{2}. Nylon was used in place of Teflon for the other parts of the counter because the foil seals to nylon more easily than to Teflon. The tight seal has been accomplished using Schjelbond tape (Supplied by the G. T. Schjeldahl Co., Northfield, Minn., used to seal the Echo satellites). Although it is not recommended as being "particularly good" for nylon, the seal has remained intact during six years of continuous use in the two detectors. The counter can be maintained by removing the end plates. With experience, replacement of all wires and membrane, as well as cleaning, can be accomplished by one man within an 8-hour day.

The shielding for the II detector consists of cadmium-paraffin and 8 inches of old steel. For the UW detector, the shield is as follows:

(a) Concentric steel tubes containing distilled mercury to a thickness of 1 inch

(b) Paraffin blocks with boric acid

(c) 8 Inches of old steel from a 16-inch gun barrel of the battleship USS Colorado.

Electronics and Counting Performance

The UW detector uses Sharp low beta anticoincidence electronics and scalers (low beta I) with voltage sensitive preamplifiers (Sharp is a division of Beckman Instrument Co.). The electronic "window" selected by a pulse generator is 0.75–100 mv. input for the anticoincidence channel and 0.5–∞ mv. for the guard channel. The discriminators were set up for use only in natural radiocarbon measurements.

The II detector has been calibrated for carbon-14 as well as tritium and argon-37. This detection system uses electronics developed for semiconductor detectors. Low noise, field effect transistorized (FET) preamplifiers, supplied by Technical Measurement Corp. (TMC), are used as the initial charge-sensitive pulse amplifiers. The pulse is amplified further by ORTEC linear amplifiers, and the pulse rate is registered by Hamner scalers. A Fluke 0–10 kv. power supply is used. The electronic components are shown in Figure 4. These electronics permit proportional counting spectra to be measured by simply feeding the amplifier output into a pulse height analyzer. Window discriminators are easily set by placing a radioactive standard gas, such as argon-37 or tritium, in the detector and recording the events on a pulse height analyzer. The

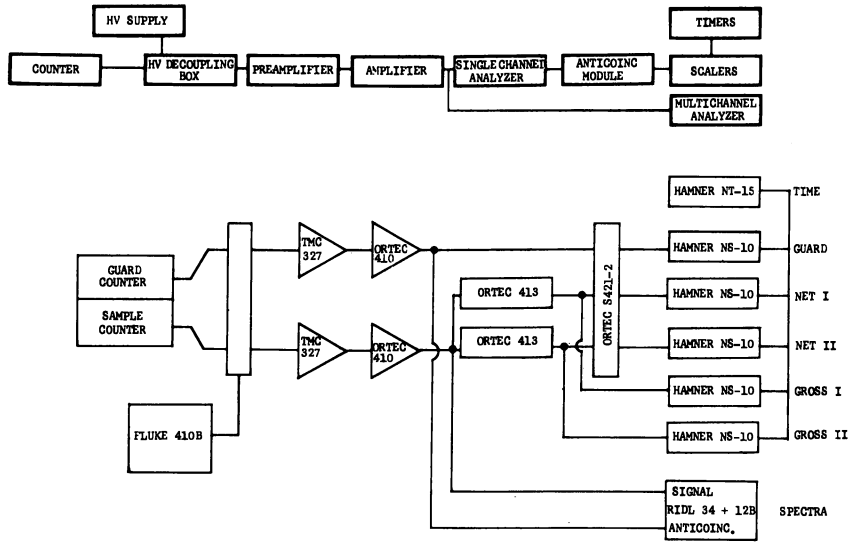

Figure 4. Electronic components and logic

discriminators are then set just below and just above the proportional peak of interest. The integrated noise level for the II detector, preamplifier, amplifier, and high voltage power supply is less than 0.1 mv. input, as determined by a pulser and oscilloscope. This low noise level permits the detector to be used in determining low energy electrons and x-rays of such gases as argon-37. The effect of recombination of electrons by gas mentioned by Loosli *et al.* (*14*) and Curran (*4*) could be significant at high pressures. However, this effect has not been apparent in counting tritium electrons of 18 kev. maximum energy at 10 atm. total pressure.

The counting modes for the II and UW detectors are given in Table I. All these channels are not necessary to perform accurate, low level radioactivity analysis. They do, however, permit rapid determination of ratios for systematic checks on the operation of the electronics and purity of the gas.

Table I. Counting Modes for II and UW Detectors

Mode	*Ortec*	*Mode*	*Sharp*
Net I	Anticoincidence-lower window	Net I	Anticoincidence-lower window
Gross I	Non-anticoincidence-lower window	Gross	Non-anticoincidence
Net II	Anticoincidence-upper window	Net II	Anticoincidence-upper window
Gross II	Non-anticoincidence-upper window	Guard	—
Guard	—		

The "plateau" (count rate *vs.* voltage) curve for the UW detector is shown in Figure 5. Setting the upper discriminator from 100 mv.–∞ permits rapid determination of the operating voltage without running a series of counts at different voltages. To obtain the operating voltage, an external source, such as sodium-22, is placed near the axis of the sample counter center wire. External gamma photons interact with the gas in the detector, forming electrons. When the "operating plateau" is exceeded as the voltage is increased, counts are recorded in the upper channel (Net II). Reproducible results can be obtained routinely by decreasing the voltage 50–100 volts below the voltage where counts are

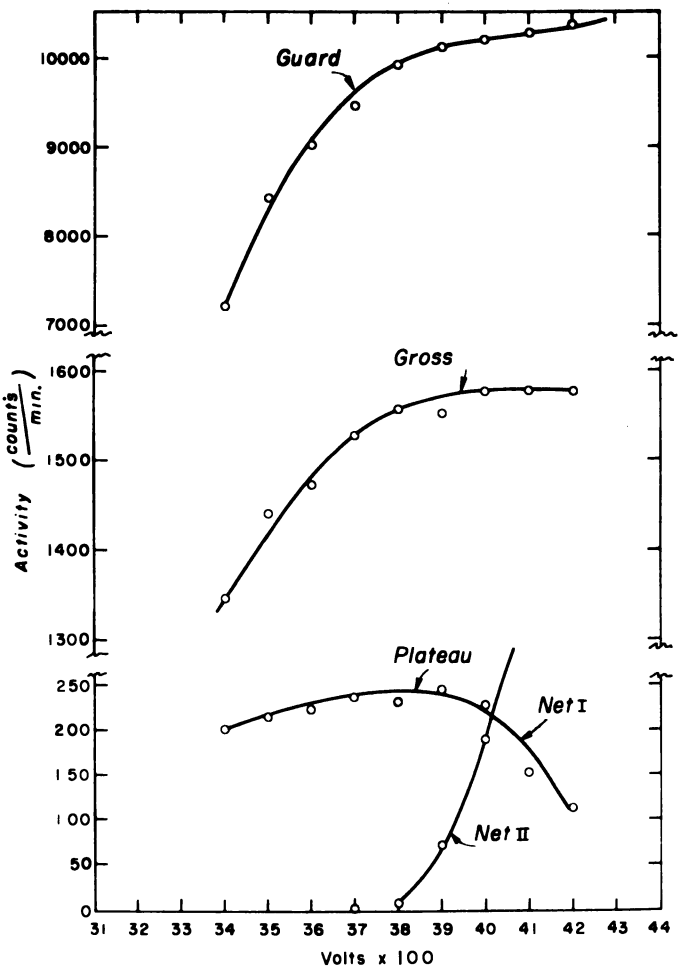

Figure 5. Carbon-14 "plateau" curve for UW detector electronics

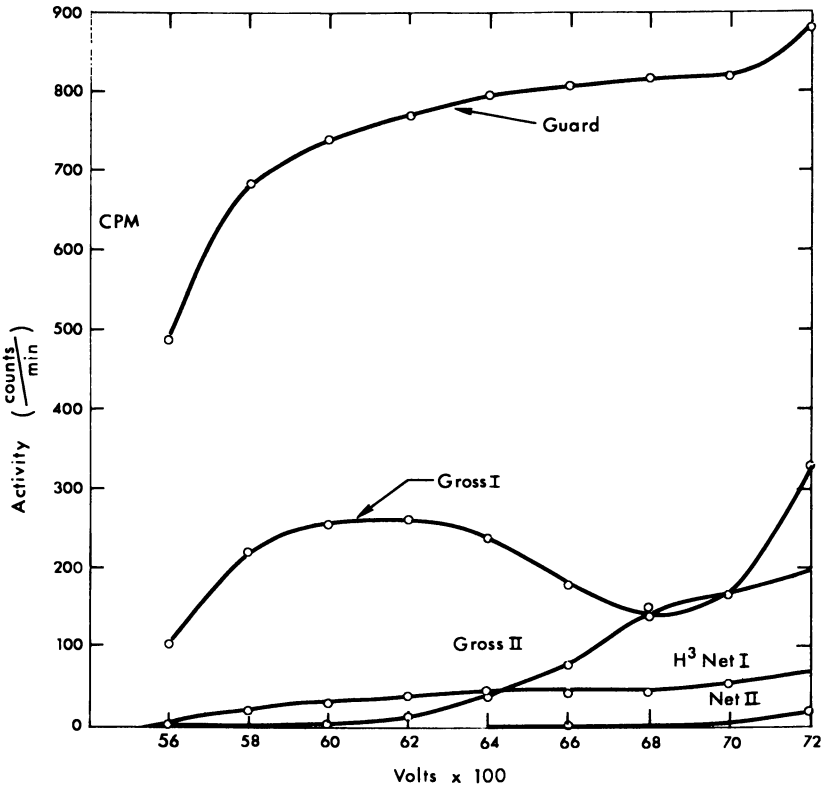

Figure 6. Tritium "plateau" curve for II detector electronics

observed in the upper channel. The time necessary to set the operating voltage is usually less than one minute.

A tritium "plateau" determination is shown in Figure 6, for the II detector. Using the TMC and ORTEC electronics, the observed results are slightly different than from the Sharp electronics, owing to different logic. The usable range of the tritium counting plateau is *ca.* 400 volts at 400 cm. Hg pressure.

The counting characteristics for subtracting external radiation are shown in Figure 7 and Figure 8. These figures illustrate the effect of placing a sodium-22 source at various distances from the axis of the center counter, and at various distances along the side of the counter respectively. The guard counter eliminates external radiation effectively. The effect of radiation entering the center counter along the axis was, at first, thought to be a serious problem. However, external radiation must enter the ends almost parallel to the counter and must fall within the window discriminators to be counted as a real event. The probability of this occurrence appears to be low for this detector design.

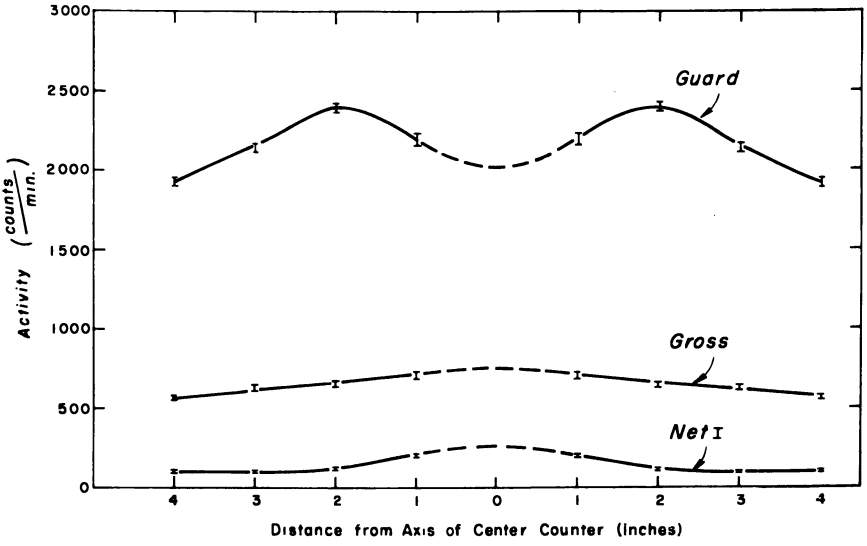

Figure 7. Effect of external source and geometry on count rate. Source used was 1-μCi sodium-22 at end of detector

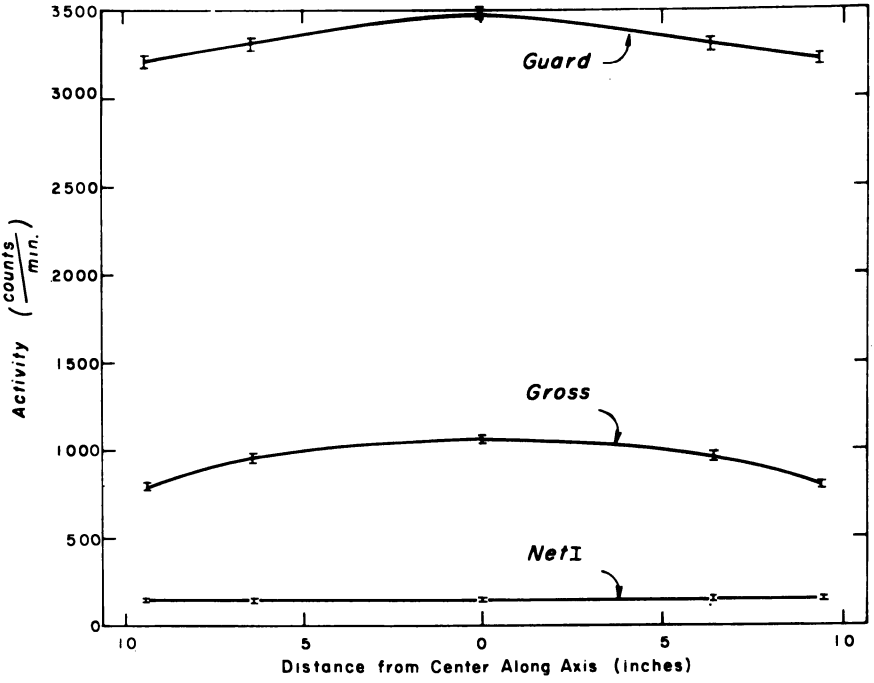

Figure 8. Effect of external source and geometry on count rate. Source used was 1-μCi sodium-22 on top of detector

One problem which might arise is from diffusion of sample gas through the membrane into the inactive or dead methane guard counter gas, especially at the butt seal. To check for this diffusion, the same methane prepared from N.B.S. oxalic acid standard was measured at least weekly for six months. The sample was left in the counter during each counting period for about 1000 minutes. No change was observed in the activity of the standard sample during the six months, showing that diffusion of sample methane is negligible. The membrane also maintained 0.5 cm. pressure differential.

In counting tritium as hydrogen in a 3 : 1 $H_2 : CH_4$ counting gas mixture, a small change in the counting gas occurs, probably by diffusion of hydrogen through the membrane during a 1000-minute counting interval. The potential for diffusion exists since: (1) hydrogen is a small molecule; (2) the sample counter is at 0.5 cm. Hg pressure higher than the guard counter; and (3) the gas composition is different in the two chambers, giving a concentration gradient. During a 1000-minute time period, the pressure differential decreases approximately 0.3 cm. This appears to be consistent and does not cause significant problems during a 1000-minute count. An internal laboratory standard, PAL-II 2150 TU (a tritium unit or TU is defined as a concentration ratio $^3H/H = 10^{-18}$), showed no change in count rate above statistical deviations during the counting period of 1000 minutes. When a radioactive tritium source of 120,000 TU was added to the sample counter, the count rate decreased by 1.5% during a 1000-minute period. This 1.5% decrease in count rate could be caused by changes in the counting gas mixture, owing either to high counting rates or to diffusion through the membrane. For routine counting of samples, the counting time is seldom longer than 1000 minutes. Since the background count rate is approximately 1.7 c.p.m., 1σ standard deviation of the background gives a counting error of about 2%—an error greater than the error caused by gas diffusion. Further studies should be made on counting rate change over a longer time if better than 2% statistical counting efficiencies are required for proportional counting of hydrogen in this gas counting mixture.

Another potential error is a "memory" effect, or contamination, between samples. No memory effect is found by counting methane prepared from N.B.S. oxalic acid standard and then background. Between each sample, the detector is evacuated to about 10μ pressure. The tritium memory effect also was checked using a 120,000 TU sample. After counting the high radioactivity gas, the counter was evacuated to 10μ pressure. Background gas was then added to the detector. The background increased 0.2 c.p.m., indicating a memory effect of 0.2/2800, or 0.007%. Upon evacuating the detector again to 10μ, the background count rate was normal. This test indicates that only a single counter fill

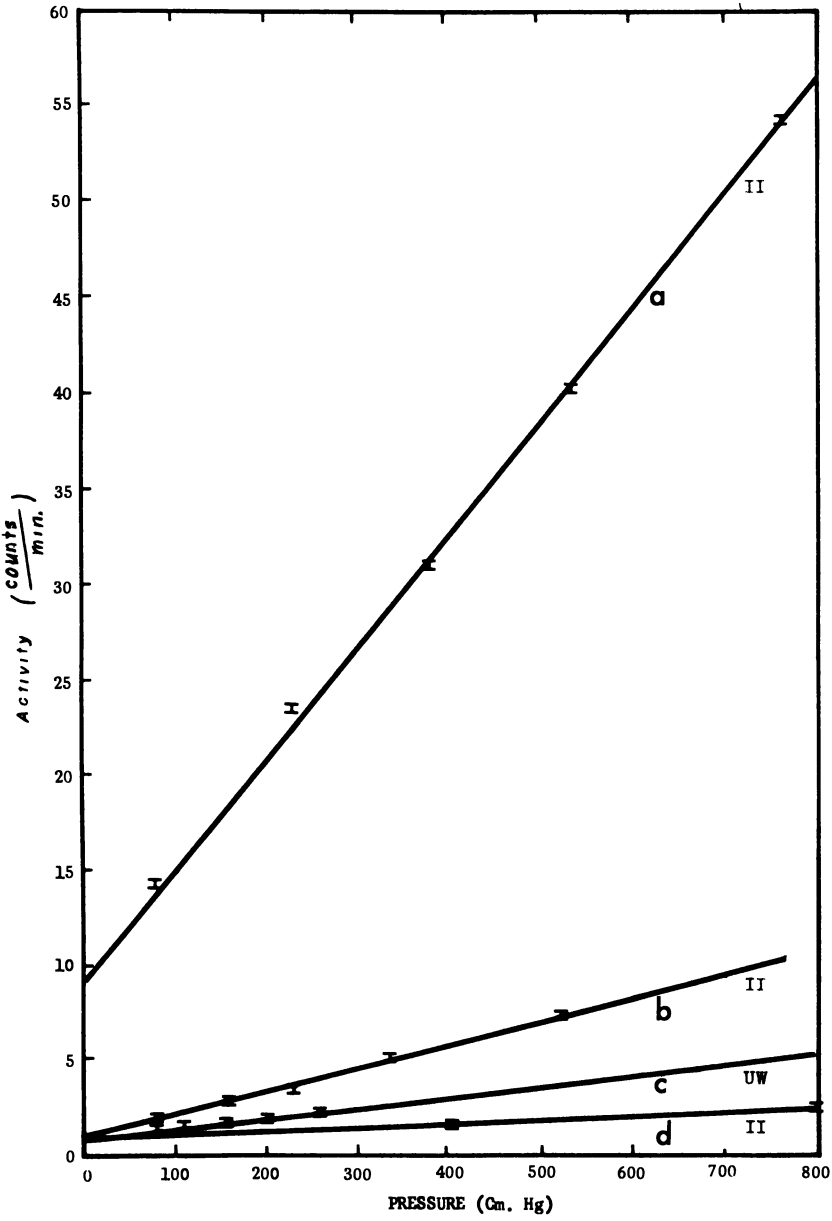

Figure 9. Background of counter under various shielding conditions and "window" settings and gas mixtures

(a): II—no shielding, CH_4
(b): II—8-inch steel shielding, CH_4
(c): UW—1-inch mercury, 8-inch steel, boron paraffin shielding, CH_4
(d): II—8-inch steel, 2-inch paraffin, 0.030-inch Cd shielding tritium "window," 3 : 1 $H_2 : CH_4$

is necessary to eliminate memory effects with tritiated hydrogen. For normal low level counting—*i.e.*, less than 2000 TU, the memory effect between samples is less than the counting statistics, and thus can be disregarded. Geyh (*6*) investigated construction components of the quartz-tube counter, Oeschger-type counters, and plastic scintillation counters and found low memory effect in the quartz-tube, but high memory effect in the Oeschger-type counters. The selection of different construction materials and levels of radioactivity used by Geyh may explain this discrepancy.

Results and Discussion

The backgrounds of the UW and II detectors, determined under various shielding conditions, are shown in Figure 9. The UW detector is used exclusively for carbon-14 analysis by counting methane, while the II detector is used for other gases as well. Background radioactivity of the II detector using methane, while outside the shield (*i.e.*, no shield except the electronic anticoincidence guard) varies from 10 to 55 c.p.m. at pressures from 1 to 10 atm., respectively (Curve a). Inside the 8-inch steel shield, background varies from 1.5 to 10 c.p.m. (Curve b). For the UW detector inside steel, mercury, and boron paraffin shielding, and in the basement of a four-story concrete and steel building, the extrapolated background would be from 1.1 to 5 c.p.m. (Curve c). The highest pressure measured in the UW detector is 3-1/3 atm., owing to limitations in the pressure gage and high voltage power supply. Background for tritium counting at different pressures is shown in Curve d. The highest pressure measured in the II detector is 11 atm., the limit of the 10-kv. power supply.

Effect of Wall Thickness on Background. The effects of different gas mixtures, wall thicknesses, and shielding are shown in Table II. Oeschger (*17*) first illustrated the wall thickness and pressure effects using ethylene as the counting gas at pressure less than 1 atm. From the measurements he derived an empirical formula explaining the resulting background. These measurements at high pressures generally agree with Oeschger's results.

Effect of Paraffin on Background. A large decrease in the background of hydrogen–methane counting gas mixture was achieved by placing a 0.030-inch carmium sheet next to the guard counter wall and 2 inches of paraffin around the counter inside the steel shield. The counter background within the tritium "window" decreased from 2.62 to 1.68 c.p.m., at 400 cm. Hg pressure. The 36% decrease in background indicates that a significant component of the background arises from fast neutrons produced by cosmic muons in the shielding and counter. Additional paraffin could decrease the background further.

Table II. Effects of Gas Mixture, Gas Pressure, Wall Thickness, and Shielding on Background

Wall Thickness mg./cm.²	Filling Gas $H_2 : CH_4$ Ratio	Filling Gas Pressure cm. Hg	Window Width	System[a]	Background, c.p.m.[b] Without Paraffin	Background, c.p.m.[b] With Paraffin
7.7	3 : 1	133	tritium	II	2.16 ± 0.07	
7.7	3 : 1	400	tritium	II	3.34 ± 0.05	
7.7	3 : 1	800	tritium	II	5.34 ± 0.08	
7.7	1 : 1	100	tritium	II	2.21 ± 0.05	
7.7	1 : 1	200	tritium	II	2.79 ± 0.06	
3.5	3 : 1	400	tritium	II	2.62 ± 0.05	1.69 ± 0.04
3.5	3 : 1	800	tritium	II		2.82 ± 0.06
3.5	2 : 1	76	tritium	II	1.42 ± 0.04	
3.5	0 : 1	76	open	II	1.62 ± 0.05	1.15 ± 0.05
3.5	0 : 1	400	tritium	II	4.89 ± 0.07	2.11 ± 0.05
3.5	0 : 1	400	open	II	5.80 ± 0.07	
7.7	0 : 1	76	open	UW		
7.7	0 : 1	253	open	UW		

[a] *See* text for details of II and UW shielding.
[b] Errors are ± σ for 1000-minute counts.

Effect of Gas Composition and "Window" on Background. If the background were caused simply by adsorption of energy in the counting gas, the background of the different gases would be proportional to the different gas densities. The results did not show this effect with various $H_2 : CH_4$ gas mixtures. In detecting tritium, a background component will be present when using hydrogen or hydrocarbons because of neutrons which are not completely absorbed.

Backgrounds of hydrogen and methane gas mixtures were measured at different pressures. The 3 : 1 $H_2 : CH_4$ mixture counted at a total pressure of 400 cm. Hg gave a background of 2.62 c.p.m. while pure methane gave a background of 4.89 c.p.m. The ratio of the number of hydrogen atoms in the two mixtures should be directly proportional to the ratio of the background count rate if the background is related to the number of hydrogen atoms in the counter. This relation was found to hold with different gas mixtures to within 10%. It appears that the background increases in proportion to the increase in hydrogen atoms. Pure hydrogen should give the lowest background but is not a good counting gas. Gas counting mixtures of 1 : 1, 2 : 1, 3 : 1, 4 : 1, and 6 : 1 $H_2 : CH_4$ were tried at various pressures up to 10 atm. It was found that 1 : 1, 2 : 1, and 3 : 1 mixtures were the most stable and free from spurious pulses. Gas mixtures of 4 : 1 and 6 : 1 gave good pulses, as measured on the oscilloscope, but reproducible data were not obtained. Only limited time was spent on these higher gas ratio mixtures so that conclusions given are subject to change following further work. With

the 3 : 1 ratio gas mixture, double pulsing and "ringing" were observed. This problem was eliminated by extending the amplifier time constant to greater than 2 μsec.

For carbon-14 counting of methane and other hydrocarbons, the lower window can be set high enough to limit the secondary effects of external radioactivity. This should reduce the background significantly. In the UW detector, the lower window was increased from 0.75 to 2 mv. input signal, and the background decreased from 2.1 to 1.0 c.p.m. (*10*). This decreased the counter efficiency for carbon-14 slightly, but the figure of merit for the counter increased significantly. There has been no systematic change in the background counting rate attributable to barometric pressure changes or solar flares in either the UW or II detectors.

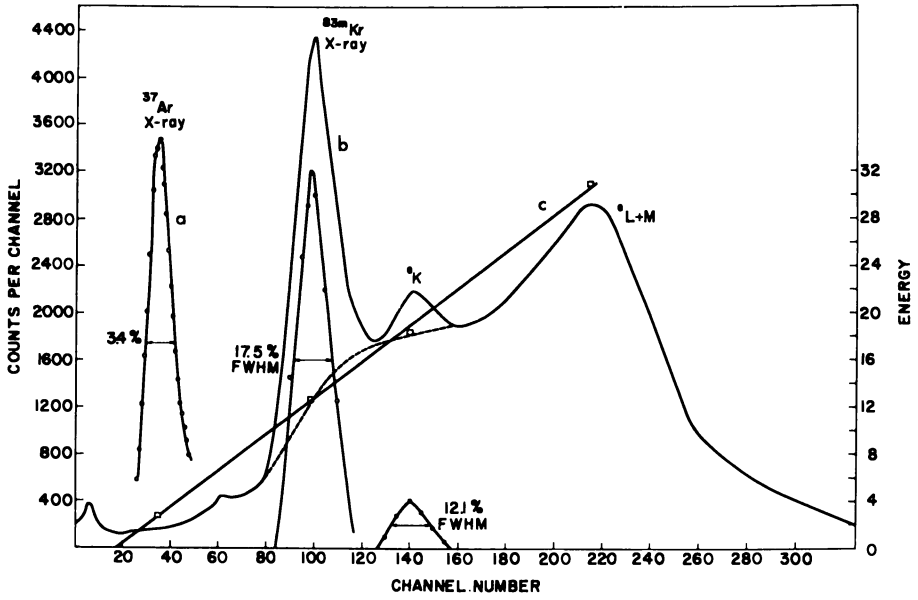

Figure 10. Proportional spectra of argon-37 and krypton-83m using 9 : 1 Ar : CH_4 gas counting mixture at a pressure of 760 cm. Hg and 5600 volts (c): Energy calibration

(a): Argon-37
(b): Krypton-83m
(c): Energy calibration

Proportional Spectra of the Counter. The proportional pulses resulting from ionization of electrons and x-rays in the counter have been measured using a pulse height analyzer. Argon-37 and krypton-83*m* have been found to be excellent calibration gases. Argon-37, with a

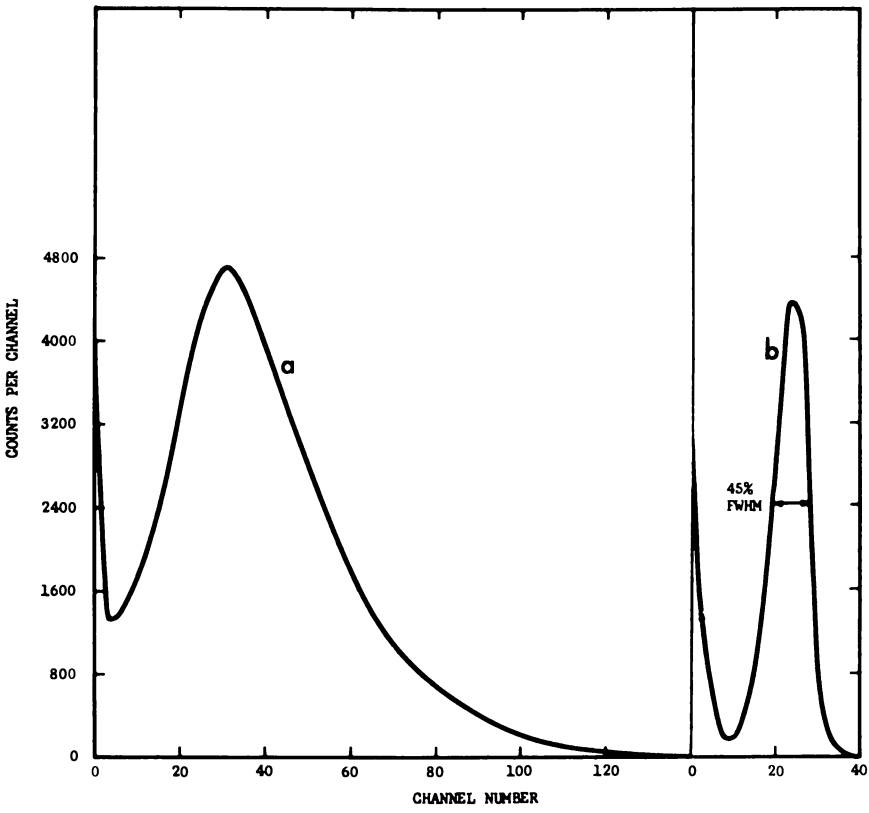

Figure 11. Proportional spectra of (a) tritium and (b) argon-37 in 3 : 1 $H_2 : CH_4$ gas counting mixture at 400 cm. Hg pressure using RIDL-400 channel pulse height analyzer

35.1-day half-life of the 2.62 k.e.v. x-ray and Auger electrons, was used to check the counter. Krypton-83*m* has a half life of 1.8 hours and decays by converting electrons, gammas, and x-rays of energies from 7–32 k.e.v. Using these sources, the energy linearity and resolution of the detector were determined. Krypton-83*m* was obtained by milking a ^{83}Rb ($t_{1/2}$ = 83 days) cow. Figure 10 shows the spectra of argon-37 and krypton-83*m* using 1 : 9 CH_4 : Ar gas counting mixtures at 10 atm. The energy of the counter is linear from 1.5 to 31 k.e.v., as determined by the pulse height analyzer. It was found that at 200 volts below operating voltage, the energy was linear up to 18 k.e.v., but the 31-k.e.v. peak was low by about 4 k.e.v. This effect must be caused by charge collection of primary ionization and acceleration of secondary electrons in the high electric field of the counter.

Tritium and argon-37 spectra are shown in Figures 11a and b. The spectra were collected using a 3 : 1 $H_2 : CH_4$ counting gas mixture at

400 cm. Hg. The argon-37 spectra were taken immediately after counting tritium and under identical conditions using inactive hydrogen and methane.

Low Energy Background. Figure 12a shows the background spectra for 10% methane and 90% argon. Figure 12b shows the background spectra for $H_2 : CH_4$, 3 : 1 gas mixture. It is noted that a low energy x-ray peak is present in both the argon–methane and hydrogen–methane gas mixtures. This peak has an energy of about 1.5 k.e.v. Apparently the aluminized foil is being excited by radiation in the detector which is not being removed by the anticoincidence guard. This excitation energy could arise from radioactive contamination in the foil, inefficient anticoincidence guarding of the incident external radiation, or radiation entering the counter through the unguarded ends. The photons either interact directly with the aluminum or first interact with the gas molecules and the secondary photons excite the aluminum. If the external radiation interacts directly with the aluminum foil, there should be no change in the background radioactivity in the 1.5-k.e.v. peak with different densities of counting gas.

However, if the external radiation (1) interacts with the gas molecules, (2) excites electrons or photons which (3) then excite aluminum giving off the characteristic x-rays, the ratio of density of two different

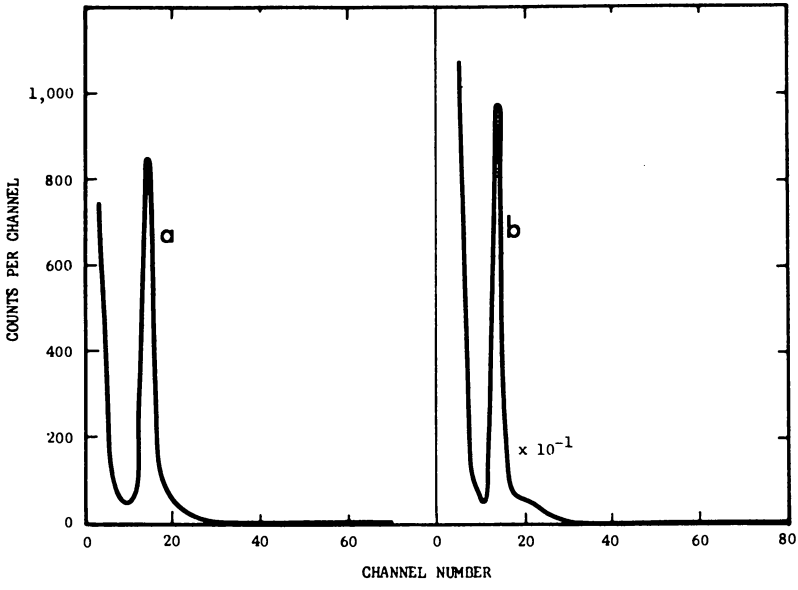

Figure 12. Background spectra of membrane detector
(a): 9 : 1 Ar : CH_4 gas counting mixture at 760 cm. Hg
(b): 3 : 1 H_2 : CH_4 gas counting mixture at 400 cm. Hg

gases should be proportional to the ratio of the background radioactivity under the peaks.

For Ar : CH_4 at 760 cm. Hg, the density is 16.78 grams/liter, and the integrated background of the peak, determined by the pulse height analyzer, is 2.02 ± 0.06 c.p.m. For H_2 : CH_4 at 400 cm. Hg pressure, the gas density is 1.298 grams/liter, and the background under the peak is 0.21 ± 0.01 c.p.m. The ratio of the densities of the two gases is 0.08, whereas the ratio of the radioactivity in the peaks is 0.10. The difference is about 20%. This error is surprisingly small considering the simple assumption made. Other effects probably occur which are not considered in this explanation.

These data indicate that the effect of gas density is important in attempting to achieve extremely low background counting of gases. The lower discriminator can be set to eliminate part of this low energy back-

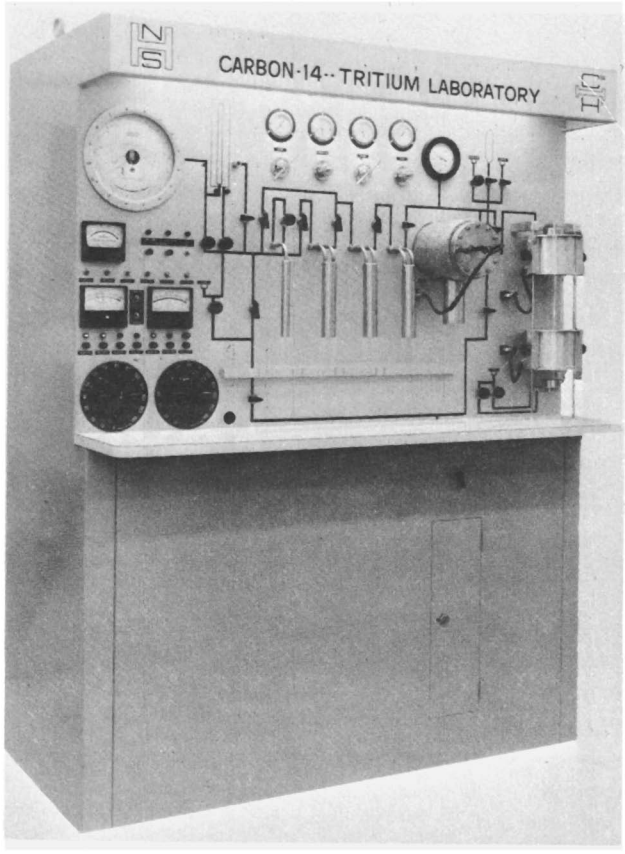

Figure 13. Laboratory equipment for sample preparation and counter filling

ground. However, in detecting low radioactivity levels of argon-37, the aluminum x-ray cannot be eliminated entirely owing to the similarity in energy. Gold on Mylar foil is known to have low background radioactivity and may be substituted to eliminate the aluminum x-ray since the characteristic gold x-ray energy is about 66 k.e.v. However, the L and M x-rays (2–10 k.e.v.) may be present, and the contribution to the background must be checked.

Use of the Equipment

The detectors have been used to date accurately carbon-14 samples, low level tritium samples, and environmental levels of argon-37. The limit of counting sensitivity is equivalent to a carbon-14 sample age of greater than 60,000 years. Since the detectors are *ca.* 1-liter volume and can be operated at different pressures—*i.e.*, 0.5–10 atm.—the versatility in sample counting is great. The UW detector has been used to date samples as small as 0.2 gram carbon (Fairhall *et al.* (*8*), Sample UW-28). The detectors with no massive shielding (*see* background data, Figure 10) could be used to date carbon-14 samples to at least 10,000 years. Tritium samples have been analyzed by direct counting at levels of 2 TU without enrichment. Argon-37 has been analyzed in atmospheric air at levels about 40 times the estimated cosmic particle produced level.

Tritium Analysis. Figure 13 shows the laboratory equipment used for sample preparation and counter filling. The bomb converter is designed to prepare methane for both carbon-14 and tritium analysis. The chemical reactions are:

For carbon-14 (*9*)

$$CO_2 + 4H_2 \xrightarrow[475°C.]{\text{Ru catalyst}} CH_4 + 2H_2O \qquad (1)$$

For tritium (*1*)

$$H_2O + Zn \xrightarrow[400°C.]{} ZnO + H_2 \qquad (2)$$

$$CO_2 + 4H_2 \xrightarrow[475°C.]{\text{Ru catalyst}} CH_4 + 2H_2O \qquad (3)$$

In the bomb converter, the water formed in Reaction 3 is used up by excess zinc giving a total reaction:

$$CO_2 + 2H_2O + 4Zn \rightarrow 4ZnO + CH_4 \qquad (4)$$

The reaction rates can be followed by observing the decrease in pressure with time as the products are formed.

It is desirable to count tritium as methane since four atoms of hydrogen per mole of gas are present. At 10 atm. using the II counter, approximately one mole of water can be counted. The background count rate would be less than 5 c.p.m. in the tritium window. The sensitivity of this method would be about 1 TU without enrichment.

After extensive effort to perfect the method, it was found that environmental water and "memory" effects occurred in the bomb reactors. Since the reactor had to be opened to change the zinc and add the water sample, environmental water was adsorbed in the reactor. Neither the environmental contamination nor "memory" effects could be removed completely by evacuating the reactor within a reasonable time. This technique is promising, but further work must be done to eliminate these problems before it can be used routinely for low level tritium analysis.

In preparing hydrogen for analysis of tritium in the counter, water is vaporized through Mg turnings at 600°C., and the resulting hydrogen condensed on activated charcoal at −195°C. A test tube with 5–10 cc. of water is placed inside the vertical combustion tube at the level of the lower heater. About 40 grams of magnesium turnings are placed in the combustion tube at the level of the upper heater. After evacuation, the upper heater is turned on and set to control at 600°C. When all the water has been reduced and the hydrogen trapped in the small charcoal trap, the lines and counter are evacuated. The counter is filled by allowing the trap to warm and the gas to expand into the sample counter. Tank methane is added to the guard counter using the automatic fill controller. When the desired pressure of hydrogen is reached as determined on the pressure gage, the counter valves are closed, and the lines are evacuated. Tank methane is then added to both sample and guard counters simultaneously while maintaining a positive pressure in the lines. The positive pressure in the lines limits back diffusion of sample gas. No apparent isotopic fractionation of hydrogen occurs if the trap is warmed nearly to room temperature while filling the counter. Other non-condensible gases such as argon are added to the counter using the hydrogen fill technique. Condensible gases such as methane are added to the counter using a filling trap which does not contain charcoal.

For routine tritium analysis, the gas counting mixture is 3 : 1 H_2 : CH_4, and the total pressure is 400 cm. Hg. It is possible to measure water samples of a few cubic centimeters at levels of 4 TU without enrichment and a 1000-minute counting period. At 800 cm. Hg, the limit of sensitivity is 2 TU, counting a 3 : 1 H_2 : CH_4 gas mixture for 1000 minutes counting time. There is approximately 1 c.p.m. per 25 TU at a total pressure of 800 cm. Hg with a background count rate of approximately 2 c.p.m.

One of the best checks of the counting method is sample comparison with other laboratories and reproducibility in counting standards and background. Table III shows such comparison. The counting efficiency for the tritium window used is 76%. All samples and background were measured at 400 cm. Hg pressure, using a 3 : 1 H_2 : CH_4 counting gas mixture.

Table III. Interlaboratory Comparison Standards Expressed in Tritium Units and Background Counting of Samples

	Laboratory				
Sample	*UCLA*	*La Jolla*	*IAEA*	*PAL-II*	*WL-II*
IAEA Std.[a]		558 ± 35	536 ± 10	572 ± 15	
La Jolla Std.		2705 ± 20		2780 ± 70	
Sierra Snow Melt[b]	350 ± 35			410 ± 38	
Groundwater					
No. 1				132 ± 11	91 ± 13[c]
No. 2				318 ± 34	308 ± 14[c]
No. 3				25 ± 25	40 ± 11[c]

	c.p.m.	
Counting Sequence	*Background*	*Standard*
1	1.47	39.7
2	1.58	39.8
3	1.44	38.5
4	1.45	39.7
5	1.56	38.4

[a] Sample supplied by H. Suess, La Jolla, who participated in the interlaboratory comparison standards from IAEA. The IAEA standard result is an average of the results from 12 laboratories with range 492–600 TU.
[b] Sample supplied by W. Libby of sample measured several times in his laboratory.
[c] Samples enriched and counted by Isotopes, Inc., Westwood Laboratories (WL-II).

The standard and background counting rates averages are 39.2 and 1.50 c.p.m., respectively. Using a 2σ standard deviation for the counting data, the values all agree within counting errors. The data were taken over a period of six months and show that the counter gives reproducible results using the 3 : 1 H_2 : CH_4 counting gas mixture.

Since the level of tritium in the atmosphere is presently greater than 10 TU, it is possible to study many physical and chemical processes using this equipment for sample analysis. Since isotopic enrichment is unnecessary for most samples, direct rapid analysis is possible. The equipment is being used presently to analyze water samples from Nevada in a hydrology project. Table IV shows the analytic data. No attempt has yet been made to evaluate these data. What is apparent qualitatively

Table IV. Tritium Analysis of Nevada Well and Ground Water

Sample Description	*Collection Date*	*TU ± 2σ*
Blue Jay Station	4/11/67	50 ± 10
6N/51-22b	8/16/67	18 ± 6
	10/1/67	137 ± 16
Base Camp Tap Water	9/29/67	80 ± 20
5N/51-7bc		
Carvers Flowing Well	3/28/67	61 ± 22
11N/43-29		
Dugan Place Spring	9/29/67	29 ± 10
8N/49-25		
Eureka Town Supply	4/10/67	76 ± 8
19N/53-24		
Fallini Well	4/11/67	148 ± 29
5N/51-19ba	6/21/67	24 ± 10
	8/16/67	30 ± 10
	10/1/67	138 ± 16
Fish Creek Ranch	4/10/67	16 ± 6
16N/53		
Pony Canyon TUN (Austin)	3/30/67	55 ± 24
19N/44-29ad		
J. Bars Ranch	3/30/67	28 ± 22
14N/43-28ac		
Moores Station	4/11/67	87 ± 17
10N/51-36ba		
6 Mile Well	4/9/67	17 ± 8
8N/51-34cd	5/11/67	66 ± 8
	6/26/67	14 ± 6
	8/16/67	84 ± 14
	10/2/67	76 ± 10
Spring Above Dugan Place	4/9/67	8 ± 6
8N/49-25		
Tonopah Airport	3/30/67	234 ± 56
2N/43-1bc		
Tonopah Well No. 9	3/28/67	55 ± 28
4N/44-8baa		
Twin Springs 60′ Well	4/11/67	18 ± 16
4N/51-13da	9/29/67	22 ± 8
Twin Springs Pond Near 140′ Well	9/29/67	96 ± 14
Twin Springs 140′ Well	4/11/67	127 ± 20
4N/51-13da2		
Twin Springs Spring	4/11/67	28 ± 8
4N/51-13da		
TYBO	4/9/67	141 ± 36
6N/50-35ab		

Table IV. Continued

Sample Description	*Collection Date*	*TU ± 2σ*
UE 1 Zone 1 N. 1,395,000 E. 429,400	2/1/67	22 ± 12
UE 1 Zone 2 N. 1,395,000 E. 429,400	2/2/67	122 ± 12
UE 1 Zone 3 Tonopah N. 1,395,000 E. 429,400	2/10/67	20 ± 6
UE 1 Zone 4	2/12/67	10 ± 12
UE 1 Zone 5	2/13/67	19 ± 16
UE 2 Packer Zone 5 1208′–1406′ N. 1,293,700 E. 523,800	1/19/67	240 ± 14
UE 2 Packer Zone 6 Swab Test 1300′–1498′ N. 1,293,700 E. 523,800	1/22/67	36 ± 12
UE 2 Packer Zone 7 Swab 1498′–bottom N. 1,293,700 E. 523,800	1/27/67	19 ± 8
UE 2 Swab 812′–1010′ N. 1,293,700 E. 523,800	1/17/67	20 ± 6
UE 11 N. 1,401,351 E. 626,475	4/22/67	32 ± 8
Upper Hot Creek Ranch	4/9/67	19 ± 16
8N/50-29da	9/26/67	88 ± 18
Warm Springs	4/11/67	63 ± 20
4N/50-20cb	9/29/67	73 ± 10

from the data is the variation in the tritium concentration at the same well at different collection times and at different locations. Samples collected at the same location and at different months during 1967 show that water is coming from different sources. Infiltration of water from the surface to the producing aquifer could give the high tritium values found in the winter and spring months at Blue Jay station, Fallini well, and 6-mile well. During the winter and spring the use of water is low, and the deeper storage water which is lower in tritium may not be tapped.

Well use, mixing of high level environmental water with deep ground water, permeability, and storage time are potential problems which can be evaluated with careful sampling techniques and hydrogeological methods of analyzing the data. These topics will be the subject of later studies.

Hydrologic studies are being conducted using environmental tritium in enclosed aquifers and for measuring water movement over large distances (*11*). Cloud physics and other meteorological studies of air mass identification can be augmented by analyzing the tritium content of water vapor. Maritime air has low tritium content, whereas continental and stratospheric air have higher tritium contents. Simplified analytic techniques of high sensitivities make many experiments feasible that were not feasible before.

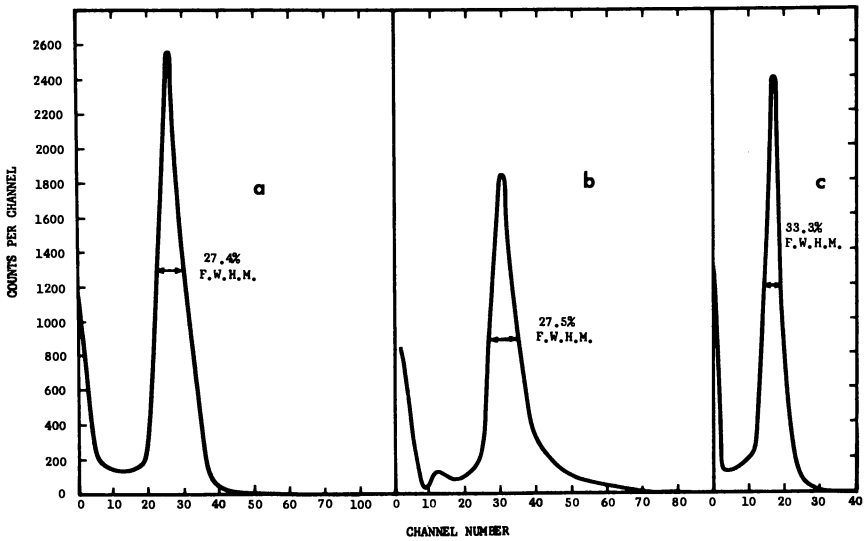

Figure 14. Proportional counter spectra of argon-37 at different pressures and voltages

(a): Spectra at pressure of 400 cm. Hg and 4000 volts
(b): Spectra at 760 cm. Hg and 5600 volts
(c): Spectra at 760 cm. Hg and 5400 volts

Argon-37 Analysis. The II counter has been calibrated for analysis of the 2.62-k.e.v. x-rays and Auger electrons emitted in the decay of argon-37. Figure 14a and b show the argon-37 spectra measured in 9 : 1 Ar : CH_4 gas mixture at pressures of 400 and 760 cm. Hg, respectively. The resolution full width at half maximum (FWHM) in both cases is 27% or 0.82 k.e.v. In both cases the spectra were measured in the center

of the voltage "plateau." Figure 14c shows the argon-37 spectra at 760 cm. Hg, measured at a lower voltage—*i.e.*, closer to the "knee" of the plateau. There is no indication of the activity above the argon-37 peak which occurred in the spectra taken in the center of the plateau at 760 cm. Hg. At 400 cm. Hg, there was no activity above the argon peak. The reason for the counts in channels above the argon peak at the higher voltages and pressures has not been investigated.

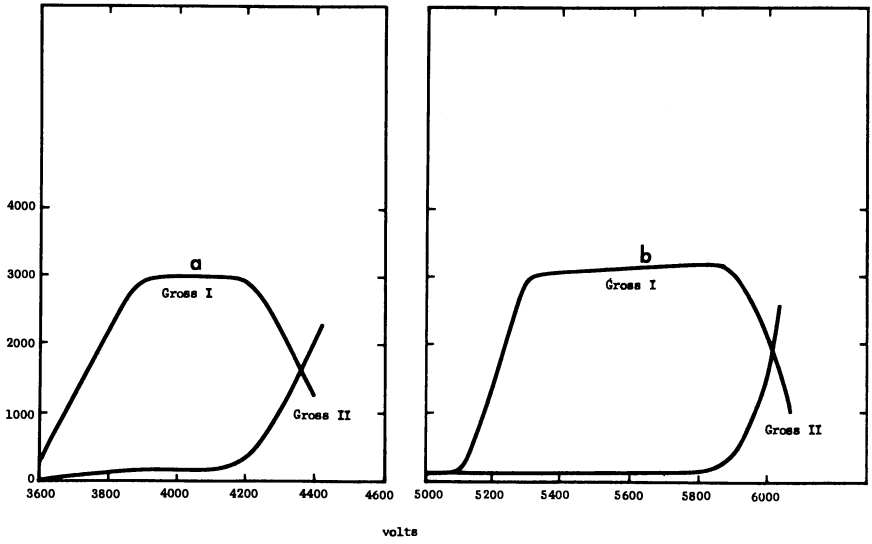

Figure 15. Argon-37 counting "plateau" in tritium window using 9 : 1 Ar : CH_4 gas counting mixture

(a): At 400 cm. Hg
(b): At 760 cm. Hg

Figure 15 shows the "plateau" curve for argon-37 at pressures of 400 and 760 cm. Hg. The length of the plateau increases with pressure, but as shown in Figure 14b, electrons may be accelerated in the electric field, giving pulses of a higher energy. Thus, a compromise must be made in "window width" for detecting argon-37 with maximum efficiency and minimum background. Small changes in gas purity might change the operating voltage. The argon-37 window must be set wide enough to accommodate these small changes in gas composition.

In the absence of a calibrated standard, the radioactivity in an argon-37 sample, supplied by Oak Ridge National Laboratory, has been approximated, using calibration data foar tritium and a pulse height analyzer to observe the peak. In the counter set up, a long line connects the counter to the fill system. The volume of the line is about 310 $cm.^3$,

or 27.2% of the total volume. The tritium efficiency was calculated using a 1650 d.p.m./cm.^{3} standard hydrogen and a standard of known tritium concentration (2150 TU). A few cm.^{3} of the 1650 c.p.m./cm.^{3} sample were added to the detector, and sufficient time was allowed for line-counter gas equilibrium. The over-all efficiency (counting volume/total volume) was found to be 72.8%. Using the known TU standard, the counting efficiency (counting rate/disintegration rate) for the tritium window is 76%.

For argon-37 counting, radioactivity in the peak is observed on a pulse height analyzer, and the window is set wide enough to count all the radioactivity. The argon-37 "standard" was 1830 d.p.m./cm.^{3} at Nov. 1, 1967, calculated from the value given by ORNL and our dilution. Using the counting data, the efficiency for counting with 9 : 1 Ar : CH_4 in the membrane detector at 400 cm. Hg of 9 : 1 Ar : CH_4 is 72%. At 760 cm. Hg, using 9 : 1 Ar : CH_4, the counting efficiency is measured at 74%. In the counting setup, the lines and the counter are at the same pressure. Thus, efficiency can be applied directly to the counting data to give the disintegration rate of argon-37 per cm.^{3} in the counter of 1.14-liter volume. The major error is the exact disintegration rate of the "standard." This error is estimated at less than 10%.

Figure 16 shows the variation of operating "plateau" voltage with gas pressure, extrapolated to high pressure. Using the present 10-kv. power supply, it should be possible to count at pressures as high as 22 atm. The figure also shows the expected variation in background with pressure within the argon-37 "window." The curve is extrapolated at high pressure and thus is subject to uncertainty. Such effects as gas impurities, spurious pulses, high voltage breakdown might invalidate the extrapolation and need to be measured. It is not yet known if the background increase with pressure is significantly different at 10–20 atm. than at 1–10 atm. However, extensive measurements from 1–10 atm., using various gas mixtures and window settings, indicate that the extrapolated curve is realistic.

Using the window width of approximately 1–8 k.e.v., the background was found to be 1.81 ± 0.05 c.p.m. at 10 atm. total pressure. Since the counter volume is 1.14 liters, 10 liters of argon can be counted at 10 atm. Previous measurements of background give variations of not more than ±0.05 c.p.m. for 1000-minute counting time. Thus, it should be possible to measure 0.1 d.p.m. ^{37}Ar per 10 liters argon within 95% confidence limits and a counting time of 1000 minutes. This is equivalent to a sensitivity of 0.1 d.p.m./meter^3 air. Since the counter has been pressure checked at 20 atm., it should be possible to count 20 liters of argon with the existing equipment. This would double the sensitivity or be equivalent to 0.05 d.p.m./meter^3 air for a 1000-minute counting time.

For higher pressure operation of the counter, extensive calibration and background studies must be made.

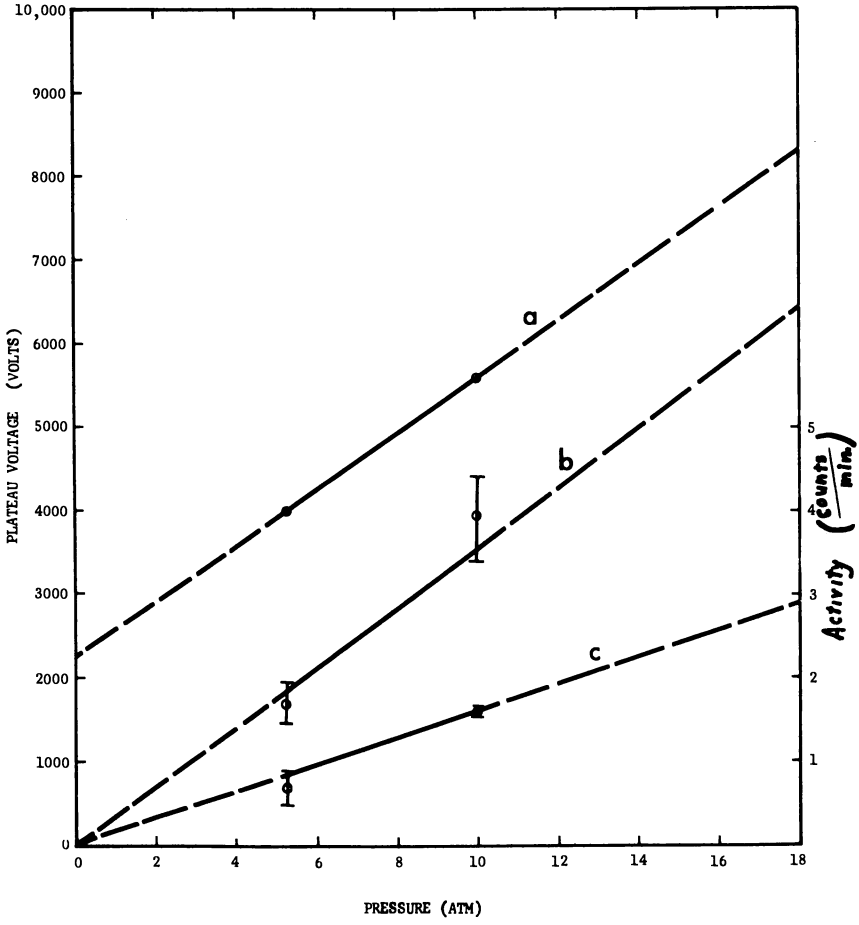

Figure 16. Variation of plateau voltage and background with pressure

(a): Plateau voltage
(b): Background in tritium window
(c): Background in argon-37 window

Preliminary results from measurements of an argon sample collected at Oakland, Calif., Dec. 12, 1967, indicate that the atmospheric argon-37 concentration is approximately 40 times the estimated cosmic particle-produced level. The sample was measured during three months, and the decay followed the argon-37 half-life. This value is preliminary and must be verified by additional sample analysis. Owing to weapons testing,

nuclear reactors, and the nuclear industry near Oakland, Calif., the present radioactive argon concentration in the local atmosphere could be significantly higher than the cosmic particle-produced level.

Lal (*13*) gives the specific activity of argon-37 in the atmosphere produced by cosmic particle reactions as 0.19 d.p.m./kg. air in the stratosphere and 2.1×10^{-2} d.p.m./kg. air in the troposphere. The radioactivity expected in a 10-liter sample of purified argon from the troposphere would be 3.98×10^{-2} d.p.m. It should be possible to measure less than twice this radioactivity level using this detector.

Loosli *et al.* (*14*) are attempting to measure cosmic particle-produced argon-39. Their detector is a matrix array detector, similar to the one constructed by Drever *et al.* (*5*), and is designed to limit the loss of primary electrons by formation of negative ions. It should also be possible to measure cosmic particle-produced argon-39 with the membrane detector at high pressures since the measured cosmic particle-produced activity is 0.12 d.p.m./liter argon, Loosli and Oeschger (*15*). Argon-39 could be a valuable tracer in ocean mixing studies owing to its 269-year half-life.

Conclusions

The counting properties of a membrane proportional counter similar to the one designed by Oeschger have been detailed. The system is reliable for measuring low levels of radioactivity in gas samples at high pressures. No barometric fluctuations in the background have been observed during the six years of continuous use. The detector is simple to construct and maintain.

Properties of the detector for reducing background radiation were measured. Part of the background arises from x-rays of aluminum caused by external radiation exciting the atoms, resulting in the characteristic x-rays. The background in the tritium window was reduced 36% by 2 inches of paraffin and a thin sheet of cadmium. The detector is valuable for measuring cosmic particle-produced levels of carbon-14, tritium, and radioactive argon. Carbon-14 samples can be measured using the equipment at ages of about 60,000 years. Tritium radioactivity has been measured at levels of 2 TU. The hydrogen is prepared contamination free and measured in the counter with a 3 : 1 $H_2 : CH_4$ counting gas mixture.

Atmospheric argon-37 has been measured in the counter at a concentration of about 40 times the estimated cosmic particle concentration. The minimum detectable limit for measuring argon at 10 atm. for a 1000-minute counting is 0.1 d.p.m./meter^3 air, or about two times the cosmic particle-produced concentration in the troposphere. It should be possible to measure cosmic particle produced argon in the stratosphere.

Acknowledgments

I express my appreciation to A. W. Fairhall and the University of Washington, Department of Chemistry, where the first detector was designed and tested; to Robert Breedlove, who assisted in constructing and setting up the gas handling and electronic equipment; to David Castagnola, who assisted in testing the equipment, analyzing samples, and reducing data; and to R. Charnell, who reviewed the paper.

Literature Cited

(1) Anand, J. S., Lal, D., *Nature* **201**, 775, 4921 (1964).
(2) Cameron, J. F., "Radioactive Dating and Methods of Low-Level Counting," STI/PUB/152, IAEA, Vienna, 1967.
(3) Charalambus, St., Goebel, K., *Nucl. Inst. Methods* **25**, 109 (1963).
(4) Curran, S. C., "Metrology of Radionuclides," STI/PUB/6, Vienna, 1959.
(5) Drever, R. W. P., Moljk, A., Curran, S. C., *Nucl. Inst.* 1, 41 (1957).
(6) Geyh, M. A., "Radioactive Dating and Methods of Low-Level Counting," STI/PUB/152, IAEA, Vienna, 1967.
(7) Fairhall, A. W., Schell, W. R., *Radiocarbon* **5**, 80 (1963).
(8) Fairhall, A. W., Schell, W. R., Young, J., *Radiocarbon* **8**, 489 (1966).
(9) Fairhall, A. W., Schell, W. R., Takashima, Y., *Rev. Sci. Instr.* **32**, 3, 323 (1961).
(10) Fairhall, A. W., personal communication.
(11) Haskell, E. E., Sr., Leventhal, S. S., Bianchi, W. C., *J. Geophy. Res.* **71**, 3849 (1966).
(12) Houtermans, F. G., Oeschger, H., *Helv. Phys. Acta* **31**, 117 (1958).
(13) Lal, D., "Earth Science and Meteoritics," pp. 115-142, North Holland Publishing Co., Amsterdam, 1963.
(14) Loosli, H. H., Oeschger, H., Wahlen, M., "Radioactive Dating and Methods of Low-Level Counting," STI/PUB/152, IAEA, Vienna, 1967.
(15) Loosli, H. H., Oeschger, H., *Earth Sci. Planetary Sci. Letters* **5**, 191 (1968).
(16) Moljk, A., Drever, R. W. P., Curran, S. C., *Proc. Roy. Soc. (London)* **239A**, 433 (1957).
(17) Oeschger, H., "Radioactive Dating," STI/PUB/68, IAEA, Vienna, 1962.
(18) Schell, W. R., Ph.D. Thesis, University of Washington (1963).

RECEIVED July 29, 1968. Work performed at Isotopes, Inc., Palo Alto Laboratory, Palo Alto, Calif. and sponsored by A.R.P.A. Contract No. DA-49-146-XZ-517.

12

A Ge(Li) Gamma-Ray Spectrometer of High Sensitivity and Resolution for Biological and Environmental Counting

PAUL L. PHELPS, KEITH O. HAMBY, BERNARD SHORE, and GILBERT D. POTTER

Bio-Medical Division and Electronic Engineering Department, Lawrence Radiation Laboratory, University of California, Livermore, Calif. 94550

*A high resolution, anticoincidence-shielded, gamma-ray spectrometer has been developed to analyze complex, low level mixtures of gamma-emitting radionuclides in environmental and biological samples. The primary detector is a planar, lithium-drifted, germanium diode contained within a plastic annulus (76 cm. × 76 cm.). This configuration was found to reduce significantly the Compton background with a resultant improvement in detection of weak spectral lines. The sensitivity permits the detection of radionuclides in environmental samples at levels below 0.05 pCi/gram—*e.g., *10 pCi of ^{137}Cs can be detected easily in 2 liters of cows' milk. Examples are presented of the spectral analysis of radionuclides in various biological and environmental samples contaminated with worldwide fallout, with debris from nuclear cratering experiments, or with reactor effluent.*

Radionuclides are a major concern of our nuclear age, whether they arise from peaceful events such as Plowshare excavations and reactor releases or from military events such as nuclear weapons tests. In each of these events different kinds and amounts of radionuclides can be produced. After they are produced, the radionuclides are transported from the site of the event by various chemical and physical processes; they can enter into the food chains leading to man and can become localized in his tissues.

One of the major objectives of the Bio-Medical Division is to determine the impact upon the biosphere, particularly upon man, of the

release of radiation and radionuclides from nuclear events. For most of these events it may be not the total radioactivity released but rather the kind and amount of specific significant radionuclides released that are important. In general, it is essential that the different kinds of nuclear events be characterized, in terms of the quantitative documentation of the life histories of the radionuclides that are produced, so that their biological significance can be evaluated in a meaningful way.

In the past, environmental and biological samples containing radioactive debris were assayed for gamma-emitting radionuclides by techniques involving radiochemical separation followed by spectrometry with sodium iodide [NaI(Tl)] scintillators. These techniques are frequently so laborious and time consuming as to discourage experimenters from undertaking the extensive samplings needed in some experiments. This is especially true in biological and environmental programs. There is no doubt that the introduction of solid-state lithium-drifted germanium [Ge(Li)] detectors has revolutionized gamma-ray spectroscopy, primarily because of the great increase in spectral resolution with Ge(Li) detectors compared with that of sodium iodide. This advantage is illustrated by a complex gamma-ray spectrum (Figure 1) from particulate fallout, presumably from a Chinese test, collected on filter paper. A 30- to 40-fold improvement in resolution has not been uncommon. In addition, data reduction can be simplified because the complicated spectrum-stripping required with NaI(Tl) scintillators can be bypassed.

This report describes an anticoincidence-shielded gamma-ray spectrometer developed for assaying complex low level mixtures of gamma-emitting radionuclides in large volume environmental and biological samples. It has given excellent resolution and at the same time has been highly efficient in assaying large volume as well as small samples. These results are attributed to four special features of the spectrometer:

(1) The incorporation of a planar Ge(Li) detector of large surface area (6 cm. × 3 cm.) and 1 cm. depletion depth, developed especially for the spectrometer by our laboratory (*1*).

(2) The Ge(Li) detector is surrounded by a plastic phosphor shield, and the two are operated in anticoincidence, reducing the Compton continuum and increasing the sensitivity for detection of noncoincident photons.

(3) Inside the vacuum chamber a cooled first-stage field-effect-transistor (FET) preamplifier adjacent to the Ge(Li) detector ensures maximum resolution.

(4) The anticoincidence and coincidence spectra are recorded separately in order to realize the increased sensitivity for noncoincident events without loss of sesitivity for truly coincident events.

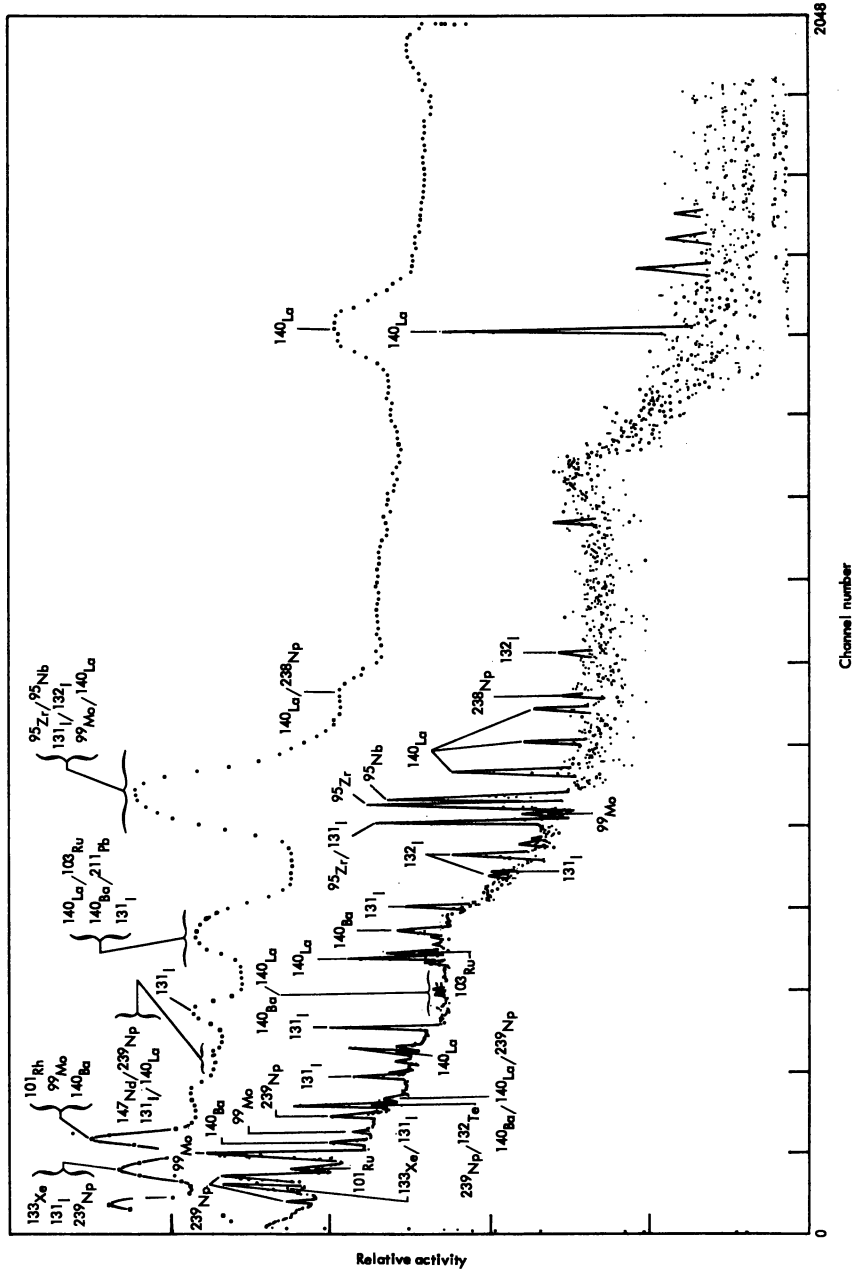

Figure 1. Two spectra from the same air-filter sample (presumed Chinese test, Jan. 16, 1968). Upper spectrum obtained with a 4 × 4 inch NaI(Tl) scintillator system. Lower spectrum obtained with our 8-cm.³ planar Ge(Li) detector

Spectrometer Design

For the spectrometer to be suitable for the radionuclide assay of large biological and environmental samples it must be capable of isolating the photopeaks typical of complex mixtures of fission products and induced activities. To achieve this goal, several important design characteristics had to be met. These included: (1) a resolution better than 3 k.e.v. (FWHM) at 1.33 M.e.v. which permits separation of most (but certainly not all) of the photopeaks in typical complex gamma spectra; (2) a dynamic range of from 50 k.e.v. to 2.0 M.e.v., which covers most photopeaks of biological interest; (3) a surface area of between 15 and 20 cm.^{2} to give as high an absolute detection efficiency as is commensurate with the art of diode manufacture; (4) the accommodation of large (200 ml.) samples, and (5) the reduction of the Compton continuum to maximize the effective sensitivity. The gamma-ray spectrometer is shown in Figures 2 and 3.

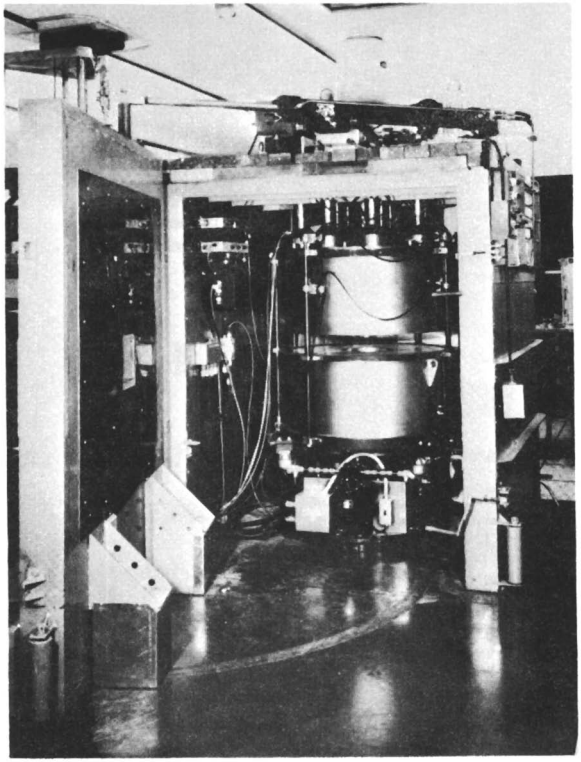

Figure 2. The anticoincidence-shielded, high resolution, Ge(Li) gamma-ray spectrometer. The annulus is in position for inserting a large environmental sample

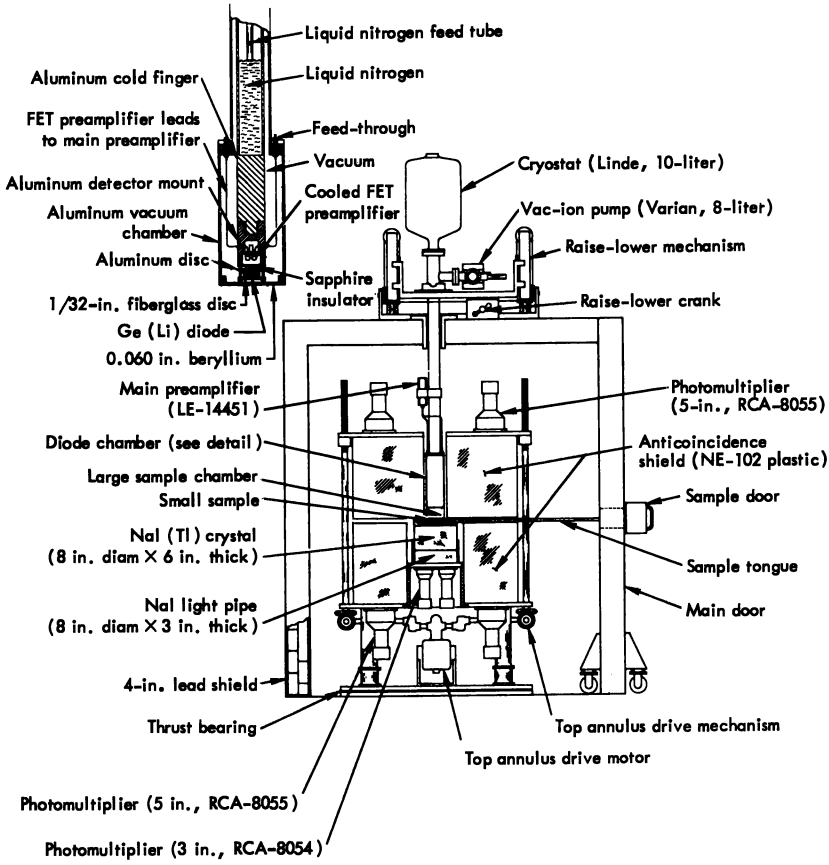

Figure 3. Schematic of the gamma-ray spectrometer shown in Figure 2. Details of the Ge(Li) chamber and cooled FET preamplifier are given in the upper left corner

Lithium-Drifted Germanium Detectors. Two kinds of planar Ge(Li) diodes were fabricated in our Laboratory for the spectrometer (*1*). The chief consideration was maximum cross section with a resolution of less than 3 k.e.v. at ^{60}Co FWHM (full width half maximum). The available single-crystal germanium material dictated the shape of the detector. The first detector was fabricated from a 15-cm. long Sylvania ingot with a trapezoidal cross section; its finished dimensions were 6 cm. × 3 cm. × 1 cm. Our second detector was fabricated from circular Hoboken stock (NPC Metal and Chemical Co., Los Angeles); its finished dimensions were 2.8 cm. diameter × 1.2 cm. thick.

Cryogenics. At room temperature, thermal excitation of charge carriers within the Ge(Li) detector produces unacceptable levels of electrical noise in the external counting circuits. To overcome this effect it

is necessary to operate the detector at cryogenic temperatures, usually near that of liquid nitrogen. Another factor requiring low temperature operation is the instability of the lithium drifted within the germanium crystalline structure to form the "intrinsic" region.

In the cryogenic system developed for the spectrometer (*see* Figure 3), the Ge(Li) detector is mounted at the end of an aluminum rod 70 cm. long (commonly referred to as a "cold finger"). Aluminum provides good thermal conduction and because of its relatively low atomic number produces less backscatter than copper [Recently, however, Cooper (*2*) has reported success with electrolytic-quality magnesium replacing the aluminum.] It is desirable that low-background aluminum be used.

The cold finger is hollow except for the last 10 cm., which are solid. Thermal insulation is provided by a vacuum chamber. After initial rough pumping, operating pressures between 10^{-7} and 10^{-8} mm. of mercury are maintained by an 8-liter Varian ion pump. The vacuum is not only necessary for thermal insulation but also is required to minimize contamination of the surfaces of the Ge(Li) detector.

Anticoincidence Shielding. The preferred gamma-ray interaction in the Ge(Li) detector is one in which the total energy of a gamma-ray is absorbed by an electron of a germanium atom. The electrical charge generated as the electron moves through the crystalline structure represents the actual energy of the absorbed gamma-ray. However, total absorption or photoelectric interaction competes with the Compton effect and with pair production. Most of the counting we do is below the energy at which pair production becomes a problem, but at 150 k.e.v. the probability of the photoelectric interaction relative to Compton absorption is 1:1, and at 1 M.e.v. the probability is 1:100 in favor of the Compton interaction. A Compton event deposits only part of its energy in the detector, and this appears as a continuum below the original photon energy. In time, the Compton scattering produces a continuum of increasing amplitude with a maximum at the low energy end of the spectrum. This continuum reduces the ratio of photopeak to background, making it difficult to detect weak photopeaks as well as reducing the accuracy of determining the actual number of counts within the photopeak.

To reduce interference from Compton scattering, an anticoincidence shield, 76 cm. × 76 cm., was constructed as shown in Figures 2 and 3. The shield consists of two independent type NE-102 plastic phosphor annuli. A 10-cm. bore through the top annulus accommodates the Ge(Li) detector chamber and the cryogenic assembly. The bottom annulus (i.d. diameter 25 cm.) houses a 20-cm. diameter by 15-cm. thick NaI(Tl) scintillator. Normally, the plastic phosphor is used in conjunction with the NaI(Tl) to form a "well"-shaped anticoincidence shield. Alterna-

tively, the Ge(Li) detector may be operated in coincidence with the NaI(Tl), with both detectors in anticoincidence with the plastic phosphor.

A drive mechanism raises the annulus for inserting the sample. Most samples are accommodated in a position just above the midline of the anticoincidence shield. The Ge(Li) detector is just above the sample; a raise-lower mechanism provides approximately a 10-cm. vertical range in its position. The counting of small planchets does not require separation of the annuli; a long plastic tongue may be used to insert the sample through a small door in the shield.

Twelve RCA type-8055 photomultipliers are attached to the surface of the top annulus. The bottom annulus, which has the larger bore, has 8 photomultipliers of the same kind. A NaI light pipe 7.5 cm. thick couples four RCA type-8054 photomultipliers to the NaI(Tl) scintillator.

The outer container for the plastic phosphor and the NaI(Tl) is stainless steel. Aluminum sheet, 0.25 mm. thick, is used on the conjoining surfaces of the two annuli and on the inside walls. Shielding from external radiation is provided by a lead shield 10 cm. thick.

Ge(Li) Detector Characteristics. Resolution measurements for the 18-cm.[3] Ge(Li) detector were made with the anticoincidence shield in the inoperative mode, with a normal operating bias of 1700 volts, and with a preamplifier designed in our Laboratory (*3, 4*), and operated in conjunction with a Tennelec TC-200 linear amplifier. Resolution at 1.33 M.e.v. was 2.62 k.e.v., FWHM (Figure 4). The electronic pulser resolution for the amplifier system at a slightly lower energy was 1.86 k.e.v., the total capacitance of the detector was 28 pF, the noise slope was 0.035 k.e.v./pF, and the leakage current at 1700 volts was 0.5×10^{-9} amp.

Mounting of the Detector. The Ge(Li) detector was clamped between a thin fiberglass disc (on the n^+ layer side) and an aluminum disc (on the p^- layer side), with indium foil on both sides to ensure good electrical contact. Nylon screws secured the detector to the aluminum FET preamplifier housing and cold finger. Heat transfer to the detector from the aluminum was through a block of sapphire that simultaneously provided a good thermal path and electrical insulation. A spacing of 3 mm. was maintained between the beryllium radiation entrance window and the detector to allow adequate dielectric for the 1700-volt bias required in detector operation. Thermocouple measurements showed the operating detector temperature to be approximately −194°C. Experimental results indicate that the detector mount (Figure 3) allowed a minimum of acoustical noise coupling between the bubbling liquid nitrogen and the detector.

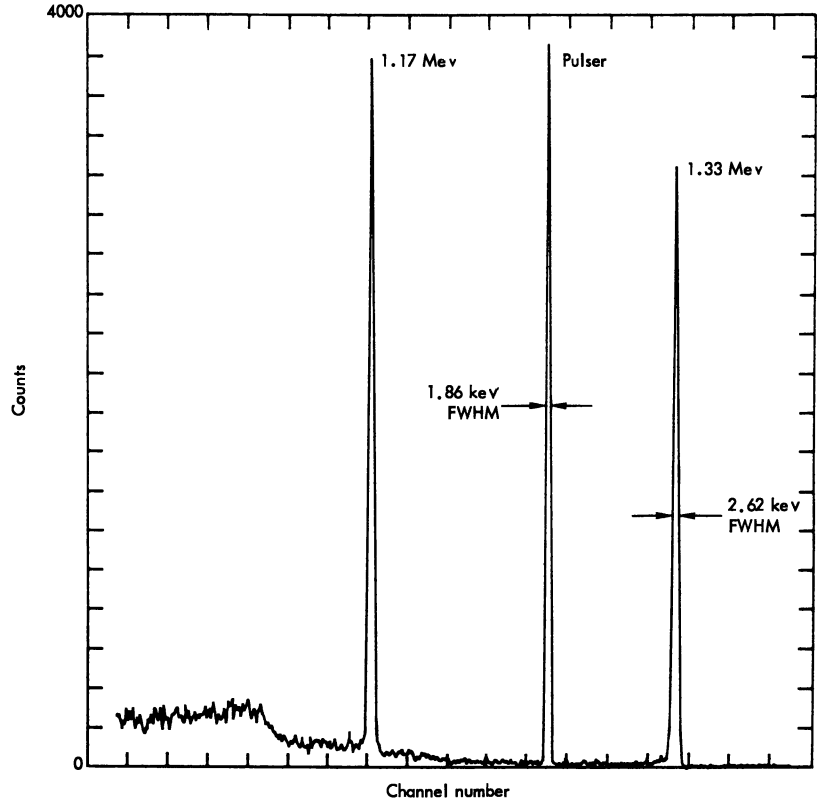

Figure 4. Spectral resolution of the 18-cm.³ planar Ge(Li) detector for ^{60}Co

Spectrometer Characteristics

Background Reduction. Two sources of radiation are the major cause of trouble in gamma-ray spectroscopy. The first is the gamma-rays emitted by radioactive contaminants contained in the shielding lead or in iron, aluminum, and stainless steel used in the detector housing and cryogenics system. The second source is the Compton radiation mentioned above.

Photopeaks observed in the background include the more prominent x-rays and gamma-rays of the natural uranium and thorium decay series and the natural ^{40}K. As reported by Cooper *et al.* (5), background peak heights are relatively unaffected by suppression, but the reduction in the background continuum is significant. For our 8-cm.³ Ge(Li) detector, the background at 150 k.e.v. was reduced from 0.1 to 0.02 counts/min./k.e.v., and that at 1.5 M.e.v. was reduced from 0.0013 to 0.0005 counts/min./k.e.v.

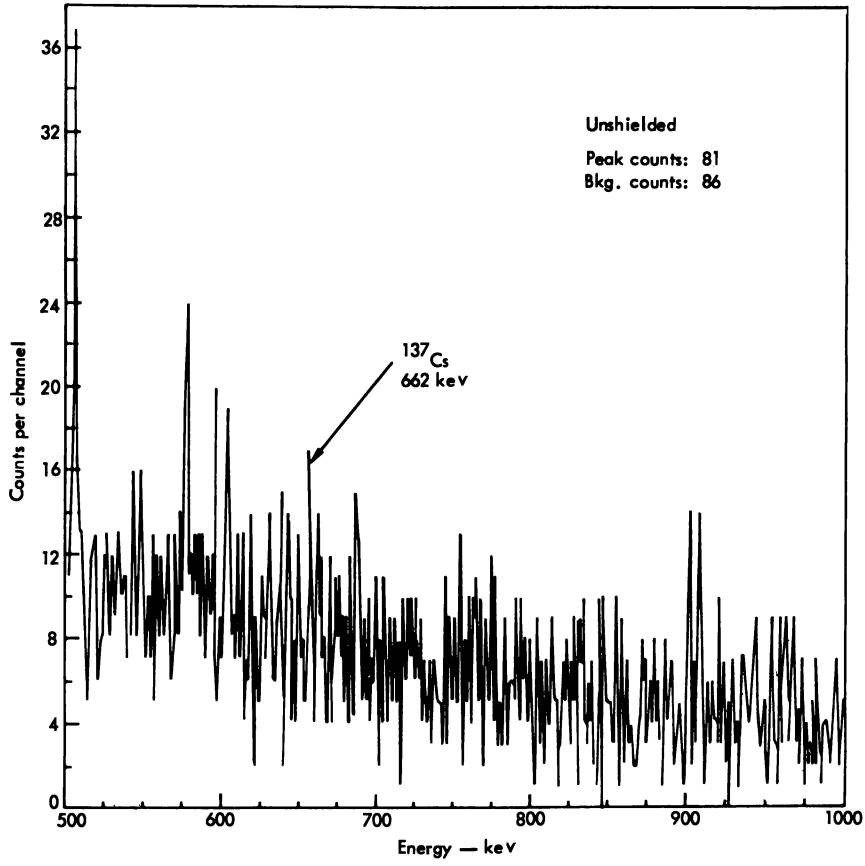

Figure 5. Spectra from 10 pCi of ^{137}Cs

Left: without anticoincidence shielding. Right: with shielding. The presence ing. The sample was counted in 200 ml. of water in each

Sensitivity. The spectra in Figures 5 and 6 illustrate the increased sensitivity of detection of a ^{137}Cs sample counted with an anticoincidence shield compared with the same sample counted with the shield removed. Both sets of data were obtained with the smaller (8-cm.^{3}) Ge(Li) detector. Without the shield in place, it was impossible to ascertain the presence of the 10-pCi ^{137}Cs photopeak. The peak height at the 100-pCi level is approximately the same with and without background suppression. Suppression, however, reduces the Compton continuum on either side of the peak by a factor of 6 at this activity level. This is illustrated in both Figures 5 and 6, where the background-suppressed ^{137}Cs photopeaks are clearly resolved and unequivocal. In all cases counting time was approximately 1000 minutes.

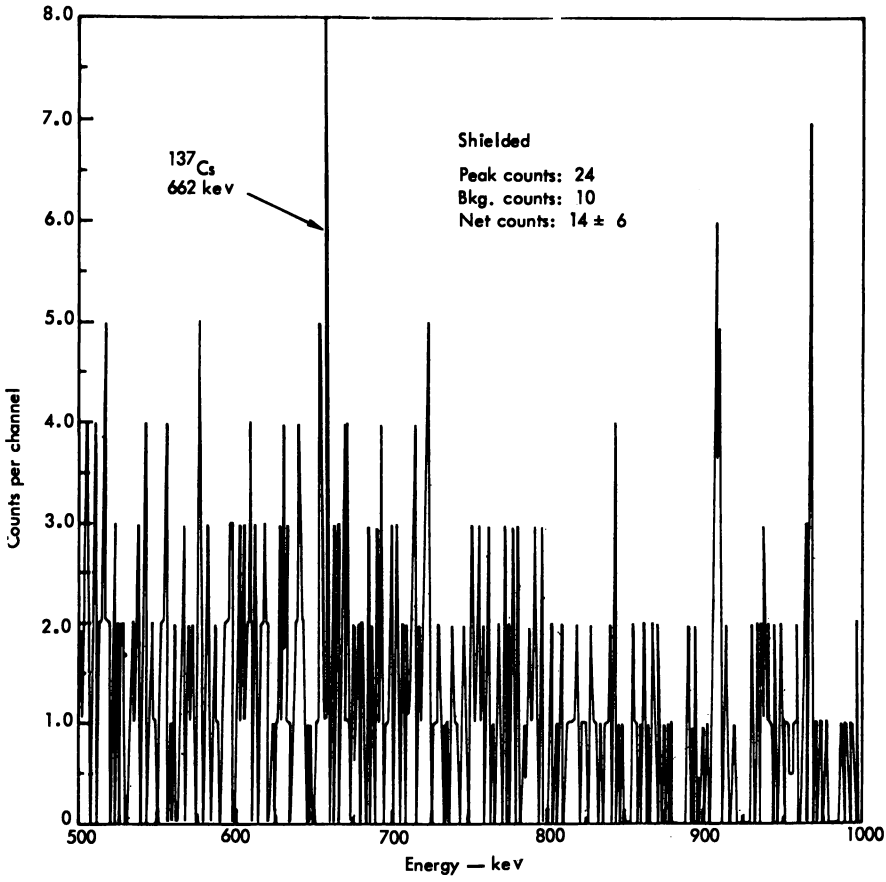

obtained with the 8-cm.³ Ge(Li) detector.

of ¹³⁷Cs cannot be verified statistically in the spectrum obtained without shield-case. Counting time was approximately 1000 minutes

Sensitivity was also tested with a canned sample containing 100 pCi ^{137}Cs plus 0.5 μCi ^{60}Co in 200 grams water. This represents an activity ratio of 0.5×10^4 between ^{137}Cs and ^{60}Co, which would correspond to a typical extreme in activities in our environmental samples. The ^{137}Cs photopeak falls in the left trail of the Compton continuum from the ^{60}Co (Figure 7); this spectrum was generated by the 18-cm.³ Ge(Li) detector with the anticoincidence shield in place. Without anticoincidence the ^{137}Cs peak is virtually lost in the Compton continuum.

The same samples were counted on the NaI(Tl) spectrometer shown in Figure 8. It was not possible to detect the 10 pCi of ^{137}Cs in 200 cm.³ of water nor 100 pCi mixed with 0.5 μCi of ^{60}Co in 200 cm.³ of water.

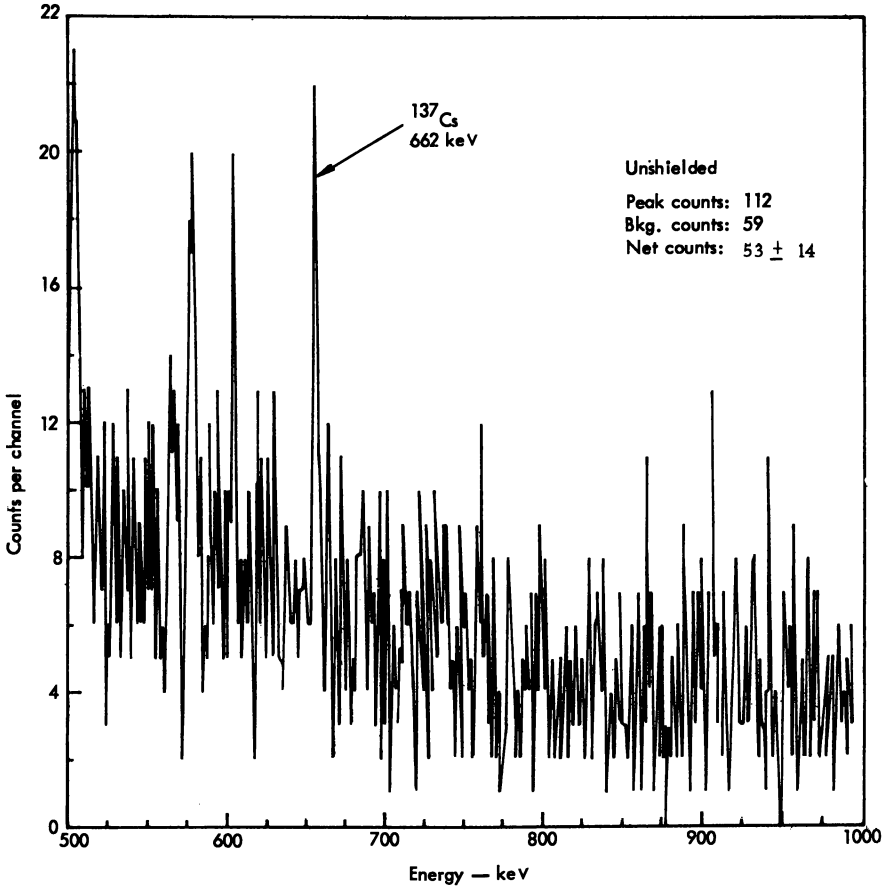

Figure 6. Spectra from 100 pCi of ^{137}Cs

Left: without anticoincidence shielding. Right: with shielding. Note the each case. Counting time was

Large Surface-Area Detectors. The advantage of large surface-area Ge(Li) detectors becomes quite apparent when large biological samples are counted. A 10-pCi, 200-gram ^{137}Cs source was counted first with an 8-cm.^{3} and then with an 18-cm.^{3} planar Ge(Li) detector, with the anticoincidence shield in place in each case. Figure 9 compares the ^{137}Cs photopeaks from the two detectors. The net counts were 14 ± a standard deviation of 6 for the smaller detector, and 51 ± a standard deviation of 10 for the larger 18-cm.^{3} Ge(Li) detector. The lower limit of sensitivity would be between 2 and 10 pCi for the 200-gram sample using the 18-cm.^{3} detector with the aluminum-can geometry; this corresponds to a minimum of 0.01 pCi/gram or 0.01 count/min.

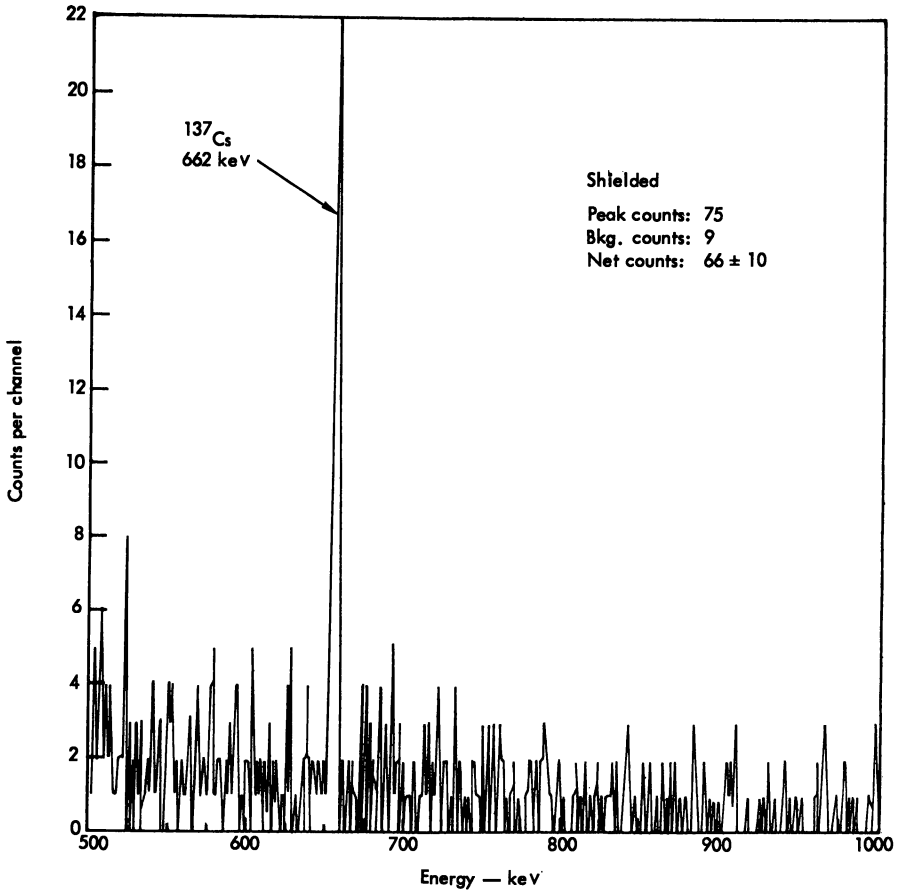

obtained with the 8-cm.³ Ge(Li) detector.

difference in background. The sample was counted in 200 ml. of water in approximately 1000 minutes

Statistical Accuracy. Galloway has dealt with the change in statistical accuracy expected from the application of background suppression (*6*). He expressed this change as a function of the change in counting efficiency, the unsuppressed peak-to-background ratio, and the change in the peak-to-background ratio with suppression. This factor (A/A′) is 1.20 for the 100-pCi ^{137}Cs sample and 1.01 for the 1000-pCi ^{137}Cs samples on the 8-cm.³ diode. An improvement in accuracy corresponds to A/A′ greater than 1.0. For the 1-μCi ^{137}Cs sample, A/A′ is 0.92; this indicates that for high activity samples, where the initial peak-to-background ratio is high and there is a significant decrease in efficiency owing to accidental coincidence in the shield, background suppression may result in decreased statistical accuracy.

Efficiency. Counting efficiencies (ratio of observed counts/min. to disintegrations/min.) over a range of gamma energies for the aluminum can and the 8-cm.^{3} Ge(Li) detector are given in Figure 10. The isotope standards were prepared with Cab-O-Sil and water very much as the biological samples are prepared. A spacing of 9-mm. including a 1.25-mm. thick beryllium radiation window is maintained between the Ge(Li) detector and the aluminum can.

The difference in efficiency between the large planar 18-cm.^{3} Ge(Li) detector and the small round 8-cm.^{3} Ge(Li) detector depends essentially on their cross-sections since they have approximately the same depletion depths. This is apparent in comparing the peaks from 10 pCi of ^{137}Cs generated by the large and small detectors (Figure 9). The geometry of the aluminum can was determined to be less efficient by approximately a factor of 10 than a disc-mounted point source.

With the shield in place and operating, the counting rate in the shield tends to affect the efficiency of photon detection in the anti-

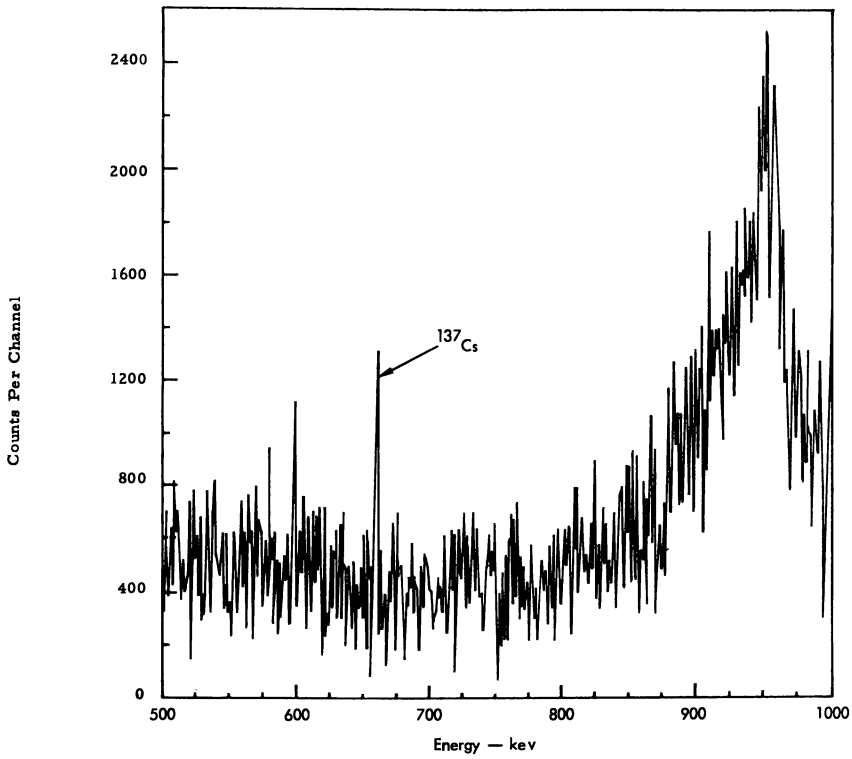

Figure 7. Spectrum from 100 pCi of ^{137}Cs mixed with 0.5 μCi of ^{60}Co in 200 ml. of water. The spectrometer was an 18-cm.^{3} Ge(Li) detector with anticoincidence shielding

coincidence mode. With samples of higher activity the counting rate in the shield increases, and the probability increases that an accidental coincidence will route a detector pulse into the wrong spectrum. Figure 11 shows (for a range of ^{137}Cs activities) the change in the ratio of anticoincidence counts to total counts as a function of activity for a truly noncoincident photon. Certainly at high counting rates of noncoincident photons the accidental events must be taken into account, but Figure 11 shows that the loss at 0.1 μCi of ^{137}Cs with the aluminum can geometry is only 1:5%. For the 100% coincident gamma-rays of ^{60}Co, the ratio of anticoincident to coincident photons is relatively constant over a wide range of activity levels. About 20% of all full-energy ^{60}Co detector pulses are not in coincidence with a shield pulse, indicating an over-all shield efficiency for ^{60}Co of about 80%.

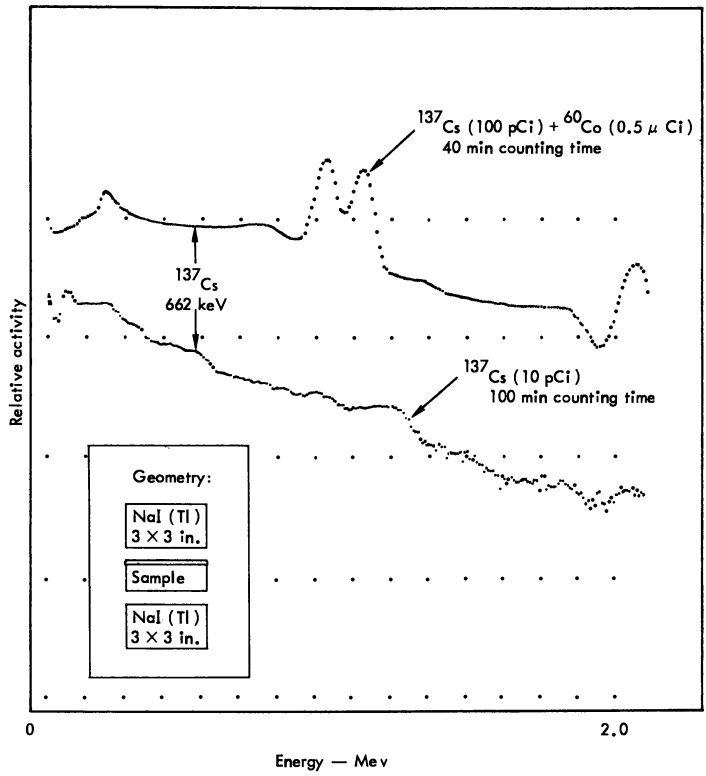

Figure 8. Spectra obtained with two 3 × 3 inch NaI(Tl) crystals. Lower: an attempt to measure 10 pCi of ^{137}Cs in 200 ml. of water. Upper: an attempt to measure 100 pCi of ^{137}Cs in the presence of 0.5 μCi of ^{60}Co. Compare these two spectra with those of Figures 5 and 7

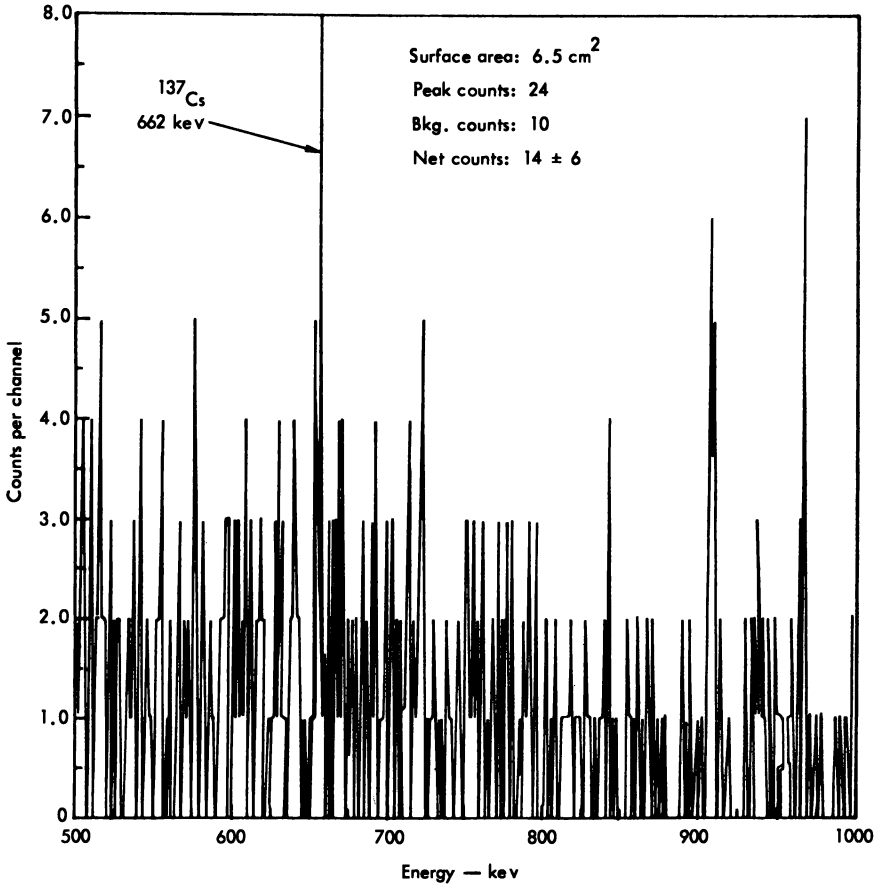

Figure 9. Detector efficiency at the ^{137}Cs energy for Ge(Li) detectors of proximately the same. The sample, 10 pCi ^{137}Cs in

Although the source full energy peak efficiency [after Crouthamel (7)] of NaI(Tl) scintillators is higher than that of Ge(Li) detectors (8), owing to the much larger volumes possible with NaI(Tl), the incident full energy peak efficiency (per unit volume) (7) of Ge(Li) was found to be higher than that of NaI(Tl).

Efficiency can be improved by operating Ge(Li) detectors in parallel. A technique worked out by Saunders and Maxwell (9) of this Laboratory resulted in a Ge(Li) detector system (four individual detectors connected in parallel) having an effective surface area of 30 cm.^{2} with a resolution at 1.33 M.e.v. of 2.91 k.e.v.

Resolution. System resolution for the 18-cm.^{3} Ge(Li) detector was evaluated at a bias voltage of 1700 volts. Leakage current was 0.5×10^{-9}

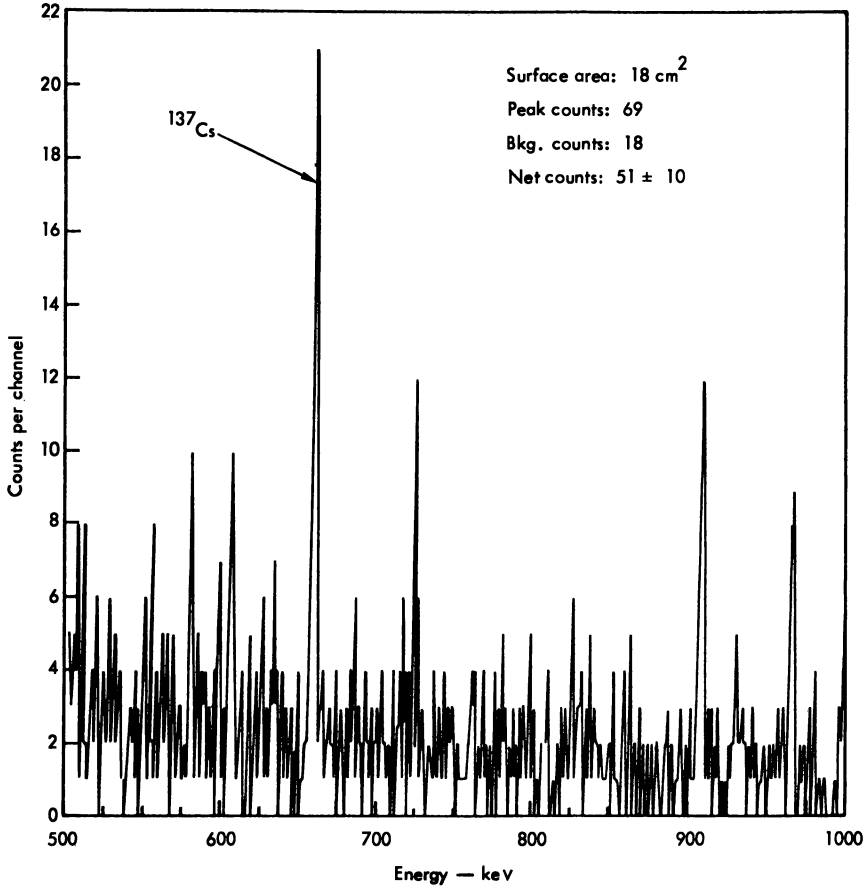

6.5-cm.^{3} (left) and 18-cm.^{3} (right) surface area. Depletion depths were ap-200 ml. water was counted for 1000 minutes in each case

amp. The electronic system was as shown in Figure 12, except that the linear amplifier was a Tennelec TC-200 with integration and differentiation times set to 1.6 μsec. Resolution measurements were made both with a ^{60}Co source and with an electronic pulser (Figure 4). For the ^{60}Co 1.33-M.e.v. peak, the resolution was 2.62 k.e.v. at FWHM. At a slightly lower energy, an electronic pulse injected into the first stage of preamplification (cooled FET preamplifier) gave an energy resolution of 1.86 k.e.v. at FWHM. The 8-cm.^{3} Ge(Li) detector gave a slightly better result for the same peak.

Instrumentation. The over-all counting system is diagrammed in Figure 12. Maximum energy resolution was achieved by installing an internally cooled FET preamplifier adjacent to the Ge(Li) detector.

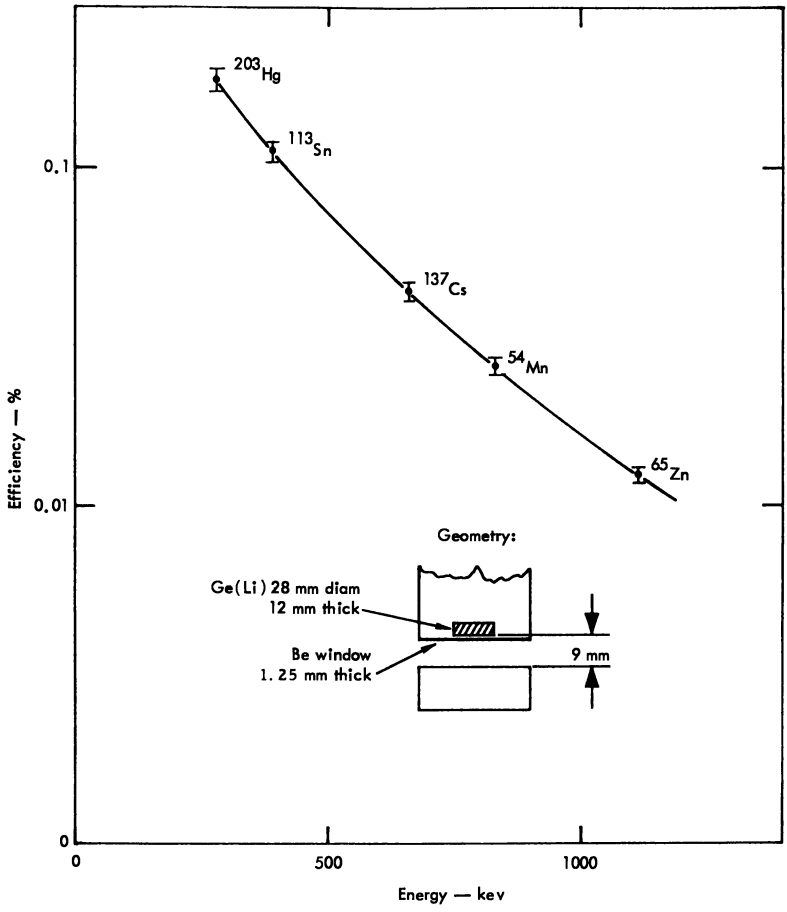

Figure 10. Detector efficiency as a function of gamma-ray energy for an 8-cm.³ (Ge(Li)) detector (samples in aluminum cans). The efficiency of the 18-cm.³ detector increases in proportion to the surface area

The electrical connection between detector and transistor was approximately 3 cm., the short lead distance is important in reducing stray electrical capacitance and microphonic noise owing to mechanical vibration. The circuit is a modified version of that of Bradley (3), with transistor types 2N4861 or 2N3823.

The optimum operating temperature for minimum noise from the FET was found to be slightly higher than the operating temperature of the Ge(Li) detector. A thermal heater made from a 100-ohm carbon resistor was therefore installed next to the FET and operated at a current that heated the transistor to a temperature just above that of liquid nitrogen.

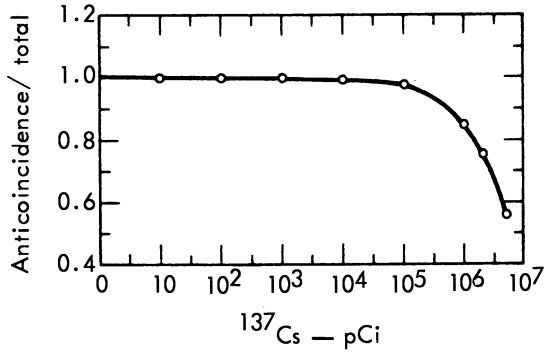

Figure 11. Ratio of anticoincidence events to the sum of events recorded in anticoincidence and coincidence as a function of activity for ^{137}Cs

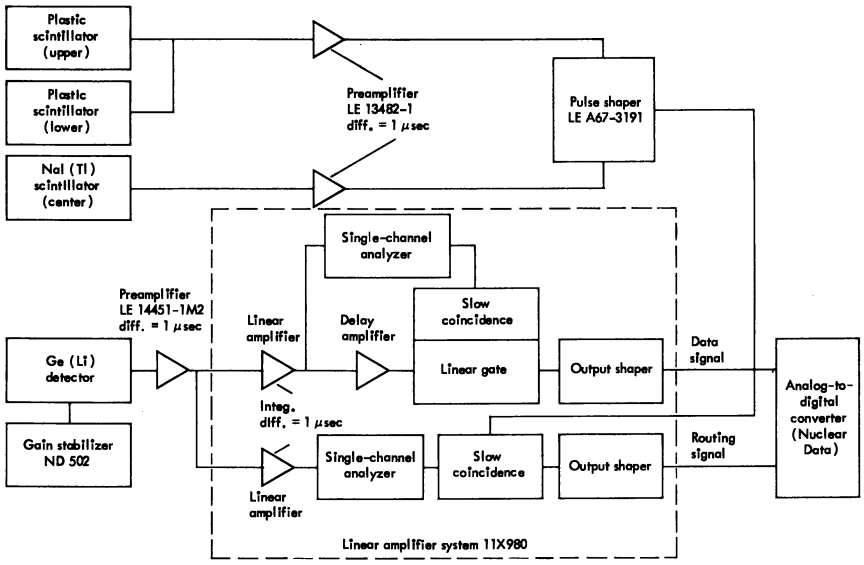

Figure 12. Schematic of the electronic system for recording simultaneously anticoincidence and coincidence events

An external charge-sensitive preamplifier (type LE 14551) also designed by A. Bradley (*3*, *4*), completes the preamplifier loop.

A linear amplifier system designed by Goulding (*10*) includes the necessary circuits for anticoincidence counting. The system is contained in a 7-inch high standard-rack mounting chassis. Pulse-shaping from

the anticoincidence shield was done by a system that incorporated adjustable threshold-detector circuits and an emitter-follower output stage.

Anticoincidence, Coincidence Recording. An inherent problem in an anticoincidence-shielded spectrometer is that a decay scheme having gamma-rays in coincidence will appear to produce the same interaction between the Ge(Li) detector and anticoincidence shield as that of a Compton event. If only the events from the Ge(Li) detector are counted in the absence of a signal from the shield, those nuclides that decay

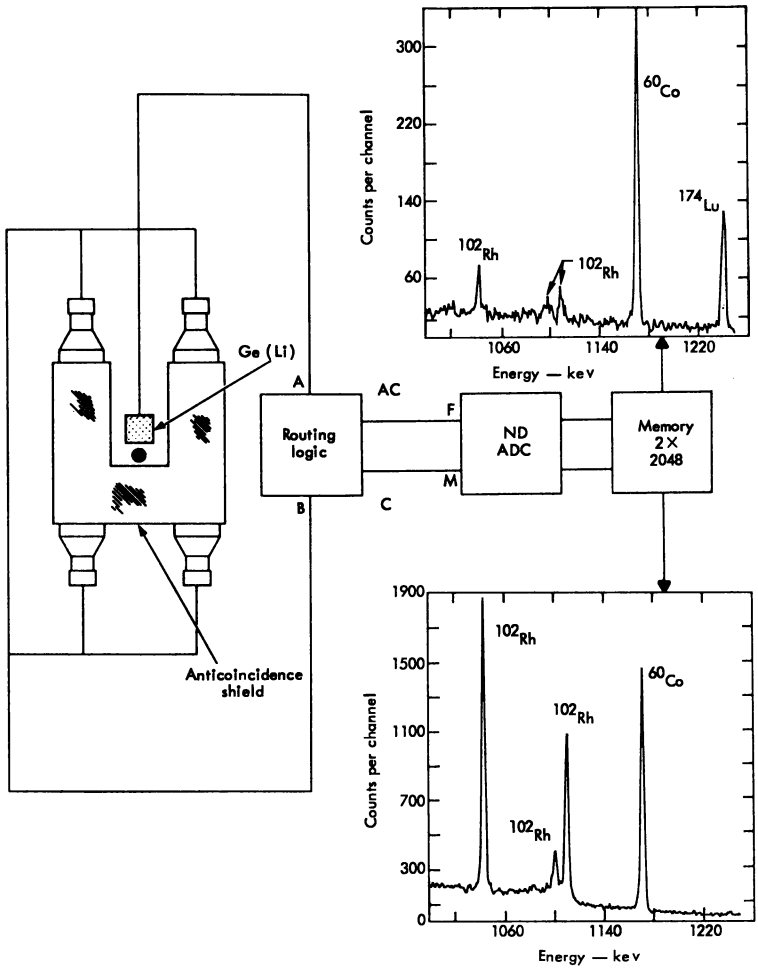

Figure 13. Method for recording simultaneously anticoincidence and coincidence events, with examples of the spectra so derived

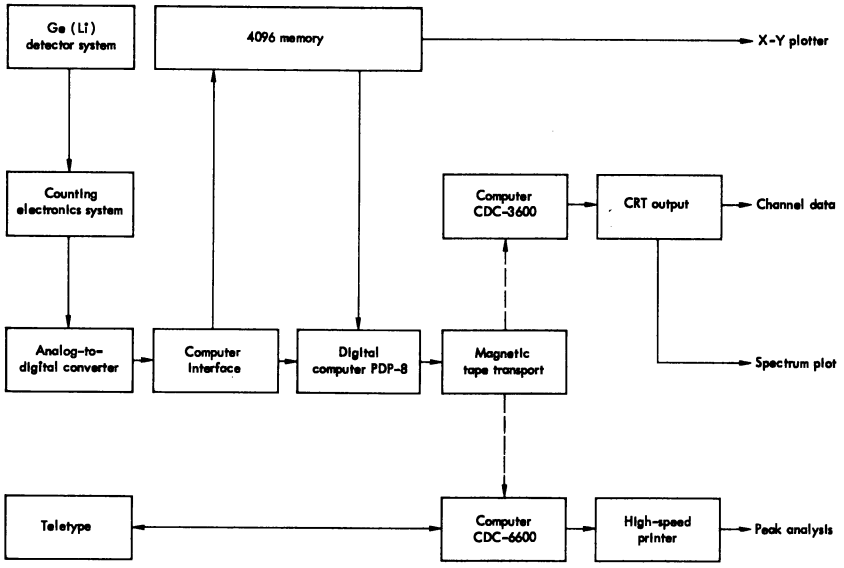

Figure 14. System for collecting and processing data from the Ge(Li) spectrometers. The data may be either stored in core memory or collected at random on magnetic tape

primarily by gamma coincidence emission will be detected inefficiently. This has been overcome by using a signal from the anticoincidence shield as a routing signal to the ND-161 pulse height analyzer. Those signals that represent total absorption in the Ge(Li) detector are collected in one side of the pulse height analyzer memory, while those events that appear simultaneously in the Ge(Li) detector and in the anticoincidence shield are routed to a different side of the memory (Figure 13).

The presence in the anticoincidence spectrum of significant amounts of fully coincident ^{60}Co photons is indicative of the detection efficiency of the shield which is approximately 80% for ^{60}Co.

Data Reduction. The spectral data can be collected on-line and stored directly on magnetic tape under control of a PDP-8 digital computer (*11*). Alternatively, they can be collected on a magnetic core memory, then transferred in bulk fashion (Figure 14). The choice of method is dictated by the length of counting required and by the method of treatment of the data (*i.e.*, simple *X-Y* plot or complete channel information).

After several spectra have been accumulated on magnetic tape, they are read by a CDC-3600 computer and obtained both as plotted and tabular output. The existence and the approximate energies of the photo-peaks of interest can be determined visually or with a CDC-3600 program.

Figure 15. First step in preparing biological samples. Shown here is the lyophilizer manifold for removing water from samples. The flasks shown are 1200 ml. in volume and contain muscle tissue

A CDC-6600 program, executed remotely [The CDC-3600 and the CDC-6600, part of the main computer complex at LRL, are located at a distance from the counting facilities] by Teletype is given, as input, the magnetic tape, a zero time, and the nominal energies of the photopeaks of interest. This program determines the precise peak energies, identifies the isotope and calculates net counts per minute and disintegrations per minute corrected for decay to zero time. This output, for all spectra on the magnetic tape, then can be printed out in any of several ways as illustrated schematically in Figure 14.

Preparation of Samples for Counting

In general, large samples of biological materials containing low levels of radionuclides (in the picocurie range) present certain problems

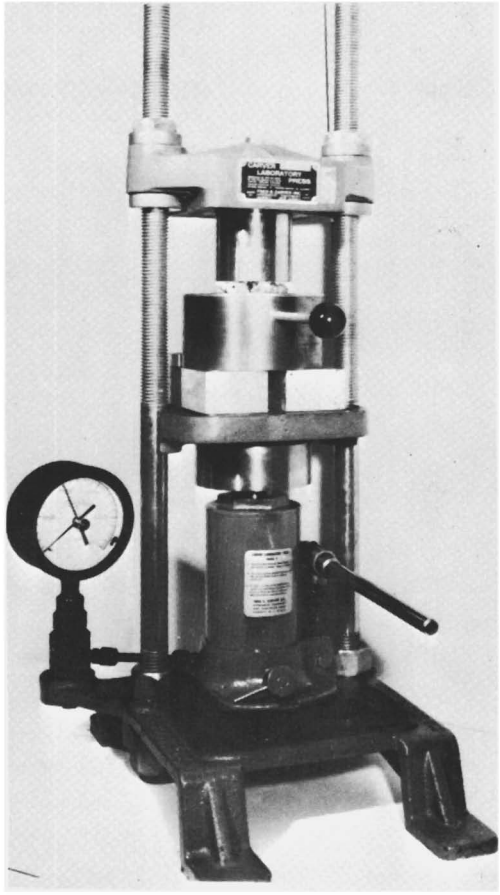

Figure 16. Lyophilized muscle tissue being compressed into an aluminum can. Between 150 and 250 grams of tissue can be compacted for counting

including the geometry of the sample itself, self-absorption, and distance between detector and sample. These factors can all affect the counting of the nuclides in the samples. Hence, we have standardized the geometry of the samples. Our aim has been to put a maximum amount of material within this fixed geometry with the absolute minimum of pretreatment. Radiochemical techniques are avoided since they are usually laborious and time consuming, and can result in loss of material as in dissolution or ashing. Since many biological materials are 50–90% water, removal of water and reduction of sample volume improve the counting within a fixed geometry. The sequence of steps for preparing samples is illustrated in Figures 15–17.

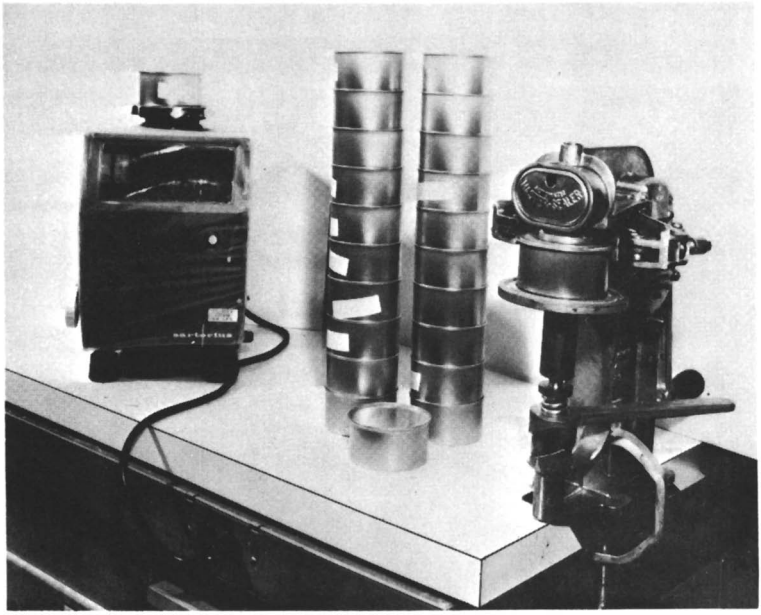

Figure 17. The aluminum cans are sealed to prevent the escape of radioactivity and the spoilage of biological materials. One can holds 2 liters of lyophilized milk

Freeze-Dried Samples. SOLID MATERIALS AND TISSUES. These are first cut into approximately 1-inch cubes, frozen on a Teflon cookie sheet in a freezer, and placed in 1200-ml. freeze-dry flasks to capacity. The flasks are attached to the freeze-dried (lyophilizer) manifold, the valves are opened to vacuum, and the flasks are evacuated. The water from the tissues is trapped on a condenser. The dry tissues (drying time about 2–3 days) are removed from the lyophilizer and compressed into thin-walled aluminum cans with a Carver Laboratory press fitted with a special die, at about 24,000 lb. pressure (total). From 150–250 grams of the dry material, representing 500–1000 grams of fresh tissue, can be packed into a single can. The cans are sealed with a hand sealer and set aside for counting. Samples can be removed from the cans at a later date for chemical analysis or beta-emitter analyses.

LIQUID SAMPLES. Liquid samples such as plasma or milk are shell-frozen in the lyophilizer flasks using a mixture of crushed dry ice and 2-propanol. They are then dehydrated in the same way as the solid samples. The resulting material, which is brittle and spongy and easily broken up, is then pressed into cans and sealed. No preservative is added to the dried materials; they can be stored indefinitely at room temperature. Approximately 2 liters of fresh milk can be dried and compressed into one can.

The cans are standard-sized seamless "tuna" cans made of extruded aluminum (8–10 ml.), approximately 3.25 inches × 1.75 inches; they are obtainable from the Central States Can Co. (Massillon, Ohio). So far these cans have been found to contain no detectable amounts of

radioactivity. The sealer is the All American Automatic Master Sealer (Wisconsin Aluminum Foundry Co., Inc.).

Fresh Samples. Fresh samples with adequate activity are canned without freeze-drying. However, they tend to ferment and produce gas, and the cans expand unless a preservative is added. At present we fill the cans with 200 grams of materials and add 5 $cm.^3$ of undiluted formalin (40%) before sealing. The contents often expand very slightly, but since the swelling is not progressive, these cans also can be stored at room temperature indefinitely after counting.

Small Samples. Very small samples and counting standards are also counted in the same geometry. They are mixed thoroughly with added warm agar (2%) or Cab-O-Sil to a final weight of 200 grams and allowed to set before they are sealed in cans.

Gaseous daughter radionuclides such as xenon or krypton are also trapped in sealed cans for counting; they do not dissipate.

Examples of Biological Counting

Radioactive Debris in Cows. Nuclear detonations produce a complex mixture of radionuclides that includes both the fission products and those induced by neutron activation. Experiments relating to such events

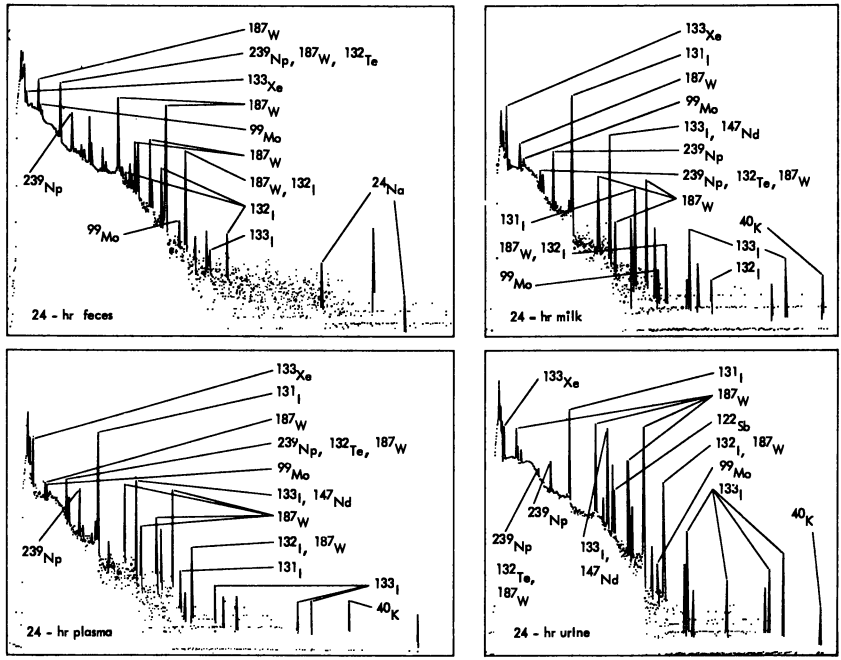

Figure 18. Gamma-ray spectra from various biological materials from a dairy cow that had been previously fed radioactive debris collected at the site of a nuclear detonation

therefore invariably involve extremely complex mixtures, especially if the debris is collected immediately after the explosion.

Several biological experiments were conducted in conjunction with experiments held at the Nevada Test Site. One of these is illustrated in Figure 18, which shows spectra from samples of feces, plasma, milk, and urine from a dairy cow 24 hours after it was fed radioactive debris obtained at the site of a nuclear detonation.

These biological materials were prepared for counting by freeze-drying and compressing into aluminum cans as described in the previous section. After counting, the spectra were printed out on an *X-Y* plotter for purposes of illustration; normally the data presentation would have been by computer printout.

From this example it is apparent that complex experiments can be carried out with relative ease. The mixture of approximately 10 isotopes in these samples has been resolved as to the specific radionuclides and their amounts.

Radionuclide Analyses of Foods. A few food items purchased at a local grocery store were similarly prepared and counted. The results are tabulated in Table I. In all cases the only radionuclides detected were ^{137}Cs and ^{40}K. The photopeaks were easily discernible; the lowest level was 12.7 pCi, ^{137}Cs for a 228-gram sample of shrimp.

Pacific Coast oysters collected at four major growing sites were also assayed for radionuclide content. Trace amounts of ^{65}Zn, detected in two cases, are probably related to ^{65}Zn discharge from nuclear reactors. The results are tabulated in Table II.

Table I. ^{137}Cs in Some Components of the Human Diet

Sample	*Milk*	*Beef*	*Shrimp*
Dry weight, grams	194	214	228
Counts in peak	88	74	46
Counts in background	30	32	23
Net counts, ± S.D.	58 ± 11	42 ± 11	23 ± 8
Counting time, min.	1020	1022	1187
Net counts/min., ± S.D.	0.057 ± 0.011	0.041 ± 0.011	0.019 ± 0.007
Specific activity, pCi/gram	0.175 ± 0.034	0.113 ± 0.031	0.056 ± 0.021
Total activity, pCi	34	24.2	12.7

Table II, ^{65}Zn in Pacific Coast Oysters

Location	*^{65}Zn, pCi/gram dry wt.*
Washington	0.79
Extreme Northern California	0.47
California (Drakes Bay)	Not Detectable
California (Morro Bay)	Not Detectable

Radionuclide Analyses of Human Liver. Several specimens (*12*) of human liver obtained at autopsy were prepared similarly, except that after they were freeze-dried they were ball-milled to insure homogeneity of radionuclide distribution in the counting sample. The powdered samples were then compressed into aluminum cans and counted for approximately 2000 minutes.

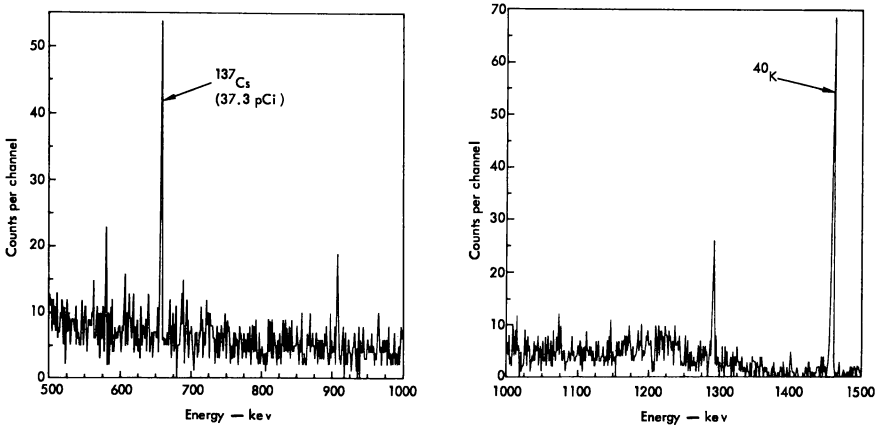

Figure 19. Spectral analysis of radioactivity in a sample of human liver. Two radionuclides, ^{137}Cs and ^{40}K, were detected. The unidentified photopeaks represent background radiation

A typical liver spectrum is shown in Figure 19. The prominent peaks are ^{137}Cs and ^{40}K. The smaller peaks were accounted for as background contaminants. Total radioactivity ranged from below 17 pCi to 45 pCi for the various samples; these two values correspond to a low specific activity of 0.156 pCi/gram and a high of 0.307 pCi/gram. For the liver of the "standard man" (*13*) the ^{137}Cs burden would be approximately 100 pCi. The liver data are summarized in Table III.

Table III. ^{137}Cs in Human Liver

Sample No.	*Total Activity (pCi)*	*Specific Activity, pCi/gram dry wt.*	*Estimated Total ^{137}Cs,[a] pCi*
0708	16.8	0.156	53
8374	28.8	0.278	94.5
4454	45.1	0.296	101
5024	37.3	0.307	104

[a] Based on a 1700-gram liver (*13*).

Discussion

The system has a specific capability for the resolution of very complex mixtures in which large energy peaks tend to mask small adjacent ones. It is therefore particularly suitable for rigorous studies of the slow incorporation of low levels of radionuclides into biological or environmental systems. It should encourage investigation in these areas, where up to now the accumulation of data has been slow, laborious, and expensive.

Experience already indicates that the system should also be useful for purposes of national defense. Debris from foreign weapons tests can be examined quickly for identification and quantitation of its radionuclide content.

As the nuclear age progresses, man will be continually exposed to radiation from the radionuclides that are produced in the nuclear events and eventually localize in him. Accordingly, one of the most critical questions is that of assessing the effects upon man of low doses of radiation delivered at low rates or moderate doses delivered at low rates. It is well-known that exposure to 25 to 50 rads may cause biological harm. But what about lower doses? Is all radiation harmful? Should the extrapolation to a zero-rad dose be linear or curvilinear? These questions are the subject for active experimentation in this Laboratory and in others. If the correct extrapolation is linear, it will be crucial to measure accurately the amount of radiation to which a person has been exposed. Such data on gamma-emitting radionuclides can be obtained with a system of the resolution and sensitivity we have described.

Summary

A gamma-ray spectrometer using a Ge(Li) detector has been constructed that offers the biologist a powerful analytical tool. It should serve to complement and to support other sophisticated analytical gamma-ray spectrometers that may be available—*i.e.*, multidimensional NaI(Tl) (*14*), unshielded Ge(Li) diodes (*8*). High spectral resolutions coupled with high sensitivity have been achieved that allow assaying small as well as large (200 cm.^{3}) biological and environmental samples.

The use of anticoincidence shielding significantly reduces the Compton continuum and allows the detection of weak spectral lines usually masked by interfering Compton radiation. Further improvement resulted from separate recording of the coincidence and anticoincidence; thus, radionuclides that normally decay with a coincidence scheme can be recorded without loss of efficiency.

Threshold limitations have been demonstrated to be approximately 0.01 count/minute. Milk samples of 2-liter volume have been assayed for ^{137}Cs with a total activity of 10 pCi.

The spectrometer has also been applied successfully to the counting of environmental samples contaminated with worldwide fallout, reactor effluent, and debris from nuclear cratering experiments. In addition, it has been possible to carry out a variety of laboratory experiments not practical in the past because of the need for laborious radiochemical analysis; such experiments have involved the analysis of several hundred samples each containing up to 20 isotopes.

Reduction of background radiation owing to natural radioactivity in the metal parts of the detector chamber and shielding can be reduced as shown by using electrolytic quality metals. In addition, backscatter can be reduced significantly by improvements in the counting geometry. These improvements are worthy of consideration.

Acknowledgments

The authors thank W. O'Neal (Mechanical Engineering Department) for the mechanical engineering involved in the various assemblies, and D. Hansen and J. Masters of the same department for constructing the detector assemblies. They are indebted to D. Sawyer and F. Newbold (Electronics Engineering Department), and R. E. Heft, W. Ralston, and W. Phillips (Bio-Medical Division) for their many practical and invaluable suggestions and original contributions. G. Armantrout, C. J. Maxwell, E. Saunders, and D. Okubo of the Electronic Engineering Department were responsible for the fabrication of the Ge(Li) detectors. The authors are also indebted to V. J. Evertsbusch (Technical Information Department) for assistance in the preparation of this report.

Literature Cited

(1) Camp, D. C., Armantrout, G. A., University of California, Lawrence Radiation Laboratory, **UCRL-12245** (1965).
(2) Cooper, J. A., Battelle-Northwest, Pacific Northwest Laboratory, Richland, Wash., private communication (1967).
(3) Bradley, A. E., *IEEE Trans. Nucl. Sci.* **13**, 611 (1966).
(4) Bradley, A. E., University of California, Lawrence Radiation Laboratory, private communication (1966).
(5) Cooper, J. A., Wogman, N. A., Perkins, R. W., Battelle-Northwest, Pacific Northwest Laboratory, Richland, Wash., *Rept.* **BNWL-SA-1522** (1968).
(6) Galloway, R. B., *Nucl. Instr. Methods* **55**, 29 (1967).
(7) Crouthamel, C. E., "Applied Gamma-Ray Spectrometry," p. 96, Pergamon Press, New York, 1960.
(8) Camp, D. C., University of California, Lawrence Radiation Laboratory, **UCRL-50156** (1967).
(9) Saunders, E., Maxwell, C. J., University of California, Lawrence Radiation Laboratory, **UCRL-70545** (1967).

(10) Goulding, F. S., *Natl. Acad. Sci.-Natl. Res. Council Publ.* **1184** (1963).
(11) Uber, D. C., University of California, Lewrence Radiation Laboratory, **UCRL-70547** (1967).
(12) Anspaugh, L. R., Phelps, P. L., unpublished data.
(13) "Radiological Health Handbook," p. 191, U. S. Department of Health, Education and Welfare, Washington, D. C., 1960.
(14) Perkins, R. W., *Nucl. Instr. Methods* **33** (1965).

RECEIVED August 5, 1968. Work performed under the auspices of the U. S. Atomic Energy Commission.

X-ray and β–γ Coincidence Spectrometry Applied to Radiochemical Analysis of Environmental Samples

FRED P. BRAUER, JAMES H. KAYE, and ROBERT E. CONNALLY
Battelle Memorial Institute, Pacific Northwest Laboratory, Richland, Wash.

Various β-γ and x-ray-γ coincidence spectrometers have been used for low level γ spectrometry measurements at our laboratory. The sample to be analyzed is counted simultaneously with a gas flow proportional counter or plastic scintillator and a NaI(Tl) detector. By requiring a coincidence between the detectors the background γ spectrum counting rate can be reduced by more than a factor of 1000. This allows γ spectra to be obtained on samples containing less than 1 d/m *of γ activity. A high degree of discrimination is provided against nuclides which do not meet the coincidence requirement. Detector arrangements and sensitivities are discussed for the measurement of ^{131}I, ^{125}I, ^{134}Cs, ^{106}Ru–^{106}Rh, ^{54}Mn, ^{60}Co, and other nuclides present in environmental samples.*

The identification and estimation of gamma radioactivity in environmental samples is often hindered by the low radioactivity levels or small available sample sizes. Large NaI(Tl) detectors are desirable to obtain high counting efficiencies (*7, 8, 11*). As the detector size is increased, however, the background also increases. By requiring an x-ray or β event in coincidence with the γ event the γ spectrum background can be reduced several orders of magnitude (*1, 4, 8*). Special sample preparation or chemical separations may be required to reduce self-absorption of the β or x-ray radiation. Even after chemical separation, γ spectra measurements are preferred to β counting since they allow discrimination against impurities and determination of isotopic ratios.

Several different detector configurations have been evaluated and are being used for low level γ spectrometry. Various sizes of plastic beta

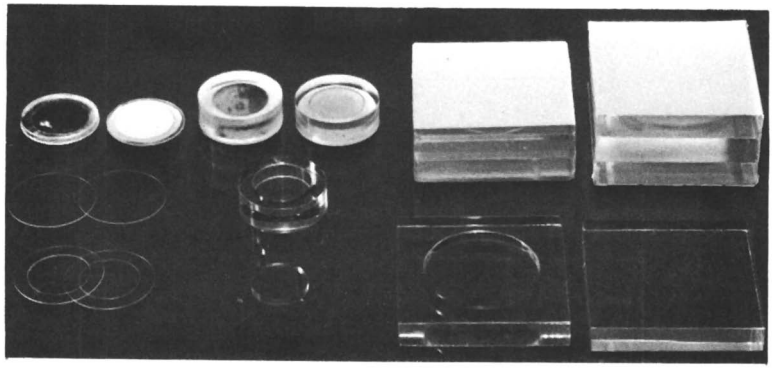

Figure 1. Plastic β scintillators

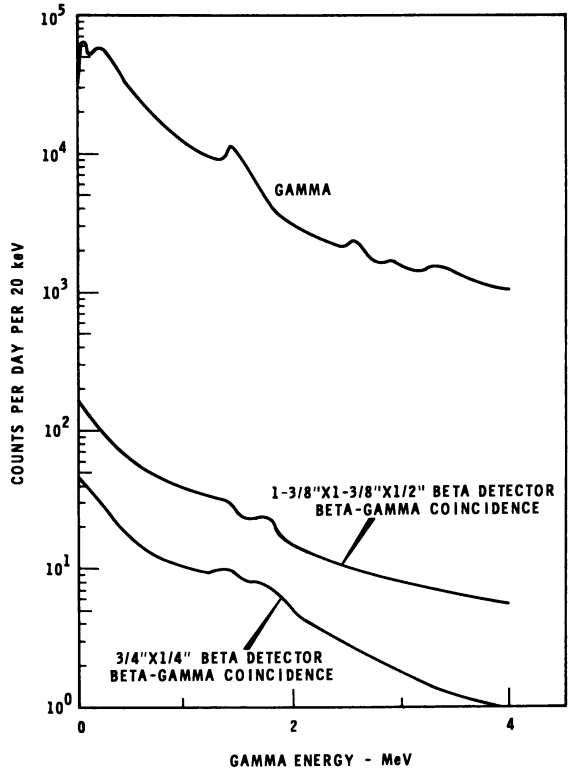

Figure 2. γ Background for an 8-inch × 8-inch NaI(Tl) well crystal with 4-inch lead shielding

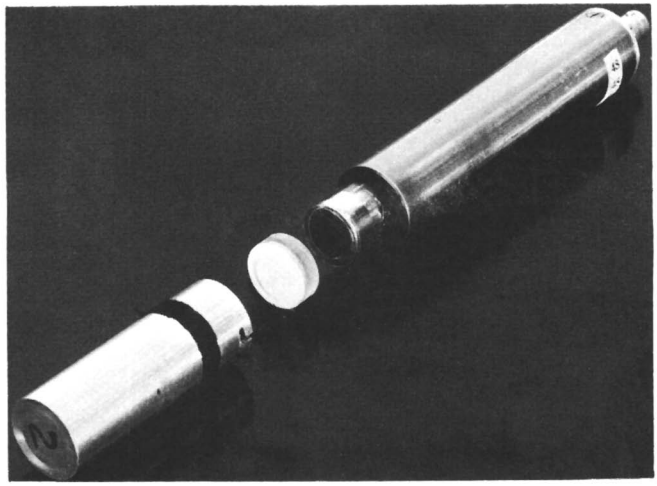

Figure 3. ¾-Inch multiplier phototube assembly

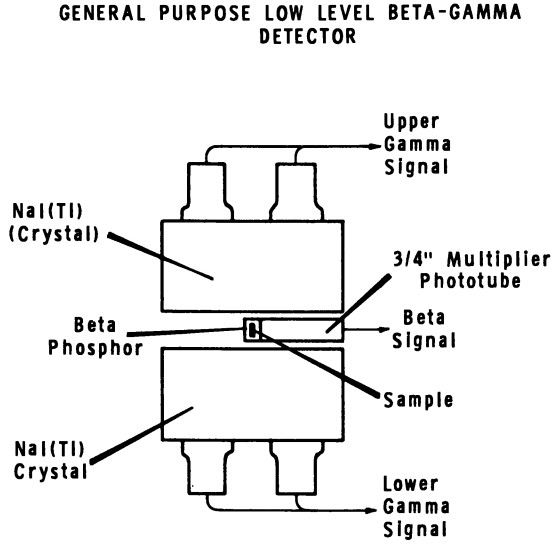

Figure 4. General purpose low level β–γ detector

scintillators (NE-102 or Pilot B) (5) containing the sample are used as detectors with well-type or opposed crystal NaI(Tl) γ detectors. Two opposed 5-inch diameter gas flow β proportional counters mounted

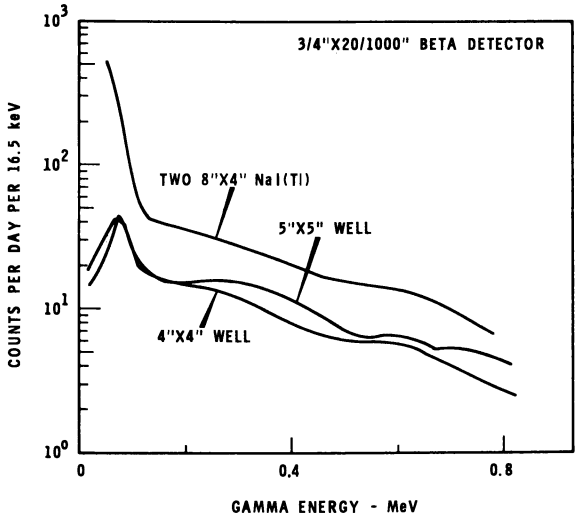

Figure 5. Background β–γ coincidence spectra

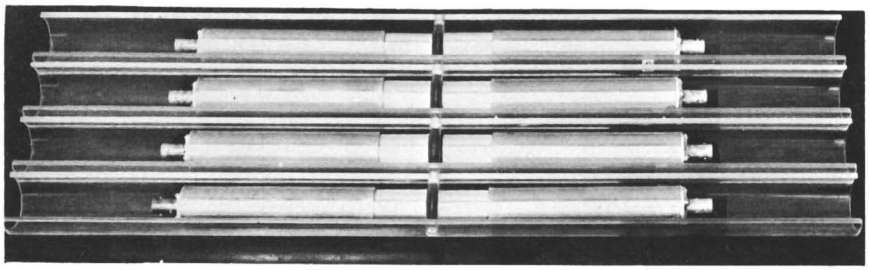

Figure 6. Multisample β scintillation detectors

between 8-inch diameter × 4-inch thick NaI(Tl) detectors are used for counting larger samples. A 2-inch diameter × 5-inch long gas flow x-ray counter has been used with a well-type NaI(Tl) detector for x-ray–γ coincidence spectrometry. Two opposed 2-inch diameter × 1/32-inch thick NaI(Tl) detectors are used for low energy γ–x-ray coincidence spectrometry.

Detectors

Systems Using Plastic Scintillators. The lowest backgrounds have been achieved by mounting the sample between 3/4-inch diameter × 1/100-inch thick plastic scintillators. Larger scintillators are used when

required by larger sample sizes to reduce self-absorption and improve counting efficiency. Various plastic scintillators are shown in Figure 1. The scintillators shown include 3/4-inch diameter × 1/100-inch thick discs, 3/4-inch diameter × 1/4-inch thick pieces with 1/2-inch diameter × 1/8-inch deep wells and caps, and 1-3/8-inch × 1-3/8-inch squares 1/4-inch thick which contain 1-inch diameter × 1/8-inch deep wells. The samples are mounted in the wells of the β scintillators or between the discs. The discs are heat sealed, and the large scintillators are held together using white pressure-sensitive plastic tape. Three of the square scintillators are sometimes stacked to accommodate samples mounted as two fractions.

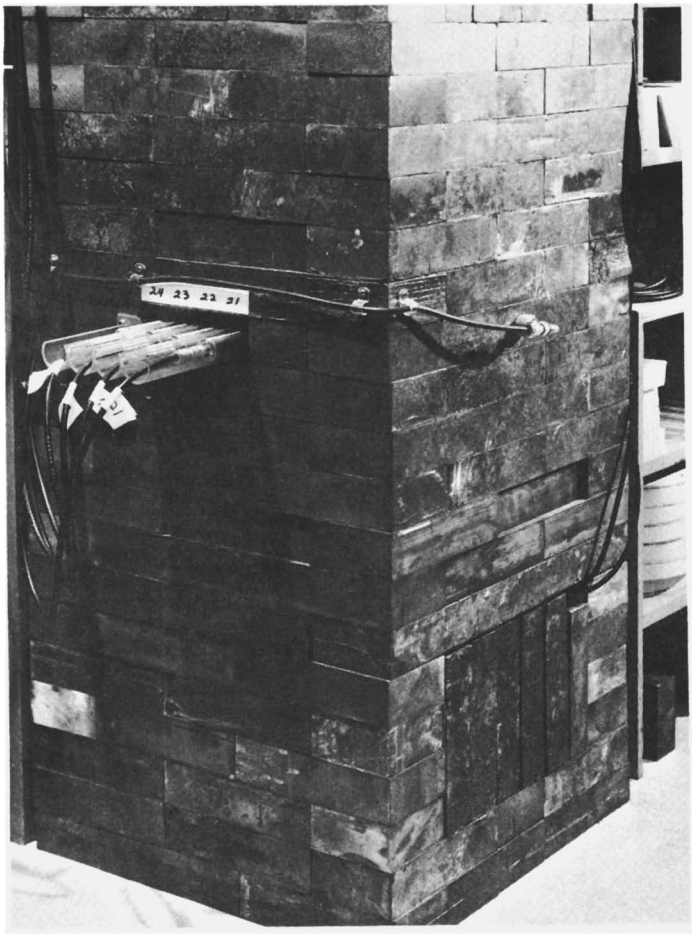

Figure 7. Eight-sample β–γ coincidence spectrometer

The larger square β scintillators are viewed edgewise by 1-1/2-inch diameter 10-stage multiplier phototubes and used in 2-inch diameter wells of 8-inch $\times$ 8-inch NaI(Tl) crystals. The larger scintillators are used for sample sizes up to several hundred milligrams. Figure 2 illustrates the reduction in background achieved by the β coincidence requirement.

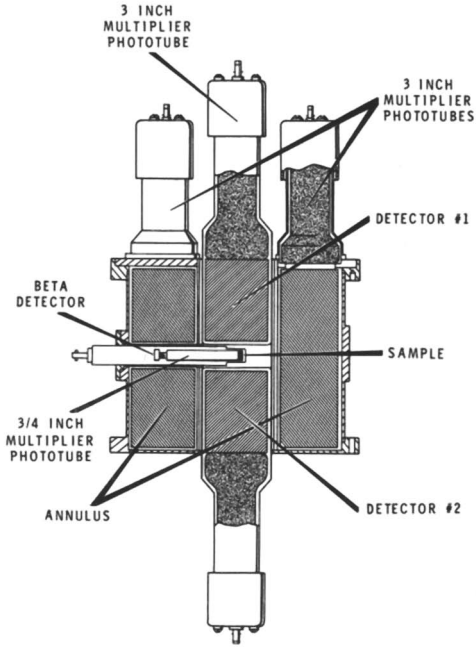

Figure 8. Schematic of dual γ detector with side-hole annulus and scintillation β detector

The 3/4-inch diameter scintillators are mounted on 3/4-inch diameter 10-stage multiplier phototubes using silicone stopcock grease. A light tight multiplier phototube assembly (Figure 3) was designed for use in 1-inch diameter wells or between opposed crystals, as shown in Figure 4. The multiplier phototube high voltage is adjusted to give a 70% β counting efficiency for a standard ^{60}Co source. The background noise level is required to be below 10,000 counts per minute.

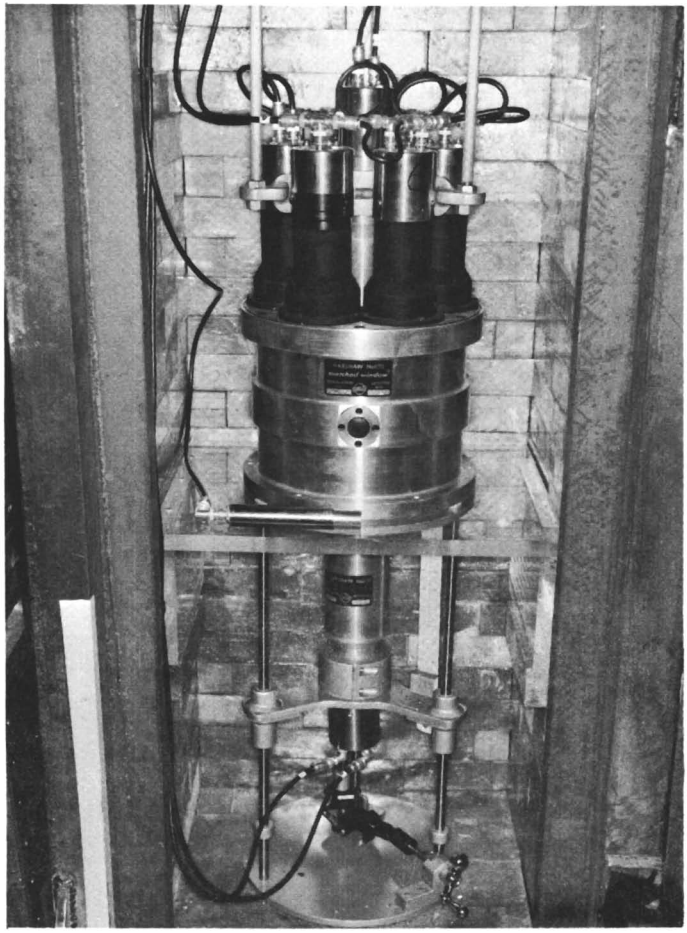

Figure 9. Dual γ detector with side-hole annulus and scintillation β detector

The background γ spectra for various sized NaI(Tl) crystals in coincidence with this β detector assembly are compared in Figure 5. Lead shields, 4 inches thick, are used around all detector assemblies. Although the background is greater when opposed 8-inch diameter × 4-inch high NaI(Tl) crystals are used, this arrangement can be used with more than one β detector. An assembly of eight separate β detectors (Figure 6) has been used with two opposed NaI(Tl) crystals. Multiplex electronics is used to route the γ spectrum in coincidence with each β detector to a separate 50-channel group in a 400-channel analyzer (*1*).

Such an arrangement is useful for taking long counts on many samples with a minimum investment in NaI(Tl) and electronics. Figure 7 shows an eight-sample β-γ coincidence spectrometer. The single β detector seen on the right side of the lead shield is a gain stabilizer probe utilizing a ^{106}Ru–^{106}Rh source in a β scintillator. Because of the high energy of the ^{106}Rh β^- the beta efficiency of the detector is greater than 99%;

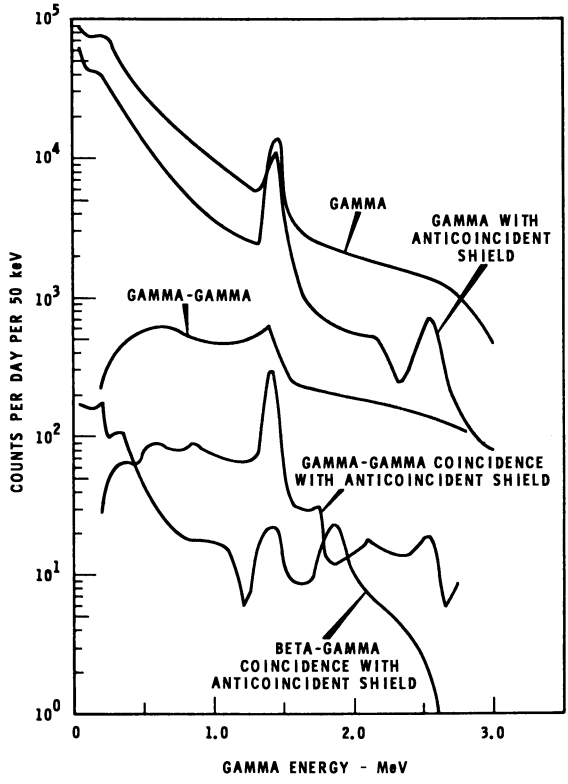

Figure 10. Background for opposed 3-inch × 4-inch NaI(Tl) crystals

γ events in coincidence with the ^{106}Rh β^- are routed to the gain stabilizer circuits and are not stored by the multichannel analyzer.

An anticoincidence-shielded γ spectrometer utilizing a scintillation β detector is shown in Figures 8 and 9. The assembly consists of two

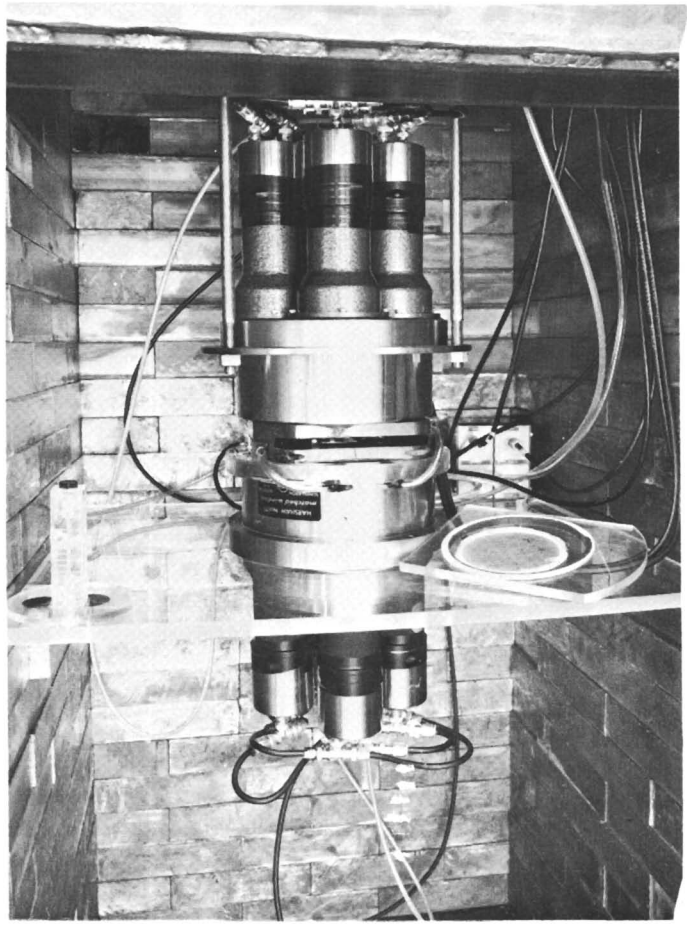

Figure 11. β–γ Coincidence spectrometer utilizing gas flow proportional counters and 8-inch × 4-inch opposed NaI(Tl) detectors

opposed 3-inch diameter × 4-inch thick NaI(Tl) crystals and a 9-3/8-inch diameter × 9-inch thick NaI(Tl) annulus. The annulus, when operated in anticoincidence with the center crystals, serves to reduce both the background and the Compton spectrum. A comparison of the γ backgrounds obtained for various modes of operation is plotted in Figure 10. The γ-γ coincidence curves illustrate the relative background reductions that are obtained by multidimensional γ spectrometry (*9*, *10*).

Systems Using Gas Flow Proportional Counters. Two types of gas flow proportional counters have been used with large area samples to

reduce β self-absorption and to study x-ray–γ coincidence techniques. One system is pictured in Figure 11. Two opposed 5-inch diameter × 1/2-inch thick gas flow proportional counters with gold plated Mylar windows were placed between opposed 8-inch diameter × 4-inch thick

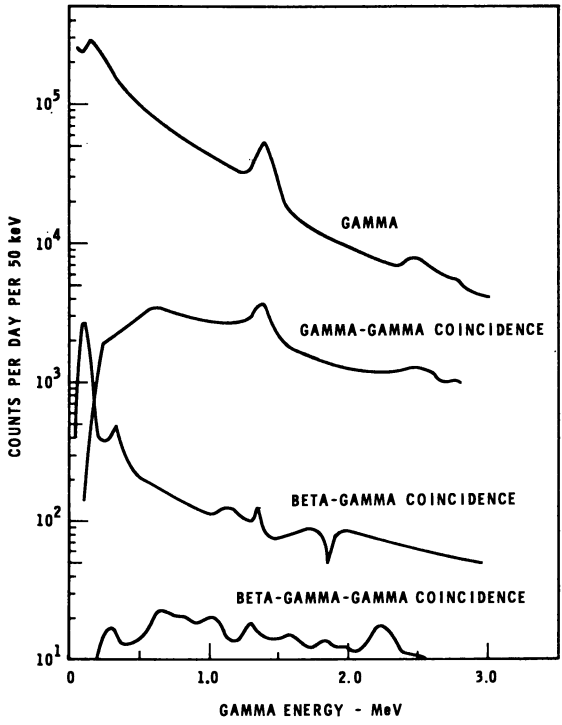

Figure 12. Background for opposed 8-inch × 4-inch NaI(Tl) crystals with opposed 5-inch diameter proportional β counters

NaI(Tl) crystals. The sample to be counted is mounted between Mylar sheets on a 1/4-inch thick × 5-inch diameter plastic ring. This system is presently used with a four quadrant, multiplexed, 4096-channel, multidimensional analyzer. The multidimensional γ spectrum in coincidence with the proportional counter events is recorded in one quadrant, and the anticoincident multidimensional γ spectrum is recorded in another quadrant; thus, no data are lost. The various background γ spectra obtained with this detector assembly are compared in Figure 12. The γ-γ coinci-

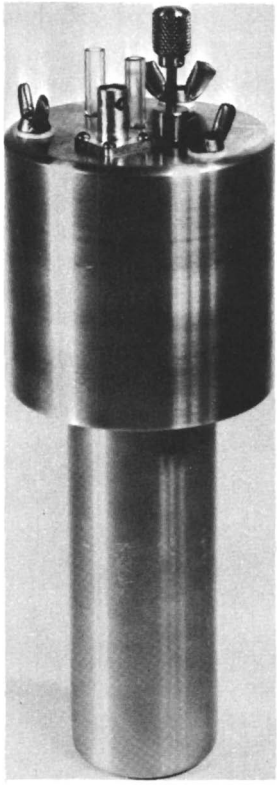

Figure 13. Gas flow proportional x-ray detector

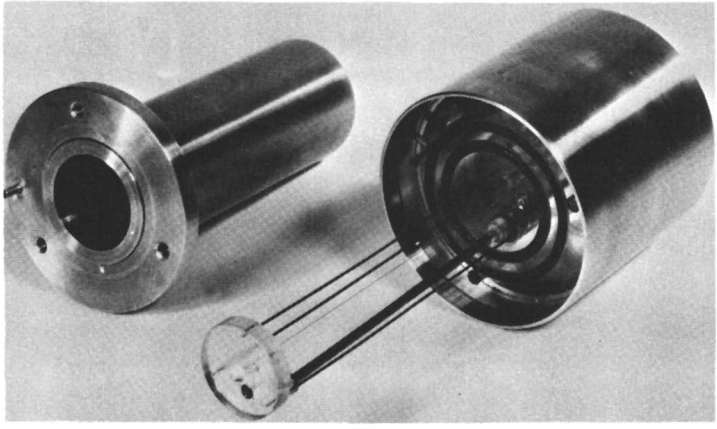

Figure 14. Partly disassembled gas flow proportional x-ray detector

dence curves illustrate the magnitude of the background in the multi-dimensional region of the γ spectrum.

The gas flow proportional counter shown in Figures 13, 14, and 15 was developed primarily for use in an x-ray–γ coincidence system. The counting chamber of the detector is 2-inch o.d. $\times$ 5-inch long and is used

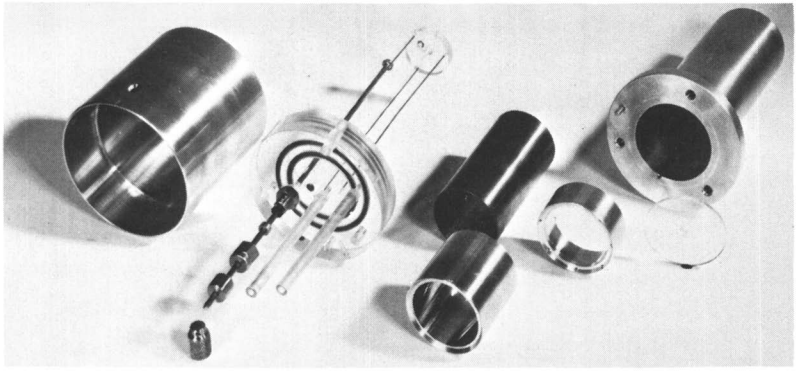

Figure 15. Disassembled gas flow proportional x-ray detector

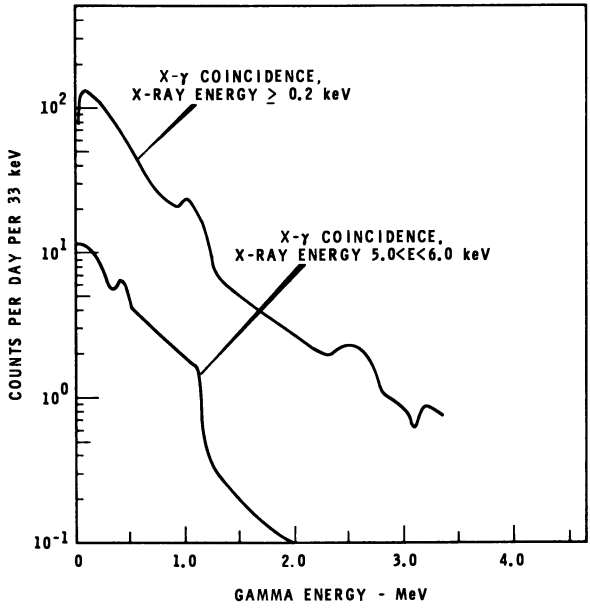

Figure 16. Background of x-ray γ detector system

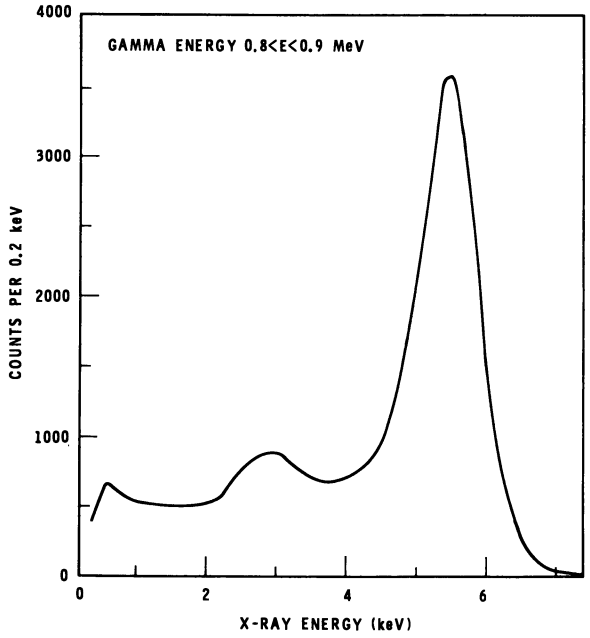

Figure 17. X-ray γ coincidence spectrum of ^{54}Mn

Table I. Background Comparisons

Detector		*0.2–4.0 M.e.v. Gamma Background c/m*
NaI(T1)	*Beta*	
5-in. × 5-in. well type	None	400
	¾-in. × ¼-in.	1
	¾-in. × 20/1000-in.	0.4
8-in. × 8-in. well type	None	2300
	1⅜-in. × 1⅜-in. × ¾-in.	5.1
	1⅜-in. × 1⅜-in. × ½-in.	3.8
	¾-in. × ¼-in.	1.4
	¾-in. × 20/1000-in.	0.8
8-in. × 4-in. pair	None	2300
	5-in. dia. gas flow	8
3-in. × 4-in. pair	None	630
3-in. × 4-in. pair with AC	None	306
	¾-in. × 20/1000-in.	1
6-in. × 5-in. pair[a]	None	1000
6-in × 5-in. pair with AC	None	250
11-in. × 6-in. pair	None	7800
8-in. × 4½-in. annulus	2-in. × 5-in. gas flow	1.6

[a] With 6-in. × 4-in. NaI light pipe.

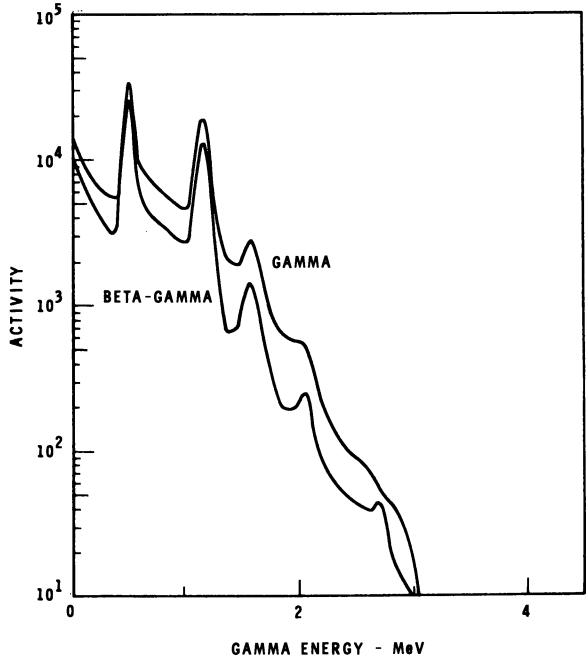

Figure 18. $^{106}Ru^{106}Rh$ spectra, 8-inch × 8-inch NaI(Tl) well crystal

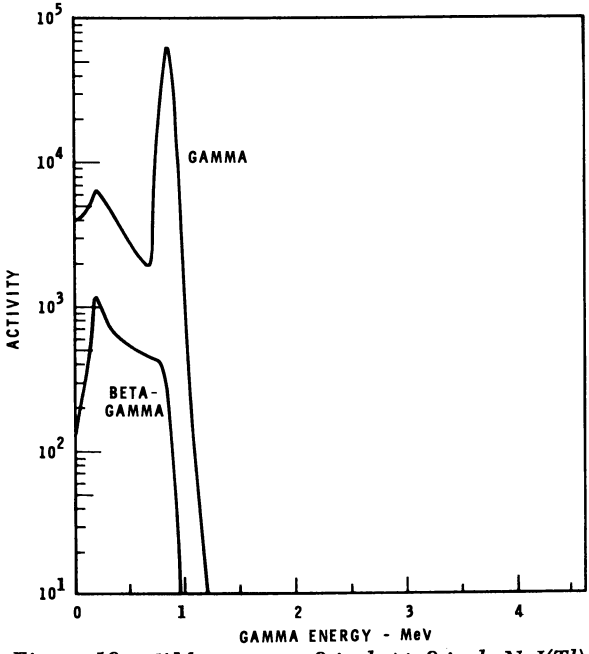

Figure 19. ^{54}Mn spectra, 8-inch × 8-inch NaI(Tl) well crystal

with an 8-inch diameter × 4-1/2-inch long NaI(Tl) annulus. The sample to be counted is mounted on the inside of a copper tube which serves as the detector cathode. The detector design includes a probe for inserting an x-ray source into the counting chamber without removing the sample. The detector system is used with a multidimensional ana-

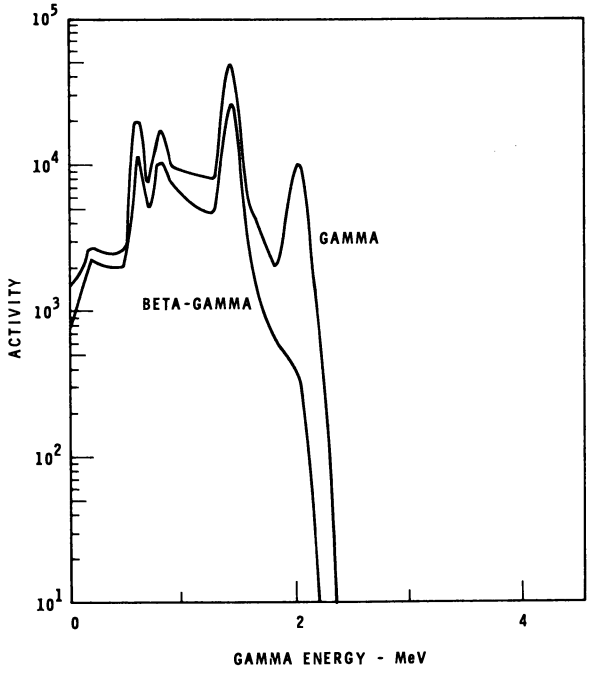

Figure 20. ^{134}Cs spectra, 8-inch × 8-inch NaI(Tl) well crystal

lyzer (2) to record both the x-ray and γ energy spectra. The background γ spectrum in coincidence with two x-ray energy ranges is plotted in Figure 16. The resolution of the x-ray detector for the x-ray associated with the decay of ^{54}Mn can be seen in Figure 17.

Results

Background. The total γ backgrounds from 20 k.e.v. to 4 M.e.v. for various types of NaI(Tl) detector systems are compared in Table I. Total γ background reductions of 10^3 can be obtained by requiring a β

coincidence. γ Spectrometry at the 1 d/m level is possible with this technique. The background increase associated with the larger, more efficient, NaI(Tl) detectors is not as great when a β coincidence is required. The background levels of our 6-inch diameter $\times$ 5-inch thick multidimensional detectors, which are shielded from the radioactiivty in their multiplier phototubes by 4-inch thick NaI light pipes and

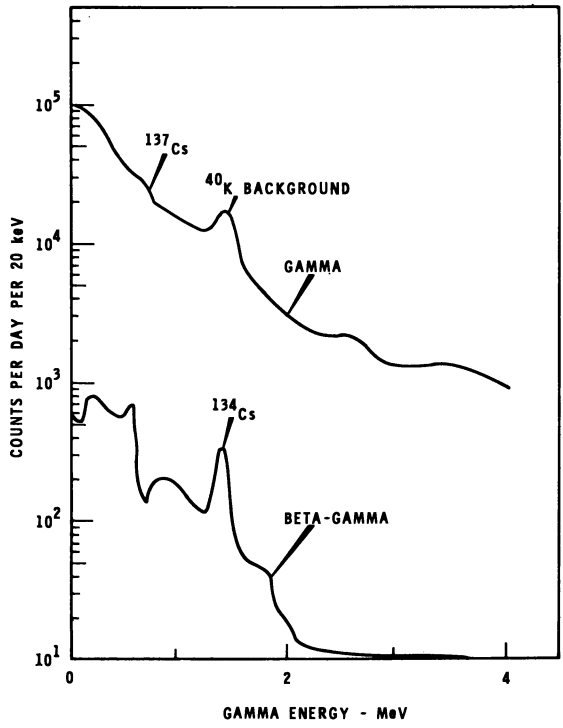

Figure 21. γ Spectra of separated Cs sample in 8-inch $\times$ 8-inch NaI(Tl) well crystal

shielded from other extraneous activity by a large 32-inch diameter plastic scintillator operated in anticoincidence, are seen to be over 10^2 times greater than our β coincident systems. The β coincidence requirement also eliminates photopeaks such as the ^{40}K peak from the background since the background observed with these systems results primarily from γ-ray detection by the β detectors.

Spectra Shapes. The γ spectrum in coincidence with β events is similar to the normal γ spectrum for many nuclides. This is shown by

the ^{106}Ru–^{106}Rh spectrum in Figure 18. The β–γ coincidence method is limited to β-emitting nuclides. The ^{54}Mn spectrum shown in Figure 19 illustrates the response of the β–γ coincidence method for an electron-capture nuclide utilizing a plastic scintillator as the β detector. The events recorded in the β–γ coincidence mode correspond to Compton γ events occurring in both the NaI(Tl) and plastic detectors. Thus, the photopeak is lost from the spectrum. The utilization of an x-ray–γ

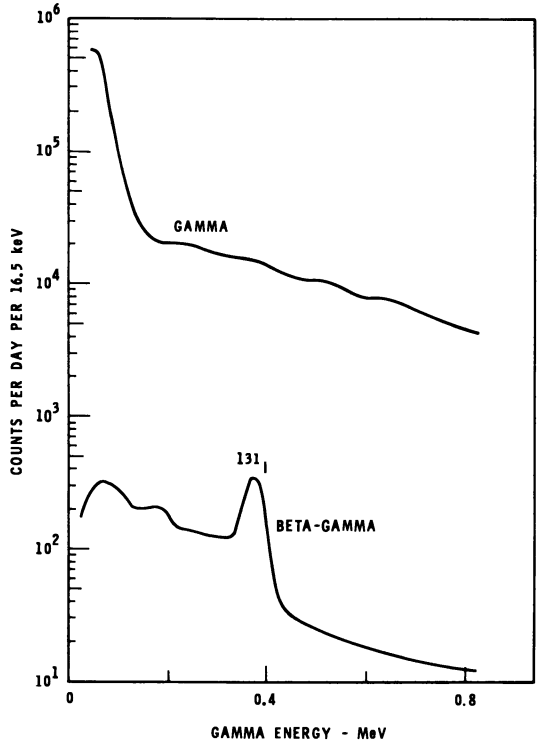

Figure 22. γ-Spectra of separated iodine sample in 5-inch × 5-inch NaI(Tl) well crystal

system such as described above can be used for low background analysis of nuclides which decay by electron capture.

Very low energy β particles are not detected by plastic scintillators. This can result in the loss of photopeaks from the β–γ coincidence spectrum as illustrated by the spectrum of ^{134}Cs shown in Figure 20. Self-absorption of the β particles by the sample can also result in similar

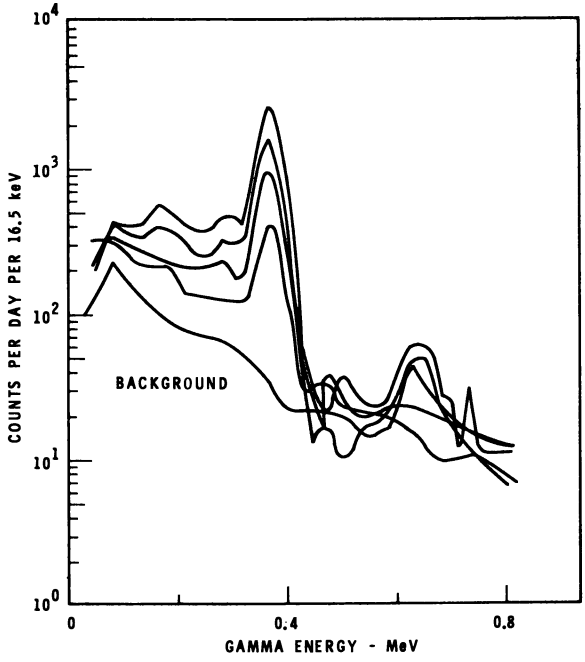

Figure 23. Decaying β–γ coincidence spectra of separated iodine sample between opposed 8-inch × 4-inch NaI(Tl) crystals

Table II. ^{131}I Detection Limits

Detector		*^{131}I Detection[a] Limit (d/m)*
NaI(Tl)	*Plastic Beta Scintillation*	
8-in. × 8-in. well type	None	5.0
	1⅜-in. × 1⅜-in. × ½-in.	0.07
8-in. × 4-in. pair	¾-in. × ¼-in.	0.14
	¾-in. × 20/1000-in.	0.04
5-in. × 5-in. well type	None	2.0
	¾-in. × ¼-in.	0.05
	¾-in. × 20/1000-in.	0.02
4-in. × 4-in. well type	None	2.0
	¾-in. × ¼-in.	0.05
	¾-in. × 20/1000-in.	0.02
3-in. × 4-in. pair with anti-coinc.	None	1.4
6-in. × 5-in. pair with anti-coinc. & NaI light pipes	None	1.4
9-in. × 9-in. three component	None	20.0
11-in. × 6-in. pair	None	40.0

[a] Standard error for zero-level sample; weekly 1000-minute counts.

spectrum changes. Quantitative analyses require control of the sample thickness and/or calibrations using sources of various sizes.

Applications. The β–γ coincidence method can be used to determine trace amounts of a β-emitting isotope in the presence of large quantities of a γ emitter with no coincident beta. The application of this technique is illustrated by the spectrum of a separated cesium sample

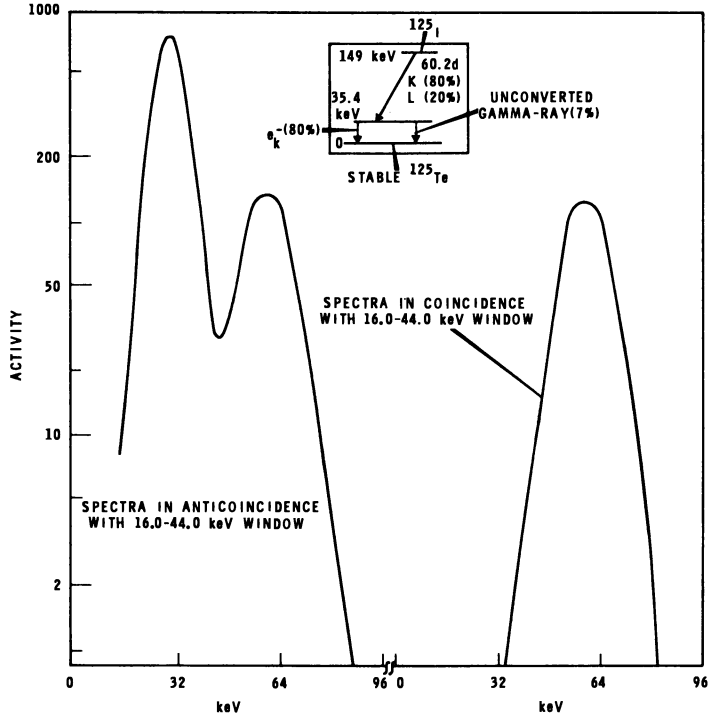

Figure 24. ^{125}I spectra, with opposed 2-inch diameter × 1/32-inch NaI(Tl) crystals

shown in Figure 21. The ^{40}K photopeak in the normal γ spectrum background and the high general background level prevent the measurement of the ^{134}Cs by normal γ spectrometry. The β coincidence spectrum is seen clearly to resolve the ^{134}Cs with complete discrimination against the ^{137}Cs γ rays.

The β–γ coincidence spectrometry technique has been used for low level ^{131}I measurements in various environmental samples. The presence of other γ emitters in the samples and the sample bulk have often required

chemical separation before counting. ^{125}I is used as a spike for radiochemical yield measurements. Figure 22 illustrates the detection of ^{131}I by β–γ coincidence spectrometry when no indication of the ^{131}I is seen in the γ spectrum. A decay study utilizing the same sample is shown in Figure 23. The counting system has been found to be stable over the

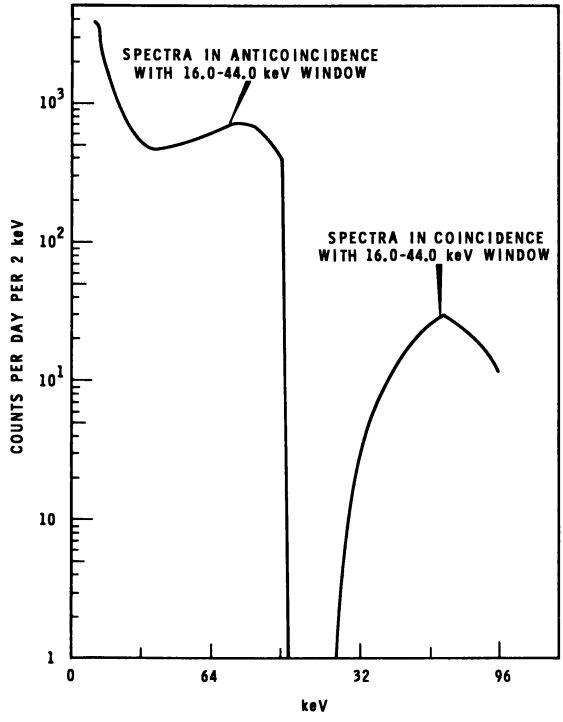

Figure 25. Background for two opposed 2-inch diameter × 1.32-inch NaI(Tl) crystals with 2-inch thick lead shielding

times required for following the decay of ^{131}I as demonstrated by the good fit of the data to the half-life.

The GEM computer program (*6*) was used to calculate the detection limits for ^{131}I by the detector systems described above. The detection limit for these comparisons has been defined as the standard error for a zero-level sample utilizing weekly 1000-minute counts to follow the decay. These results are tabulated in Table II. The β–γ system improves the sensitivity by a factor of 10^2.

Small amounts of ^{125}I must be estimated frequently in analyzing environmental iodine samples (*3*). We have used a low energy x-ray–γ

coincidence system for these measurements. The detector system consists of two opposed 2-inch diameter × 1/32-inch-thick NaI(Tl) crystals with 5 mil Be windows. The electronics associated with the system records the summed outputs from the two detectors in one set of 50 channels if a ~ 30-k.e.v. event is not observed in the upper crystal. If an event is observed, the spectrum is recorded in a different set of 50 channels. The spectrum of ^{125}I obtained with this system is shown in Figure 24 as is the

Table III. Detection Limits for 8-inch by 8-inch NaI(Tl) Well Crystal

	Sensitivity, Counts/Disintegration		*Detection Limit[a] (d/m)*			
			Individual		*Composite*	
Nuclide	γ	β–γ	γ	β–γ	γ	β–γ
^{22}Na	.80	.56	1.5	.04	5.0	.08
^{46}Sc	.58	.30	2.1	.07	3.7	.11
^{51}Cr	.089	(.0065)	20.	(4.)	25.	(9.)
^{54}Mn	.90	(.044)	1.4	(.7)	1.7	(3.)
^{57}Co	.10	(.016)	15.	(.9)	64.	(2.3)
^{60}Co	.95	.67	1.4	.05	3.0	.09
^{65}Zn	.37	(.04)	3.5	(.8)	7.0	(1.7)
^{88}Y	.92	(.13)	1.2	(.2)	2.0	(.6)
$^{95}Zr^{95}Nb$	.87	.28	1.4	.06	1.7	.12
^{103}Ru	.82	.12	2.0	.15	5.2	.4
$^{106}Ru^{106}Rh$	.36	.34	8.0	.08	24.	.26
^{125}Sb	.91	.24	2.5	.09	4.5	.16
^{134}Cs	.92	.52	2.2	.05	4.2	.08
^{137}Cs	.67	(.05)	2.0	(.6)	2.6	(2.)
^{141}Ce	.38	.23	4.0	.06	9.0	.13
$^{144}Ce^{144}Pr$	.13	.085	22.	.3	130.	1.2
^{226}Ra + daughters	1.4	.91	2.1	.035	4.2	.08
^{232}Th + daughters	1.1	.52	2.8	.07	8.0	.13

[a] Standard error for zero-level sample, 1000-minute count.

^{125}I decay scheme. The coincidence detection of the x-ray associated with the electron capture and the 35-k.e.v. γ ray or the x-ray associated with the internal conversion of the 35-k.e.v. γ results in the coincidence spectrum. A significant background reduction is obtained with this system as shown in Figure 25. The system also has a high degree of discrimination against other x-ray and low energy γ events as well as Compton events associated with higher energy γ rays.

Sensitivity. The detection limit for a number of radionuclides has been calculated using the GEM computer program (*6*). The calculations are based on a 1000-minute count of a zero-level sample. The

computations were performed assuming one nuclide present in the sample and assuming all nuclides present in the sample. The results obtained for an 8-inch × 8-inch well crystal with a 3/4-inch × 1/4-inch β scintillator are listed in Table III. The variation in sensitivity is associated with the various decay scheme differences. The numbers in parentheses identify nuclides which do not decay by β^- emission.

Table IV. Detection Limit Comparison of Various Detectors

Detection Limit[a] *(d/m)*

				Two Parameter γ–γ		
				AC Shield		
Nuclide	*χ–γ 8-in. × 4.5-in. Annulus*	*β–γ 8-in. × 8-in. Well*	*γ 8-in. × 8-in. Well*	*6-in. × 5-in. Pair*	*6-in. × 5-in. Pair*	*11-in × 6-in. Pair*
^{7}Be				40.	8.	330.
^{22}Na		.08	5.	.5	.4	.5
^{40}K				10.	10.	160.
^{46}Sc		.11	3.7	.6	.2	.4
^{51}Cr	2.1		25.	19.	.6	340.
^{54}Mn	.2		1.7	1.3	.7	7.
^{57}Co			64.	3.5	1.0	25.
^{58}Co					1.0	
^{59}Fe				3.0	1.3	20.
^{60}Co		.09	3.0	.7	.3	.5
^{65}Zn	.4		7.0	4.2	1.7	20.
^{88}Y			2.0	.7	.14	.38
^{95}Zr^{95}Nb		.12	1.7	1.3	1.0	7.
^{103}Ru		.4	5.2	4.4	1.2	42.
^{106}Ru^{106}Rh		.26	24.	7.0	2.3	13.
^{124}Sb				1.3	.6	1.0
^{125}Sb		.16	4.5	4.2	1.7	31.
^{131}I		.1	5.0	2.6	.7	
^{134}Cs		.08	4.2	.7	.3	1.3
^{137}Cs			2.6	1.	.6	10.
^{140}Ba^{140}La				2.6	1.6	10.
^{141}Ce		.13	9.0	5.7	1.4	80.
^{144}Ce^{144}Pr		1.2	130.	87.	19.	240.
^{147}Nd				9.0	2.5	
^{226}Ra + daughters		.08	4.2	3.3	1.4	4.
^{232}Th + daughters		.13	8.0	2.4	1.8	19.

[a] Standard error for zero-level sample, 1000-minute count.

Table IV compares the performance of several γ spectrometry systems for many nuclides found in the environment. The β–γ coincidence system is seen to offer significantly lower detection limits for many of the nuclides. Longer counting times could be used to establish even lower limits of detection, especially for low background systems.

Summary

β–γ Coincidence spectrometry has been used for measurement of many radiochemically separated environmental samples. Small samples can also be counted directly. Air filters and various particulate samples can often be counted without prior chemistry. The method is especially useful when γ spectra are desired and the available sample contains insufficient activity for analysis by normal or multiparameter γ spectrometry.

Acknowledgments

The authors thank H. G. Rieck for his assistance in design and assembly of the multiplier phototube β detectors.

Literature Cited

(1) Brauer, F. P., Connally, R. E., **HW-SA-2932** (1963).
(2) Brauer, F. P., Connally, R. E., Kaye, J. H., Schlosser, J. E., **BNSA-121** (1965).
(3) Eldridge, J. S., Crowther, P., *Nucleonics* **22,** 6 (1964).
(4) Grenier, R. P., Samuelson, R. R., *Rev. Sci. Instr.* **35,** 11 (1964).
(5) Harley, J. H., Hallden, N. A., Fisenne, S. M., *Nucleonics* **22,** 1 (1962).
(6) Nicholson, W. L., Schlosser, J. E., Brauer, F. P., *Nucl. Instr. Methods* **25,** 45 (1963).
(7) Perkins, R. W., *Health Phys.* **7,** 81 (1961).
(8) Perkins, R. W., *Proc. Conf. Modern Trends Activation Anal. (1961).*
(9) Perkins, R. W., *Nucl. Instr. Methods* **33,** 71 (1965).
(10) Wogman, N. A., Robertson, D. E., Perkins, R. W., *Nucl. Instr. Methods* **50,** 1 (1967).
(11) Wogman, N. A., Robertson, D. E., Perkins, R. W., *Health Phys.* **13,** 767 (1967).

RECEIVED June 4, 1968. Based on work performed under U. S. Atomic Energy Commission Contract AT(45-1)-1830.

14

The Characterization of Radioactive Particles from Nuclear Weapons Tests

ROBERT E. HEFT

Bio-Medical Division, Lawrence Radiation Laboratory, University of California, Livermore, Calif. 94550

Early time aerial filter samples of the stabilized clouds produced by past nuclear weapons tests have been re-examined to determine mass and radioisotopic distribution as a function of particle size. The particles, after removal from the cellulose fiber filter by ashing, were separated into size groups by sedimentation in stabilized fluid columns. The mass and radioisotopic composition of the particle groups were determined and used to generate distribution functions. For airburst detonations the distribution data can be fitted by a single normal distribution function; for Coral Island surface bursts a linear combination of two lognormal functions is needed; for cratering detonations, a linear combination of three lognormal distribution functions is required. The number of functions required is related to the number of discrete particle classes generated by the detonation.

Except for tritium, carbon-14, and the long lived rare gases, the radioactive atoms produced by a nuclear detonation are accounted for completely within a population of radioactive particles. The nature of the particle population and the manner in which the individual radionuclides are distributed within it will vary with the conditions under which the detonation occurred. Characterization of the radioactive particle population requires:

(1) The determination of mass and radionuclide distributions as a function of particle size and type.

(2) The expression of these distributions in simple mathematical form.

Characterization is based on the analysis of aerial cloud and local fallout samples taken at the detonation site shortly after detonation. Radiochemical analysis of such samples at early time provides data from which the relationships of radionuclide partitioning may be deduced. In general, the partitioning of all radionuclides may be described in terms of that of two members of the set, providing one of the two is representative of the refractory isotopic species and the other is representative of the volatile isotopic species (*1*). [Whether a particular isotope behaves as a refractory or a volatile depends on its chemical form at the time condensation occurs. Thus, a fission product such as strontium-89 may behave as a volatile because at condensation time the mass chain is principally in the form of bromine, krypton, and rubidium.] At any subsequent time, residual portions of the samples collected at early time may be subjected to size analysis to determine how a long lived refractory isotope, a long lived volatile isotope, and mass are distributed with particle size and type. These distributions together with the internal isotope relationships based on early time analysis provide the complete information required to characterize the particle population. The experimental procedures used for the systematic separation of particle samples according to size and type are described elsewhere (*3*) and will not be treated here.

Particle Population

From the standpoint of particle population all nuclear detonations fall into one of two principal categories:

(1) The radioactive particle population consists of environmental materials introduced into the fireball as pre-existing particles. These may be completely or partially melted, but if vaporized, they do not reappear as an identifiable part of the particle population.

(2) The radioactive particle population consists of metal oxide spheres formed by condensation from the vapor state of metallic constituents of the detonated device.

Detonations which produce particle populations of the first category are land surface bursts, land subsurface bursts, vented underground bursts, and tower bursts.

Land Surface Burst. The particle population clearly consists of two distinct components—crystalline particles and "glass" particles. The crystalline particles are local soil material which entered the fireball at a late time and hence were not melted.

The "glass" population which entered the fireball earlier and was subjected to more heating is the more abundant and is peaked at larger particle diameter than is the crystalline population. The size range of the over-all population is from a few tenths of a micron to perhaps a

thousand microns diameter. Crystalline particle densities are those of the local soil material. "Glass" particle densities are equal to or slightly less than those of the local soil particles. Radionuclide partition can be described by a series of linear relationships of the form

$$A/R = a + b\ (V/R) \tag{1}$$

where A/R and V/R are atom ratios for an arbitrary radionuclide, A, and a volatile radionuclide, V, to a refractory radionuclide, R. The parameters a and b are constants for a particular isotope set (A, V, R) for a particular detonation.

Land Subsurface Burst. Everything which was said above about land surface burst applies exactly to the aerial cloud particle population produced by a land subsurface burst in which an aboveground fireball appears. However, a third component of the particle population is found. This component appears to result from soil material which interacted with the fireball at high temperature but which was separated from the fireball early, before the temperature had fallen below the melting point of the soil materials. The particles in this component have diameters ranging from tens of microns to several centimeters and have densities which are apt to be quite low compared with those of the original soil components. The relative abundance of radionuclides in this component is quite constant from sample to sample and is independent of particle size. If we indicate by subscript 1 this third component and by 2,3 the aerial cloud components, radionuclide partitioning can be described by a series of equations of the forms

$$A_{2,3}/R_{2,3} = a + b\ (V_{2,3}/R_{2,3}) \tag{2}$$

$$A/{}_1R_1 = c\ (V_1/R_1) \tag{3}$$

Vented Underground Burst. An underground detonation which produces no visible fireball, but which results in the release of volatile radionuclides through fissures or other vents, produces a single particle class—atmospheric aerosol particles with condensable radionuclides deposited on their surface. Radionuclide abundance is independent of particle size.

Tower Burst. If the energy of the detonation is sufficient to vaporize the entire tower mass, the particle population is like that described for the land surface burst. If, however, the entire tower is not vaporized, the particle population will consist of three identifiable components—the crystalline and "glass" components of the surface detonation plus a metal sphere population which arises from melted (not vaporized) tower materials resolidifying as spheres. Such spheres are metallic rather than metal oxide and exhibit the density and magnetic properties of the tower material. The size range of the spherical component is from a few microns to perhaps a few hundred microns diameter. If we indicate by

subscript 1 the metal sphere component and by 2, 3 the glass, crystalline soil components, radionuclide partitioning can be described by a series of equations of the form

$$A_1/R_1 = a_1 + b\ (V_1/R_1) \tag{4}$$

$$A_{2,3}/R_{2,3} = a_{2,3} + b\ (V_{2,3}/R_{2,3}) \tag{5}$$

The constant coefficient, b, which is related to late surface deposition, is independent of particle composition; hence, it is the same for the soil and the metal sphere populations. The coefficients, a_1, are related to volume deposition and depend on chemical composition of the particles; hence, they would be expected to be different for soil and metal sphere constituents. It would also be expected that the individual types of particles which make up a particular soil (*e.g.*, quartz and feldspar) would exhibit different radionuclide compositions; however, in the soil case the composition variation is independent of particle size so that a single average coefficient, $a_{2,3}$, applies. However, the sphere/soil ratio in general varies with size, so that the radionuclide composition of the sphere population needs to be considered separately.

Detonations of the second category—those which produce particles by condensation from the vapor state—include airbursts and water surface bursts.

Air Burst. Particles produced by condensation are spherical, and range in size from about 0.01μ to perhaps 20μ in diameter. The particles are metal oxides and exhibit densities in the range of the metal oxides of the condensable materials vaporized by the detonation. Radionuclide partitioning can be described (*2*) by a series of equations of the form

$$A/R = (V/R)^n \tag{6}$$

where A, V, and R are as described above, and n is constant for a given radionuclide set for a particular detonation.

Water Surface Burst. When the entire platform of a water surface detonation is vaporized, the primary particle population is exactly like that described under airburst. However, the particles of the primary population act as condensation nucleii for the late-time condensation of sea salts. The salt particles are hygroscopic and eventually dissolve and leave the primary population behind. However, particle transport is affected by the sea salt particle growth which temporarily, at least, produces larger particles than does an airburst.

The above categories of particle forms can be rationalized on the basis that if a condensed-phase material enters the fireball from the environment, vapor condensation will occur onto this material. If no condensed phase is available, condensation from the vapor state will produce a population of metal oxide spheres. Exactly where the transition occurs

in the case of a low altitude airburst, for example, is not known. However, it is to be expected that the transition region is relatively narrow and that almost all detonations will fall clearly into one class or the other.

The following discussion gives an example of the data treatment required to characterize the population for three cases—a land surface burst, a land subsurface detonation, and an airburst detonation. These three examples cover the complete range of types of solutions to the characterization problem.

Characterization of a Land Surface Burst

In this section, the process of characterization of the particle population from a megaton level, Coral Island surface detonation is described. [While the general features of the particle population are illustrated by this example, it should be kept in mind that particular details of behavior could be altered significantly for a similar detonation conducted in a different soil environment.]

The data of Table I are derived from early time radiochemical data reported by Stevenson (*5*). The linearity of the radionuclide ratios was first pointed out in that report. The aerial filter samples were taken at successively later times, 1 and 2, below the reported cloud base, and 3, 4, and 5 in the cloud. The tabulated values of r^A correspond to atom ratio of isotope A to an arbitrary refractory isotope normalized by dividing by the atom ratio in which the two species were formed. Refractory species include the isotopes of the rare earths Eu and Tb as well as ^{45}Ca, ^{89}Zr, ^{44}Sc, and others produced by neutron reactions on stable isotopes. The tabulation has been limited to fission product species. However, the

Table I. Normalized Atom Ratios (Land Surface Detonation)

$$r^A = \frac{N^A/N^{Ref}}{N_0{}^A/N_0{}^{Ref}}$$

	Aerial Filter Samples					
Isotope	*1*	*2*	*3*	*4*	*5*	α^A
^{89}Sr, ^{137}Cs	.616	.635	2.76	10.86	30.82	1.000
^{90}Sr	.629	.796	1.93	6.37	20.39	.545
^{91}Y	.839	.843	1.65	4.92	13.43	.408
^{95}Zr	.973	.947	1.05	1.27	2.21	.034
^{99}Mo	.924	.945	1.18	2.18	4.86	.124
^{140}Ba	.810	1.044	1.77	5.44	14.20	.447
^{141}Ce	.860	.894	1.48	4.34	11.56	.347
^{144}Ce	.938	.970	1.08	1.89	3.89	.094
^{147}Nd	.917	.962	1.13	2.00	4.17	.104
Refractories	1.000	1.000	1.00	1.00	1.00	.000

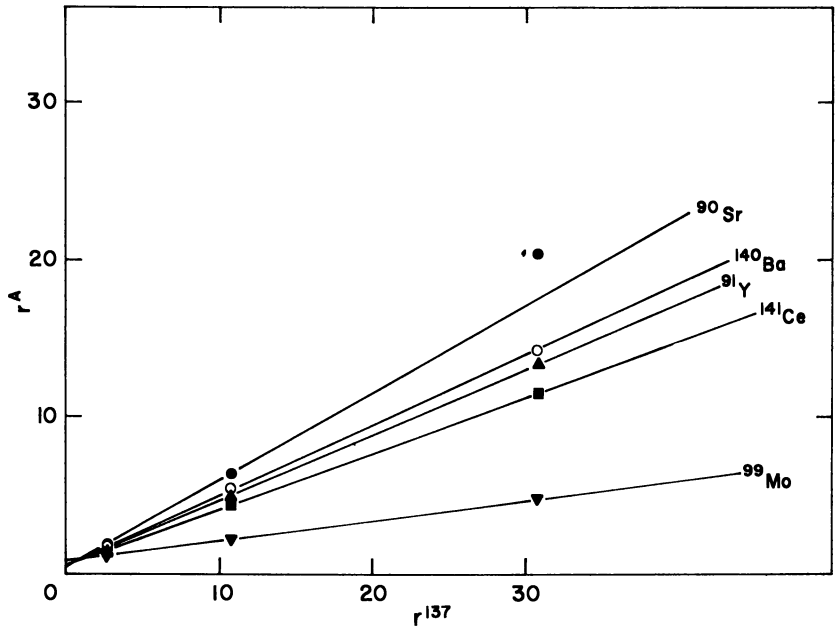

Figure 1. Land surface detonation. Linear relationship of normalized inter-isotopic ratios.

complete study included numerous neutron capture isotopes which behave in completely analogous fashion to the fission products.

The values α^A, listed in the last column of Table I, correspond to the slopes obtained by plotting normalized atom ratios of isotope A against those for ^{137}Cs.

$$\alpha^A = \frac{1}{5} \sum_{i=1}^{5} \left(\frac{r^A - 1}{r^{137} - 1} \right)_i \tag{7}$$

Graphs of r^A *vs.* r^{89} for several isotopes are shown in Figure 1. It is important to note that all the normalized isotopic ratios are equal to unity when the cesium-137/refractory ratio is unity. This fact implies quite clearly that the samples analyzed are representative of the complete particle population. The linearity of the r^A values relative to r^{137} indicates that there are two and only two isotopic compositions present in the particle population and that the isotopic composition of any arbitrary particle sample is a linear combination of these. In the case of subsurface detonations where a third particle class *is* observed, the normalized isotopic ratios for the other isotopes are not equal to unity when the cesium-137 ratio is. A minimum conclusion is that for this particular Coral Island

surface detonation there is no missing particle class which carries a significant fraction of the radionuclide population.

A second implication of the linearity can be seen better if the equation is rewritten in terms of atoms, N^A.

$$\frac{N^A/N^{Ref}}{N_0{}^A/N_0{}^{Ref}} = (1 - \alpha^A) + \alpha^A \frac{N^{137}/N^{Ref}}{N_0{}^{137}/N_0{}^{Ref}} \quad (8)$$

This form of the equation describes the manner in which r^A values were determined. However, Equation 8 can be replaced by its exact equivalent

$$N^A/N_0{}^A = (1 - \alpha^A)\ N^{Ref}/N_0{}^{Ref} + \alpha^A\ (N^{137}/N_0{}^{137}) \quad (9)$$

The equation in this form states that in the samples analyzed the distribution of any radionuclide, A, can be expressed as a linear combination of the distribution of two species, a refractory and ^{137}Cs. Therefore, we need to determine only refractory distribution, ^{137}Cs distribution, and mass distribution with particle size and the distribution of all other isotopic species for which α^A values are known and can be calculated. The refractory species used is ^{155}Eu. It has a half-life of 1.811 years and two easily resolved gamma photopeaks so that its abundance as well as that of ^{137}Cs can be determined readily by gamma spectrometry.

Table II. Specific Activity Data

Particle Diameter, μ	*<D>, μ*	*^{155}Eu Atoms / Mg (× 10^{-9})*	*Atoms − 22.32/<D> / Mg (× 10^{-9})*
> 710	830	—	—
500-710	585	.26	.22
350-500	412	—	—
250-350	291	1.35	1.27
177-250	207	3.00	2.89
125-177	146	3.24	3.09
53-125	74	5.52	5.22
37-53	44	8.95	8.44
25-37	30	12.64	11.90
18.5-25	21	13.46	12.38
12.5-18.5	15	13.46	11.97
9.25-12.5	10.6	12.78	10.67
6.25-9.25	7.5	8.45	5.47
4.6-6.2	5.3	7.57	3.37
3.1-4.6	3.7	7.35	1.30
2.3-3.1	2.6	8.45	0
1.6-2.3	1.9	11.88	0
1.2-1.6	1.4	17.35	0
.8-1.2	1.0	20.48	0

Separated weighed particle fractions from residual portions of the filter papers listed in Table I were analyzed to determine the ^{155}Eu specific activity data shown in Table II. The mean diameter, $<D>$, listed in the table is the harmonic mean for the diameter range indicated. The origin time values of ^{155}Eu atom/Mg listed in the third column of Table II are shown graphically in Figure 2. The sloping lines correspond to a $1/<D>$ variation of the specific activity. Specific activity which varies as $1/<D>$ implies surface attachment of the isotope. Specific activity which does not vary with particle size implies that the isotope is volume distributed. The graph shows clearly two regions of surface distribution separated by an intermediate region which may reflect a volume distribution or be caused by a combination of two surface distributions. The surface distribution in the small diameter region is attributed to late condensation on the crystalline component of the population. That is, ^{155}Eu which was still uncondensed at late times, deposits uniformly on the surface of all particles present in the cloud. The smaller of these particles were ones which had entered late and were not melted and hence retained their original crystalline form.

The surface distribution in the large diameter region of the graph is refractory rich and thus corresponds to particles which entered the cloud early. In the intermediate size range there is a transition between the two surface distributions. The $^{155}Eu/Mg$ values in this region can

(Land Surface Detonation)

$\left(\frac{W_{xtal}}{W_{total}}\right)_1$	$\left(\frac{W_{xtal}}{W_{total}}\right)_2$	$\frac{^{137}Cs\ Atoms}{Mg\ (\times 10^{-9})}$
0	0	3
0	0	3
0	0	4
0	0	4
0	0	5
0	0	6
0	0	—
0	0	—
.041	0	—
.338	0	—
.550	.018	—
.731	.125	—
.946	.551	141
.927	.725	233
1.000	.893	—
1.000	1.000	—
1.000	1.000	—
1.000	1.000	—
1.000	1.000	1170

be accounted for by assuming that the two particle populations overlap in this region and that the observed values result from mixing of the two different ^{155}Eu/Mg values. For the crystalline population and for late time condensation on the glass this value is given by

$$(^{155}\text{Eu atoms/Mg}) = 22.32 \times 10^9/\langle D\rangle \text{ (microns)} \quad (10)$$

To arrive at the ^{155}Eu atoms/Mg caused by early condensation, this value is subtracted from the observed ratio and recorded in Column 4, Table II. For particle diameters greater than $\langle D\rangle = 30\mu$, the values in Column 4 can be fitted by

$$(^{155}\text{Eu atoms/Mg}) = 371.4 \times 10^9/\langle D\rangle\ (\mu) \quad (11)$$

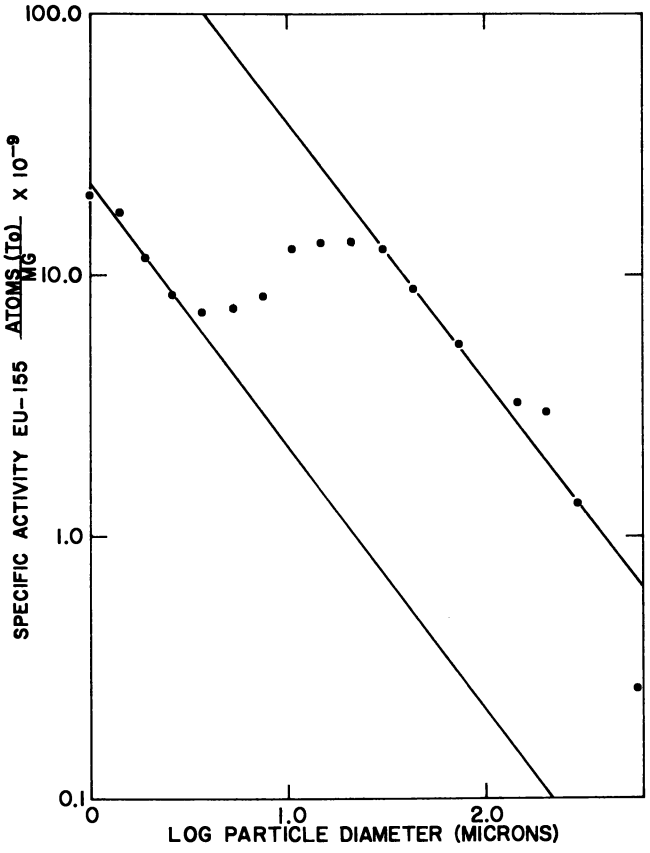

Figure 2. Land surface detonation. Refractory specific activity vs. *particle diameter.*

Below $<D> = 30\mu$ this relationship may continue, or at the other extreme if all deposition is volume distributed,

$$\frac{^{155}\text{Eu atoms}}{\text{Mg}} = \text{Constant} = 12.38 \times 10^9 \tag{12}$$

The values derived in Column 4 are presumed to result from a linear combination of the value given by Equations 10 and either 11 or 12. The calculated fraction of particle mass which was associated with Equation 10 is given in Column 5 for Equation 11 being true, and Column 6 for Equation 12. These mass fractions were calculated using the following two relationships

$$\left[\frac{W_{\text{xtal}}}{W_{\text{total}}}\right]_1 = \frac{371.4 - <D> (^{155}\text{Eu/Mg})_{\text{Col 4}}}{371.4 - 22.32} \tag{13}$$

or

$$\left[\frac{W_{\text{xtal}}}{W_{\text{total}}}\right]_2 = \frac{12.38 - (^{155}\text{Eu/Mg})_{\text{Col 4}}}{12.38 - 22.32/<D>} \tag{14}$$

The values will be used below in connection with determination of the size distribution of the over-all particle population.

In Column 7 of Table II, a limited number of values for ^{137}Cs atoms/Mg are recorded. These data are incomplete at this time because only recently has it become possible to recover the particles from aerial filters without losing ^{137}Cs activity. Additional separations are in process to provide additional data points for the ^{137}Cs distribution. The limited data can be described adequately by the single equation

$$\frac{^{137}\text{Cs atoms}}{\text{Mg}} = \frac{1170 \times 10^9}{<D>} \tag{15}$$

This implies that all ^{137}Cs is surface deposited at late time, a not unreasonable finding in view of the 3.9 minute half-life of ^{137}Xe, the ^{137}Cs precursor. In any event, it is not expected that a very large fraction of the ^{137}Cs will be associated with the early-time condensation phase.

Up to this point, the evidence for two particle populations has been based solely on the refractory specific activity. Additional confirmation is based on the observed particle size distribution by mass of an aerial filter sample. A portion of the aerial filter sample designated as "2" in Table I, was separated into size fractions, and the weight distribution of the fraction is shown in Figure 3. The ordinate values are simply:

$$\frac{dN_w}{dx} = \frac{W_i/\Sigma W_i}{\Delta \log D} \tag{16}$$

where W_i is the weight of the i^{th} size fraction, and x is the logarithm of the particle diameter in microns. The data points are fitted by a linear

combination of two gaussian curves to obtain a two component log-normal representation of the data. It is not proposed that the distribution is representative of the over-all population. First, the radiochemical data of Table I say that this sample is depleted in volatile species. Second, the sample, which was the earliest collected, was taken 1.5 hours after detonation so that it may be expected to be depleted in larger size particles. Because of the lateness of sampling, no really precise determination of the over-all size distribution can be made. However, it is

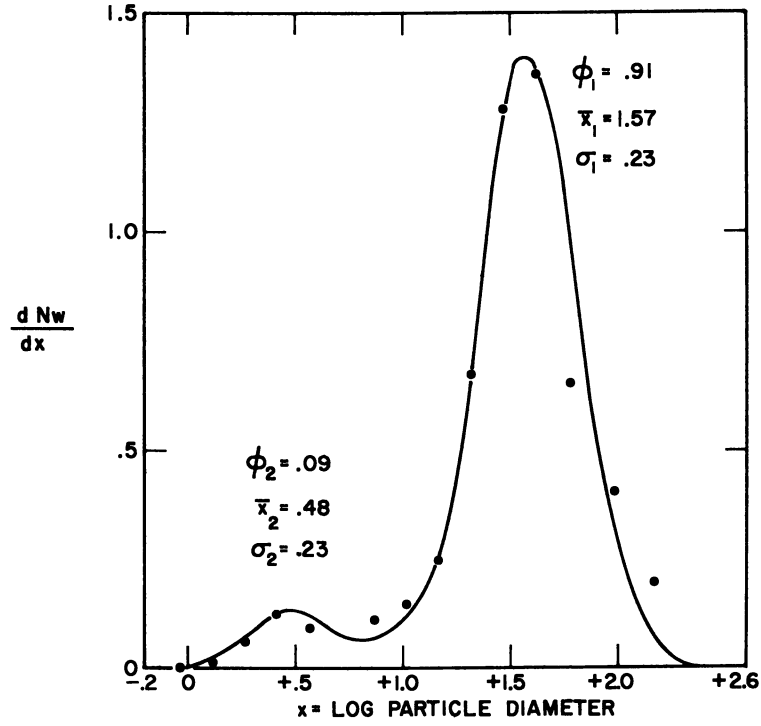

Figure 3. Land surface detonation. Particle size distribution (mass).

possible to set some reasonable limits on the nature of the distribution using the information from the specific activity measurements. The resolution is based on four premises as follows:

(1) The population consists of two components. This is based on specific activity data and size distribution observed in aerial sample.

(2) The upper size limit of the larger sized population is 1000μ. This is based on review of the size/frequency data for close-in, early-time fallout collections. All reported size-frequency curves were dropping vertically between 800 and 1000μ.

(3) The lower size limit of crystalline population is 0.31μ. This is based on experimental determination that ^{137}Cs atoms/Mg $\cong$ 2400 $\times$ 10^9 for fractions consisting of all particles less than 1.2μ in diameter. This value coupled with the equation $^{137}\text{Cs/Mg} = 1170 \times 10^9/\langle D \rangle$ implies that $\langle D \rangle$ is 0.49μ. However, if $1/2\ (1/2 + 1/D_{\min}) = 1/.49$, $D_{\min}$ is equal to 0.31μ.

(4) The over-all distribution function consists of a linear combination of two lognormal functions. This is based on the observation that size distribution from very early aerial clouds samples from subsurface detonations are described accurately by the lognormal form of distribution. (This is shown below in connection with subsurface detonation analyses.) It is also supported by the work of particle analysts in industry, who find that particle population produced by crushing or grinding are described by lognormal distributions.

The complete description of a two-component population in the lognormal form requires the determination of five parameters. Where x is used to denote the logarithm of the particle diameter in microns, σ the standard deviation of the variable x, ϕ the fraction of the total mass in one of the two populations and subscript 1 to denote the "glass" component, 2 the crystalline, we have:

$$\frac{dN_w}{dx} = \phi_1/\sqrt{2\pi}\,\sigma_2 \exp\left[-\left(\frac{(x_1 - x)^2}{2\,\sigma_1^2}\right)\right] + \phi_2/\sqrt{2\pi}\,\sigma_1 \exp\left[-\left(\frac{(x_2 - x)^2}{2\,\sigma_2^2}\right)\right] \tag{17}$$

Since $\phi_1 + \phi_2 \equiv 1$, there are five parameters to be determined, σ_1, σ_2, x_1, x_2, and ϕ_1. Since the estimation is based on the range of sizes observed for each population and since these ranges depend on the form assumed for the ^{155}Eu/Mg function in the less than 37-μ range, it is necessary to consider the two cases separately.

Case I. For the "glass" population $^{155}\text{Eu/Mg} = \dfrac{371.4 \times 10^9}{\langle D \rangle}$ for all $\langle D \rangle$. Referring to Column 5, Table II, it is seen that $D_{\min}$ for the "glass" population is 4.6μ, and $D_{\max}$ for the crystalline population is 37μ. If we take 6 σ equal to the particle size range and use subscripts 1 and 2 to denote "glass" and crystalline components respectively, then

$$\sigma_2 = \frac{\log 37 - \log .31}{6} = .3461 \tag{18}$$

$$\sigma_1 = \frac{\log 1000 - \log 4.6}{6} = .3895 \tag{19}$$

If we then take $x = x_{\max} - 3\,\sigma = x_{\min} + 3\,\sigma$,

$$x_1 = \log 1000 - 1.1685 = 1.8315 \quad (67.84\mu) \tag{20}$$

$$x_2 = \log 37 - 1.0383 \quad = 0.5299 \quad (3.39\mu) \tag{21}$$

We now wish to determine ϕ_1 and ϕ_2 so that the ratio of ^{137}Cs to ^{155}Eu for the whole population is equal to the ratio in which they were formed. Based on the r^{137} values of Table I, and the atom ratios observed for residual portions of the filter samples, we find:

$$\frac{N_0{}^{137}}{N_0{}^{155}} = \frac{N^{137}/N^{155}}{r^{137}} = 8.14 \tag{22}$$

This value falls below the theoretical ratio for these isotopes but is based on the same efficiency and half-life data which were used to derive the atoms/Mg relationships. Therefore, we will find ϕ_1 and ϕ_2 so that the ratio of the total ^{137}Cs to the total ^{155}Eu equals 8.14. It is a property of the lognormal form of distribution function that if particle mass distribution is described by x and σ, then the surface/volume distribution is given by (*4*):

$$x^1 = x - \frac{2.303\,\sigma^2}{2} = x - 1.1515\,\sigma^2 \tag{23}$$

$$\sigma^1 = \sigma$$

Therefore

$$x_1{}^1 = 1.6568\ (<D>_1{}^1 = 45.37\mu)$$
$$x_2{}^1 = 0.3920\ (<D>_2{}^1 = 2.466\mu) \tag{24}$$

where $<D>_i{}^1$ is the reciprocal of the arithmetic mean of $1/D$.

$$\left(\frac{^{137}Cs}{Mg}\right) = \left(\phi_1 \frac{1170}{45.37}\,{}^1\phi + \frac{1170}{2.466}\right) \times 10^9 \tag{25}$$

$$\left(\frac{^{155}Eu}{Mg}\right) = \left(\phi_1 \frac{341.4}{45.37}\,{}^2\phi + \frac{22.32}{45.37} + \phi_2 \frac{22.32}{2.466}\right) \times 10^9 \tag{26}$$

$$\phi_1 = 1 - \phi_2 \tag{27}$$

$$^{137}Cs = 8.14\ ^{155}Eu \tag{28}$$

The simultaneous solution of Equations 25–28 gives:

$$\phi_1 = .910 \qquad \phi_2 = .090 \tag{29}$$

so that $(^{137}Cs/Mg)_{total} = 66.16 \times 10^9$ and $(^{155}Eu/Mg)_{total} = 8.13 \times 10^9$. For Case I, the complete description of the particle size distribution by mass is:

$$\frac{dN^w}{dx} = \frac{.910}{.3895\sqrt{2\pi}} \exp\left[-\left(\frac{1.8315 - x}{.3895\sqrt{2}}\right)^2\right] + \frac{.090}{.3461\sqrt{2\pi}} \exp\left[-\left(\frac{.5299 - x}{.3461\sqrt{2}}\right)^2\right] \tag{30}$$

For the ^{137}Cs distributions of the same two populations

$$\frac{\phi_1^{137}}{\phi_2^{137}} = \frac{.91/45.37}{.09/2.466} \text{ so that } \phi_1^{137} = .355 \quad \phi_2^{137} = .645 \tag{31}$$

and for surface distribution, the geometric mean x_2 is equal to the geometric mean of the mass distribution x, less $2.303\,\sigma^2$, so that the ^{137}Cs distribution is given by:

$$\frac{dN^{137}}{dx} = \frac{.355}{.3895\sqrt{2\pi}} \exp\left[-\left(\frac{1.4281 - x}{.3895\sqrt{2}}\right)^2\right] + \frac{.645}{.3461\sqrt{2\pi}} \exp\left[-\left(\frac{.1760 - x}{.3461\sqrt{2}}\right)^2\right] \tag{32}$$

For the ^{155}Eu distribution of the same two populations

$$\frac{\phi_1^{155}}{\phi_2^{155}} = \frac{(^{155}\text{Eu/Mg})_1\,\phi_1/\langle D\rangle_1^1}{(^{155}\text{Eu/Mg})_2\,\phi_2/\langle D\rangle_2^1} \tag{33}$$

$$\frac{\phi_1^{155}}{\phi_2^{155}} = \frac{393.7 \times 91/45.37}{22.32 \times .09/2.466} \text{ so that } \phi_1^{155} = .906,\ \phi_2^{155} = .094 \tag{34}$$

$$\frac{dN^{155}}{dx} = \frac{.906}{.3895\sqrt{2\pi}} \exp\left[-\left(\frac{1.4281 - x}{.3895\sqrt{2}}\right)^2\right] + \frac{.094}{.3461\sqrt{2\pi}} \exp\left[-\left(\frac{.1760 - x}{.3461\sqrt{2}}\right)^2\right] \tag{35}$$

Case II. For the "glass" population $^{155}Eu/Mg$ is:

$$\text{If } \langle D\rangle >> 30\text{: } ^{155}\text{Eu/Mg} = \frac{371.4 \times 10^9}{\langle D\rangle} \tag{36}$$

$$\text{If } \langle D\rangle < 30\text{: } ^{155}\text{Eu/Mg} = 12.38 \times 10^9 \tag{37}$$

Referring to Column 6, Table II, D_{min} for the "glass" population is 3.1μ, and D_{max} for the crystalline population is 18.5μ. The method for calculating the parameters of the distribution functions for Case II is completely analogous to that used in Case I and will not be given in detail. In Table III the parameters of the distribution functions for the two cases are given. The data of Table III together with the values of α^A listed in Table I constitute a complete characterization of the particle for a land surface detonation.

Land Subsurface Detonation

A subsurface detonation in the low kiloton yield range which produced an aboveground fireball and a three component particle population is treated in this section.

Table III. Parameters of Distribution Functions (Land Surface Burst)

	Case I			*Case II*		
Quantity	*Mass*	*^{137}Cs*	*^{155}Eu*	*Mass*	*^{137}Cs*	*^{155}Eu*[a]
ϕ_1	.910	.355	.906	.918	.378	(.296) .607
σ_1	.3895	.3895	.3895	.4181	.4181	.4181
x_1	1.8315	1.4821	1.4821	1.7457	1.3431	(1.7457) 1.3431
$<D>_1$ (μ)	67.8	30.4	30.4	55.7	22.0	(55.7) 22.0
ϕ_2	.090	.645	.094	.092	.622	.097
σ_2	.3461	.3461	.3461	.2960	.2960	.2960
x_2	.5299	.1760	.1760	.3792	.2008	.2008
$<D>_2$ (μ)	3.39	1.50	1.50	2.39	1.59	1.59
Atoms/Mg $\times 10^{-9}$	—	66.2	8.13	—	81.2	9.97

[a] Values in parentheses apply below 30μ; companion value applies above 30μ.

Table IV. Normalized Atom Ratios (Subsurface Detonation)

$$r_A = \frac{N^A/N^{147}}{N_1^A/N_1^{147}}$$

		Aerial Filter Samples						
Iotope	*Local Fallout*	*1*	*2*	*3*	*4*	*5*	*6*	*Remote Fallout*
^{89}Sr	1.00	87.5	87.9	161.2	181.0	200.3	992.1	2.81
^{99}Mo	1.00	1.10	1.18	1.08	1.24	1.17	1.14	1.06
^{95}Zr	1.00	1.06	1.10	1.04	1.03	1.08	.88	1.05
^{137}Cs	1.00	104.4	108.6	200.6	203.9	238.5	1292.2	2.91
^{140}Ba	1.00	7.26	7.00	11.6	12.5	12.5	60.8	1.37
^{141}Ce	1.00	2.14	2.05	2.76	2.93	3.04	9.98	1.07
^{144}Ce	1.00	1.00	1.04	0.96	1.00	.99	1.07	0.98
^{156}Eu	1.00	1.01	.98	—	.98	1.00	—	1.02

In Table IV, the atom ratio data obtained by radiochemical analysis of a series of aerial filter and fallout samples are presented. The analyses were performed by the Radiochemistry Division at Lawrence Radiation Laboratory, Livermore. The atom ratios, which we designate by r_1^A in this case, are in the form $\frac{N^A/N^{147}}{N_1^A/N_1^{147}}$ where the denominator, N_1^A/N_1^{147} is the atom ratio observed for isotope A relative to Nd^{147} in the extreme close-in fallout collections. These samples all gave the same isotopic analyses, *and* when separated into particle size fractions, both the isotopic abundances and isotopic specific activities were independent of particle size. This is positive evidence that none of the isotopes were surface distributed, and this is taken to indicate that this particle population left the condensing system at very early time, before the temperature had

decreased to below particle melting temperature. The aerial filter samples 1 through 6 were taken at successively later times in the radioactive cloud. These data internally fit a linear relationship, $r_1^A = a + br_1^{89}$, but the point 1, 1 which would represent the isotopic ratio relationship for the close-in fallout does *not* fall on the line. Thus, the aerial cloud particles exhibit the same type of two-component isotopic distribution as the aerial cloud samples from the Coral Island surface burst. However, a third component which is missing from the cloud is required to account for the total isotopic partitioning. The column of Table IV which is labeled "remote fallout" corresponds to a sample taken a few miles from the detonation point and is a mixture of all three components.

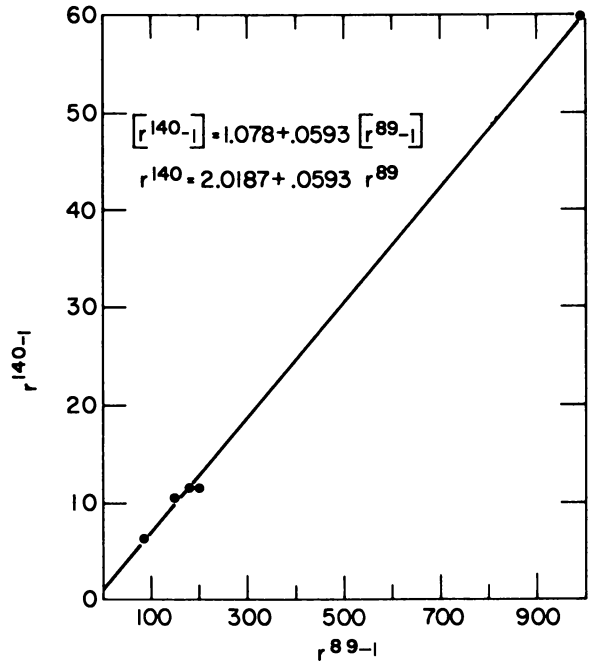

Figure 4. Land subsurface detonation. Aerial filter samples.

The isotopic data can be used to calculate the partitioning. In the calculation the subscript 0 indicates original amount formed, 1 indicates extreme close-in fallout population, 2 indicates the total aerial cloud population. To resolve a three-component system, it is necessary to use three isotopes. ^{140}Ba, ^{89}Sr, and ^{147}Nd are used in this illustration. Other isotope sets may be used providing only that their relative abundance

of formation is known. The internal relationship between the three isotopes in the aerial cloud sample is shown in Figure 4. To minimize the use of superscripts in the equations we define:

$$\mathrm{Ba}_i = N_i^{140}/N_0^{140} \tag{38}$$

$$\mathrm{Sr}_i = N_i^{89}/N_0^{89} \tag{39}$$

$$\mathrm{Nd}_i = N_i^{147}/N_0^{147} \tag{40}$$

From analysis of aerial cloud samples:

$$N_2^{140}/N_1^{140} = 2.019\, N_2^{147}/N_1^{147} + .0593\, N_2^{89}/N_1^{89} \tag{41}$$

Hence:

$$\frac{N_2^{140}/N_0^{140}}{N_1^{140}/N_0^{140}} = 2.019\, \frac{N_2^{147}/N_0^{147}}{N_1^{147}/N_0^{147}} + .0593\, \frac{N_2^{89}/N_0^{89}}{N_1^{89}/N_0^{89}} \tag{42}$$

or:

$$\frac{\mathrm{Ba}_2}{\mathrm{Ba}_1} = 2.019\, \frac{\mathrm{Nd}_2}{\mathrm{Nd}_1} + .0593\, \frac{\mathrm{Sr}_2}{\mathrm{Sr}_1} \tag{43}$$

From atom ratios observed in local fallout and expected values for these ratios:

$$\mathrm{Ba}_1/\mathrm{Nd}_1 = .7481 \tag{44}$$

$$\mathrm{Sr}_1/\mathrm{Nd}_1 = .1891 \tag{45}$$

Hence, combining Equations 43, 44, and 45:

$$1.3368\, \mathrm{Ba}_2 = 2.019\, \mathrm{Nd}_2 + .3136\, \mathrm{Sr}_2 \tag{46}$$

But

$$\mathrm{Ba}_2 = 1 - \mathrm{Ba}_1 = 1 - .7481\, \mathrm{Nd}_1 = 1 - .7481 + .7481\, \mathrm{Nd}_2 \tag{47}$$

and

$$\mathrm{Sr}_2 = 1 - \mathrm{Sr}_1 = 1 - .1891\, \mathrm{Nd}_1 = 1 - .1891 + .1891\, \mathrm{Nd}_2 \tag{48}$$

since isotopes are accounted for completely between the aerial cloud and local fallout populations. Solving Equations 46, 47, and 48, we find

$$\mathrm{Nd}_2 = .076 \qquad \mathrm{Nd}_1 = .924 \tag{49}$$

$$\mathrm{Ba}_2 = .310 \qquad \mathrm{Ba}_1 = .690 \tag{50}$$

$$\mathrm{Sr}_2 = .826 \qquad \mathrm{Sr}_1 = .174 \tag{51}$$

The partition of other isotopes may be calculated from the above partition values and the equations of the aerial cloud data.

$$r_1^{\mathrm{A}} = a + b r_1^{89} \tag{52}$$

so that

$$N_2^{\mathrm{A}}/N_1^{\mathrm{A}} = a\, N_2^{147}/N_1^{147} + b\, N_2^{89}/N_1^{89} \tag{53}$$

Values *a* and *b* for the fission product isotopes and the partition factors α_1 and α_2 are listed in Table V; α_1, for a given isotope, is the fraction which was retained by the local fallout "glass" particles, and α_2 is the fraction released to the cloud. Thus, from Table V, α_1^{137} is 0.153 which indicates that 15.3% of the ^{137}Cs is retained by the local glass particles. It is interesting to note that the independent yield of cesium in the 137 mass chain is approximately 17%—the balance of the chain is formed as tellurium, iodine, and xenon.

Table V. Fission Product Distribution Parameters (Land Subsurface Detonation)

Isotope	a	b	α_1	α_2
^{89}Sr	—	—	.174	.826
^{95}Zr	1.000	0.0	.924	.076
^{99}Mo	1.147	0.0	.916	.084
^{137}Cs	− .190	1.190	.153	.847
^{140}Ba	2.019	.0593	.690	.310
^{141}Ce	1.220	.00875	.863	.137
^{147}Nd	—	—	.924	.076

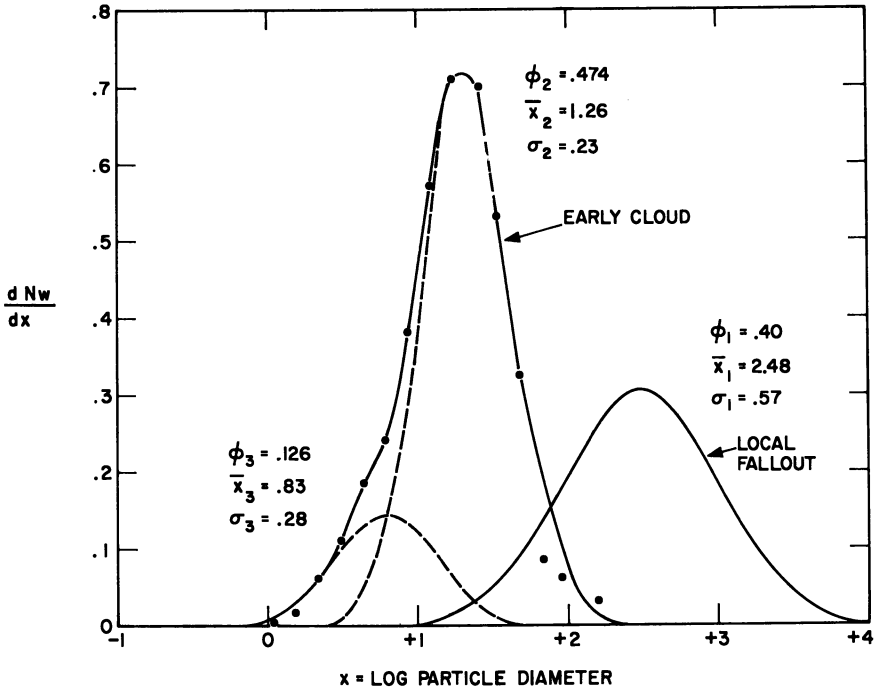

Figure 5. Land subsurface detonation. Particle size distribution (mass).

Note that although only fission product species have been listed, comparable analytical data for numerous neutron capture isotopes show that these behave in a manner completely analogous to the fission products.

As in the case of the land surface burst, complete characterization of the particle population requires only that particle mass, a volatile species, and a refractory species distribution with particle size be determined. All other isotopic distributions may be deduced from the istotope partition calculations described above. In the subsurface detonation, the earliest aerial cloud sample was obtained in the cloud 15 minutes after detonation. The early sample was, therefore, completely representative of the aerial cloud particle population. In Figure 5 the results of the size analysis on a weight basis are shown. Included for comparison is a size distribution for the early, local fallout material. The local fallout population and the aerial cloud population are separated completely from the time of their formation.

The values of ϕ_1, the fraction of the mass in the three populations may be calculated from the specific activity of the ^{147}Nd, together with the previously derived ^{147}Nd partition. The ^{147}Nd specific activity for the local fallout samples was found to be:

$$\frac{N_1{}^{147}}{Mg_1} = 1.05 \times 10^9 \frac{\text{atoms}}{\text{Mg}} \tag{54}$$

(Where Mg_1 designates the fraction of particle mass in the i^{th} component.) This value is corrected from that observed for the gross fallout samples by about a factor of two. The radioactive particles in this population are uniformly of low density because they have been melted and resolidified. These particles contain numerous voids and occlusions and hence have densities well below normal soil density. A density separation in fluid of density just below normal density produces a division of the particles so that essentially 100% of the activity is associated with the light fraction, while perhaps 50% of the original mass is in this fraction. The specific activity used is that for the light fraction. The gross specific activity of ^{147}Nd in the early air filter sample, which represents the entire cloud population, was found to be:

$$\frac{N_2{}^{147}}{Mg_2} = .0515 \times 10^9 \frac{\text{atoms}}{\text{Mg}} \tag{55}$$

Equations 54 and 49 combine to give:

$$\frac{Mg_1}{N_0{}^{147}} = \frac{N_1{}^{147}/N_0{}^{147}}{N_1{}^{147}/Mg_1} = \frac{.924}{1.05 \times 10^9} = 1.48 \times 10^{-9} \tag{56}$$

Similarly Equations 55 and 49 give:

$$\frac{Mg_2}{N_0^{147}} = \frac{N_2^{147}/N_0^{147}}{N_2^{147}/Mg} = \frac{.076}{.0515 \times 10^9} = 0.88 \times 10^{-9} \quad (57)$$

The mass partition from Equations 56 and 57 is then,

$$\frac{Mg_1}{Mg_{total}} = \frac{.88}{.88 + 1.48} = 0.40 \text{ and } \frac{Mg_2}{Mg_{total}} = \frac{1.48}{.88 + 1.48} = 0.60 \quad (58)$$

Thus, 60% of the total radioactive particle mass is found in the aerial cloud population. This is partitioned between the early, "glass" fraction and the late, crystalline fraction in accordance with the areas under the two lognormal curves which combine to produce the observed size distribution with mass.

The behavior of the refractory and volatile species in the various particle populations may be summarized.

(1) Volatile species (^{137}Cs) is volume distributed in the local fallout and exhibits constant specific activity

$$\left(\frac{N_1^{137}}{Mg_1}\right) = .55 \times 10^9 \frac{\text{atoms}}{Mg} \quad (59)$$

(2) In the aerial cloud the ^{137}Cs is distributed uniformly over the surfaces of both populations, and its specific activity can be described by

$$\left(\frac{N_1^{137}}{Mg}\right)_{2,3} = \frac{29.6 \times 10^9}{\langle D \rangle} \quad (60)$$

(3) The refractory species, of which ^{147}Nd is typical, appear not to be associated at all with the late entering crystalline population. In the local fallout, ^{147}Nd exhibits constant specific activity 1.05×10^9 atoms/Mg, and in the early entering "glass" population the refractories appear on the basis of data obtained thus far to be primarily surface distributed.

$$\frac{N_2^{147}}{Mg_2} = \frac{.875 \times 10^9}{\langle D \rangle} \frac{\text{atoms}}{Mg} \quad (61)$$

However, the observed values in the intermediate size range are obscured by the crystalline population contribution which contributes to mass but not to ^{147}Nd.

There are two size ranges of the over-all population in which isotopic composition does not vary with particle size. Particles greater than about 200μ in diameter exhibit the uniform composition of the local fallout particles. Particles less than 2μ in diameter exhibit a constant isotopic composition which consists of a mixture of the surface deposited volatile species. The parameters of the functions which describe the mass, refractory, and volatile distributions are given in Table VI. As in the

Table VI. Parameters of Distribution Functions (Land Subsurface Burst)

Quantity	*Mass*	*Volatile* (^{137}Cs)	*Refractory* (^{147}Nd)
ϕ_1	.400	.153	.924
σ_1	.570	.570	.570
x_1	2.480	2.480	2.480
$<D>_1$ (μ)	302.	302.	302.
$(Atoms/Mg)_1 \times 10^{-9}$	—	.55	1.05
ϕ_2	.474	.480	.076
σ_2	.230	.230	.23
x_2	1.260	1.138	1.138
$<D>_2$ (μ)	18.2	13.7	13.7
$(Atoms/Mg)_2 \times 10^{-9}$	—	1.87	.052
ϕ_3	.126	.367	0.00
σ_3	.280	.280	—
x_3	.830	.649	—
$<D>_3$ (μ)	6.8	4.5	—
$(Atoms/Mg)_3 \times 10^{-9}$	—	.55	0.00

case of the land surface detonation the complete distribution is a linear combination of the components:

$$\frac{dN}{dx} = \sum_{i=1}^{3} (\phi_i/\sigma_i \sqrt{2\pi}) \exp\left[-\left(\frac{x_i - x}{\sigma_i \sqrt{2}}\right)^2\right] \quad (62)$$

where x is the logarithm of particle diameter, ϕ_i is the fraction of the constituent associated with particle group, i, and σ_i is the standard deviation of x relative to its mean value x_i. Since there are three particle groups, a total of eight parameters are needed to characterize each quantity—mass, volatile species, and refractory species. The behavior of the other isotopes can be reconstructed from the volatile, refractory behavior combined with partition data given in Table V. The three-component distribution produced by the land subsurface detonation appears to be the most complex pattern produced.

Airburst Detonation

Airburst detonations produce particles in the smaller size ranges so that the earliest air filter samples are generally completely representative of the entire population. However, the analysis of submicron size particles is more difficult than the analysis of the larger particles found in surface detonation samples. The LRL Particle Analysis Program is currently engaged in analyzing airburst particle populations. However, data are incomplete, and to illustrate the characterization problem for

this type of event, we will use data obtained in the analysis of a low kiloton range yield airburst and reported by K. Johnston (5). The radiochemical data obtained by analyzing early and late aerial filter samples from this event are presented in Table VII. These are unpublished data from the LRL Radiochemistry Division. The number of analyses performed on this event are not sufficient to establish the log-log relationship between the radioisotopic ratios. However, this relationship has been explored and justified by Freiling (2), and we will accept its validity.

Table VII. Normalized Atom Ratios (Air Burst)

$$r_A = \frac{N^A/N^{95}}{N_0{}^A/N_0{}^{95}}$$

Isotope	*Early Air Sample*	*Late Air Sample*	*Exponent in* $r_A = (r_{137})^x$
^{89}Sr	1.00	1.474	1.045
^{90}Y	1.00	1.297	.700
^{91}Y	1.00	1.346	.801
^{99}Mo	1.00	1.012	.0321
^{111}Ag	1.00	1.328	.765
^{115}Cd	1.00	1.386	.877
^{136}Cs	1.00	1.419	.943
^{137}Cs	1.00	1.449	1.000
^{140}Ba	1.00	1.351	.811
^{141}Ce	1.00	1.215	.525
^{144}Ce	1.00	1.011	.0295
^{147}Nd	1.00	1.022	.0585
^{153}Sm	1.00	1.00	0.00
^{156}Eu	1.00	1.00	0.00

For a series of successively later air samples, the interisotopic ratios can be represented accurately by a series of equations of the form:

$$\frac{A}{R} = \left(\frac{V}{R}\right)^{N_A} \tag{63}$$

The problem again reduces to one of determining the distribution of mass, a volatile species, and a refractory species, all with particle size. These distributions together with the interisotopic relationships would constitute complete characterization of the particle population. However, at the present time the form of various distribution functions cannot be specified uniquely. In Table VIII, the distribution data for a refractory species, ^{95}Zr, and a volatile species, ^{137}Cs, are given in the integral form. Also listed are values for the number distribution estimated on the basis that the ^{95}Zr atoms are volume distributed so the number of particles in each size interval is proportional to the number of ^{95}Zr atoms

Table VIII. Distribution Data (Airburst Particles)

Particle Diameter, μ	*Logarithm of Diameter*	*Percent in Particles Greater than Indicated Size*		
		^{95}Zr	^{137}Cs	*Number (est.)*
.1	−1.0	99.95	87.63	21.60
.25	− .602	99.87	86.39	8.31
.50	− .301	99.60	81.75	5.25
1.0	0.0	97.86	59.05	2.75
2.5	+ .399	84.86	8.05	.59
3.75	+ .575	47.36	—	.13
5.0	+ .699	24.96	—	.037

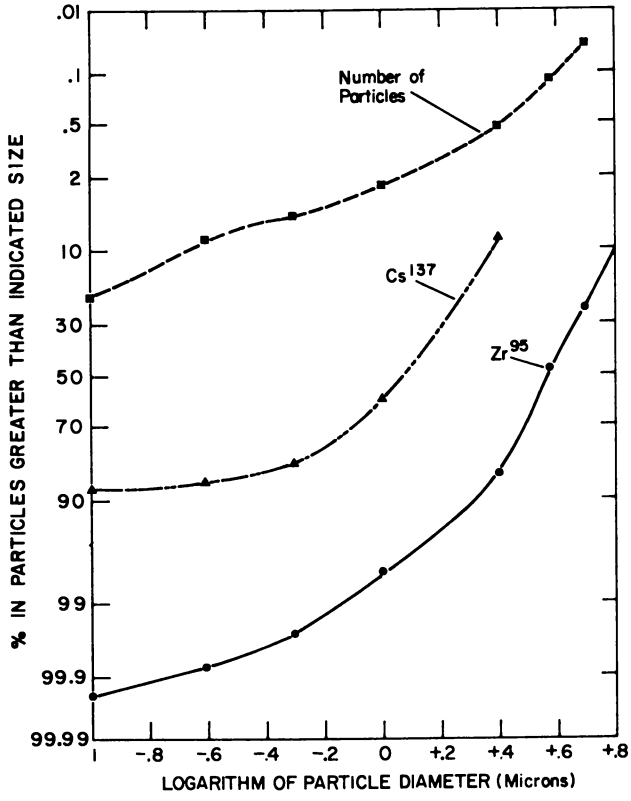

Figure 6. Airburst distribution. Data lognormal form.

divided by the mean diameter cubed. [On this basis, the size distribution by mass would be the same as that for the ^{95}Zr which is assumed to be volume distributed. Such an assumption may or may not be valid and should be compared with that of Johnston which was that gross gamma

activity per unit volume is constant.] In Figure 6, these data are presented as percent oversize *vs.* logarithm of particle diameter on a normal probability coordinate graph. If the distribution were a single, log-normal distribution function, a straight line would result, whose intercept with the 50% ordinate would be x and whose slope would be related to σ. The curvature of the plots indicates that if the quantities are distributed normally with respect to the logarithm of particle diameter, the distribution consists of more than a single component. Since all particles are observed to fall into a single class of metal oxide spheres, it is perhaps unreasonable to expect that the distribution function would be bimodal.

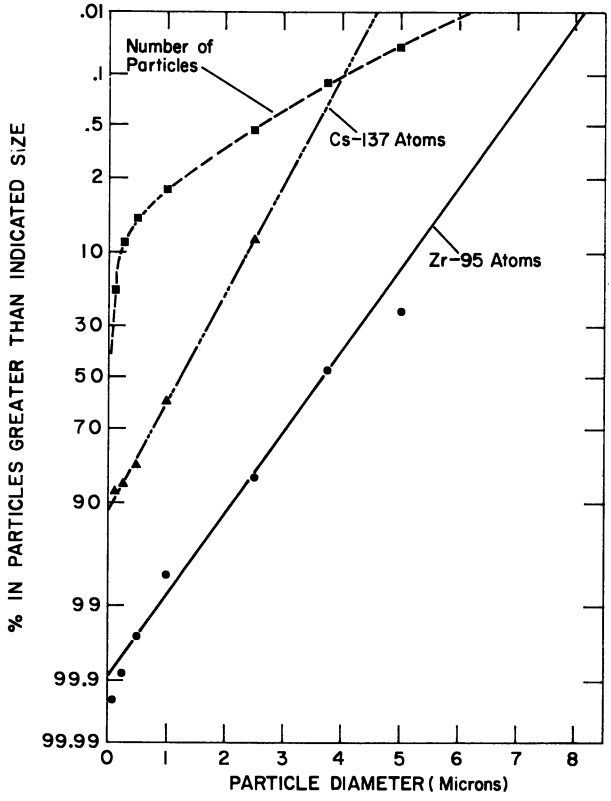

Figure 7. Airburst distribution. Data normal form.

However, in the particular airburst event analyzed, the condensable metallic system was essentially two component. That is, roughly equivalent masses of aluminum and iron constituted the principle amount of condensable material. Aluminum oxides would condense earlier than iron oxides so that it is not inconceivable that a two-component particle

population would be produced—a larger diameter component rich in aluminum and depleted in iron, and a smaller diameter component in which the converse held. Data available at this time are not adequate to confirm or reject a two-component hypothesis.

In Figure 7 the same distribution data are shown in the form of a probability coordinate plot against the particle diameter rather than the logarithm of diameter. In this form it is possible to approximate the ^{137}Cs and ^{95}Zr data points with a linear relationship. However, it is somewhat unexpected for *both* a surface related quantity and a volume related one to follow a normal distribution with respect to particle diameter. That is, if D^2 is normally distributed with respect to D, then D^3 cannot be nor can D be. In the case of lognormal functions, of course, if log D is normally distributed, then so are 2 log D (or log D^2) and 3 log (or log D^3).

The equation, in differential form, which corresponds to the lines in Figure 7 are:

$$\frac{dN^{137}}{dD} = \frac{1}{.89\sqrt{2\pi}} \exp\left[-\left(\frac{1.22 - D}{.89\sqrt{2}}\right)^2\right] \tag{64}$$

$$\frac{dN^{95}}{dD} = \frac{1}{1.19\sqrt{2\pi}} \exp\left[-\left(\frac{3.63 - D}{1.19\sqrt{2}}\right)^2\right] \tag{65}$$

In Figure 8, a plot of dN^{137}/dN^{95} *vs.* D is shown together with experimental values of the ratio for indicated particle size fractions. The excellence of the fit shows that the data analysis is consistent, although it cannot be used to establish the uniqueness of the normal distribution function in describing the data.

One other form of distribution function which has been suggested as appropriate for condensation particles is the exponential distribution. In terms of a particle number distribution, its form is

$$\frac{n_i/\Sigma n_i}{\Delta r} = \frac{dN}{dr} = \frac{1}{\bar{r}} \exp\left[-r/\bar{r}\right] \tag{66}$$

The distribution of a property, p, dependent on r^n is given by

$$\frac{dN^p}{dr} = \frac{r^n \bar{r}^{(n+1)} \exp\left[-r/\bar{r}\right]}{\Gamma(n+1)} \tag{67}$$

where $\Gamma(n+1)$ is the gamma function. For integral values of n, $\Gamma(n+1) = n!$ Hence, if ^{137}Cs were distributed on the surface of the particles, its distribution would be given by

$$\frac{dN^{137}}{dr} = \frac{r^2 \bar{r}^3 \exp\left[-r/\bar{r}\right]}{2!} \tag{68}$$

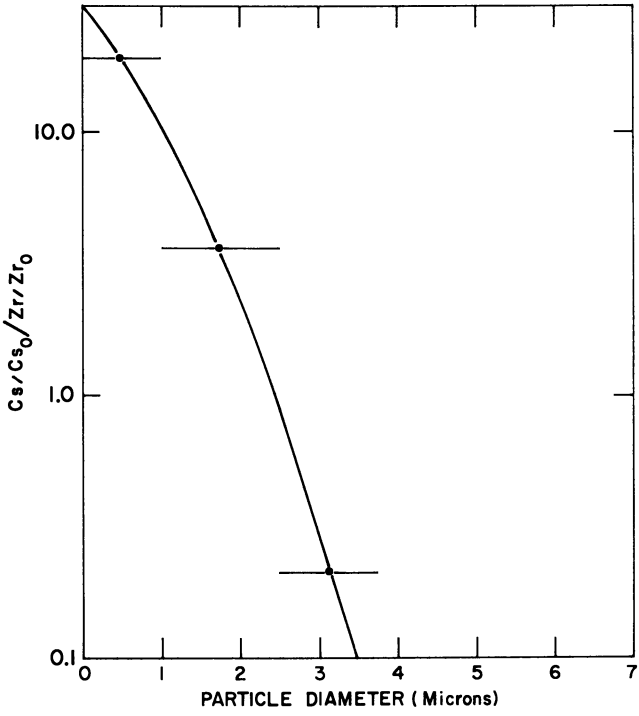

Figure 8. Airburst detonation. Volatile/refractory isotope partition vs. *particle diameter.*

The experimental data of Table VIII were converted to differential form and plotted on semilogarithmic paper

$$\frac{1}{\langle r \rangle^2}\left(\frac{n_i^{137}}{\Sigma n_i}\Big/\Delta r\right) = \frac{1}{r^2}\frac{dN}{dr} \; vs. \; \frac{r^3}{2!}\exp\left[-r/\bar{r}\right] \qquad (69)$$

The data, except for the 0–0.1μ fraction, fall on a straight line. However, the value of $\bar{r}$ calculated from the intercept is larger by about a factor of 100 than the value of $\bar{r}$ calculated from the slope. On the basis of this limited trial, the fit of the data to this form of distribution function appears to be quite unsatisfactory. A correct form of distribution function should apply to the entire class of airburst populations, and additional work now underway is devoted largely to resolving the problem of determining an appropriate form of distribution function to apply to airburst particle size distributions. However, there may be no simple function which reflects adequately the over-all behavior of the particle population. Indeed, Johnson (5) was able to demonstrate that his experimental results on isotope distribution with particle size were compatible with theoretical distributions obtained by following a modified version

of a thermodynamic treatment suggested by Carl Miller (*6*). In this treatment, each radionuclide exhibits a unique distribution with particle size.

Conclusions

The over-all problem of characterizing quantitatively the populations of radioactive particles produced by nuclear detonations is subject to solution on a systematic basis.

(1) Based on the interisotopic ratios obtainable from the analysis of various early time gross particle samples from a given event, it is possible to relate the behavior of all isotopes to that of a single pair of isotopes—a volatile species and a refractory species.

(2) The distribution of the volatile species, the refractory species, and mass within the particle population can be determined by analysis of size separated fractions of early samples from the aerial cloud and close-in fallout.

(3) For land surface and subsurface detonations, the distribution functions may be expressed as linear combinations of two or three log-normal distribution functions. Each component corresponds to a particle group which interacted with the radioactive cloud at a different time. Earlier interaction generally corresponds to larger particles, more high temperature effect on the particles, and greater enrichment in refractory radioisotopic sphere. Later interaction corresponds to smaller particles, less temperature effect on the particles, and greater enrichment in surface distributed volatile species. All particles consist of environmental soil material. The interisotopic relationships are linear in form.

(4) For airbursts the form of the distribution functions is still under investigation. All particles consist of metal oxide spheres produced by condensation from the vapor state of the device materials. The number of population components may be related to the number of major condensable components of the device. Large particles are enriched in refractory isotopes, small particles in volatile. The interisotopic relationships may be expressed best as power functions.

Literature Cited

(1) Freiling, E. C., *Science* **133**, 1991 (1961).
(2) Freiling, E. C., Paper in: Radioactive Fallout from Nuclear Weapons Tests, TID-7632, Atomic Energy Commission, February, 1962.
(3) Heft, R. E., Steele, W. A., University of California, Lawrence Radiation Laboratory, *UCRL Rept.*, in press.
(4) Herdan, G., "Small Particle Statistics," pp. 84-85, Academic Press, New York, 1960.

(5) Johnston, K., Atomic Weapons Research Establishment, Aldermaston, *SSCD Memo No.* **161** (Title U, Report SRD) (1965).
(6) Miller, C. F., "Fallout and Radiological Countermeasures," Vol. I, Stanford Research Institute, Menlo Park, Calif., 1963.
(7) Stevenson, P. S., Hicks, H. G., Nervik, W. E., Levy, W. B., University of California, Lawrence Radiation Laboratory, **UCRL-2057** (Title U, Report SRD) (1957).

RECEIVED June 4, 1968. Work performed under the auspices of the U. S. Atomic Energy Commission.

15

The Interpretation of Fractionation in Fallout Fields

P. C. STEVENSON

Lawrence Radiation Laboratory, University of California, Livermore, Calif.

The fractionation of fission-product radionuclides in fallout fields can be understood at least qualitatively in terms of the chemical nature and relative abundances of the short lived precursors of the observed long lived species. This consideration leads by way of reasonable assumptions detailed herein to the conclusion that the composition of any sample is specified to a defined degree of precision by the concentration of relatively few radionuclides. Identification of these species may then give insight into the physical and chemical processes of fallout phenomenology. A computerized algorithm is given for identifying the "best" nuclides for the purpose and determining the minimum number necessary.

Many of the less-understood phenomena leading to the observed fallout distribution resulting from a nuclear explosion occur on a relatively short time scale (a few tens of seconds or less). These short term phenomena lead to an initial distribution of radioactive material referred to as the "source term" in a fallout study. Many predictive calculations are based on an assumed source term, which of necessity has been quite oversimplified. Two typical simplifications made for purposes of model development are: (1) that the radiochemical composition of "fallout" is well defined and uniform; (2) that the particles comprising the initial debris are uniform with respect to settling rate in the atmosphere. The latter assumption has received considerable attention elsewhere, notably in the work of Miller (2). However, the former assumption concerning the radiochemical uniformity of the debris has received far less systematic attention.

Many workers have made it a practice to consider "debris" as a single uniform radioactive species, well defined by gross gamma intensity, and with known decay properties with time—this assumption is grossly in error. Even for consideration of external radiation effects, the variation of composition of debris with location exerts a definite and sometimes major influence, while any mechanism which depends on ingestion of a particular species into a biological food chain may be perturbed by orders of magnitude. This paper examines the origin of the source term in the light of known processes, makes some qualitative inferences regarding the results to be expected by modifying the assumptions of uniformity of debris, and examines some existing data to evaluate the results of such inferences.

It has been known for many years that the "fission products" observed in the field or in the laboratory some time after the event are in fact not usually the species produced in fission at all but the result of one or several consecutive beta disintegrations of shorter lived isobaric precursors which are formed directly in the fission process. From the chemist's point of view this is important because the β-decay process is an actual transmutation of elements, and the time scale involved is frequently comparable with that for the formation of fallout particles.

Unfortunately, precise knowledge of the distribution of direct yield among several competing isobars is generally not available; furthermore, the radioactive half-lives involved are frequently completely unknown since the fission process gives rise directly to between 300 and 400 radioactive species, and the separation of such a complex mixture usually involves a time which is quite long compared with the lifetimes of interest. We do know that each isobaric chain is formed directly as a number of different isobars and that the width of the isobaric yield distribution is such that to account for 90% or more of a chain one must consider at least three or perhaps four chemical elements.

It is apparent, then, that to understand the physical and chemical processes which govern the distribution of a particular long lived species —*e.g.*, ^{140}Ba—in a fallout field, one must consider the properties not of barium, or not only of barium, but of cesium, xenon, and perhaps even iodine, and tellurium (in fact in this case the relevant species appear to be barium, cesium, and xenon).

Parenthetically, it should be obvious that those radionuclides of interest which are not fission products do not suffer from this complication; such species either are formed directly by a nuclear reaction or are produced exclusively by a known β-decay process from a well defined precursor of (usually) known characteristics—*e.g.*, ^{239}Np formed by β-decay from ^{239}U.

Mechanism of Inclusion of Activity in Fallout

A relatively crude physicochemical model can give a basis for understanding fallout formation. It is assumed first that the preponderance of material comprising the fallout forms an inert condensed matrix in which the active species are included as impurities in such low concentrations that the vapor pressure of the matrix is not perturbed. One then considers the behavior of each trace impurity in terms of a distribution ratio between the matrix phase and the vapor phase. The behavior of such a ratio with temperature can be described roughly as a step function. At a high enough temperature, assuming there is a high enough partial pressure of matrix material to permit the existence of a condensed phase, the trace impurity will be largely in the vapor phase, while at a low temperature, the trace impurity will be largely in the condensed phase. Intermediate behavior will be governed by Raoult's or Henry's law, depending on the possibility of compound formation between the impurity and the matrix; for our present discussion the transition range may be neglected until later.

In actual practice, of course, there is a well defined temperature above which a condensed phase does not exist since the amount of matrix material is limited. This leads to a logical (though oversimplified) three-stage division of the process of fallout formation from the very high temperature gas resulting from a nuclear explosion: Stage 1—the earliest stage—ends when condensed matrix formation occurs; Stage 2 ends far less sharply, when the temperature reaches an equilibrium with the surroundings; Stage 3 includes all subsequent processes. Based on our simple model, one may divide the elements into three classes: (1) refractory species, which becomes condensable at or before the end of Stage 1 and consequently condense as soon as matrix material appears; (2) semivolatile species, which are not condensed into the matrix at high temperatures but are absorbed or adsorbed by the particles as the temperature approaches ambient; (3) volatile species, which condense only below ambient temperature, the extreme examples being the noble gases.

It should be apparent that the allocation of a particular element to a particular class is a function of both the matrix material (considering condensation temperature and compound formation) and the conditions of the event. A nuclear explosion in the atmosphere gives rise to a cloud of debris which within a few minutes cools to the temperature of the tropopause; a nuclear explosion conducted underground, for example to loosen up a gas-bearing formation, cools rapidly only to the melting point of the surrounding rock.

A further complication ensues when the time scale of radioactive decay is compared with the time scale of debris condensation. If con-

densation is rapid compared with all the half lives in a particular isobaric chain, the isobars will distribute according to their nature, and those chemical species that remain volatile into the third stage of debris formation will condense only after transmutation *via* β-decay. If, however, the half-lives are of the same order of magnitude as the condensation times, the changing nature of the species during condensation can make the process quite complicated. In the extreme case, in which all half-lives are short compared with condensation time, the activity will show behavior characteristic of the end-product species.

This series of phenomena exerts a profound influence on the composition and distribution of radioactive material in fallout, the effect depending on the environment of the nuclear explosion. An explosion in the atmosphere, high enough so that the underlying terrain does not affect the debris, results in particles which begin to form at the end of Stage 1 and incorporate the refractory species present at that time. The debris cloud is so dilute that the particles formed are small and do not separate from the vapor during Stages 2 and 3, so that the over-all composition of the debris at the end of all condensation, say 20 minutes after the burst, is uniform. It is still true that the refractory species tend to be distributed through the bulk of the debris particles and that the semivolatile species and condensable descendants of volatile species tend to be on the particle surfaces, so that particles with different surface-to-volume ratios will differ in composition. Therefore, any mechanism that tends to segregate particles on the basis of size will separate a nonrepresentative sample.

In an explosion that includes condensable matter from the environment, the time scale is reduced; in particular, the rate of post-condensation segregation mechanisms is accelerated enormously. In bursts at very low altitude or at the surface, large amounts of dust, gravel, rocks, and water vapor at relatively low temperature are swept into the debris cloud, presumably to exert a scrubbing and scavenging action on those species condensable at that time. The volatile radioelements, of course, are not condensed, and their radioactive descendants deposit preferentially on the suspended fine particles that remain after the settling of the gross lumps and droplets. One might expect close-in fallout under such conditions to be highly enriched in refractory radionuclides and depleted in radionuclides with volatile precursors, while the debris remaining airborne would be expected to consist primarily of those nuclides with volatile precursors. To estimate the effect of such enrichment and depletion, one must know the fraction of a given isobaric chain formed as a volatile chemical species or its very short lived precursors; this knowledge, as mentioned before, is currently inaccurate and incomplete.

When the amount of surrounding or entrapped material is very large, as in a buried explosion, the scrubbing and scavenging effect is completely predominant. A deeply buried event releases no activity whatever; one buried at a somewhat shallower depth releases only those radionuclides that can pass through a thick filter bed of cool material; these consequently consist almost exclusively of noble gases and their decay products. An explosion buried to produce a crater will liberate nuclides able to pass through a filter bed that is both thinner and more diffuse, but the emergent debris is still highly enriched in volatile species; those condensable elements that emerge are probably attached to the relatively coarse dust that is blown through the filter and may be expected to be enriched in the close-in fallout and severely depleted in the long range airborne cloud. Again, for full understanding, it is necessary to know the isobaric yield distribution and nuclide lifetimes in each β-decay chain of interest.

In any case, this simple model indicates that the distribution of long lived activities in fallout debris should be the result of not more than three different mechanisms—not, in fact, more than two different mechanisms if there is no separation of the vapor and condensed phases until after a time that is long compared with all precursor half-lives. This in turn signifies that one should be able to predict the entire radioactive composition of a particular fallout sample, whatever the mechanism of fractionation may be, given an analysis for only two or three consituents of sufficiently different behavior, and given full knowledge of the relative isobaric yields and half lives and the condensation time scale of the events. As mentioned previously, such knowledge is not yet available; however, this simple approach can be tested by examining the available data to see whether it is possible to express the compositions of all samples from a given event in terms of a small number of radionuclides.

Measurements have been made (*see* Figures 1–4) on sets of samples obtained with aircraft from debris clouds resulting from atmospheric explosions. In many cases it has been observed that the behavior of the active products was determined by the behavior of two and only two different radionuclides and that for an entire set of samples from a single event, the amount of nuclide i in sample j was given, usually to within 10%, by an equation such as

$$A_{ij} = k_{i1} A_{1j} + k_{i2} A_{2j} \quad (1)$$

where Nuclide 1 was a radionuclide that had one or more volatile or semivolatile precursors, and Nuclide 2 was a radionuclide having only refractory precursors. In practice, this relationship has usually been expressed in terms of ratios by dividing by A_{1j} or A_{2j} and using suitable normalizing factors to convert the resulting activity or atom ratios to the

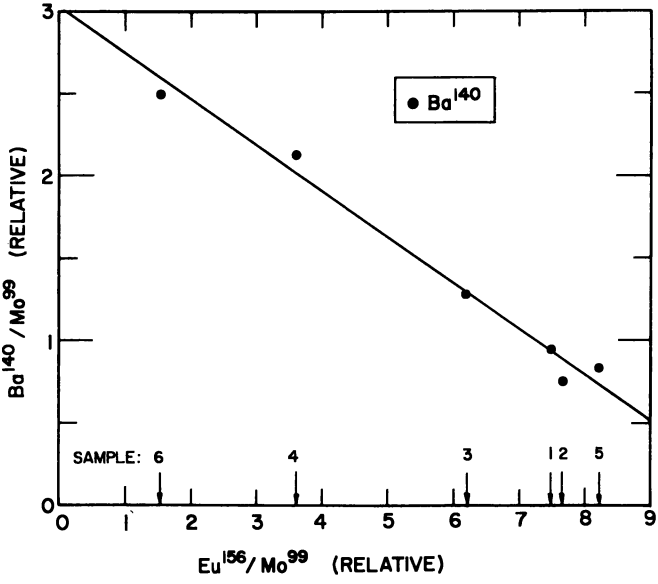

Figure 1. Correlation of the ratio $^{140}Ba/^{99}Mo$ with the ratio $^{156}Eu/^{99}Mo$ in a set of airborne-debris samples from a nuclear event. ^{156}Eu has only refractory species for precursors; the mass-99 chain exhibits volatile behavior, perhaps owing to the volatility of MoO_3. The strong negative correlation indicates that ^{140}Ba has at least some volatile precursors.

so-called "*R* values," which are equivalent to activity ratios corrected for counter sensitivity. Equation 1 is clearly a matrix equation that can be written conveniently as:

$$A = K\alpha \tag{2}$$

where α is a submatrix of A consisting of the first two rows.

By the ordinary rules of matrix algebra, it is obvious that A is a matrix of rank not greater than *two* since both K and α are of rank two.

It is clear that this simplest case is a selected set of samples taken from the debris that remains airborne for relatively long periods. One might therefore expect that any early time separation processes that would separate debris condensed during Stage 2 from that to be condensed later in Stage 3, such as prompt filtration or "scrubbing" by heavy early fallout, would exert a constant bias on all samples remaining airborne, so that the presence or absence of a third mechanism would not be apparent in the selected data. However, it is not unreasonable to attempt to evaluate activities in debris fields in terms of a relatively small number of species, and the data from large sets of samples could be represented by a matrix

equation of the form of Equation 2, where the rank of the matrix A is small compared with the number of species of interest. Our simple theory says the rank should not be greater than three, but it is now time to abandon our simplifications and to realize that actual distribution-function/time (or temperature) curves may depart quite widely from step functions and that we should give up the arbitrary division of all elements into three classes.

The question is: in the data from a real experiment, where many radionuclides are measured in many samples collected under a wide variety of conditions, what is the least number of classes of chemical behavior that will describe the observed results to the desired precision? Or, in mathematical terms, what is the rank of the matrix A, and what nuclides should be selected to make up the submatrix α? Finally, can any physical significance be attached to the combination of coefficients making up the elements of K, and can these elements of K or quantities thus derived be carried over from one event to the next?

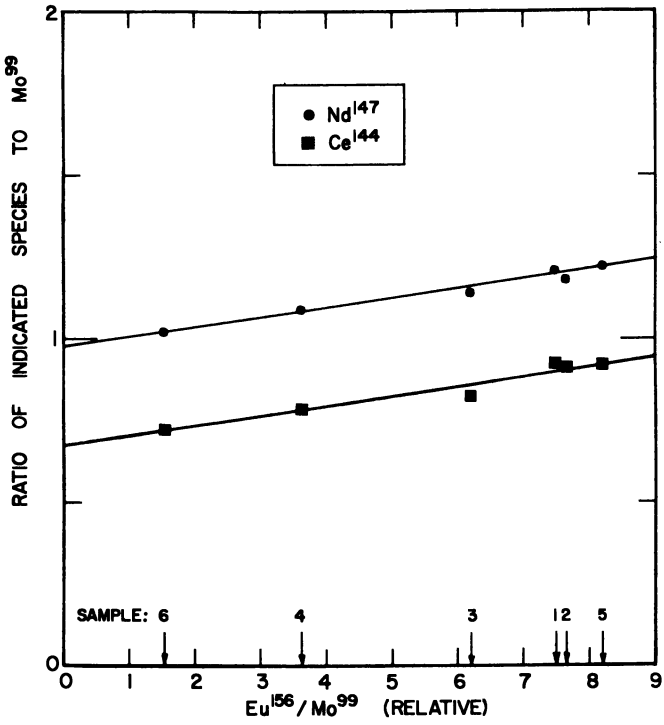

Figure 2. Correlation of the ratios $^{147}Nd/^{99}Mo$ and $^{144}Ce/^{99}Mo$ with the ratio $^{156}Eu/^{99}Mo$. Slight positive correlation indicates that both the mass-144 and mass-147 chains are somewhat less volatile than the mass-99 chain.

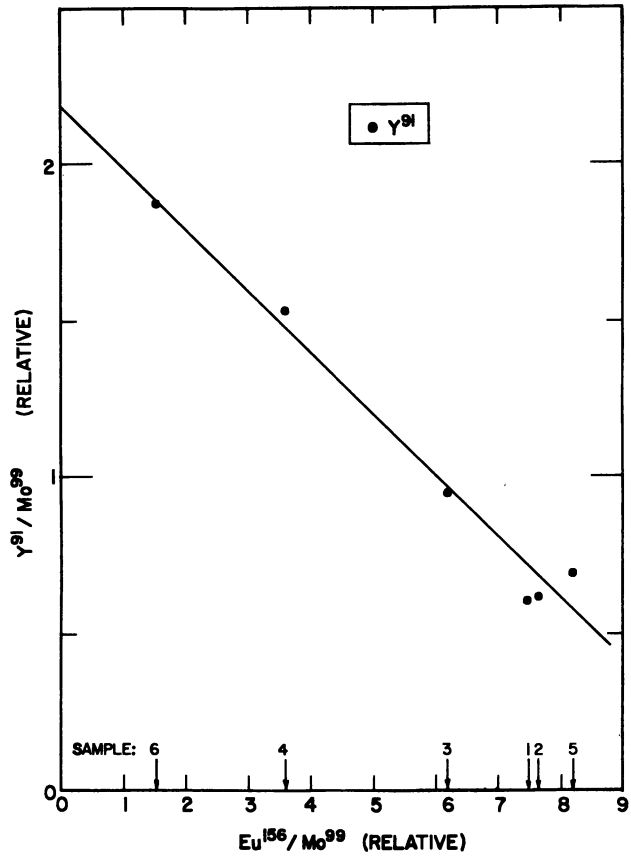

Figure 3. Correlation of the ratio $^{91}Y/^{99}Mo$ with the ratio $^{156}Eu/^{99}Mo$. Negative correlation indicate volatile behavior in the mass-91 chain.

These questions have practical importance. The number of radionuclides contributing significant radiation to a fallout field is large; furthermore, some of the chemical elements that contribute a small fraction of the total radiation may be of biological importance out of all proportion, owing to efficient biological concentration mechanisms. If an accurate survey of all radionuclides could be accomplished by, for example, surveying a set of samples with a gamma spectrometer of adequate resolution, such as a lithium-drifted germanium diode (*1*), the reduction in total work load would be enormous. The variation in composition of fallout samples is significant; a survey for total γ-radiation in the close-in fallout pattern is practically useless for giving a measure of the source term for further predictions unless it is interpreted in terms of the radiochemical composition of the fallout as a varying function of

position and especially so if it is reduced to an essentially meaningless term like "kilotons/unit area" or "fraction of fissions released."

The determination of the rank of a matrix is fairly simple and straight-forward. Unfortunately, the orthodox methods applied to a matrix such as A in Equation 2 give an answer which is exact mathematically but useless physically, namely that the rank of A is the number of radionuclides measured or the number of samples analyzed, whichever is less. This unfortunate result arises from presence of experimental imprecision in the elements of A. One must therefore rewrite Equation 2 in the form

$$A - K\alpha = E \tag{3}$$

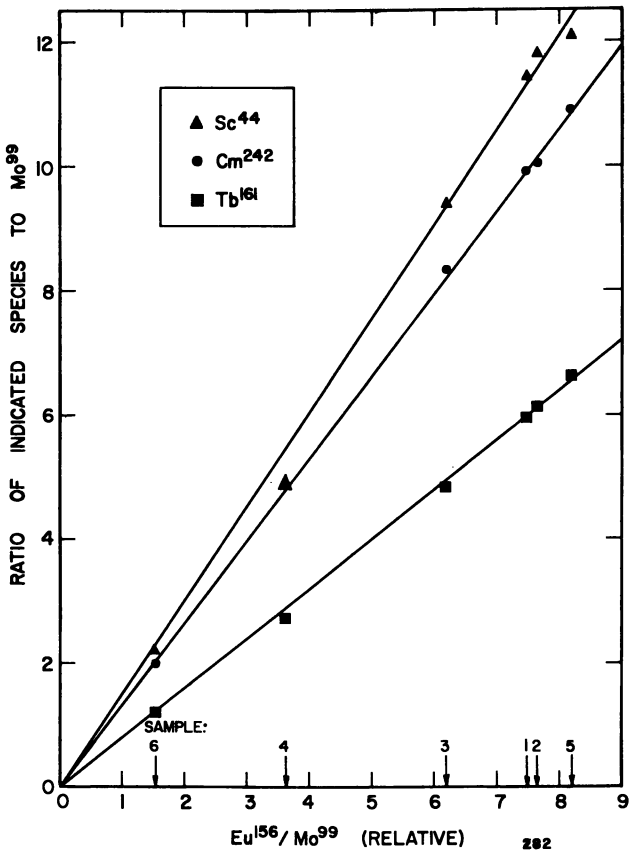

Figure 4. Correlation of the ratios $^{44}Sc/^{99}Mo$, $^{242}Cm/^{99}Mo$ and $^{161}Tb/^{99}Mo$ with the ratio $^{156}Eu/^{99}Mo$. Positive correlations with intercept at the origin indicate refractory behavior.

where E is a matrix whose elements are not significantly different from zero, the significance being judged in terms of the known imprecisions of the elements of A and α.

The algorithm used is attributed to J. B. J. Read. For many manipulations on large matrices it is only practical for use with a fairly large computer. The data are arranged in two matrices by sample i and nuclide j: one matrix, V, contains the amount of each nuclide in each sample; the other matrix, E, contains the variances of these numbers, as estimated from counting statistics, agreement between replicate analyses, and known analytical errors. It is also possible to add an arbitrary term F_{ik} to each variance to account for random effects between samples not considered in the model; this is usually done in terms of an additional fractional error. Zeroes are inserted for missing data in cases in which not all nuclides were measured in every sample.

The "best nuclide" is selected from the two matrices, the selection criteria being: (1) the nuclide must be one of those for which the largest number of samples were analyzed; and (2) that of these species, the one is selected for which the measurements are most precise, that is for which

$$S_k^2 = \sum_i \frac{(V_{ik})^2}{E_{ik}} \tag{4}$$

has the largest value.

The other columns of V are then made orthogonal to the *k*th ("best") column by adding an appropriate multiple of the *k*th column to each. (Zero elements must be skipped.) The same operation is also performed on a unit matrix M having the same number of columns as V. The resulting transformed V matrix now has all other columns orthogonal to the pivot column *k;* the matrix M has been converted into the matrix which, multiplied into the original V matrix from the right, transforms it into the new V matrix, V^1—*i.e.*,

$$V^1 = VM \tag{5}$$

If each row of V^1 is considered as a separate row vector, then it can be shown (3) by transposing the matrices that the variances of the elements of V^1 are the diagonal elements of the matrices obtained by

$$M_l = M^t E_l M \tag{6}$$

where E_l symbolizes the *l*th column of the matrix E. This gives a matrix E^1, whose elements are the variances of the elements of V^1. One then evaluates S_m^2 again, using the new V^1 and E^1 to find the second pivot column (other than the *k*th column) having the largest number of non-zero elements and the highest value of S_m^2. Again a unit matrix, M, and V^1 are operated on to orthogonalize the remaining columns in V^1 (since

the kth column is already orthogonal, it is not altered by this operation); the column of the twice-altered V matrix (other than the two previously used) that has the largest number of non-zero elements and the highest new value of S^2 is then used as the third pivot, and so on until each column of the matrix, except the last, has been used as a pivot column for orthogonalization. The resulting transformed V matrix now has all columns mutually orthogonal, and we may calculate a quantity X_j^2 for each column of V^1

$$X_j^2 = \Sigma \frac{(V_{ij}^1)^2}{E_{ij}^1} \tag{7}$$

which is analogous to S^2 of Equation 4; in fact, for the original pivot column the two quantities are identical. For the other columns (nuclides) X^2 is equivalent to a χ^2 test of the assumption that the data for each nuclide can be fitted, within statistics, by a linear expression only in those significant radionuclides which were previously used as pivots. The reliability with which one concludes that each nuclide must be used is then evaluated from a χ^2 significance table, using for the number of degrees of freedom the number of non-zero elements in the column, less the number of previously used significant pivot columns.

Results

This technique has been applied to data from a set of 42 samples from a nuclear detonation. Samples were taken both from fallout collectors and from airborne-debris samplers. Twenty-seven radionuclides could be identified and measured with acceptable precision (better than 10%) in at least some of the samples. The results are presented in Table I. This calculation was performed without the added variance term F_{ik}. The nuclides include both fission and activation products.

From Table I it is essentially certain that four radionuclides must be used to interpret the data, these being ^{132}Te (the original pivot species), ^{140}Ba, ^{196}Au, and ^{203}Pb. The two nuclides ^{237}U and ^{147}Nd, which also show a level of significance greater than 5%, can almost certainly be disregarded since they were detected in only a few samples, and the appreciable value of X^2 is probably caused by an erroneous value on one or two samples. If we disregard these two nuclides, it is a reliable conclusion at the 97% confidence level that no more than four nuclides are necessary, and at a confidence level of greater than 99% that no more than five are needed. It is worth noting that two nuclides which are clearly fractionated from each other, ^{140}Ba and ^{132}Te, are major contributors to the gamma field but have very different lifetimes.

Table I. Data for 27 Species Analyzed in 42 Samples Collected from a Nuclear Event

Nuclide	X^2	*Degrees of Freedom*	*Level of Significance, %*
^{132}Te	23,088	42	100 (Original Pivot)
^{140}Ba	1,533	34	99 +
^{196}Au	418	40	99 +
^{203}Pb	141	36	99 +
^{198}Au	11.8	22	<3
^{122}Sb	9.71	25	<1
^{131}I	8.73	30	<1
^{141}Ce	3.25	28	<1
^{237}U	1.44	4	<20[a]
^{103}Ru	0.819	11	<1
^{99}Mo	0.425	15	<1
^{147}Nd	0.411	1	<50[a]
^{187}W	0.261	19	<1
^{24}Na	0	0	0
^{54}Mn	0	0	0
^{88}Y	0	0	0
^{91}Sr	0	0	0
^{95}Zr	0	0	0
^{97}Zr	0	0	0
^{124}Sb	0	0	0
^{127}Sb	0	0	0
^{133}I	0	0	0
^{135}I	0	0	0
^{137}Cs	0	0	0
^{139}Ba	0	0	0
^{143}Ce	0	0	0
^{203}Hg	0	0	0

[a] Caused by the presence of a single "outlier" in the data which is probably the result of nonrandom error.

Table II. Data for 12 Species Analyzed in 25 Samples Collected from a Nuclear Event

Nuclide	X^2	*Degrees of Freedom*	*Level of Significance, %*
^{89}Sr	2500	25	100 (Original Pivot)
^{147}Nd	821	24	99 +
^{136}Cs	63.7	23	99 +
^{140}Ba	61.0	22	99 +
^{131}I	15.3	19	~30
^{98}Zr	14.1	21	~15
^{99}Mo	13.7	16	~30
^{132}Te	10.9	16	~10
^{156}Eu	8.1	16	~5
^{144}Ce	5.9	16	~1
^{137}Cs	4.5	13	~1
^{141}Ce	0.1	16	~0

Results from a second nuclear event were also analyzed by this technique. Data were obtained from radiochemical analyses for 12 elements on a set of 25 samples. Since the data were not analyzed completely for errors, an estimate of 10% was used for the standard deviation of each measurement.

Table II shows the result of the analysis. In this event only fission-product radionuclides were considered. As before, four nuclides are significant at well above the 99% confidence level; all other nuclides have a level of significance at or below 30%. Since the estimated experimental errors are probably not realistic, a level of significance below 50% is probably not meaningful. Four nuclides are then necessary and sufficient.

Summary and Conclusion

It has been shown that the data on many fractionated radionuclides in a fallout field can be expressed in terms of the data on a small number of nuclides. This suggests that the phenomena leading to fractionation are the result of a small number of competing mechanisms and that the observed effects could be understood if these mechanisms could be identified, the factors affecting them evaluated, and the chemical species present at the time (*e.g.*, short lived precursors of fission-product radionuclides) characterized adequately. The similarity between the number of required nuclides observed (four in each event) and the number predicted on the basis of a very crude model does not, of course, justify the model, but it is suggestive that the four radionuclides clearly indicated in the first event have among them a refractory element (barium as BaO)), semivolatile elements (gold and the cesium precursor of ^{140}Ba) and volatile elements (tellurium and the xenon precursor of ^{140}Ba). The behavior of lead in debris has not been studied enough to characterize its volatility. In the second event, also, the four necessary nuclides include refractory (^{147}Nd, ^{140}Ba), semivolatile (^{89}Rb, ^{140}Cs, ^{136}Cs) and volatile (^{89}Kr, ^{140}Xe) elements. The independent yield of ^{89}Sr is believed to be quite low; it would be refractory.

It remains for workers to develop a method of selecting correlations based on mechanism rather than on adequacy of measurement and to attempt some interpretation of these results in terms of mechanisms of source-term formation. This paper has attempted to show only that the complexity of the phenomenology, while enough to cause trouble, is not beyond analysis.

Acknowledgments

The data used for analysis in this paper represent a large amount of work on the part of many members of Radiochemistry Division of the

Lawrence Radiation Laboratory, Livermore. I would like to express my appreciation to them for their efforts, and especially to J. B. J. Read for his contribution to the mathematical analysis used.

Literature Cited

(1) Gunnink, R., Levy, H. B., Niday, J. B., University of California, Lawrence Radiation Laboratory, Livermore, *Rept.* **UCID-15140** (May 16, 1967).
(2) Miller, C. F., "Fallout and Radiological Counter Measures," Vol. I, Stanford Research Institute, Menlo Park, Calif., 1963.
(3) Stevenson, P., *Natl. Acad. Sci.–Natl. Res. Council Monograph* **NAS/NS 3109,** 52 (1965).

RECEIVED June 20, 1968. Work performed under the auspices of the U. S. Atomic Energy Commission.

16

Observed Fractionation in Ground Level Fallout from Three Nuclear Cratering Detonations

THOMAS A. GIBSON, JR.

University of California, Lawrence Radiation Laboratory, Livermore, Calif. 94550

Data relating to radionuclide deposition (fallout) within a few miles of the Danny Boy, Sedan, and Palanquin nuclear cratering shots are examined for evidence of fractionation. The fractionation index is computed for several fission-product mass chains produced in each event. For the three events studied only Danny Boy showed unambiguous evidence of fractionation in the early fallout, and the degree of fractionation was small. In Danny Boy there was only a factor of four difference between most enriched and most depleted species, compared with the factors of several hundred that have been observed in many late time samples of airborne debris. If this small amount of fractionation proves to be true in general for cratering shots, predictions of early-fallout gamma-radiation patterns will be simplified.

The radioactive products of a nuclear explosion are said to have undergone fractionation if their relative proportions in samples taken at various locations differ significantly from their relative proportions as formed. This report describes a study of fractionation in the early fallout from the nuclear cratering shots Danny Boy, Sedan, and Palanquin. Published fallout data for these shots was the basic information used in the study. A normalization procedure was applied to the published data as follows: the amount of each radionuclide (or mass chain) of interest measured on a fallout tray is related to the gamma-radiation exposure rate measured at the tray location and to the amount of that radionuclide produced per kiloton of fission by the device. The result is an index

number for each radionuclide of interest. These "fractionation indices" show the degree of fractionation that has occurred in the deposited early fallout debris.

This technique has the advantage of reducing many individual measurements to a meaningful, manageable, and a comprehensive set of fractionation index numbers. It is useful and illuminating because the quantitative measure of ground deposition for a particular mass chain (or a specific nuclide in the case of a shielded nuclide) can be compared directly with the ambient gamma-radiation field. The index allows the deposition of the various mass chains to be compared with one another, and it enables the deposition from one cratering event to be contrasted with that from another on a mass chain-by-mass chain basis. Furthermore, the method is independent of fission yield, total yield, and total amount of radioactive material deposited in the close-in fallout patterns.

The Fractionation Index

The fractionation index I_i is calculated for each measured fission product at each tray location in the fallout field as follows:

$$I_i = \frac{\text{No. atoms in tray}}{\text{area of tray}} \times \frac{1}{\text{No. atoms from 1 kt fission}} \times \frac{1}{\text{gamma exposure rate at tray}}$$

or, symbolically,

$$I_i = \frac{M_i}{A_{tr}} \times \frac{1}{N_i} \times \frac{1}{(d\gamma/dt)_{H+1\,hr.}}$$

where:

I_i = index for mass chain i as represented by nuclide i

M_i = atoms of nuclide i measured in tray, corrected to zero time

A_{tr} = area of tray in ft.^{2}

N_i = atoms of nuclide i produced by 1 kiloton of fission, corrected to zero time (in practice, usually the total yield of chain i per kiloton, expressed as number of atoms)

$(d\gamma/dt)_{H+1\,hr.}$ = gamma exposure rate in roentgens/hr. measured with a 4π detector 3 ft. above surface at tray location and decay corrected to a time of H + 1 hr.

Since the gamma exposure rate at a particular location is directly proportional to the area concentration of gamma-emitting nuclides in the vicinity, one notes that, in the absence of fractionation the index will have

the same value for all nuclides at all locations. When fractionation takes place, the index gives a quantitative measure of the enrichment or depletion of a mass chain relative to the total assemblage. If present, neutron-induced gamma-emitting nuclides will add to the exposure rate and thus decrease the magnitude of the index. This consideration is of interest when comparing different cratering events. The utility of this index is demonstrated below by examining its application to the cratering events Danny Boy, Sedan, and Palanquin.

Sources of the Data

The report of Miskel and Bonner (*1*) was the source of Danny Boy information. They used measurements from nine tray locations extending from 2500 to 25,000 ft. from ground zero and studied 11 fission product nuclides. The gamma-radiation exposure rates measured at the tray locations varied by more than a factor of 100 with distance from ground zero, as did the radiochemical determinations of each nuclide expressed as disintegrations per minute per square foot. Miskel and Bonner divided the latter by the former to give a factor designated as J_i. While the J_i for any one nuclide was not exactly constant with distance from ground zero, the values were reasonably consistent, and furthermore, no discernible trend with distance was apparent. Also, the ratios of J_i values between different nuclides showed no trend with distance. Thus, there was no change in fractionation over the distances involved, and the determinations for the various trays at different distances were averaged.

Information concerning Sedan was obtained from the report by Lane (*2*). He reports equivalent fissions per gram for material from fallout trays between 5800 and 19,200 ft. from ground zero for a series of nuclides. The determinations show random scatter and do not indicate a trend with distance. Therefore, the values for different trays were averaged. A report by Nordyke and Williamson (*3*) provided the experimental determination of fallout-mass area density divided by gamma field readings in units of (kg./sq. meter)/(roentgens/hr.) over the same fallout area. These two sources provided the necessary input to calculate the fractionation indices for Sedan.

Schwartz (*4*) provided the early fallout field tray information for Palanquin. He reported a fraction of total atoms produced per square foot divided by the field exposure rate at the tray locations in roentgens/hr. at H + 1 hr. for the different nuclides studied. The trays were placed from about 2500 to 25,000 ft. from ground zero; the data show no trend with distance, so the determinations for the different trays were averaged.

Calculated Fractionation Indices

Table I gives the fractionation indices obtained for the various mass chains in these three cratering events. The mass chains are divided into the conventional three groups: volatile, intermediate, and nonvolatile.

Table I. Calculated Fractionation Indices for Early Fallout Debris from the Danny Boy, Sedan, and Palanquin Nuclear Cratering Shots

		Index (units[a] of 10^{-11} kiloton-hr./ft.^{2}-roentgens)		
Group	*Nuclide*	*Danny Boy*	*Sedan*	*Palanquin*
Volatile	^{89}Sr	1.46	0.81	0.30
	^{90}Sr	1.94	1.26	—
	^{91}Y	—	1.11	—
	^{132}Te	—	0.77	1.04
	^{137}Cs	1.72	0.59	0.35
	^{140}Ba	1.21	0.98	0.74
Intermediate	^{103}Ru	—	0.54	—
	^{106}Ru	—	0.71	—
	^{131}I	—	0.95	0.58
	^{136}Cs	1.57	0.99	1.12
	^{141}Ce	0.90	1.12	0.88
Nonvolatile	^{95}Zr	0.38	1.19	0.72
	^{99}Mo	0.42	0.91	0.79
	^{144}Ce	0.38	1.13	0.62
	^{147}Nd	0.37	—	0.69
	^{156}Eu	0.34	—	0.78

[a] Kilotons may be converted to equivalent fissions by multiplying by 1.45×10^{23}.

For Danny Boy the indices are roughly four times as high for the volatiles as for the nonvolatiles, while the intermediates fall between these extremes. This clear-cut, systematic difference in the indices is taken as evidence that fractionation occurred in the Danny Boy early fallout but to a much smaller degree (factor of four) than might have been predicted on the basis of other fractionation studies. (For example, late time samples of airborne debris have shown fractionation involving factors of several hundred.)

For Sedan the indices show little or no evidence of fractionation. They scatter somewhat, but not greatly for this type of information.

For Palanquin the indices suggest that some slight fractionation is present. Since the nonvolatile group forms such a consistent set, one is tempted to infer that the ^{89}Sr and ^{137}Cs mass chains are depleted and that all other nuclides are present in just about their production proportions.

These observations support the theoretical arguments advanced by Fedorov (5) for weak (little) fractionation in the early fallout from cratering events.

As a rough check on the magnitude of the indices in Table I, a theoretical estimate of the fractionation index for unfractionated fission products can be calculated as follows. The index has the units kiloton-hr./ft.^{2} roentgens; if we use the most probable value of 2500 roentgens/hr. for 1 kiloton/sq. mile over Nevada Test Site terrain for unfractionated fission products, we obtain (since 1 square mile $= 2.78 \times 10^7$ ft.^{2})

$$I = \frac{1}{2.78 \times 10^7 \times 2.5 \times 10^3} = 1.44 \times 10^{-11}.$$

This independently calculated theoretical value for the unfractionated index agrees closely with the experimental indices in Table I, thus giving support to their validity.

The relatively small spread of the numbers in Table I (about a factor of six from smallest to largest) is remarkable in view of the considerable differences in venting phenomenology among the three shots and the variety of sources for the radiochemical data used. Danny Boy data were supplied by the U.S. Air Force; Sedan data by Tracerlab, Nuclear Science and Engineering Corp., and Hazleton Nuclear Science Corp.; Palanquin data were supplied by Lawrence Radiation Laboratory.

To summarize, there appears to have been little fractionation in the early fallout from these three cratering events, with Danny Boy being the only one of the three to show unambiguous evidence of fractionation. If this observation proves to be true in general for cratering shots, then predictions of early fallout gamma-radiation patterns will be simplified.

Literature Cited

(1) Miskel, J. A., Bonner, N. A., University of California, Lawrence Radiation Laboratory, **WT-1817** (Dec. 31, 1964).
(2) Lane, W. B., U. S. Naval Radiological Defense Laboratory, **PNE-229F** (Jan. 7, 1964).
(3) Nordyke, M. D., Williamson, M. M., University of California, Lawrence Radiation Laboratory, **PNE-242F** (Aug. 6, 1965).
(4) Schwartz, L. L., University of California, Lawrence Radiation Laboratory, private communication of Project Palanquin radiochemical results.
(5) Fedorov, Ye. K., *Dokl. Akad. Nauk* **169,** 575 (1966).

RECEIVED June 4, 1968. Work done under the auspices of the U. S. Atomic Energy Commission.

Small Boy Revisited: An Exercise in the Recovery of Questionable Data from a Field Operation

G. R. CROCKER[1] and E. C. FREILING[1]

Naval Radiological Defense Laboratory, San Francisco, Calif. 94135

The large body of radiochemical data available from the low yield land-surface event Small Boy has been re-examined for internal consistency by a variety of methods. It was possible to show that certain portions of the data are not sufficiently reliable to be useful for establishing the fractionation behavior of fission-product radionuclides in the nuclear debris. Certain other parts of the data are shown to need adjustment for calibration differences which existed between the four laboratories which performed the analyses. Despite the shortcomings of the data, it was possible to establish that the relationships which existed among the fractionating radionuclides were qualitatively similar to those previously observed for other events. Other features of the data appear to be unique to Small Boy.

The radiation properties of debris from nuclear bursts depend on the concentrations of the fission products in the debris. It is not possible to predict these concentrations from a knowledge of the yields of the radionuclides for the fission process in question since the fission products undergo severe fractionation during fallout formation—*i.e.*, the proportions of the fission products found in samples of nuclear debris are often very different from the production ratios, sometimes being much larger and at other times much smaller than expected. In principle, fractionation phenomena are understood since they have their basis in the large differences in volatility of the fission products relative to the inert mate-

[1] Present address: FCA, U. S. Naval Weapons Laboratory, Dahlgren, Va. 22448.

rial (soil, device casing, associated hardware, etc.) in the fireball. Thus, fission products which exist as inert gases during fallout formation will be distributed quite differently from those that exist as refractory oxides. However, a direct calculation of the fractionated compositions of fallout formed in various situations is handicapped by a shortage of appropriate thermodynamic and kinetic input data, as well as by uncertainties regarding the hydrodynamic and meteorological processes involved. Accordingly, reliance is placed on the empirical analysis of experimental radiochemical data on fallout. For many burst conditions, correlation methods have resulted in the discovery of several rather simple relationships among the fission-product mass chains with regard to their fractionation behavior. The relationships provide a practical means for predicting the radiochemical composition of fallout.

Earlier reports from this Laboratory presented the results of correlations of radiochemical data from some coral and seawater surface events of Operation Redwing (*4*), from some similar events of Operation Hardtack (*2*), and from some airburst events (*7*). This report presents the results of studies of data from Small Boy, a silicate-soil surface event of Operation Sunbeam.

Background

The treatment of radiochemical results on fractionated fallout samples is greatly facilitated if the data are expressed in equivalent fissions. The number of equivalent fissions of a particular nuclide is the number of atoms of the fissionable material in the device which must have undergone fission to produce the amount of the radionuclide observed in the sample. If the sample contains a_n atoms of nuclide n (at the time of detonation), and if the fractional yield of nuclide n for the device was y_n, the number of equivalent fissions, f_n, is:

$$f_n = \frac{a_n}{y_n}$$

If the sample is unfractionated, the value of f_n for all nuclides will be the same, but in the fractionated case very different values of f_n for some of the nuclides will be observed. Any pair of nuclides, i and j, may be compared by formation of the ratio:

$$r_{i,j} = \frac{f_i}{f_j}$$

If i and j have been incorporated in the fallout to the same extent, the ratio will be 1. If they have been incorporated to different extents (and, presumably, by different mechanisms), the ratio may be much less than or much greater than 1. Samples of fallout collected in the field may

show considerably different values of the ratio for the same pair of nuclides, particularly if the sampling locations are widely separated. The set of ratios for debris collected by aircraft flying through the cloud will generally differ significantly from the ratios for fallout deposited on the ground in the local area. Any sample which is subdivided into fractions of different particle sizes will generally show different values of the ratios for the various fractions.

In discussing the fission-product composition of fallout samples it is advantageous to choose some fission product as a reference nuclide, j, and express the composition of the other fission products i by a set of $r_{i,j}$ ratios. For local fallout from land-surface bursts the choice of ^{95}Zr as reference nuclide has proved convenient. A ratio of particular interest is $r_{89,95}$ since ^{89}Sr and ^{95}Zr generally fractionate from each other about as severely as any pair of nuclides. Thus, $r_{89,95}$ indicates approximately the maximum extent of fractionation that will be observed in the sample.

Freiling (*4*, *7*) pointed out that $r_{i,95}$ correlates logarithmically with $r_{89,95}$. If, on log-log paper, the values of $r_{i,95}$ for several samples are plotted as ordinates against corresponding $r_{89,95}$ values as abscissas, the data can be fitted to a straight line of the form:

$$\log r_{i,95} = a_i + b_i \log r_{89,95} \quad (1)$$

with coefficients of correlation usually greater than 0.70 for values of b_i between 0.5 and 1.0. The slope of the line indicates the degree of fractionation of nuclide i from ^{95}Zr, relative to the fractionation of ^{89}Sr from ^{95}Zr. If the slope is 1, then i and ^{89}Sr have fractionated in the same way and to the same extent. A slope of zero indicates that i has not fractionated at all from ^{95}Zr. Intermediate values indicate intermediate fractionation behavior, while values greater than 1 indicate that i has fractionated from ^{95}Zr more extensively than ^{89}Sr. Small negative values of the slope of the correlation line are encountered occasionally. These are interpreted to mean that nuclide i has fractionated from ^{95}Zr in a sense opposite to the fractionation of ^{89}Sr. That is, increasing enrichment in ^{89}Sr, relative to ^{95}Zr, is correlated with increasing depletion in i.

The parameter a_i in Equation 1 is the value of the ordinate corresponding to $\log r_{89,95} = 0$; in other words, it leads to the value of $r_{i,95}$ which corresponds to $r_{89,95} = 1$. Statistical treatment does not give satisfactory assignment of values to this parameter since it is very sensitive to errors in analysis and calibration. Within rather large uncertainties, a_i can usually be considered zero. This implies that if, in a given sample, ^{89}Sr is not fractionated from ^{95}Zr, no other fission products should be appreciably fractionated in that sample. Although this expectation appears reasonable, the data do not always support it strongly, and for airbursts there are theoretical reasons for expecting otherwise.

The results of correlation studies reported in Refs. 2, 4, and 7 indicated that the fractionation behavior of most fission products was remarkably similar for coral surface bursts, bursts on the surface of deep and shallow seawater, and bursts at altitudes sufficiently great to avoid entrainment of soil or water in the fireball and cloud. Furthermore, the correlations showed no clear-cut dependence on the explosive yield of the device. This report extends the treatment to a near-surface event on silicate soil.

The data utilized in this report pertain to the event called Small Boy, which occurred at Nevada Test Site in 1962. Small Boy was a low yield shot fired from a wooden tower slightly above the surface of alluvial soil. The Naval Radiological Defense Laboratory (NRDL) collected many samples of debris deposited on the ground at 43 stations within 8.7 miles of ground zero and took other samples on a line 15 miles from ground zero. Further samples were supplied by the University of California at Los Angeles (UCLA) sampling network at distances of 18, 27, 36, 52, and 70 miles. Four cloud samples were supplied by Los Alamos Scientific Laboratory (LASL). The discussion in this report is concerned mainly with samples taken within 8.7 miles of ground zero and the cloud samples. The number of samples analyzed from each station varied, and many samples were subdivided by sieving into seven sieve fractions which were analyzed individually. Radiochemical data on a total of about 187 samples were suitable for the correlation studies reported here. All of these samples were analyzed for ^{89}Sr, ^{90}Sr, ^{91}Y, and ^{95}Zr. In addition, about one-third of them were analyzed for ^{99}Mo, ^{103}Ru, ^{106}Ru, ^{136}Cs, ^{137}Cs, ^{140}Ba, ^{141}Ce, ^{144}Ce, ^{239}Np, and ^{239}Pu. Some of the latter group of samples were analyzed also for ^{131}I and ^{132}Te. The details of the collection of the NRDL and UCLA samples, along with some gross physical and radiological properties, are documented in Ref. 9.

Since in-house facilities for handling a large volume of samples for routine analysis were not available, the analytical work was contracted out to three commercial laboratories. We will refer to them as Laboratories A, B, and C. The contractors were selected on the basis of qualification tests which were intended to serve also for interlaboratory calibration. The results were reported to NRDL as d.p.m. or equivalent ^{235}U thermal-neutron fissions at detonation time. All of the radiochemical data obtained from the laboratories are reported in Ref. 5. These values were punched on cards and converted by computer to equivalent fissions of the device, based on mass-chain yield values supplied by the weapons laboratories. At the same time, the calibration factors derived from qualification-test analyses were applied. Values of the ratios, $r_{i,95}$, were formed. All of the ratios for a given nuclide i were then selected along with the corresponding values of $r_{89,95}$, and the data points were fitted

to Equation 1 by the computer. Values of the parameters a_i and b_i were printed out along with their 95% confidence limits and the coefficients of correlation.

A study of the effect of fractionation on the radiation levels in the local fallout field, as revealed by the radiochemical data, was reported by Crocker (*1*). A preliminary presentation of the correlations is given in Ref. 3.

In considering the correlation results, it is well to keep in mind the range of fractionation, as indicated by the values of the $r_{89,95}$ ratio, shown by the samples in question. For the Small Boy event most of the gross samples from the collecting stations in the local fallout field yielded values of $r_{89,95}$ in the range between 0.1 and 0.2. However, when cloud samples, sieve fraction samples, and samples from the peripheral stations are also considered, the range of the ratio runs from about 0.01 to about 7.0.

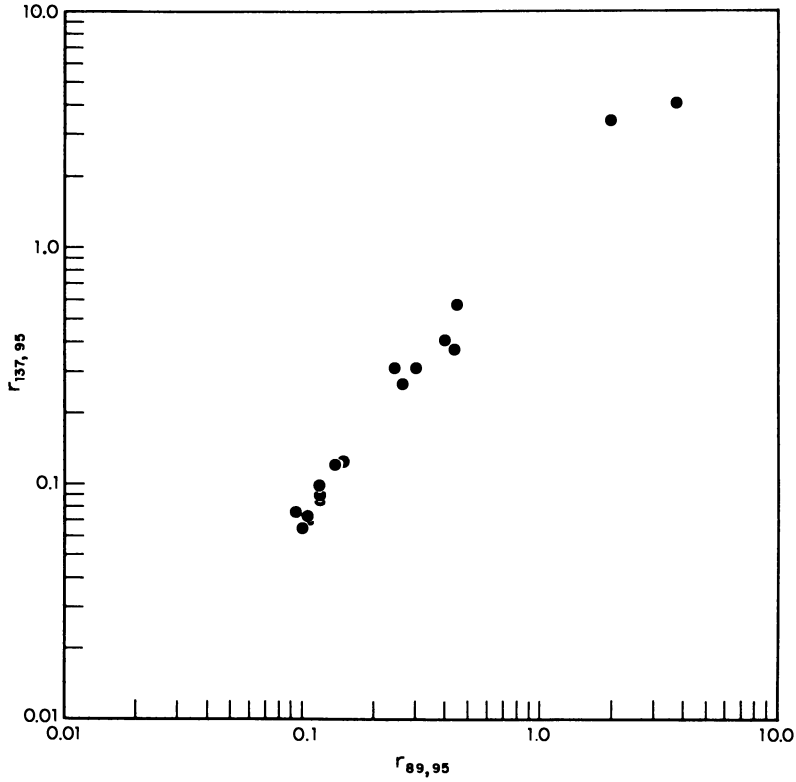

Figure 1. Correlation of ^{89}Sr and ^{137}Cs data reported by Laboratory A

All of the data were plotted on log-log paper along with the correlation lines as given by the parameters from the computer-fitting routine. Figure 1 shows the results for ^{137}Cs and ^{89}Sr, which illustrate a reasonably satisfactory fit. Much of the data do not fit a linear log-log correlation line this well. Figure 2, for example, shows part of the results for ^{90}Sr.

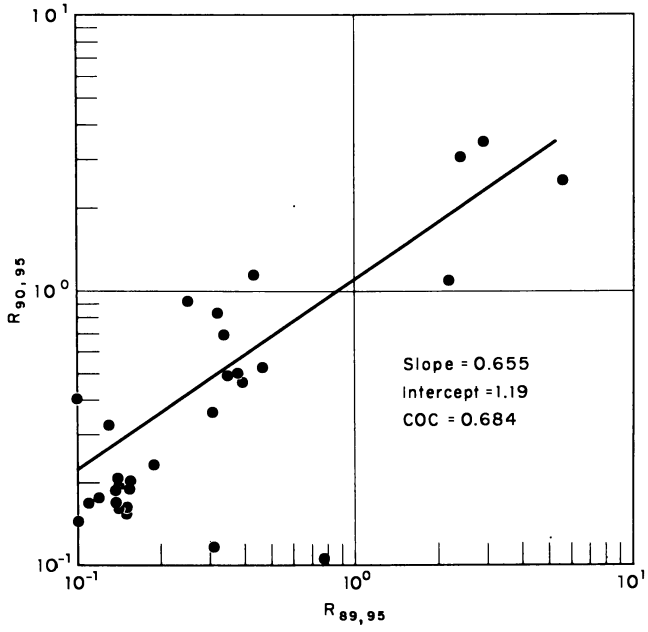

Figure 2. Correlation plot for ^{90}Sr data

The data were originally fitted by lumping together data points from all three contracting laboratories. While investigating a poor fit of ^{141}Ce data, we noticed that points from Laboratory A could be fitted fairly well, while those from Laboratory B scattered so badly as to suggest that Laboratory B was experiencing difficulty with this particular analysis. Figure 3 shows these data. Investigation of the ^{103}Ru and ^{106}Ru data showed the same situation but reversed with respect to the two laboratories—Laboratory B points correlated better than Laboratory A points.

In some instances, calibration differences among the laboratories also appeared to be obscuring the correlation. Figure 4 illustrates this effect. When ^{91}Y data from the three laboratories are treated separately, one attains the three lines with a reasonable degree of confidence. Note that their slopes do not differ greatly, but that the intercepts differ appreciably. Consequently, when the data are lumped together, the correlation is much less clear.

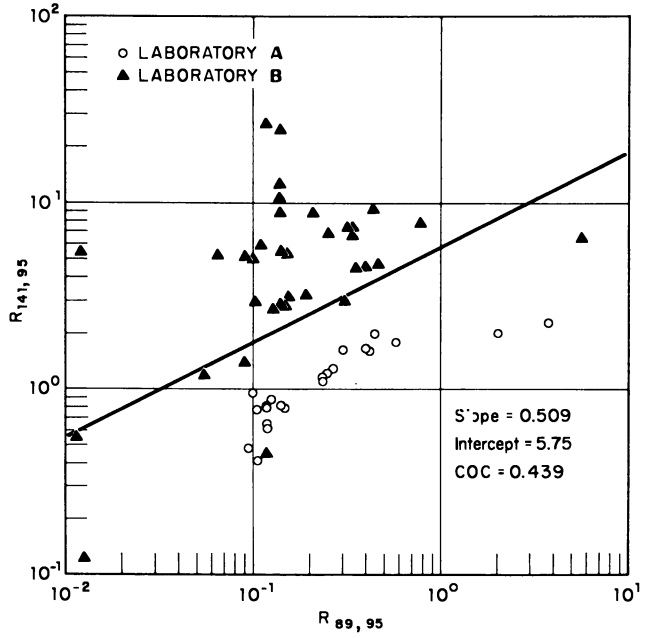

Figure 3. Correlation plot for the ^{141}Ce data

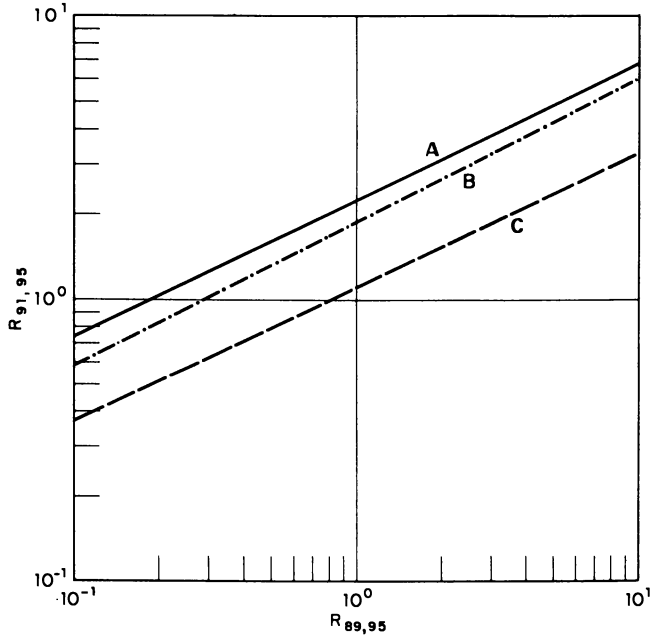

Figure 4. Correlation lines for ^{91}Y data from three different laboratories

Considerations such as these made it evident that if useful information were to be obtained from the Small Boy effort and if misleading results were to be avoided, a complete re-examination of the data was called for.

Method

Our objective in re-examining the 1446 pieces of Small Boy data has been to extract the maximum amount of information and the minimum amount of misinformation with the least amount of tampering. Our method has turned out to be a loop which we have traveled innumerable times. The first step of the loop was to choose, for a given laboratory, the best substantiated correlation available and select the outliers. We next traced the outliers through every other meaningful correlation to corroborate their spuriousness. The procedure was repeated for the next best substantiated correlation, and so on, as far as we could carry it. The data from the other laboratories were treated similarly in turn. We have thus examined the data exhaustively for mutual consistency. In many cases we were able to show that a datum violated more than one criterion, and we rejected it on that basis. In other cases, data were so far out of line that there was no question as to their abnormality. In still other situations we found that correlations could be established with the data from one laboratory but not with the data from another. We then rejected the irregular data *in toto*.

Whatever success we have achieved has been greatly assisted by the eventual availability of highly reliable data from a fourth laboratory, Laboratory D.

Some highlights of the method follow. Space limitations prohibit a complete account. [Complete details can be found in Ref. 6.]

Correlation of the ^{95}Zr, ^{99}Mo, ^{144}Ce, and ^{239}Pu Data. Since the correlation method used in these studies was based on plotting the ratio $r_{i,95}$ *vs.* $r_{j,95}$, it is important to establish that the ^{95}Zr data used in forming the ratios were reliable. A check on the internal consistency of the ^{95}Zr values can be made by inspecting the $r_{99,95}$ and $r_{144,95}$ ratios, both of which should be near 1. If the ^{95}Zr value for a sample is erroneous, both $r_{99,95}$ and $r_{144,95}$ should be anomalous, barring a compensatory error in the ^{99}Mo or ^{144}Ce value. For one of the 18 data points (for the sample group under discussion here) from Laboratory A, and for five of the 29 data points from Laboratory B, one (but not both) of the ratios $r_{99,95}$ and $r_{144,95}$ was anomalous. These anomalies, therefore, probably reflect questionable ^{99}Mo or ^{144}Ce values rather than ^{95}Zr values. The average values of the ratios (after discarding the anomalous ones) and the standard deviations are shown in Table I.

Table I. Average Values and Standard Deviations of $r_{99,95}$ and $r_{144,95}$

	$r_{99,95}$	$r_{144,95}$
Laboratory A	1.13 ± 0.04	1.23 ± 0.07
Laboratory B	0.90 ± 0.09	1.35 ± 0.20

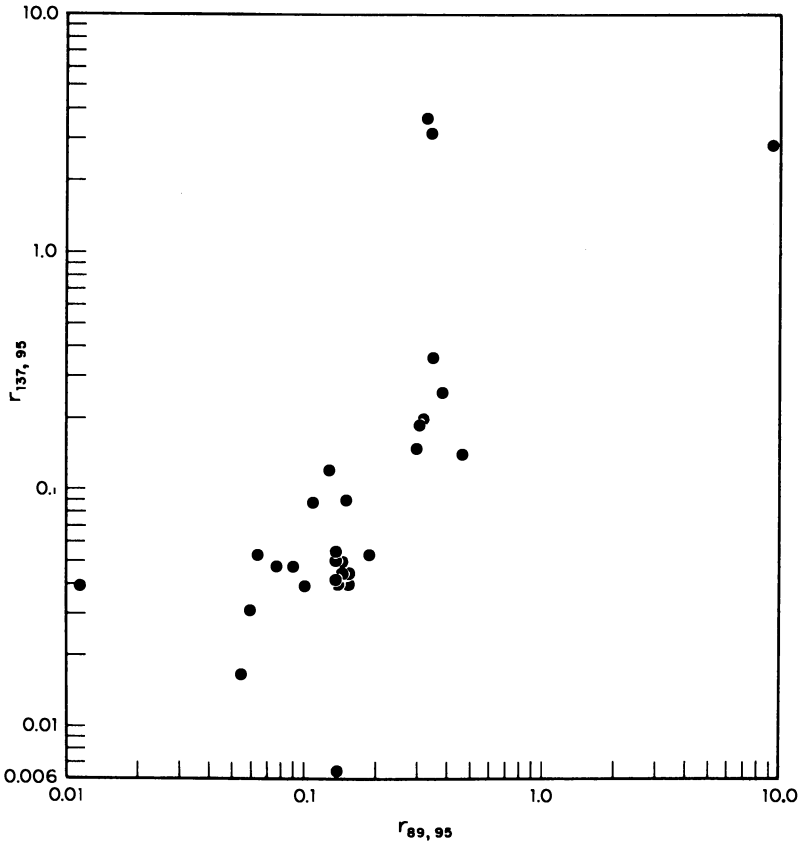

Figure 5. Correlation of ^{89}Sr and ^{137}Cs data reported by Laboratory B

The uncertainties shown in Table I are acceptable in data for correlation purposes, with the possible exception of the $r_{144,95}$ values from Laboratory B. The rather large deviations here probably reflect uncertainty in the ^{144}Ce values, rather than in the ^{95}Zr values since (as mentioned in connection with Figure 3) the ^{141}Ce data from Laboratory B also appeared to contain large uncertainties. Table I also shows that calibration differences with respect to ^{99}Mo probably existed between the two laboratories. From the preceding discussion and that data in Table I it is reasonable to conclude that the ^{95}Zr data from both labora-

tories were reliable and were not responsible for the correlation difficulties encountered.

The $r_{239,95}$ values reported by Laboratory A for 25 samples averaged 1.03 ± 0.14 after two values were discarded as anomalous. These data, taken with those quoted in the preceding paragraphs, clearly indicate that ^{95}Zr, ^{99}Mo, ^{144}Ce, and ^{239}Pu formed a group of nuclides which did not fractionate from each other significantly.

Correlation of ^{89}Sr and ^{137}Cs Data. The ratio $r_{89,95}$ is important since it is ordinarily used as the reference with which the ratios for all of the other fractionating mass chains are compared. Experience in correlating fallout radiochemical data has shown (*2*, *4*, *7*) that the behavior of $r_{89,95}$ is closely similar to that of $r_{137,95}$. This provides a way of checking the reliability of the ^{89}Sr and ^{137}Cs data. Figure 1 showed a plot of $r_{137,95}$ *vs.* $r_{89,95}$ for the group of samples analyzed by Laboratory A. The correlation here was sufficiently good to assure that the ^{89}Sr and ^{137}Cs analyses are not in serious error, at least in a relative sense. [Absolute

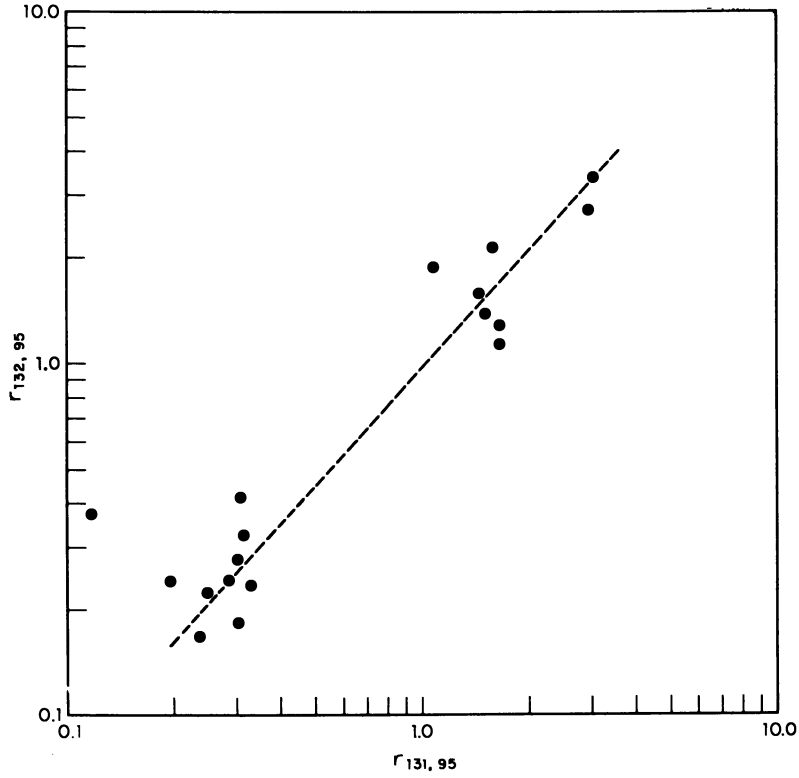

Figure 6. Correlation of ^{131}I and ^{132}Te data reported by Laboratory A

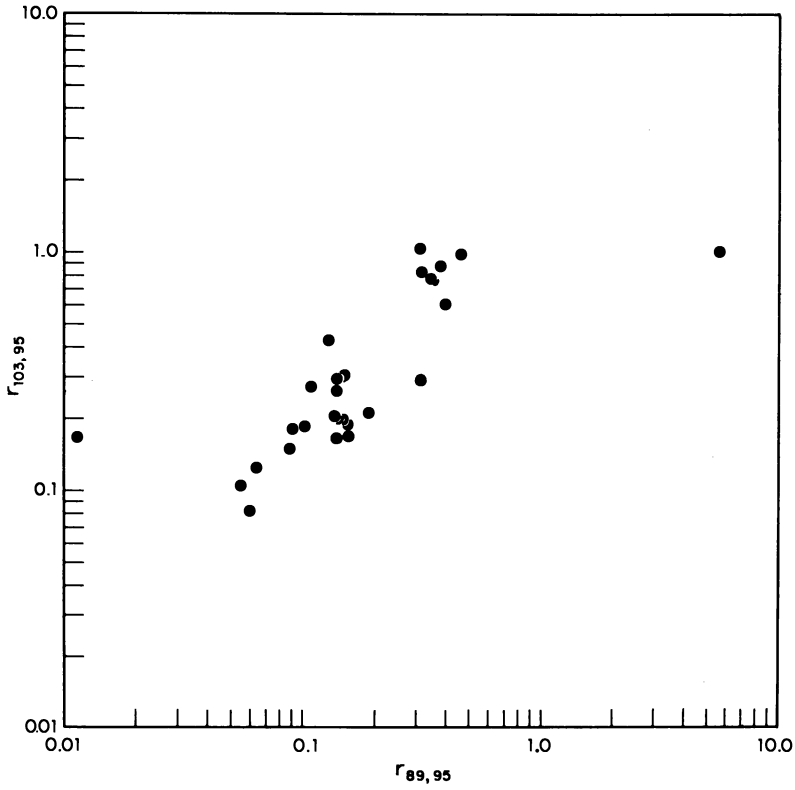

Figure 7. Correlation of ^{103}Ru and ^{89}Sr data reported by Laboratory B

values come into question only in determining the intercept of the correlation line. Since some calibration differences between the laboratories existed (*see* Figure 4 and Table I), it is not appropriate to compare the data on an absolute basis.] On the other hand, the data from Laboratory B, shown in Figure 5, correlate poorly. Since the groups of samples supplied to Laboratories A and B were quite alike, it is difficult to escape the conclusion that either the ^{89}Sr or the ^{137}Cs data (or both) from Laboratory B are not sufficiently accurate for correlation. As shown later, there are reasons for believing that the ^{137}Cs data are more reliable than the ^{89}Sr data. Hence, $r_{137,95}$ was used as the reference ratio in most of the correlations of Laboratory B data in the remainder of this section.

The ^{131}I and ^{132}Te Data from Laboratory A. Attempts to correlate $r_{131,95}$ and $r_{132,95}$ with $r_{89,95}$ or $r_{137,95}$ for the group of samples analyzed by Laboratory A were unsatisfactory. Since confidence had been established in the ^{89}Sr, ^{137}Cs, and ^{95}Zr values, the ^{131}I and ^{132}Te data invited scrutiny. The elemental compositions of the mass-131 and mass-132

chains are predicted to be similar at the time of fallout formation, and accordingly, one would expect the $r_{131,95}$ and $r_{132,95}$ values to correlate closely. Figure 6 shows a log-log plot of these ratios, but the expected correlation is absent. There is no good way to explain this plot unless one is willing to suppose that the mass-131 and mass-132 chains fractionate appreciably from each other in a random way. The alternative is to assume that random errors in the data are obscuring a correlation line such as that which has been dotted in on the figure. This line, which has a slope slightly greater than unity and passes near the point ($r_{131,95} = 1$, $r_{132,95} = 1$), was drawn in by inspection. Although the procedure is hardly justifiable, it is interesting to note that by arbitrary "correction" of the data points so that they lie on the dotted line the correlation of both the $r_{131,95}$ and $r_{132,95}$ ratios with the $r_{137,95}$ ratio can be considerably improved. [Either $r_{137,95}$ or $r_{89,95}$ could be chosen here. Since correlation between these two ratios has been established, a satisfactory correlation of some third ratio with one of them will assure correlation with the other.]

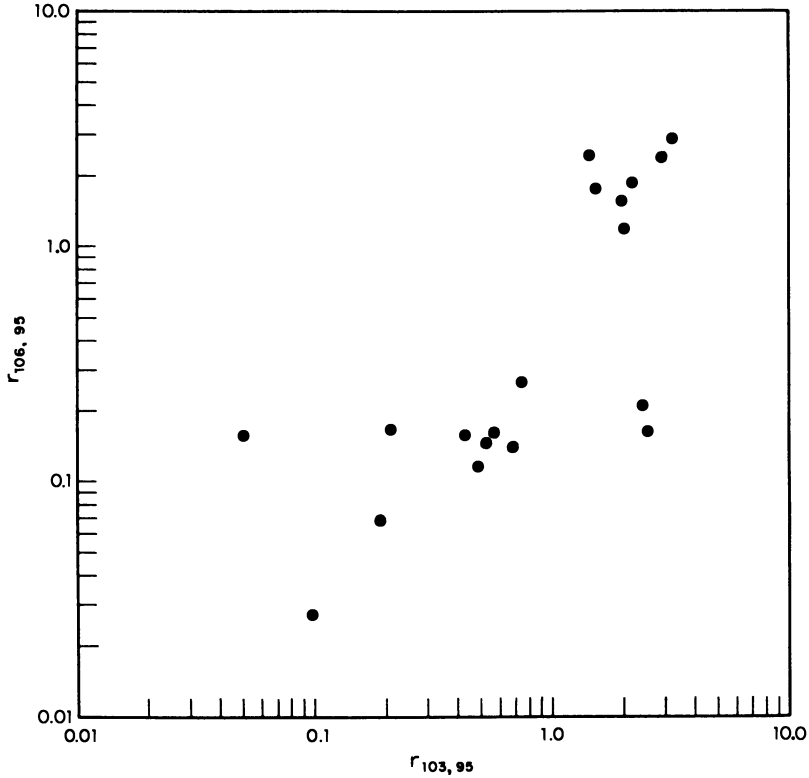

Figure 8. Correlation of ^{103}Ru and ^{106}Ru data reported by Laboratory A

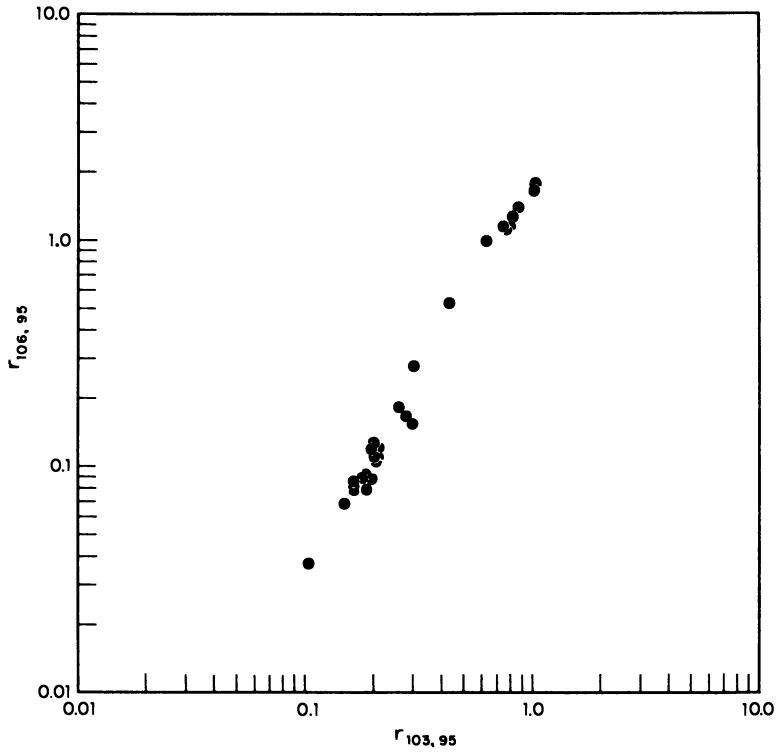

Figure 9. Correlation of ^{103}Ru and ^{106}Ru data reported by Laboratory B

Analysis for ^{131}I was not requested from Laboratory B on its group of samples. The ^{132}Te data reported by Laboratory B are discussed below.

Correlation of the ^{103}Ru and ^{106}Ru Data. The results on ^{103}Ru and ^{106}Ru offer another opportunity for evaluating the data for internal consistency. Both Laboratory A and Laboratory B reported data on these two radionuclides, but neither set of data yielded satisfactory correlation with $r_{89,95}$. A typical example of these correlations is shown in Figure 7. The mass-103 and mass-106 chains, like mass-131 and mass-132, are expected on theoretical grounds to fractionate in the same way and should correlate closely. Figure 8 shows the data on the two ruthenium isotopes as reported by Laboratory A. The points scatter badly with only a vague indication of the expected correlation. In contrast, the ruthenium data reported by Laboratory B, shown in Figure 9, display a remarkably good correlation. Again, as in the case of the ^{89}Sr–^{137}Cs correlations, one cannot easily avoid the conclusion that one set of data is reliable and the other is not. Note that the position of the two laboratories is reversed;

the questionable ^{89}Sr–^{137}Cs data were submitted by Laboratory B, while Laboratory A submitted the questionable ^{103}Ru–^{106}Ru data.

The failure of the ^{103}Ru and ^{106}Ru data to correlate with the ^{89}Sr data thus appears to be caused by bad ruthenium data for Laboratory A and by bad strontium data for Laboratory B. This also provides a partial explanation of the poor ^{89}Sr–^{137}Cs correlation (Laboratory B) of Figure 5. The question remains as to whether the poor correlation arises solely from bad ^{89}Sr data—*i.e.*, it is possible that the ^{137}Cs data are reliable. To test this, the ^{103}Ru data and the ^{137}Cs data were plotted in Figure 10. The correlation in this case is noticeably better than in Figure 7, where the same ^{103}Ru data are plotted with the ^{89}Sr data. We conclude, accordingly, that the ^{137}Cs data reported by Laboratory B are more reliable than the ^{89}Sr data.

The shape of the correlation plot in Figure 10 is unusual. It appears that sufficient data of satisfactory quality would dictate a curvilinear correlation line. This behavior is not entirely unprecedented since curvi-

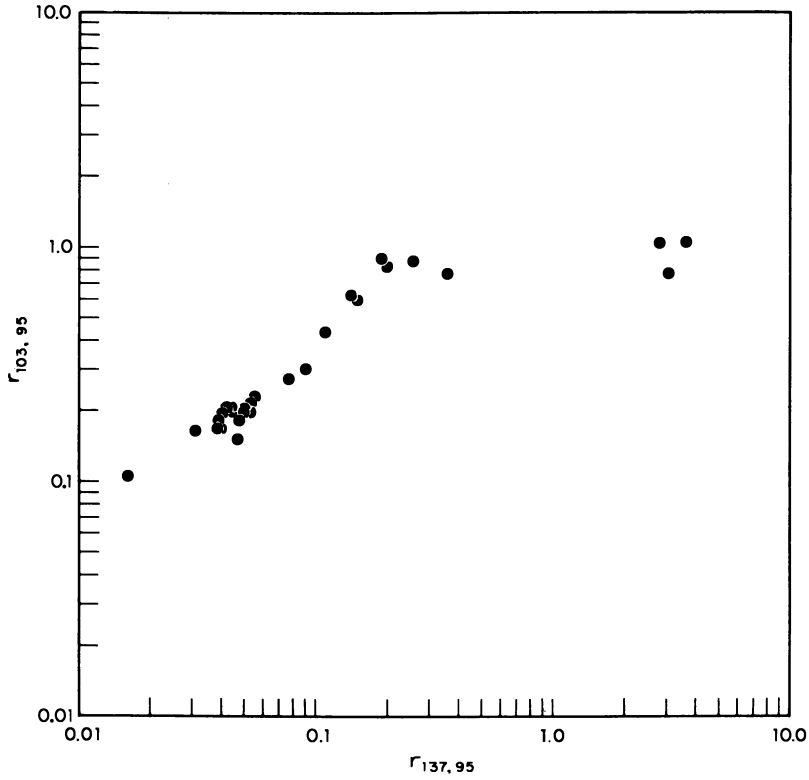

Figure 10. Correlation of ^{103}Ru and ^{137}Cs data reported by Laboratory B

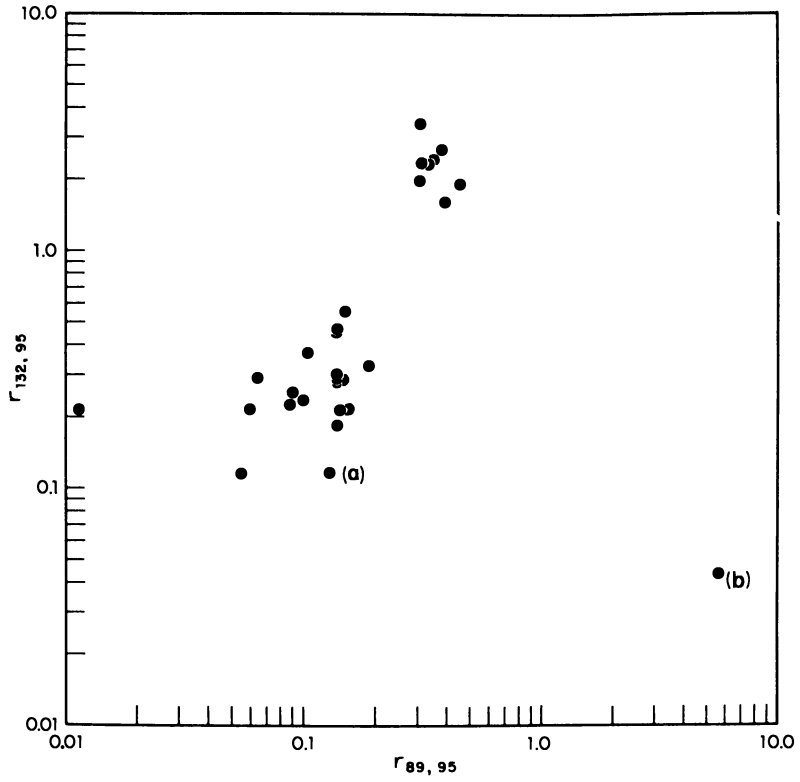

Figure 11. Correlation of the ^{132}Te with ^{89}Sr data reported by Laboratory B

linear correlations were noted in study of the radiochemical data (8) on debris from the Kiwi Transient Nuclear Test (TNT). [In the Kiwi-TNT experiment, a rapid reactivity insertion vaporized about 5% of the core of a Kiwi reactor and converted some 68% of it to a cloud of finely divided material. The conditions under which this debris was formed were very different from those under which fallout from weapons tests is formed. Nonetheless, certain similarities were observed in radionuclide fractionation behavior in the two kinds of debris.]

The excellent correlation shown in Figure 9 indicates that the mass-103 and mass-106 chains fractionate in the same way, the latter being considerably more volatile than the former.

Correlation of the ^{132}Te Data from Laboratry B. Laboratory B determined ^{132}Te on its samples but not ^{131}I. The values of $r_{132,95}$ are plotted *vs.* $r_{89,95}$ and $r_{137,95}$ in Figures 11 and 12, respectively. The plots resemble Figures 7 and 10, inasmuch as the correlation with $r_{137,95}$ is better than that with $r_{89,95}$, and they support the contention that the

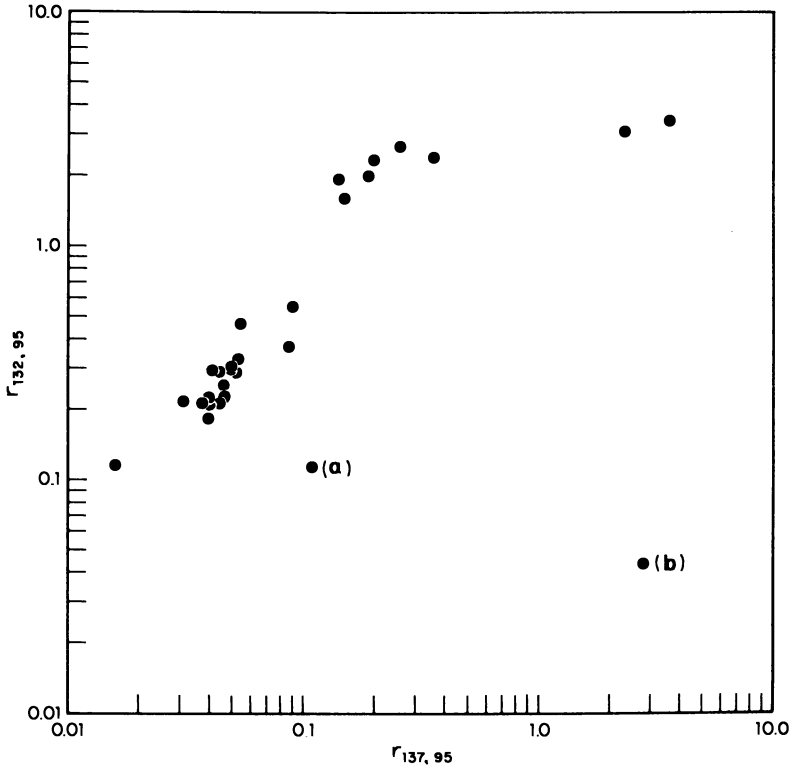

Figure 12. Correlation of the ^{132}Te with ^{137}Cs data reported by Laboratory B

^{137}Cs values reported by Laboratory B are more reliable than the ^{89}Sr values. In fact, the resemblance between Figures 10 and 12, aside from the outlying points (a and b), is close enough to suggest that the ^{103}Ru data for these samples should correlate with the ^{132}Te data. As shown in Figure 13, the correlation is indeed remarkably good. Inspection of Figures 11, 12, and 13 now strongly suggests that the $r_{132,95}$ value for Point a is low by a factor of 10 and for Point b is low by a factor of 10^2. Powers-of-ten errors in data of this kind are not uncommon.

The success of the correlation of the ^{103}Ru and ^{132}Te data from Laboratory B in Figure 13 suggested that a similar attempt should be made with the data on these nuclides from Laboratory A. Since these data, as discussed earlier, had already appeared to be inconsistent, it was not surprising that the correlation of $r_{132,95}$ and $r_{103,95}$ (shown in Figure 14) failed. Similar attempts to correlate the ^{103}Ru data with the ^{131}I data and to correlate the ^{106}Ru data with either the ^{132}Te or ^{131}I data failed for the Laboratory A samples.

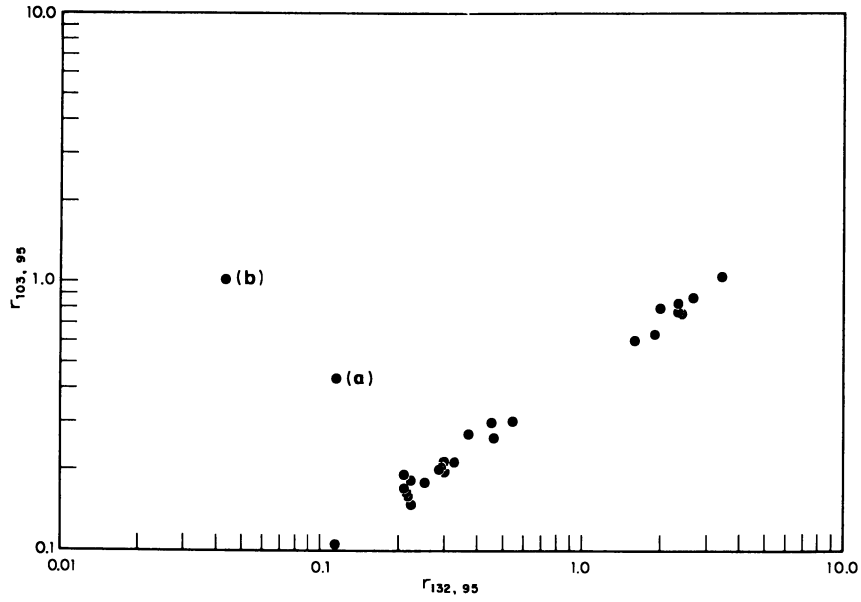

Figure 13. Correlation of ^{103}Ru with ^{132}Te data as reported by Laboratory B

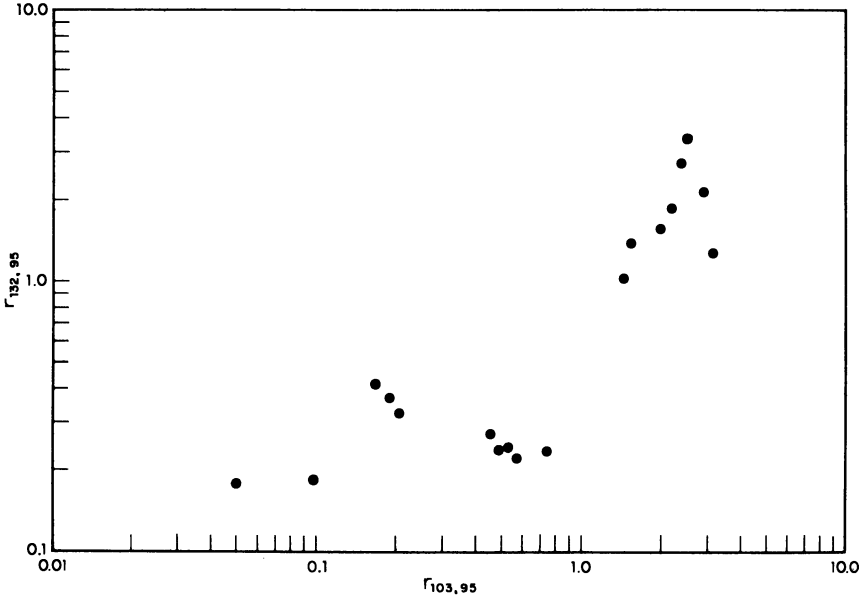

Figure 14. Correlation of the ^{132}Te and ^{103}Ru data from Laboratory A

Correlation of the ^{136}Cs, ^{140}Ba, and ^{141}Ce Data. The correlations discussed so far provide standards for evaluating the reliability of the remaining data on fractionating mass chains as reported by Laboratories A and B in a fairly straightforward manner. With the exception of two outlying points, the ^{136}Cs data reported by Laboratory A correlated well with the ^{137}Cs data. On the other hand, the ^{136}Cs data reported by Laboratory B show almost no correlation with the corresponding ^{137}Cs data (which have been established to be of reasonable reliability). We thus conclude that with regard to ^{136}Cs Laboratory A data are good and Laboratory B data are poor. Exactly the same conclusion can be reached

Table II. Selected, Adjusted, and Condensed Results for Laboratory A

A. Krypton Daughters[a]

	Sample	f_{89}	f_{90}	f_{91}	$f_{90}{}^2/f_{91}K$[b]	f_V[b] Ave. S.D.	Exp.[c]
	Cloud Samples						
1.	245-L1-2	R[f]	5.62	4.84	R	—	13
2.	842-R1-1A	7.96	8.09	6.00	7.05	7.50 ± 0.64	13
	Close-in Gross Fallout Samples						
1.	S1S-PC-2	3.33	9.45	18.3	3.14	3.24 ± 0.15	13
2.	S1N-PC-1	2.20	5.96	9.24	2.49	2.34 ± 0.21	11
3.	S2-PC-21	9.25	26.3	46.7	9.49	9.37 ± 0.12	13
4.	S3-PC-16	1.92	4.70	6.91	2.06	1.99 ± 0.09	10
5.	S5-PC-1	1.04	2.84	6.02	0.86	0.95 ± 0.13	14
	Close-in Sieve Fractions						
1.	101-AO-6-7	1.04	2.84	5.43	0.95	1.00 ± 0.07	14
2.	101-AO-6-24	1.32	3.70	7.54	1.17	1.24 ± 0.11	14
3.	101-AO-6-PAN	2.05	5.66	9.32	2.14	2.10 ± 0.07	12
4.	403-AO-4-7-12	1.13	2.57	3.32	1.29	1.21 ± 0.11	13
5.	403-AO-4-80	1.80	5.18	10.0	1.72	1.76 ± 0.06	14
6.	403-AO-4-PAN	3.67	8.46	12.7	3.65	3.66 ± 0.01	13
7.	S5-PC-4-80	1.40	4.24	8.50	1.36	1.38 ± 0.03	14
8.	707-AO-3-24	1.13	4.01	6.55	1.59	1.36 ± 0.32	12
9.	707-AO-3-170	1.55	4.36	8.70	1.41	1.48 ± 0.10	14
10.	707-AO-3-PAN	1.02	2.68	4.02	1.14	1.08 ± 0.08	13
	Long Range Sieve Fractions						
1.	13-LA-1-10-12	5.00	13.9	25.0	5.00	5.00 ± 0.00	13
2.	13-LA-1-10-42	7.52	22.1	34.2	9.20	8.36 ± 1.18	12
3.	13-LA-1-10-170	1.46	R	8.89	—	1.46 —	13
4.	13-LA-1-10-PAN	2.10	6.00	9.15	2.53	2.32 ± 0.31	12
5.	18-12B-LT-2	2.78	5.44	7.65	2.49	2.64 ± 0.21	11
6.	18-12B-GT-44	1.02	2.67	5.45	0.85	0.93 ± 0.13	13
7.	56-12B-LT-2	7.68	10.3	12.8	5.35	6.52 ± 1.64	10
8.	56-12B-GT-44	1.05	2.78	5.30	0.94	1.00 ± 0.08	12

Table II. Continued

B. Primary Properties

	Sample	Weight, grams	100-h Ionization Current (10^{-8} ma.)	f_R[d] Ave. S.D.	Exp.	$r_{V,R}$[e]
	Cloud Samples					
1.	245-L1-2	—	174	2.46 ± 0.08	13	—
2.	842-R1-1A	—	212	2.42 ± 0.01	13	3.10 ± 8.5%
	Close-in Gross Fallout Samples					
1.	S1S-PC-2	2.39	495	3.18 ± 0.09	14	0.102 ± 5.4%
2.	S1N-PC-1	1.15	3.17	1.02 ± 0.08	12	0.230 ± 12 %
3.	S2-PC-21	1.25	1070	8.89 ± 0.02	14	0.105 ± 1 %
4.	S3-PC-16	2.61	0.274	4.81 ± 0.17	10	0.414 ± 6.1%
5.	S5-PC-1	0.50	1200	1.13 ± 0.03	15	0.084 ± 14 %
	Close-in Sieve Fractions					
1.	101-AO-6-7	0.3090	1330	7.96 ± 0.40	14	0.126 ± 8.6%
2.	101-AO-6-24	3.2922	U[b]	1.26 ± 0.03	15	0.099 ± 9.2%
3.	101-AO-6-PAN	3.2903	374	8.73 ± 0.20	12	0.240 ± 4.0%
4.	403-AO-4-7-12	0.0196	259	2.35 ± 0.42	13	0.516 ± 20 %
5.	403-AO-4-80	0.8232	235	1.92 ± 0.12	15	0.092 ± 7.2%
6.	403-AO-4-PAN	0.0814	542	9.62 ± 0.28	13	0.380 ± 2.9%
7.	S5-PC-4-80	0.2050	2000	1.72 ± 0.14	15	0.080 ± 8.5%
8.	707-AO-3-24	0.0046	51.1	5.91 ± 0.80	12	0.230 ± 28 %
9.	707-AO-3-170	0.1474	1790	1.62 ± 0.09	15	0.091 ± 8.8%
10.	707-AO-3-PAN	0.0955	150.8	3.02 ± 0.26	13	0.358 ± 11 %
	Long Range Sieve Fractions					
1.	13-LA-1-10-12	0.0460	645	3.73 ± 0.41	14	0.134 ± 11 %
2.	13-LA-1-10-42	0.1120	148	3.45 ± 0.06	13	0.242 ± 14 %
3.	13-LA-1-10-170	3.5672	203	1.41 ± 0.04	14	0.104 ± —
4.	13-LA-1-10-PAN	5.6493	32.7	7.56 ± 0.29	12	0.307 ± 14 %
5.	18-12B-LT-2	U	U	3.39 ± 0.29	11	0.779 ± 12 %
6.	18-12B-GT-24	U	U	9.32 ± 0.08	13	0.100 ± 14 %
7.	56-12B-LT-2	U	U	6.49 ± 0.50	10	1.01 ± 26 %
8.	56-12B-GT-44	U	U	6.53 ± 0.17	12	0.153 ± 8.4%

C. Intermediate and Volatile Nuclides

	Sample	f_I[g] Ave. S.D.	f_{137}	f_J[h] Ave. S.D.	Exp.
	Cloud Samples				
1.	245-L1-2	4.41 ± 0.43	7.19	6.24 ± 0.03	13
2.	842-R1-1A	5.21 ± 0.43	8.62	7.04 ± 0.85	13

Table II. Continued

Sample	f_I[g] Ave.	S.D	f_{137}	f_J[h] Ave.	S.D.	Exp.
Close-in Gross Fallout Samples						
1. S1S-PC-2	18.8	± 2.8	2.74	8.38	± 0.21	13
2. S1N-PC-1	0.92	± 0.085	0.199	0.92	—	12
3. S2-PC-21	4.84	± 0.90	0.673	1.90	± 0.07	14
4. S3-PC-16	7.35	± 0.82	2.44	6.16	± 1.39	10
5. S5-PC-1	5.07	± 0.83	0.723	2.07	± 0.40	14
Close-in Sieve Fractions						
1. 101-AO-6-7	49.6	± 5.8	8.75	18	± 14	13
2. 101-AO-6-24	6.54	± 0.92	0.997	3.05	± 0.22	14
3. 101-AO-6-PAN	0.96	± 0.032	0.204	1.20	± 0.13	13
4. 403-AO-4-7-12	3.48	± 0.20	1.13	0.53	—	13
5. 403-AO-4-80	10.3	± 4.0	1.16	4.04	± 0.74	14
6. 403-AO-4-PAN	1.28	± 0.09	0.324	1.34	± 0.57	14
7. S5-PC-4-80	7.70	± 0.57	1.12	5.56	± 1.41	14
8. 707-AO-3-24	6.6	± 1.6	1.99	0.72	—	12
9. 707-AO-3-170	8.1	± 2.2	1.07	3.74	± 1.15	14
10. 707-AO-3-PAN	4.00	± 0.17	1.04	4.95	± 1.27	13
Long Range Sieve Fractions						
1. 13-LA-1-10-12	23.7	± 3.7	4.37	12.0	± 0.06	13
2. 13-LA-1-10-42	3.35	± 0.25	0.970	4.60	± 0.59	13
3. 13-LA-1-10-170	7.5	± 1.7	1.20	3.56	± 0.66	13
4. 13-LA-1-10-PAN	0.99	± 0.14	0.219	1.04	± 0.01	13
5. 18-12B-LT-2	7.6	± 1.4	1.52	15.5	± —	11
6. 18-12B-GT-44	4.9	± 2.1	0.754	3.21	—	13
7. 56-12B-LT-2	0.144	± 0.029	0.074	0.17	—	12
8. 56-12B-GT-44	3.7	± 1.4	0.727	5.12	—	12

[a] Units are in fissions for the cloud samples and fissions/gram for all other samples.
[b] f_V is the average of f_{89} and $f_{90}^2/f_{91}K$ where K is the average over-all samples of $f_{90}^2/f_{89}f_{91}$.
[c] Although shown only once, the exponent applies to the power of 10 to be associated with each number in the row.
[d] f_R is the average of f_{95}, f_{99}, f_{144}, and f_{239}(Pu).
[e] $r_{V,R}$ is defined as f_V/f_R.
[f] U = undetermined, R = rejected.
[g] f_I is the average of f_{91}, f_{136}, f_{140}, f_{141}, and f_{239}(Np).
[h] f_J is the average value of f_{131} and f_{132}.

regarding the ^{141}Ce data by the same plotting methods. However, the ^{140}Ba data from both laboratories correlate reasonably well with the ^{137}Cs data (and, for Laboratory A with the ^{89}Sr data).

Correlation of ^{90}Sr and ^{91}Y Data. With regard to these nuclides, there is a third set of data to consider along with the data from Laboratories A and B. The laboratory responsible for the third set, Laboratory

Table III. Selected, Adjusted, and Condensed Results for Laboratory B

		A. *Primary Properties*[a]				
	Sample	*Weight, grams*	*100-h Ionization Current (10^{-8} ma.)*[a]	f_R[b] *Ave. S.D.*	f_I[c] *Ave. S.D.*	*Exp.*
			Cloud Sample			
1.	842-R1-1D	—	205	2.34 ± 0.03	5.46 ± 0.28	13
			Close-in Gross Fallout Samples			
1.	101-AO-1	10.2	U[d]	4.29 ± 0.02	2.66 ± 0.03	14
2.	201-AO-7	4.0	U	6.25 ± 0.50	3.80 ± 0.37	14
3.	305-AO-2	1.88	U	8.7 ± 1.5	4.23 ± 0.17	14
4.	403-AO-2	1.85	U	11.3 ± 0.8	4.88 ± 0.17	14
5.	505-AO-1	1.53	U	7.12 ± 0.73	2.96 ± 0.01	14
6.	603-AO-4	0.61	U	— —	2.98 ± 0.67	14
7.	707-AO-6	0.38	U	— —	2.81 ± 0.02	14
			Close-in Sieve Fractions			
1.	S1S-PC-1-12	0.0320	979	5.41 ± 0.27	3.33 ± 0.62	14
2.	S1S-PC-1-80	0.1335	1140	7.92 ± 0.47	4.20 ± 0.20	14
3.	S1S-PC-1-PAN	1.0804	37.5	6.15 ± 0.51	7.2 ± 1.2	12
4.	S2-PC-16-12	0.0399	1890	9.77 ± 0.89	4.67 ± 0.18	14
5.	S2-PC-16-42	0.3960	1710	12.9 ± 1.4	5.64 ± 0.61	14
6.	S2-PC-16-170	0.2498	79.3	3.22 ± 0.35	2.25 ± 0.02	13
7.	S2-PC-16-PAN	0.1262	84.8	2.02 ± 0.06	2.14 ± 0.30	14
8.	201-AO-10-7	0.0322	1130	4.76 ± 1.3	3.31 ± 0.03	13
9.	201-AO-10-42	1.3357	1880	11.4 ± 1.4	5.40 ± 0.16	14
10.	201-AO-10-PAN	0.5360	102.1	1.59 ± 0.11	2.17 ± 0.50	13
11.	305-AO-4-7	0.0245	889	6.0 ± 0.21	2.03 ± 0.24	14
12.	305-AO-4-42	0.7198	1805	13.0 ± 0.8	5.35 ± 0.43	14
13.	305-AO-4-PAN	0.0809	298	7.69 ± 0.79	7.52 ± 0.84	14
14.	403-AO-3-80	0.7897	—	14.7 ± 1.1	6.80 ± 0.61	14
15.	S5-PC-5-12	0.0034	41.2	1.40 ± 0.28	R[e]	12
16.	S5-PC-5-80	0.2410	2590	11.9 ± 0.2	5.24 ± 0.43	14
17.	S5-PC-5-PAN	0.0500	63.4	0.51 ± 0.06	6.70 ± 0.42	14
18.	505-AO-6-7,24	0.0288	9.48	1.00 ± 0.23		12
19.	505-AO-6-80	0.5565	2210	16.8 ± 3.1	6.46 ± 0.63	14
20.	505-AO-6-PAN	0.5001	177.4	2.53 ± 0.30	3.7 ± 1.7	13
21.	603-AO-1-12,24	0.0151	3.64	3.60 ± 0.59	4.64 ± 0.77	12
22.	603-AO-1-80	0.1958	2130	3.68 ± 0.32	1.37 —	15
23.	603-AO-1-PAN	0.1123	150.5	3.02 ± 0.15	4.6 ± 1.7	13

Table III. Continued

	Sample	Weight, grams	100-h Ionization Current (10^{-8} ma.)[a]	f_R[b] Ave. S.D.	f_I[c] Ave. S.D.	Exp.
			Long Range Sieve Fractions			
1.	18-12B-2-44	U	U	2.29 ± 0.12	3.56 ± 0.24	12
2.	27-1B-LT-2	U	U	1.32 ± 0.07	4.7 ± 1.2	12
3.	27-1B-2-44	U	U	2.38 ± 0.52	39.7 ± 1.8	10
4.	27-1B-GT-44	U	U	5.91 ± 0.11	0.25 ± 0.06	11
5.	35-19B-LT-2	U	U	1.87 ± 0.11	6.5 ± 2.6	10
6.	35-19B-2-44	U	U	4.44 ± 0.16	5.42 ± 0.07	11
7.	35-19B-GT-44	U	U	6.57 ± 0.37	R	12
8.	56-12B-2-20	U	U	— —	2.49 ± 0.82	11
9.	56-12B-20-44	U	U	2.63 ± 0.16	2.77 ± 0.11	11
			Early Recovery Fractions			
1.	ER-2	U	U	3.22 ± 3.05	U	11
2.	ER-4	U	U	5.33 ± 2.50	U	11
3.	ER-5	U	U	5.97 ± 0.22	R	13
4.	ER-6	U	U	3.57 ± 0.06	2.51 ± 0.37	13

B. Volatile Nuclides

	Sample	f_{103}	f_{106}	f_{132}	f_{137}	Exp.
			Cloud Sample			
1.	842-R1-1D	8.20	5.86	(0.0918)	9.75	13
			Close-in Gross Fallout Samples			
1.	101-AO-1	4.41	1.02	1.77	(0.0417)	14
2.	201-AO-7	4.80	1.13	1.78	0.493	14
3.	305-AO-2	6.67	1.54	2.47	0.576	14
4.	403-AO-2	7.45	1.80	2.78	0.699	14
5.	505-AO-1	4.50	1.21	1.77	0.486	14
6.	603-AO-4	5.86	1.41	2.07	0.347	14
7.	707-AO-6	4.02	1.11	1.50	0.451	14
			Close-in Sieve Fractions			
1.	S1S-PC-1-12	4.21	1.06	1.68	0.454	14
2.	S1S-PC-1-80	4.96	1.17	1.62	0.558	14
3.	S1S-PC-1-PAN	1.76	1.13	1.16	0.181	13
4.	S2-PC-16-12	8.33	2.28	2.98	1.16	14
5.	S2-PC-16-42	8.03	1.63	2.30	0.726	14
6.	S2-PC-16-170	3.60	1.48	1.71	0.464	13
7.	S2-PC-16-PAN	4.44	2.64	3.09	0.472	14

Table III. Continued

	Sample	f_{103}	f_{106}	f_{132}	f_{137}	*Exp.*
			Close-in Sieve Fractions			
8.	201-AO-10-7	4.99	1.56	2.33	0.454	13
9.	201-AO-10-42	7.42	1.66	2.73	0.817	14
10.	201-AO-10-PAN	4.31	2.89	3.19	0.448	13
11.	305-AO-4-7	2.66	0.419	0.761	0.178	14
12.	305-AO-4-42	6.45	1.28	2.53	0.879	14
13.	305-AO-4-PAN	12.4	6.75	0.859	1.37	13
14.	403-AO-3-80	8.91	1.89	2.98	0.890	14
15.	S5-PC-5-12	7.39	4.44	4.68	(21.7)	12
16.	S5-PC-5-80	7.06	1.61	2.01	0.730	14
17.	S5-PC-5-PAN	1.40	0.943	1.15	0.284	14
18.	505-AO-6-7,24	0.421	0.315	0.360	0.625	13
19.	505-AO-6-80	9.27	2.07	2.94	0.856	14
20.	505-AO-6-PAN	8.26	5.86	6.62	1.05	13
21.	603-AO-1-12,24	9.95	6.51	7.84	17.4	12
22.	603-AO-1-80	19.0	4.28	6.49	1.54	14
23.	603-AO-1-PAN	6.83	4.77	5.37	0.657	13
			Long Range Sieve Fractions			
1.	18-12B-2-44	U	U	5.36	1.56	12
2.	27-1B-LT-2	U	U	6.15	20.7	10
3.	27-1B-2-44	U	U	1.24	0.205	12
4.	27-1B-GT-44	U	U	2.45	4.33	9
5.	35-19B-LT-2	U	U	7.60	3.25	10
6.	35-19B-2-44	U	U	7.39	0.916	11
7.	35-19B-GT-44	U	U	2.81	0.391	12
8.	56-12B-2-20	U	U	3.01	1.19	11
9.	56-12B-20-44	U	U	2.94	0.946	11
			Early Recovery Fractions			
1.	ER-2	U	U	U	U	—
2.	ER-4	U	U	U	U	—
3.	ER-5	U	U	U	2.49	11
4.	ER-6	U	U	1.52	4.10	12

[a] Cloud sample results are in ma. or fissions; all other results are in ma./gram or fissions/gram. The exponent in the last column applies to all columns.
[b] f_R is the average of f_{95}, f_{99}, and f_{144}.
[c] f_F is the average of f_{136} and f_{140}.
[d] U = unreported.
[e] R = rejected.

Table IV. Selected and Adjusted

No.	Sample	Weight, grams	Current, 10^{-8} ma.	f_{95}
				Cloud Samples (fissions/
1.	827-L1-2A	—	552	8.36
2.	837-R1-1A	—	478	R[j]
3.	842-R1-1C	—	130	2.72
				Close-in Fallout Samples (fissions/
1.	103-AO-9	15.98	R	55.1
2.	200-AO-9	1.12	54.2	38.0
3.	202-AO-9	0.71	0.575	96.6
4.	204-AO-9	0.63	0.237	21.6
5.	207-AO-9	2.95	0.0722	75.2
6.	209-AO-9	5.17	R	R[i]
7.	300-AO-9	0.27	45.2	36.5
8.	302-AO-9	0.68	U	U
9.	303-AO-9	2.46	R	R[i]
10.	305-AO-9	1.62	1333	132.0
11.	311-AO-9	0.91	0.179	2.51
12.	400-AO-9	0.18	122.8	15.7
13.	401-AO-9	2.68	940	10.2
14.	405-AO-9	1.38	725	73.7
15.	407-AO-9	0.90	8.31	7.01
16.	409-AO-9	1.51	U	U
17.	413-AO-9	3.74	R	15.6
18.	501-AO-9	0.12	R	18.3
19.	502-AO-9	1.10	0.886	1.46
20.	503-AO-9	1.08	832	76.4
21.	509-AO-9	0.83	1.63	11.3
22.	513-AO-9	1.42	9.93	2.63
23.	601-AO-9	0.09	5.43	45.8
24.	605-AO-9	0.46	1922	13.3
25.	607-AO-9	0.30	203	20.5
26.	700-AO-9	0.15	4.61	4.10
27.	701-AO-9	0.07	R	14.1
28.	703-AO-9	0.21	390	40.7
29.	704-AO-9	0.25	2.51	10.4
				Close-in Sieve
1.	S1S-PC-1-24	0.21	1563	11.0
2.	S1S-PC-1-42	0.21	1720	15.0
3.	S1S-PC-1-170	0.51	503	3.14
4.	S1S-PC-1-325	1.37	149	2.60

Results for Laboratory C

f_{89}	f_{90}	f_{91}	f_{131}	*Exponent*
sample and current/sample)				
2.05	R[b]	R[b]	—	14
2.03	R[b]	1.62	—	14
7.49[f]	6.37[f]	4.99[f]	—	13
gram and current/gram)				
1.79	3.31	R[c]	—	10
3.95	9.55	23.9	—	12
4.54	6.95	17.8	—	10
1.56	6.59	17.3	—	10
R[d]	R[d]	R[d]	—	—
1.12	4.55	15.1	—	10
2.90	7.67	18.4	—	12
R[e]	R[e]	R[e]	—	—
8.96	R[d, e]	55.6	—	12
10.4	19.6	R[e]	—	13
R[f]	1.43	0.692	—	11
1.08	3.19	7.14	—	13
0.737	2.36	4.58	—	14
5.59	24.0	R[e, g]	—	13
0.631	1.68	2.94	—	12
1.23	3.35	2.58	—	10
2.24	5.59	11.1	—	10
1.39	3.63	8.48	—	13
R[e, g]	R[e, g]	R[e, g]	—	11
8.87	16.4	35.6	—	13
1.12	2.64	6.11	—	13
U	U	R[e]	—	11
3.31	9.94	21.4	—	13
1.18	2.51	6.43	—	14
1.37	3.88	7.90	—	13
1.85	R[g]	1.72	—	12
0.79	3.59	4.86	—	12
2.69	6.70	16.0	—	13
1.50	2.91	R[h]	—	11
Fraction Samples				
1.24	3.17	6.19	—	14
1.35	3.19	7.80	—	14
0.345	0.830	1.68	—	13
0.607	1.96	4.36	—	12

Table IV.

No.	*Sample*	*Weight, grams*	*Current, 10^{-8} ma.*	f_{95}
				Close-in Sieve
5.	101-AO-6-12	1.57	1637	10.4
6.	101-AO-6-42	1.26	1700	12.9
7.	101-AO-6-80	0.24	897	6.59
8.	101-AO-6-170	0.41	312	17.1
9.	101-AO-6-325	1.39	40.1	2.29
10.	S2-PC-16-24	0.19	1521	13.8
11.	S2-PC-16-80	0.05	1430	11.0
12.	S2-PC-16-325	0.43	28.6	9.66
13.	201-AO-10-12	0.31	1423	9.74
14.	201-AO-10-24	1.01	1675	11.1
15.	201-AO-10-80	0.28	1430	12.7
16.	201-AO-10-170	0.61	110.6	62.3
17.	201-AO-10-325	1.15	32.2	9.05
18.	305-AO-4-12	0.07	1135	10.1
19.	305-AO-4-24	0.31	1593	12.1
20.	305-AO-4-80	0.14	1210	7.98
21.	305-AO-4-170	0.13	428	2.81
22.	305-AO-4-325	0.14	237	11.3
23.	403-AO-4-24	0.02	532	3.24
24.	403-AO-4-42	0.62	1749	13.6
25.	403-AO-4-170	0.13	931	7.82
26.	403-AO-4-325	0.14	213	5.75
27.	S5-PC-5-24	0.003	573	4.89
28.	S5-PC-5-42	0.01	893	8.67
29.	S5-PC-5-325	0.09	97.7	4.20
30.	505-AO-6-42	0.09	1023	8.36
31.	505-AO-6-170	0.21	1077	10.0
32.	505-AO-6-325	0.34	103.1	2.24
33.	603-AO-1-42	0.008	899	8.74
34.	603-AO-1-170	0.15	2060	20.6
35.	603-AO-1-325	0.12	89.9	6.89
36.	707-AO-3-42	0.004	168	18.3
37.	707-AO-3-80	0.016	943	6.50
38.	707-AO-3-325	0.10	150.8	5.09
				Long Range
1.	14-LA-3-4	—	—	23.6
2.	15-LA-9-10	—	—	28.1
3.	16-LA-15-16	—	—	24.0
4.	18-10A	—	—	3.44

Continued

f_{89}	f_{90}	f_{91}	f_{131}	*Exponent*
Fraction Samples				
1.07	3.07	5.95	—	14
1.17	3.75	6.26	—	14
0.637	1.76	2.88	—	14
2.08	R[c]	9.89	—	13
0.362	0.955	1.62	—	13
1.09	3.12	7.21	—	14
0.837	2.44	6.04	—	14
1.62	4.39	7.44	—	12
1.03	R[c]	5.61	—	14
1.32	2.95	6.29	—	14
0.929	2.00	6.22	—	14
5.84	R[c]	35.4	—	12
1.67	4.47	7.31	—	12
0.920	2.55	5.31	—	14
1.13	2.95	6.39	—	14
0.790	2.23	4.40	—	14
0.262	0.838	1.90	—	14
1.18	3.04	7.75	—	13
0.363	0.877	2.00	—	14
1.03	3.19	7.51	—	14
0.649	1.88	3.86	—	14
1.07	2.72	4.05	—	13
0.501	1.36	3.13	—	14
0.867	2.16	46.0[k]	—	14
0.579	1.88	3.08	—	13
0.820	2.53	5.02	—	14
0.725	2.07	4.20	—	14
0.661	1.22	2.18	—	13
0.561	1.52	3.53	—	14
1.04	3.44	6.80	—	14
1.12	3.19	5.26	—	13
3.18	9.24	R[d]	—	13
0.649	1.52	3.44	—	14
0.796	2.16	3.70	—	13
Gross Samples				
0.247	0.750	1.41	—	13
2.22	6.79	17.6	—	12
2.03	5.47	14.2	—	12
0.743	1.60	R[d]	—	9

Table IV.

No.	*Sample*	*Weight, grams*	*Current, 10^{-8} ma.*	f_{95}
				Long Range
5.	27-2A	—	—	40.4
6.	115-19A	—	—	9.13
				Long Range
1.	13-LA-1-10-24	0.08	234	9.51
2.	13-LA-1-10-80	0.50	202	20.8
3.	13-LA-1-10-325	8.44	70.2	4.20
4.	18-9B-LT-44	—	—	6.29
5.	18-9B-GT-44	—	—	3.51
6.	18-10B-2-44	—	—	3.32
7.	18-10B-88-125	—	—	11.4
8.	18-10B-88-125	—	—	12.6
9.	18-10B-125-149	—	—	36.4
10.	18-10B-149-177	—	—	10.5
11.	18-10B-177-210	—	—	2.68
12.	18-10B-210-250	—	—	4.94
13.	18-10B-250-297	—	—	20.8
14.	18-10B-297-500	—	—	15.6
15.	18-11B-LT-44	—	—	2.19
16.	18-11B-GT-44	—	—	6.68
17.	27-2B-LT-44	—	—	3.90
18.	27-2B-GT-44	—	—	5.54
19.	27-3B-LT-2	—	—	19.0
20.	27-3B-2-44	—	—	7.04
21.	27-3B-44-88	—	—	2.88
22.	27-3B-88-105	—	—	20.8
23.	27-3B-105-125	—	—	7.04
24.	27-3B-125-149	—	—	8.97
25.	27-3B-149-177	—	—	6.44
26.	27-3B-177-250	—	—	18.7
27.	27-4B-LT-44	—	—	1.82
28.	27-4B-GT-44	—	—	20.1
29.	35-17B-LT-44	—	—	2.07
30.	35-17B-GT-44	—	—	4.97
31.	35-18B-LT-44	—	—	3.14
32.	35-18B-GT-44	—	—	21.8
33.	35-20B-LT-2-44	—	—	7.64
34.	35-20B-44-88	—	—	11.5

Continued

f_{89}	f_{90}	f_{91}	f_{131}	*Exponent*
Gross Samples				
3.31	7.19	17.8	—	8
4.97	7.99	R[g]	—	7
Sieve Fractions				
1.45	4.55	7.29	—	13
1.64	4.85	9.75	—	13
0.563	1.48	3.43	—	13
1.42	4.47	7.41	6.68	13
0.392	1.16	1.99	0.582	13
0.773	1.64	2.80	—	12
0.975	2.76	4.90	—	12
0.814	2.20	3.73	—	12
2.48	6.79	R[c]	—	11
1.77	2.40	3.75	—	11
0.235	1.20	R[d]	—	11
R[a]	R[a]	R[a]	—	11
1.30	4.79	R[a,b]	—	10
1.57	3.99	9.50	—	10
0.754	2.16	3.27	3.19	13
0.714	2.64	4.15	1.32	13
1.27	3.99	5.62	5.76	12
0.466	1.28	2.81	0.971	13
2.57	4.79	6.58	—	10
2.21	R[d]	R[d]	—	11
0.351	0.799	1.63	—	12
1.08	3.19	5.22	—	11
0.773	2.00	3.34	—	11
0.661	1.60	2.58	—	11
0.315	1.16	3.73	—	11
2.26	7.59	23.2	—	10
0.365	0.955	1.34	2.04	12
1.91	6.23	10.2	3.00	11
0.498	1.20	1.62	1.11	12
0.690	2.40	3.70	1.65	12
0.920	2.00	4.15	1.97	12
2.91	7.80	16.0	6.38	12
2.46	4.39	1.07[b]	—	11
1.27	3.59	4.51	—	11

Table IV.

No.	Sample	Weight, grams	Current 10^{-8} ma.	f_{95}
				Long Range
35.	35-20B-88-105	—	—	4.64
36.	35-20B-105-125	—	—	33.8
37.	35-20B-125-177	—	—	14.3
38.	56-11B-LT-44	—	—	2.80
39.	56-11B-GT-44	—	—	2.58
40.	56-14B-LT-44	—	—	3.93
41.	56-14B-GT-44	—	—	4.15

[a] Geometric-mean test failed.
[b] $f_{90} < f_{91} < f_{89}$.
[c] $f_{90} < f_{89} < f_{91}$.
[d] $f_{89} < f_{91} < f_{90}$.
[e] f_{91} does not correlate with ionization current.

Table V. Values of $r_{i,R}$ for Laboratory D[a]

Nuclide	Sample: Surface	245	827	837	842
^{89}Sr	0.0645	2.02	3.30	3.49	3.73
^{111}Ag, ^{115}Cd	0.184 ± 0.001	2.43 ± 0.04	3.28 ± 0.01	3.34 ± 0.01	3.36 ± 0.02
^{136}Cs	0.399	1.94	2.49	2.58	2.51
^{137}Cs	0.198	1.87	3.21	3.41	3.48
^{140}Ba	0.420	1.84	2.45	2.51	2.54
^{239}Np[b]	1.00 ± 0.02	0.94 ± 0.00	1.18 ± 0.01	1.18 ± 0.02	1.21 ± 0.00
Refractories (^{99}Mo, ^{144}Ce, ^{147}Nd, ^{156}Eu)	1.00 ± 0.05	1.00 ± 0.01	1.00 ± 0.03	1.00 ± 0.04	1.00 ± 0.04

[a] No alteration of Laboratory D data was required.
[b] The values shown are the averages of two identically behaving quantities.

C, determined only ^{89}Sr, ^{90}Sr, ^{91}Y, and ^{95}Zr. The samples supplied to them were the same kind supplied to Laboratories A and B and should have shown the same fractionation behavior. It is unfortunate that there is no way of verifying the reliability of the ^{95}Zr data from Laboratory C,

Continued

f_{89}	f_{90}	f_{91}	f_{131}	*Exponent*
Sieve Fractions				
0.326	1.20	1.56	—	11
3.26	7.19	R[e]	—	10
2.18	5.19	10.2	—	10
2.10	R[d]	4.01	0.580	12
R[e,d]	R[e,d]	R[e,d]	2.93	12
1.03	3.44	4.38	2.20	12
R[e,d]	R[e,d]	R[e,d]	1.28	12

[f] $f_{91} < f_{90} < f_{89}$.
[g] $f_{91} < f_{89} < f_{90}$.
[h] Apparent factor-of-10 error.
[i] Rejected on the basis of Ref. 7.
[j] Rejected on the basis of comparisons on cloud samples.

as was done for the Laboratory A and B data, since no other refractory fission-product chains (such as mass-99 or mass-144) were determined on this group of samples.

The mass-89, 90, and 91 chains are expected to show close correlation with each other, both on theoretical grounds and from past experience with fallout radiochemical data. The data from Laboratory A bear out this expectation since a plot of $r_{90,95}$ *vs.* $r_{91,95}$ and plots of either of these ratios *vs.* $r_{89,95}$ show excellent correlation. For Laboratory B, the ^{89}Sr data (as we have already shown) are not reliable. Furthermore, there is essentially no correlation between $r_{90,95}$ and $r_{91,95}$ and $r_{91,95}$ shows little correlation with $r_{137,95}$. The correlation of $r_{90,95}$ with $r_{137,95}$ is somewhat better, suggesting that the ^{90}Sr data are about as reliable as the ^{137}Cs data.

In the data from Laboratory C a similar failure of correlation between ^{90}Sr and ^{91}Y is observed. However, in this case the ^{89}Sr and ^{90}Sr data correlate reasonably well, whereas the ^{89}Sr and ^{91}Y data fail to correlate. We conclude provisionally that the ^{91}Y data are at fault, reserving the possibility that the data for each of the two Sr isotopes may contain the same errors since they were resolved from the decay curve of a single precipitate. Errors of this kind would not be apparent from a single correlation plot. One would expect, in fact, that classical radiochemical procedures for determining such pairs as ^{89}Sr–^{90}Sr, ^{103}Ru–^{106}Ru, and ^{136}Cs–^{137}Cs would always yield correlatable data from any individual laboratory. The Small Boy data show that this is frequently not true, and one is led to suppose that the difficulty lies in inadequate or erroneous counting data or faulty resolution of the decay curve.

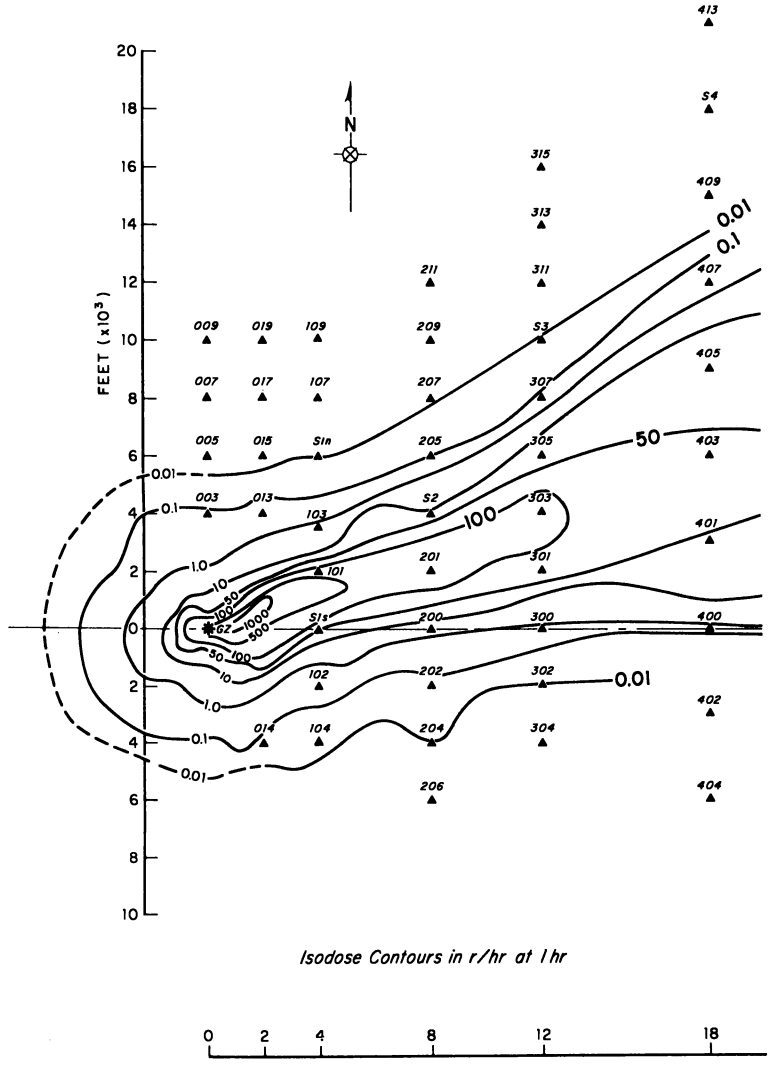

Figure 15. Close-in station array

The data from Laboratory A showed that, for any sample, f_{90} was closely related to both the arithmetic and geometric means of f_{89} and f_{91}. Subsequent investigation has shown that this rule applies to other types of bursts as well as the Transient Nuclear Test (*8*). Application of this rule, and requirements that f_{89}, f_{90}, and f_{91} have the proper order, helped to eliminate many spurious results.

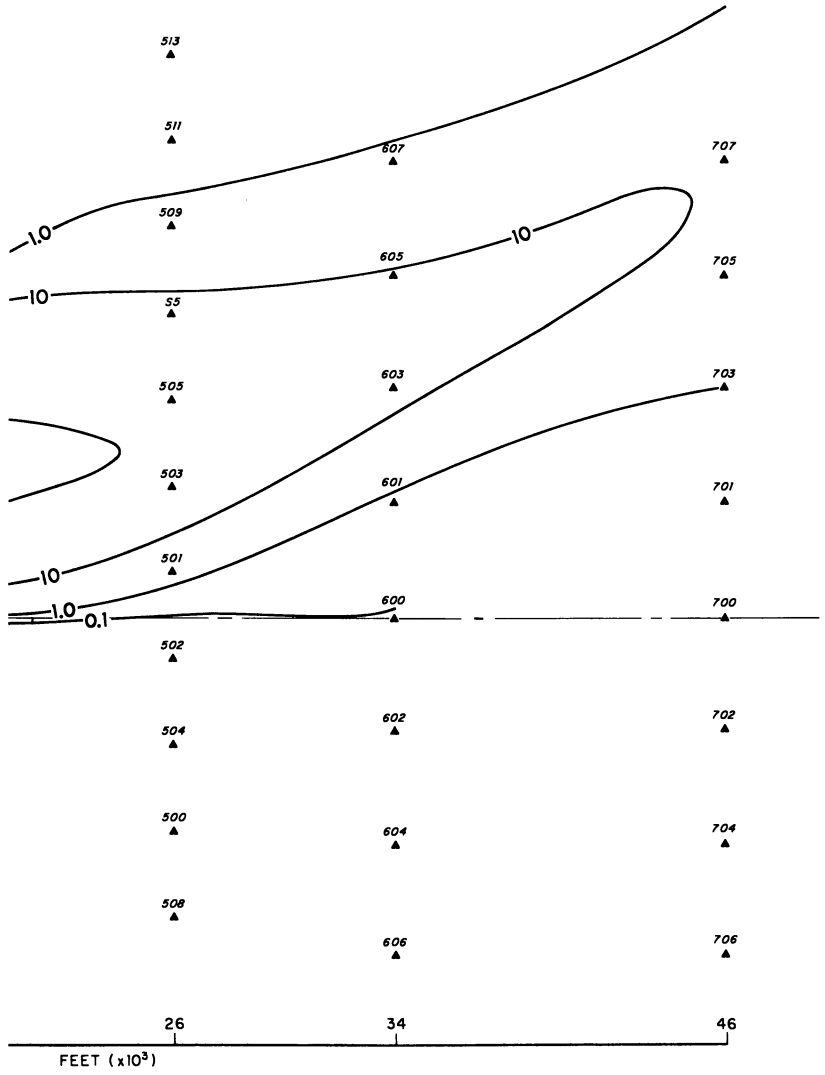

and 1-hour radiation pattern

Other Correlations. Other correlations found helpful in reassessing Small Boy data are worthy of mention, if not lengthy discussion. These included the similarity of behavior among ^{91}Y, ^{136}Cs, ^{140}Ba, ^{141}Ce, ^{239}Np, and the 100-*h* ionization current and the 10-*h* field exposure rate; the similarity of ^{111}Ag, ^{115}Cd, and ^{137}Cs; the identity of ^{147}Nd and ^{156}Eu behavior to that of ^{95}Zr, ^{99}Mo, ^{144}Ce, and ^{239}Pu; and the correlation of ionization current and field exposure rate with $r_{89,95}$.

Results

Tables II through V give the final selected and recalibrated data for Small Boy in alphabetical order of the performing laboratory. In a number of cases, data from similarly behaving nuclides are grouped and averaged in the belief that little or no information is lost in the process. Inspection of these tables indicates a gratifyingly high precision in many cases. The data should form a fruitful basis for subsequent analysis of the fallout-formation phenomena occurring in Small Boy. The relation of sample designation to sample source and treatment is as follows:

Cloud samples 245 were collected between 40 and 45 minutes after detonation at a height of 15,000 feet. Cloud samples 827 were collected one hour after detonation between 16,500 and 17,500 feet. Cloud samples 837 were collected one hour after detonation between 16,500 and 17,500 feet. Cloud samples 837 were collected at 16,000 feet approximately 1.5 hours after shot time. Cloud sample 842 was collected at 16,700 feet approximately 2 hours after shot time.

Figure 15 shows the close-in fallout collection array (NRDL) and the radiation pattern at 1 hour. The first three numbers of the close-in samples correspond to the numbers of the stations shown here. The letters AO and PC indicate always-open collectors and platform collectors, respectively. These collectors were identical, but the PC collectors received better protection from dust prior to shot time. The next number indicates which of the 9 or 16 pans in the array has been taken. Additional numbers indicate sieve sizes retaining the debris.

Figure 16 shows the relation of the fallout pattern to the long range collection array (UCLA). For these samples, the first two digits give the approximate mileage from ground zero. LA indicates large-area collectors which were used at Indian Springs. The abbreviations GT and LT represent greater than and less than and are followed by particle sizes in microns. For some samples (*e.g.*, 18-10B) size ranges in microns follow the sample designation.

Conclusion

The large body of radiochemical data reported on samples from event Small Boy contained a considerable proportion of unreliable results and calibration factors. For successful use of the data to establish the fractionation behavior of fission products in nuclear debris, it was necessary to examine the individual values by all available methods, to discard those which fail to show internal consistency, and to revise the calibrations. The authors of this report have undertaken such an evaluation, and a number of meaningful relationships have already resulted.

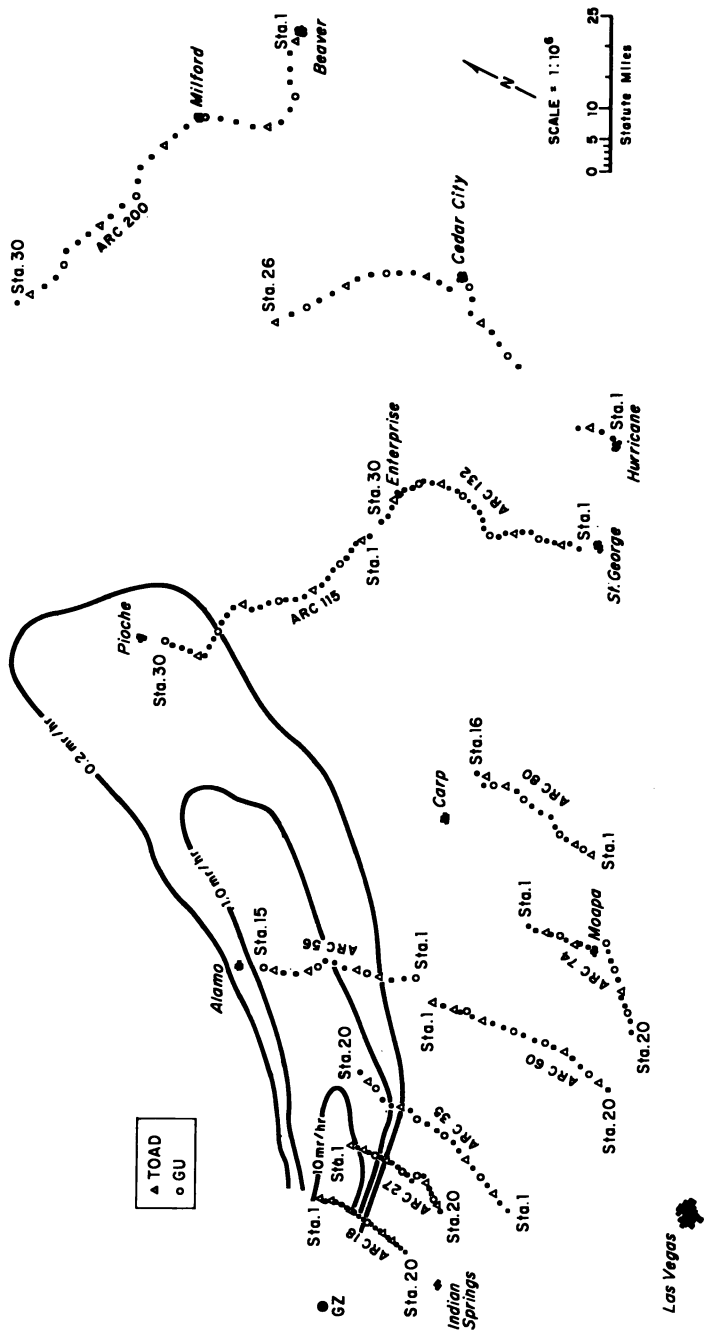

Figure 16. Long range collection stations and 1-hour radiation pattern

In particular ^{95}Zr, ^{99}Mo, ^{144}Ce, ^{147}Nd, ^{156}Eu, and ^{239}Pu formed a group of nuclides which did not fractionate from each other; ^{89}Sr, ^{90}Sr, and ^{91}Y followed an arithmetic or geometric mean rule among themselves and fractionated from the ^{95}Zr group; ^{111}Ag, ^{115}Cd, and ^{137}Cs fractionated strongly from the refractory ^{95}Zr group; ^{103}Ru and ^{106}Ru formed a pair which behaved similarly but not identically, as did the pair ^{136}Cs and ^{140}Ba; the differences in behavior among ^{91}Y, ^{136}Cs, ^{140}Ba, ^{141}Ce, and ^{239}Np were of no operational significance, and ^{91}Y correlated well with 100-hr. ionization current and the 10-*h* field exposure rate. ^{132}Te, ^{131}I, and ^{106}Ru behaved very similarly. The correlation plots show curvilinearities which would imply that a simple two-component model of fallout formation is not applicable to the Small Boy event.

Literature Cited

(1) Crocker, G. R., Naval Radiological Defense Laboratory, *Tech. Rept.* **USNRDL-TR-892** (Aug. 4, 1965).
(2) Crocker, G. R., *Nature* **210,** 1028 (1966).
(3) Crocker, G. R., Kawahara, F. K., Freiling, E. C., *U. S. At. Energy Comm./ Div. Tech. Info.* **CONF-765** (Nov. 1965).
(4) Freiling, E. C., *Science* **133,** 1991 (1961).
(5) Freiling, E. C., Bunney, L. R., Kawahara, F. K., Operation Sunbeam, Shot Smallboy, Project 2.10, POR-2216, Naval Radiological Defense Laboratory (Oct. 15, 1964) (Classified).
(6) Freiling, E. C., Crocker, G. R., Naval Radiological Defense Laboratory, *Tech. Rept.* **NRDL-TR-68-140** (June 28, 1968).
(7) Freiling, E. C., Kay, M. A., *Nature* **209,** 236 (1966).
(8) Lai, J. R., Freiling, E. C., ADVAN. CHEM. SER. **93,** 337 (1969).
(9) LaRiviere, P. D., Sartor, J. D., Lane, W. B., Operation Sunbeam, Shot Smallboy, Project 2.9, POR-2215, Naval Radiological Defense Laboratory (Oct. 23, 1964) (Classified).

RECEIVED January 18, 1969. Work sponsored by the U. S. Atomic Energy Commission under Contract AT(49-7)-163 and by the Defense Atomic Support Agency.

Correlation of Radionuclide Fractionation in Debris from a Transient Nuclear Test

J. R. LAI and E. C. FREILING[1]

U. S. Naval Radiological Defense Laboratory, San Francisco, Calif. 94135

Fractionation correlation techniques have been applied to cloud, fallout, and ground-filter samples from the Transient Nuclear Test of January 1965. Although safety analysts do not consider fractionation effects to be of operational importance for this type of event, analysis of such data provides insight into the mechanisms of debris formation. The results show many similarities to the correlations observed for fallout. Those dissimilarities found indicate the importance of escape processes to the formation mechanisms for this type of debris.

This paper describes the physical and radiochemical characteristics of selected debris from the Kiwi Transient Nuclear Test (TNT) (*6, 7*). This transient test was conducted in Nevada by the Los Alamos Scientific Laboratory (LASL), and produced approximately 3×10^{20} fissions (*1*). Zero time was 1059 PST on 12 January 1965. About 5% of the reactor core was vaporized, and some 68% was converted to a cloud of particulate. The measured maximum temperature was 4250°K. (*7*). Large pieces of fuel rods were recovered near ground zero.

The purpose of this test was to ascertain the hazard that would result from a rapid reactivity insertion into a Kiwi reactor. The test provided an occasion to study radionuclide fractionation in debris from a reactor excursion. Because fractionation processes distribute hazardous radionuclides among debris particles in different manners, their effects require documentation and study. Chapter 17 by Crocker and Freiling in this volume will provide background for the reader who is unfamiliar with fractionation phenomena.

[1] Present address: FCA, U.S. Naval Weapons Laboratory, Dahlgren, Va. 22448.

Methodology and Gross Properties of the Debris

Three types of test samples were studied at NRDL: (1) cloud-filter samples (KC) obtained by aircraft flying at heights of 5000–8000 ft., (2) a ground-filter sample (KG) obtained by ground-level filtration of air at a point 4000 ft. from ground zero, and (3) a ground-fallout sample (KH), aliquotted by weight from a plastic-strip collector located 4000 ft. from ground zero. The cloud and ground-filter samples consisted mainly of small, irregular particles, most of which were less than 50μ in diameter (*see* Figure 1). By contrast, the size of the particles in the

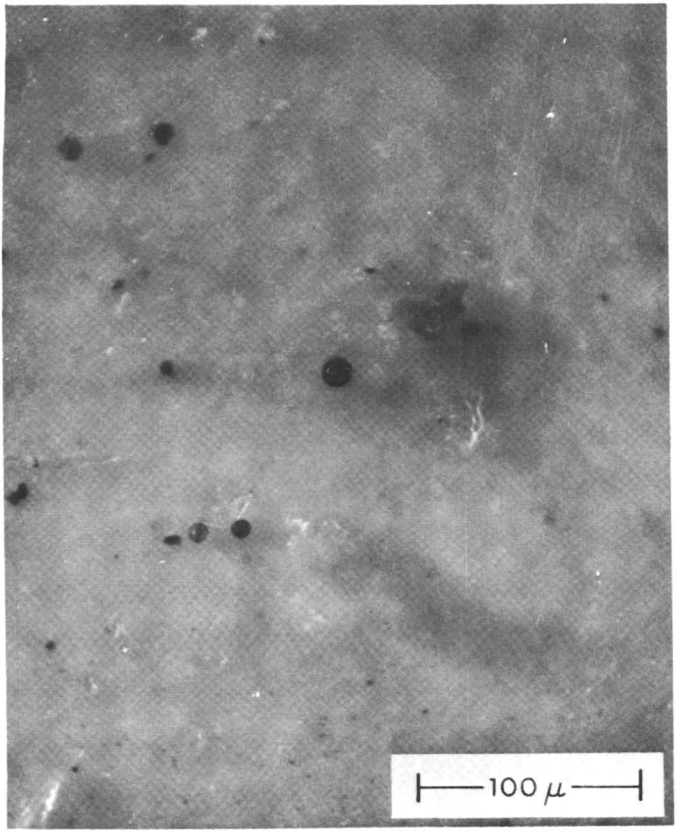

Figure 1. Particles from the cloud sample KC-1, showing both spherical and irregular particles

ground-fallout sample ranged from a few microns to several millimeters (*see* Figures 2, 3, and 4). Prior to radiochemical analysis, the ground-fallout sample was sieved into eight fractions. Table I summarizes the

associated data on mass and activity. The radioactive assay was obtained with a 4-π gamma-ionization chamber.

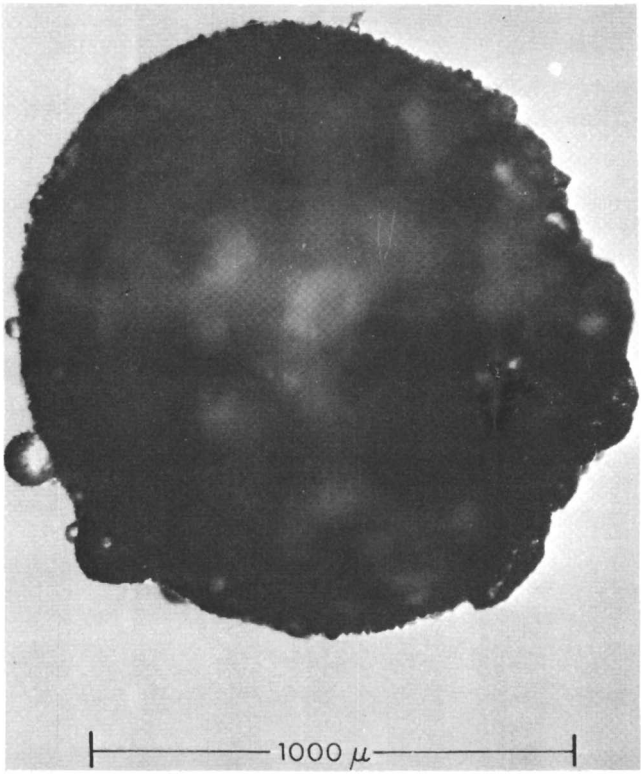

Figure 2. A large particle from sample fraction KH-3. The particle is spherical with many spheres stuck to its surface

Figures 2 through 4 show photomicrographs of selected spheroidal and irregularly shaped particles from fallout sample fraction KH-3. Figure 2 also shows the effect of agglomeration, which was evidenced by only a small portion of the debris. In fraction KH-3, about one-fifth of the total weight consisted of spheroids, and these ranged in density from 1.1 to 2.3 grams/cm.^{3}. The spheroids, shown in Figure 3, ranged from translucent green to black. Gross samples and separated fractions were analyzed further by γ-spectrometry and radiochemistry.

Fractionation Information from γ-Ray Spectra

γ-ray spectra were taken of all debris samples with a 400-channel, Technical Measurement Corp. (TMC) pulse-height analyzer equipped

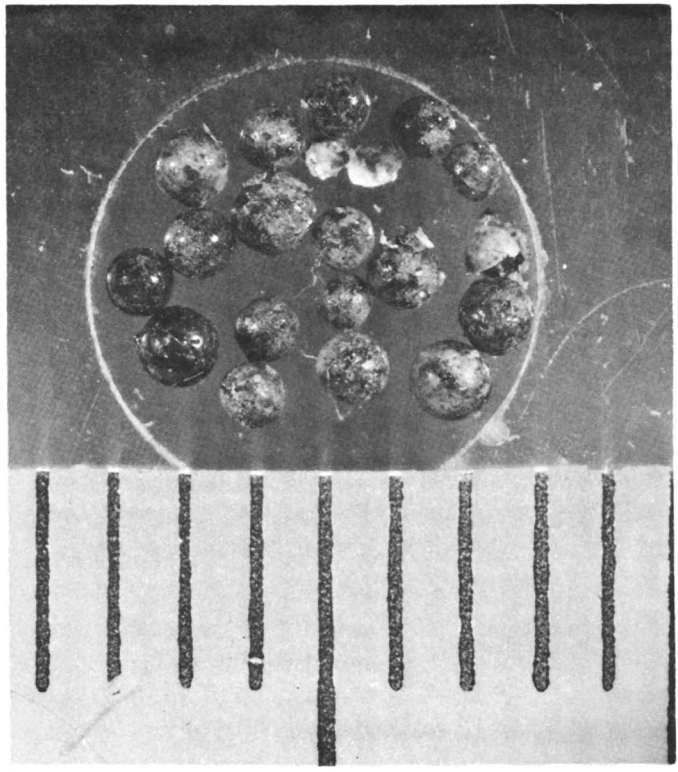

Figure 3. Large spheroidal particles from fraction KH-3s. Scale divisions are 1 mm.

with a 4 × 4-inch NaI(Tl) crystal. In general, the spectra of a majority of samples agreed qualitatively with the corresponding radiochemical data and were especially valuable in identifying radionuclides at early times.

Some typical gross γ-spectra are illustrated in Figure 5. This figure shows the 13-day γ-spectra of a typical cloud-filter sample KC-1, the ground-filter sample KG, and two fractions, KH-1 and KH-8 (largest and smallest sizes, respectively), of the ground-fallout sample. The figure compares these spectra with the unfractionated fission-product spectrum of irradiated $^{235}UC_2$. Various degrees of fractionation can be seen between samples and between different size fractions of the same sample. For instance, the spectrum of the cloud-filter sample shows, by comparison with the unfractionated $^{235}UC_2$ spectrum, a relatively small degree of fractionation. By contrast the spectrum of the ground-filter sample indicates a strong enrichment in the volatile behaving nuclides ^{131}I and ^{132}Te–^{132}I, and a deficiency in ^{99}Mo. Subsequent radiochemical results, described below, substantiate these findings. As

to the fallout sample KH, the largest size fraction (KH-1) shows a slight depletion of the volatiles (^{131}I, ^{132}Te, etc.); the small size fraction (KH-8), shows a strong depletion of the volatiles, an absence of ^{140}Ba–^{140}La, and a very strong enrichment of ^{103}Ru.

Various degrees of fractionation of ^{133}Xe ($\gamma = 0.081$ M.e.v.) can be seen in Figure 5, after the adjustment for interference arising from ^{147}Nd ($\gamma = 0.091$ M.e.v.; assumed not to fractionate from ^{235}U). The extent of the ^{147}Nd interference is estimated by comparison with the reference spectrum as indicated above. The cloud sample KC-1 shows a substantial depletion of ^{133}Xe; the ground-filter KG shows a slight depletion; and the ground-fallout fraction KH-1, no discernible depletion. No data are available for sample KH-8. The wide variation in ^{133}Xe activity may well be attributed to differences in the shock and thermal history of the samples and reflects the fission-product release rate from the fuel of the ^{133}Xe precursors—namely, 21-hour ^{133}I and 2-min. ^{133}Te (*14*). Recent calculations by Crocker have shown that, at 13 days after an event, the ^{133}Xe should constitute about 13% of the total fission-product activity. Laboratory investigations (*9*) with $^{235}UC_2$ microspheres (similar to

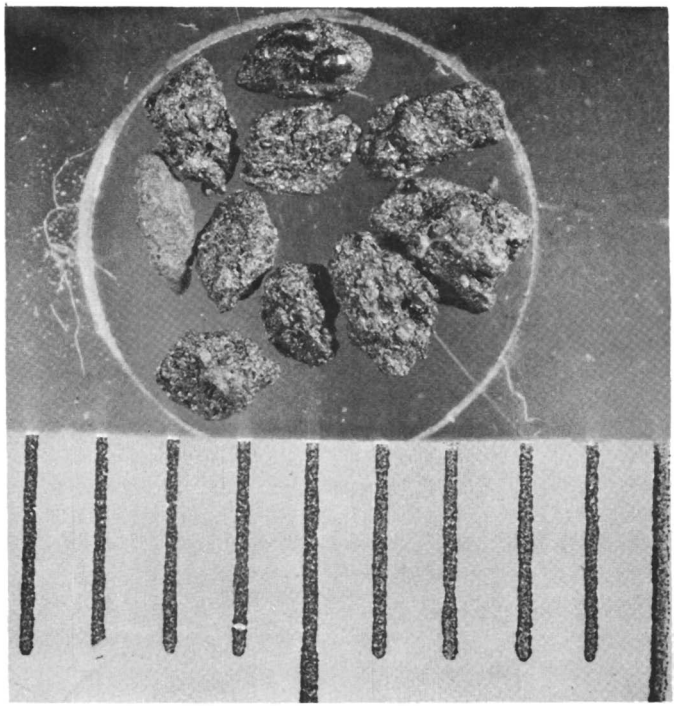

Figure 4. Large irregularly shaped particles from fraction KH-3f. Scale divisions are 1 mm.

Table I. Weight and Activity Measurements of Ground-Fallout Sample KH After Sieve Size Separation

Designation	*Sieve Size Range, mm.*	*Weight, gram*	*Ionization Chamber Reading, Feb. 2, 1965*[a] *ma.*	*Specific Ionization ma./gram*
KH-1	>2.794	0.1455	510×10^{-10}	3.50×10^{-7}
KH-2	1.397–2.794	0.4478	770×10^{-10}	1.72×10^{-7}
KH-3	0.701–1.397	0.8210	152×10^{-9}	1.85×10^{-7}
KH-4	0.351–0.701	0.6198	100×10^{-9}	1.61×10^{-7}
KH-5	0.175–0.351	0.127	234×10^{-10}	1.92×10^{-7}
KH-6	0.088–0.175	0.0508	146×10^{-10}	2.87×10^{-7}
KH-7	0.044–0.088	0.0206	85×10^{-10}	4.13×10^{-7}
KH-8	<0.044	0.0046	219×10^{-11}	4.76×10^{-7}

[a] On this day a 105-μgram Ra standard read 668 × 10^{-9} ma.

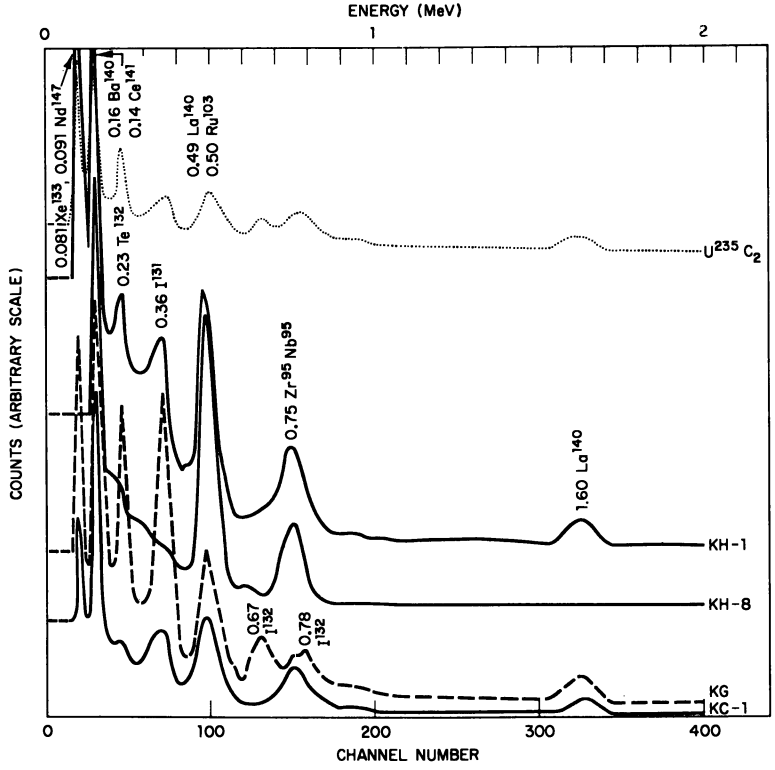

Figure 5. Comparison of gamma spectra from cloud, ground-filter, and fallout samples at thirteen days after the event, and of unfractionated $U^{235}C_2$ eleven days after irradiation

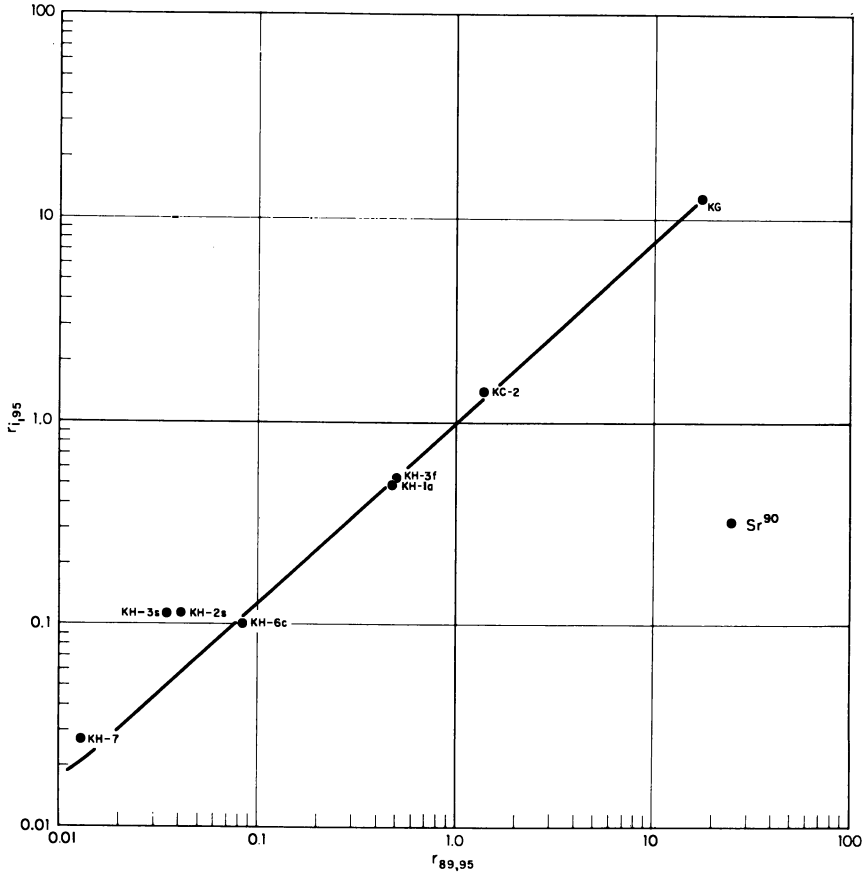

Figure 6. Fractionation plot for Sr^{90}

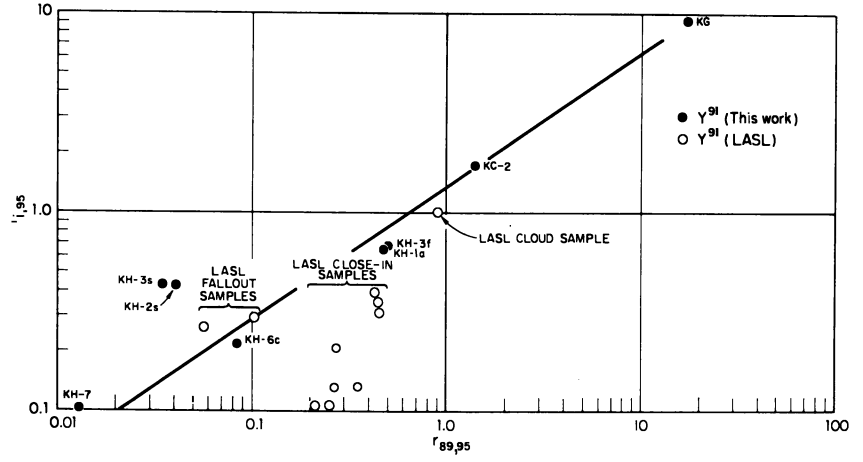

Figure 7. Fractionation plot for Y^{91} (LASL data is from Ref. 1)

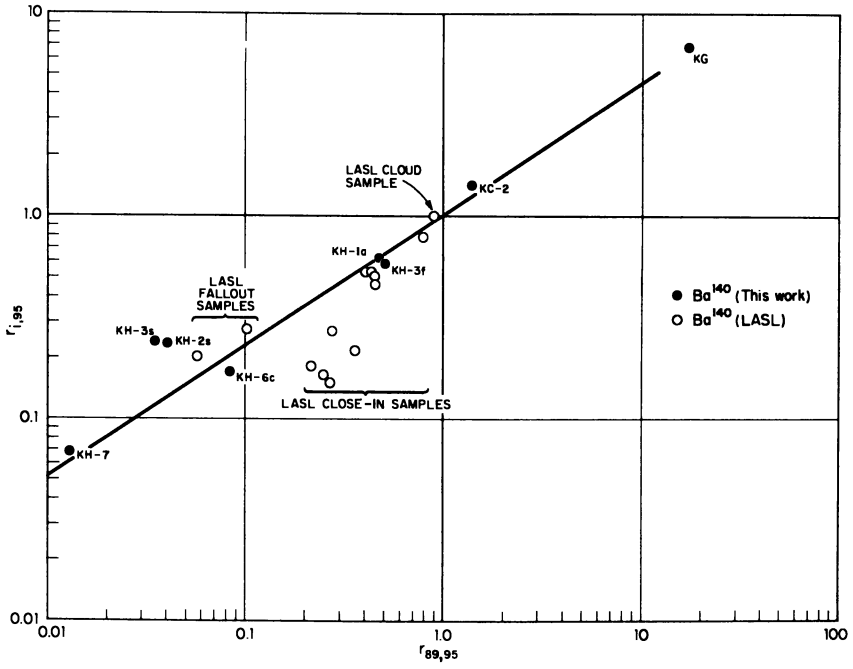

Figure 8. Fractionation plot for Ba^{140} (LASL data is from Ref. 1)

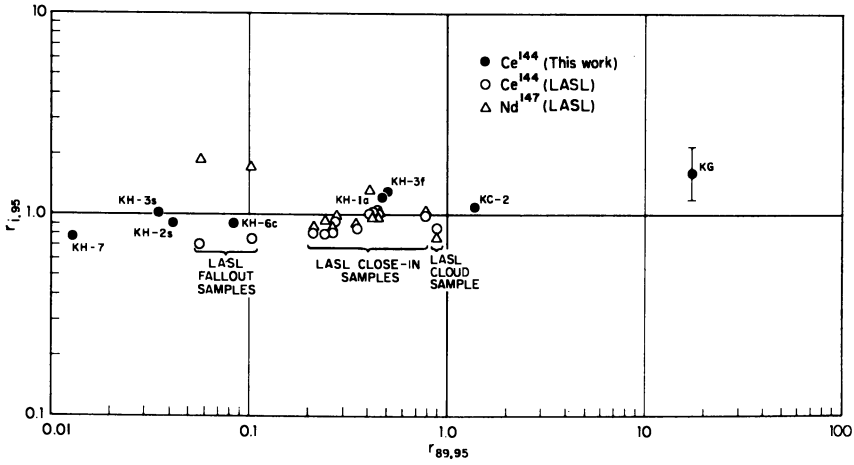

Figure 9. Fractionation plot for Ce^{144} and Nd^{147} (LASL data is from Ref. 1)

NERVA fuel) have shown that the fission product ^{133}Xe was found in the calculated abundance following irradiation with thermal neutrons at ambient temperatures. In the latter instance the surface integrity of the fuel spheres was maintained during irradiation; hence, the fission products were unfractionated.

Radionuclide Composition and Fractionation Correlations

The contribution of the γ-spectra to knowledge about radionuclide fractionation is limited: pure and nearly pure β emitters (*e.g.*, ^{89}Sr, ^{90}Sr, and ^{91}Y) are not detectable by γ-spectrometry; only relative magnitudes of the γ-emitters can be determined from the spectra. Quantitative information on the radiochemical composition was obtained by radiochemical analyses performed by Tracerlab, Division of Laboratory for Electronics, Inc., Richmond, Calif.

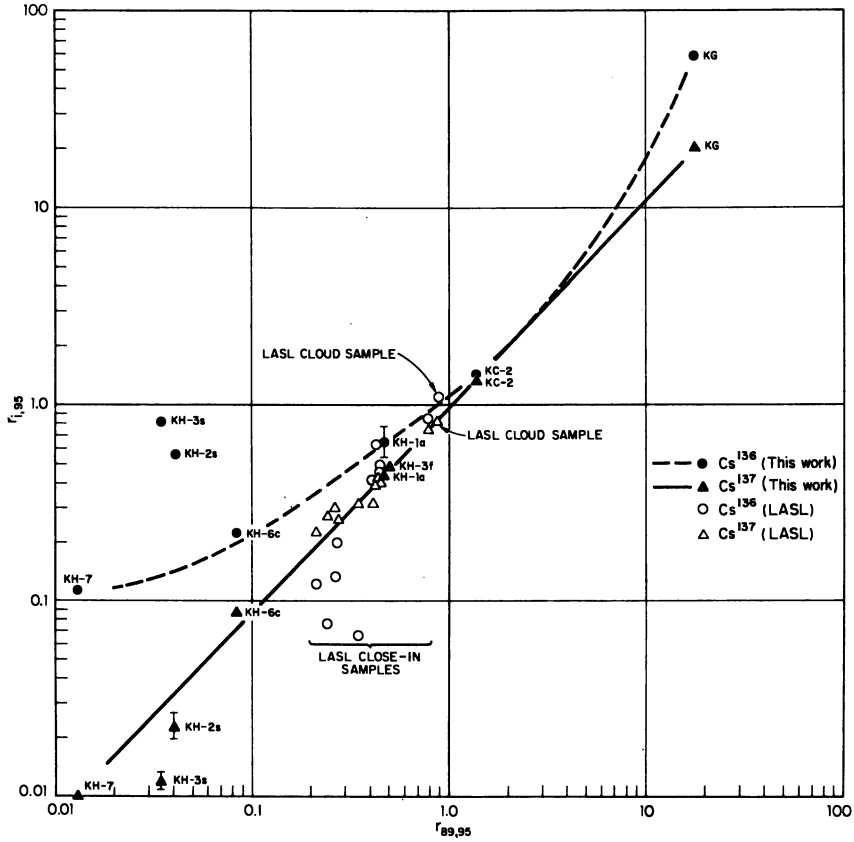

Figure 10. Fractionation plot for Cs^{136} and Cs^{137} (LASL data is from Ref. 1)

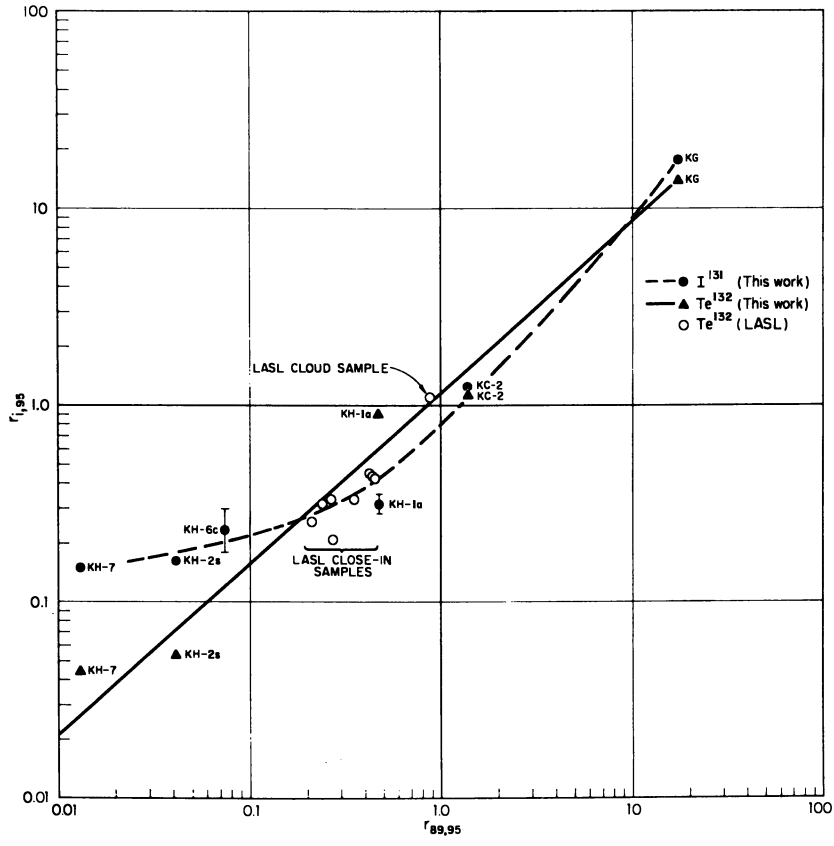

Figure 11. Fractionation plot for I^{131} and Te^{132} (LASL data is from Ref. 1)

The radiochemical results were first converted to equivalent fissions. The number of equivalent fissions f_i of mass chain i in a sample is the number of device fissions required to produce the number of atoms of mass chain i that were observed in the sample. In the transient test the device fissions were essentially all thermal-neutron fissions of ^{235}U. The f_i values were converted to $r_{i,95}$ ($= f_i/f_{95}$) ratios, and the $r_{i,95}$ ratios were then plotted logarithmically against $r_{89,95}$ in the usual manner (*3*, *4*). The choice of $r_{89,95}$ provides easy comparison with similar plots of fractionation data obtained from fallout samples. When the points can be fitted with straight lines, the slopes of the lines provide correlation parameters.

Figures 6 through 13 are fractionation plots of the total sample data. Bryant *et al.* (*1*) provided LASL data for comparison. The scatter of these data reflects differences among the fuel fragments that LASL

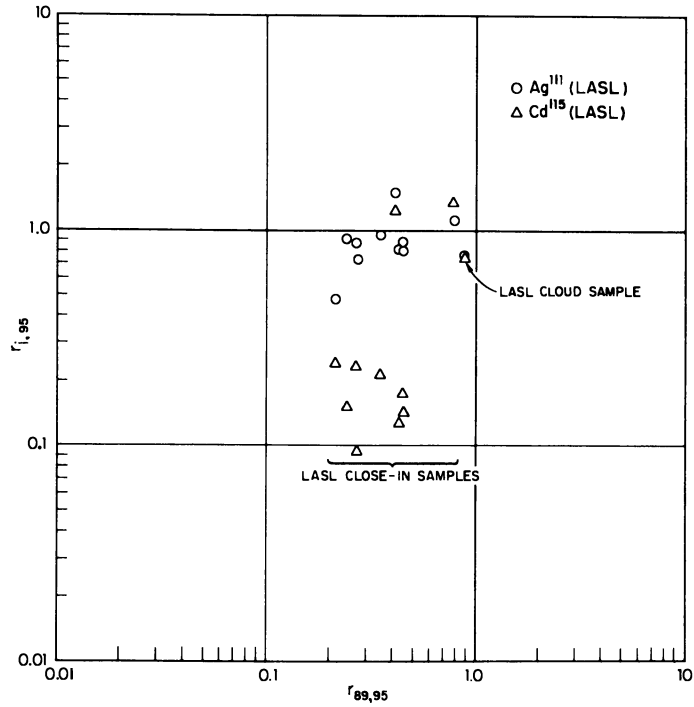

Figure 12. Fractionation plot for Ag^{111} and Cd^{115} (from Ref. 1)

analyzed; it does not indicate poor radiochemistry. Several characteristics of the fractionation behavior are apparent. Table II compares the fractionation behavior observed for the transient test with that observed in nuclear weapons tests (*3, 4, 5*). Inspection of this table shows that for the transient test:

(1) ^{144}Ce, ^{147}Nd, and radionuclides with gaseous precursors correlate linearly and have nearly the same correlation parameters as have been observed in air bursts.

(2) ^{132}Te also correlates linearly.

(3) ^{131}I and the shielded nuclide ^{136}Cs correlations have definite curvature.

(4) ^{99}Mo, ^{103}Ru, ^{106}Ru, and ^{237}U do not correlate well with ^{89}Sr and ^{95}Zr, although they tend to follow each other.

The curvature in the case of ^{136}Cs is related to its greater abundance with respect to ^{137}Cs in both fallout and ground-filter samples. This difference cannot arise from different ^{136}Cs fission yields in these portions of debris caused by difference in neutron spectra in different parts of the reactor. Thus, for the thermal-neutron fission of ^{235}U, the ratio of ^{136}Cs yield to the total chain yield of ^{137}Cs can be calculated from the

data of Weaver *et al.* (*13*) to be 0.0613, while for fission-spectrum neutrons this ratio is 0.0585. The difference must therefore be attributed to the fact that the gaseous precursors of ^{137}Cs escaped more readily from the fallout particles than did ^{136}Cs. (The fact that ^{136}Cs appears to be always more abundant than ^{137}Cs probably indicates an inaccuracy in the ^{136}Cs calibration factor.) An alternative view would be to say that in the fallout samples ^{136}Cs is behaving more like ^{140}Ba, while in the ground filter sample it is behaving more like ^{137}Cs. The fact that Cs is prominent in the 140 chain at earlier times than it is in the 137 chain is equivalent to saying that the fractionation processes for the fallout sample operated at earlier times than those which appear to have operated on the ground-filter sample and therefore are reasonably associated with escape rather than with condensation phenomena.

The behavior of the 131 and 132 chains can also be explained on the basis of escape. Tellurium has a larger fractional independent yield in the 132 chain than in the 131 chain (*12*) and also has a larger fractional release than iodine at elevated temperatures (*11*).

The behavior of ^{99}Mo, ^{103}Ru, ^{106}Ru, and ^{237}U is difficult to account for. In view of the wide scatter of the data, which may indicate analytical difficulties, the results on these nuclides need to be confirmed.

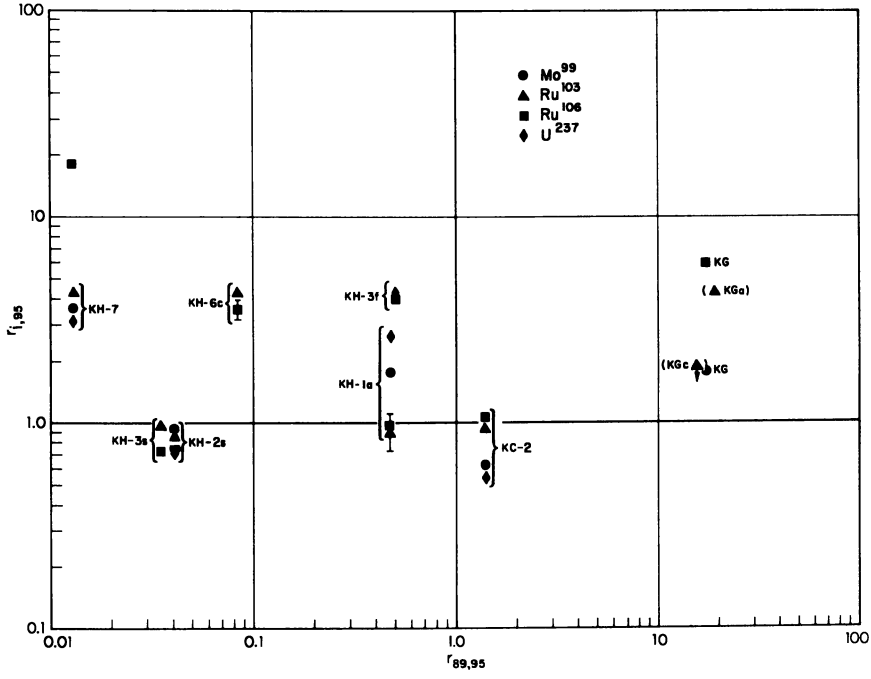

Figure 13. Fractionation plot for Mo^{99}, Ru^{103}, Ru^{106}, and U^{237}

Table II. Comparison of Fractionation-Correlation Parameters with Those from Nuclear Weapons Tests

	Transient Test	*Air Bursts*	*Coral Surface Burst*	*Silicate Surface Bursts*
^{89}Sr[a]	1.000	1.000	1.000	1.000
^{90}Sr	0.9	0.92 ± 0.08	0.73	0.5–0.7
^{91}Y	0.7	0.56 ± 0.03	0.54	0.4–0.5
^{95}Zr[b]	0.000	0.000	0.000	0.000
^{99}Mo	irregular[c]	(0.30 ± 0.05)[c]	−0.10	−0.02–0.04
^{103}Ru	irregular[c]	—	—	0.5
^{106}Ru	irregular[c]	—	—	—
^{111}Ag	irregular[c]	0.80 ± 0.05	—	—
^{115}Cd	irregular[c]	0.80 ± 0.06	—	—
^{131}I	curved	—	—	0.6–1.1
^{132}Te	0.9	—	—	0.4–1.1
^{136}Cs	curved	0.67 ± 0.08	—	0.4–0.8
^{137}Cs	1.0	0.90 ± 0.09	1.0	1.0–1.2
^{140}Ba	0.7	(0.62 ± 0.04)[c]	0.6	0.5–0.6
^{144}Ce	0.1	0.17 ± 0.20	0.08	0.0–0.2
^{237}U	irregular[c]	0.80 ± 0.05	−0.02	0.5[d]

[a] All ^{89}Sr slopes are 1.000 by definition.
[b] All ^{95}Zr slopes are 0.000 by definition.
[c] Although none of these nuclides correlate well with $r_{89,95}$, they appear to correlate well among themselves.
[d] This value is actually from ^{239}Np which does not fractionate from ^{237}U in silicate surface bursts.
[e] Yield dependent.

Table III. Behavior of ^{89}Sr, ^{90}Sr, and ^{91}Y in the Kiwi-TNT Event

Sample	$f_{90}\,(f_{89}f_{91})^{-1/2}$
KC-2	0.91
KG	1.00
KH-1a	0.87
KH-2s	0.87
KH-3s	0.93
KH-3f	0.91
KH-6c	0.73
KH-7	0.70
	0.86 ± 0.10

Table III tests the applicability of the geometric-mean rule to the transient data. This rule states that $f_{90}^2 \approx f_{89}f_{91}$. Table III shows that the average value of $f_{90}\,(f_{89}f_{91})^{-1/2}$ for the transient debris is within 14% of the predicted value of unity.

Combination of sample weights and radiochemical results for the KH fractions allowed several types of specific activity (s) to be calculated. Table IV shows these results. In terms of s_{95}, the number of

equivalent fissions of ^{95}Zr per gram, the data show no correlation with either particle size or shape. The specific activity of ^{89}Sr (s_{89}), on the other hand, appears definitely higher for the irregular particles. This observation, which is the opposite of that found in fallout particles, is consistent with the belief that spheroidization is the result of exposure to high temperatures and that this exposure preferably volatilized the ^{89}Sr precursors.

Table IV. Specific Activity(s) of Fallout Particles

Sample	Weight, mg.	s_{95}, $10^{14}f_{95}/g$	s_{89}, $10^{13}f_{89}/g$	Oralloy Content,[b] wt. %	s_{95}/Oralloy, $10^{14}f_{95}/g$ Oralloy	s_γ[c] 10^{-7} ma./gram	s_γ/s_{95}, ma./$10^{21}f_{95}$
KH-1a[a]	98.0	12.5	5.98	10.3	12.1	2.93	2.35
KH-2s	44.2	6.02	0.27	7.1	8.5	—	—
KH-3s	23.5	8.85	0.31	—	—	—	—
KH-3f	52.0	2.81	1.40	—	—	—	—
KH-6c	14.8	8.04	0.68	17.9	4.0	2.40	2.98
KH-7	20.6	14.8	0.20	41.6	3.5	3.45	2.33

[a] Single irregularly shaped particle.
[b] Oralloy was 93% ^{235}U.
[c] At 1415 on Feb. 2, 1965 or $D + 21$ days or $H + 507$ hours.

The variation in oralloy content shown in Column 5 explains some of the variability in s_{95}. Column 5 is calculated on the assumption that the oralloy is 93% ^{235}U. When one considers that UC_2 has 90 wt. % of uranium, the concentration of uranium in KH-7 indicates that about half this fraction arose from primary fuel material.

The value of s_{95} is normalized in terms of the uranium content in Column 6 to give the number of equivalent ^{95}Zr fissions per gram of oralloy. This value for the large fritted particle (KH-1a) exceeds the calculated fragmentation threshold of $10^{15}f_{95}/g$ (*8*). The evident negative correlation of this ratio with degree of fragmentation is noteworthy. Evidently, either degree of burn alone is an insufficient criterion of fragmentation, or large fractions of the mass 95 chain escaped as ^{95}Sr. The latter conclusion is supported by independent, unpublished observations.

Finally, the ionization current per gram, s_γ, has been calculated for 21 days after the event and compared with s_{95}. Unlike the cloud sample, the KH sample was fractionated. The standardized (*i.e.*, corrected to a reading of 560×10^{-9} ma. for a 100-μgram radium standard) unfractionated value of this ratio at 21 days has been determined by Mackin to be 4.7×10^{-21} ma. per fission (*10*). The value determined here is only half of the theoretical value. Crocker's calculations show that ^{140}La contributes 60% of the ionization rate from an unfractionated sample at this time (*2*). Depletion in ^{140}La therefore undoubtedly contributes to the

low value of this parameter. However, the ratio s_γ/s_{95} is relatively constant while the degree of depletion in the 140 chain varies considerably among the samples, and hence other causes must be contributing. The variation of ^{99}Mo, ^{103}Ru, ^{106}Ru, and ^{237}U indicates that variability in the content of other mass chains may be compensating.

Conclusions

Although the transient test was orders of magnitude below a nuclear weapon in regard to energy release and temperature achieved, the debris showed many similarities to fallout. These included not only the size and appearance of the particles but also the correlation properties of various radionuclides. Dissimilarities in the correlations and the variation of specific activity with particle type confirm expectations of the importance of escape processes to the formation mechanisms for this type of debris. This study shows that data-correlation techniques developed for fallout characterization are also useful in studying reactor debris.

Literature Cited

(1) Bryant, E. A., Sattizahn, J. E., Wagner, G. F., Los Alamos Scientific Laboratory, **LA-3290** (June 23, 1965) (Classified).
(2) Crocker, G. R., U. S. Naval Radiological Defense Laboratory, **USNRDL-TR-1009** (Dec. 28, 1965).
(3) Crocker, G. R., *Nature* **210**, 1029 (1966).
(4) Crocker, G. R., Kawahara, F. K., Freiling, E. C., "Radioactive Fallout from Nuclear Weapons Tests," A. W. Klement, Ed., p. 72 (Nov. 1965).
(5) Freiling, E. C., *Science* **133**, 1991 (1961).
(6) Fultyn, R. V., *Intern. Symp. Fission Prod. Release, Transport, Accident Conditions*, Oak Ridge, Tenn., **CONF-650407**, 537 (1965).
(7) Henderson, R. W., *Intern. Symp. Fission Prod. Release, Transport, Accident Conditions*, Oak Ridge, Tenn., **CONF-650407**, 557 (1965).
(8) King, L. D. P., Mills, C. B., *Trans. Am. Nucl. Soc.* **8**, 565 (1965).
(9) Lai, J. R., Pascual, J. N., Wong, D. T., U. S. Naval Radiological Defense Laboratory, **USNRDL-TR-68-68** (Nov. 24, 1967).
(10) Mackin, J. L., Weisbecker, L. W., Zigman, P. E., U. S. Naval Radiological Defense Laboratory, **USNRDL-TR-811** (Jan. 18, 1965).
(11) Rymer, G. R., Grandy, G. L., Henninger, W. A., Roll, J. A., Westinghouse Astronuclear Laboratory, **WANL-TNR-162** (July 1, 1964) (Classified).
(12) Strom, P. O. *et al.*, U. S. Naval Radiological Defense Laboratory, **USNRDL-935** (Nov. 5, 1965).
(13) Weaver, L. E., Strom, P. O., Killeen, P. A., U. S. Naval Radiological Defense Laboratory, **USNRDL-TR-633** (March 5, 1963).
(14) Zumwalt, L. R., Gethard, P. E., Anderson, E. E., *Nucl. Sci. Eng.* **21**, 1-12 (1965).

RECEIVED September 25, 1968. Work sponsored by the Space Nuclear Propulsion Office under Contract AT-(49-5)2505 (5).

19

The Specific Activity of Nuclear Debris from Ground Surface Bursts as a Function of Particle Size

M. W. NATHANS

Trapelo Division of LFE Corp., 2030 Wright Ave., Richmond, Calif. 94804

Cloud samples from five coral surface bursts and one silicate surface burst were subjected to a size separation by means of a density gradient column. The fractions were analyzed for ^{90}Sr, ^{147}Pm, and uranium. One sample was also analyzed for ^{137}Cs and ^{144}Ce. Fraction weights were obtained by direct weighing or by matrix element analysis. Mean diameters of the particles in the size fractions were determined from size distribution measurements by optical and electron microscopy. The specific activities are varying functions of the radioactive species. No systematic differences between the behavior of ^{147}Pm and ^{90}Sr are apparent as a function of yield. Uranium behaves almost identically to ^{90}Sr. There is evidence of a strong decrease in the specific activity at particle sizes above 60μ.

Some years ago Freiling proposed that the specific activity (activity per unit weight or volume) of individual fission products in nuclear debris, particularly from air bursts, be expressed as an inverse power function of the particle size (2, 3). Thus:

$$A^{(i)} = A^{(i)}\ (r = 1)^{-m} \qquad (1)$$

In this expression $A^{(i)}$ is the specific activity of radionuclide i, $A^{(i)}\ (r = 1)$ is the specific activity of nuclide i at $r = 1$, r is the radius of a debris particle, and m is a number between 0 and 1. A value of $m = 0$ implies that the activity is proportional to the volume of the particles. Such a volume dependence results for nuclides which combine with the matrix material in the cooling fireball and applies to the so-called refractory chains, such as the 95-, 11-, and 147-chains. A value of $m = 1$ or a surface-

area dependence results for nuclides which are still in the gas phase or whose precursors are still in the gas phase when solidification is essentially complete. In this latter case, the last radioactive member or members of the chain condense on the surface of the particles, provided these end members are not volatile. Examples are the 89- and 137-chains. If both volatile and nonvolatile members of a mass chain are present during condensation and solidification, volume as well as surface deposition occurs. For such cases a fractional value of m between 0 and 1 is found. Examples are the 90- and 140-chains. The over-all result is a fractionation of fission products to an extent which depends upon the particle size.

The "radial distribution model" sketched above has been found to be a good approximation for airbursts in the particle size range above about 3μ (*1*). No data were available for particles below 3μ in diameter. [Recently, some strong evidence was obtained in our laboratory that the specific activities in airburst debris increase with decreasing size below about 0.5μ]. The model is inadequate, however, for describing the specific activities of debris particles from ground surface and near-surface bursts. For such events, the underlying hypothesis certainly breaks down. In airbursts one has to consider only the condensation and subsequent solidification of material which has been in the gas phase exclusively. In ground surface bursts a great quantity of soil material is drawn into the fireball and later into the rising cloud. Only a small portion of this material fuses, and even less vaporizes. Thus, the greater part of even the refractory chains condense on the surface of the particles only and may migrate into the particles primarily by diffusion. Thus, a more complicated size dependence of the specific activities is expected to be present in the debris from surface and near-surface bursts. The determination of this size dependence is important for predicting dose rates in fallout fields. Therefore, a systematic investigation was carried out to determine the size–activity relationships for several representative nuclides in debris resulting from four coral surface bursts and one silicate surface burst.

Experimental

Samples from the following events were analyzed: Castle Bravo, Castle Koon, Redwing LaCrosse, Redwing Zuni, Redwing Tewa, and from Johnie Boy. Koon samples from three different altitudes were analyzed but only one of the Johnie Boy samples (842L). Additional Johnie Boy samples have been analyzed by Russell (*6*). Details of all events and samples are reported elsewhere in this volume (*5*), except for LaCrosse and for Tewa. LaCrosse was a coral surface burst of about 40 kilotons whose cloud topped out at 12,000 meters. The sample analyzed (054) was collected at 6500 meters and at 2.6 hours after the event.

Tewa was detonated on a barge on a shallow portion of the Bikini lagoon. Its yield was about 4.6 megatons, and its cloud topped at about 32,000 meters. The sample analyzed (501) was taken at 16,000 meters at 2.2 hours after the event.

Prior to radiochemical analysis the samples were ashed and separated into size fractions by means of procedures described by Nathans *et al.* The determinations of the fraction weights and of the mean diameters of the particles in the fractions have also been described extensively in the same paper. An aliquot of each size fraction was dissolved and subjected to a separation procedure to isolate Sr, Ru, Sb, Cs, Ce, Pm, U, and Pu fractions. The procedure is sketched in Figure 1. Further decontamination of Ru and Ce was carried out only with the Johnie Boy sample. The Sb and Pu fractions were set aside for later analysis. After complete analysis of the Cs fractions, anomalies were found in the data for the coral samples. These samples had been ashed at about 475°C. Apparently some Cs had volatilized at this temperature. Such a behavior explained the anomalies, and this was confirmed by Heft by more extensive experimentation (*4*). Thus, Cs data are reported only for the Johnie Boy sample, which was ashed at low temperature in a Tracerlab low temperature asher.

The methods used for analyzing the activities are summarized in Table I. The $^{143,144}Pm$ tracer was prepared at the Oak Ridge National Laboratory by cyclotron bombardment of enriched ^{143}Nd with protons. The ^{90}Sr was counted within 24 hours of final separation so that the growing ^{90}Sr activity could be neglected. Most size fractions contained sufficient ^{90}Sr and ^{137}Cs activity such that the counting statistics could be kept within $\pm 3\%$ without the need for excessive counting times. The ^{147}Pm and ^{144}Ce data include a possible counting error of $\pm 6\%$ or less, except for the fractions containing the largest particles, for which the counting error was as high as $\pm 20\%$. The uranium data are associated with errors not exceeding 3%.

Specific activities were calculated by dividing the fraction weights into the counting results corrected for chemical yield. Consideration was given to the question of whether the weights and the radiochemical data were obtained from the same portion of the filter containing the particle fractions or from different portions as described by Nathans *et al.* Radiochemistry and matrix element analysis on the *same* particles were performed on the Zuni sample and on Koon samples 1086 and 7269. Thus, for these samples corrected weights based on the matrix element analyses were certainly indicated. In regard to the remaining samples, fraction weights from matrix analyses were used for Zuni, LaCrosse, and Koon sample 051 because any errors introduced by the inhomogeneity of the filter surface were deemed less than the errors in the directly measured fractions from the Bravo sample, so that for this sample the directly-sults indicated that the relation between these errors was reversed in the fractions from the Bravo sample, so that for this sample the directly-measured fraction weights were used. Since no matrix analyses were performed on the fractions of the Johnie Boy sample, in this case again the directly measured weights were used.

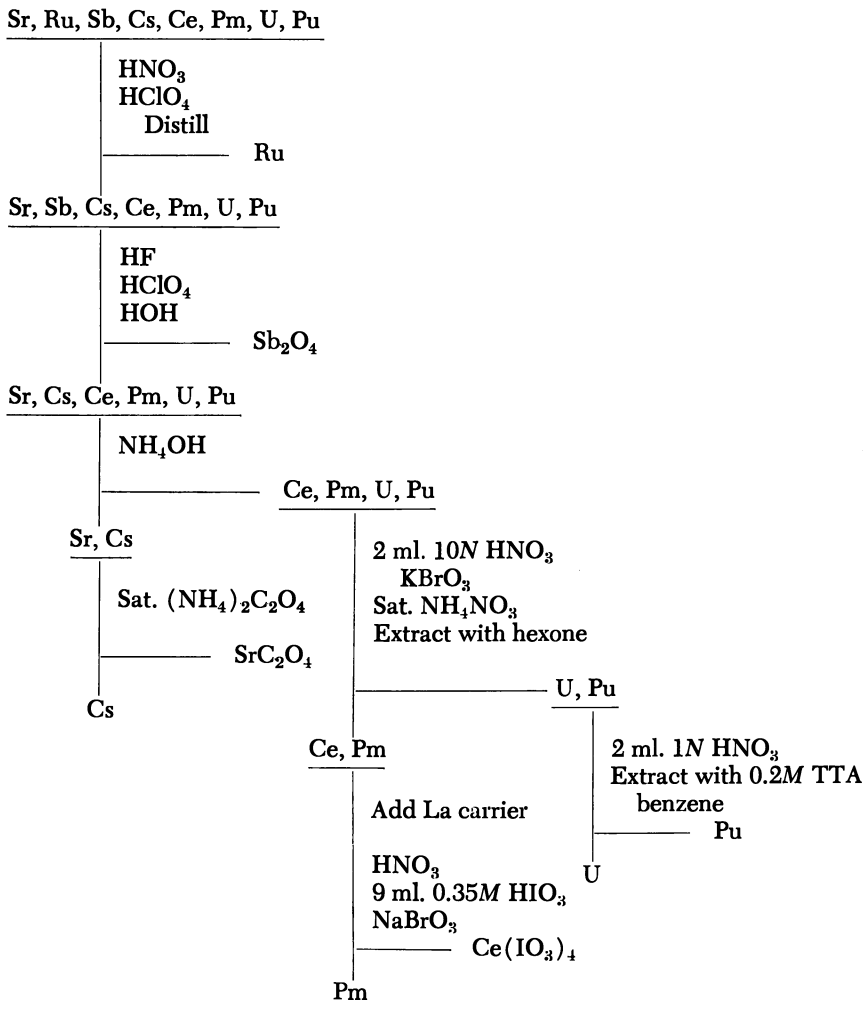

Figure 1. Flow diagram of separation procedure

Table I. Methods of Analyzing Some Radionuclides

Nuclide	*Yield Tracer*	*Chemical Form*	*Activity Counted*
^{90}Sr	Stable Sr	$SrCO_3$	Beta
^{106}Ru	Stable Ru	Ru metal	Beta
^{137}Cs	Stable Cs	$CsClO_4$	Gamma
^{144}Ce	Stable Ce	Ce_2O_3	Beta
^{147}Pm	$^{143,144}Pm$	Metal plated on Pt disc	Beta, x-ray
U	^{233}U	Determined by mass spectrometry	

Table II. Relative Specific Activities in a Bravo Cloud Sample

		Specific Activity					
Event	$\overline{a}$,[a] μ	^{90}Sr	^{106}Ru	^{137}Cs	^{144}Ce	^{147}Pm	*U*
Bravo	69	1.20				1.33	1.59
	57	1.48				3.56	1.78
	41	1.94				5.18	2.74
	24	1.85				5.08	2.98
	19	2.32				6.77	3.58
	15	2.25				7.15	3.45
	12.3	3.11				8.98	4.02
	8.1	3.64				5.46	4.18
	(5)	4.76				13.50	3.40
	(1.5)	4.03				15.02	3.18
	1.0	5.62				47.07	2.28
Tewa	41	3.78				2.7	0.61
	32	6.39				1.86	—
	25	13.0				14.8	0.17
	11.8	14.0				13.7	0.46
	8.2	24.0				20.2	1.8
	[a]	43.1				37.2	3.01
	[a]	48.7				43.4	3.22
	[a]	57.3				38.9	4.48
	[a]	49.6				55.4	3.21
	[a]	40.5				22.3	(10.4)
	[a]	49.4				29.1	3.34
	[a]	38.3				35.0	3.69
	[a]	25.1				31.9	3.51
Zuni	58	0.80				0.67	13.1
	42	0.79				1.10	9.6
	36	0.99				2.49	11.2
	22	1.16				2.24	13.7
	18	1.46				2.87	14.5
	11.5	2.03				2.71	17.8
	7.5	1.79				2.71	18.6
	5.4	1.66				3.92	13.1
	3.1	2.33				2.03	43.3
	2.4	2.47				2.26	—
	1.2	4.27				2.55	65.6
	0.58	5.58				1.05	13.9
Koon 051	(90)	0.19				—	1.73
	(60)	0.16				—	2.47
	54[b]	0.19				0.11	—
	43[b]	0.27				0.037	—
	33	0.38				0.29	2.25
	32.5[b]	0.54				0.20	—
	23	0.77				0.81	5.12
	23[b]	0.95				0.71	—
	(18)	0.90				—	6.92
	15.8[b]	0.95				0.82	—

Table II. Continued

Event	$\bar{a}$,[a] μ	*Specific Activity* ^{90}Sr	^{106}Ru	^{137}Cs	^{144}Ce	^{147}Pm	*U*
	14	1.15				—	8.08
	10.7[b]	1.07				1.18	—
	9	1.50				1.22	8.97
	8.3[b]	1.35				0.93	—
	(5.3)	1.32				—	8.22
	(3)	3.12				0.83	8.06
	2.75[b]	2.79				1.49	—
	(2)	1.42				1.24	19.0
	1.70[b]	2.65				1.34	—
	(1)	3.99				2.46	39.0
	0.91	6.57				3.94	—
	(0.6)	4.67				—	74.5
	0.6[b]	6.72				4.73	—
Koon 1086	16	42.1				2.15	61
	11	124				21.7	220
	1.4	130				28.9	261
	0.98	161				16.7	325
	0.45	146				44.9	238
	0.47	126				11.7	238
	0.30	135				15.0	309
	0.28	95.6				13.3	255
Koon 7269	68	2.23					4.34
	42	6.05					8.30
	27	11.3					13.4
	23	15.1					16.8
	21	(11.4)					(14.5)
	20	(31.2)					(30.4)
	6.8	(61.8)				(24.0)	(70.0)
	5.2	(6.16)				(21.1)	(98.3)
	4.3	49.2				30.5	93.7
	3.6	72.1				6.41	116
	1.2	63.7				9.60	76.5
	0.74	80.3				15.0	98.5
	0.39	79.7				21.4	124
LaCrosse	(50)	0.050				0.015	1.83
	30	2.09				0.58	2.35
	18	9.14				2.57	1.71
	(13)	14.7				4.25	1.05
	9	14.3				3.44	0.88
	4.8	17.6				2.94	1.02
	(3)	18.8				3.14	1.08
	(2)	19.3				3.45	1.11
	(1.5)	19.0				3.45	1.14
	(0.9)	(11.1)				(1.63)	(0.85)
	0.50	(13.2)				(1.72)	(0.86)

Table II. Continued

Event	$\bar{a}$,[a] μ	Specific Activity					
		^{90}Sr	^{106}Ru	^{137}Cs	^{144}Ce	^{147}Pm	U
Johnie Boy	120	1.89	0.045	1.48	0.32	0.67	1.25
	114	0.27	0.10	0.16	0.55	0.63	1.59
	102	0.11	0.12	0.054	0.46	0.51	1.46
	70	0.11	0.36	0.070	0.41	0.50	1.40
	46	0.085	0.33	0.076	0.37	0.42	0.95
	27.5	0.11	0.40	0.13	0.35	0.43	0.93
	21.5	0.15	0.59	0.28	0.54	0.67	1.02
	13	0.21	0.68	0.50	—	—	1.11
	9.3	0.23	(2.52)	0.68	0.33	0.41	0.88
	5.5	0.25	0.58	0.83	0.18	0.51	0.75
	3.4	0.49	0.32	1.33	0.18	0.56	1.26
	(2.0)	0.76	1.00	1.51	0.26	0.91	1.84
	1.1	1.35	1.97	1.84	0.83	0.92	3.10[b]
	0.62	0.58	0.67	0.65	1.16	1.21	1.34

[a] Not measured.
[b] From analysis of a second portion of the same filter sample.

Results and Discussion

The experimental results are shown in Table II. The indicated diameters, *a*, are the mean diameters of the size fractions.

The data show that the specific activity is generally not a simple function of particle size, confirming the composite nature of the samples. The sharp decrease of the ^{147}Pm specific activities in coral burst samples toward large particle sizes is particularly significant. Systematic differences as a function of yield or soil type between refractory ^{147}Pm behavior and semivolatile ^{90}Sr behavior are not apparent. Uranium behaves very much like ^{90}Sr.

Of particular importance is the evidence of strong geometric fractionation effects in the Koon cloud. Not only do order of magnitude differences exist between the average specific activities of samples taken from different portions of the cloud, but there are also differences in the relation between the specific activity and the particle size in those samples. One cannot draw the inference, however, that similarly large effects are the rule in clouds from ground bursts. Indeed, Russell did not find any significant geometric effects in the Johnie Boy cloud. Yet our results pose strongly the question of the uniqueness of the specific activity as a function of particle size and therefore of the representativeness of any one sample.

The question of representativeness is also posed by the specific activities of ^{90}Sr and ^{147}Pm relative to each other in Bravo, for example.

Integration of the specific activities over the particle size yields a much lower amount of ^{90}Sr than of ^{147}Pm produced, even if estimates from analyses of particles greater than 100μ are included (7). Such a result suggests that the sample was not representative of the true radioactive cloud distribution.

Finally, it should be noted that the samples may have been altered by weathering. Oxide is at least partly converted to carbonate and hydroxide as a result of moist storage conditions. In addition, surface-deposited activity may have been redistributed since moisture could have provided a path between particles. Such an effect would be more significant for ^{90}Sr than for ^{147}Pm but is probably not very large. It was found that the 2-propanol used for the size separations was capable of leaching some activity from the particles. However, the amount of ^{147}Pm leached was only about 1%; the amount of ^{90}Sr was never more than about 5% of the total, so that only a small fraction of these nuclides must be considered capable of migrating.

Conclusions

(1) The specific activities of radionuclides in debris from ground surface bursts are generally complicated functions of the particle size, in accordance with the composite nature of the debris.

(2) The specific activities of radionuclides in samples from surface burst debris are not necessarily unique functions of the particle size. The uniqueness is determined by the degree of mixing in the cloud, and is, therefore, expected to be a function of the time elapsed between the shot time and the sampling time.

Literature Cited

(1) Benson, P., Gleit, C. E., Leventhal, L., *Proc. Conf., Radioactive Fallout Nucl. Weapons Tests, 2nd, Germantown, Md., 1964,* 108 (1965).
(2) Freiling, E. C., U. S. Naval Radiological Defense Laboratory, Rept. **USNRDL-TR-680** (Sept. 12, 1963).
(3) Freiling, E. C., *Science* **139,** 1058 (1963).
(4) Heft, R. E., private communication, February 1968.
(5) Nathans, M. W., Thews, R., Russell, I. J., ADVAN. CHEM. SER. **93,** 360 (1969).
(6) Russell, I. J., Operation Sunbeam, Shot Johnie Boy, Rept., **POR-2291 (WT-2291)** (May 5, 1965).
(7) Tompkins, R. C., Krey, P. W., Rept. **WT-918** (Feb. 1956).

RECEIVED February 26, 1969. Work supported by Defense Atomic Support Agency under Contract DA-49-146-XZ-484.

20

The Particle Size Distribution of Nuclear Cloud Samples

M. W. NATHANS and R. THEWS[1]

Trapelo Division of LFE Corp., 2030 Wright Ave., Richmond, Calif. 94804

I. J. RUSSELL

Boston College, Chestnut Hill, Boston, Mass. 02167

The size distributions of the particles in cloud samples from three coral surface bursts and one silicate surface burst were determined by optical and electron microscopy. These distributions were approximately lognormal below about 3μ, but followed an inverse power law between 3 and ca. 60 or 70μ. The exponent was not determined unequivocally, but it has a value between 3 and 4.5. Above 70μ the size frequency curve drops off rather sharply as a result of particles having been lost from the cloud by sedimentation. The effect of sedimentation was investigated theoretically. Correction factors to the size distribution were calculated as a function of particle size, and theoretical cutoff sizes were determined. The correction to the size frequency curve is less than 5% below about 70μ, but it rises rather rapidly above this size. The corrections allow the correlation of the experimentally determined size distributions of the samples with those of the clouds, assuming cloud homogeneity.

The size and mass frequency distributions of the particles in clouds from ground surface bursts have an essential bearing on predictions of the fallout field resulting from such nuclear explosions. Fallout models that are still in use employ size distributions which have been derived

[1] Present address: Department of Physics, University of Rochester, Rochester, N. Y. 14627.

from the analysis of fallout collections from events that occurred in the early 1950's. These distributions are lognormal, with mass medians of the order about 100μ and logarithmic standard deviations of 1.68 to 1.98 (*3*). It is clear, however, that the fallout by itself cannot provide adequate information about the distribution in the smaller size ranges ($<$ 50–100μ) because they are not completely removed from the cloud during the relatively short period of sampling.

The reason for deriving the size distributions from fallout collections was the lack of cloud sampling during the first one to two hours after the event. Earlier cloud penetrations by aircraft were not possible because of the high radiation field. A rocket sampling program tried in the late 1950's to obtain cloud samples within the first 15 minutes was unsuccessful, and geopolitical considerations prevented further work. Thus, all available cloud samples were depleted in the particles larger than 50–100μ, the cutoff size depending upon the time and altitude of sampling and, therefore, were devoid of those particles which were most prominent in the fallout. The lack of information on the size distribution of cloud samples is, therefore, quite understandable.

As already mentioned, cloud sampling normally did not commence until between one and two hours after the shot. By this time, the cloud had long since stabilized—*i.e.*, its rise had come to a complete stop. The clouds from large yield devices, such as Zuni (3.4 megatons) and Bravo (15 meagtons), had penetrated the tropopause and had topped out at altitudes of 30 km. or more. The cloud bottoms were approximately at the tropopause height of about 15 km. Nevertheless, significant concentrations of particulate matter were present at lower altitudes, resulting both from those portions of the stem that never penetrated the tropopause and from sedimentation out of the cloud. These were usually the particles found in the collections originating with clouds of high yield, megaton-range shots. Occasionally, the tropopause was penetrated so that samples from the bottom of the cloud above the tropopause are also available, but, in a "vertical" sense the largest part of the cloud was not sampled. Thus, even cloud sampling itself may cause a bias against the smallest particles. Further distortions of the gross particle size distribution may have resulted from sampling only the edges of the visible cloud.

For lower yield events, when all or most of the cloud remains below the tropopause, sampling has been more extensive, although still not necessarily representative. The Johnie Boy (0.5 kiloton) cloud, whose top was at about 4.3 km. (15,000 ft.), was sampled at several altitudes by airplanes flying through the cloud. The Koon (150 kilotons) cloud, with a top at about 17 km. (55,000 ft.), was sampled at the periphery only, but one sample was obtained from the region near the top of the

cloud. In both cases, therefore, one can derive data that show the variation of size distributions with respect to altitude at some hours after the shot.

Finally, some distortion of the particle size distribution is caused by deviations from Stokes' law during particle sedimentation. These deviations are a function of the particle size such that the retardation of Stokesian settling becomes larger with increasing particle size. This effect can be evaluated theoretically, however, and corrections can be made to determine size distributions experimentally.

In this paper we report on the results of size distribution measurements of cloud samples from three coral surface bursts and one silicate surface burst and present the results of the calculations of the sedimentation correction.

Experimental

Samples. Table I lists the events from which samples have been analyzed. The individual sample tabulation is given in Table II.

Ashing. Sections of filter papers containing the samples from Johnie Boy were ashed in a Trapelo low temperature asher to prevent volatilization of some of the fission products of interest for different portions

Table I. Characteristics of Some Nuclear Ground Bursts

Event	*Yield, Megatons*	*Soil*	*Cloud Top, Meters*	*Cloud Bottom, Meters*
Castle Bravo (1954)	15	coral	34,000	16,600
Redwing Zuni (1956)	3.4	coral	24,500	15,000
Castle Koon (1954)	0.15	coral	16,500	[a]
Johnie Boy (1962)	0.0005	silicate	4,300	

[a] A strong wind shear at about 11 km. directed the bottom portion of the cloud away from the remainder of the cloud.

Table II. Sampling Data for Some Cloud Samples from Ground Surface Bursts

Event and Sample No.	*Time of Collection, Hours*	*Altitude of Collection, Meters*
Bravo—1086	4.0	15,500
Zuni—049	3.1	12,700
Koon—1086		
—051	3.1	11,950
—7269		
Johnie Boy—842R	0.6	2,950
—842L	0.4	3,400
—245L	0.8	3,700
—827L	0.35	4,350

of the program. This method of ashing left too much incompletely ashed residue in the coral samples because of differing characteristics of the filter paper. It was necessary, therefore, to ash the coral samples in a muffle furnace at about 475°C. At this temperature, any $Ca(OH)_2$ present decomposes, but $CaCO_3$ does not.

Size Separation. Measurements for the complete particle size distribution on samples thus prepared were extremely difficult to perform. Because small particles are often masked by larger ones the results are biased seriously in favor of the larger particles. By successive dilutions of the sample it was possible to obtain what appears to be a reasonable size distribution of the Johnie Boy sample. Better results were obtained by separating the particles into fractions of different, although overlapping, size ranges; determining the size distributions in the fractions; and combining these distributions with appropriate weighting factors.

Two methods were used for size separation. In the first method, used only with some of the Johnie Boy samples, the sample was dispersed in 500 ml. of benzene in a graduated cylinder (column length: 30 cm.) and was allowed to settle for 120 minutes. The top 400 ml. were removed and filtered to give the smallest size fraction. Benzene (400 ml.) was added to the remainder in the cylinder, and the particles were redispersed. Settling was allowed to proceed for 60 minutes before the top 400 ml. were again removed and filtered. This procedure was repeated a number of times with ever shorter settling times to yield size fractions containing successively larger particles. Particle agglomeration was not apparent under the microscope.

The second method, first applied by Heft and Steele (*4*) to cloud and fallout samples, consisted of adding the particles, well dispersed and deagglomerated, in a small amount of 2-propanol, to the top of a 30-cm. long density-gradient column. The column liquid was 2-propanol and contained concentrations of CCl_4 which varied from 6% at the bottom of the column to 5% at the top. The small density gradient thus established suppressed local convection currents which would tend to diffuse the size ranges of the particles in the various fractions. The particles were allowed to settle through the column into a container containing some CCl_4. The container was changed, starting 2 minutes after administration of the sample to the column, after settling periods which increased by a factor of 2 each time. The last few fractions were obtained by draining the column in segments.

The 2-propanol had some leaching effect on the radioactivity contained in or on the particles. This effect was rather insignificant with the Johnie Boy sample (silicate surface), but quite pronounced for ^{90}Sr and ^{137}Cs with the coral samples. Some experiments were carried out with anisol–CCl_4 and with silicone–CCl_4 mixtures. In both cases, the leaching was considerably reduced. Sample recovery from the anisol column was poor, however, because particles tended to adhere to the wall. The silicone caused problems because it was difficult to remove quantitatively from the filters, and the residue interfered with the microscopy. Complete removal of the silicone from the size fractions may be effected by ultracentrifugation and washing with CCl_4 before filtration. Such a procedure will cause some losses, however, that will be difficult to eliminate.

Size Measurement. After the fractions were filtered, the millipore filters were sectioned to provide separate portions for chemical analysis and for size distribution measurements. One-eighth or one-fourth was set aside in reserve. The section designated for optical microscopy was transferred to a microscope slide and placed in a covered petri dish with a few drops of acetone. The acetone vapor is absorbed by the millipore and renders the filter transparent.

The size fractions measured by electron microscopy were redispersed before filtration in a sonic shaker. About 100–200 λ was transferred to a microscope slide. After drying, a small amount of collodion (4% in amyl acetate) was added, and the solvent was allowed to evaporate. The collodion film was scribed into 3 mm. squares, floated off on water, and gathered on electron microscope grids.

The size distribution of the particles in the fractions was determined by measuring the size of about 100 particles in each fraction by optical or electron microscopy, as appropriate for the size range of the fraction. The size of the particles in most of the Johnie Boy samples was measured along a line parallel to the base of the field of view. This procedure extends the size range a little on both ends, because the particles are not all spherical, but otherwise has little effect on the size distribution because the particles are randomly oriented. In some of the Johnie Boy samples, the particles were measured along the longest and the shortest directions, and the averages were taken.

In the optical microscope, measurements were made with a Crookes image-splitting eyepiece that was calibrated with a measuring slide. The electron microscope (Hitachi HU-11) was calibrated with latex spheres of known size.

Fraction Weights. To arrive at the size distribution of the unseparated sample, it is necessary to know the relative number of particles in each size fraction. Three different approaches have been applied:

(a) The simplest approach is a weighing of the fractions. It was found, however, that sometimes "negative weights" were obtained. This observation could be ascribed to a weight loss of the millipore by the action of the CCl_4 (from the collectors and the washings). An improvement was made by prewashing the filters with about 150 ml. of CCl_4, but it was found that the problem could not be entirely eliminated. Variable errors of up to several tenths of a milligram were still present. Such errors are not too important when the fraction weights are high (of the order of 10 mg. or more) but may be significant when fraction weights are low.

(b) Fraction weights may be derived from a complete chemical analysis. Atomic absorption analyses have been carried out for Ca, Mg, Fe, and Na. Fraction weights have been reconstructed from these analyses by assuming the elements to have been present in the form of $CaCO_3$, $MgCO_3$, Fe_2O_3, and NaCl. However, the analyses were often performed on one-eighth sections of the millipore filters, and when the particles were not uniformly distributed on the millipore, erratic results were sometimes obtained.

(c) The number of particles in the fractions may be obtained by counting. This method was evaluated with several samples. The total

number of particles in 20 randomly selected fields of view was determined in each fraction selected for this purpose. The total number of particles in each fraction was calculated by relating the total area viewed to the area of the filter paper. This method has its own statistical errors, in addition to the errors associated with the gross inhomogeneity of particle deposition on the filters.

The most consistent data were found to be derived by the use of Method b. The only exception was the Bravo sample, where Method a was used.

Treatment of Data

The size distributions of the fractions were plotted on log-probability paper as particle diameter (in microns) against cumulative percent of particles smaller than the indicated size. Figure 1 shows such a plot for the Johnie Boy size fractions. Such plots were compared for several samples with similar plots on linear-probability paper. Almost always the data could be described better by a lognormal rather than by a normal distribution law, after proper allowance for the presence of a maximum and a minimum size in each fraction. The parameters of the distributions were determined from the graph: the geometric mean as the 50% point (median) and the logarithmic standard deviation as the ratio of the diameters at the 84 and 50% points.

By adding the size distributions of the fractions with the proper weighting factors the size distribution of the total sample can be obtained. The relative numbers of particles in the fractions may be used as the weighting factors. These numbers are calculated by dividing the fraction weights by the average weight of a particle in each fraction computed as $(\pi\rho/6)\ a^3$ where ρ is the density (assumed to be 2.75 grams/cm.^{3}) and a^3 is the mean of the cube of the particle diameter as determined from a lognormal distribution.

The Sedimentation Correction

Gravitational sedimentation causes a change in the particle size distribution anywhere in and below the cloud compared with the size distribution at stabilization time. Thus, to reconstruct the size distribution at stabilization time, corrections must be applied to the size distributions measured in the samples. These corrections were calculated by assuming Stokesian settling modified by a drag slip correction. It was assumed further that at stabilization time the cloud was axially symmetric and consisted of spherical particles. Wind and diffusion effects were neglected.

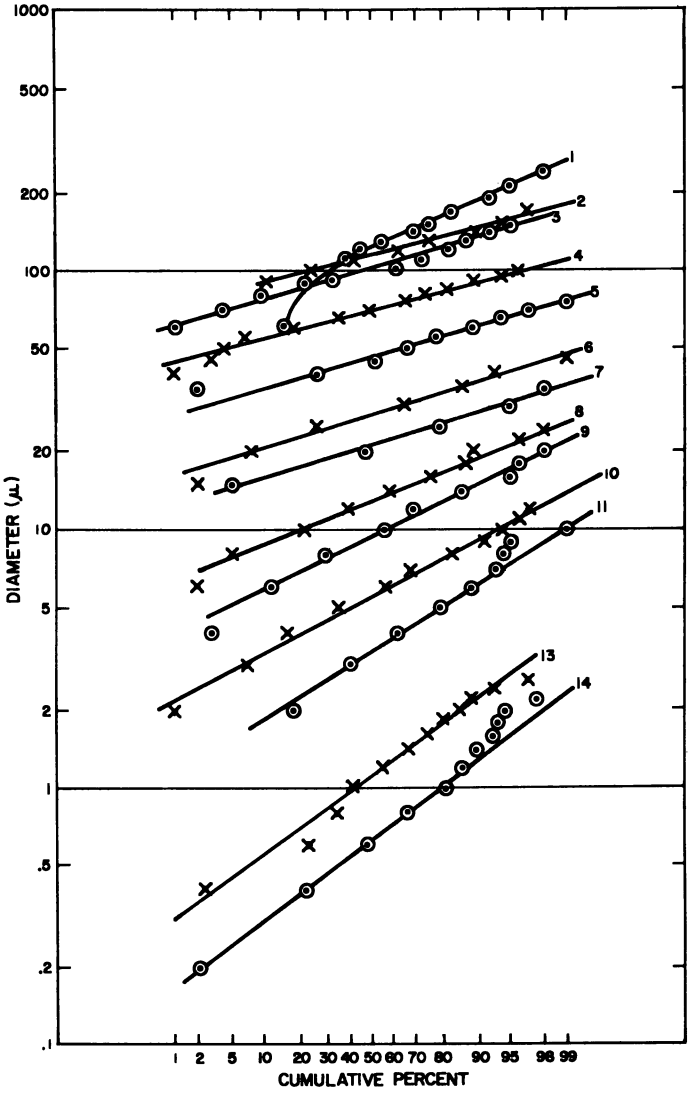

Figure 1. Size distributions in the fractions from a Johnie Boy sample

If $f(a,z,t)$ denotes the number density of particles with diameter a at position z and time t, the continuity equation is

$$\frac{\partial f}{\partial t} + v\,\frac{\partial f}{\partial t} + f\,\frac{\partial v}{\partial z} = 0 \qquad (1)$$

where $v = v(a,z)$ is the velocity of the particles. A formal solution for f in terms of the initial ($t = 0$) value is

$$f(a,z,t) = \left(\frac{\partial z_1}{\partial z}\right)_{a,t} f[a,z(a,z,t)0] \tag{2}$$

The value of the function $z(a,z,t)$ is the position which as particle of diameter a must have occupied at $t = 0$ to arrive at position z at time t. It is defined through the relation

$$t = \int_{z}^{z_1(a,z,t)} \frac{dn}{v(a,n)} \tag{3}$$

Specifically, the calculations had as their goal the computation of $(\partial z_1/\partial z)$ as a function of particle size for clouds of different heights at various altitudes and sampling times, including the parameters applicable to the samples analyzed. A detailed exposition of the theory and its limitations is presented in the Appendix. The values of $(\partial z_1/\partial z)$ are divided point by point into the measured size distribution—*i.e.*, $f(a,z,t)$—to arrive at the size distribution at stabilization time—*i.e.*, $f[a,z(a,z,t),0]$, according to Equation 2. An additional output of the calculations are the cutoff diameters (smallest and largest diameters) in the samples.

Results

Figure 1 shows, as a typical plot, the particle size distributions of the size fractions from a Johnie Boy sample. Only the first fraction, containing the largest particles, deviates significantly from lognormality. The standard deviations are almost the same for the first nine fractions as is apparent from the parallelism of the cumulative frequency curves. When the particle size decreases further, the standard deviations of the size distributions in the fractions increase.

The Johnie Boy sample contained a considerable number of spherical particles in the three smallest size fractions. These particles have a size distribution which differs from that of the irregularly shaped debris particles, being lognormal with a mean below 1μ. They have not been included in the size and mass frequency curves for convenience of calculation since their effect on the curves is small. However, the fraction weights and hence the number of particles in the fractions were corrected for the presence of these spherical particles.

The size and mass frequency curves of the complete cloud samples, derived from those of the fractions and the fraction weights, are shown in Figures 2 through 6. The sedimentation corrections have been applied. They are quite small for all but the largest particles found.

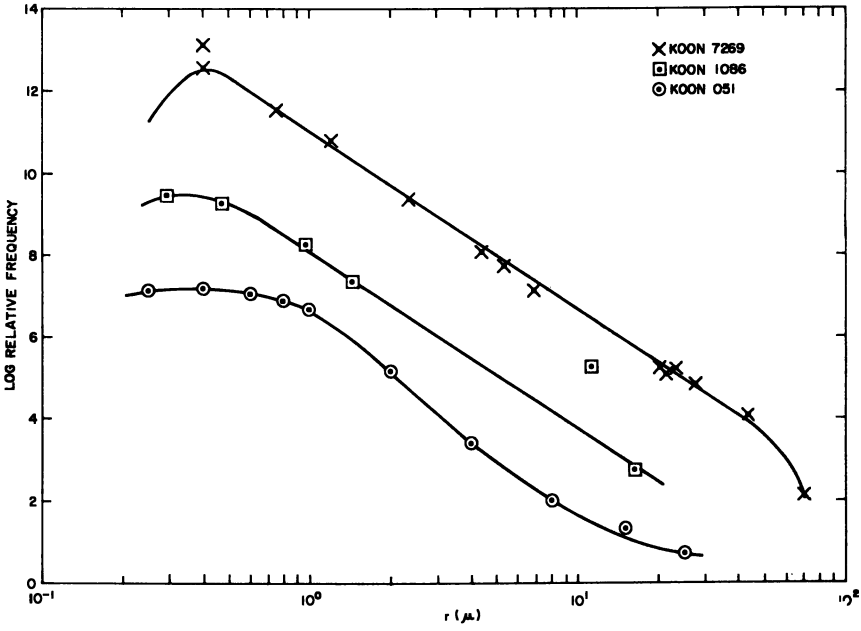

Figure 2. Size frequency curves for three Koon samples

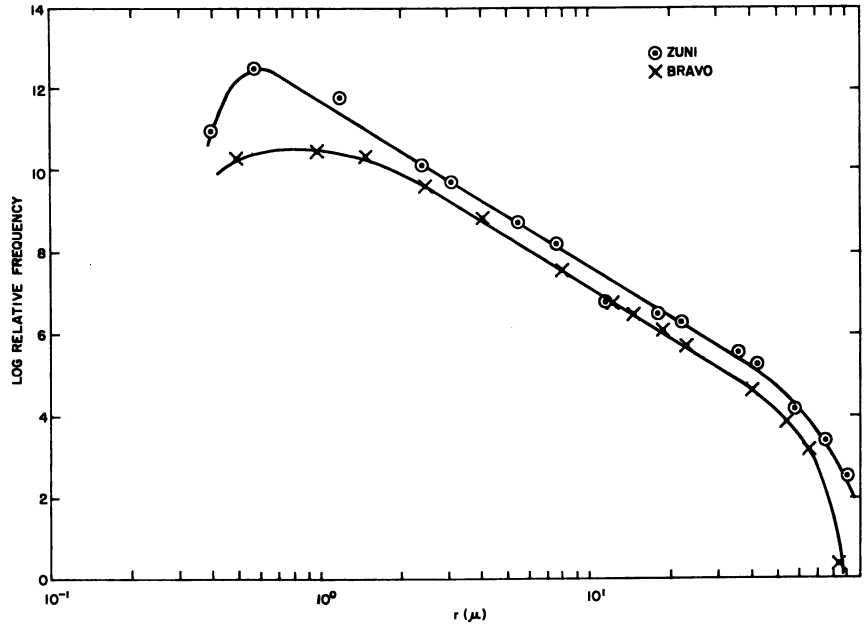

Figure 3. Size frequency curves for a Bravo and a Zuni sample

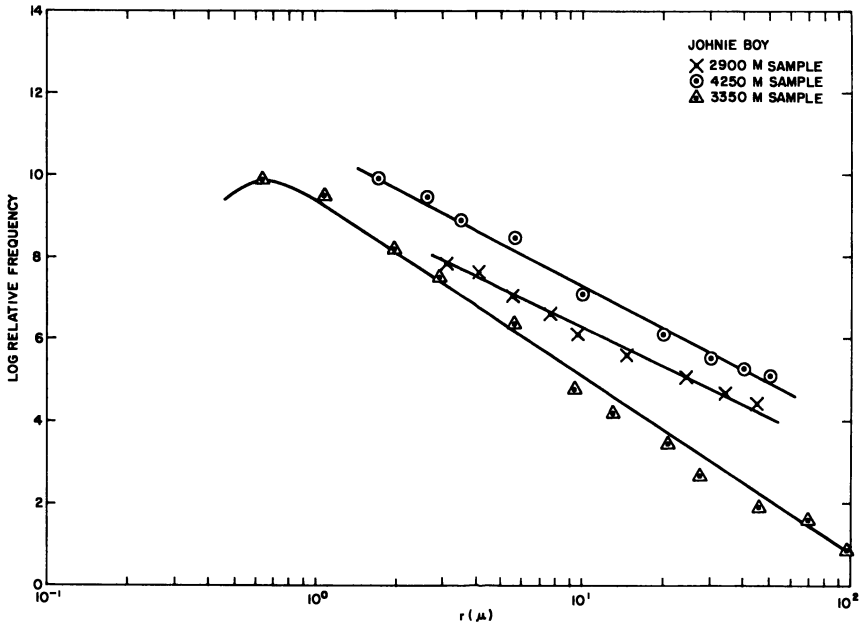

Figure 4. Size frequency curves for some Johnie Boy samples

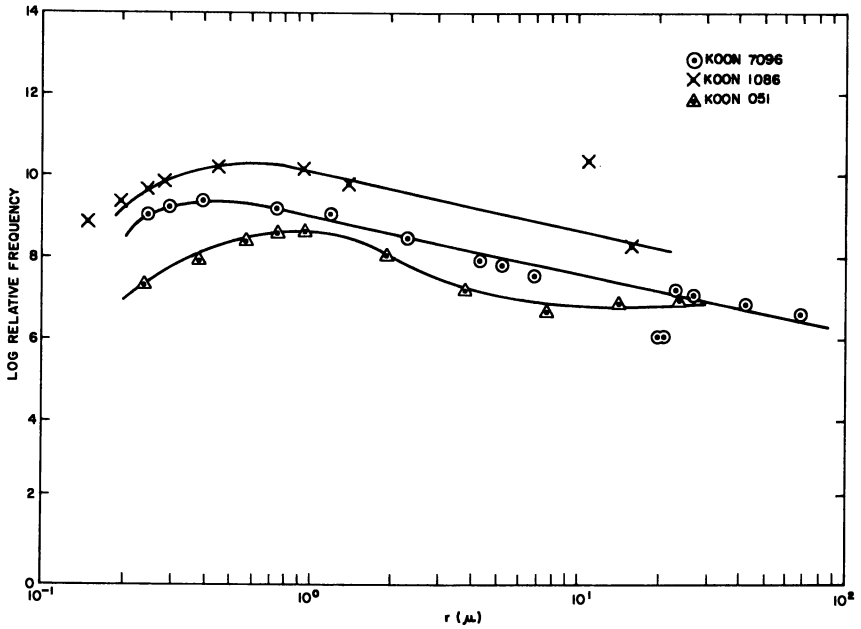

Figure 5. Mass frequency curves for three Koon samples

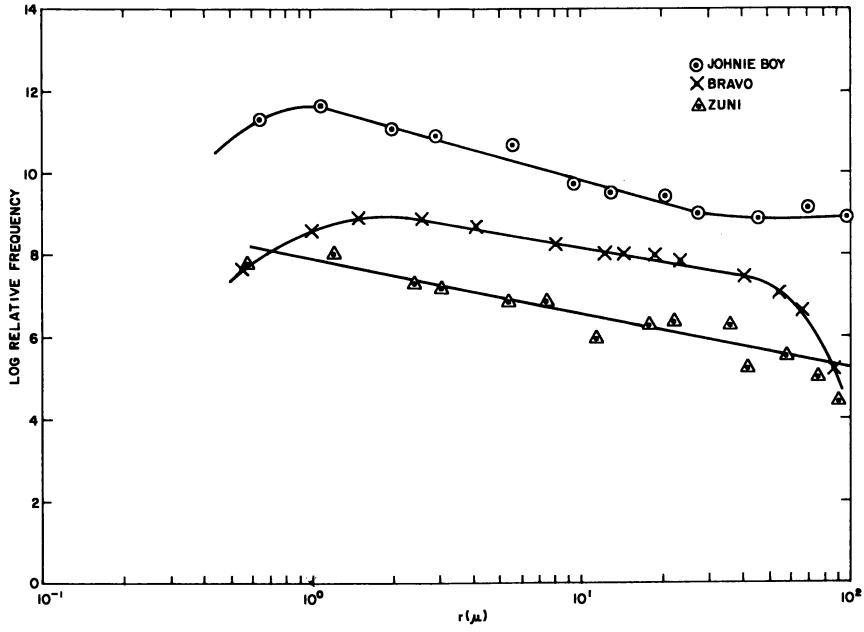

Figure 6. Mass frequency curves for a Bravo and a Zuni sample and for a Johnie Boy sample

The curves have the following characteristics in common: below a few microns they are approximately lognormal with medians between 0.5 and 1μ. Above a few microns the size frequency decreases as a^{-p} until a diameter a little smaller than the cutoff diameter is reached. For larger sizes the size frequency curves drop off rapidly.

Table III. Characteristics of Particle Size Distributions

Sample	*Modal Diameter, μ*	*Slope*	*Exp. Upper Bound,[a] μ*	*Calc. Upper Bound, μ*	*Exp. Lower Bound, μ*
Bravo	1.0	−4.1	115	117	0.3
Zuni	0.6	−4.07	110	106	0.2
Koon—051	0.4	—	65	65	0.2
—1086	0.3	−4.23	80	20	0.09
—7269	0.4	−4.35	86	53	0.17
Johnie Boy—842	0.6	−4.4			
—245		−3.3			
—827		−3.3			

[a] Since a few large size "stragglers" were always present, the upper bound was taken here as that size below which 90% of the particles are contained.

Some of the parameters of the size distributions are listed in Table III. The calculated and experimentally found upper bounds agree well, except for Koon sample 1086, which originated at the top of the cloud. The a^{-p} portion of the curves yielded values of p slightly greater than 4, with the exception of one series of measurements of Johnie Boy samples. In this series, values of about 3.3 were found. Although there is, therefore, no doubt about the shape of the curves; quantitative details are still subject to some argument.

The calculation of the sedimentation correction also suggested the presence of a lower cutoff diameter, but experimentally this cutoff would not be as sharp as at the large particle end of the distribution. The reason is that the model neglected diffusion effects and the presence of a stem. A lower cutoff is indicated by the size-frequency curve for the Bravo sample when compared with the curve for Koon (filter 051) and Zuni. The maximum in the size frequency curve for Bravo, about 1 μ, is at a larger diameter than those in the curves for the other samples, which occur at about 0.5–0.6 μ. A further indication is obtained by comparing the results from the three Koon samples (Figure 2). This clearly shows that the largest and smallest cutoff diameters in samples 1086 and 7269 are considerably smaller than the corresponding values for sample 051. This is in accordance with the theory provided that the lower portion of the Koon cloud, which yielded sample 7269 and which became separated from the main cloud, is indeed treated as a separate cloud.

Conclusions

(1) The size frequency curves for debris in cloud samples from surface and near-surface nuclear bursts generally has a lognormal shape below a few microns but obeys an r^{-p} law between a few microns and about 70 μ. The value of p is probably about 4 but is still subject to some conjecture. Removal of large particles prior to sampling as a result of sedimentation does not allow for any definitive conclusions about the shape of the size frequency curve in the cloud.

(2) The sedimentation process causes an increasing relative number density of particles with increasing size at the sampling altitudes. Applicable correction can be calculated.

(3) Although the size frequency curves of samples obtained at different altitudes below and in a cloud differ in regard to their upper and lower bounds, the shapes are essentially the same.

Appendix

Particle Sedimentation Model

Consider an axially symmetric cloud of spherical particles in the atmosphere. If wind and diffusion effects are neglected, the only change will be caused by gravitational settling of individual particles. Denote by $f(a,x,t)$ the number density of particles with diameter a at position z and time t. The continuity equation is

$$\frac{\partial f}{\partial t} + v\frac{\partial f}{\partial z} + f\frac{\partial v}{\partial z} = 0 \tag{1}$$

where $v = v(a,z)$ is the velocity of the particles. A formal solution for f can be written in terms of the initial ($t = 0$) value.

$$f(a,z,t) = \frac{\partial z_1}{\partial z}_{a,t} f[a,z(a,z,t)0] \tag{2}$$

The value of the function $z_1(a,z,t)$ is the position at which a particle of diameter a must have occupied at $t = 0$ in order to arrive at position z at time t. It is defined implicitly through the relation

$$t = \int_{z}^{z_1(a,z,t)} \frac{dx}{v(a,x)} \tag{3}$$

Analytic expressions for the velocity $v(a,x)$ are available only for small particles falling in low density media. However, approximate formulas have been obtained by Davies (*1*), which are valid over a wide range of conditions. The formalism leading to these expressions is reviewed briefly.

Consider a particle with diameter a, mass m, and density ρ_p, falling with velocity v, in a medium of density ρ, and viscosity η, under the influence of a resistance force W. The problem can be stated as a relation between the two independent dimensionless variables

$$\mathrm{Re} = g(\psi \mathrm{Re}^2) \tag{4}$$

where the Reynolds number is

$$\mathrm{Re} = \frac{v\rho a}{\eta} \tag{5}$$

and the drag coefficient is

$$\psi = \frac{8W}{\pi a^2 \rho v^2} \tag{6}$$

For steady fall in the atmosphere, $W = mg = \frac{\pi}{6}\rho_p g a^3$, and one can write

$$v = \frac{\eta \mathrm{Re}}{\rho a} \tag{7}$$

where Re is determined by solving Equation 4, with

$$\psi \mathrm{Re}^2 = \frac{4}{3}\frac{\rho_p g}{\eta^2}\rho a^3 \tag{8}$$

For the empirical formula (Equation 4), Davies divides the Reynolds number range into two parts. The data for Re are fitted with a fourth-order polynomial in $4\mathrm{Re}^2$ for the higher values. To integrate Equation 3 analytically, one must fit the same data with second-order polynomials. The results are as follows:

$$\mathrm{Re} = \frac{\psi \mathrm{Re}^2}{24}(1 - \epsilon \psi \mathrm{Re}^2) \qquad 0 \leqslant \psi \mathrm{Re}^2 \leqslant 100 \tag{9}$$

$$\mathrm{Re} = 10^d (\psi \mathrm{Re}^2)^b \qquad 100 \leqslant \psi \mathrm{Re}^2 \leqslant 3200 \tag{10}$$

The parameters are $\epsilon = 0.003$, $d = -1.02$, and $b = 0.744$. From a comparison with the tabulated data (Equation 1), it is found that the maximum errors in Equations 9 and 10 are 3% and 10%, respectively, both occurring at the upper limits.

When the air density is low and particle diameter is small compared with the mean free path, Equation 7 for the velocity must be modified by the drag slip correction. This corrects for the acceleration of particles during the time between collisions with air molecules, which increases the average velocity. The correction factor may be written (*4*):

$$v = \frac{\eta \mathrm{Re}}{\rho a}\left(1 + \frac{A}{\rho a}\right) \tag{11}$$

where $A = 2.33 \times 10^{-7}$ kg./meter^2. This factor has been verified experimentally for $A/\rho a \leqslant 200$ (*3*).

The dependence of v on particle diameter is explicit, but the z-dependence is still implicit through the z dependence of atmospheric density and viscosity. For this application, it is a good approximation to assume η = constant and

$$\rho(z) = \rho_0 e^{-cz} \tag{12}$$

From a fit to standard atmospheric data (*4*), the following parameters were determined.

$$\eta = 1.4 \times 10^{-5} \text{ kg./meter-sec.}$$
$$\rho_0 = 2.14 \text{ kg./meter}^3$$
$$c = 1.56 \times 10^{-4} \text{ meter}^{-1}$$

The maximum errors in η and ρ are 6% and 8% respectively for $10{,}000 \leqslant z \leqslant 30{,}000$ meters. These errors increase to 20% and 25% if the range is extended to $500 \leqslant z \leqslant 50{,}000$ meters.

One may now evaluate Equation 3 and solve for z_1 and $\partial z_1/\partial z$. For each particle size, the atmosphere is divided into two regions where Equations 9 and 10 are valid. The upper limit above which the drag slip correction has not been verified and the lower limit below which neither Equations 9 nor 10 are valid are also needed. With the definition

$$B \equiv \frac{4\,\rho_p g}{3\,\eta^2} \tag{13}$$

the boundary values can be written:

$$x_0 = \frac{1}{c}\ln\left(\frac{200\,a\rho}{A}\right) \tag{14}$$

$$x_1 = \frac{1}{c}\ln\left(\frac{B\rho_0 a^3}{100}\right) \tag{15}$$

$$x_2 = \frac{1}{c}\ln\left(\frac{B\rho_0 a^3}{3200}\right) \tag{16}$$

To evaluate the integral (Equation 3), Equation 9 plus the correction (Equation 11) is used for $x_1 \leqslant x \leqslant x_0$, and Equation 10 is used alone for $x_2 \leqslant x \leqslant x_1$. The error in neglecting the correction (Equation 11) in the second region is less than 0.01%. For $x > x_0$ or $x < x_2$, neither Equations 9 nor 10 is valid.

First consider the case where $x_1 \leqslant z \leqslant x_0$. Then the particle motion is entirely in the region where Equation 9 plus Equation 11 is valid, and Equation 9 nor 10 is valid.

$$t = -\frac{24}{\eta Bac}\int_{\rho(z_1)}^{\rho(z)} \frac{dy}{[A + (1 - \varepsilon ABa^2)ay - \varepsilon Ba^4y^2]} \tag{17}$$

where the integration variable has been changed from x to $y = \rho_0 e^{-cx}$. This can be evaluated, to give

$$t = \frac{24}{\eta Ba^2c}\left(\frac{1}{1 + \varepsilon ABa^2}\right)\ln\left[\frac{1 - \varepsilon Ba^3\rho(z_1)}{1 - \varepsilon Ba^3\rho(z)} \cdot \frac{A + a\rho(z)}{A + a\rho(z_1)}\right] \tag{18}$$

It is convenient to define

$$K = \frac{1}{24}\eta Ba^2c(1 + \varepsilon ABa)^2 \tag{19}$$

If Equation 12 is inserted in Equation 18, one may solve for $z_1(a,z,t)$, yielding

$$z_1 = z + \frac{Kt}{c} - \frac{1}{c}\ln\left[\frac{F_1(t)}{F_2(t)}\right] \tag{20}$$

where

$$F_1(t) = 1 + \varepsilon ABa^2 e^{Kt} + \frac{A}{a\rho(z)}(1 - e^{-Kt}) \tag{21}$$

and

$$F_2(t) = 1 + \varepsilon ABa^2 e^{-Kt} - \varepsilon Ba^3\rho(z)(1 - e^{-Kt}) \tag{22}$$

This may be differentiated with respect to z to obtain the normalization factor for the distribution function. The result is

$$\left(\frac{\partial z_1}{\partial z}\right)_{a,t} = \frac{(1 + \varepsilon ABa^2)^2}{F_1(t)F_2(t)} \tag{23}$$

If $x_2 < z < x_1$, part or all of the motion is in the region where Equation 10 is valid. If all of the motion is in this region, Equations 3 and 10 give

$$t = \frac{10^{-d}[B\rho(z)a^3]^{1-b}}{\eta Ba^2c(1-b)}[1 - e^{-c(1-b)(z_1-z)}] \tag{24}$$

The quantities z_1 and $\partial z_1/\partial z$ may be obtained from Equation 24. The results are

$$z_1 = z - \frac{1}{c(1-b)}\ln\left[\frac{1 - \eta Ba^2c(1-b)t}{10^{-d}[B\rho(z)a^3]^{1-b}}\right] \tag{25}$$

and

$$\left(\frac{\partial z_1}{\partial z}\right)_{a,t} = \frac{1}{1 - \dfrac{\eta Ba^2c(1-b)t}{10^{-d}[B\rho(z)a^3]^{1-b}}} \tag{26}$$

If t is large enough, part of the motion will be in the region $x > x_1$, and Equation 9 must be used for this part. The minimum time is that required for a particle to fall from x_1 to z. This time is denoted by t_1, and from Equation 24 it may be expressed as

$$t_1 = \frac{10^{-d}[B\rho(z)a^3]^{1-b}}{\eta Ba^2c(1-b)}[1 - e^{-c(1-b)(x_1-z)}] \tag{27}$$

For $t < t_1$, Equations 27 and 28 are valid, but for $t > t_1$, z and $\partial z_1/\partial z$ must be recalculated, using Equation 20 for part of the time. The resulting expressions are:

$$z_1 = x_1 + \frac{k(t-t_1)}{c} - \frac{1}{c}\ln\left[\frac{F_1(t-t_1)}{F_2(t-t_1)}\right] \tag{28}$$

and

$$\left(\frac{\partial z_1}{\partial z}\right)_{a,t} = \frac{10^{-d}[B\rho(z)a^3]^{1-b}}{24} \frac{(1 + \varepsilon ABa^2)^2\left(1 + \dfrac{A}{\rho(x_1)a}\right)(1 - \varepsilon Ba^3\rho(x_1))}{F_1(t - t_1)F_2(t - t_1)} \tag{29}$$

For $z < x_2$, Equations 9 and 10 are not valid. For a given z and t, the restriction, Equation 16, places an upper limit on the particle size. This can be written in the form:

$$a_M = \left[\frac{3200}{B\rho_0}e\right]^{1/3} \tag{30}$$

For t large enough so that part of the motion is in the region $x > x_0$, the drag slip correction is not valid. This is evident from Equations 20 and 21 since $z_1 \to \infty$ as $t \to t_M(z)$, where

$$t_M(z) = \frac{1}{k}\ln\left[\frac{1 + \dfrac{a\rho(z)}{A}}{1 - \varepsilon Ba^3\rho(z)}\right] \tag{31}$$

The results from the exponential density in the drag slip correction which modifies the velocity with a factor $\sim e^{cx}$, so that a particle can apparently fall an infinite distance in a finite time.

From Equations 14, 20, and 31 it is clear that the difference in the two t values for which $z_1 \to \infty$ and $z_1 = x_0$ is negligible, so that Equation 31 is an accurate cutoff value. The restriction becomes $t \leqslant t_M(z)$ for $z > x_1$, or $t - t_1 \leqslant t_M(x_1)$ for $< x_1$. The limits imposed on maximum particle size by both the drag-slip and Davies equation cutoff are shown in Figure 7.

To reconstruct an initial particle size distribution from observations at a later time, one must either have particle size distribution measurements at many different space-time points or make some assumption about the initial spatial distribution. The simplest assumption is that the initial spatial and particle size distributions are independent.

$$f(a,z,0) = m(a)g(z) \tag{32}$$

If this is used in Equation 2, one can write

$$m(a) = \frac{f(a,z,t)}{g(z_1(a,z,t))\left(\dfrac{\partial z_1}{\partial z}\right)_{a,t}} \tag{33}$$

The quantities $z_1(a,z,t)$ and $(\partial z_1/\partial z)_{a,t}$ can be calculated from Equations 20–29, and if the function $g(z)$ is known, the initial particle size distribution can be calculated from the observed distribution $f(a,z,t)$ at one z and t. If the simplest assumption, g = constant, is made, the only cor-

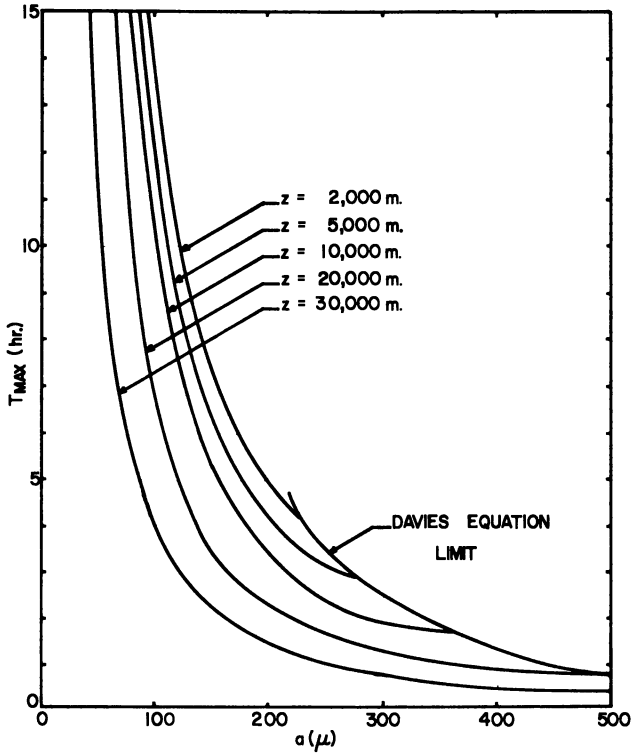

Figure 7. Particle size limits imposed by the drag-slip and the Davies equation cutoff

rection factor is $\partial z_1/\partial z$. It is seen that $(\partial z_1/\partial z)_{a,t} \geq 1$ for all a, t, and z. This is because the particle velocity is a decreasing function of altitude. The particles at the top of the cloud fall faster than those at the bottom, causing an increase in density at the bottom. Dividing by the factor $\partial z_1/\partial z$ just corrects the observed distribution for this bunching effect.

If observations are made at two points in space, it is possible to check the assumption $g(z) =$ constant by comparing the initial distributions obtained from the two measured values. In general, if observations are made at n different space (or time) points, and an initial distribution $g(z)$ is assumed with m arbitrary parameters, these parameters may be determined from consistency relations among the various observations, and there will be an additional n-m consistency relation to test the validity of the assumptions. Note that each test is actually multiplied by the number of particle size divisions, so that the initial distribution function can be determined quite accurately if multiple observations are available.

In addition to the $\partial z_1/\partial z$ correction, there is also a cutoff size above which no particle should be seen. This occurs because the particle velocity is an increasing function of particle size. At a given observation point, a time will occur when all of the particles of a given size which were initially at the top of the cloud have fallen past this point, so that only smaller particles should still be seen. If a_c denotes this cutoff size, y the initial cloud top, and z the observation altitude, then

$$y - z = z_1(a_c,z,t) \tag{34}$$

gives the relation between cutoff size and cloud geometry. The comparison of this theoretical cutoff size with the observation gives a test of the basic assumption of the particle sedimentation model, since it is independent of assumptions about the initial distributions. Note that if the observation point is below the initial cloud bottom, Equation 34 gives a minimum particle size. This is seen easily by inverting the arguments for a cutoff size. Since the initial cloud bottom is much less well defined than the top, this is not expected to be a very useful test of the model.

Figure 8 shows values of $(\partial z_1/\partial z)_{a,t}$ plotted *vs.* particle size for times ranging from one to 10 hours and an observation altitude of 15,000 meters. The calculations were done with the atmospheric parameters mentioned previously, and with a particle density $\rho_p = 2.6$ g./cm.^{3}. Superimposed on the graph are lines corresponding to various initial cloud tops. The intersection of these lines with the $\partial z_1/\partial z$ lines gives the cutoff size values. As expected, the correction factor increases with time and particle size. For an initial cloud top at 35,000 meters, observations at $t = 3$ hours give a maximum particle size of 138μ, with the correction factor varying from zero for small sizes to 1.02, 1.15, and 1.62 at 50, 100, and 138μ, respectively. If the observation time is increased to five hours, the maximum particle size decreases to 113μ, and the correction factor values increase to 1.03, 1.33, and 1.78 at 50, 100, and 113μ.

An estimate of the probable errors in the correction factors and cutoff values follows. From Equation 3 one sees that the fractional errors in both are of the same order of magnitude as the fractional error in the velocity, $\Delta v/v$, averaged over the region of motion. There are three main contributions to this error. One comes from the approximation to the Davies equations (8 and 10). The average fractional error is of the order of $\Delta v/v \simeq -5\%$, the minus sign occurring since Equations 9 and 10 underestimate the true values of Re and v. The other error contributions come from the approximations for air density and viscosity. One sees from Equations 7–9 that the first-order term in v is independent of ρ and has a $1/\eta$ dependence. The second-order term is directly proportional to ρ. Since this term contributes a maximum of 30% to the velocity and the maximum error in ρ is 8%, this contribution to $\Delta v/v$ should be

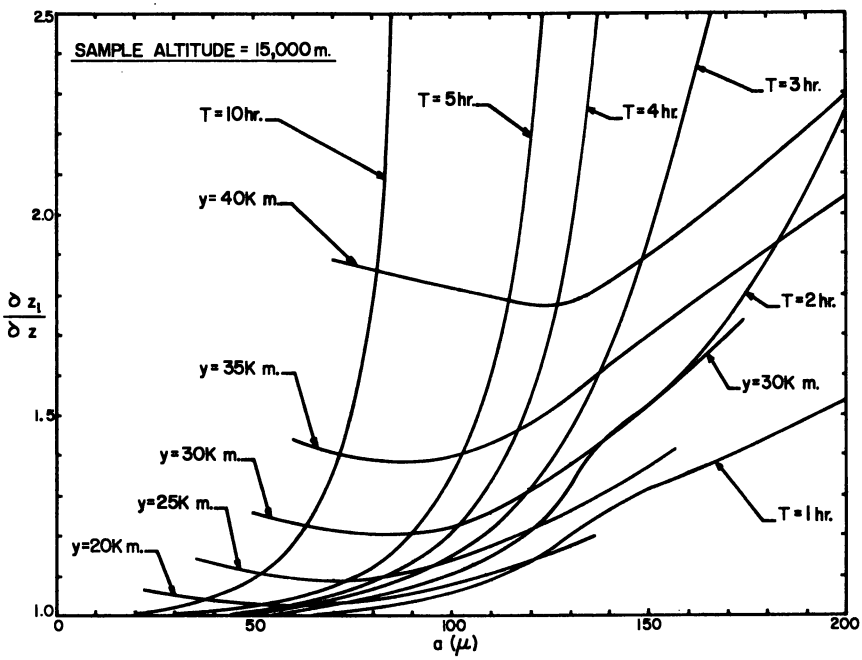

Figure 8. Size distribution corrections as a function of particle size for samples taken at 15,000 meters altitude at various times after cloud stabilization

only 1–2%. The maximum error in η is about -6% since the minimum value was used in the calculations. This causes an error $\Delta v/v \approx +3\%$, which tends to cancel the error from the approximations for the Davies equations. An estimate of the combined contributions of all errors yields an average $\Delta v/v$ of the order of 4%.

An estimate of the errors arising from effects not included in the model is much more difficult. Some of the qualitative effects are listed below.

(1) Nonspherical particles. Little is known about the fall velocity of nonspherical particles. It would be expected that needle-shaped particles would feel less air resistance per unit mass and fall faster but that irregularly shaped particles would, in general, feel more resistance and fall more slowly. The net effect depends upon the distribution of particle shapes, which is also uncertain.

(2) Collective motion. A large number of small particles may move as a unit, carrying along part of the atmosphere. It has been shown (5) that for small Reynolds numbers the velocity of such systems with total number of particles between 25 and 125 is from 30 to 100% higher than the velocity of an isolated particle. This effect would certainly increase the correction factor $\partial z_1/\partial z$ for small particle size and would probably

also reduce the cutoff size. However, the formation of the particle cluster depends on the unknown factors of interparticle forces and distances.

(3) Horizontal diffusion. As the cloud expands horizontally, the particle size distribution may vary as a function of distance from the center if the diffusion coefficient is a function of particle size. This would cause the true correction factor to vary with horizontal position, and should be observable if observations are made for horizontal positions at the same altitude and time. Since the diffusion coefficient for clouds is known only within a factor of 10–100, no estimate of the variation with particle size is possible at this time.

Literature Cited

(1) Davies, C. N., *Proc. Phys. Soc* **57**, 18 (1945).
(2) Department of Defense, Land Fallout Prediction System, **DASA 1800-IV** (June 27, 1966).
(3) Freiling, E. C., Rept. **NRDL-TR-680** (Sept. 12, 1963).
(4) Heft, R., Steele, W. A., Rept. **UCRL-50428** (May 17, 1968).
(5) Khoorguani, V. G., *Phys. Atmos. Ocean (Moscow)* **2**, 394 (1966).

RECEIVED February 26, 1969. Work performed under Contract No. DA-49-146-XZ-484 with the Defense Atomic Support Agency.

A Comparison between Cloud Samples and Close-In Ground Fallout Samples from Nuclear Ground Bursts

R. C. TOMPKINS[1]

U. S. Army Ballistic Research Laboratories, Aberdeen Proving Ground, Md.[1]

I. J. RUSSELL

Boston College, Chestnut Hill, Boston, Mass.

M. W. NATHANS

Tracerlab/LFE, 2030 Wright Ave., Richmond, Calif.

In several instances the radiochemical composition of fallout samples could not be derived by extrapolating the specific activity–particle size curves obtained from cloud samples. This may be explained by assuming that the close-in fallout originates primarily from soil horizons close to the exploding device which are ejected from the device environs without spending an appreciable amount of time in the cloud. Related observations show that the specific activities of individual particles of comparable size in cloud samples may vary considerably, apparently as a function of the degree of alteration resulting from the thermal history of the particles. Thus, the activities of samples may vary according to the relative amounts of altered and unaltered material present in the samples.

Data from the Bravo test (15 megatons on a coral surface) and the Johnie Boy test (0.5 kilotons on silicate surface) suggested a generalized picture of the specific activity *vs.* particle size of nuclear debris as shown in Figure 1.

[1] Present address: Nuclear Effects Laboratory, Edgewood Arsenal, Md. 21010.

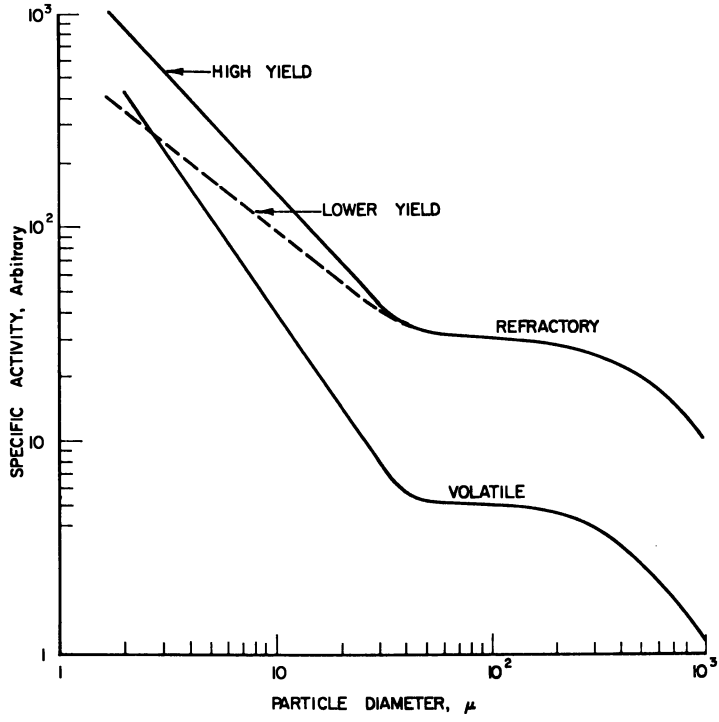

Figure 1. Specific activity and yield (schematic)

A knowledge of the size distribution function of the radioactive debris and the specific activity of individual fission product chains as a function of particle size suffice to define many important radiological properties of the land-surface nuclear explosion. If Φ_i is the function of a radionuclide or fission mass chain distributed between particle sizes D_1 and D_2, then

$$\Phi_i = \frac{\int_{D_1}^{D_2} S_i(D) \cdot f(D) \cdot D^3 \cdot dD}{\int_0^{\infty} S_i(D) \cdot f(D) \cdot D^3 \cdot dD} \quad (1)$$

$S_i(D)$ is specific activity, expressed in some suitable unit such as atoms of radionuclide or of fission product mass chain per unit mass of debris. A commonly used unit is equivalent fissions per gram of debris, where an equivalent fission is defined as the number of fissions that must have occurred in the device to produce the amount of a particular radionuclide observed in the sample.

The size distribution function $f(D)$ pertaining to the event as a whole has variously been taken as a log-normal or as a power law distri-

bution from approximately 1 to 1000μ diameter (*10*). In defining the size distribution, one must specify whether the distribution pertains to radioactive particles only or to undifferentiated debris. The same precaution applies to specific activity. The value of Φ_i calculated from Equation 1 is independent of whether active or undifferentiated debris is under consideration, provided a consistent approach is adopted.

If S_i is expressed in equivalent fissions per gram, then fractionation factors of any two isotopes i and j at a given particle size D are

$$r_{i,j} = \frac{S_i}{S_j} \tag{2}$$

where, for the fractionation factor $r_{i,j}$, we use Freiling's notation (*3*). If we desire the fractionation factor averaged over the size interval D_1 to D_2, then $r_{i,j} = \Phi_i/\Phi_j$.

If the initial distribution of radioactive debris is known spatially, Equations 1 and 2 suffice to define the partition of radioactive debris between local and long range fallout, the decay rate of radioactive debris in a given size interval, and other properties of the radiation fallout field.

Because of the sparsity of information on the particle size and specific activity behavior of radioactive cloud samples originating from land-surface nuclear explosions over a range of yields, a *post-facto* study was instituted in 1967 by Nathans and co-workers (*7, 8*). Aircraft samples collected within a few hours near the detonation site were, in some instances, still extant. Despite the long time that had intervened between the collection and analysis of the samples, it was possible to investigate the distribution of three long-lived fission product isotopes as a function of particle size. These were 30-year ^{137}Cs, typical of a volatile-behaving fission product mass chain; 28-year ^{90}Sr, a chain of intermediate volatility; and 2.7-year ^{147}Pm, a refractorily behaving chain. The particle size distribution of the cloud particulates was also determined. Here, we note only those aspects related to the validity of the results and the generality of their application. Further, we discuss only a small fraction of the cloud sample data, restricting our attention to the Zuni event, a 3.5-megaton burst on a coral surface.

Choice of Zuni is dictated partly by the fact that prompt fallout samples were obtained near the test site and that a fallout collection ship was located about 85 km. from ground zero. Thus, the opportunity exists to compare samples in the same size range but collected under quite different conditions. The Zuni cloud samples were obtained at an altitude of 12.5 km. about 3 hours after the explosion. The Zuni cloud at stabilization extended from approximately 15 to 24 km. vertically.

With respect to the cloud samples, which were analyzed 11 years after collection, their chemical form may have been altered. Also, it is

possible that storage of the sample under moist conditions may have facilitated diffusion of the more mobile ions within a particle or from one particle to another.

To elucidate some interesting differences between particles that were altered significantly by the thermal history to which they had been subjected and particles that were relatively unaltered, we present data obtained by personnel at the Nuclear Effects Laboratory, who analyzed prompt fallout from the 5-megaton surface coral explosion, Tewa. These samples were obtained within 16 km. of ground zero.

Debris and Radioactive Mixing

The character of the radioactive debris from a land surface explosion is determined largely by the extent of mixing between the extraneous debris injected into the cloud and the fission product radioactivities. Within the early cloud there is a well developed toroidal circulation (*5*), which is clearly evident in the case of air bursts and large yield surface bursts. In low yield surface explosions it may be obscured quickly by the dirt cloud and by rapid damping of a systematic circulation.

The detailed structure of the radioactive cloud after stabilization has occurred (within 10 minutes) has not been studied extensively. Figure 2 shows some relative radiation intensity data obtained by rockets following the Zuni explosion (3.5-megatons, coral island surface). The data pertain to the situation 15 minutes after the explosion. The evidences of a toroidal structure are still marked. Note that the bulk of the radioactivity is in the core of the cloud and that the distribution, either horizontally or vertically, is far from uniform. The aircraft samples on Zuni were collected at 41 kft., well below the core of concentration as found at 15 minutes. Since only the lower fringes of the nuclear cloud were penetrated, analyses probably do not represent fairly the nuclear cloud as it existed at the time of sampling.

The specific activity of a debris sample will depend upon the thermal history experienced by the sample, the time after fission when the melted or heated soil was exposed to the fission product vapors, the time-temperature history of the exposure, and a number of undefined and complex parameters.

The population of fission product elements as a function of time is changing rapidly. These may be estimated from a knowledge of the half-lives of the fission product chain members, the mass chain yield, and the independent yield distribution along the mass chains. Although there are some uncertainties in these procedures largely because of lack of data on short-lived species, and a less than perfect understanding of the charge distribution function, reasonable estimates of radioactive atom

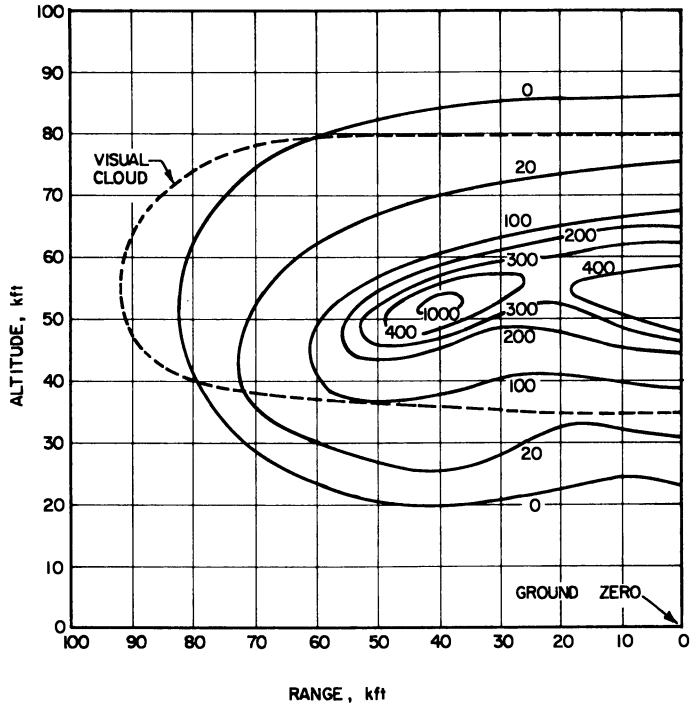

Figure 2. Typical cloud radioactivity intensity contours 15 minutes after burst. Intensity is in arbitrary units

population as a function of time, satisfactory for the purpose, can be made. Some typical calculates are indicated in Figure 3 for mass chains 89, 90, 95, and 103 for ^{235}U, ^{239}Pu, and ^{238}U fission. The differences in populations of common precursor elements arise from a shift in Z_p, the charge of the most probable fission product along a given mass chain. Z_p is a function of the relative number of neutrons and protons in the fissioning nucleus. In the case of ^{238}U, fission product decay chains are longer, and a greater fraction of the chain is formed farther from stability.

Elements from selenium through the middle rare earths will be present in the mixed fission product population; they exhibit a wide variety of volatilities (*1*). The elements Y, Zr, and Nb and the rare earth oxides are high boiling and condensable at low partial pressures, whereas the noble gases, and the alkali metals Mo, Tc, Pd, Ag, Cd, Sn, Sb, Te, Ru, and perhaps Rh, are very volatile in a relative sense; Sr and Ba are predicted to be of refractory or intermediate behavior.

The fireball is in approximate pressure equilibrium with the atmosphere when the temperature has dropped to ~4000°K. (*5*). At the time of the second temperature maximum, the volume of a 1-megaton fireball

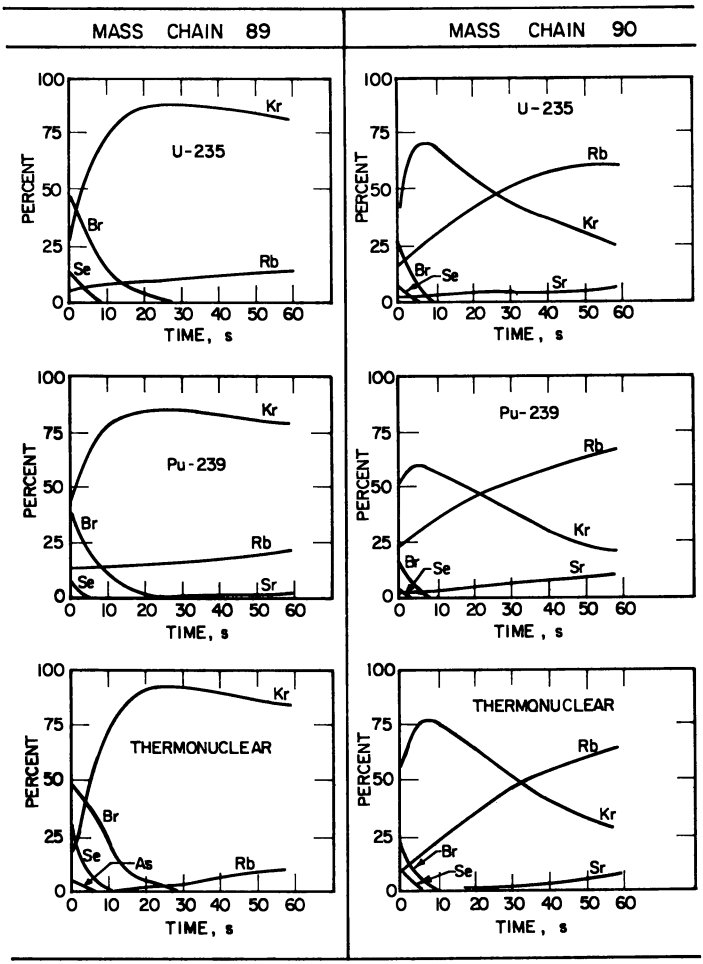

Figure 3a. Fractional chain yields for mass chains 89 and 90

is ~6.5 × 10^{14} cm.^{3}. This volume is achieved ~1 sec. after the explosion. A megaton of fission yield corresponds to the fissioning of approximately 50 kg. of fissile material and produces ~2.5 kg. or 25 moles of an element having a mass chain yield of 5% and a mass of 100. Hence, there are approximately 10^{10} atoms or molecules of fission product per cubic centimeter. The partial pressure of a typical fission product is estimated to be around 10^{-8} atm.

The time required to cool to 1450°C.—the approximate melting point of silicate rock—is estimated as $t = .49W^{.5}$ sec., where W is in kilotons (9). Thus, condensation times of ~50 sec. are predicted for 10

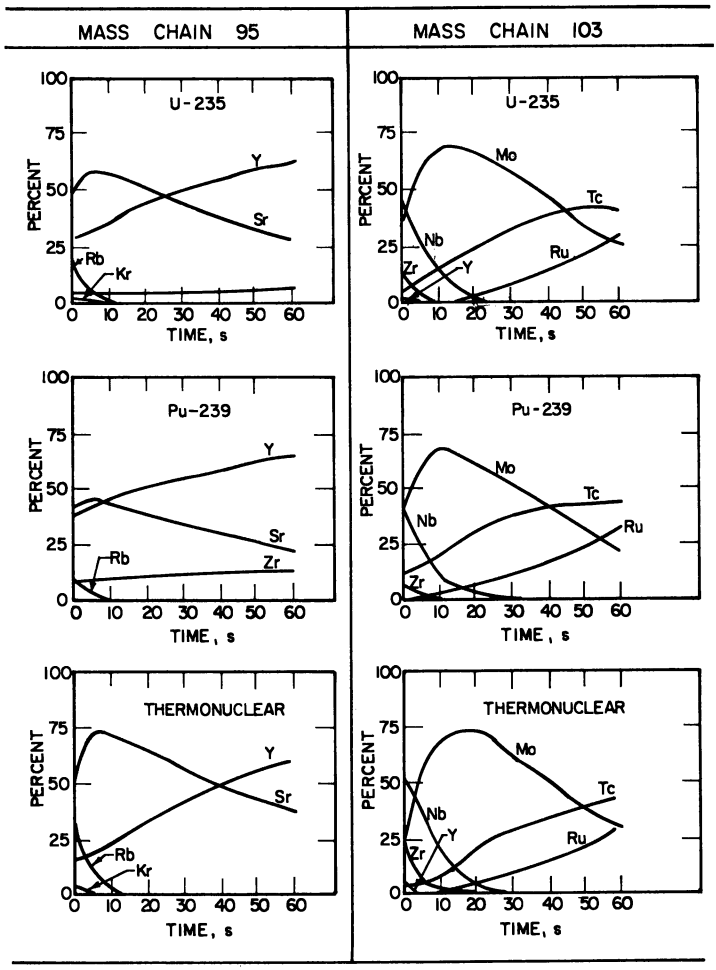

Figure 3b. Fractional chain yields for mass chains 95 and 103

megatons and ~15 sec. for 1 megaton. At 1750°K. equilibrium vapor pressures well below 10^{-8} atm. would be predicted for the most refractory elements—*e.g.*, Zr and the rare earths. Since the halogens, noble gases, and some other elements would have pressures well above 10^{-8} atm., they will be late in condensing, and the phenomenon of fractionation will result.

If only a few percent of the energy is expended in volatilizing the soil, several tens of thousand tons of soil will be entrained in the vapor cloud. The partial pressure of the vaporized soil constituents will then be of the order of a million times that of the fission products. There will

be a fractionation, based upon the volatility spectrum, of the soil constituents on recondensation, but the more refractory components, such as CaO, MgO, and SiO_2, will be expected to condense out earlier than fission products having approximately the same boiling points but much lower partial pressures.

Coincident, or nearly coincident with the injection of a large mass of vaporized soil and structural materials into the fireball, a large mass of melted or partially melted soil is swept through the cloud of hot radioactive gases and is mixed to a greater or lesser degree by the toroidal circulation within the cloud. The mass of material introduced in this fashion is probably at least an order of magnitude greater than that which is volatilized directly, as can be inferred from the magnitude of the specific activity of the fallout debris accessible for sampling. We note that the average specific activity (for the debris as a whole) is given by $1.4 \times 10^{14}\ a/b$ equivalent fissions per gram, where a is the fraction of energy derived from fission and b is the number of tons of debris per ton of total yield. Specific activities, normalized to 100% fission, of $\sim 1.4 \times 10^{14}$ equivalent fissions per gram would be observed if 1 ton of soil were mixed intimately with the fission products from 1 ton of yield. The observation of 10^{16} equivalent fissions per gram would correspond to a mixing ratio (tons soil/ton energy) of 0.01.

We can distinguish roughly three classes of specific activity behavior depending upon the thermal and mixing history of the debris. If F_v, F_m, F_I and W_v, W_m, and W_I are the number of equivalent fissions and the masses corresponding to volatilized and recondensed, melted only, and non-melted or irregular portions of the debris respectively, and S_v, S_m, and S_I are the corresponding specific activities, we can expect $S_v(D)$, $S_m(D)$, and $S_I(D)$ to exhibit quite different behavior as a function of particle size. Only a complete assay and sampling of the cloud and fallout debris will permit such a description. Lacking these, it is necessary to deduce something of the fundamental debris formation.

Table I. Summary of Samples Reported

Lacrosse	40 kilotons		
	Fallout	21 km.	downwind
Zuni	3.5 megatons		
	Fallout	18 km.	crosswind
	Fallout	85 km.	downwind on shipboard
	Cloud	12.5 km.	altitude at H + 3 hr.
Tewa	5 megatons		
	Fallout	17.5 km.	upwind
Bravo	15 megatons		
	Fallout	30 km.	downwind

The size distribution of the radioactive debris containing the majority of the fission products may bear little relationship to the size distribution of the environmental soil. Vaporization, agglomeration, condensation, and coagulation will probably lead to particles smaller than and larger than those found in the soil. A striking demonstration of this is found in the size distribution of radioactive debris of a low yield explosion over an alluvial salt bed in Nevada (*6*). While the mean diameter of the pre-shot soil particles was about 6μ, the prompt fallout contained many intensely radioactive particles of 1000μ or greater.

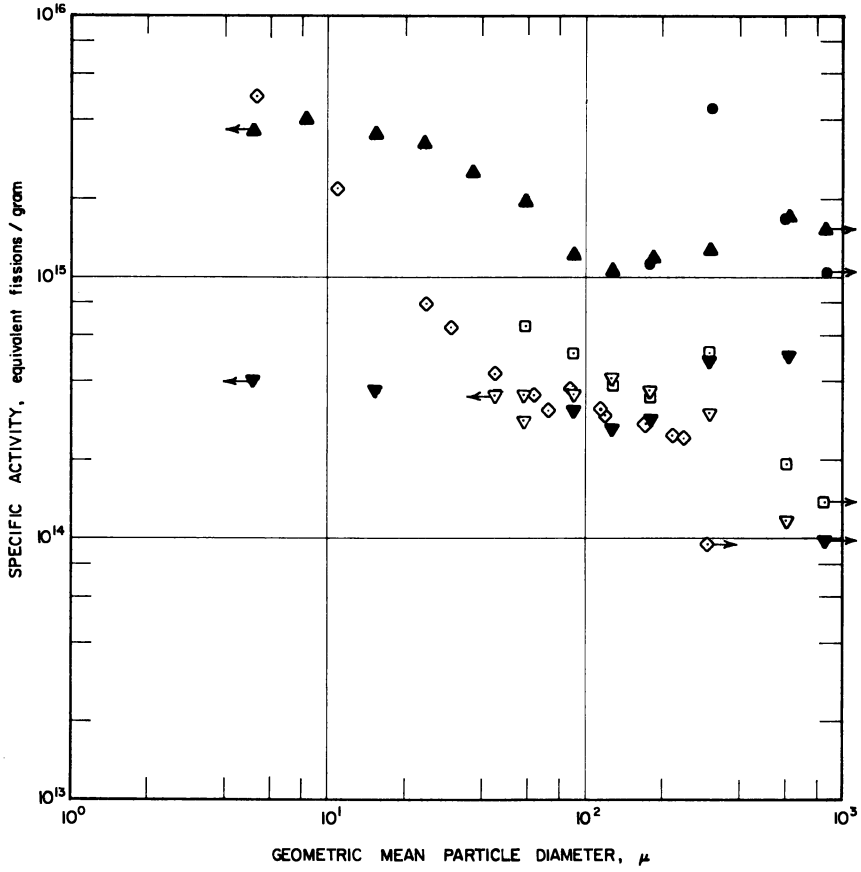

Figure 4. Specific activity of ^{144}Ce in fallout vs. *particle size*

● *Tewa spheres*
▲ *Zuni distant sample*
▼ *Zuni close-in sample*
◇ *Bravo*
□ *Tewa irregulars*
▽ *Lacrosse*

Experimental Data

The data were obtained from the samples summarized in Table I. The fallout samples were separated into particle-size classes by standard sieves for particles larger than 44μ and by the Roller analyzer for particles smaller than 44μ. In the sequel the size classes are characterized by their geometric mean diameters. The larger size classes of the Tewa sample were separated mechanically under the microscope into spherical and irregular fractions. Very few spheres could be found below the 177-μ class. The ratio of active to inactive particles was measured auto-

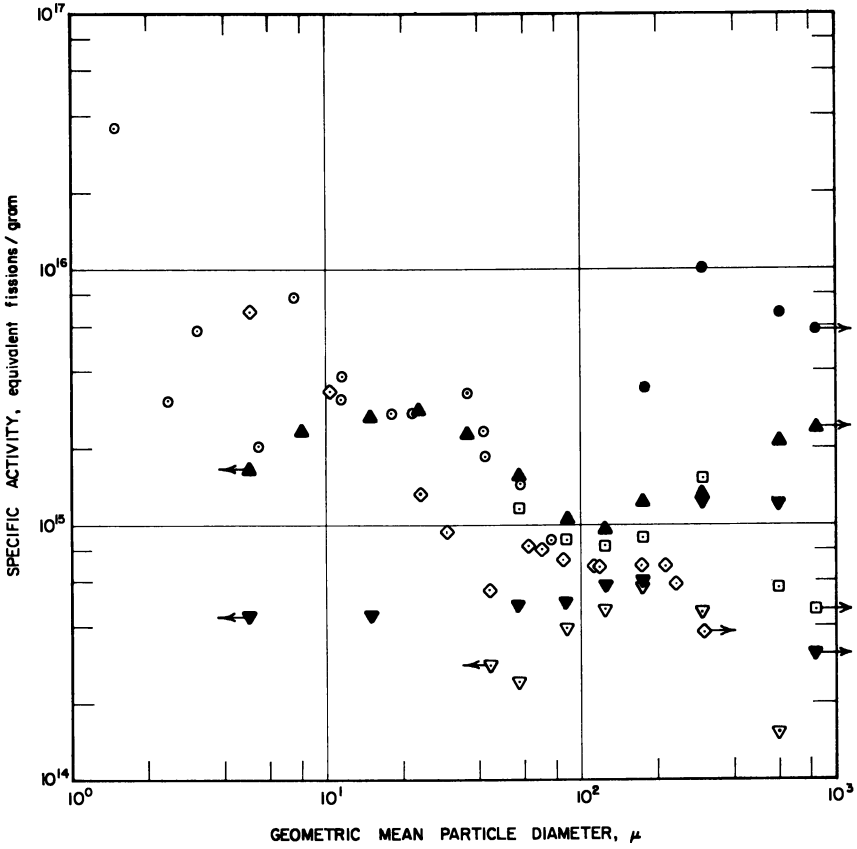

Figure 5. Specific activity of ^{99}Mo in fallout and ^{147}Pm in cloud vs. *particle size*

- ● *Tewa spheres*
- ▲ *Zuni distant fallout*
- ▼ *Zuni close-in fallout*
- ◇ *Bravo fallout*
- ○ *Zuni cloud*
- □ *Tewa irregulars*
- ▽ *Lacrosse fallout*

radiographically as a function of particle size on the Bravo sample, and the specific activities were adjusted to represent radioactive particles only (*11*).

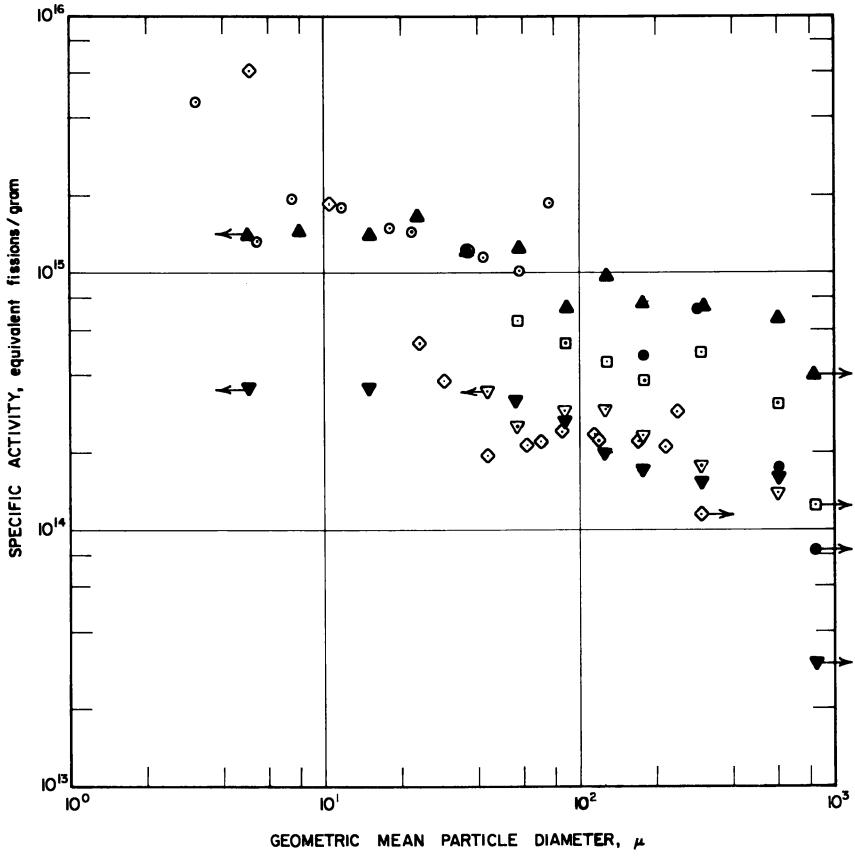

Figure 6. Specific activity of ^{140}Ba in fallout and ^{90}Sr in cloud vs. *particle size*

- ● *Tewa spheres*
- ▲ *Zuni distant fallout*
- ▼ *Zuni close-in fallout*
- ◇ *Bravo fallout*
- ○ *Zuni cloud*
- □ *Tewa irregulars*
- ▽ *Lacrosse fallout*

Figure 4 shows the specific activity (equivalent fissions per gram, normalized to 100% fission) for ^{144}Ce. We note without surprise that the close-in curve for Zuni lies considerably below the more distant curve. The Tewa spheres lie far above the irregulars. In varying degrees there is

a general tendency for a minimum between 100 and 200μ and a peak at somewhat larger sizes. The close-in samples from all four events tend to converge at the minimum. The percent active particles in the Bravo sample was constant at about 90 above 50μ. The different shapes of the specific activity curves below 100μ may be attributable to differences in the active/inactive function.

Figure 5 is a similar plot for ^{99}Mo that also includes data for ^{147}Pm (7) in the Zuni cloud. This cloud sample shows remarkable agreement with the distant Zuni fallout sample. In other respects the comments on Figure 4 are applicable to Figure 5.

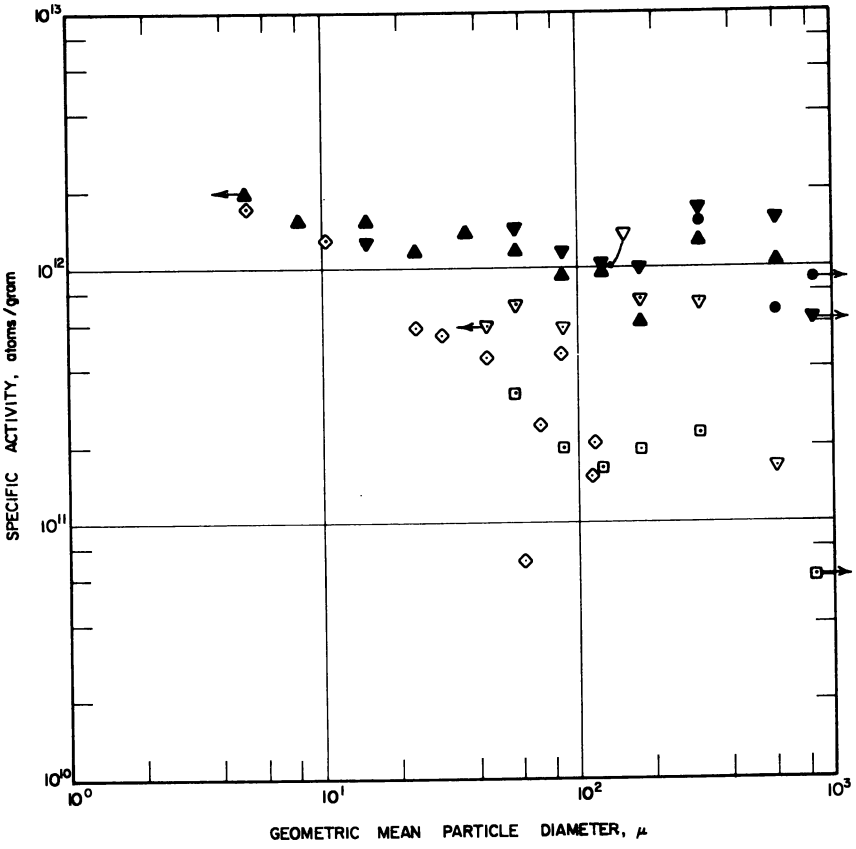

Figure 7. Specific activity of ^{45}Ca in fallout vs. *particle size*

● *Tewa spheres*
▲ *Zuni distant sample*
▼ *Zuni close-in sample*
◇ *Bravo*
□ *Tewa irregulars*
▽ *Lacrosse*

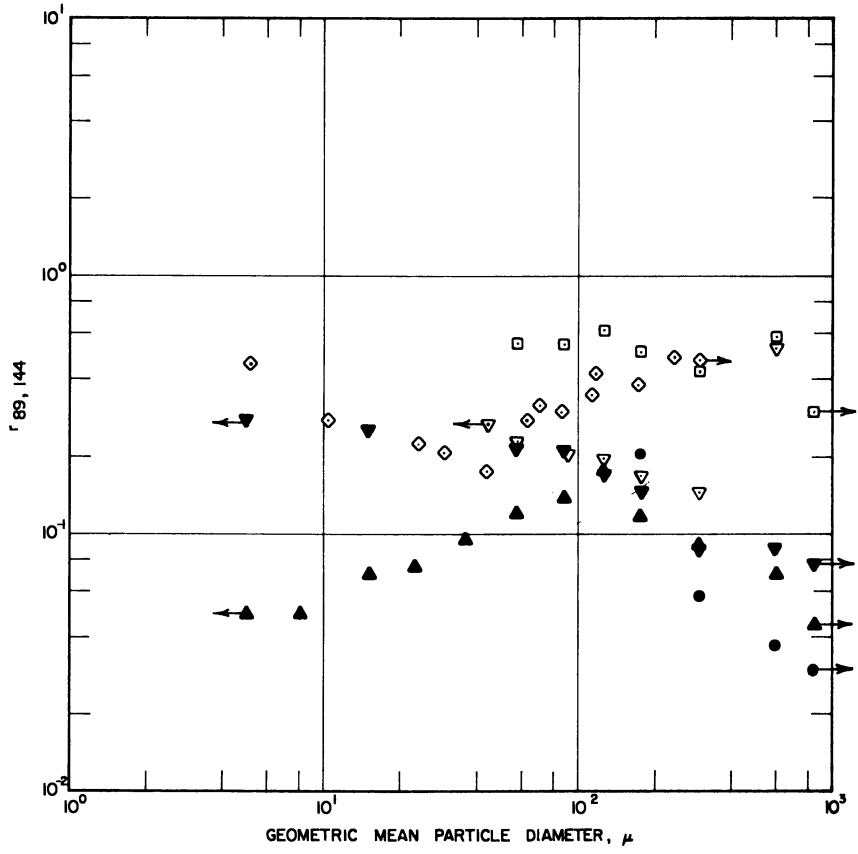

Figure 8. Fractionation of ^{89}Sr with respect to ^{144}Ce in fallout vs. *particle size*

- ● *Tewa spheres*
- ▲ *Zuni distant sample*
- ▼ *Zuni close-in sample*
- ◇ *Bravo*
- □ *Tewa irregulars*
- ▽ *Lacrosse*

Figure 6 shows the specific activity of ^{140}Ba in the fallout and ^{90}Sr in the Zuni cloud (7). The similarity in the shapes of the curves for the various samples is quite evident. Again the Zuni 85-km. fallout agrees quantitatively with the cloud. For the semivolatile mass chain 140, the distinction between the Tewa spheres and irregulars is less marked than it was for the refractory 99 and 144.

Figure 7 depicts the specific activity of ^{45}Ca (atoms per gram, not normalized). There appears to be no significant difference between the 18-km. and 85-km. Zuni samples, except perhaps at large particle sizes.

The calcium activation varies inversely with the weapon yield. The Tewa spheres are much more activated than the irregulars.

Figure 8 is a plot of $r_{89,144}$ *vs.* particle size. We define $r_{i,j}$ as the ratio of equivalent fissions of i to equivalent fissions of j. These ratios have several advantages: (1) they are independent of the percent active particles, (2) they are independent of errors in weighing the samples, and (3) in a truly representative sample of weapon debris, $r_{i,j} = 1$ for all i and j. Figure 8 presents two surprises: (1) for Zuni, $r_{89,144}$ is generally lower in the more distant sample, and (2) the Zuni 85-km. curve below 150μ and the Bravo curve above 50μ have positive slopes (and appear to

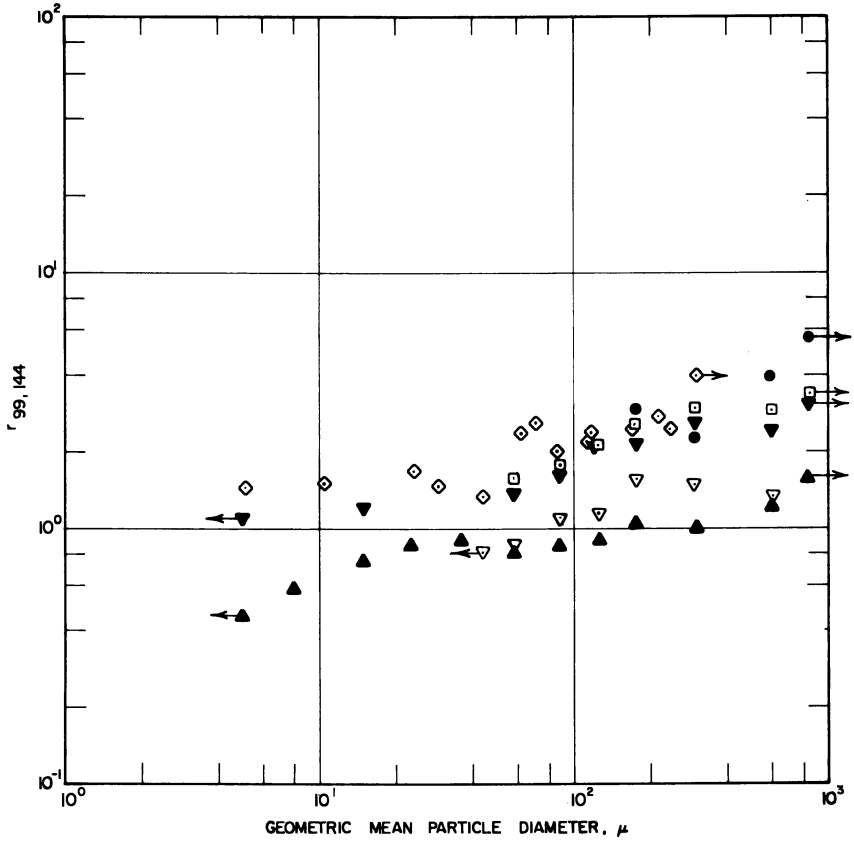

Figure 9. Fractionation of ^{99}Mo with respect to ^{144}Ce in fallout vs. *particle size*

- ● *Tewa spheres*
- ▲ *Zuni distant sample*
- ▼ *Zuni close-in sample*
- ◇ *Bravo*
- □ *Tewa irregulars*
- ▽ *Lacrosse*

be parallel). It is less surprising that the Tewa spheres lie well below unity, and it is difficult to extrapolate any of the curves to particle sizes having the complementary r's greater than unity. Two possibilities come to mind for the location of the complements: (1) the cloud and (2) rain-out. The observation of $r_{89,144}$ greater than unity in cloud samples is well known. It is of interest that samples of aqueous fallout from Tewa and Zuni yielded $r_{89,144}$ of 4.18 and 11.9, respectively.

Figure 9 reveals a systematic fractionation of ^{99}Mo with respect to ^{144}Ce.

Discussion

An exhaustive discussion of the data presented in graphical form will not be attempted. However, the following conclusions can be drawn with some confidence.

Absolute Magnitude of Specific Activities. In the Tewa and Zuni atoll samples absolute magnitude of specific activities for particles of the same kind (*e.g.*, irregulars) are not too different when a refractory chain such as Chain 144 is compared. The absolute magnitudes on a normalized basis are around 3×10^{15} to 5×10^{15} equivalent fissions per gram. Bravo (15 megatons on coral) and Lacrosse (40 kilotons on coral) also give similar values.

Slope of Specific Activity *vs.* Size for Prompt Fallout. The relatively small slope of specific activity *vs.* particle size undoubtedly is a consequence of mixing of relatively inert debris from more distant soil horizons with debris which has had a more intimate mixing with the radioactive components of the fireball. In fact, particles below 100μ must have originated in the stem of the cloud for the most part. They could not have fallen from the cloud itself.

Magnitude of Specific Activities in Sphere Samples. The high specific activity of sphere samples relative to irregulars indicates a more intense thermal history for the spheres. Probably most of the refractory chain was acquired by the particle during a hot, early phase that the irregular particles never experienced. We note that the specific activities of volatile chains, such as ^{89}Sr in the Tewa spheres and irregulars are not too different. This can signify that the spheres and irregulars of the same size had roughly the same mean residence time in the cloud, and experienced roughly the same environment. However, the very high specific activities of the spheres (*e.g.*, more than 10^{16} fissions per gram for ^{99}Mo at the maximum near 300μ) must signify that these particles arose either from primary condensed vapor in the fireball proper, which later coagulated to larger sizes, or from melted soil. In the latter case, temperatures must have been very high a sufficient period of time to have permitted

essentially equilibrium between the vapor phase and the melt phase of the particle, and these processes must have occurred at a time when the fission product concentration was very high.

Fraction of the Activity in Spheres. Spheres constituted approximately 25% of the total Tewa activity (10 days after the explosion) in particles in the 420- to 840-μ range. The spheres, however, constituted only a few percent of the mass in this range.

Magnitude of Specific Activity in Cloud Samples. The specific activities of all nuclides—refractory and volatile—show higher values in the cloud samples and in the 85-km. downwind fallout samples from Zuni. It is to be emphasized that these are undifferentiated samples—*i.e.*, no attempt is made to distinguish between radioactive and nonradioactive particles—and that both the cloud and the downwind fallout samples are not representative of the core of the nuclear cloud but only of its lower fringes. Accordingly, specific activities within the core of the cloud should be even higher than those observed.

The specific activity for a refractory chain in cloud and fallout samples of lower yield surface bursts may not be too different. Data exist for Johnie Boy (*10*) and for Lacrosse (*7*) which bear this out. Apparently mixing of the fission products with the debris is much more efficient in low yield explosions where the toroidal circulation is weaker and less persistent and where cloud rise is heavily damped by the atmosphere. This is the basis for drawing the specific activity of the refractory chain at low particle diameters more flatly for lower yield cases, as illustrated schematically in Figure 1.

We note that fission product activity balance requires that the specific activity of a volatile chain increase more rapidly than a refractory chain with decreasing diameter because of the large depletion factors noted in $^{89}Sr/^{144}Ce$ in large sizes.

^{45}Ca Specific Activity Behavior. The $^{45}Ca/^{144}Ce$ ratio for the irregulars is essentially constant for 50μ to greater than 840μ, whereas the sphere population shows a very high $^{45}Ca/^{144}Ce$ ratio at 177μ. This is a troublesome point which would be eliminated if the 177-μ datum were a factor of 10 too high for ^{45}Ca. In any event, the behavior of the refractory fission products in spheres and irregulars closely parallels that of ^{45}Ca; this suggests that the coral in the immediate vicinity of the detonation, which received the highest neutron flux, was also most intimately mixed with the fission products in the hottest part of the cloud. Since the irregulars have a ^{45}Ca content roughly one-ninth that of the spheres, they may have originated at a slant range averaging about three times that of the soil that gave rise to the spheres.

We have no ready explanation for the form of the ^{45}Ca specific activity *vs.* size behavior in the spheres. If the point at 177μ is valid, it

would seem to eliminate vaporization and condensation as the source of the spheres or at least suggest that mixing in the fireball was very poor.

Specific Activity Maximum of Refractory Chains. The maximum in the specific activity in the vicinity of 300μ for the refractory fission product chain appears to be real. This maximum is difficult to interpret on the basis of melting of the pre-shot soil, with preservation of its size distribution. (Coincidentally, the size distribution of the pre-shot soil also peaks in the vicinity of 300μ on a mass basis.) If we were dealing merely with movement of soil into the fireball, soil melting, and the diffusion of the fission products from the vapor phase into the soil particles, we should expect an increase in specific activity with decreasing size. When vapor-phase diffusion is the rate-determining step, the rate of pickup by the particle is proportional to the first power of the particle diameter (*4*). Vapor-phase diffusion will be the rate-determining step when reaction rate at the particle surface (proportional to diameter squared) and diffusion into the particle are both rapid. We note further that smaller particles will achieve equilibrium *via* diffusion faster than larger particles in accordance with the magnitude of the parameter Dt/r^2. The rate of fall of a particle is approximately proportional to D^2, and hence the time a particle can spend, on the average, in the fission product environment is related to $1/D^2$.

These effects can compound to explain the rapid decrease in specific activity of spheres at diameters greater than the maximum; they do not explain, however, the observed decrease in specific activity in spheres below 300μ.

If uniform mixing of the fission product vapors and volatilized materials results, the recondensed particles might be expected to have a constant specific activity of elements having similar boiling points. Note parenthetically that studies of fission-product incorporation into the metal and oxide products of vaporized iron wires (in which iron-metal spheres and iron-oxide irregulars are formed) indicate no simple relationship between specific activity and size. For example, a refractory element like zirconium is found most enriched in particles of intermediate size. This is probably in part caused by a concentration effect—*i.e.*, in these experiments the zirconium represented a mole fraction of about 10^{-9}. As indicated earlier, the fission products are a minor constituent in the fireball, and a very complex pattern of incorporation can be anticipated, especially if coagulation with melted but unvaporized particles ensues.

If only melting occurs, an explanation for the bell-shaped distribution of specific activity must take into account an incursion of material of low specific activity at the small sizes which still experienced sufficiently high temperatures to melt.

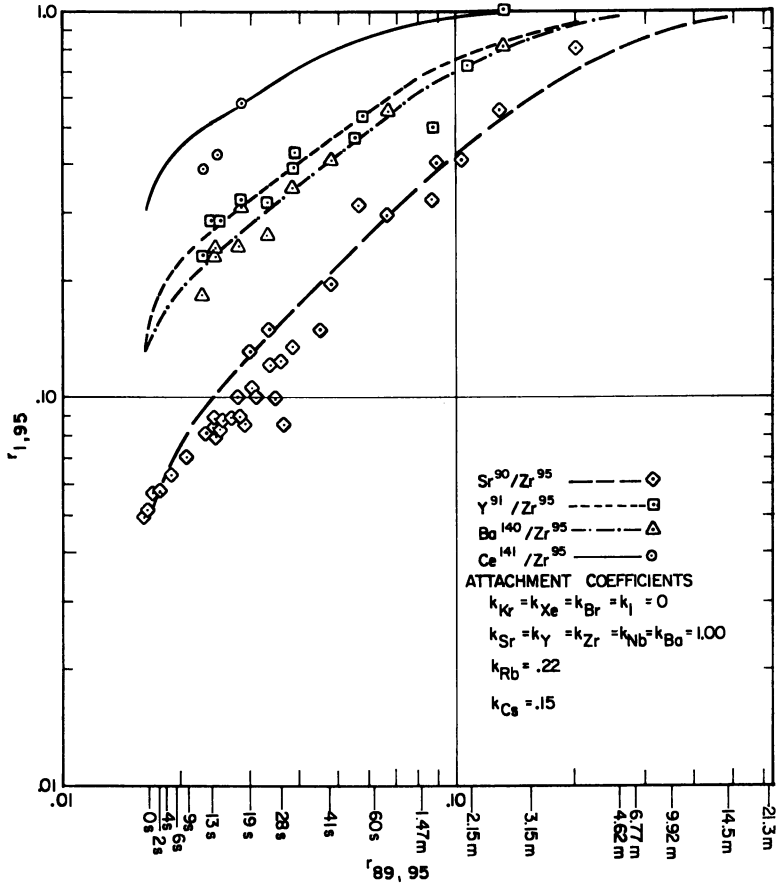

Figure 10. Radiochemical composition and time

Radiochemical Composition of Prompt Fallout Particles and Time. It was possible to fit the Johnie Boy radiochemical data (*see* Figure 10) for some fission product chains having gaseous and alkali-metal precursors, as follows. The abundances of the fission-product elements along the chains were calculated by the method of Bolles and Ballou (2), and an arbitrary set of attachment coefficients was assigned to the elements. This procedure left certain conceptual difficulties. On the basis of the Tewa data for spheres and irregulars, we now believe that the refractory chain content of these particle samples represents the thermal and mixing history more than the time spent in the cloud since the bulk of the refractory chain in the large particles is acquired during the early thermal phase. Thus, the times indicated on the scale of Figure 10 are too short. It is probable, too, that the relative attachment coefficients of rubidium

and cesium of 0.22 and 0.15, respectively, have little true significance. At the times that rubidium and cesium are formed and are attaching, the temperatures are quite low, and attachment may be quite effective. Laboratory studies are now underway to test this point.

Conclusions

In the light of the data presented here, the generalized specific activity curve drawn in Figure 1 finds some substantiation and requires some refinement. There appears to be a persistent peak in the refractory isotope chain around 300μ. Normalized specific activities are, within a factor of 2 or 3, independent of yield in the larger irregular particles. Consequently, a roughly equivalent mixing history is indicated. Spheres, which are definitely melted and which to some extent may reflect volatilized and recondensed material, have specific activities for refractory chains (but not for volatile chains) an order of magnitude higher than for irregulars. Evidence exists for the acquisition of the refractory chain at an earlier time than is the case with volatile chains. Therefore, calculations of the time spent in the cloud must be made with caution when they are based upon the ratio of volatile to refractory chains.

The ^{45}Ca and fission product data, taken as a whole suggest two disparate sources of large debris; one, originating at more distant soil horizons, consists of unmelted or partially melted soil particles; the other, originating in the immediate vicinity of the fireball, is completely melted, with perhaps some volatilization.

The data are worthy of a more careful study than that presented here. The implications of applying Equation 1 to an estimate of the fraction of activity in various size ranges need to be investigated further since these bear on the distribution of local and long range fallout from land-surface explosions. It is becoming increasingly evident that we still lack a complete description of the debris produced by large yield land surface nuclear events and that the question of the radiochemical composition and its variation with particle size in the true cloud must remain unsettled, despite the cloud analysis data reported here.

Fundamentally, the thermal and mixing history of the debris will determine the degree of fission product scavenging and the complementary radiochemical composition of the fine particles remaining in the cloud. Of considerable significance is the tendency for the specific activity of refractory chains to exhibit higher values at low particle sizes. It is possible that, in very high yield land surface explosions, a portion of the cloud core never gets well mixed with debris (or if it does, only transiently), and that a portion of debris which is essentially unfrac-

tionated, and exhibiting very high specific activity characteristic of air burst debris, would be found in the core of the cloud if sampling in this region had been possible.

Literature Cited

(1) Bedford, R. G., Jackson, D. C., University of California, Lawrence Radiation Laboratory, *Rept.* **UCRL-12314** (1965).
(2) Bolles, R. C., Ballou, N. E., U. S. Naval Radiological Defense Laboratory, *Rept.* **USNRDL-457** (1956).
(3) Freiling, E. C., *Science* **133,** 3469 (1961).
(4) Freiling, E. C., Crocker, G. R., Adams, E. C., *Symp. Radioactive Fallout Nucl. Weapons Tests* **5,** 17 (1965).
(5) Huebsch, I. O., U. S. Naval Radiological Defense Laboratory, *Rept.* **USNRDL-TR-741,** 8 (1964).
(6) La Riviere, P. D., private communication (1965).
(7) Nathans, M. W., ADVAN. CHEM. SER. **93,** 352 (1969).
(8) Nathans, M. W., Thews, R., Russell, I. J., ADVAN. CHEM. SER. **93,** 360 (1969).
(9) Rainey, S. C., *USNRDL-DASA Fallout Symp. Project* **3,** 29 (1962).
(10) Russell, I. J., *DASA Rept.* **POR-2291** (1965).
(11) Tompkins, R. C., Krey, P. W., *AFSWP Rept.* **WT-918** (1956).

RECEIVED November 13, 1968. Work supported by the Defense Atomic Support Agency, Contract DA-49-146-XZ-484.

Radiocarbon in the Environment

A. W. FAIRHALL and J. A. YOUNG

University of Washington, Seattle, Wash. 98105

Prior to 1950 the worldwide inventory of ^{14}C was 2.2×10^{30} atoms. Nuclear tests added an additional 6×10^{28} ^{14}C atoms to the atmosphere. This had a dramatic effect: for a time the ^{14}C concentrations of the troposphere at mid-latitudes of the northern hemisphere were double their pre-1950 levels. The decline of the ^{14}C levels of the atmosphere, owing to atmospheric mixing and exchange of CO_2 with the sea, has given valuable insight into both of these processes. The ^{14}C levels in the oceans are increasing as a result of this exchange. This increase should prove valuable as a tracer in oceanography. Other potential applications of the increase of ^{14}C in the atmosphere and the sea are discussed.

Before the development and testing of nuclear weapons the atmosphere, sea, and biosphere contained an estimated 2.16×10^{30} atoms (*cf.* Table I) or 51 metric tons of ^{14}C. This radioactive isotope of carbon, which decays with a half-life of 5730 years, is produced by the nuclear reaction $^{14}N(n,p)^{14}C$. For natural ^{14}C the neutrons are produced by the action of cosmic ray primaries on atoms in the upper atmosphere. Natural ^{14}C therefore originates mostly in the stratosphere. By some mechanism which is not understood the nascent ^{14}C atoms eventually are oxidized to $^{14}CO_2$. The 315-p.p.m. of the atmosphere which is ordinary $^{12,13}CO_2$ dilutes this $^{14}CO_2$ by a factor of the order of 10^{12}. Thus, atmospheric CO_2 has always been radioactive to the extent of about 13.5 ± 1 disintegrations per minute (d.p.m.) per gram of carbon (*10, 22, 29, 34, 52*), although deviations from this value amounting to several percent are known to have occurred during the past several thousand years.

The nascent ^{14}C mixes into the lower atmosphere where it eventually enters the sea and biosphere. Thus, all living things contain radioactive carbon to about the same extent. Upon their death any carbon which survives chemical decomposition gradually loses its radioactivity with the

half-life of 5730 years. This forms the basis of the well known radiocarbon dating method (*34*).

With the advent of nuclear weapons, particularly thermonuclear devices (hydrogen bombs), additional ^{14}C was added to the atmosphere. This ^{14}C, which we shall refer to as "excess ^{14}C," was produced by neutrons which escaped from the fireball interacting with nitrogen atoms of the atmosphere in the same manner as the neutrons from cosmic rays. Since the bulk of this ^{14}C was probably produced by a few very high energy devices exploded high in the atmosphere, most of the excess ^{14}C was likewise deposited in the stratosphere.

In assessing the environmental effects of the excess ^{14}C it is convenient to measure the excess with respect to the natural levels of ^{14}C which prevailed in the terrestrial biosphere prior to about 1950. By convention, the natural level of ^{14}C in the terrestrial biosphere is represented by a sample of oxalic acid distributed by the National Bureau of Standards, weighted by the factor 0.95 to bring its specific radioactivity into agreement with measurements on 19th century wood (*11*). For purposes of computing ^{14}C inventories we have arbitrarily adopted the value 13.5 d.p.m./gram carbon, corresponding to 5.85×10^{10} ^{14}C atoms/gram carbon, as the specific activity of the terrestrial biosphere, unperturbed by nuclear testing or by the combustion of fossil fuels during recent decades.

We note in passing that the total natural ^{14}C inventory of 2.16×10^{30} atoms which is based on this value (*cf.* Table I) corresponds to a ^{14}C decay rate of 1.63 disintegrations/sec./cm.^{2} of the earth, considerably below the estimated production rate of ^{14}C atoms averaged over the last 10 solar cycles (111 years) of 2.50 ± 0.50 atoms/sec./cm.^{2} (*35*). From a geophysical point of view it would be very surprising if the decay rate and the production rate of ^{14}C were out of balance as seriously as the difference between the above two numbers would suggest. It is difficult to reconcile this discrepancy by errors in computing the ^{14}C inventory since the bulk of the ^{14}C is in the sea, where the ^{14}C concentration relative to the terrestrial biosphere is known fairly well. Since the ^{14}C inventory is directly proportional to the value assumed for the concentration of ^{14}C in the terrestrial biosphere, a specific activity of 20.6 d.p.m./gram carbon would bring the decay rate into balance with the present-day production rate. However, it is doubtful that the several direct measurements (*10, 22, 29, 34, 52*) of the specific activity could have underestimated this quantity by the $\sim$ 35% required to achieve concordance. The source of the discrepancy is therefore unknown unless the present-day production rate is indeed significantly higher than the average production rate over the last 8000 years, the mean life of ^{14}C.

The ^{14}C concentration in samples of atmospheric CO_2 or CO_2 extracted from sea water is also conveniently measured relative to the oxalic acid standard with due allowance for isotope fractionation effects. Experimentally, the quantities which are measured are the net radioactivity, A (counting rate of the sample after subtracting the background of the counting apparatus), per unit weight of carbon, of the sample and of the NBS standard; and the ratio $^{13}C/^{12}C$ of isotopic abundances of ^{13}C to ^{12}C in the sample relative to a standard. Most laboratories use proportional counting of either CO_2, CH_4, or C_2H_2 to measure A. Samples will typically contain from 1 to 5 grams of carbon. The overall precision of the measurements is around 0.5%.

The experimental quantities are related to three others by the following equations (*12*):

$$\delta\,^{14}C = \left(\frac{A_{sample} - 0.95\,A_{std}}{0.95\,A_{std}}\right) \times 1000$$

$$\Delta\,^{14}C = \delta\,^{14}C - (2\,\delta\,^{13}C + 50)\left(1 + \frac{\delta\,^{14}C}{1000}\right)$$

$$\delta\,^{13}C = \left(\frac{(^{13}C/^{12}C)_{sample}}{(^{13}C/^{12}C)_{std}} - 1\right) \times 1000$$

In these equations $(^{13}C/^{12}C)_{std}$ refers to a sample of PDB belemnite, and $\delta^{13}C$ is a measure of the isotope fractionation of the sample; $\delta^{14}C$ is a measure of the difference in radioactivity between the sample and the NBS standard, uncorrected for isotope fractionation; $\Delta^{14}C$ is the corresponding quantity corrected for isotope fractionation. Both $\delta^{14}C$ and $\Delta^{14}C$ are in units of per mil ($^o/_{oo}$), but the excess ^{14}C is so large, up to $1000^o/_{oo}$, that it is convenient to express this excess in percent. We shall therefore define "excess ^{14}C" to be 0.1 $\Delta^{14}C$.

This procedure gives a correct measure of the perturbation of nuclear testing on the atmosphere and terrestrial biosphere, but in the sea it should be born in mind that pre-1950 levels of ^{14}C were generally significantly less than those of the atmosphere or terrestrial biosphere. Pre-1950 surface ocean water is generally taken to have had a $\Delta^{14}C$ value of $-50^o/_{oo}$ (*19*), and in the deep sea $\Delta^{14}C$ values as low as $-320^o/_{oo}$ have been observed (*5*). Thus, our definition of excess ^{14}C when applied to sea water underestimates the perturbation of nuclear testing by at least 5 percentage points. The absence of data on the sea in the early 1950's prevents a direct comparison of present ^{14}C levels in sea water with pre-atomic era levels. However, the measurements which were made on the sea in the late 1950's (*5, 6, 10, 13, 14, 18, 23, 49*) are probably indicative of pre-bomb levels of ^{14}C except for those samples from near the sea surface in the northern hemisphere where excess ^{14}C was already being detected.

The nuclear testing which took place in the 1950's added an estimated 25×10^{27} ^{14}C atoms to the atmosphere (27). Although this represents only a small increment to the total ^{14}C inventory of the world, it produced a significant perturbation on the prevailing ^{14}C levels of the atmosphere since the latter contains only a small fraction, *ca.* 2%, of the total ^{14}C reservoir. Thus, by 1961 atmospheric CO_2 in the northern troposphere was 25% above the pre-1950 level of ^{14}C.

The 1958–1961 moratorium on testing of nuclear weapons in the atmosphere was broken by the U.S.S.R. in the fall of 1961. The U. S. resumed testing in May 1962, and both nations conducted numerous tests until the end of 1962. Except for minor amounts from the small-scale tests by the Chinese and French there has been no significant production of ^{14}C from nuclear testing in the atmosphere since 1962.

Table I shows our estimate of the situation which prevailed in the various carbon reservoirs in the pre-nuclear era and at the end of 1962. The 1961–1962 tests contributed an additional $\sim 35 \times 10^{27}$ ^{14}C atoms into the atmosphere, principally the stratosphere. These atoms therefore

Table I. Distributions of Natural ^{14}C and of Excess ^{14}C in the Several Carbon Reservoirs at the End of 1962

Reservoir	*Total Carbon, grams*	*Pre-1950 ^{14}C Concentration, atoms/gram C*	*Total Natural ^{14}C, 10^{27} atoms*	*Total Excess ^{14}C, 10^{27} atoms*
Atmospheric CO_2	6.8×10^{17}	6.07×10^{10}	41	54
Terrestrial biosphere	3.1×10^{17} (19)	5.85×10^{10}	18	<1
Humus	1.1×10^{18} (19)	$<5.8 \times 10^{10}$ [a]	<64	<1
Marine biosphere (living)	3×10^{15} [b]	6.0×10^{10}	0.2	<0.1
Oceanic detritus	2×10^{16} [c]	6.0×10^{10}	1	$\sim$<0.1
Dissolved organic in sea	8×10^{17} [d]	5.3×10^{10} [e]	42	<<1
Inorganic carbon in sea				
top 100 meters	1.0×10^{18}	5.8×10^{10}	58	~3
below 100 meters	3.8×10^{19}	5.1×10^{10} [f]	1940	~1
All reservoirs	42×10^{18}		~2160	~60

[a] The average age of humus is unknown.
[b] Estimated from data in Ref. 2 on the assumption that zooplankton makes up the bulk of the biomass.
[c] Based on a world ocean average of 15 μgrams C/l. (*cf.* Refs. 36, 37).
[d] Based on a world ocean average of 0.6 mg. C/l. (*cf.* Ref. 37).
[e] The age of the dissolved organic matter in the sea is unknown, but the total amount present compared with the estimated rate of production suggests that it has accumulated over many hundreds of years. We have used a value of 800 years for the age of this material in estimating its total ^{14}C content.
[f] Based on a $\Delta^{14}C$ value for the entire ocean of $-160^0/_{00}$ (Ref. 14).

represented a perturbation on prevailing ^{14}C levels in the stratosphere which was relatively localized in time and place compared with pre-1958 tests. Whereas the monitoring of ^{14}C produced in the early tests had been rather haphazard, a number of laboratories set out systematically to monitor this fresh ^{14}C. As anticipated, this large increment of ^{14}C has proved to be a valuable tracer for gaining insight into a number of geophysical processes, and it shows promise of being potentially useful in a number of others. We shall discuss several of these in this review.

Radiocarbon in the Atmosphere

Studies of fission products and other tracers from nuclear weapons tests have shown that whereas meridional mixing of the atmosphere is comparatively slow, zonal—*i.e.*, longitudinal—mixing is fairly rapid, the time scale being of the order of a few weeks. Although vertical mixing of the stratosphere is extremely slow, the time scale being several years, the turbulent troposphere mixes vertically rather quickly, on the order of a fortnight. Thus, the monitoring of ^{14}C in the stratosphere requires vertical as well as meridional sampling, whereas meridional sampling at ground level suffices for the troposphere. Hagemann and co-workers (*27, 28*) have carried out an extensive program of ^{14}C monitoring in the stratosphere and upper troposphere, the samples which were collected and measured numbering in the thousands. A number of radiocarbon dating laboratories have monitored the troposphere and occasionally the sea (*3, 5, 6, 7, 9, 10, 13, 14, 15, 17, 18, 23, 24, 25, 31, 32, 33, 38, 39, 40, 42, 43, 44, 45, 46, 47, 48, 49, 50, 53,54, 55, 56*). As we shall see many more measurements are needed on the sea, including the deep sea below *ca.* 50 meters.

Figure 1 shows graphically the levels of excess ^{14}C which have prevailed in the troposphere since the beginning of 1963. Two features are striking: the pronounced seasonal fluctuations in ^{14}C levels in the northern hemisphere and the strong north-south gradients which developed in 1963 but which subsequently decreased to nearly zero by 1967. Both are a consequence of the seasonally varying pattern of injection of excess ^{14}C from the stratosphere into the troposphere and of the meridional mixing of the troposphere. The bulk of the excess ^{14}C enters the troposphere mainly through the mid-latitude tropopause gap in the northern hemisphere during the spring and early summer. During this period meridional mixing is weakest. Unlike particulate debris, which is quickly scavenged from the troposphere by rain, CO_2 has a comparatively long residence time in the troposphere. The levels of excess ^{14}C in tropospheric air were therefore highest at mid-latitudes in the northern hemisphere, and they reached their maximum concentration by late summer.

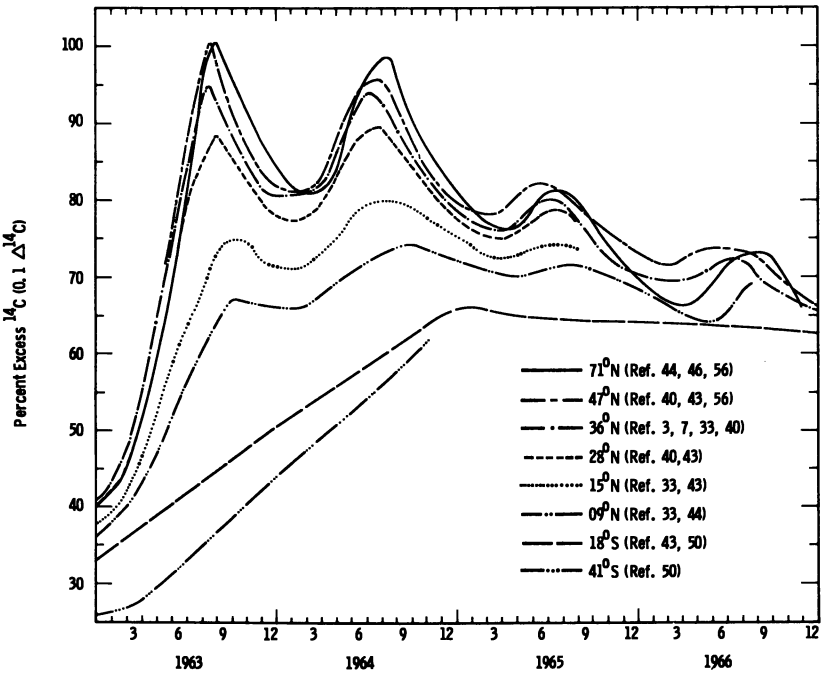

Figure 1. Concentrations of ^{14}C in tropospheric CO_2 measured at several latitudes since the beginning of 1963

Meridional mixing, which occurs most strongly in the fall and winter months, mixed the bulk of this injected ^{14}C southward and into the southern hemisphere troposphere. Thus, each year from September through February the levels of ^{14}C declined at more northerly latitudes while at more sourtherly latitudes the levels of ^{14}C rose, until by about mid-1966 the entire troposphere became fairly homogeneous in ^{14}C.

In comparing the changes which took place at the different latitudes, shown in Figure 1, one should bear in mind the relative volumes of tropospheric air which are involved. The convergence of the meridians and the decrease in the mean altitude of the tropopause at high latitudes result in the volume of the troposphere per degree of latitude being very much larger in the equatorial region than it is at high latitudes. As seen in Figure 1, a comparatively small injection of stratospheric air at 71°N suffices to raise the ^{14}C levels in the troposphere at that latitude to somewhat higher values than were observed at mid-latitudes even though the bulk of the ^{14}C is injected there.

From the data of Figure 1 and the mean altitude of the tropopause as a function of latitude the computation of the tropospheric inventory of ^{14}C is straightforward. Although the stratosphere is more difficult to

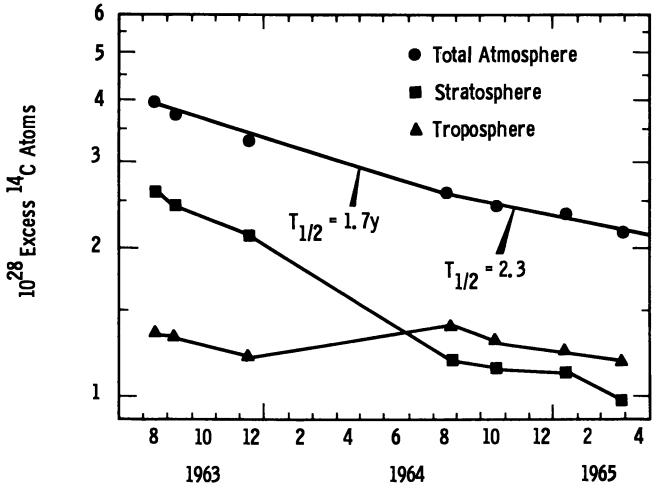

Figure 2. Inventories of excess ^{14}C in the Northern Hemisphere atmosphere

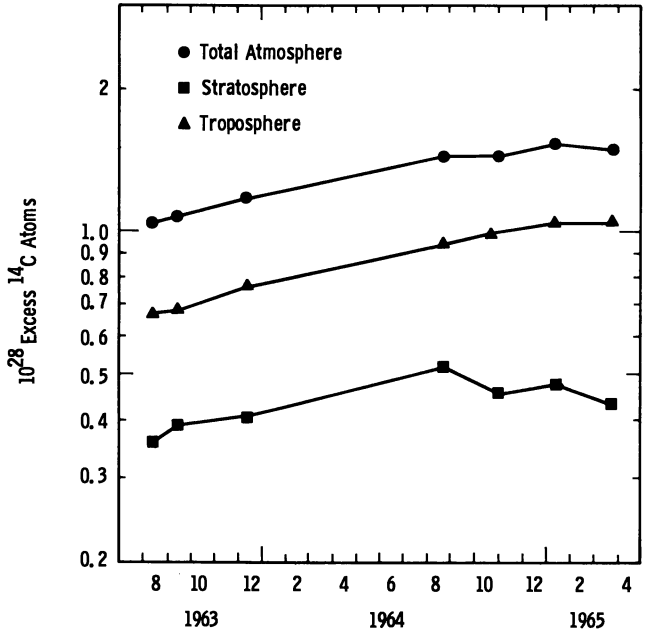

Figure 3. Inventories of excess ^{14}C in the Southern Hemisphere atmosphere

sample as adequately as the troposphere, the data from the high altitude sampling program (*27, 28*) may be used to estimate the distribution of ^{14}C in the stratosphere, and from it the ^{14}C inventory can be computed. Figures 2 and 3 show these inventories for the northern and southern hemispheres. The total atmospheric inventory of excess ^{14}C, shown in Figure 4, declines with a half-time of 3.3 years.

The rate of decrease of the inventory of excess ^{14}C in the stratosphere is proportional to the difference in ^{14}C concentration between the stratosphere and troposphere. This difference, expressed in ^{14}C atoms/

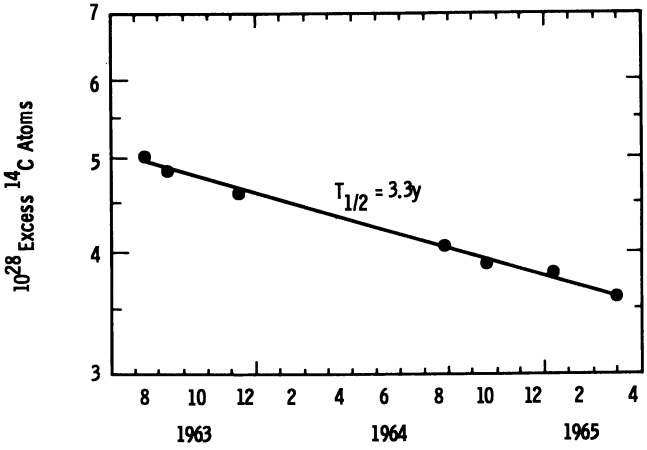

Figure 4. Inventory of excess ^{14}C in the atmosphere

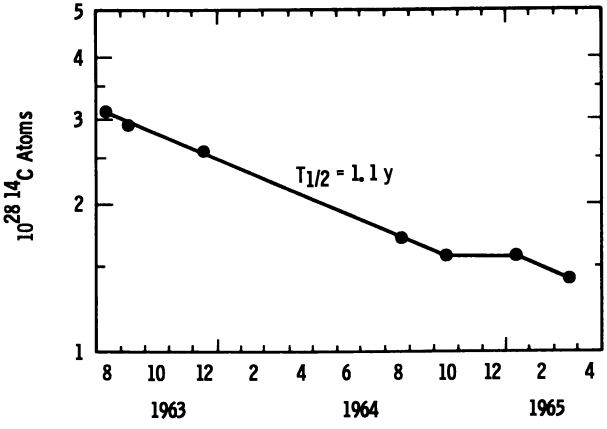

Figure 5. Difference between the stratospheric and the tropospheric ^{14}C concentrations, expressed in atoms/gram of air, summed by 10° zones of latitude over the earth

gram air, was summed by 10° of latitude over the global stratosphere for 6 different dates during 1963 and 1964. The results, plotted in Figure 5, show that during this period the inventory of excess ^{14}C in the stratosphere decreased with a half-time of 1.1 years.

Radiocarbon in the Sea

The decline of the atmospheric inventory of excess ^{14}C is caused by uptake by the terrestrial biosphere and by exchange of CO_2 between the atmosphere and the surface of the sea. Of these two sinks the latter is undoubtedly the more important. Craig (*19*) has estimated that of the CO_2 which leaves the atmosphere each year, 82% goes into the sea and only 18% goes into the terrestrial biosphere. That part of the biosphere which is utilized for food by animals, including man, quickly returns most of its carbon to the atmosphere by metabolic processes. Only a portion of the terrestrial biosphere is relatively permanently fixed in long lived trees or as slowly decaying humus. Therefore, most of the observed decline in the atmospheric ^{14}C reservoir shown in Figure 4 must be explained by uptake by the sea.

In contrast to the atmosphere, where much can be learned from a relatively small number of ^{14}C sampling locations, the sea presents a formidable sampling problem. The sea does not achieve the nice vertical and zonal uniformity characteristic of the troposphere. The well-mixed surface layer of the sea, generally 50–100 meters deep but occasionally deeper, appears to achieve a uniform concentration but only vertically; the levels of excess ^{14}C in the mixed layer varies considerably from place to place. This arises partly from the upwelling of subsurface water of lower ^{14}C content which perturbs the concentration of surface water in many areas of the ocean, adding to the difficulty of interpreting sea water ^{14}C measurements.

Below the mixed surface layer, in the region of the thermocline, the few vertical profiles of excess ^{14}C which have been measured show that rather strong concentration gradients exist. This is illustrated in Figure 6, where vertical profiles were taken at about the same location in 1965, 1966, and 1967 (*16, 56*). Owing to the movement of water in the eastward drift of the Pacific gyre, the water which was sampled was different each time so that the obvious differences between the profiles is difficult to interpret. However, in addition to the strong vertical ^{14}C gradients exhibited by these profiles they also show that a significant amount of excess ^{14}C is found below the mixed layer. In the case of the profiles of Figure 6, more than two-thirds of the excess ^{14}C is below the well mixed surface layer. Therefore, ^{14}C measurements on surface water alone are not sufficient to establish the distribution of excess ^{14}C in the

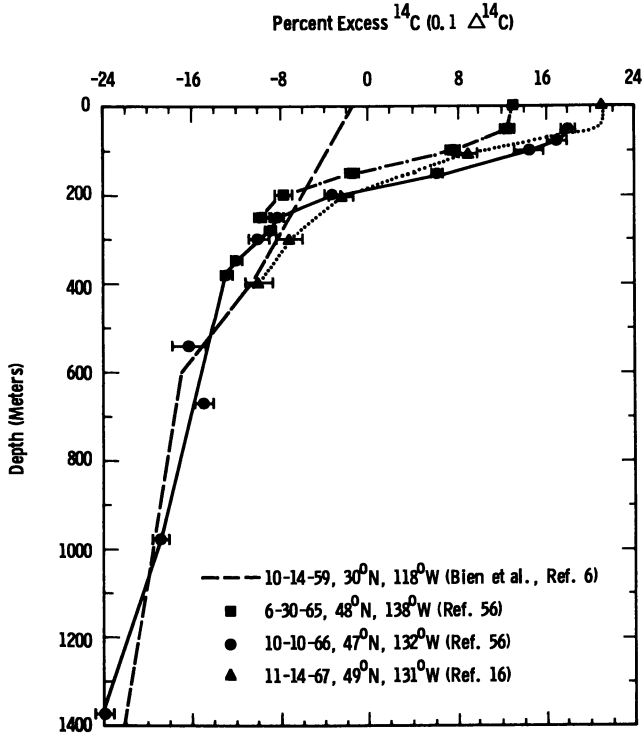

Figure 6. Some vertical profiles of ^{14}C in the North Pacific Ocean

sea. Sampling to considerable depths will be necessary to do this, and in view of the immense expanse of the world's ocean the sampling problem is obviously a formidable one.

Despite the difficulty of interpreting ^{14}C measurements on surface ocean water such measurements are of great interest. The net transport of excess ^{14}C from the atmosphere to the sea depends on the difference between the ^{14}C concentration in atmospheric CO_2 and that in the carbonate system at the sea surface. The decline in the atmospheric reservoir of excess ^{14}C is therefore controlled by the ^{14}C concentration at the sea surface. This in turn depends upon diffusion and advection into the deep sea. As the levels of excess ^{14}C in the troposphere and the mixed layer of the sea begin to approach each other, mixing from the mixed layer of the sea into the deep sea will be the factor controlling the levels of excess ^{14}C in the atmosphere.

Figure 7 shows a plot of excess ^{14}C in surface ocean water from the Pacific and Indian Oceans in 1965, 1966, and 1967 as a function of latitude (*7, 16, 44, 56*). Figure 8 shows a similar plot for the Atlantic Ocean (*16,*

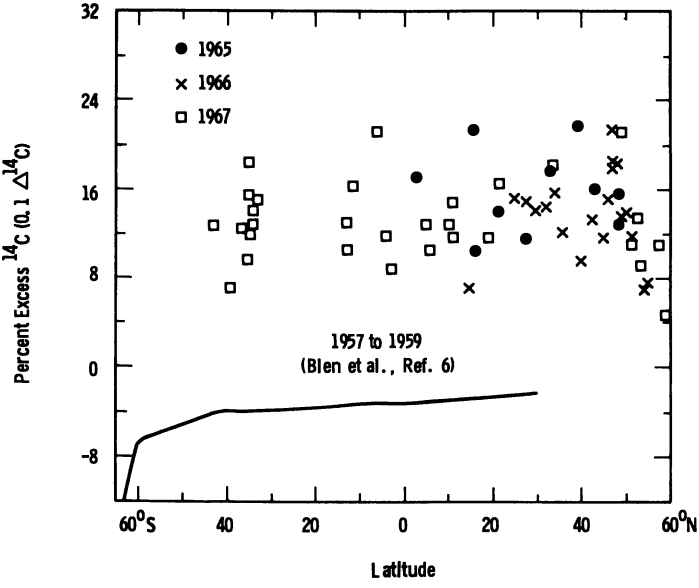

Figure 7. ^{14}C *concentrations in* CO_2 *extracted from Pacific and Indian Ocean surface waters* (7, 16, 44, 56)

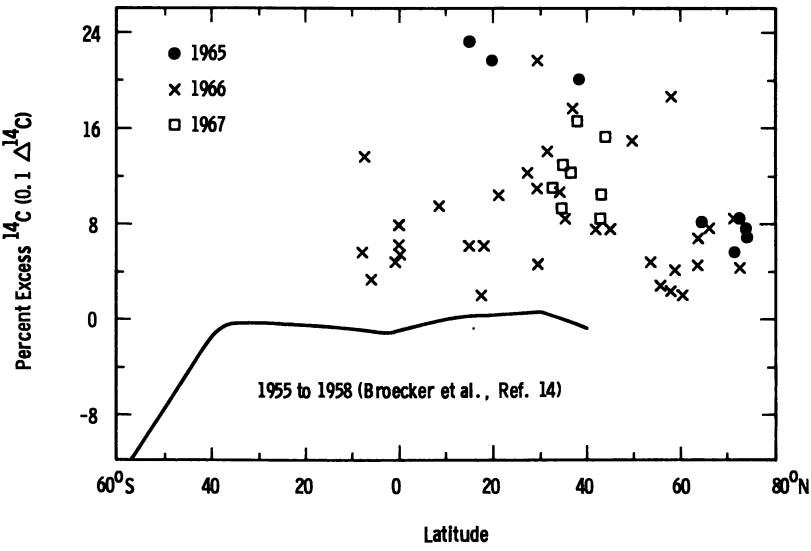

Figure 8. ^{14}C *concentrations in* CO_2 *extracted from Atlantic Ocean surface waters* (16, 40, 44, 56)

40, 44, 56). Note the considerable amount of scatter among the data from different stations at similar latitudes. This presumably reflects the complexity of the advective and diffusive processes near the sea surface, compounded by upwelling of deep water.

Another significant feature is the level of excess ^{14}C which is found in the Pacific and Indian oceans at latitudes around 40°S in 1967. These levels are comparable with those observed at 40°N, or for that matter, at other latitudes between these two. Although the concentrations of excess ^{14}C in the northern hemisphere troposphere were initially (1963) much higher than those in the southern hemisphere and the two did not reach near equality until about mid-1966, by 1967 the southern hemisphere ocean had achieved levels of excess ^{14}C in surface waters which are comparable with the levels which were achieved much earlier by the oceans of the northern hemisphere. This rapid catching up by the oceans of the southern hemisphere is most likely caused by a higher rate of CO_2 exchange across the sea surface. The higher average wind speeds over the sea surface which prevail in the southern hemisphere at latitudes near 40°S is expected to result in a higher rate of CO_2 exchange between the atmosphere and the sea (*56*).

Discussion

Two general approaches are used to interpret the observations on excess ^{14}C in the atmosphere and the sea: the box model approach (*30, 33, 44, 45*) and tropospheric mixing by eddy diffusion (*10, 39, 56*). For box models the atmosphere and the sea are divided into a number of boxes, each of which is assumed, for purposes of calculation, to be internally well mixed. The object is to derive mean residence times for exchange between the carbon reservoirs represented by the boxes. Residence time in the context of this approach is defined as the mean concentration of a given reservoir divided by the rate of change of concentration of that reservoir owing to transfer into some other reservoir. This rate of change, which corresponds to a first-order rate law (residence time being the reciprocal of the rate constant) is generally not the observed rate of change of the reservoir since the exchange goes both ways; furthermore, exchange with several reservoirs may be involved.

In the spirit of the box model approach, of the several residence times of geophysical interest two now seem to be fairly well established—the mean residence time of a trace substance in the lower stratosphere before entering the troposphere and the mean residence time of CO_2 in

the troposphere before entering the mixed layer of the sea. The decline of the stratospheric inventories of various bomb debris all point to a residence time in the lower stratosphere ($<$ *ca.* 25 km.) of 1–1.5 years (*20, 21, 26, 30, 56*). The decreasing level of excess ^{14}C in the stratosphere relative to the troposphere shown in Figure 5 likewise gives a mean stratospheric residence time of 1.6 years. In none of these cases can the stratosphere truly be considered well mixed, so in the strict sense of the box model approach the decline of the inventories or the concentration levels does not define a residence time. However, to the extent that these follow a first-order rate law, they may be regarded as empirical or "effective" residence times and as such are in reasonable agreement with each other.

Table II gives the residence time of CO_2 in the atmosphere before entering the sea as estimated from various data. The results of several different approaches to the data of Figure 1 (Column 4) suggest that the mean atmospheric residence time of CO_2 before entering the mixed layer of the sea is around 4 to 5 years, in good agreement with some of the earlier estimates based on natural ^{14}C. A residence time of 10 years or more, which has sometimes been advocated, now seems to be untenable.

Table II. Estimates of the Mean Residence Time of CO_2 in the Atmosphere Before Entering the Sea

	Basis of Estimate		
Authors	*Natural ^{14}C*	*Industrial Effect*	*Bomb ^{14}C*
Arnold and Anderson (*1*)	10–20 yr.	~20 yr.	
Bien and Suess (*7*)			25 yr.
Bolin and Erickson (*8*)		5 yr.	
Craig (*19*)	7 ± 3		
Fergusson (*23*)		~2 yr.	
Munnich and Roether (*40*)			5.4 yr.[a]
Nydal (*44*)			4.5 ± 1.0 yr.[b]
(*45*)			4.0 ± 1.0 yr.[b]
Rafter and Fergusson (*49*)			1.7 yr.
Revelle and Suess (*51*)	>7 yr.	~10 yr.	
Young and Fairhall (*56*)			4 yr.

[a] Value deduced for the Northern Hemisphere only. The larger ratio of ocean to land areas in the Southern Hemisphere may be expected to give a shorter residence time for that hemisphere. This value is therefore an upper limit for the atmosphere as a whole.

[b] Including also uptake by the terrestrial biosphere. The mean residence time for exchange with the sea alone is expected to be larger than this value by about 25%.

The mean residence time of carbon in the mixed layer of the sea before transfer into the deep sea is of considerable interest, for as has already been pointed out, the rate of this transfer will eventually govern the levels of excess ^{14}C in the atmosphere. There have been several estimates of this residence time. Craig (*19*) concluded that it was most probably not more than 10 years, and in one of his calculations he deduced a value of 4 years. Broecker *et al.* (*14*) concluded it was 5 years in the Atlantic Ocean and 8 years in the Pacific Ocean. Nydal (*45*) found that for the North Atlantic it was around 3 years or less. The profiles of Figure 6, and a few others which are not shown, all show a significant penetration of excess ^{14}C below the mixed surface layer, pointing to a short residence time, of the order of 2 years, in the mixed layer of the sea before transfer below the thermocline into the deep sea. Considering the size of the oceans these data are very meager, and no firm conclusions can be drawn from them. However, continued measurements of ^{14}C in the sea should help to establish a firmer estimate of this quantity.

Besides the box model approach, the data of Figures 1, 7, and 8 have also been analyzed using an eddy diffusion model to account for the observed changes occurring in the troposphere (*40, 56*). Taking the exchange of CO_2 between the atmosphere and the sea to be proportional to the square of the wind speed over the sea surface, Young and Fairhall (*56*) were able to give a reasonable explanation of the observations using this model. This approach predicts that the oceans of the southern hemisphere will be the principal sink for excess ^{14}C. The rapid increase in the levels of excess ^{14}C in surface ocean water at latitude near 40°S confirms this expectation.

Besides these applications to geophysical problems, the excess ^{14}C has interesting possibilities in other areas of research. The large increase in ^{14}C in tropospheric air which took place in 1963 means that so far as ^{14}C is concerned plant material which grew later than 1962 is significantly different from plant material which grew before 1963. Using this fact Berger and Libby (*4*) have shown that the body organs, such as the heart, liver, and brain, turn over their carbon on a time scale of the order of weeks. It would be of interest if similar studies could be carried out on DNA extract to see if the same is true of the molecules carrying the genetic code.

Another example is illustrated in Figure 9 (*17*). The outer, sapwood rings of a western redcedar, *Thuja plicata* Donn, which grew about 50 miles south of Seattle, show an increase in ^{14}C which lags slightly behind the levels of ^{14}C which prevailed in the atmosphere. This lag is attributed to a holdover of food supply from the previous year; a sizeable

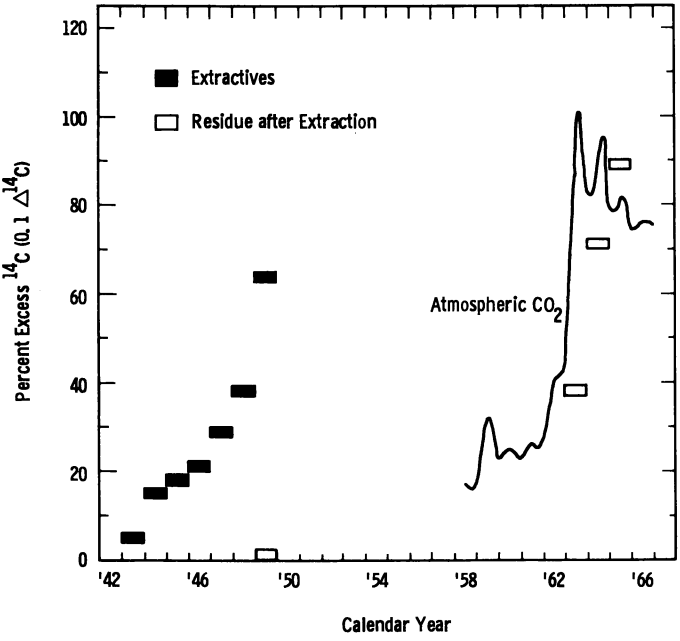

Figure 9. ^{14}C concentration in tree rings and in heartwood extractives of western redcedar

holdover from the previous year, on the order of 80–90%, is required to fit the observations. More likely the holdover is less than this each year but it extends over several years. The ^{14}C content of the dark component, extracted with acetone, which is present in the outermost heartwood rings was also examined. These data are also shown in Figure 9. The cellular structure of the outermost heartwood ring was laid down in 1949, well before excess ^{14}C perturbed the atmosphere significantly. The insoluble residue from the acetone extraction shows no excess ^{14}C. However, the extractives, which amount to *ca.* 6% by weight of the dry heartwood, show significant amounts of excess ^{14}C. In the heartwood ring laid down in 1949 it measures nearly 65% above normal, comparable with the excess ^{14}C in the outermost sapwood ring. This illustrates what botanists already know: that the extractives are formed as metabolites in the outermost growth ring and are deposited in the dead cells at the periphery of the heartwood. It appears that further ^{14}C studies could elucidate the chemistry of wood formation and provide interesting information on the utilization of stored food supply by trees.

A number of other interesting possibilities for utilizing the excess ^{14}C in the atmosphere as a tracer of natural processes come easily to mind. Not much is known about the rate of turnover of humus in the soil. Measurements of ^{14}C in soil humus over the next several years, while the terrestrial biosphere continues to fix carbon with significant amounts of excess ^{14}C, should help to determine the rate of turnover of carbon in the reservoir of humus. Some work along these lines is already in progress (*41*).

In the marine biosphere organisms which live near the surface show significant levels of excess ^{14}C. It would be of interest to know if the organisms which live at great depth show similar amounts of excess ^{14}C, implying a rapid downward propagation of the food chain. If the food chain propagates downward very slowly, deep-feeding organisms will be slow to show evidence of excess ^{14}C. Another problem of marine biology is the very large reservoir of dissolved organic matter in the sea. Not much is known about this material besides its distribution, which in the deep sea is remarkably uniform (*37*). The mechanisms of its formation and destruction are unknown. It is not known whether it has accumulated over long periods of time, thousands of years perhaps, or whether it is a reservoir which turns over fairly rapidly. Measurements of ^{14}C would be desirable to help answer some of these questions.

Conclusion

The large perturbation produced in the level of ^{14}C in tropospheric CO_2 in 1963–65 has left its mark in the terrestrial biosphere and is producing measurable changes in near-surface waters of the sea. It is clear that man has unwittingly initiated a geophysical experiment on a global scale. Provided that the present moratorium on atmospheric tests by the two major nuclear powers is continued, the 1962–62 nuclear tests will have provided an unparalleled opportunity—we hope a unique opportunity—for gaining increased insight into many of the processes taking place in our environment.

Literature Cited

(1) Arnold, J. R., Anderson, E. C., *Tellus* **9**, 28 (1957).
(2) Banse, K., *Progr. Oceanog.* **2**, 55 (1964).
(3) Berger, R., Fergusson, G. J., Libby, W. F., *Am. J. Sci. Radiocarbon Suppl.* **7**, 336 (1965); **8**, 467 (1966).
(4) Berger, R., Libby, W. F., *Am. J. Sci. Radiocarbon Suppl.* **9**, 477 (1967).
(5) Bien, G. S., Rakestraw, N. W., Suess, H. E., *Limnology Oceanog. Suppl.* **10**, R25 (1965).

(6) Bien, G. S., Rakestraw, N. W., Suess, H. E., *Tellus* **12,** 436 (1960).
(7) Bien, G., Suess, H., *Radioactive Dating Methods Low Level Counting, I.A.E.A. Vienna,* 105-115 (1967).
(8) Bolin, B., Eriksson, E., "The Atmosphere and the Sea in Motion," pp. 130-142, Rockefeller Institute Press and Oxford University Press, New York, 1959.
(9) Brodie, J. W., Burling, R. W., *Nature* **181,** 107 (1958).
(10) Broecker, W. S., Tucek, C. S., Olson, E. A., *Intern. J. Appl. Radiation Isotopes* **7,** 1 (1959).
(11) Broecker, W. S., Olson, E. A., *Am. J. Sci. Radiocarbon Suppl.* 1, 111 (1959).
(12) *Ibid.,* **3,** 176 (1961).
(13) Broecker, W. S., Olson, E. A., *Science* **132,** 712 (1960).
(14) Broecker, W. S., Gerard, R., Ewing, M., Heezen, B. C., *J. Geophys. Res.* **65,** 2003 (1960).
(15) Broecker, W. S., Walton, A., *Science* **130,** 309 (1959).
(16) Buddemeier, R. W., Fairhall, A. W., Yang, I. C., Young, A. W., unpublished data.
(17) Buddemeier, R. W., Fairhall, A. W., unpublished data.
(18) Burling, R. W., Garner, D. M., *New Zealand Geol. Geophys.* **2,** 799 (1959).
(19) Craig, H., *Tellus* **9,** 1 (1957).
(20) Fabian, P., Libby, W. F., Palmer, C. E., *J. Geophys. Res.* **73,** 3611 (1968).
(21) Feely, H. W., Seitz, H., Lagomarsino, R. J., Biscaye, P. E., *Tellus* **18,** 316 (1966).
(22) Fergusson, G. J., *Nucleonics* **13,** 18 (1955).
(23) Fergusson, G. J., *Proc. Roy. Soc.* **A243,** 561 (1958).
(24) Fergusson, G. J., *J. Geophys. Res.* **68,** 3733 (1963).
(25) Garner, D. M., *Nature* **182,** 466 (1958); *New Zealand J. Geol. Geophys.* 1, 577 (1958).
(26) Gudiksen, P. H., Fairhall, A. W., Reed, R. J., *J. Geophys. Res.* **73,** 4461 (1968).
(27) Hagemann, F., Gray, J., Machta, L., Turkevich, A., *Science* **130,** 542 (1959).
(28) Hagemann, F. T., Gray, J., Machta, L., *U. S. At. Energy Comm. Health Safety Lab. Rept.* **HASL-159** (1965); **HASL-166** (1966).
(29) Hayes, F. N., Williams, D. L., Rogers, B., *Phys. Rev.* **92,** 512 (1953).
(30) Junge, C. E., *J. Geophys. Res.* **68,** 3849 (1963).
(31) Kigoshi, K., *J. Radiation Res.* **1,** 111 (1960).
(32) Kigoshi, K., Endo, K., *Bull. Chem. Soc. Japan* **34,** 1740 (1961).
(33) Lal, D., Rama, *J. Geophys. Res.* **71,** 2865 (1966).
(34) Libby, W. F., "Radiocarbon Dating," 2nd ed., University of Chicago Press, Chicago, 1955.
(35) Lingenfelter, R. E., *Rev. Geophys.* **1,** 35 (1963).
(36) Menzel, D. W., Goering, J. J., *Limnol. Oceanog.* 11, 333 (1966).
(37) Menzel, D. W., *Deep-Sea Res.* **14,** 229 (1967).
(38) Munnich, K. O., Vogel, J. C., *Naturwiss.* **45,** 327 (1958).
(39) Munnich, K. O., Vogel, J. C., *Proc. Symp. Radioactive Dating, I.A.E.A. Vienna,* 189-197 (1963).
(40) Munnich, K. O., Roether, W., *Radioactive Dating Methods Low Level Counting, I.A.E.A. Vienna,* 93-104 (1967).
(41) Nakhla, S. M., Delibrias, G., *Radiometric Dating Methods Low Level Counting, I.A.E.A. Vienna,* 169-176 (1967).
(42) Nydal, R., *Nature* **200,** 212 (1963).
(43) Nydal, R., *Tellus* **18,** 272 (1966).

(44) Nydal, R., *Radioactive Dating Methods Low Level Counting, I.A.E.A. Vienna*, 119-128 (1967).
(45) Nydal, R. J., *Geophys. Res.* **73,** 3617 (1968).
(46) Olsson, I. U., Karlen, I., *Am. J. Sci. Radiocarbon Suppl.* **7,** 331 (1965).
(47) Olsson, I. U., Karlen, I., Stenberg, A., *Tellus* **18,** 293 (1966).
(48) Patterson, R. L., Blifford, I. H., *Science* **126,** 26 (1957).
(49) Rafter, T. A., Fergusson, G. J., *New Zealand J. Sci. Technol.* **B38,** 871 (1957).
(50) Rafter, T. A., *New Zealand J. Sci.* **8,** 472 (1965).
(51) Revelle, R., Suess, H. E., *Tellus* **9,** 18 (1957).
(52) Suess, H. E., *Science* **122,** 415 (1955).
(53) Tauber, H., *Science* **131,** 921 (1960).
(54) *Ibid.*, **133,** 461 (1961).
(55) Willis, E. H., *Nature* **185,** 552 (1960).
(56) Young, J. A., Fairhall, A. W., *J. Geophys. Res.* **73,** 1185 (1968).

RECEIVED February 24, 1969. Work supported by the U. S. Atomic Energy Commission under Contracts AT(45-1)-1776 and AT(45-1)-2091.

Analysis and Public Health Aspects of Environmental Tritium

A. A. MOGHISSI[1]

U. S. Department of Health, Education, and Welfare, Southeastern Radiological Health Laboratory, P.O. Box 61, Montgomery, Ala. 36101

An advanced dioxane-based liquid scintillation solution is developed which incorporated 5 ml. of water and yields a Y *value of approximately*

$$1\ \text{nCi/liter}\left(Y = \frac{\sqrt{\text{background (c.p.m.)}}}{2.22 \times \text{volume of water (ml.)} \times \text{efficiency (c.p.m./d.p.m.)}}\right)$$

A new detergent, Triton-101, in association with p*-xylene is used for the suspension of 10 ml. of water with a* Y *value of approximately 0.5 nCi/liter. The application of a new instrumental technique with three photomultipliers decreases further the* Y *value of both mixtures. A Teflon cylinder with a volume of 250–300 ml. is used as sample container for low level counting with a* Y *value of approximately 0.2 nCi/liter. Selected results of samples collected during 1967 are reported, and the radiation dose to the population of the United States from tritium is estimated to be approximately 0.2 mrem./year.*

Tritium is a radionuclide with considerable public health significance. Starting with the atmospheric thermonuclear tests, tritium concentration in the Northern Hemisphere has increased considerably above the natural background of approximately 10 pCi/liter of water (5). Since the cessation of these tests, environmental tritium concentrations have decreased gradually. Tritium is, however, produced in every nuclear reactor to some extent as a product of fission (*1*) or the activation of deuterium. In particular, reactors with heavy water as the moderator or cooling agent produce a large amount of tritium. Inasmuch as no

[1] Present address: Southwestern Radiological Health Laboratory, P.O. Box 15027, Las Vegas, Nev. 89114.

economically feasible process is known for separating tritium in nuclear waste water, the expanding nuclear industry will introduce tritium into the environment. In addition, kCi amounts of tritiated compounds are produced annually for various applications. A portion of this tritium escapes into the environment as waste water. Consequently, a constant and careful observation of the tritium concentration in the environment, and research to understand its effect in biological systems are necessary.

This paper summarizes some of the recently developed methodology used at the Southeastern Radiological Health Laboratory to determine environmental tritium concentrations. Since some of the methods used are not yet available in the literature, their development and essential features are discussed. Selected data on environmental tritium concentrations are presented and interpreted.

In recent years, several developments have generated new possibilities in liquid scintillation counting. The most important event was the development of the bialkali photomultipliers with considerably improved quantum efficiency. In addition, several new scintillators and solvents of higher purity have become available. With the resulting counting systems it has been possible to achieve sensitivities comparable with gas counters, with much less time and effort involved.

Criteria for Comparing Counting Systems

The selection of an appropriate technique for low level counting has been discussed by Moghissi *et al.* (9). If M *ml.* of water with a specific activity of Y nCi/liter are counted with an efficiency of E c.p.m./d.p.m. for t minutes, the number of counts obtained are as follows:

$$(M \times 10^{-3}) \times Y \times (2.22 \times 10^{3}) \times E \times t$$

If background (B in c.p.m.) is counted for t minutes, its standard deviation will be $\sqrt{Bt}$. The minimum limit of detection at 1σ confidence level and one-minute counting time requires:

$$(M \times 10^{-3}) \times Y \times (2.22 \times 10^{3}) \times E \times t = \sqrt{Bt}$$

where 2.22 is c.p.m./pCi.

Rearrangement of this equation yields:

$$Y = \frac{\sqrt{B}}{2.22 \times E \times M}$$

This equation is applicable to background dominant counting systems and cannot be used to compare counters such as those used in tracer studies. In addition, it disregards the importance of convenience and time requirements in using a particular procedure. However, if internal

gas and liquid scintillation counters are compared, these factors should also be considered.

The manufacturer rates the performance of his instrument by a figure of merit, F, defined as S^2/B, where S is reported as the counting efficiency of an unquenched sample. Unfortunately, F is inadequate for evaluating low level counting systems. This value, for an instrument using S11 type photomultipliers, for example, is only slightly lower than those with bialkali photomultipliers. The use of the latter instruments for low level counting, however, reveals that the Y value is decreased by a factor of 3–4. The reason is the necessity of applying highly quenched samples in low level counting where the majority of radioactive decays produce only 2–3 photons. The difference in the quantum efficiency of the two photomultiplier types, in this case, affects the counting efficiency considerably more than an unquenched sample where more photons are available.

Materials

A Beckman liquid scintillation counting system was used to study scintillation solutions and to analyze environmental samples. All scintillators were obtained from Pilot Chemicals, Boston, Mass. *p*-Dioxane, spectroscopic grade, and *p*-xylene (m.p. 12°–13°C.) were received from Matheson, Coleman, and Bell, Rutherford, N. J.

Scintillation Solution

The first attempt to develop an efficient scintillation method for low level counting consisted of evaluating the dioxane-based solution and studying the many factors influencing the efficiency and the background (9).

The resulting solution consisted of 5 ml. of water and 20 ml. of dioxane containing 7 grams 2,5-diphenyloxazole (PPO), 1.5 grams bis-(*o*-methylstyryl)benzene (bis-MSB), and 120 grams naphthalene/liter dioxane. The Y-value of this solution was approximately 1 nCi/liter.

The presence of oxygen in this solution as in all dioxane-based scintillators adversely affects the efficiency and background. Also, light excitation produces phosphorescence. Therefore, it is necessary to use high purity compounds and avoid contact with air and exposure to light.

Many successful suspension counting systems have been reported where water is suspended in a scintillation mixture by a detergent. Van der Laarse (8) reported a system consisting of 4 ml. of water and 16 ml. of a mixture of toulene containing 4 grams PPO, 0.3 gram POPOP/liter mixed with Triton X-100 in a ratio of 55:25. He obtained a counting efficiency of 21% and a Y-value of 1.3 nCi/liter.

Williams (*12*) compared suspension and homogeneous scintillation for tritium low level counting. He showed, in agreement with van der Laarse, that higher $E \cdot M$ values can be obtained using Triton X-100 as detergent. His most sensitive solution consisted of toluene (7 grams PPO, 0.5 gram POPOP/liter) and Triton X-100 mixed in a volume ratio of 65:35. Water (7.5 ml.) was counted with an efficiency of 15.5% and a background of 10 c.p.m. resulting in a Y-value of 1.2 nCi/liter.

An important factor in using suspension counting is the counting vial. Glass vials usually decrease the counting efficiency by 10–20% and increase the background by approximately 10 c.p.m. as compared with polyethylene vials. Unfortunately, aromatic solvents migrate through polyethylene vials with considerable speed (120–180 mg./d), placing limitations and inconvenience on the application of these vials in suspension counting. The new nylon vials (Nuclear Chicago) are resistant to aromatic solvents. Their resistance to water, however, is low, and owing to the resulting change in their shape, they cannot be used for water counting in instruments with automatic sample changers.

These factors should be weighed carefully against the small decrease in Y value before a decision is made regarding the application of the reported procedures. Recognizing this fact, many commercial detergents were tested in the author's laboratory. A Y value of 0.5 was obtained with several detergents; for example, Triton N-101 (Rohm and Haas Co., Philadelphia, Pa.) using *p*-xylene as solvent and a ratio of xylene to detergent of 2.75:1. The optimum concentration of water was 10–12 ml. in a 25 ml. mixture. It was of considerable interest to find that the instabilities reported by Benson (*2*) and confirmed by others (*12*) were absent in room-temperature operated liquid scintillation equipment. On the other hand, it was found that phosphorescence and chemiluminescence were severe in suspension counting. The possible temperature effect is under study in this laboratory. From the preliminary results it can be concluded that the increased sensitivity is to some extent responsible for the detection of the mentioned undesirable effects in suspension counting.

Large Volume Liquid Scintillation Counting

The lowest Y value obtainable using the above-mentioned liquid scintillation counting systems is limited by the volume of the vial used (25 ml.). For lower Y values, a larger volume is necessary (*3*, *7*). To determine the optimum volume, a system was designed as shown in Figure 1. A Teflon tube with a 5-cm. internal diameter was used as the container and reflector. Two Teflon sheets (0.3-mm. thick) closed both ends of the tube by two O-rings and two aluminum devices pressed

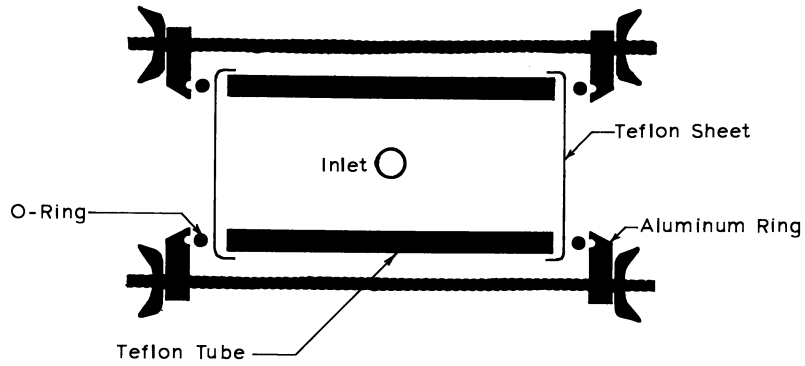

Figure 1. Large volume cell for low level counting of tritium by liquid scintillation

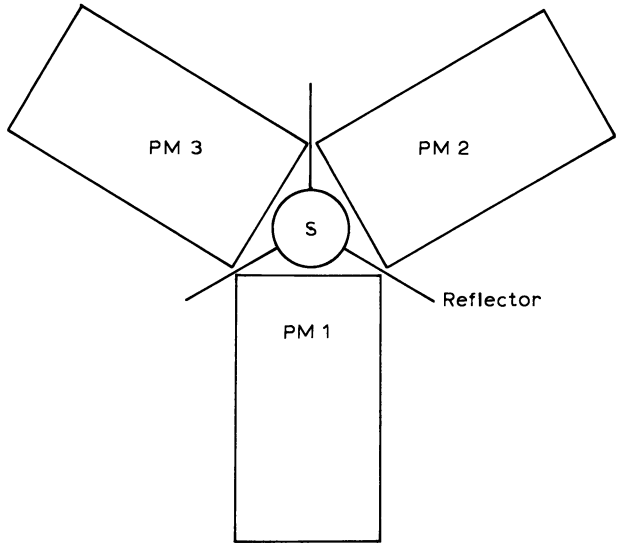

Figure 2. Block diagram of the three photomultiplier system for low level counting of tritium

together by four long screws. This system permitted volume variation by using tubes of different lengths. A volume of 250–300 ml. was found to have a minimum Y value of approximately 0.4 nCi/liter for dioxane and 0.2 nCi/liter for the suspension system. The latter figure approaches the lowest Y value of any tritium low level counting system, including the most sensitive gas counters (*4*). An anticoincidence ring is being prepared for this system.

Tritium Counting with Three Photomultipliers

A triple-coincidence technique has been described by Schwerdtel (*11*) for determining counting efficiency of quenched samples by using coincidence rules. A similar system was designed independently and used in this laboratory for the same purpose and, contrary to Schwerdtel's method, also for low level counting. The block diagram is shown in Figure 2. During this study it was found that if the system were designed in such a manner that a pulse were registered when any two of the three photomultipliers observe an event (simultaneous double coincidence), the counting efficiency increases by approximately 10–20% as compared with the usual two-photomultiplier system. The *Y* value in this case is correspondingly lower. This is explainable by the increased surface of photomultipliers by 50%.

Environmental Levels of Tritium during 1967

The Bureau of Radiological Health (BRH) of the Public Health Service for many years has been analyzing and evaluating environmental tritium. Several networks comprising various media have been established. Surface waters, rain, urine, and food are analyzed by the Southeastern Radiological Health Laboratory, and the results are reported periodically in *Radiological Health Data and Reports.*

During 1967 the dioxane-based liquid scintillation solution was used to analyze tritium samples. The minimum limit of detectability of this system at 2 σ confidence level was 0.2 nCi/liter. An example of the networks' operating during 1967 is the one carried out in cooperation with the South Carolina State Board of Health. Samples are collected from the Savannah River near Beaufort, S. C., and Augusta, Ga.; and the Broad River near Columbia, S. C. These three stations are part of the environmental surveillance program of the South Carolina State Board of Health and include two stations located near the Savannah River Plant operated by E. I. du Pont de Nemours and Co. for the Atomic Energy Commission. Figure 1 shows the results of the analysis of the collected samples from these stations and the difference between the tritium levels of the samples from the two latter stations. Inasmuch as the Savannah River plant is located between these stations, the difference can be attributed to the operation of this major nuclear facility (Figure 3).

Radiation Dose from Environmental Tritium

The ultimate purpose of the surveillance activities was to determine the radiation dose to the population. Moghissi and Porter (*10*) reported

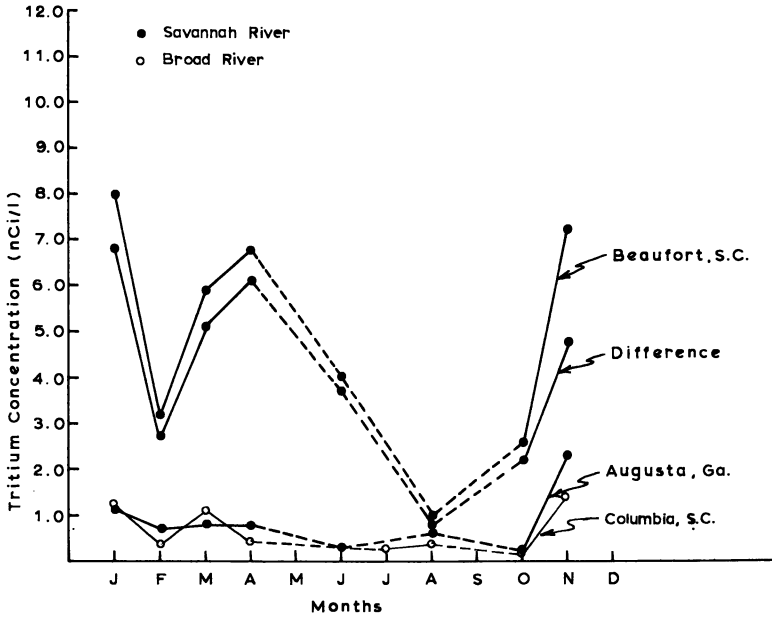

Figure 3. Tritium concentration of samples collected during 1967 from the Broad River at Columbia, S. C., and the Savannah River at Beaufort, S. C., and Augusta, Ga., as well as the difference in tritium concentration of samples from the latter two stations

the following equation for correlating dose equivalent (DE) and the concentration of tritium (C) in body water:

$$DE \text{ (mrem./}a\text{)} = 0.17C \text{ (nCi/liter)}$$

This equation is based on several assumptions as discussed by Moghissi and Porter (*10*) requiring further study and, as such, should be used with caution.

Among several media analyzed during 1967, urine is probably the best for calculating DE. The tritium concentration in urine during 1967 averaged approximately 1 nCi/liter, corresponding to 0.2 mrem./a. In terms of Federal Radiation Council guidance (*6*) this represents 0.1% of the radiation protection guide (170 mrem.) for an average dose to a suitable sample of the population. The average tritium concentration in surface waters is 5 to 6 nCi/liter. If it is assumed that the specific activity of tritium in surface water is identical to that in the body, this corresponds to 1.0 mrem./a. This discrepancy between DE values calculated from urine and surface waters is explained by the fact that the stations where surface waters are collected are not necessarily representative for the

areas monitored by urine analysis and are generally located around nuclear facilities. Often the relatively high concentrations are diluted by rain and other waters before the river water is consumed by the population. Food results do not follow any pattern because of the composite nature of the samples.

It is particularly interesting to evaluate the contribution of a major nuclear facility, such as the Savannah River Plant, to the radiation dose to the population. Inasmuch as Beaufort, S. C., receives its drinking water primarily from the Savannah River, the expected body burdens may be extrapolated from tritium concentrations of the river at Beaufort. As mentioned previously, the difference between the concentrations at Augusta, Ga., and Beaufort, S. C., may be attributed to the operation of the Savannah River Plant. The difference averages approximately 4 nCi/liter and corresponds to 0.8 mrem./*a*. This represents 0.5% of the radiation protection guide for an average dose to a suitable sample of the population.

It should be emphasized that there are a number of factors in the public health aspects of tritium which are not well established and whose discussion is beyond the scope of this paper. Studies should continue to develop more sensitive techniques for tritium measurement and to increase present knowledge in this field of radiological health.

Acknowledgment

The support of many staff members of the Southeastern Radiological Health Laboratory, in particular my co-workers, is greatly appreciated.

Literature Cited

(1) Albenesius, E. L., *Phys. Rev. Letters* **3**, 274 (1959).
(2) Benson, R. H., *Anal. Chem.* **38**, 1353 (1966).
(3) Boyce, I. S., Cameron, J. F., "Tritium in the Physical and Biological Sciences," Vol. I, p. 231, IAEA, Vienna, 1962.
(4) Cameron, J. F., "Radioactive Dating and Methods of Low-Level Counting," p. 543, IAEA, Vienna, 1967.
(5) Kaufman, S., Libby, W. F., *Phys. Rev.* **93**, 1337 (1954).
(6) Federal Radiation Council, Background Material for the Development of Radiation Protection Standards, *Rept. No.* 1, 1960.
(7) Kaufmann, W. J., Nir, A., Parks, G., Hours, R. M., "Tritium in the Physical and Biological Sciences," Vol. I, p. 249, IAEA, Vienna, 1962.
(8) van der Laarse, J. D., *Intern. J. Appl. Radiation Isotopes* **19**, 337 (1967).
(9) Moghissi, A. A., Kelley, H. L., Regnier, J. E., Carter, M. W., *Intern. J. Appl. Radiation Isotopes* **20**, 145 (1969).
(10) Moghissi, A. A., Porter, C. R., *Rad. Health Data Rept.* **9**, 337 (1968).
(11) Schwerdtel, E., *Atomkernenergie* **11**, 324 (1966).
(12) Williams, P. H., *Intern. J. Appl. Radiation Isotopes* **19**, 377 (1968).

RECEIVED July 22, 1968. Mention of commercial products used in connection with work reported here does not constitute an endorsement by the Public Health Service.

Decrease of Bovine Cesium-137 Concentrations Following the Cessations of Atmospheric Nuclear Weapons Testing

CLIFTON BLINCOE and V. R. BOHMAN
University of Nevada, Reno, Nev.

Cattle have been used since 1958 to study the fallout cesium-137 concentration in the biosphere. These studies have been made at three locations in Nevada and have included measurement of both liver and skeletal muscle concentrations of ^{137}Cs twice yearly. A comparison of yearling and mature cattle indicated no effect of these ages at slaughter on the ^{137}Cs concentration. The half-period for decrease of bovine soft-tissue ^{137}Cs in the absence of atmospheric nuclear weapons testing averaged 0.9 year (0.5 ± 0.1 to 1.3 ± 0.5 years). There was no significant difference in the rate of decrease following the cessation of atmospheric nuclear weapons testing in 1959 and in 1963. The same rate of decrease was observed at all three locations and in both muscle and liver.

Cesium-137 is the principle radionuclide of appreciable half-life and high fission yield found in the edible tissues of animals. It also has gaseous precursors (^{137}I and ^{137}Xe) and can thus be expected in fallout from low temperature fission product releases to the atmosphere.

Range beef cattle have been used as monitors of fallout radionuclides in the biosphere. They forage over large areas eating a variety of desert plants, thus integrating the biologically available fallout over a wide area. They are also large enough to provide the large samples necessary for determining quantitatively low concentrations of radionuclides. The ability of cattle to survive exclusively on desert range and their importance as human food also increases their desirability as monitors of biologically available radionuclides.

Cattle have been maintained on desert range in three locations in Nevada since 1958 for studies of fallout accumulation. The data for ^{137}Cs,

^{131}I, and ^{90}Sr through 1962 have been published (*4, 5, 6*). These indicated that bovine thyroid ^{131}I concentration was a good monitor of fresh fallout, that soft-tissue ^{137}Cs was a good monitor of biosphere contamination with long half-life radionuclides, and that ^{90}Sr concentrations were largely cumulative.

This report concerns the changes in concentration of ^{137}Cs in edible tissues of range cattle following the cessation of atmospheric nuclear weapons test series.

Methods

Three herds of Hereford cattle have been maintained at three locations in Nevada since 1958. One herd is on the Nevada Test Site of the U. S. Atomic Energy Commission (NTS), another 80 km. east in Delemar Valley (DV), and the third 480 km. north of the DV herd at the Knoll Creek Field Laboratory of the University of Nevada (KC). These locations are indicated in Figure 1. The locations, herds, and sampling procedures have been described in detail (*4, 5, 6*). Samples are taken twice yearly from all herds. Prior to 1963 a calf, a yearling, a two-year old, a three-year old, and a mature animal were slaughtered at each sampling period from each herd. Analysis of the data from these studies indicated that more useful data would be obtained by limiting the number of age groups used (*5*). Since 1963, three yearling and three mature animals have been taken from each herd at each sampling period. In all cases, the animals have lived their entire life in the location indicated and have existed entirely on desert range except for winter supplementation with locally produced hay necessary at the KC location.

Samples of liver and skeletal muscle from the round were analyzed for cesium-137 after wet digestion with nitric acid (*3*). The radiocesium was then separated by coprecipitation with cobalt cobalticyanide (*2*). ^{137}Cs was measured with a well-type scintillation counter (5.1 cm. diameter and height NaI(Tl) crystal), single-channel analyzer, and scaler by counting γ-ray energies of 0.662 $\pm$ 0.025 Mev. The standard deviation of analysis was found to be $\pm$ 0.032 pCi. ^{137}Cs/gram of tissue prior to 1963 and $\pm$ 0.050 pCi ^{137}Cs/gram in 1964–1965.

Multichannel γ-ray spectrometry of the counting samples indicated that measurable quantities of ^{134}Cs or other fallout nuclides were not present, confirming that this procedure gives good decontamination from other fission products. Previous studies have failed to demonstrate the presence of ^{135}Cs in cattle (*5*).

Analysis of variance, linear regression, and other statistical procedures were performed using computer programs based on standard procedures (*12, 14*).

Results and Discussion

This study encompasses two periods without extensive atmospheric contamination by nuclear weapons testing. An informal voluntary testing moratorium was observed from Oct. 31, 1958 until Sept. 1, 1961. A limited

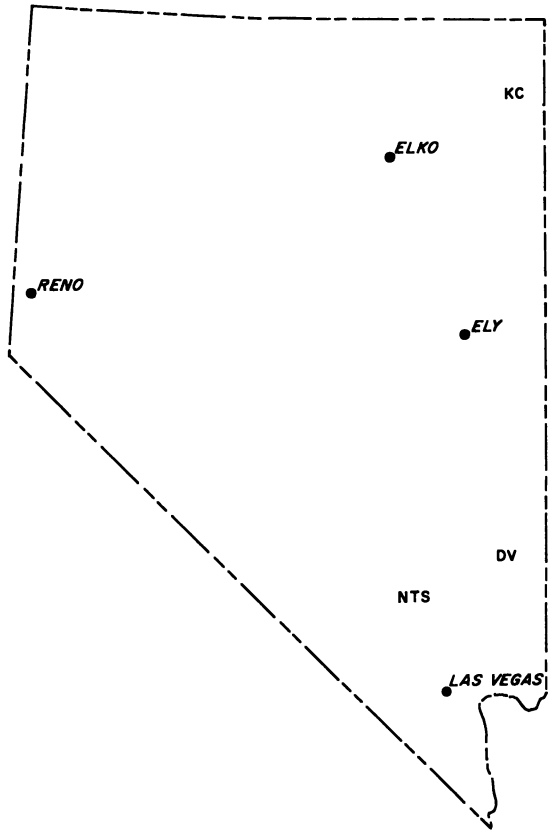

Figure 1. Locations of the test herds of range cattle

nuclear test ban treaty was signed on Aug. 5, 1963 and continues in effect to the present time. Only occasional, low fission yield, atmospheric nuclear detonations by France and China have occurred during these periods before 1967. Otherwise all detonations ceased during the informal testing moratorium, but underground testing continued during the limited test ban treaty. These tests have occasionally released limited quantities of radioactivity to the atmosphere. The data collected following these cessations of atmospheric nuclear weapons tests were first studied to ascertain the experimental variables influencing the ^{137}Cs concentration in bovine soft tissues and then to ascertain the rates of decrease of ^{137}Cs in these tissues in the absence of atmospheric nuclear weapons testing.

Analysis of variance was made on the 1960 muscle data and the 1961 liver data as representative of concentrations during the informal

testing moratorium. Time was not a factor in the analysis of variance, and spring and fall data for a given year were considered replicates of each other since only one animal per age group was slaughtered at any location at any one time (5). Analysis of variance was also made on the data collected from 1963 to and including the spring 1966 sampling as representative of tissue concentrations during the first few years of the limited nuclear test ban treaty period. The major factors studied were the tissue sampled (muscle or liver), age of the animals (yearling or mature), location in the state (KC, DV or NTS), and time. All factors and interactions not containing age as a variable were highly significant ($P > 0.01$). Location in the state significantly affected soft-tissue concentrations of ^{137}Cs. This was expected since the study was designed originally to ascertain the effect of distance from the Nevada Test Site on fallout in cattle. The observation that liver and muscle had significantly different concentrations of radiocesium was in agreement with a previously reported study (5) indicating a highly significant correlation of liver and muscle fallout ^{137}Cs concentration with the liver increasing in ^{137}Cs relatively slower than muscle. Since age was not a factor in the concentrations of ^{137}Cs in soft tissues, data from yearling and mature cattle were combined in all subsequent statistical studies.

The samples collected after cessation of atmospheric nuclear weapons tests in 1958 and 1963 were examined to ascertain the relative rate of decrease of soft-tissue cesium-137 (Table I). In view of the analysis of variance studies, each tissue and location were considered separately,

Table I. Half-Period for Decrease of Bovine Cesium-137 Concentrations Following the Cessation of Atomospheric Nuclear Weapons Tests

		1959[a,b]		*1963*[a]		
Tissue	*Location*	*No. of Samples*	*Half-Period, years*	*No. of Samples*	*Sampling Periods Included*[c]	*Half-Period, years*
Muscle	KC	10	0.84 ± 0.14[d]	36	F63-S66	0.96 ± 0.11[d]
	DV	10	0.54 ± 0.10	30	S64-S66	1.33 ± 0.39
	NTS	9	2.29 ± 2.67	42	S63-S66	0.78 ± 0.06
Liver	KC	8	0.88 ± 0.17	36	F63-S66	1.01 ± 0.11
	DV	6	0.59 ± 0.04	30	S64-S66	1.34 ± 0.52
	NTS	6	0.83 ± 0.27	42	S63-S66	1.00 ± 0.12
Average	—		0.74 ± 0.07[e,f]			1.07 ± 0.09[f]

[a] Year of termination of atmospheric nuclear weapon tests.
[b] S59-S61 data used.
[c] S = spring sampling; F = fall sampling.
[d] Standard error of estimate.
[e] The muscle-NTS value excluded from the average.
[f] Standard error of the mean.

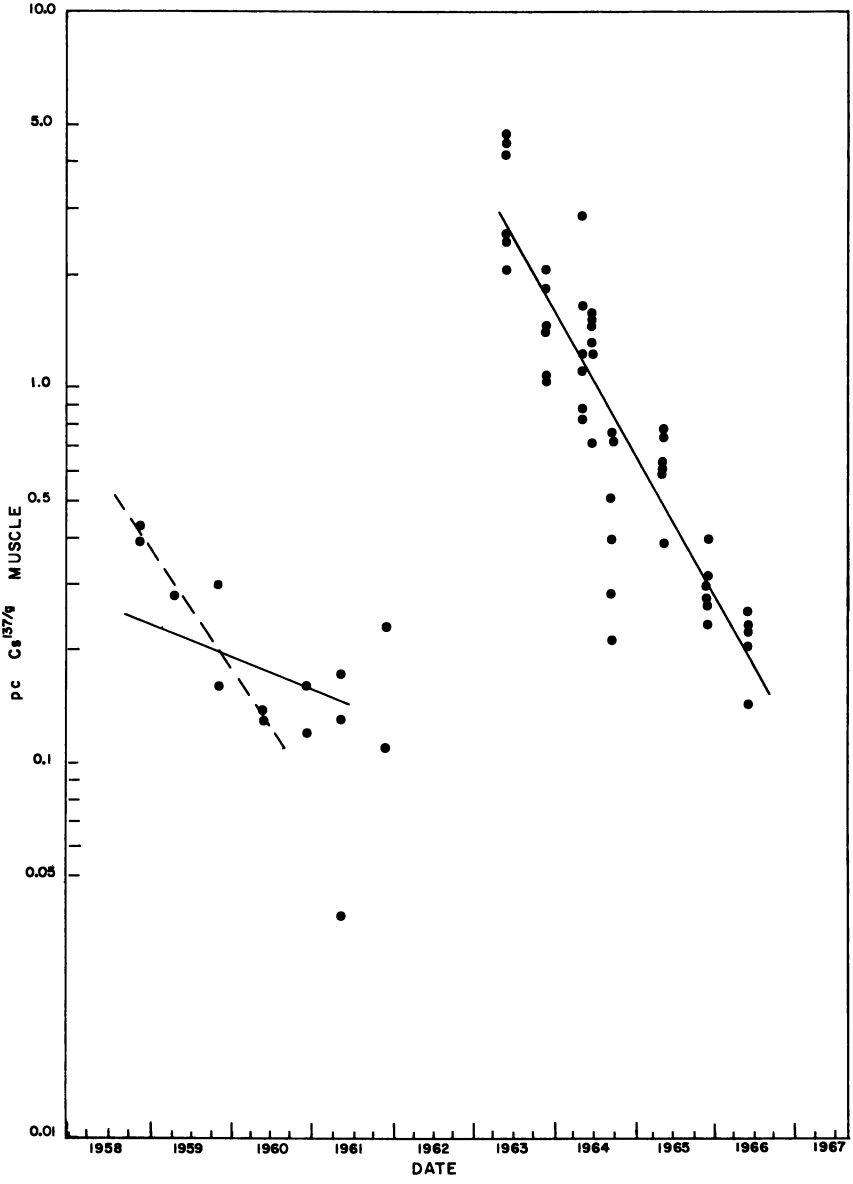

Figure 2. Decrease of muscle cesium-137 concentrations in range cattle following the cessation of atmospheric nuclear weapons testing. Dashed line indicates the regression equation calculated only on 1959 and 1960 data.

but data from yearling and mature cattle were pooled. The relative rate of decline is expressed as half-periods. Figures 2 and 3 give data for muscle and liver ^{137}Cs concentrations at the NTS location. These data

are representative of those collected and indicate the regression equations used to calculate the half-period. It should be pointed out that these half-periods have little relation to the biological half-life of ^{137}Cs. The

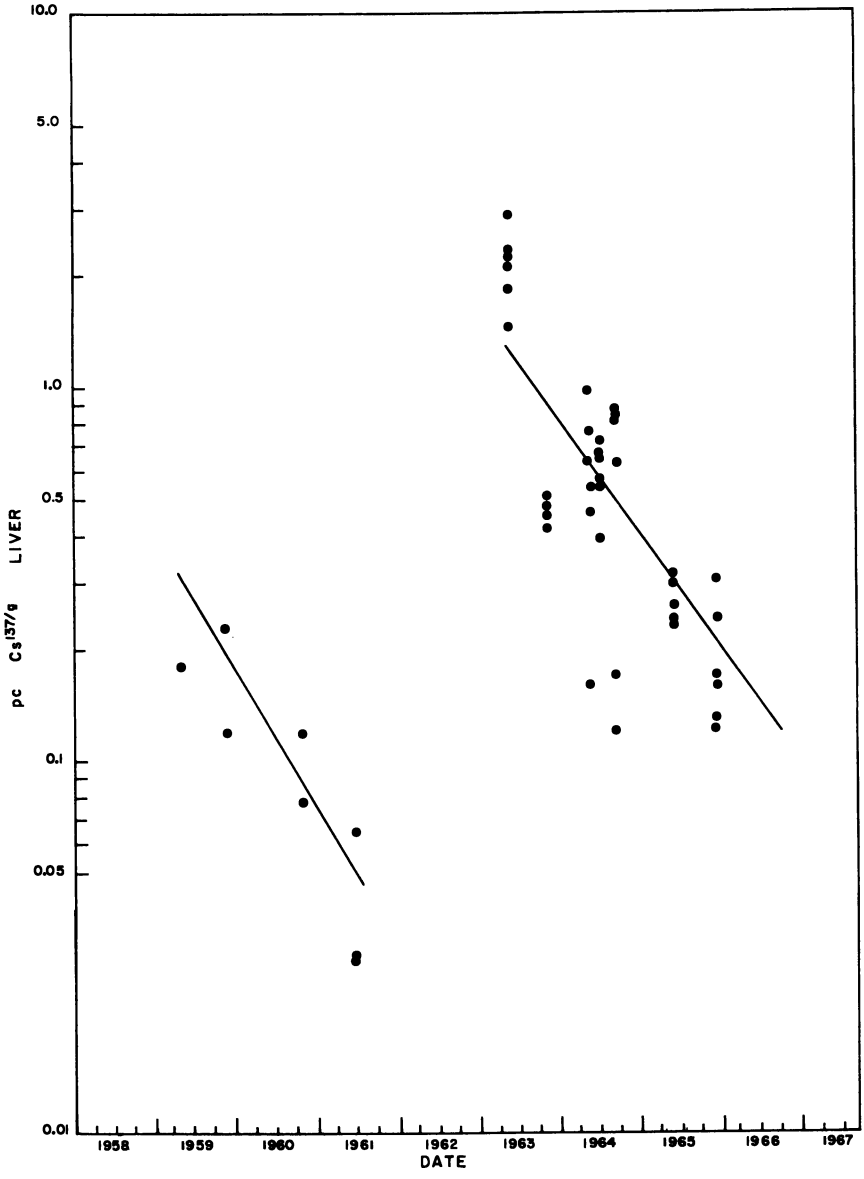

Figure 3. Decrease of liver cesium-137 concentrations in range cattle following the cessation of atmospheric nuclear weapons testing

biological half-life in cattle is reported to be 15–30 days (*11, 13*), which is more than an order of magnitude less than the observed half-period for loss of ^{137}Cs following the cessation of atmospheric nuclear weapons testing. The relatively short biological half-life and the long half-period observed in these studies indicate that range cattle are always in a steady state with their intake of fallout cesium-137. The levels of soft tissue ^{137}Cs in range cattle, thus, depend almost exclusively on their intake of cesium-137. Since pulmonary absorption of ^{137}Cs would be a very minor source of this isotope, except in specialized circumstances, we feel the soft-tissue ^{137}Cs concentrations found reflect the oral intake of this isotope and, hence, the plant contamination, both internal and external, of the range species grazed. Foliar contamination is the most significant route of entry of ^{137}Cs into the food chain (*10*) and can be affected by many factors. It would be changed by rain removal of surface contamination, wind removal of surface contamination, death and removal of plants and parts of plants, changing rate of atmospheric fallout deposition, etc.

All half-periods observed were similar. The average half-period for decrease of muscle and liver fallout ^{137}Cs in Nevada range cattle following the cessation of atmospheric nuclear weapons testing in 1959 was 0.7 year, and that following the cessation of atmospheric nuclear weapons testing in 1963 was 1.1 years. This difference was not significant. Thus fallout ^{137}Cs in the biosphere behaved the same, following the cessation of atmospheric nuclear weapons testing in 1959 and in 1963. This would indicate that the limited releases of fission products, which have occurred during the limited test ban treaty, have not significantly influenced the biosphere concentration of cesium-137.

The half-period for decrease of muscle cesium-137 concentration in NTS animals after the cessation of atmospheric nuclear weapons testing in 1959 appears anomalous (Table I and Figure 2). In addition to being considerably greater (2.3 years) than the other half-periods found, its standard deviation was larger than the value. If one considers only the initial rate of decrease of radiocesium in these muscle samples, one finds a half-period of 0.9 year which is quite consistent with other data. Examination of these data, in comparison with data from liver (Figures 2 and 3), indicates that only muscle decreased its rate of decline in 1960. It should also be noted that the values during 1960 were only about twice the standard error of analysis. Thus, analytical error alone is not an improbable cause of these anomalous values.

The three test herds were exposed to different mixtures of local and world-wide fallout. When atmospheric nuclear weapons testing ceases, animals in the NTS herd reach a greater maximum in soft-tissue ^{137}Cs concentration faster than animals in the other two herds (*5*). This is because the DV and KC herds respond primarily to world-wide fallout which

continues to rise for some time after testing stops, whereas the NTS herd also responds to local fallout deposited simultaneously with testing. By the time the KC and DV herds reach their maximum ^{137}Cs concentrations, this higher radiocesium concentration in the NTS herd has decreased to the same level as the other two herds. After atmospheric nuclear weapons testing stops, the factors decreasing the radiocesium concentration of the animal diets would operate at the same relative rate for both world-wide and local fallout, and the continued deposition of world-wide fallout would be at the same absolute rate in all three locations. One would thus expect the ^{137}Cs concentration to decrease somewhat faster at the NTS location because of the local nature of more of the fallout. This tendency is apparently masked by the continual deposition and removal of world-wide fallout. Our data (Table I) indicate the relative rate of decrease of ^{137}Cs in the biosphere is essentially the same at all three locations. One would expect the initial rate of decline to be affected most by local fallout, but the dispersion of the data is too great to calculate a reliable initial rate of decrease of the NTS herd compared with the other two herds. Also, the NTS herd moves from place to place within the Nevada Test Site, thus ingesting various mixtures of fresh and world-wide fallout. This would also tend to obscure the presumably more rapid decrease in local than world-wide fallout ^{137}Cs.

The half-periods observed here are about the same as the half-period in humans calculated from published data (*1*, *8*, *9*). Data for the radiocesium concentration in milk is subject to appreciable variation within a given year, owing primarily to the varying feed sources of dairy cattle during a year. Using the yearly data published by Campbell *et al.* (*7*) and Anderson *et al.* (*1*) we calculated a half-period of 1 to 1.7 years—again somewhat longer than in Nevada range cattle. The slower decline of fallout ^{137}Cs in cow's milk probably reflects the consumption of stored feed. While range cattle are continually exposed to biosphere cesium-137, dairy cattle consume a large portion of their radiocesium from stored feeds which represent biosphere contamination at least six months before consumption. This decreases the rate of decline of fallout ^{137}Cs in milk.

Measurement of milk cesium-137 secreted by range beef cattle is not practical because of the limited lactation period and milk production of beef cattle and because of the added handling of the cattle that would be required.

Acknowledgments

The authors acknowledge the assistance of G. R. Farmer, D.V.M. and E. L. Fountain, D.V.M. with the early sampling periods and of the Southwestern Radiological Health Laboratory, U. S. Public Health Service with the later sampling periods.

Literature Cited

(1) Anderson, E. C., Ward, G. M., Holland, J. Z., Langham, W. H., *U. S. At. Energy Comm. Rept.* **TID-7632**, 1962.
(2) Blincoe, C., *J. Agr. Food Chem.* **9**, 127 (1961).
(3) Blincoe, C., *Anal. Chem.* **34**, 715 (1962).
(4) Blincoe, C., Bohman, V. R., Fountain, E. L., *J. Agr. Food Chem.* **12**, 414 (1964).
(5) *Ibid.*, **13**, 157 (1965).
(6) Bohman, V. R., Blincoe, C., Wade, M. A., Lesperance, A. L., *J. Agr. Food Chem.* **14**, 413 (1966).
(7) Campbell, J. F., Murthy, G. K., Lewis, K. H., Straub, G. P., "Radioactive Fallout, Soils, Plants, Foods, Man," E. B. Fowler, Ed., Elsevier, New York, 1965.
(8) Eisenbud, M., *Federation Proc.* **22**, 1410 (1963).
(9) McNeill, K. G., Harrison, J. E., *Nature* **216**, 1340 (1967).
(10) Russell, J. S., "Atomic Energy Waste: Its Nature, Use and Disposal," Interscience, New York, 1961.
(11) Sansom, B. F., *J. Agri. Sci.* **66**, 389 (1966).
(12) Snedecor, G. W., "Statistical Methods Applied to Experiments in Agriculture and Biology," Iowa State University Press, Ames, Iowa, 1956.
(13) Wasserman, R. H., Lengemann, F. W., Thompson, J. C., Jr., Comar, C. L., "Radioactive Fallout, Soils, Plants, Foods, Man," E. B. Fowler, Ed., Elsevier, New York, 1965.
(14) Youden, W. J., "Statistical Methods for Chemists," p. 17, Wiley, New York, 1951.

RECEIVED June 4, 1968. This project was supported in part by the U. S. Atomic Energy Commission, Contracts AT(04-3)34 and AT(04-3)509. Nevada Agricultural Experiment Station Projects 190 and 394. Journal Series 84.

25

Relation of Radon Concentration in the Atmosphere to Total Moisture Detention in Soil and Atmospheric Thermal Stability

WILLIAM M. COX, RICHARD L. BLANCHARD, and BERND KAHN

Department of Health, Education, and Welfare, Division of Environmental Radiation, Radiological Engineering Laboratory, 5555 Ridge Ave., Cincinnati, Ohio 45213

Average monthly morning radon concentrations in ground-level air at Cincinnati, Ohio, based on daily measurements of radon-daughter concentrations, are reported for the period 1959–1966. Monthly averages ranged from 120 to 1520 pCi/cu. meters; maxima occurred from August to October and minima from February to April. Two alternative linear equations for predicting average monthly radon concentrations from atmospheric stability and total moisture detention in soil were derived. Radon concentrations varied directly with atmospheric stability and inversely with total moisture detention. Both correlation coefficients were 0.94, and 50 mean monthly values were predicted within 20% on the average.

Gaseous radon-222 and its particulate short lived daughters are usually the major radioactive constituents in air. Presented here are monthly average radon-222 concentrations based on the measurement of short lived radon-222 daughters in ground-level air at the same location daily in the morning for eight successive years. To aid in predicting radon-222 concentrations, results are analyzed for seasonal trends and the effects of atmospheric thermal stability and soil moisture content. In an earlier paper (*1*), morning values during the first four years of the study were compared with afternoon radon-222 concentrations, morning radon-220 concentrations, wind speeds, and amount of precipitation, and typical diurnal cycles of radon-222 concentrations were shown.

The concentrations of radon-222 and its daughters in ground-level air depend on the concentration and distribution of their radium-226 precursor in soil and rock, the emanating power of radon from its point of formation, the diffusion of radon to the surface of the ground, the resistance of ground cover (snow or vegetation) to the passage of radon, the vertical and horizontal transport of radon in the atmosphere, particle formation and attachment to larger particles by radon daughters, and washout from the atmosphere by precipitation (*1, 2, 3, 4, 5, 6, 7, 8, 9, 10, 11, 12, 13, 14*). At a specific location, atmospheric thermal stability and soil moisture content appear to be especially significant in predicting radon concentrations, as indicated by accumulation of radon during inversions and by higher radon concentrations during drier seasons (*2, 4, 8, 9, 12, 14*).

To evaluate among numerous other factors the influence of atmospheric thermal stability and soil moisture content, their monthly average values were compared with monthly average radon-222 concentrations by least squares analysis in terms of linear equations. Radon-222 concentrations were computed from radon-daughter measurements at Cincinnati from 1959 to 1966. The Cincinnati station of the U. S. Weather Bureau provided temperature and rainfall records from 1962 to 1966 for computing atmospheric thermal stability and soil moisture content. The latter was derived in terms of total moisture detention (*TMD*) as defined by Thornthwaite (*15, 16*). This presentation of soil moisture data has been applied to irrigation problems for the past 20 years and has been tested and improved in this context. Its use appears advantageous because only Weather Bureau records and determination of soil water-holding capacity are required, and direct measurements of soil moisture content are unnecessary. In correlated studies the influence of precipitation on radon-daughter concentrations was observed for specific stability ranges, and radon concentrations computed from radon-daughter measurements were compared with directly measured radon concentrations in 114 morning observations.

Procedure and Calculations

Airborne particles were collected outside the laboratory by drawing air at the rate of 30 cu. meters/day through a 4.7 cm. diameter, 0.8-μ pore size, membrane filter (*1*). The air intake was 5 meters above ground and was shielded from precipitation by a glass tube. Air was drawn through the filter for 24-hour periods. The filter was collected at 8:30 a.m. (either EST or EDT, as applicable), Tuesdays through Fridays, and the α-activity was measured with a scintillation detector within 2 minutes of collection.

The concentration of radon in air was computed from the α-count by assuming that 3.8-day ^{222}Rn and its short-lived daughters—2.0 min.

^{218}Po, 27-min. ^{214}Pb, 20-min. ^{214}Bi, and 164-μsec. ^{214}Po—were in secular equilibrium. The measured α-radiation, emitted by ^{214}Po, was corrected for the decay of its parents ^{214}Pb and ^{214}Bi between collection and counting, for slight periodic changes in counter efficiency as determined with a long lived standard, and for the presence of short lived daughters of ^{220}Rn. The corrected count rates were converted to radon concentrations in air by taking into account the counter efficiency and the amount of air that passed through the filter. For the eight-year record, all daily morning values were averaged on a monthly basis; for comparisons with stability and *TMD* values, radon values were averaged only on days for which stability data were available, and monthly averages were used if stability data were available for more than one-half of the days. As a result, only 50 monthly averages were considered for the period 1962–1966.

During 1965, morning concentrations of radon and radon daughters were compared by passing 1.4 cu. meters of air in 2 hours through a membrane filter and then through 60 grams of activated charcoal at a temperature of −78°C. (*13*). The radon daughters on the membrane filter were measured in an α-counter immediately after collection; the radon adsorbed on the charcoal was measured three hours after collection by counting with a spectrometer the γ-rays from the ^{214}Pb and ^{214}Bi daughters.

Stability values—differences between temperatures at elevations of 30 and 3 meters—were obtained from records of the U. S. Weather Bureau station at Gest St., 6 miles from the laboratory and in a topographically similar location. Stability records were begun in 1962. Hourly values were averaged for 3, 6, 9, 12, and 15 hours before collecting the radon-daughter filter and then averaged for each month. Average daily temperatures at the same location were also obtained from this source and converted to monthly averages. Hourly precipitation data at Abbe Observatory, 1 mile from the laboratory, were also obtained from the U. S. Weather Bureau. Monthly averages were derived for TMD calculations, and monthly averages for the 12 hours prior to filter collection were computed to evaluate the combined effect of stability and rainfall.

Total moisture detention was computed by a monthly bookkeeping procedure developed by Thornthwaite for precipitation, evapotranspiration, storage of water in the ground and as snow, and run-off (*15*). Briefly, TMD values are derived from the mean monthly rainfall at Cincinnati, an average water-holding capacity of soil at Cincinnati of 300 mm. (*16*), and potential evapotranspiration values that were obtained from a nomogram based on mean monthly temperatures and the number of daylight hours. Every month, the retained rainfall is added to, and evapotranspiration subtracted from, the water stored during the previous months. When the water-holding capacity of the soil is reached, the *TMD* remains constant, subject to the retention of additional water as snow and ice, and the presence of some water in the process of running off. Thornthwaite provides examples of this lengthy but not complex procedure (*15*).

Table I. Average Monthly Morning Radon-222 Concentrations, pCi/cu. meter

Month	*1959*	*1960*	*1961*	*1962*	*1963*	*1964*	*1965*	*1966*	*Average*
Jan.	230	170	310	180	350	390	260	270	270
Feb.	240	160	280	130	200	360	240	210	230
March	270	150	120	180	120	—	120	280	180
April	—	320	170	360	260	170	200	200	240
May	—	290	230	420	320	350	400	400	340
June	390	280	450	470	580	420	300	720	450
July	540	610	440	490	590	640	610	590	560
Aug.	840	580	640	640	720	640	700	970	710
Sept.	700	790	570	560	1050	870	530	690	720
Oct.	620	660	820	500	1520	1130	440	910	830
Nov.	310	320	360	460	620	660	440	370	440
Dec.	280	210	240	470	410	390	410	280	310

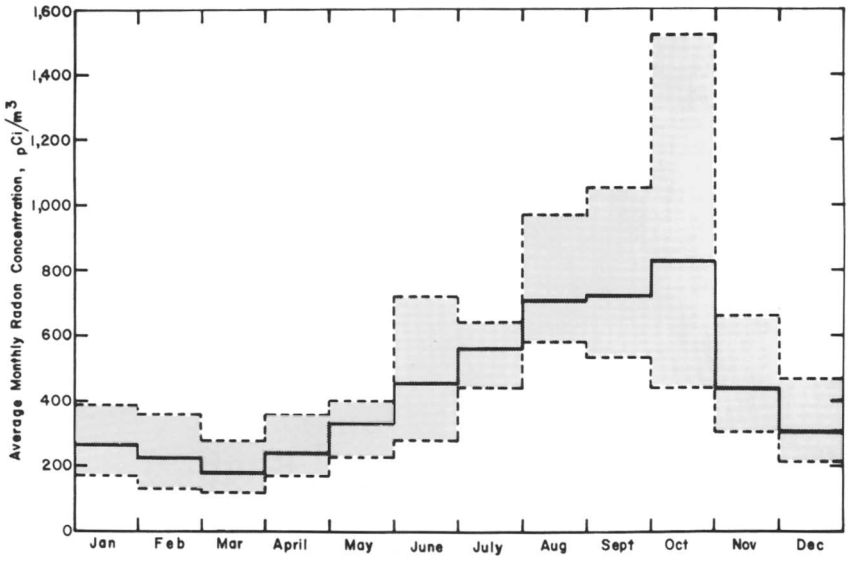

Figure 1. Mean and extreme average monthly morning radon concentrations, 1959–1966

Results and Discussion

Average monthly morning radon concentrations in air computed from radon-daughter measurements (Table I and Figure 1) consistently reached annual maxima during August–October and minima during February–April. Individual monthly averages ranged from 120 to 1520 pCi./cu. meters, and October averages in the eight-year period were more

than four times as high as March averages. The same pattern has been observed at other inland locations (*5, 7, 9*), but it is not universally applicable (*7*).

Monthly averages based on daily average radon concentrations would differ from the values in Table I and Figure 1 in that (a) morning values usually are daily maxima, and (b) radon concentrations appear to be underestimated by measuring radon daughters. At Livermore, Calif., for example, afternoon radon concentrations (usually the daily minima) were on the average 0.5 of morning values (*5*), and the average concentration measured in the morning by radon daughters relative to direct measurement was 0.77 ± 0.09 (*6*). At Cincinnati, the average ratio of 8:30 a.m. to 3:00 p.m. concentrations was 0.41 ± .18 (1 σ of individual monthly values) from 1959 to 1962 (*1*). The average ratio of morning radon concentration by radon-daughter measurement to direct measurement was 0.87 ± 0.14 (1 σ of individual values), as measured in this study. Neither ratio varied greatly from month to month. Thus, the average computed from the mean of maximum and minimum daily values would be approximately $(1 + 0.41)/(2 \times 0.87) = 0.8$ of the values shown in Table I and Figure 1.

To indicate numerically the correlation of trends for average monthly radon concentrations in air, nighttime atmospheric stability, and soil moisture content, coefficients for alternative simple empirical equations were obtained by least-square analysis:

$$C = k_1 S + k_2 (TMD)^{-1} + k_3 \quad (1)$$

and

$$\ln C = k_1' S - k_2' (TMD) + k_3' \quad (2)$$

C is the average monthly morning radon concentration in pCi./cu. meter computed from radon daughter measurements, S is the stability in °F./27 meters, and TMD is the total moisture detention in mm. The constants k and k' and the correlation coefficients for the equations were obtained for all three variables and also separately for C *vs.* stability and C *vs.* TMD.

Figure 2 shows the trend in average monthly radon concentrations with average monthly nighttime atmospheric stability. The squared correlation coefficients, R^2, of 0.53 and 0.54 (F ratios of 54 and 56) indicate that the two variables are definitely correlated. The scattering of values about the curves in Figure 2, however, suggests that the indicated equations do not alone explain the variation in radon concentrations. [R^2 provides the F ratio according to:

$$F \text{ ratio} = \frac{(n - p)R^2}{1 - R^2}$$

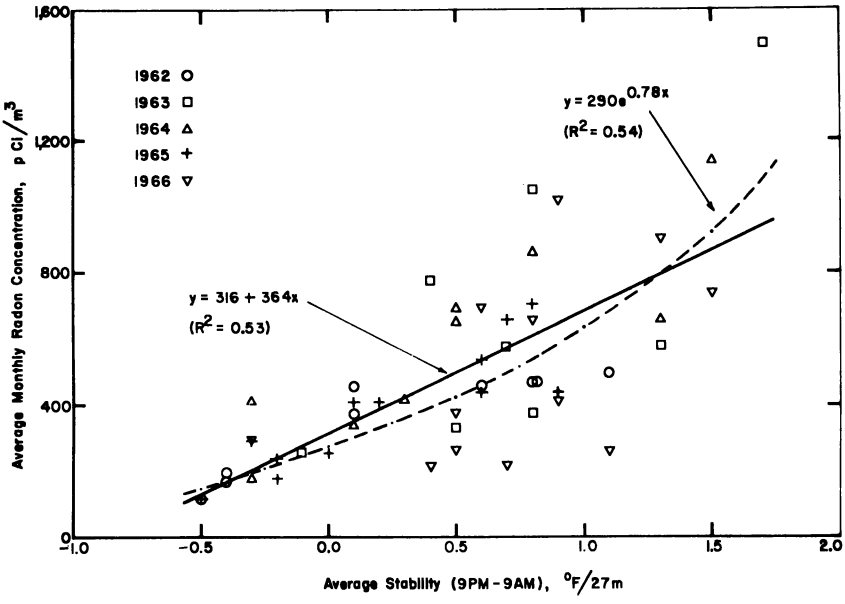

Figure 2. Average monthly radon concentration as function of stability

where n is the number of observations, and p is the number of parameters. In this study, $n = 50$, and $p = 2$ or 3. Relations are significant according to the F ratio at the 99.9% confidence level if $F > 13$.]

The 12-hour averages for stability used in Figure 2 yield a higher correlation than averages over shorter or longer periods as shown below:

Period	R^2
3 hours	0.05
6	0.32
9	0.46
12	0.53
15	0.51

That the R^2 value for the 12-hour period is largest suggests that radon-daughter measurements were affected more by the accumulation of radon near ground level during the entire night than by the accumulation of the short lived radon daughters in air immediately before collection.

Precipitation during the 12-hour period before filter collection decreased the radon concentration, as shown in Table II for three stability categories. The effect is especially apparent at high stabilities: radon concentrations were almost two-fold lower during precepitation at sta-

Table II. Effect of Stability and Rainfall on Average Morning Radon Concentrations, pCi/cu. meter

	Average Stability (9 p.m.–9 a.m.), °F./27 meters		
Precipitation	*<−0.5*	*−0.5 to 0.5*	*>0.5*
none	194 (91)[a]	337 (281)	793 (290)
>0.01 inch	158 (16)	218 (54)	398 (17)

[a] Number of values in parentheses.

Table III. Total Moisture Detention in Soil at Cincinnati, Ohio, mm.

Month	*1962*	*1963*	*1964*	*1965*	*1966*
Jan.	405	321	187	331	387
Feb.	464	344	227	383	417
March	450	452	398	378	382
April	351	388	408	387	392
May	314	364	279	257	328
June	226	244	277	177	223
July	239	197	186	141	147
Aug.	172	154	136	113	116
Sept.	156	116	119	201	144
Oct.	191	91	107	254	129
Nov.	229	89	146	280	217
Dec.	269	112	256	296	300

bility values above 0.5 °F./27 meters. A decrease of radon concentration after rain had been noted previously (*1, 2*), and can be ascribed to washout of radon and/or its daughters from air and to a reduction of radon diffusion through the ground when the surface soil is moist.

The pattern of high *TMD* values in late winter and low values in late summer is shown in Table III, and the high degree of predictive power of both equations for average radon concentrations in air from *TMD* values is apparent in Figure 3. For the linear relation, R^2 is 0.84, and the *F* ratio is 252; the logarithmic relation is correlated only slightly less ($R^2 = 0.79$, *F* ratio = 181).

Prediction of average monthly morning concentrations in air is further improved by considering both stability and *TMD;* by least-squares analysis, Equations 1 and 2 are:

$$C = 139\,S + 93{,}000\,(TMD)^{-1} - 14 \qquad [R^2 = 0.89] \qquad (1a)$$

and

$$\ln C = 0.332\,S - 0.00384\,(TMD) + 6.877 \qquad [R^2 = 0.89] \qquad (1b)$$

The *F* ratios equal 380, and the two equations are the same in their over-all predictive power. Different values are predicted for individual months, however, as shown in Figures 4 and 5. Both equations predict

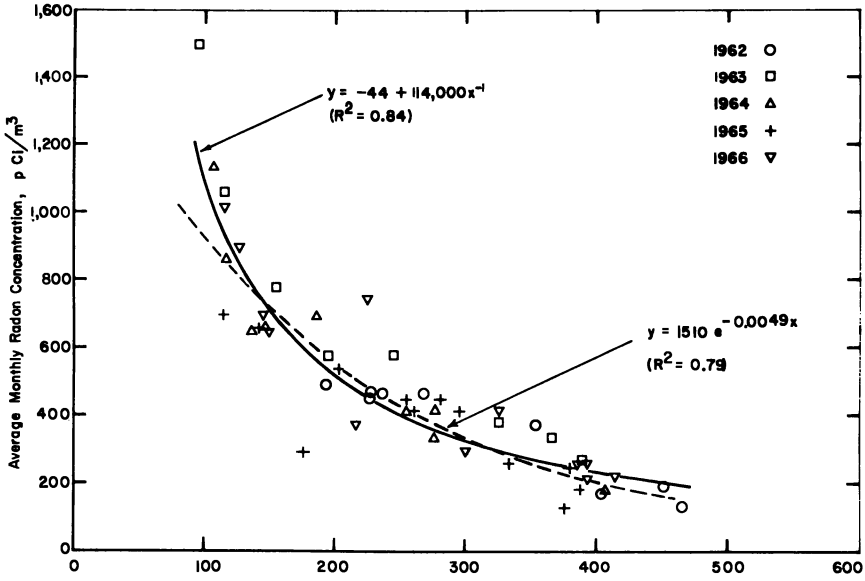

Figure 3. Average monthly radon concentration as function of total moisture detention in soil

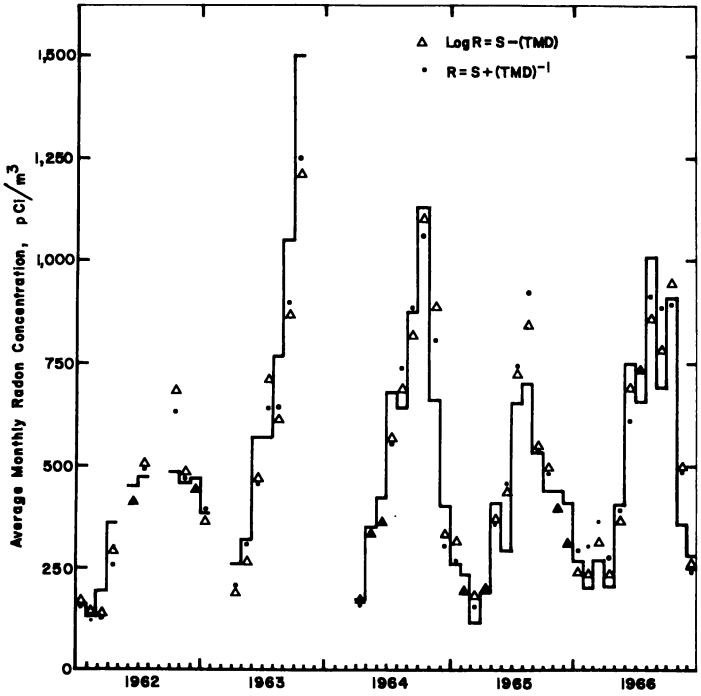

Figure 4. Measured average monthly radon concentration vs. values predicted from stability and total moisture detention in soil

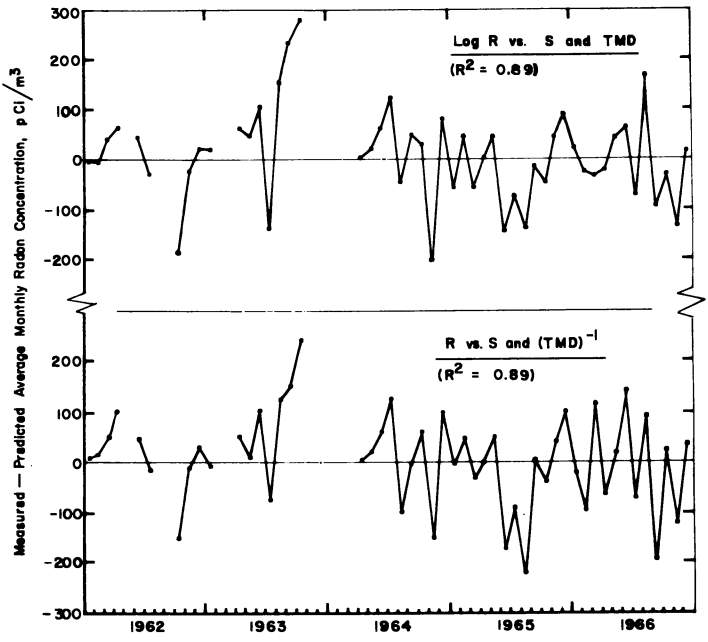

Figure 5. Difference between measured average monthly radon concentrations and values predicted from stability and total moisture detention in soil

all but two of the 50 values within less than 200 pCi./cu. meter, and the average error in prediction is 20%, compared with an average 58% error if the over-all average were predicted for every month.

It would be highly unreasonable to ascribe all variability in radon concentrations at a given location solely to variations in stability and soil moisture content, and contribution from the other cited factors would be expected to improve these predictions. Differences between predicted and measured averages are especially noticeable during high radon concentrations, in that predicted values vary less from year to year than do the measured values. The high degree of correlation, however, indicates that the monthly average radon concentrations in air were reasonably well predicted by monthly *TMD* and atmospheric stability data.

Conclusion

Monthly average ^{222}Rn concentrations in air during 1959–1966, measured daily at 8:30 a.m. by counting α-particles emitted by the short lived ^{214}Po daughter in 24-hour samples of airborne particles, showed an annual maximum in August–October and minimum in February–April.

The maximum eight-year average was 830 pCi./cu. meters in October, and the minimum was 180 pCi./cu. meters in March. Values measured at 3:00 p.m. during 1959–1962 showed the same annual pattern, but monthly averages were only 0.41 as high as morning values. The average ratio of radon concentrations computed from radon-daughter measurements to directly measured radon concentrations during 1965 was 0.87.

Average monthly morning concentrations of radon in air increased with average monthly values of atmospheric stability during the 12 hours before filter collection, but there was appreciable scatter of values about lines of best fit. The squared correlation coefficient was 0.53 for a linear relation between radon concentration and stability. Lower correlations applied to stability values averaged over periods longer or shorter than 12 hours. Precipitation during the 12-hour period before collection decreased radon concentrations.

Average monthly morning radon concentration varied inversely with soil moisture content, expressed in terms of Thornthwaite's total moisture detention. The two variables were highly correlated, the squared correlation coefficient being 0.84. By relating radon concentration in air to both *TMD* and stability, the squared correlation coefficient increased to 0.89. An alternative mathematical relation, the logarithm of the radon concentration *vs. TMD* and stability, showed identical correlation.

Acknowledgment

We thank the Cincinnati Station of the U. S. Weather Bureau for making data available to us, and David Smith of this laboratory for discussing the effect of meteorological parameters.

Literature Cited

(1) Gold, S., Barkhau, H. W., Shleien, B., Kahn, B., "The Natural Radiation Environment," J. A. S. Adams and W. M. Lowder, Eds., p. 369, University of Chicago Press, Chicago, 1964.
(2) Hosler, C. R., *Monthly Weather Rev.* **94,** 89 (1966).
(3) Hosler, C. R., Lockhart, Jr., L. B., *J. Geophys. Res.* **70,** 4537 (1965).
(4) Kraner, H. W., Schroeder, G. L., Evans, R. D., "The Natural Radiation Environment," J. A. S. Adams and W. M. Lowder, Eds., p. 191, University of Chicago Press, Chicago, 1964.
(5) Lindeken, C. L., University of California, Lawrence Radiation Laboratory, **UCRL-50007-66-1,** 41 (1966).
(6) Lindeken, C. L., *J. Geophys. Res.* **73,** 2823 (1968).
(7) Lockhart, Jr., L. B., "The Natural Radiation Environment," J. A. S. Adams and W. M. Lowder, Eds., p. 331, University of Chicago Press, Chicago, 1964.
(8) Moses, H., **ANL-6398,** 86 (1961).
(9) Moses, H., Lucas, Jr., H. F., Zerbe, G. A., *J. Air Poll. Control Assoc.* **13,** 12 (1963).
(10) Pearson, J. E., Jones, G. E., *J. Geophys. Res.* **70,** 5279 (1965).

(11) Schroeder, G. L., Kraner, H. W., Evans, R. D., *J. Geophys. Res.* **70,** 471 (1965).
(12) Servant, J., **CEA-R 2434** (1964).
(13) Shleien, B., *Am. Ind. Hygiene Assoc. J.* **24,** 180 (1963).
(14) Tanner, A. B., "The Natural Radiation Environment," J. A. S. Adams and W. M. Lowder, Eds., p. 161, University of Chicago Press, Chicago, 1964.
(15) Thornthwaite, C. W., Mather, J. R., Drexel Institute of Technology, *Publ. Climatology* **8,** (1) (1955).
(16) Thornthwaite, C. W. *et al.*, Drexel Institute of Technology, *Publ. Climatology* **17,** (3) (1964).

RECEIVED June 16, 1968.

Radiochemical Dating of Nuclear Weapon Debris Precipitated from Cyclonic Storms over the California Coast

PAUL KRUGER

Civil Engineering Department, Stanford University, Stanford, Calif. 94305

Radiochemical analyses of the fission products ^{140}Ba, ^{89}Sr, and ^{90}Sr in precipitation from three Pacific cyclones were examined as functions of time and latitude along the California coast to estimate the fractional contribution of nuclear debris from recent nuclear weapons tests. The estimates are based upon the assumptions that the observed fission products originated solely from announced tests in the atmosphere and were produced with the same relative yields as those reported for U. S. nuclear weapons. The analyses show evidences of fractionation of these fission products in the precipitation along the coast in each of the three cyclone storms studied. In accordance with the given assumptions, the fractionation seems to be associated with the precipitation patterns resulting from the meteorological features of the storms.

Radiochemical methods have proved effective for studying fractionation of radionuclides resulting from atmospheric nuclear weapon tests and the deposition of these radionuclides by meteorological processes.

The phenomena of fractionation have been studied extensively by many investigators. The extent of fractionation was shown to depend on many parameters, such as the total yield and height of the detonation and the amount and chemical composition of the earth's surface affected by the fireball. Freiling (7) distinguished between primary fractionation, resulting from processes occurring during the condensation of the fireball materials and secondary fractionation, resulting from the further contact of the condensed debris with the immediate environmental

materials. It was further shown (*8*) that radionuclide fractionation occurs even in air bursts, where the fireball does not affect the earth's surface. Potential and actual fractionation for airburst debris were distinguished, where potential fractionation was defined to exist when the radiochemical composition varies among the aerosol particles, by size, density, macroscopic composition, or history in the fireball, even though these particles contain totally among themselves an unfractionated composition of the radionuclides. Potential fractionation of the debris from air bursts has been shown (*2*). Freiling and Kay (*8*) suggested that to achieve an actual fractionation, a particle-separation process must occur—*e.g.*, as a result of unequal rates of sedimentation through the atmosphere over long periods of time.

It is well established that in non-arid regions, precipitation is the primary means by which contaminating aerosols are removed from the atmosphere. Many chemical, physical, and meteorological parameters affect the micro, meso, and synoptic scale processes through which precipitation transports radioactive aerosols from atmosphere to ground. These parameters include the radioactivity component of the natural aerosols, the processes by which water vapor condenses and grows to raindrops, and the incorporation of the radioactive aerosol into the precipitation. Thus, the prediction of specific deposition from fundamental considerations has proved to be difficult because of the many uncertainties yet prevalent in these processes. Many attempts have been made to evaluate the deposition of these aerosols by empirical studies.

The initial distribution of radioaerosols from an atmospheric nuclear explosion depends upon condensation and coagulation during the rise and cooling of the fireball. These processes result in small particle sizes of the nuclear weapon debris. For example, Stewart (*24*) calculated that for yields of about 20 kilotons, the particles coagulated from vaporized materials will reappear as very small particles (with modal radii of the order of 0.1 to 0.01μ) and remain airborne for long periods. When such particles are carried into the stratosphere by the buoyant lifting of the fireball, it is expected that they will become a quasi-conservative constituent of the stratospheric air. It has been shown that particles with diameters less than 1μ have an essentially infinite residence in the atmosphere for sedimentation processes alone (*16*).

The transport of stratospheric air and the contained aerosol particles has been examined by many investigators. For example, the intrusion of stratospheric air into the troposphere has been demonstrated by Danielson (*5*). Such intrusions occur frequently in association with cyclonic disturbances (*23*). In the troposphere, the aerosol particles may be removed effectively by precipitation processes. They may be removed by collisions between the aerosol particles and cloud or rain drops (*9*).

Aerosol particles of the size likely to contain the nuclear weapon debris radionuclides and to come from stratospheric air masses are also more likely to serve efficiently as precipitation nuclei (*13*). Either of these two precipitation removal processes could result in the actual fractionation of potentially fractionated nuclear weapon debris.

The possibility of meteorological fractionation of nuclear weapon debris has been suggested. For example, Storebö (*25*) observed more short lived fission products at a mountain station in Norway compared with those at lowland stations. He suggested that the short lived fission products were on larger particles which should be transported more easily downward by rain than smaller particles. However, another change in the radioactivity composition during a single rain has been explained with the assumption that the first rain fractions collected contained a larger number of very small particles which were potentially fractionated (*20*). The assumption was attributed to the observation of Greenfield (*9*) that collection efficiencies of 20-μ diameter raindrops was very high for aerosol particles with radius less than about 0.01μ.

Radiochemistry offers an excellent method for further examination of meteorological fractionation of nuclear weapon debris, especially during periods when known single sources of nuclear weapons testing has occurred. Three of the more biologically important fission products are 12.8-day ^{140}Ba, 50.5-day ^{89}Sr, and 27.7-year ^{90}Sr. These alkaline-earth element radionuclides have in common their production as secondary fission products from decay of rare-gas element primary fission products, high solubility in most chemical forms, and biological similarity to calcium, an element important in man. The characteristics of the decay chains leading to these three fission products are given in Table I. The relative production values for the underlined nuclide in each chain are for fission yields reported for nuclear weapon explosives (*12*). Barium and strontium have boiling points over 1100°C. and are considered to be refractory elements. However, their condensation properties during the early history of the fireball are determined by their volatile and rare-gas element precursors. Thus, during the cooling of the rapidly rising fireball, the formation of the three radionuclides by β-decay of their gaseous precursors takes place at different rates. ^{140}Ba, having the shortest lived precursors condenses first; ^{90}Sr condenses next; ^{89}Sr condenses last. Thus, these three radionuclides may be potential fractionated by being distributed unequally among the aerosol particles contained in stratospheric air masses.

The differences in condensation history of the three alkaline-earth element fission products allows examination of their radioactivity ratio as a method for determining fractionation. The recent atmospheric

Table I. Characteristics of the

Mass No.	*First Nuclide*	*Second Nuclide*	*Third Nuclide*
89	~2-sec. ^{89}Se (17)	4.5-sec. ^{89}Br (37)	3.16-min. ^{89}Kr (53)
90	~3-sec. ^{90}Br (17)	33-sec. ^{90}Kr (57)	2.7-min. ^{90}Rb (26)
140	~1.5-sec. ^{140}I (7)	16-sec. ^{140}Xe (49)	66-sec. ^{140}Cs (40)

[a] From Freiling and Kay (*8*); values in parenthesis are the fractional chain yield calculated by the theory of Present (*22*). The relative production values are from Harley

nuclear weapons tests on the China mainland offered an opportunity to use this method to examine the possibility of meteorological fractionation in precipitation from cyclonic storms affecting the California coast.

Radionuclide concentrations in precipitation reaching the ground depend upon many meteorological parameters. The concentration is influenced by the amount of radioactivity incorporated into the precipitation and the amount of precipitation reaching the ground. These two, in turn, may be divided conveniently into the following six parameters: (1) the height of the precipitation generating level, (2) the precipitation generation and growth mechanisms in the cloud, (3) the amount and characteristics of the radioactive aerosols initially in the air masses participating in the precipitation process, (4) the specific humidity at the generating level, (5) the previous precipitation experience of the air at the generating level, and (6) the descent experience of the precipitation from the cloud in which the precipitation originates to the ground.

Some of the major precipitation-producing storm systems include extratropical cyclones, convective showers, severe storms, and orographic lifting. Many of these storm types have been examined for their radioactivity deposition characteristics. One of the more important types of storms, both in duration and areal extent, is the extratropical cyclone, which in the United States, generally may last for days and cover thousands of miles of trajectory and width. An examination of deposition from extratropical cyclones in Pennsylvania was given by Kruger, Hosler, and Davis (*18*). Several meteorological parameters were observed to influence the deposition of radioactive aerosols (*i.e.*, 27.7-year ^{90}Sr). These included the effects of frontal and trough passage, the changes in precipitation growth processes, the gradient of radioactive aerosol in the cloud and in the different air masses, the amount and rate of rainfall, and the effects of evaporation below the cloud bases.

A = 89, 90, 140 Decay Chains[a]

Fourth Nuclide	*Last Radioactive Nuclide*	*Relative Production (HASL-164)*
15.4-min. ^{89}Rb (10)	50.4-day ^{89}Sr (0)	147
27.7-yr. ^{90}Sr (0) / (1384)	61-hr. ^{90}Y (0)	1
12.8-day ^{140}Ba (3) / (1140)	40-hr. ^{140}La (0)	1170

et al. (*12*) for weapon fission yields. The boiling point for the element is given below in °C.

Pacific cyclones represent the major source of precipitation over the western United States. Therefore, they also represent a major source of deposition of contaminant aerosols in the waters of these states. The examination of radioactive aerosols in precipitation resulting from Pacific cyclones is thus of interest in understanding the transport of atmospheric aerosols to the ground by precipitation.

A study of a Pacific Coast cyclone at Santa Barbara, Calif. on Feb. 7, 1962, has been reported (*19*). The effects of the overturning of the marine layer and the passage of the surface front and the troughline at 500 mbars, on the observed concentrations of ^{89}Sr and ^{90}Sr in the precipitation were noted. Similar effects have been noted at other locations—*e.g.*, a change of radioactivity concentration during the passage of a cold front over the Netherlands (3) and a marked change in ^{90}Sr concentration in rainfall associated with the presence of a trough at 500 mbars (*21*).

During the winters of 1966-1967 and 1967-1968, cyclonic storms occurred over the California coast on three occasions shortly after the detonation of a nuclear weapon on the China mainland such that measurable concentrations of 12.8-day ^{140}Ba were present in 6-hour rainfall samples. The deposition radioactivity ratios of ^{140}Ba, ^{89}Sr, and ^{90}Sr were examined in the rainfall along the California coast for each of these three storms and used to examine the fractional contribution of the longer lived strontium radionuclides from the various known Chinese nuclear explosions.

Experimental Results

A precipitation-collection network is maintained at 11 sites along the California coast. Each site has an identical stainless-steel funnel with an area of 3.62 sq. meters; rainfall drains through a small valve into polyethylene bottles. Arrangements have been made for collecting rainfall in prearranged collection increments from specific storms. The locations

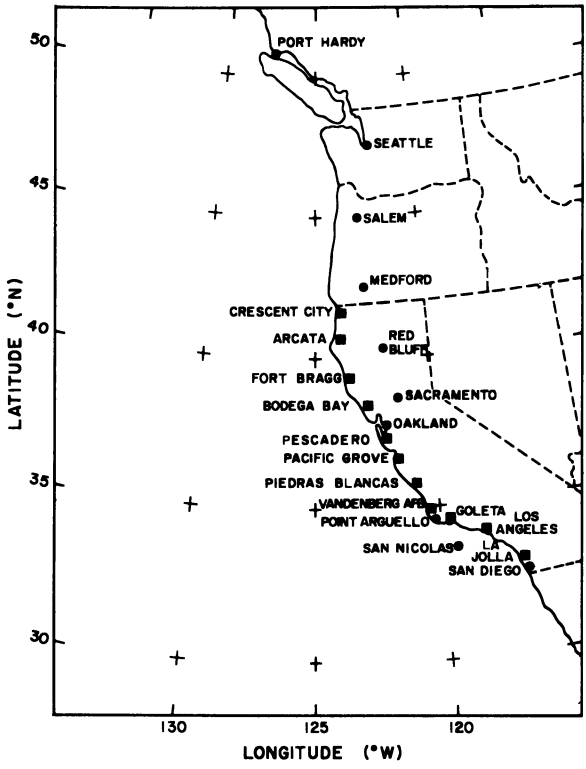

Figure 1. Collection sites along the California coast (rectangles) and the ESSA weather stations (circles)

of the collection sites are shown in Figure 1. The corresponding meteorological data for each storm are obtained from the several ESSA Weather Bureau stations also shown in Figure 1. For each storm, vertical cross sections of the atmosphere are constructed from the available radiosonde data, and the synoptic conditions are taken from the surface, 500 mbars, 300 mbars, and other facsimile charts.

Radiochemical analyses for ^{140}Ba, ^{89}Sr, and ^{90}Sr are made for each of the rain samples collected at each site affected by the storm. Standard radiochemical procedures (*11*) are used. The rainfall is acidified with HNO_3, and barium and strontium carriers are added with mixing to ensure exchange of carrier and radioisotopes. The sample is made basic with NH_4OH and run through an ion-exchange column containing Chelex-100 anion exchange resin in the ammonium form. The barium and strontium carriers are eluted with HNO_3 and evaporated to fumes to precipitate $Ba(NO_3)_2$ and $Sr(NO_3)_2$. Following dissolution and $Fe(OH)_3$ scavenging precipitations, the barium is separated as $BaCrO_4$. The strontium is precipitated as $SrCO_3$ for chemical yield determination. After reestablishment of the ^{90}Sr — ^{90}Y radioactivity equilibrium, ^{90}Y is removed quantitatively. The radioactivity measurements of the ^{140}Ba —

^{140}La, the $^{89}Sr + {}^{90}Sr$, and the ^{90}Y samples are determined in low background (0.2 c.p.m.) anti-coincidence β-counters having a sensitivity for measurement of β-activity of < 1 d.p.m. The disintegration rates are extrapolated back from time of measurement to midtime of the rainfall collection period.

Repeated analysis of ^{90}Sr standards shows a standard deviation for single measurements of about $\pm 5\%$. For the ^{140}Ba concentrations prevalent during the measurement periods, the standard deviations for single measurements were estimated to be about ± 10 to $\pm 20\%$. The reproducibility of the analytical procedures was checked with the large 146.4-liter sample from Bodega Bay for the January 1968 storm by dividing it into two equal aliquots and analyzing them as two independent samples. Table II shows that the spread in the duplicate values ranged from 1.5 to 4% for these relatively high activity samples. The ^{89}Sr value, obtained from the difference in activity of its $^{89}Sr + {}^{90}Sr$ sample free of ^{90}Y, and the ^{90}Sr value determined from the ^{90}Y measurement, shows the greater average deviation. In general, the ^{89}Sr activities were sufficiently greater than the ^{90}Sr activity (ratios ranging from 3 to 60) such that the standard deviations of the ^{89}Sr activity were of the order of ± 10 to $\pm 20\%$.

Table II. Reproducibility Measured for a Split Sample

Concentration, d.p.m./liter			*Percent Deviation,* $\frac{\Delta C}{C} \times 100$		
^{140}Ba	^{89}Sr	^{90}Sr	^{140}Ba	^{89}Sr	^{90}Sr
55.8	25.3	1.15	2.1	4.0	1.3
53.5	27.4	1.12			

During each winter rainy season, meteorological alert was established after each of the Chinese nuclear weapons tests: October 1966, December 1966, and December 1967. The criteria used to alert the collection network of a forecasted storm system included the presence of a well-defined jet stream and a forecast for precipitation in excess of 3 mm. over a majority of the sampling sites.

A cyclonic storm satisfying these criteria moved in over the California coast within 25 days after each of these three nuclear explosions affording high probability that the ^{140}Ba from the latest explosion would be measurable with adequate precision. The three Pacific cyclones examined occurred during Nov. 15-17, 1966, Jan. 20-22, 1967, and Jan. 8-11, 1968. Each of these storms exhibited different meteorological characteristics. To assist in evaluating the radiochemical data, each storm was analyzed.

Storm of Nov. 15-17, 1966. The large-scale circulation pattern leading up to this storm period was characterized by a strong blocking high building over western Canada and extending into the central Pacific. The storm which affected the California coast developed out of a deep low pressure system which moved into eastern Pacific offshore Oregon-Washington coast.

The associated frontal system moved across the Pacific northwest states into northern California and became quasi-stationary in that position on November 15. The positions of the surface front taken from the surface charts for Nov. 15-17, 1966, are shown in Figure 2. Subsequent wave developments on this front resulted in heavy precipitation in northern California throughout November 15, and into the morning of November 16 before the front started to push southward along the California coast.

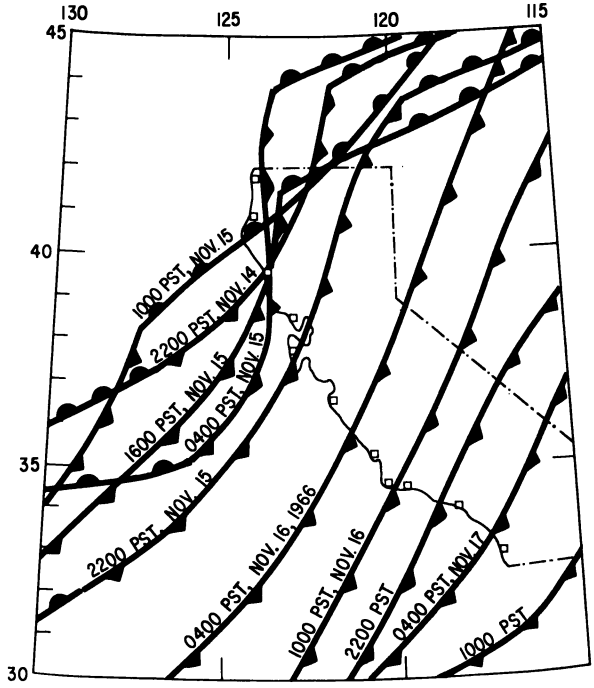

Figure 2. The 6-hourly frontal positions for the storm of Nov. 15-17, 1966

The 0400 PST upper circulation patterns at the 500-mbar level for the Nov. 15-17 period are shown in Figure 3. A deep cold low remained nearly stationary offshore Vancouver Island during this storm period,

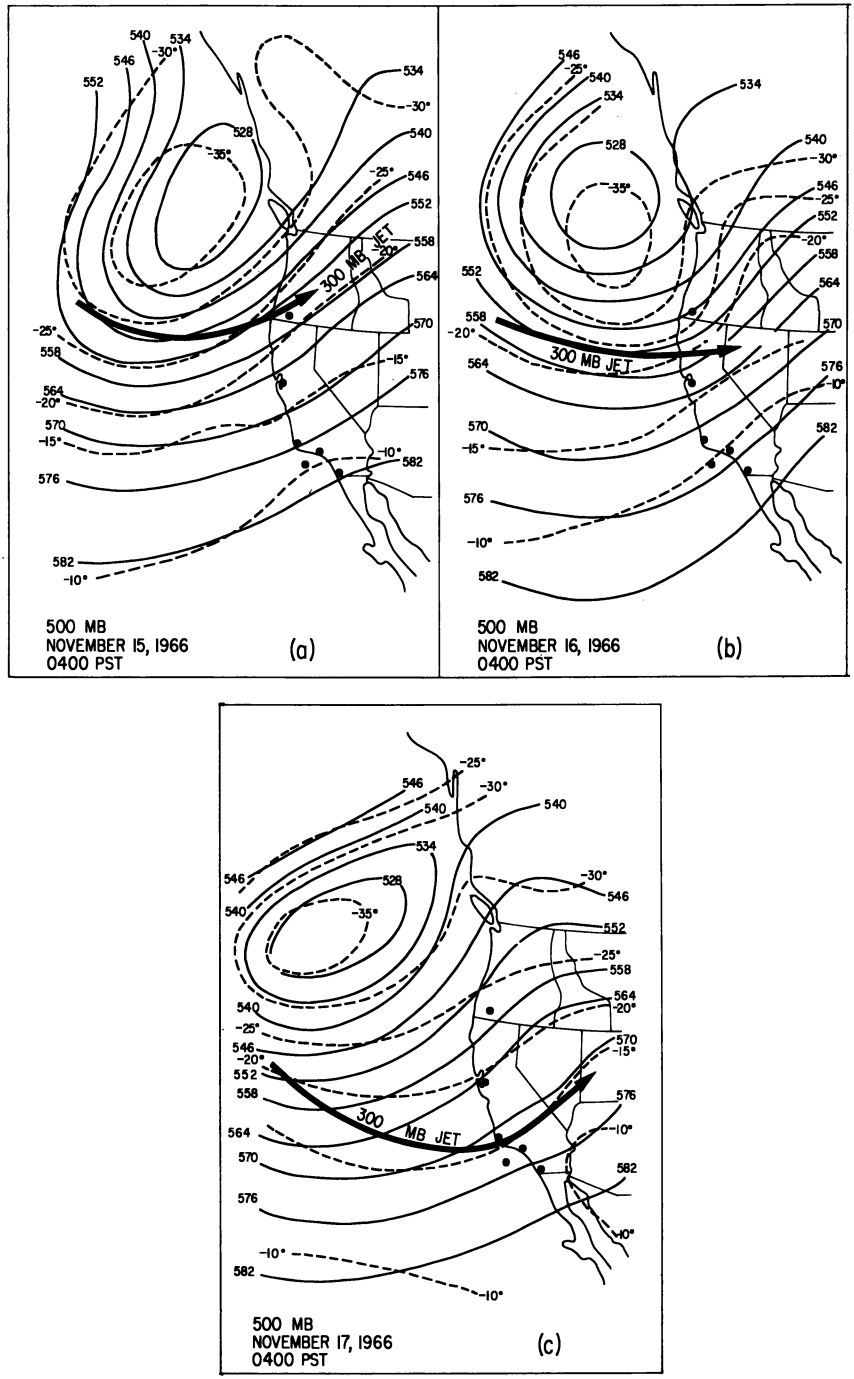

Figure 3. 0400 PST upper circulation patterns at the 500-mbar level and location of the jet stream for Nov. 15-17, 1966

while the jet stream at the 300-mbar level shifted southward from southern Oregon to near Vandenberg in southern California.

The southward shift of the jet stream core can be seen in more detail on the atmospheric cross sections presented in Figure 4. The cross sections extend from Medford (MFR) southward across the coastal range to Oakland (OAK) and onward to Vandenberg (VBG), San Nicolas Island (NSI), and San Diego (SAN). The partial soundings from Los Angeles (LAX) were used when available.

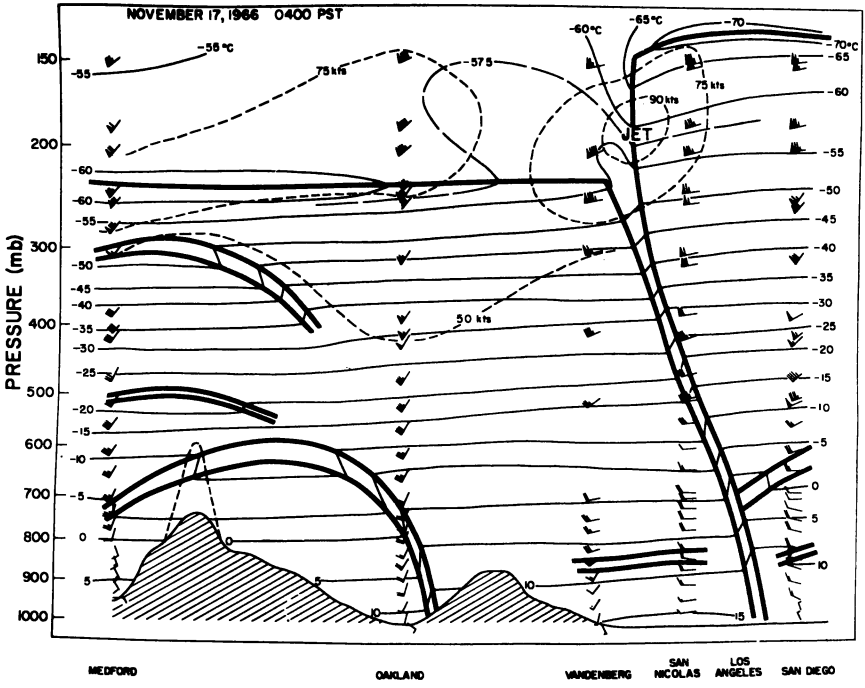

Figure 4. 0400 PST cross sections through California for Nov. 15-17, 1966

At 0400 PST, November 15, the main polar front cut across the coastal range between Medford and Oakland with the jet stream core of strength in excess of 110 knots near the 250-mbar level. This front, which remained nearly stationary until the 16th, was located between Oakland and Vandenberg with the jet stream core immediately south of Oakland showing no discernible change in its height and strength. However, during the subsequent 24 hours, the jet stream apparently weakened and lost its well-defined core as it shifted southward to near Vandenberg.

This change in strength and position of the jet stream is also reflected in the rainfall distribution observed along the coast during the

southward movement of the front. Figure 5 shows the latitudinal distribution of 6-hourly precipitation amounts relative to the time of the frontal passage.

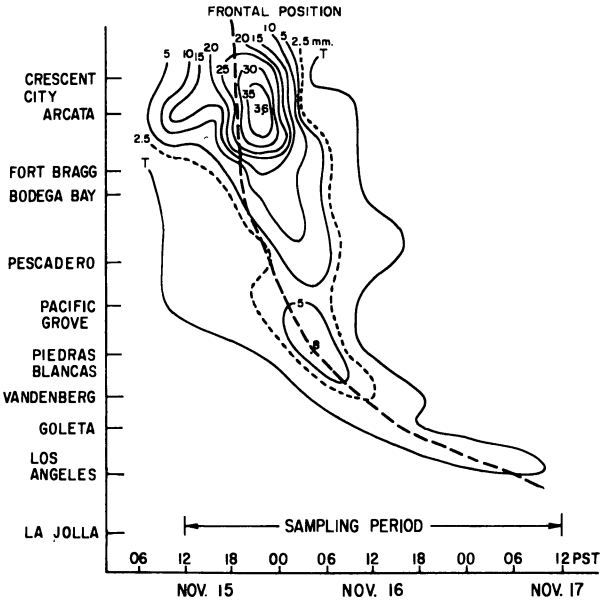

Figure 5. Time section of 6-hourly precipitation amount and frontal position along the California coast for Nov. 15-17, 1966

The isohyets show that precipitation rates in excess of 30 mm. per six hours fell in northern California near the time of the frontal passage, but as the front accelerated southward through central California the precipitation amounts decreased substantially. Thus, south of Vandenberg, where the jet stream was observed to lose its strength, the frontal precipitation was mostly in form of drizzle and light intermittent rain.

Precipitation collection was initiated at 1200 PST, November 15 and continued in 6-hour increments thereafter. From Monterey northward the collection was terminated at 1800 PST, November 16, but collections continued through southern California until 1200 PST, November 17. The rainfall and radiochemical data for this storm are given in Table III.

Storm of Jan. 20-23, 1967. The synoptic meteorological situation leading to this storm period was similar to that for the Nov. 15-17, 1966 storm. The large scale pressure distribution was again characterized by a blocking high over northwestern Canada and another strong high in the central Pacific just east of the International Date Line. A deep low pressure center developed in the Gulf of Alaska on January 19. The

Table III. Rainfall Collection
Storm of November

Collection Data Site, Times	Precip., mm.	^{140}Ba Dep., d.p.m./m.²	^{140}Ba Conc., d.p.m./l.	^{89}Sr Dep. d.p.m./m.²	^{89}Sr Conc., d.p.m./l.
Crescent City					
15:1200-15:1800	69.0	998	14.4	518	7.5
15:1800-15:2400	17.5	214	12.2	90	5.1
16:0000-16:0600	2.9	—	—	237	80.9
Arcata					
15:1200-15:1800	9.3	50	5.4	45	4.8
15:1800-15:2400	25.5	334	13.1	182	7.1
16:0000-16:0600	<0.1	—	—	—	—
Fort Bragg					
15:1200-15:1800	12.9	178	13.7	84	6.5
15:1800-15:2400	15.8	487	30.8	L	—
16:0000-16:0600	0.2	—	—	40	184.
Bodega Bay					
15:1200-15:1800	5.8	152	26.1	78	13.2
15:1800-15:2400	7.2	272	37.8	100	13.8
16:0000-16:0600	3.2	—	—	18	56.8
Pescadero					
15:1200-15:1800	10.9	310	28.4	83	7.6
15:1800-15:2400	20.0	457	22.8	157	7.8
16:0000-16:0600	4.6	117	25.5	46	9.9
Pacific Grove					
15:1200-15:1800	3.9	38	9.8	28	2.0
15:1800-15:2400	7.1	44	6.2	28	3.9
16:0000-16:0600	8.7	93	10.7	94	10.9
Piedras Blancas					
15:1200-15:1800	0.05	4	75.7	<1	<4.0
15:1800-15:2400	3.1	89	29.1	33	10.9
16:0000-16:0600	6.6	127	19.4	67	10.2
Vandenberg AFB					
16:0000-16:0600	2.1	14	6.8	7	3.4
16:1600-16:1200	0.7	—	—	5	6.4
Goleta					
16:0600-16:1200	0.2	16	71.3	8	35.5

associated frontal system moved through Washington and Oregon and became quasi-stationary in a west-southwesterly orientation through northern California and Nevada into the Pacific.

and Radiochemical Data
15–16, 1966

^{90}Sr		Ratios		
Dep.,	*Conc.,*	$\frac{^{140}Ba}{^{89}Sr}$	$\frac{^{140}Ba}{^{90}Sr}$	$\frac{^{89}Sr}{^{90}Sr}$
d.p.m./m.²	*d.p.m./l.*			
24.7	0.36	1.9	40	21
4.8	0.28	2.4	44	19
13.2	4.52	—	—	18
3.3	0.35	1.2	15	14
12.5	0.49	1.8	27	15
—	—	—	—	—
7.5	0.57	2.1	24	11
7.2	0.45	—	68	—
2.1	9.75	—	—	19
10.1	1.74	2.0	15	8
9.1	1.26	2.7	30	11
1.1	3.43	—	—	17
8.7	0.81	3.7	35	9
17.6	0.88	2.9	26	9
4.7	1.02	2.6	26	10
4.6	0.33	1.4	9	6
4.9	0.68	1.6	9	6
9.8	1.13	1.0	10	10
<0.1	<0.3	—	—	—
5.2	1.70	2.7	17	6
10.4	1.59	1.9	12	7
0.9	0.42	2.0	16	8
0.4	0.56	—	—	12
0.6	2.56	2.0	28	14

The surface frontal positions for the period Jan. 20-23, 1967 are presented in Figure 6 and show the front accelerating through central and southern California subsequent to a wave moving into Nevada on January 21.

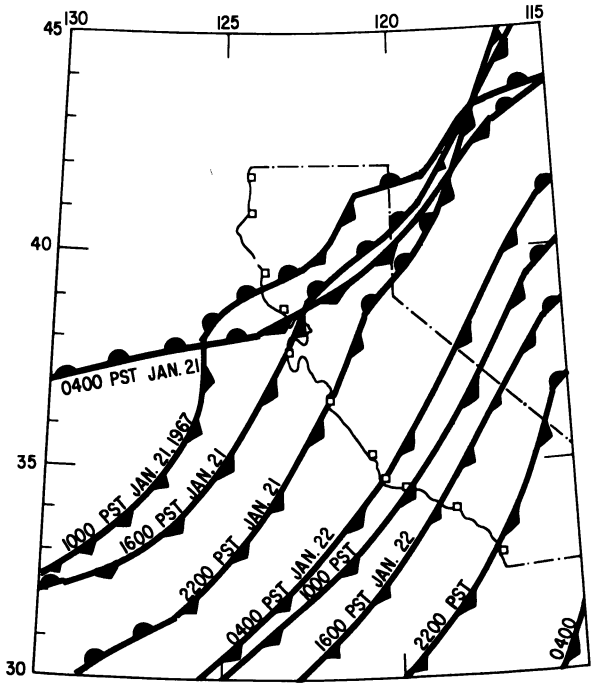

Figure 6. The 6-hourly frontal positions for the storm of Jan. 20-22, 1967

The 500-mbar charts for the same period, shown in Figure 7, reveal some basic differences in the structure between the November 1966 and January 1967 storms. In the latter, the thermal and contour fields were completely out of phase, and this baroclinic situation brought about a strong cold-air advection with deepening of the pressure trough along the West Coast. As a result, the associated jet stream, whose progress is outlined in Figure 7, moved across California into Mexico during the storm period. The isotach analysis in the atmospheric cross sections between Medford and San Diego in Figure 8 shows that the jet-stream core maintained its strength of about 150 knots as it shifted southward.

The tropopause level was near 200 mbars in the pre-frontal region, but dropped below the 300-mbar level in the post-frontal region. The strong sinking motion of the stratospheric air mass near the upper frontal zone is evident in the 10°–15°C. warming which occurred in this zone between January 21 and 23, shown in Figure 8. This rate of heating corresponds to a sinking motion of about 25 meters/hr. assuming no horizontal temperature advection. Similar computations made for the November storms shows a sinking speed of about 20 meters/hr. between the 15th and 16th when heavy precipitation fell in northern California but with

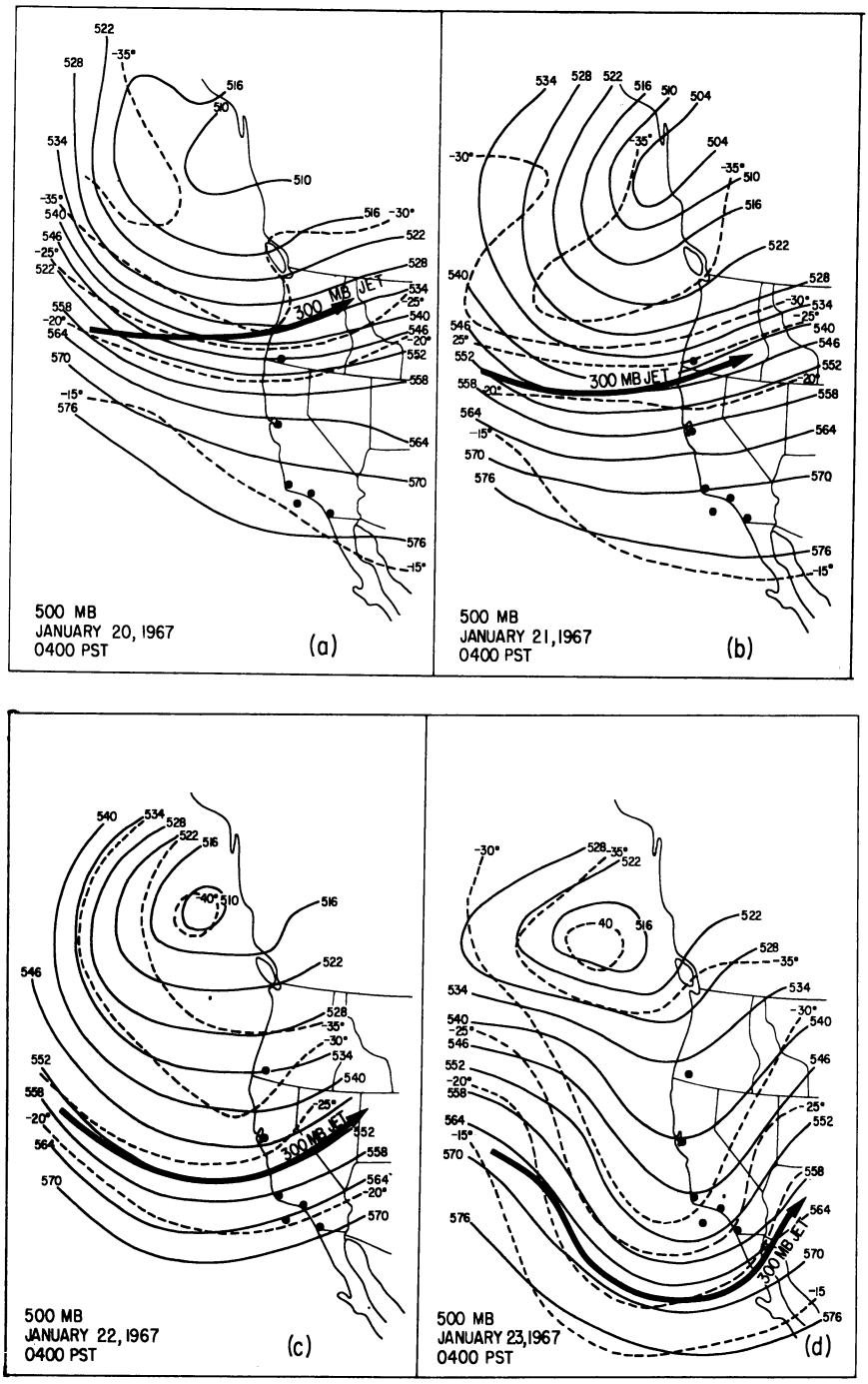

Figure 7. 0400 PST upper circulation patterns at the 500-mbar level and location of the jet stream for the period January 20-22, 1967

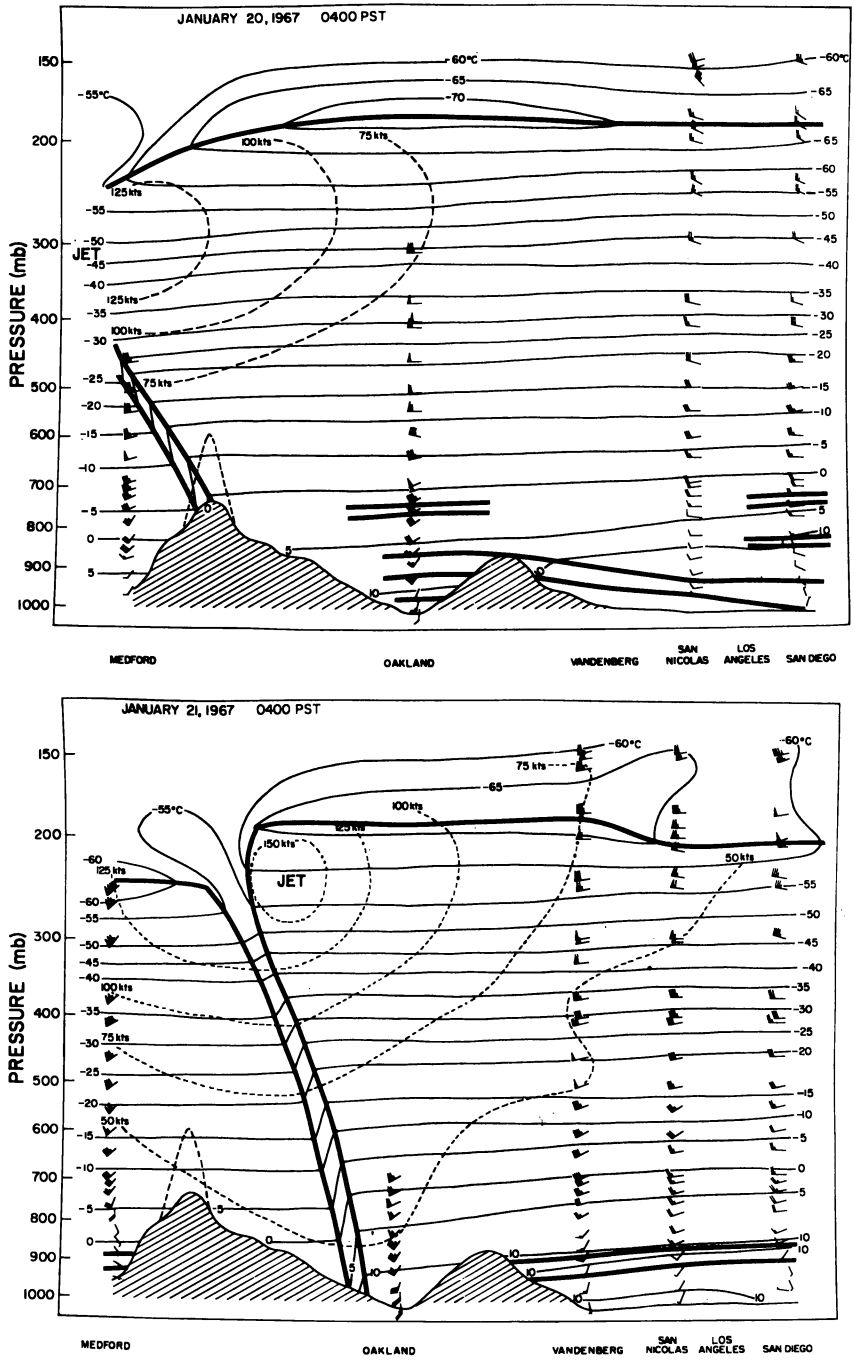

Figure 8. 0400 PST cross sections

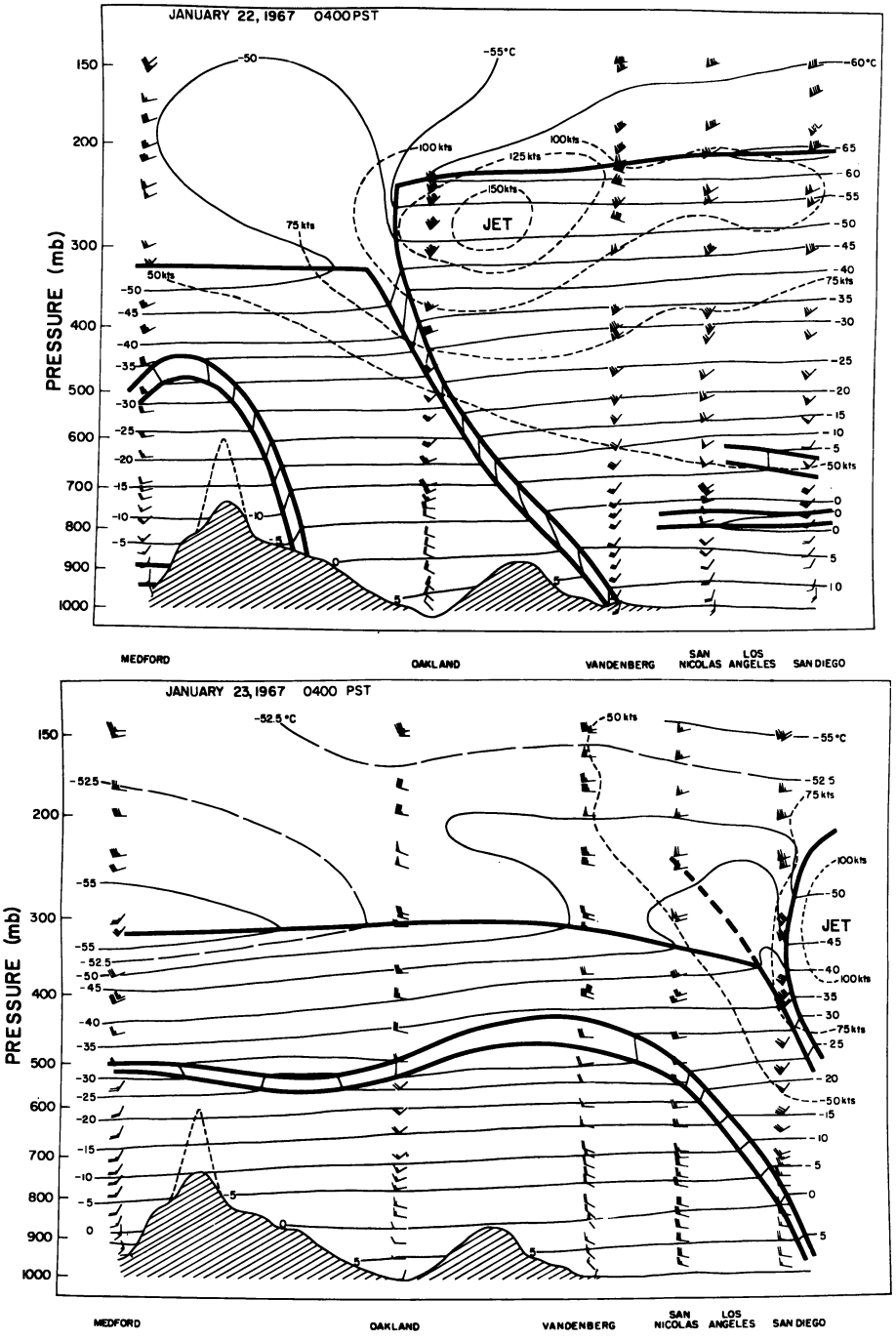

through California for Jan. 20-23, 1967

no sinking motion apparent during the subsequent 24 hours which coincided with the rapid decrease in precipitation rates.

The 6-hourly precipitation distribution for the January storm, shown in Figure 9, reflects the difference in the dynamics processes of the frontal zone between the two storms. The isohyets show an increasing 6-hourly precipitation rate as the front moved southward, reaching a maximum of over 25 mm. per six hours near San Diego which was about twice that observed in northern California, opposite the trend noted in the latitudinal distribution for the November storm.

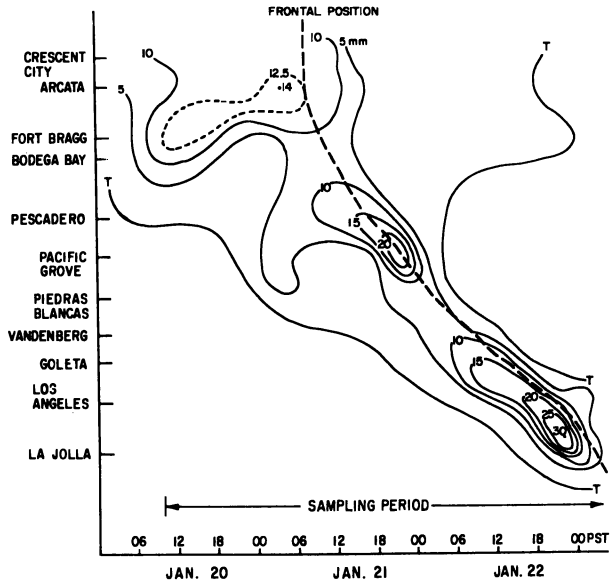

Figure 9. Time section of 6-hourly precipitation amount and frontal position along the California coast for Jan. 20-22, 1967

For this storm, precipitation collections started at 1200 PST, January 20 from Crescent City southward to Pescadero; light rain began at Vandenberg and Goleta after 1200 PST, January 21, and at La Jolla, collections did not occur until 1200 PST on January 22. The rainfall and radiochemical data for this storm are given in Table IV.

Storm of Jan. 8-11, 1968. Analysis of this storm shows that the cold front which moved into northern California during January 9 was preceded by a strong high pressure cell over the Great Basin. Considerable lifting of the air mass over the cold dome resulted well in advance of the cold front. Light precipitation started in northern California on

January 8 and became moderate to heavy with the approach of the cold front.

The 6-hourly surface positions of the frontal system are shown in Figure 10. The front weakened south of Monterey, with only light precipitation reported during the frontal passage at Paso Robles and Vandenberg Air Force Base. The 0400-PST upper circulation patterns at the 500-mbar level for the period January 9–11 are shown in Figure 11.

An added warm front-type impulse was observed in southern California well ahead of the cold front. Light rain and drizzle resulted at Vandenberg and southward at the time the cold front was approaching San Francisco. A pronounced orographic and cold-dome lifting effect was observed around Santa Barbara, accompanied by a secondary maximum in precipitation. However, the precipitation rates were generally light throughout southern California with no evidence of increased convective activity during the frontal passage.

During January 9, the jet stream located at the 40,000-ft. level moved southward to between Oakland and Vandenberg. It shifted northward to just north of Oakland by the morning of January 10 and then southward by the morning of January 11 to a region between Vandenberg and San Diego. During the same period, the tropopause lowered from near the 200-mbar level on January 9 to near 350 mbars on January 10 along the coast between Oakland and Los Angeles. Precipitation collections started at 1600 PST January 8 at Bodega Bay and continued to 0800 PST January 11 at Los Angeles. The 6-hourly precipitation pattern for the storm is shown in Figure 12. The rainfall and radiochemical data are given in Table V.

Discussion

The 6-hourly data for the storms of Nov. 15-16, 1966 and Jan. 20-23, 1966, and the longer-period data for the storm of Jan. 8-11, 1968 show many significant variations in radionuclide deposition and concentration both timewise and by collection site. For example, the data for 1200 PST to 1800 PST, Nov. 15, 1966 (in Table III) show a 250-fold range in ^{140}Ba deposition and an over 1000-fold range in precipitation. The ^{140}Ba concentration, however, showed a range of less than a factor of 5 from Crescent City to Pacific Grove, although significant differences were noted for Arcata, Bodega Bay, and Pescadero, each having about the same total rainfall. Owing to the complex nature of Pacific coast cyclonic storms, discussed earlier, such variations are not unexpected. The large areal and vertical extent of Pacific cyclones may involve radioaerosol sources ranging from stratospheric to sea-level heights and water contents influenced by long range marine conditions and by local effects from

Table IV. Rainfall Collection
Storm of January

Collection Data Site, Times	Precip., mm.	^{140}Ba Dep., d.p.m./m.²	^{140}Ba Conc., d.p.m./l.	^{89}Sr Dep., d.p.m./m.²	^{89}Sr Conc., d.p.m./l.
Crescent City					
20:1800-20:2400	11.8	147	12.4	78	6.6
21:0000-21:0600	18.5	173	9.3	107	5.7
21:0600-21:1200	13.7	138	10.1	94	6.9
21:1200-21:1800	1.2	162	134	110	91.0
21:1800-21:2400	0.7	95	134	44	62.5
22:0000-22:0600	1.0	Lost	—	Lost	—
Arcata					
20:1200-20:1800	15.6	243	15.5	69	4.4
20:1800-20:2400	15.5	48	3.1	30	2.0
21:0000-21:0600	14.5	81	5.8	54	3.7
21:0600-21:1200	10.9	64	5.9	60	5.5
21:1200-21:1800	2.6	92	35.3	69	26.6
21:1800-21:2400	0.5	60	119	17	33.9
22:0000-22:0600	0.8	58	75.0	18	22.9
Fort Bragg					
20:1200-20:1800	13.7	85	6.2	40	2.9
20:1800-20:2400	11.3	79	7.0	77	6.8
21:0000-21:0600	19.3	115	6.0	143	7.4
21:0600-21:1200	8.1	53	6.6	40	5.0
21:1200-21:1800	0.4	28	68.8	9	22.3
Bodega Bay					
20:1200-20:1800	20.4	112	5.5	21	1.0
20:1800-20:2400	6.8	49	7.1	30	4.3
21:0000-21:0600	7.0	68	9.5	64	8.8
21:0600-21:1200	9.8	112	11.3	108	11.0
21:1200-21:1800	16.0	121	7.6	67	4.2
Pescadero					
20:1200-20:1800	17.8	456	25.7	236	13.3
20:1800-20:2400	30.5	368	12.0	212	7.0
21:0000-21:0600	25.4	227	9.0	227	9.0
21:0600-21:1200	27.9	265	9.5	276	9.9
21:1200-21:1800	17.8	316	17.8	240	13.5
21:1800-21:2400	20.3	217	10.8	130	6.5
Pacific Grove					
20:1800-20:2400	2.0	119	61.2	20	10.5
21:0000-21:0600	6.9	262	38.4	68	9.8
21:0600-21:1200	3.4	207	61.1	83	24.5
21:1200-21:1800	6.7	224	33.7	159	23.9
21:1800-21:2400	37.9	376	9.9	227	6.0

and Radiochemical Data
20–23, 1967

^{90}Sr		Ratios		
Dep.,	*Conc.,*	$\frac{^{140}Ba}{^{89}Sr}$	$\frac{^{140}Ba}{^{90}Sr}$	$\frac{^{89}Sr}{^{90}Sr}$
d.p.m./m.²	*d.p.m./l.*			
12.3	1.0	1.9	11.9	6.3
18.5	1.0	1.6	9.4	5.8
14.9	1.1	1.5	9.3	6.3
13.0	10.8	1.5	12.3	8.4
5.8	8.2	2.1	16.2	7.6
Lost	—	—	—	—
12.7	0.8	3.5	19.2	5.5
4.7	0.3	1.5	10.1	6.5
10.0	0.7	1.6	8.5	5.4
11.9	1.1	1.1	5.4	5.0
7.8	3.0	1.3	11.7	8.8
2.4	4.9	3.5	24.2	6.8
2.7	3.5	3.3	21.5	6.6
6.2	0.5	2.1	13.6	6.4
14.5	1.3	1.0	5.5	5.3
25.2	1.3	0.8	4.6	5.7
7.8	1.0	1.3	6.8	5.2
2.8	7.2	3.1	9.6	3.1
5.2	0.3	5.4	21.9	4.0
6.3	0.9	1.7	7.8	4.7
14.4	2.0	1.1	4.7	4.4
44.2	4.5	1.0	2.5	2.5
21.1	1.3	1.8	5.7	3.2
28.0	1.6	1.9	16.2	8.4
22.9	0.7	1.7	16.1	9.3
43.9	1.7	1.0	5.2	5.2
54.6	1.9	1.0	4.9	5.1
55.4	3.1	1.3	5.7	4.3
26.4	1.3	1.7	8.2	4.9
2.0	1.0	5.8	59.7	10.2
8.0	1.2	3.8	32.8	8.5
9.8	2.9	2.5	21.1	8.5
12.6	1.9	1.4	17.8	12.6
19.8	0.5	1.7	19.0	11.5

Table IV.

Collection Data Site, Times	Precip., mm.	^{140}Ba Dep., d.p.m./m.^{2}	^{140}Ba Conc., d.p.m./l.	^{89}Sr Dep., d.p.m./m.^{2}	^{89}Sr Conc., d.p.m./l.
Piedras Blancas					
20:1800-20:2400	3.0	335	110	71	23.3
21:0000-21:0600	0.8	495	601	122	148
21:0600-21:1200	0.4	179	493	53	147
21:1200-21:1800	3.4	371	110	140	41.4
21:1800-21:2400	22.7	529	23.3	228	10.0
Vandenberg					
21:1200-21:1800	0.1	708	7320	50	529
21:1800-21:2400	2.0	1260	626	67	33.3
22:0000-22:0600	16.5	984	59.7	97	5.9
Goleta					
21:1200-21:1800	tr.	—	—	—	—
21:1800-21:2400	8.4	371	43.8	200	23.6
22:0000-22:0600	19.3	161	8.4	202	10.6
22:0600-22:1200	4.6	30	6.0	22	4.4
Los Angeles					
22:0000-22:0600	7.6	850	112	535	70.3
22:0600-22:1200	44.5	502	11.4	554	12.5
22:1200-22:1800	8.5	283	34.4	298	36.3
22:1800-22:2400	4.3	80	18.5	78	18.0
La Jolla					
22:1200-22:1800	1.1	448	40.7	467	42.4
22:1800-22:2400	18.9	121	6.4	112	6.0
23:0000-23:0600	1.8	42	24.2	30	17.1

convective and orographic processes. Sufficient 6-hourly meteorological data are not generally available to examine the many observed radioaerosol deposition and concentration changes. However, the general picture of each storm as a whole does allow some detailed examination, especially the changes in the fission product radionuclide ratios.

The radioactivity ratio of potentially unfractionated fission product radionuclides in precipitation should be independent of the amounts of aerosol and water vapor removed from the air masses. For an air mass containing uniformly mixed radioaerosols from the same nuclear explosion, the ratios should be the same by time and collection-site latitude along the coast. The ratios at storm date may be calculated for depositions following a specifically known atmospheric nuclear explosion with known initial production quantities. The presence of longer lived radio-

Continued

^{90}Sr		Ratios		
Dep.,	*Conc.,*	$\frac{^{140}Ba}{^{89}Sr}$	$\frac{^{140}Ba}{^{90}Sr}$	$\frac{^{89}Sr}{^{90}Sr}$
d.p.m./m.²	*d.p.m./l.*			
10.0	3.3	4.7	33.4	7.1
15.5	18.8	4.1	32.0	7.9
6.9	19.2	3.3	25.1	7.7
41.3	12.2	2.7	9.0	3.4
64.4	2.8	2.3	8.2	3.6
2.3	24.6	13.8	298	21.5
3.6	1.8	18.8	354	18.8
11.5	0.7	10.2	85.4	8.4
—	—	—	—	—
18.1	2.1	1.9	20.6	11.1
22.4	1.2	0.8	7.1	9.0
3.5	0.7	1.4	8.6	6.3
47.6	6.3	1.6	17.8	11.2
56.0	1.3	0.9	8.9	9.9
54.9	6.7	1.0	5.2	5.4
14.0	3.4	1.0	5.5	5.4
40.3	3.7	1.0	11.1	11.6
17.8	0.9	1.1	6.8	6.3
4.6	2.7	1.4	9.1	6.4

nuclides from prior explosions changes the ratios. Also, the fractionation of potentially fractionated fission product radionuclides may indeed depend on the amounts of aerosol and water vapor removed from the air masses. Thus, the ratios of fission product radionuclides with different half-lives, such as the three radionuclides used in this study, afford an additional parameter to examine their deposition by precipitation. Their properties were given in Table I. The ratio most sensitive to fresh sources of fission products is the $^{140}Ba/^{89}Sr$ activity ratio which "decays" with a half-life of 17.2 days. The activity ratio of $^{140}Ba/^{90}Sr$ "decays" with a half-life of 12.8 days, and the activity ratio of $^{89}Sr/^{90}Sr$ "decays" with a half-life of 50.5 days. The average activity ratios for these three radionuclides were determined for each of the three Pacific cyclones over the entire storm period. These ratios are listed in Table VI together with

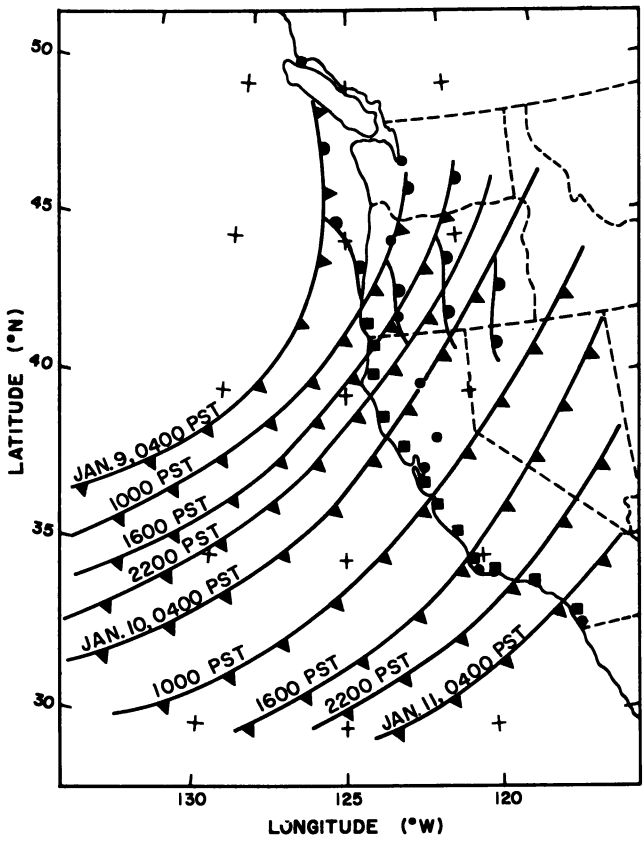

Figure 10. The 6-hourly frontal positions for the storm of Jan. 8-11, 1968

monthly ratio measurements available from other sources. In general, these limited data indicate an atmosphere containing fission product radionuclides of about the same ages.

The mean standard deviation of the storm average $^{140}Ba/^{89}Sr$ ratio of about 20–30% is about equal to the standard deviation estimated for individual ratio measurements. The larger standard deviations of the $^{140}Ba/^{90}Sr$ ratios may reflect the greater variability in ^{90}Sr sources from all prior atmospheric nuclear tests which add to the fresh ^{90}Sr from the most recent tests. Thus, the changes in the ratios of the three radionuclides given by time and location site in Tables III, IV, and V for the three respective storms may be influenced by differences in distribution of the fission products by age in the air masses and by changes in the precipitation mechanisms. To examine these possibilities further, the trends in radionuclide ratios in each storm were analyzed in the context

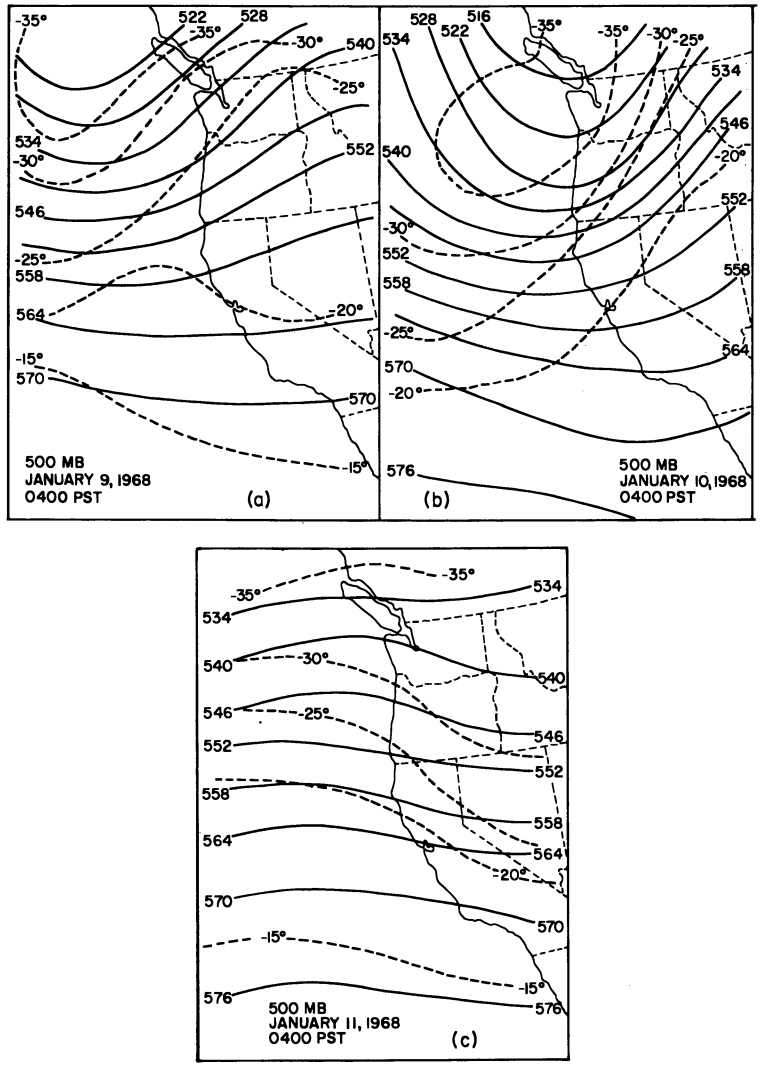

Figure 11. 0400 PST upper circulation patterns at the 500-mbar level and location of the jet stream for Jan. 8-11, 1968

of the announced nuclear explosions by the Chinese and French since the advent of the Limited Nuclear Test Ban Treaty.

The analysis was made on the assumptions that the differences in gaseous-precursor fission products resulted in a potential fractionation of the three alkaline-earth radionuclides and the radioaerosols participating in the precipitation processes in the Pacific cyclones over the

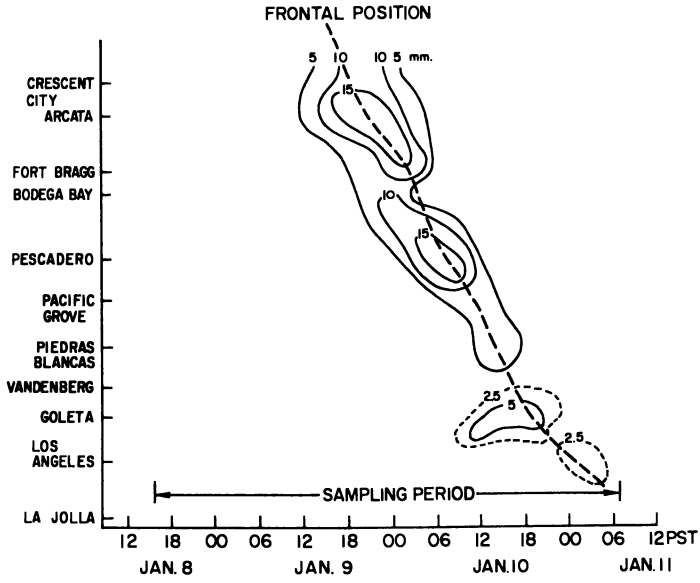

Figure 12. Time section of 6-hourly precipitation amount and frontal position along the California coast for Jan. 8-11, 1968

California coast had variable particle-size distributions according to specific nuclear-weapon test and trajectory history. The use of these three radionuclides allows the deposition of each radionuclide to be assigned by fraction to three nuclear sources on the basis of known or constant initial production ratios. ^{90}Sr present in the rainfall may have been produced by any and all nuclear explosions to date, although it has been shown that atmospheric residence times are not greater than a few years. ^{89}Sr will be present from tests occurring within the prior $\sim$ 12-month period, and ^{140}Ba will be present only from tests in the prior months. The examination of the ratios was made by assuming that the ^{140}Ba found originated solely from the most recent of the few announced nuclear explosions, that the ^{89}Sr existed from the major explosions in the prior year, and that the ^{90}Sr existed from all prior explosions in addition.

It was also assumed that the production ratios of the three radionuclides were the same as the ratios given for weapon fission yields (*12*). For each of the three storms and the reported nuclear explosions for the period, an analysis of the fractional deposition by event was made for each collection site along, and by regions of, the California coast. Based on these assumptions, the fraction of ^{140}Ba from the most recent atmospheric nuclear explosion before each storm was 1.00. The ^{140}Ba deposition on storm date was extrapolated to the explosion date. The initial

$^{140}Ba/^{89}Sr$ ratio determines the fraction of the storm deposition of ^{89}Sr which originated from that explosion. That amount of ^{89}Sr deposition is extrapolated to the storm date, and the difference of this deposition from the total ^{89}Sr deposition is attributed to the major prior explosion test. In a similar manner, the initial $^{140}Ba/^{90}Sr$ ratio determines the fraction of ^{90}Sr deposition for the most recent test, and the initial $^{89}Sr/^{90}Sr$ ratio determines the fraction of ^{90}Sr deposition from the prior test. The difference of the sum of these two fractional ^{90}Sr depositions from the total ^{90}Sr deposition gives the fraction of ^{90}Sr deposition from all prior explosions.

Storm of Nov. 15-17, 1966. The fission product ratio data by nuclear event for this storm are given in Table VII. The storm occurred 18 days after the reported Chinese fourth nuclear weapon test of about 20 kilotons on Oct. 28, 1966 and 190 days after the Chinese third nuclear explosion of about 200 kilotons on May 9, 1966. Also listed is the series of tests conducted by the French in the Southern Hemisphere (near Tahiti) in the time period between these two Chinese tests. A further possible source of fission products was the vented U.S.S.R. underground nuclear explosion of Oct. 27, 1966 (*14*). The extent of venting is not reported, and contributions to the storm deposition, if any, would appear as part of the fission products from the China-3 explosion. However, the venting process may result in significant fractionation of the fission products.

Analysis of upper wind charts for the 18-day period showed several examples of possible meridional transport of nuclear weapon debris across the equator into the Northern Hemisphere. Thus, the possibility of a contribution to the California coast storm deposition of fission products from the French test of about 400 kilotons on Oct. 4, 1966 cannot be neglected. The French explosion occurred 24 days earlier than the China-4 explosion, and the ^{140}Ba would have decayed by a factor of 4 relative to the October 28 test. However, the reported yield of this French test was 20 times greater, so that on October 28 there was still five times as much ^{140}Ba in the atmosphere from the French test of October 4 than from the China-4 test of October 28. If only 20% of the aerosol deposited in the California rain contained French debris, the ^{140}Ba activity contribution would have been 50%. Since so little ^{140}Ba could exist from the China-3 test of May 9, any contribution of ^{140}Ba from the French tests are included in the fraction assigned to China-4.

Table VIII shows the total storm rainfall and radionuclide depositions measured at each collection site. The storm description given earlier noted the diminishing rainfall as the frontal system moved down the coast. The total collected rainfall decreased from 86 mm. at Crescent City almost smoothly to the low of only 3 mm. at Piedras Blancas. The deposition of the three radionuclides follow a similar pattern; the con-

Table V. Rainfall Collection
Storm of January

Collection Data Site, Times	Precip., mm.	^{140}Ba Dep., d.p.m./m.²	^{140}Ba Conc., d.p.m./l.	^{89}Sr Dep., d.p.m./m.²	^{89}Sr Conc., d.p.m./l.
Bodega Bay					
08:1630-09:0800	2.2	368	165	134	60
09:0800-09:1630	4.0	199	50	37	9
09:1630-10:0130	40.3	2207	55	1053	26
Pescadero					
09:0000-09:0800	0.27	22	83	12	43
09:0800-10:0800	29.4	2445	83	1220	42
Pacific Grove					
10:0200-10:0800	10.8	123	11	128	12
10:0800-10:1000	2.1	88	43	74	31
Piedras Blancas					
10:0630-10:1530	15.7	403	25	262	17
Vandenberg AFB					
10:0350-10:0800	0.12	87	700	59	476
10:0800-10:1600	2.2	304	136	170	76
10:1600-10:1922	1.3	50	38	50	38
Goleta					
10:0430-10:0800	0.91	713	783	335	368
10:0800-10:2030	12.8	1198	95	557	44
Los Angeles					
10:2050-11:0845	4.2	207	49	100	24

centrations changing relatively little. The ratios of the radionuclides, however, show divergent behavior. The mean $^{140}Ba/^{89}Sr$ ratio is 2.1 ± 0.5, with no trend by collection site, whereas the $^{89}Sr/^{90}Sr$ ratio decreases steadily from north to south by a factor of over 3. These data indicate that the fraction of ^{89}Sr and ^{90}Sr from the most recent test (October 28) was reasonably constant (~ 5.5 and ~ 6% respectively), but that the remaining 94% of ^{90}Sr differed markedly in origin from north to south. The data show that ^{90}Sr originated primarily from China-3 (May 9) in the north and primarily from prior tests (1965 and earlier) in the south.

Table IX groups the site data into coastal regions. The ^{89}Sr appears to have originated equally from China-4 and China-3 in the north and south regions but with more fresh ^{89}Sr in the central region. This latter trend is emphasized by the large rainfall and ^{140}Ba deposition at Pescadero. Meteorological data are lacking to examine this observation in greater detail. The ^{90}Sr data on a regional basis emphasizes the heavier

and Radiochemical Data
8–11, 1968

^{90}Sr		Ratios		
Dep.,	*Conc.,*	$\frac{^{140}Ba}{^{89}Sr}$	$\frac{^{140}Ba}{^{90}Sr}$	$\frac{^{89}Sr}{^{90}Sr}$
d.p.m./m.²	*d.p.m./l.*			
3.9	1.8	2.7	94	34
1.6	0.4	5.4	124	23
45.9	1.1	2.1	48	23
0.33	1.2	1.8	67	37
39.1	1.3	2.0	63	31
3.4	0.3	1.0	36	38
1.2	0.5	1.2	73	62
11.4	0.7	1.5	35	23
2.1	16.6	1.5	41	29
8.4	3.8	1.8	36	20
2.1	1.6	1.0	24	25
13.2	14.4	2.1	54	26
34.7	2.7	2.2	35	16
6.0	1.5	2.1	35	17

deposition of the China-3 ^{90}Sr in the north and the increased fraction of older ^{90}Sr in central and southern California.

Storm of Jan. 20-23, 1967. This storm was characterized by the large ($\sim$ 200 kilotons) atmospheric nuclear weapon test of the Chinese (China-5) on Dec. 28, 1966. The pertinent ratio data are given in Table X. The first California storm occurred 25.6 days later. Another possible source of fresh fission products was the reported venting of a U.S.S.R. underground nuclear detonation on Dec. 18, 1966 (*17*). The prior Chinese and French atmosphere tests occurred 85 to 109 days before the storm date; less than 1% of the ^{140}Ba could have come from China-4 and less than 7% from the French tests. ^{89}Sr was still present from the prior tests; only 3% was left from the China-3 test of May 9, but the activity levels would still be measurable.

Table VI. Average Radionuclide Ratios in Precipitation Precipitation from Three Pacific Cyclones

Ratio	Date of Storm	Average Ratio[a]	Other Results			
			[b]	[c]	[d]	[e]
$^{140}Ba/^{89}Sr$	Nov. 1966	2.1 ± 0.5 (17)		1.6		
	Jan. 1967	2.0 ± 0.9 (48)		8.3+		
	Jan. 1968	2.0 ± 0.6 (14)				
$^{140}Ba/^{90}Sr$	Nov. 1966	25 ± 11 (18)				
	Jan. 1967	13.7 ± 7.5 (48)				
	Jan. 1968	55 ± 21 (14)				
$^{89}Sr/^{90}Sr$	Nov. 1966	11.9 ± 3.9 (21)	19.5	10.5	3.0	trace
					12.3	trace
	Jan. 1967	6.9 ± 2.0 (48)	10.3	0.9+	17.5	7.2
					14.9	9.2
	Jan. 1968	28 ± 8 (14)				18.0
						15.0

[a] Mean value and average deviation for number of samples given in parenthesis.
[b] *D. D. Huff* (*15*), monthly samples at Saratoga Creek, Calif.
[c] A. Aarkrog (*1*), monthly samples at Denmark; he comments that the Jan. 1967 sample showed a surprisingly low ^{89}Sr content.
[d] R. S. Cambray *et al.* (*4*), monthly samples at Abingdon (upper) and Milford Haven (lower), England.
[e] E. P. Hardy and J. Rivera (*10*), monthly samples at San Francisco (upper) and Los Angeles (lower), Calif.

Table VII. Fission Product Ratio Data by Nuclear Event
November 15, 1966

Event		China-4	France			China-3	
Date, 1966		Oct. 28	Oct. 4	Sept. 25	Sept. 11	May 9	Prior
Yield, ~kilotons		20	400	?	100	200	large
Δt, days		18	42	51	65	190	>190
Nuclide Ratio	R_o (HASL-164)						
$^{140}Ba/^{89}Sr$	8	3.84	1.45	1.01	0.59	0.0037	0
$^{140}Ba/^{90}Sr$	1170	438	120	74	35	0.05	0
$^{89}Sr/^{90}Sr$	147	11.5	83	73	60	11	0

The deposition and ratio data for this storm are given in Table XI. Immediately noticeable is the unusual data from the Vandenberg AFB site; with a minimum in total rainfall, a maximum in ^{140}Ba deposition, and a minimum in deposition of the two strontium radioisotopes. Just 80 miles south at Goleta with almost twice as much precipitation, the ^{140}Ba

deposition decreases by a factor of about 5, while the ^{89}Sr and ^{90}Sr depositions increase by a factor of about 2. These data suggest the possibility of a significant case of fission product fractionation.

The 6-hourly $^{140}Ba/^{90}Sr$ and $^{89}Sr/^{90}Sr$ ratios are shown in Figure 13 as a time section of the deposition ratio with respect to the movement of the frontal passage down the coast. It was noted in this storm that the front accelerated through central and southern California and that the jet stream remained strong as it shifted southward. The precipitation pattern, given in Figure 9, indicates three periods of precipitation as the front moved down the coast: steady rain from Crescent City down to Pescadero, light rain at Vandenberg and Goleta, and later heavy rain at Los Angeles southward. The time section in Figure 13 seems to reflect the differences in these precipitation periods. Both activity ratios go through a low (a low in the ratio implying a maximum of old ^{90}Sr) centered at about Bodega Bay and just before the passage of the front. The latitudes between Pescadero and Pacific Grove appear to be at the edge of the steepest gradient of the ratios. Below Pacific Grove, the deposition appears to occur in cells, mainly prefrontal. A major deposition cell seems to have occurred primarily at Vandenberg AFB. Although Pacific Grove and Piedras Blancas show high ratios during the early periods of precipitation, the large deposition of ^{140}Ba at Vandenberg at first appears to be a singular event. From Pescadero to Goleta, the $^{140}Ba/^{89}Sr$ ratio goes from 1.4 through the maximum of 13.8 at Vandenberg AFB and back to 1.3. However, from Vandenberg south, the ^{89}Sr deposition increases significantly, reaching a maximum at Los Angeles.

The analysis of the fractional deposition by event notes the severe fractionation that has taken place, provided, of course, that the radionuclides were produced originally with the ratios, R_o, given in Table XI. From Crescent City through Pescadero, where the maximum precipitation occurred, the three radionuclide ratios are generally constant. The resulting ^{89}Sr fractions by event may be attributed about 50% each from the China-5 and China-3 explosions. The corresponding ^{90}Sr fractions show about 3% from China-5, about 52% from China-3, and the remaining 45% from prior events.

The somewhat larger deposition of ^{140}Ba at Piedras Blancas and the very large deposition at Vandenberg AFB suggest the occurrence of the fractionation. The fraction of 1.10 for ^{89}Sr from China-5 at Piedras Blancas indicates that the deposition of 6.4 d.p.m./sq. meter of ^{89}Sr is too small by 10% to account for the deposition of 1909 d.p.m./sq. meter of ^{140}Ba, even if all of the ^{89}Sr originated from the China-5 event. This 10% is well within the uncertainty of the ratios. However, for "bookkeeping" purposes, the additional fraction of 0.10 for ^{89}Sr was "borrowed"

Table VIII. Fission Product
California Coast,

Site	Total Rainfall, mm.	Deposition, d.p.m./m.²			Ratios		
		^{140}Ba	^{89}Sr	^{90}Sr	$\frac{^{140}Ba}{^{90}Sr}$	$\frac{^{140}Ba}{^{89}Sr}$	$\frac{^{89}Sr}{^{90}Sr}$
Crescent City	86	1212	608	29.5	2.0	41	20.6
Arcata	35	384	227	15.8	1.7	24	14
Fort Bragg	28	665	lost	14.7	—	45	—
Bodega Bay	13	424	178	19.2	2.4	22	9.3
Pescadero	31	767	240	26.3	3.2	29	9.1
Pacific Grove	11	82	56	9.5	1.5	9	6.0
Piedras Blancas	3	93	33	5.2	2.8	18	6.4

Table IX. Regional Deposition of Fission Products by Nuclear Event
California Coast, November 15, 1966

Region of Coast	Fission Product	Fractional Deposition by Event		
		Ch-4	Ch-3	Prior
North	^{89}Sr	0.50	0.50	—
	^{90}Sr	0.08	0.86	0.06
Central	^{89}Sr	0.75	0.25	—
	^{90}Sr	0.06	0.21	0.73
South	^{89}Sr	0.50	0.50	—
	^{90}Sr	0.03	0.27	0.70
Total	^{89}Sr	0.57	0.43	—
	^{90}Sr	0.06	0.50	0.44

from the China-3 event, noted by the (−0.10) under China-3. The ^{90}Sr required from China-5 is comparable with data from the northern sites.

This anomaly, if for Piedras Blancas alone, might be explained by assuming the radiochemical measurements of one or more of the five ^{89}Sr samples were too low. However, the results for Vandenberg showed even greater anomalies. The radiochemical measurements were reviewed carefully, and the large ^{140}Ba content in all three of the samples could not be the result of random errors. A check was also made to determine that ^{140}Ba was not used as a radioactive tracer at Vandenberg AFB during that period. The deposition of ^{140}Ba given in Table XI required 3.85 times as much ^{89}Sr measured as being caused solely by the China-5 event. It also required 60% of the measured ^{90}Sr solely from the China-5 event. The total ^{90}Sr deposited in the 18 hours of showers at Vandenberg AFB was only 17 d.p.m./sq. meter. Table IV shows that during the period

Deposition by Nuclear Event
November 15, 1966

Fractional Deposition by Event

^{89}Sr		^{90}Sr		
Ch-4	*Ch-3*	*Ch-4*	*Ch-3*	*Prior*
0.52	0.48	0.09	0.91	0
0.43	0.57	0.05	0.75	0.20
—	—	0.10	—	—
0.61	0.39	0.05	0.33	0.62
0.83	0.17	0.06	0.15	0.79
0.38	0.62	0.05	0.34	0.61
0.73	0.27	0.04	0.16	0.80

1800 to 2400 PST on January 21, when the major deposition of 1260 d.p.m./sq. meter of ^{140}Ba deposited in 2.0 mm. rainfall at Vandenberg, less than half that amount deposited in 22.7 mm. rainfall at Piedras Blancas, just north, while less than one-third deposited in 8.4 mm. rainfall at Goleta, just south. In contrast, the ^{90}Sr deposition at Vandenberg was a minimum, 3.6 d.p.m./sq. meter, compared with 64.6 d.p.m./sq. meter at Piedras Blancas and 18.1 d.p.m./sq. meter at Goleta. Thus, the "bookkeeping" in Table XI shows by the (−10.8) in ^{90}Sr from China-3 that the deposition of ^{90}Sr from China-3 was too low by almost a factor 3 compared with the ^{89}Sr.

The increased deposition of the two strontium radioisotopes from Goleta southward restores the $^{140}Ba/^{89}Sr$ ratio to the values found at the northern sites. The fractional deposition of ^{89}Sr by event is also similar to the fractions observed at the northern sites. However, the lack of ^{90}Sr from China-3 at Piedras Blancas and Vandenberg AFB seems to change to an excess of about 14–43% from Goleta to La Jolla.

Table X. Fission Product Ratio Data by Nuclear Event
January 21, 1967

Event		*China-5*	*China-4*	*France*	*China-3*	
Date, 1966		*Dec. 28*	*Oct. 28*	*Oct. 4*	*May 9*	*Prior*
Yield, ~kilotons		200	20	400	200	large
Δt, *days*		25.6	85	109	257	>257
Nuclide Ratio	R_o *(HASL-164)*					
$^{140}Ba/^{89}Sr$	8	2.8	0.26	0.10	0	0
$^{140}Ba/^{90}Sr$	1170	292	11.7	2.8	0	0
$^{89}Sr/^{90}Sr$	147	103	46	33	4.4	0

Table XI. Fission Product
California Coast, January

Site	Total Rainfall, mm.	Deposition, d.p.m./m.²			Ratios		
		^{140}Ba	^{89}Sr	^{90}Sr	^{140}Ba / ^{89}Sr	^{140}Ba / ^{90}Sr	^{89}Sr / ^{90}Sr
Crescent City	47	715	433	77	1.6	9.3	5.6
Arcata	60	646	317	52	2.0	12.4	6.1
Fort Bragg	53	360	309	57	1.2	6.3	5.4
Bodega Bay	60	462	290	91	1.6	5.1	3.2
Pescadero	140	1849	1321	231	1.4	8.0	5.7
Pacific Grove	57	1148	550	52	2.1	22.1	10.6
Piedras Blancas	30	1909	614	138	3.1	13.8	4.5
Vandenberg AFB	19	2952	214	17	13.8	174	12.6
Goleta	32	562	424	44	1.3	12.8	9.6
Los Angeles	65	1715	1465	173	1.2	9.9	8.5
La Jolla	22	611	609	63	1.0	9.7	9.7

The examination of these individual site data by regional deposition seems to remove the apparent fractionations occurring at Vandenberg AFB and at the southern sites. For this purpose, Crescent City to Bodega Bay (all north of San Francisco) was taken as north California coast, Pescadero to Piedras Blancas as the central coast, and Vandenberg AFB was added to the other three southern sites as the southern California coast. Table XII shows the analysis made by integrating solely the prefrontal rainfall and the total storm rainfall. It is immediately noted that the data from the prefrontal and total rainfall are identical. Also, the ^{89}Sr fractions are now identical for the central and southern portions of the coast and not too different from the northern coast. The ^{90}Sr from China-5 seems to increase southward by a factor of two, from 3 to 6%, and to go through a low for China-3, with a corresponding high for prior events in the central coast and to reverse these in the southern coast.

The over-all data suggest a preferential rainout of ^{140}Ba-bearing particles from the air mass leaving Piedras Blancas and moving over Vandenberg AFB as the precipitation decreased to showers, and the subsequent preferential rainout of the ^{90}Sr-bearing particles from the same air mass as it moved from Vandenberg AFB southward along the coast as the rainfall intensified again. The ^{140}Ba might be more abundant on the larger sized aerosol particles, which are rained out preferentially as precipitation nuclei under light rainfall conditions, or they might be present at a different level in the atmosphere when the precipitation-generating level or mechanism changed. With the increased rainfall at Los Angeles, the smaller size aerosol particles might be more efficiently rained out, and since much of the ^{140}Ba was rained out earlier, the ^{89}Sr

Deposition by Nuclear Event
20–23, 1967

Fractional Deposition by Event

^{89}Sr		^{90}Sr		
Ch-5	*Ch-3*	*Ch-5*	*Ch-3*	*Prior*
0.58	0.42	0.03	0.54	0.43
0.72	0.28	0.04	0.40	0.56
0.41	0.59	0.02	0.73	0.25
0.56	0.00	0.02	0.32	0.66
0.49	0.51	0.03	0.65	0.32
0.73	0.27	0.07	0.64	0.29
1.10	(−0.10)	0.05	(−0.10)	1.05
4.85	(−3.85)	0.6	(−10.8)	11.2
0.47	0.53	0.04	1.17	(−0.21)
0.41	0.59	0.03	1.14	(−0.17)
0.36	0.64	0.03	1.43	(−0.46)

and ^{90}Sr fractions would be enriched. Alternately, the increased rainfall might be caused by another change in precipitation-generating level or mechanism. It is unfortunate that sufficient meteorological data of the vertical profiles of the atmosphere over the California coast are not available with which to examine this interesting case of apparent fractionation.

Storm of Jan. 8-11, 1968. Nuclear weapons testing in the atmosphere in 1967 was characterized by the major thermonuclear explosion of June 17 by China, by a series of three low yield ($<$ 20 kiloton) detonations during June and July by France, and the small explosion of less than 20 kilotons fission of December 24 by China. The latter has been attributed by the popular press as a "dud H-bomb," but the creation of the fission products set up a situation in January 1968, timewise, for ^{140}Ba, ^{89}Sr, and ^{90}Sr, similar to that which existed in January 1967. Table XIII lists the fission product ratio data by nuclear event as of Jan. 10, 1968. Although the ^{140}Ba content in the atmosphere from the China-7 test of December 24 was small, it was the only ^{140}Ba source from atmospheric nuclear explosions during the storm of Jan. 8-11, 1968. Assuming a fission trigger of approximately 20 kilotons for the high yield China-6 test and 207 days of decay, the ^{140}Ba would not be measurable. Similar assumptions apply to the low yield French tests that were 192–219 days old. The ^{89}Sr from the French and China-6 tests, however, would be both measurable and indistinguishable from each other. Very little ^{89}Sr remained from the Dec. 28, 1966 and earlier tests.

The storm of Jan. 8-11, 1968 was characterized by a rainfall pattern that was heaviest in the north and diminished to light rain and drizzle

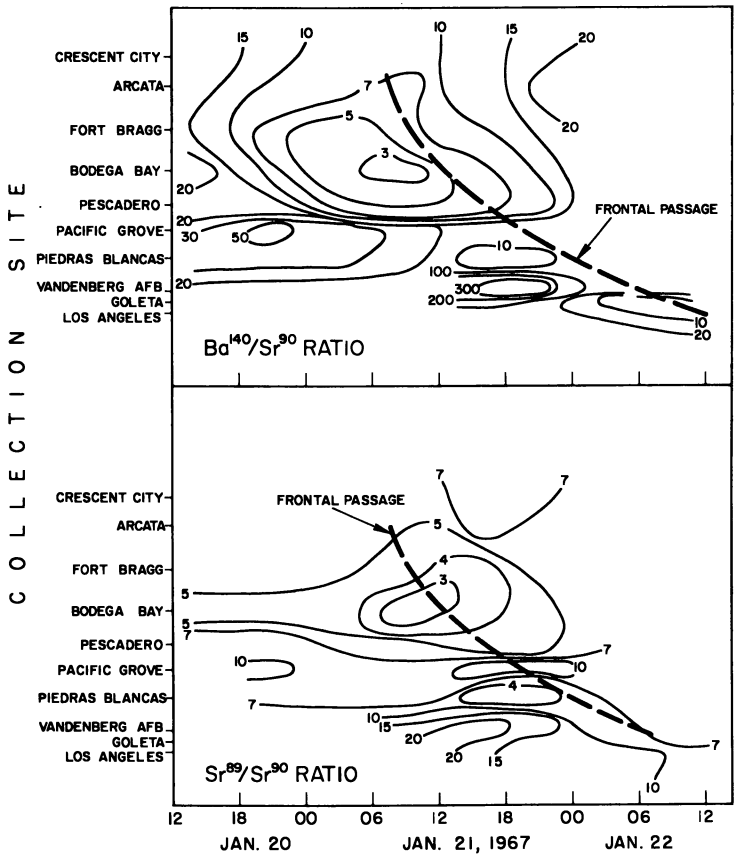

Figure 13. $^{140}Ba/^{90}Sr$ and $^{89}Sr/^{90}Sr$ ratios along the California coast for the precipitation deposition of the Jan. 20-22, 1967 storm

Table XII. Regional Deposition of Fission Products by Nuclear Event
California Coast, January 20–23, 1967

Region of California Coast	*Fission Product*	*Fractional Deposition by Event*					
		Prefrontal Rainfall			*Total Storm Rainfall*		
		Ch-5	*Ch-3*	*Prior*	*Ch-5*	*Ch-3*	*Prior*
North	^{89}Sr	0.56	0.44	—	0.57	0.43	—
	^{90}Sr	0.03	0.47	0.50	0.03	0.48	0.49
Central	^{89}Sr	0.70	0.30	—	0.69	0.31	—
	^{90}Sr	0.04	0.39	0.57	0.04	0.42	0.54
South	^{89}Sr	0.70	0.30	—	0.67	0.33	—
	^{90}Sr	0.06	0.66	0.28	0.06	0.69	0.25
Total	^{89}Sr	0.67	0.33	—	0.66	0.34	—
	^{90}Sr	0.04	0.51	0.45	0.04	0.52	0.44

Table XIII. Fission Product Ratio Data by Nuclear Event
January 10, 1968

Event		*China-7*	*France*	*China-6*	*Prior*
Date, 1967		*Dec. 24*	*June 5, 27, July 2*	*June 17*	*< Dec. 28, 1966*
Yield		⩽ 20 kilotons	small	2-7 megatons	—
Δt, *days*		17	192-219	207	> 378
Nuclide Ratio	R_0 *(HASL-164)*				
$^{140}Ba/^{89}Sr$	8	4.03	< 0.01	< 0.01	0
$^{140}Ba/^{90}Sr$	1170	465	< 0.05	< 0.01	0
$^{89}Sr/^{90}Sr$	147	116	10.9-7.4	9.9	0.7

down to Los Angeles, but with pronounced orographic rainfall at Goleta. The data in Table XIV show that the decrease in deposition of the three radionuclides qualitatively follows the decreases of rainfall southward, with an increase in all three at Goleta. The $^{140}Ba/^{89}Sr$ ratio is essentially constant over all sites, except for the one low deposition of ^{140}Ba at Pacific Grove. The $^{140}Ba/^{90}Sr$ and $^{89}Sr/^{90}Sr$ ratios also look reasonably uniform; the extent of deviations from the means can be considered to be well within the standard deviations of the individual ratio values. No significant trends are discernible. The ^{89}Sr fractional deposition appears again to be about 50% from the most recent test, China-7, and 50% for the older one, China-6, especially for the northernmost two and southernmost 2 sites. The lower $^{140}Ba/^{89}Sr$ ratios for the three central sites may be significant. The fraction of ^{90}Sr from China-7 appears to be reasonably constant at about 10% down the coast. However, extensive fractionation of ^{90}Sr from ^{89}Sr seems to have occurred, especially from Pescadero to Vandenberg AFB. At Pacific Grove, 2.38 times as much ^{90}Sr as measured would be required to meet the $^{89}Sr/^{90}Sr$ ratio if all of the ^{90}Sr came from the China-6 explosion alone. Assuming an error of 100% in the radiochemical measurement of the two samples, lowering the deposition for both samples to 101 d.p.m./sq. meter, the $^{140}Ba/^{89}Sr$ ratio would be raised to 2.0, and the $^{89}Sr/^{90}Sr$ ratio would be lowered to 22. Although both new values would "look better" in Table XIV, there is no basis for so great a radiochemical error, and such change would not affect the ratios at the neighboring sites. Thus, radiochemical error is not considered significant as a source of these greater than 1.0 fractional depositions. The results, therefore, indicate that a fractionation process has taken place either during the condensation history of the fission radionuclides or during the precipitation deposition of those radionuclides. Other possibilities include the fission products from the announced nuclear

Table XIV. Fission Product

California Coast,

Site	Total Rainfall, mm.	Deposition, d.p.m./m.²			Ratios		
		^{140}Ba	^{89}Sr	^{90}Sr	$\frac{^{140}Ba}{^{89}Sr}$	$\frac{^{140}Ba}{^{90}Sr}$	$\frac{^{89}Sr}{^{90}Sr}$
Bodega Bay	47	2774	1224	51.4	2.3	54	24
Pescadero	30	2467	1232	39.4	2.0	63	31
Pacific Grove	13	211	202	4.6	1.0	46	44
Piedras Blancas	16	403	262	11.4	1.5	35	23
Vandenberg AFB	4	441	279	12.6	1.6	35	22
Goleta	14	1911	892	47.9	2.1	40	19
Los Angeles	4	207	100	6.0	2.1	35	17

Table XV. Regional Deposition of Fission Products by Nuclear Event

California Coast, January 8-11, 1968

Region of Coast	Product Fission	Fractional Deposition by Event		
		Ch-7	Ch-6	Prior
North	^{89}Sr	0.53	0.47	—
	^{90}Sr	0.12	1.28	−0.40
Central	^{89}Sr	0.33	0.67	—
	^{90}Sr	0.08	1.96	−1.04
South	^{89}Sr	0.50	0.50	—
	^{90}Sr	0.08	0.95	−0.03
Total	^{89}Sr	0.50	0.50	—
	^{90}Sr	0.10	1.22	−0.32

weapons tests in ratios significantly different than those assumed or the presence of fission products from unannounced nuclear detonations.

Integrating these data by coastal region, as given in Table XV, shows, however, that the fractionations are not removed regionally as they were in the storm of January 1967. The storm integrated over all of the collection sites shows about 32% less ^{90}Sr deposition than required to account for the ^{140}Ba and ^{89}Sr from the two 1967 Chinese nuclear weapons tests. On the basis that the initital production ratios were the same as announced values for U. S. fission devices, fractionation of ^{90}Sr from ^{89}Sr and ^{140}Ba must have occurred at least to that extent.

One possibility that makes the January 1968 storm different from the January 1967 storm may lie in the trajectories of the two storms. The

Deposition by Nuclear Event

January 10, 1968

Fractional Deposition by Event

^{89}Sr		^{90}Sr		
Ch-7	*Ch-6*	*Ch-7*	*Ch-6*	*Prior*
0.56	0.44	0.11	1.05	−0.16
0.50	0.50	0.13	1.58	−0.71
0.26	0.74	0.10	3.28	−2.38
0.38	0.62	0.08	1.43	−0.51
0.39	0.61	0.08	1.36	−0.44
0.53	0.47	0.09	0.88	0.03
0.52	0.48	0.08	0.82	0.10

fractionation noted at individual collection sites may have been eliminated regionally by the total deposition of the potentially-fractionated aerosol in the January 1967 storm when the rainfall reintensified on its southeasterly trajectory. The lack of elimination of the local-site fractionation in the January 1968 storm may have been caused by the incomplete deposition of the aerosols over the collection sites. Trajectory analysis of these three storms, which are planned for the future, may shed additional light on these three interesting cases of possible meteorological fractionation of chemically similar radionuclides.

Acknowledgments

This program was carried out with the generous assistance of many individuals at the several rainfall collection sites along the California coast. The storm alerts and the quantitative descriptions of the storms studied were carried out by Einar L. Hovind of North American Weather Consultants, Inc., Goleta, Calif. The radiochemical analyses were performed in the water quality control radioactivity laboratory under the supervision of Gerald H. Hamada.

Literature Cited

(1) Aarkrog, A., private communication, August, 1967.
(2) Benson, P., Gleit, C. E., Leventhal, L., *Proc. U. S. At. Energy Comm. Symp. Radioactive Fallout Nucl. Weapons Tests, 2nd* **CONF-765,** CF STI (1965).
(3) Bleichrodt, J. F., Bleeker, W., Schmidt, F. H., *Tellus* **12,** 188-194 (1960).
(4) Cambray, R. S., Fisher, E. M. R., Brooks, W. L., Peirson, D. H., *UKAEA Rept.* **AERE-R5575,** November, 1967.

(5) Danielsen, E. F., *Project Springfield Rept.* **DASA-1517,** July, 1964.
(6) Edvarson, K., Löw, K., Sisefsky, J., *Nature* **184,** 1771-1774 (1959).
(7) Freiling, E. C., *Science* **133,** 1991-1998 (1961).
(8) Freiling, E. C., Kay, M. A., *Nature* **209,** 236-289 (1966).
(9) Greenfield, S. M., *J. Meteor.* **14,** 115-125 (1957).
(10) Hardy, E. P., Rivera, J., *U. S. At. Energy Comm. Rept.* **HASL-197,** July 1, 1968.
(11) Harley, J. H., Ed., "Manual of Standard Procedures," NYO-4700, 2nd ed., 1967.
(12) Harley, N., Fisenne, I., Ong, L., Harley, J., *HASL Quart. Summ. Rept.* **HASL-164,** 251-260 (1965).
(13) Hicks, B. B., *J. Applied Meteor.* **5,** 169-174 (1966).
(14) Holland, J. Z., private communication.
(15) Huff, D. D., private communication, 1967.
(16) Junge, C. E., "Air Chemistry and Radioactivity," Academic Press, New York, 1963.
(17) Kauranen, P., Kulmala, A., Mattsson, R., *Nature* **216,** 238-241 (1967).
(18) Kruger, P., Hosler, C. L., Davis, L. G., *J. Geophys. Res.* **71,** 4257-4266 (1966).
(19) Kruger, P., Miller, A., *J. Geophys. Res.* **69,** 1469-1480 (1964).
(20) Lindbloom, G., *Tellus* **13,** 106-112 (1961).
(21) Miyaki, Y., Saruhashi, K., Katsuragi, Y., Kanazawa, T., *J. Geophys. Res.* **67,** 189-193 (1962).
(22) Present, R. D., *Phys. Rev.* **72,** 7-15 (1947).
(23) Reiter, E. R., *J. Appl. Meteor.* **2,** 691-705 (1963).
(24) Stewart, K., *Trans. Faraday Soc.* **52,** 161-173 (1956).
(25) Storebö, P. B., *Tellus* **12,** 293-297 (1960).

RECEIVED November 4, 1968.

Simulation of the Hydrologic Transport of Radioactive Aerosols

DALE D. HUFF[1] and PAUL KRUGER

Civil Engineering Department, Stanford University, Stanford, Calif.

A model for the hydrologic transport of radioactive aerosols has been prepared to simulate watershed radioaerosol hydrographs. The hydrologic transport model (HTM-1) is based on the anticipated physical and chemical interactions of fallout deposited radioaerosols with watershed media during runoff. A numerical simulation of the watershed moisture balance is computed by the Stanford watershed model and is used to estimate resulting effects on radioaerosol transport. Transport calculations consider the effects of vegetal interception, soil surface interactions (including erosion), and stream channel movement to predict a continuous radioaerosol hydrograph for the two biologically important radionuclides: 27.7-year ^{90}Sr and 30.0-year ^{137}Cs. Experimental radioaerosol hydrographs have been obtained for the Saratoga Creek, Calif., watershed. These data are used to evaluate the several processes considered in preparing the HTM-1.

The increasing demand on water resources is accompanied by an increasing need for understanding and controlling the introduction of water-borne trace-concentration contaminants into water supplies. A major consideration in trace contaminant behavior is the chemical interaction between the trace materials and watershed media during hydrologic events. One class of trace pollutants which especially contributes to the concern about deteriorating water quality is the radioactive aerosols deposited after atmospheric nuclear weapons testing. Although the occurrence of radioaerosols in water supplies is of general interest from

[1] Present address: Civil Engineering Department, University of Wisconsin, Madison, Wis.

the general processes associated with the hydrologic transport of trace elements into water supplies. Radionuclides can generally be measured at low concentration with great precision.

A hydrologic transport model has been developed to summarize and evaluate present understanding of the movement of pollutants into water supplies. The model, using numerical computation methods, simulates the hydrologic transport of radioactive aerosols deposited as fallout. The results may be generalized to include other pollutants. The hydrologic transport model (HTM-1) operation is based upon relating radioaerosol transport with detailed quantitative estimates of the water budget within a basin, as calculated by the Stanford watershed model (*1*).

A schematic of the HTM-1 is shown in Figure 1. To follow the probable path of aerosol movement through a watershed, the HTM-1 simulation begins with depositional input data and an inventory of radioaerosol content throughout the basin. Incoming aerosols are divided between vegetal interception storage, land surface storage, and direct channel input. For example, in a heavily forested watershed, vegetal interception storage is the most important storage for incoming radioactive aerosols. The radioaerosols are removed from vegetal storage by the action of rainfall which transports them onto the land surface. Both direct precipitation onto the land surface and vegetal drip contribute to land surface storage, which may be divided into overland flow storage and surface soil storage. Before the onset of overland flow, all of the aerosol reaching the land surface is held in storage at the soil surface. As precipitation continues, the radioaerosol is removed from surface soil storage either by elution into overland flow and transport into the channel system, or by a gradual migration into the subsurface soil profile caused by infiltrating water. Radioaerosols which have migrated below the soil surface may be transported farther either into the stream channel by interflow (shallow subsurface flow), or to deep storage by water percolating to groundwater storage. Aerosols dissolved in overland flow and aerosols sorbed on eroded sediment are carried into the channel system by surface runoff. It is assumed that these aerosols and any eroded soil, on reaching the main channel, are carried, quantitatively, by the water flowing out of the watershed.

Soil and radioaerosol movement through the channel system is simulated in a manner analogous to the routing of water through the system by the Stanford watershed model. Computations for each reach begin with an estimate of radioaerosol input to the channel. All incoming radioaerosol is assumed to mix uniformly with the water in the reach. Radioaerosol outflow from the reach may be estimated as the product of total reach aerosol content and the ratio of channel water outflow to

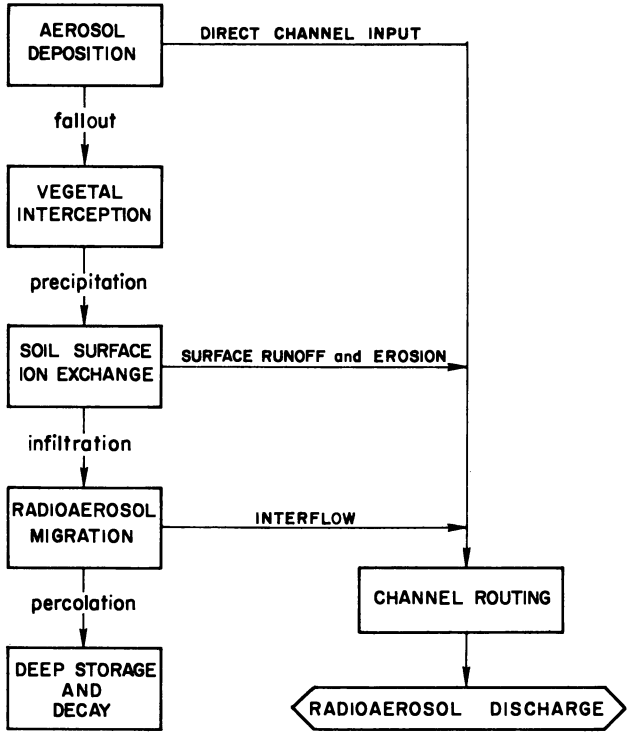

Figure 1. Schematic of the hydrologic transport model

total volume. Inflow to each reach is the sum of land surface input and a radiobiological viewpoint, such radioaerosols are useful for studying input from the adjacent upstream reach. The final output is a continuous prediction of the quantity of aerosol flowing out of the basin.

Individual Components of the HTM-1. The physical and chemical interactions between trace elements and watershed media have been examined previously (3). The data acquired from a recently completed field investigation on a small watershed have been used to re-examine some of those interactions. The results of the field study are included in the following discussions.

Deposition of Radioaerosols

A means for estimating accurately hourly radioaerosol deposition on the basis of easily obtained meteorological parameters is highly desirable. However, such relationships have not yet been satisfactorily developed. For the purpose of the HTM-1, hourly fallout estimates have been made during rainfall periods, using the assumption that

the product of the measured average monthly radioaerosol concentration in rainfall and hourly precipitation represents the hourly radioaerosol deposition total. Although actual hourly values may be in considerable error from the average hourly values, such errors may be expected to be smoothed considerably in subsequent simulation of net transport. So long as total deposition is reproduced on a monthly basis, the error caused by individual hourly results is expected to be small.

An evaluation of the expected errors in estimated hourly deposition was made from radiochemical data for three rainstorms. The results showed that the calculated values agreed with the measured values to within a factor of two, and the estimated and actual depositions rapidly approached the same value as the time period considered was increased. In general, for intervals of 6 hours, the errors do not exceed $\pm 30\%$.

The most important chemical parameter affecting the deposition and subsequent mobility of radioactive aerosols, such as the nuclides ^{90}Sr and ^{137}Cs examined in this study, is their solubility in rainwater. If these aerosols are dissolved in precipitation, the main factor in their transport is the movement of the rainwater, not the transport of insoluble aerosol particles. Huff and Kruger (*2*) examined the solubility products of strontium and chemically similar compounds which may carry trace amounts of ^{90}Sr, and they estimated that strontium should be soluble in precipitation. Solubility tables also indicate that cesium compounds likely to exist in precipitation should be soluble. It was noted that the possibility did exist that some of the fission product ^{90}Sr and ^{137}Cs might be bound within the structure of insoluble natural aerosols or nuclear weapon debris.

The problem of estimating aerosol transport is thus focused on the study of watershed media effects on the transport of substances in solution rather than in insoluble aerosol particles. Thus, sorption by watershed media is a prime factor in determining the hydrologic transport of soluble radioaerosols, such as cesium and strontium. Removal of soluble radioaerosol elements from runoff by formation of insoluble compounds is considered unlikely.

A second factor in the deposition process is the physical size of the radioaerosol particles deposited during dry deposition. Particle size affects the efficiency of foliar collection of dry aerosol particles and may also be important in determining the rate of solution of soluble constituents within the aerosol particle. Lockhart *et al.* (*7*) indicated that nuclear debris in surface level air is generally associated with aerosol particle sizes about 0.5–1.0μ in diameter. Martell (*8*) stated that high yield detonations causing condensation of ^{90}Sr at stratospheric altitudes leads to the formation of particles with diameters less than 1μ. Hence,

it may be assumed that the radioaerosol particles deposited during dry fallout are about 1μ in diameter. This size suggests rapid solution of soluble components of the particle. Such small particles may also be transported easily from vegetal surfaces to the land surface by rainfall, even if solution does not occur. Therefore, it has been assumed that aerosols are deposited in a mobile form that permits precipitation to initiate transport within the vegetal storage reservoir.

Vegetal Interception

Radioactive aerosols are intercepted by vegetation either by mechanical trapping of dry particulate matter or in the rainfall which wets the vegetation.

Menzel *et al.* (*10*) stated that aerosol particles having a diameter of less than 44μ are effectively retained on foliage. Since the radioactive aerosols considered in this investigation have particle diameters much smaller than 44μ, it is expected that during dry deposition, watershed vegetation will retain all radioaerosol deposited on foliar surfaces. In addition, "regenerated" aerosols associated with previously contaminated surface soil eroded by wind may constitute another source of input to vegetal storage. The rate of accumulation of radioactive aerosols on foliage under dry conditions is thus a function of the average atmospheric deposition rate, prior basin contamination, and the amount and type of cover in the watershed. There has been an apparent lack of investigation of the rate of dry radioaerosol accumulation by vegetation. However, results of this investigation suggest that vegetation is quite efficient in removing aerosols from the atmosphere. For the purpose of the model, the relative difference between observed deposition and the build-up of aerosols on vegetation during dry periods has been taken as a measure of the difference in collection efficiency between vegetation and deposition sampling devices.

Small amounts of precipitation, which may have correspondingly large concentrations of aerosols, and which are intercepted by vegetation may later evaporate, depositing their radioaerosol content on the foliar surfaces. However, precipitation totals quite often exceed the storage capacity of foliar surfaces, and radioaerosols previously deposited on the vegetation are washed onto the land surface. Since fallout deposition of ^{137}Cs and ^{90}Sr has been occurring for over a decade, it has been assumed that an equilibrium specific activity of these nuclides has been reached in vegetation; thus no significant plant uptake arising from isotope dilution effects should occur. Furthermore, net foliar uptake of fallout radioaerosols should be small compared with the total amount of mobile material present, partially because of the leaching effect of the

rainwater. In such cases, the net change in vegetal radioaerosol storage, assuming complete solution and mixing of radioaerosols with water on the vegetal surfaces, may be related to pre-storm contamination, amount of storm precipitation, water storage capacity of the vegetation and the rate of deposition by the equation:

$$dA = R\,dt - \frac{I \cdot A}{V}\,dt \tag{1}$$

where A = foliar aerosol content after the onset of vegetal drip.
R = deposition rate.
I = rate of vegetal drip loss from vegetal storage.
V = volume of vegetal storage capacity.
t = time.

Equation 1 may be rearranged and integrated to yield:

$$A_t = \frac{VR}{I}\,(1 - e^{-It/V}) + A_o e^{-It/V} \tag{2}$$

where A_o = initial foliar aerosol content.
A_t = foliar aerosol content after time t.

Equation 2 represents an expression for the vegetal aerosol content after any period of time during which sufficient precipitation occurs to cause vegetal drip. In simulation applications, the equation may be used to monitor the vegetal aerosol inventory during major storms throughout the year. Periods of no vegetal drip are simulated by adding all deposition to the established vegetal inventory. Losses from vegetal storage to the land surface constitute a major step in the net transport process. The total aerosol loss from vegetation storage may be found from the conservation of mass relationship:

$$A_t = A_o + Rt - \Delta A \tag{3}$$

where ΔA = total aerosol loss from vegetal storage. Substitution of Equation 2 into Equation 3 yields:

$$A = A_o\,(1 - e^{-It/V}) + R\left(t - \frac{V}{I}(1 - e^{-It/V})\right) \tag{4}$$

Equations 3 and 4 form the basis for the conceptual simulation of vegetal interception processes on the net transport of deposited aerosols. Computations begin from measured or estimated values of aerosol deposition and vegetal inventory and the quantity of vegetal drip which is estimated by the Stanford watershed model as precipitation reaching the land surface. The deposition to the land surface from vegetal storage for the current time interval and the value of vegetal aerosol inventory to be used at the next time interval are computed and held for later use. In this fashion, a continuous record of aerosol content in vegetal storage

is maintained, and depositional input to the next major step in hydrologic transport is generated.

Land Surface Interactions

The ion exchange reactions which occur while precipitation is in contact with soil in the watershed are of primary importance in describing the hydrologic transport process for any chemical constituent. The HTM-1 model assumes ion exchange as the determining factor which relates surface runoff processes to the hydrologic transport of water-borne radioactive aerosols. The complex interactions of water, radioaerosol, and soil may be described by examining the theories of ion exchange equilibria and kinetics in a dynamic soil and water system. However, for practical reasons, many simplifying assumptions have been made about these complex interactions.

The rate of reaction between trace elements in solution and those sorbed on soil has been examined in an attempt to determine the degree of departure from equilibrium conditions which might be found during overland flow conditions. In general, owing to the high ratio of soil surface area to runoff volume, and the turbulence caused by raindrop impact, it may be expected that exchange will proceed to equilibrium in a time interval that is short compared with the time of travel of overland flow. For the purpose of the HTM-1, it is assumed that exchange equilibrium between soil and water phases is attained.

For equilibrium conditions, Donnan ion exchange theory (*6*) may be used to describe quantitatively equilibria for trace quantities of chemical elements in the presence of high homologous salt concentrations. The radionuclides ^{90}Sr and ^{137}Cs constitute a very small fraction of the mass of the chemical constituents in rainfall; thus the equilibrium distribution of these nuclides between solid and liquid phases may be estimated as

$$K_d = \frac{b_r}{b_w} \frac{w}{g} \tag{5}$$

where K_d = distribution coefficient
b_r = quantity of radionuclide in the soil phase
b_w = quantity of radionuclide in the liquid phase
w = volume of the liquid phase
g = dry weight of the soil phase

Each of the parameters K_d, w, and g is an independent variable and may be measured or estimated from a knowledge of the physical system. When Equation 5 is solved simultaneously with the expression for the total surface radioaerosol inventory,

$$R = b_r + b_w \tag{6}$$

where R = total radioaerosol on the land surface, the individual values of b_r and b_w may be determined, provided the current values of the parameters K_d, w, and g are known. Thus the important parameters for determining ion exchange effects during overland flow are w, the volume of water per unit area, g, the effective weight of soil acting as an ion exchanger (per unit area), and K_d, the exchange distribution coefficient which is characteristic of the soil type in the basin. In addition, R, the total amount of radionuclide present per unit area of the system must be known to obtain an absolute measure of the ion quantities in the liquid and soil phases.

The distribution coefficient, K_d, may be found experimentally for a watershed, using representative samples of soil and runoff water. Reynolds and Gloyna (*11*), in studies of the uptake and release of radionuclides by stream sediments in the Guadalupe River in Texas, measured the distribution coefficient for strontium between river sediments and fresh water under both static (laboratory) conditions and flow (actual) conditions. For a representative sediment having a cation exchange capacity of 35 meq./liter, and a suspended sediment concentration of 500 mg./liter, K_d was 198 ml./gram. This corresponds to about 9% of the strontium sorbed on the sediments. Under actual flow conditions, the strontium K_d value was computed on the basis of mass action equations, the cation concentration of the water, and the selectivity or mass action coefficients determined in static equilibrium studies. Direct measurements of strontium K_d values in sediment were also made from ^{90}Sr content. Computed values of the strontium K_d were 72 and 128 ml./gram, from the headwaters and mouth, respectively, of the Guadalupe River. The corresponding measured K_d values were 767 and 500 ml./gram, respectively. During the HTM-1 field study, K_d values in the Saratoga Creek watershed were found to be 300 ± 30 and 25,000 ± 10,000 ml./gram for ^{90}Sr and ^{137}Cs, respectively. Individual K_d measurements for several different storms are summarized in Table I. Although the K_d values for ^{90}Sr are constant within ±10% over the three-storm sampling period, the values for ^{137}Cs appear to increase significantly. This increase may be associated with the decrease in suspended solids in the samples and reflect the possibility that the concept of an equilibrium distribution coefficient for an element held so strongly by soils may not be adequate. However, it may also be caused by the large errors associated with the measurements and the small sampling of data.

The effective weight of exchanger, g, is perhaps the most significant and difficult ion exchange parameter to measure. For the HTM-1, the soil mass available for exchange with overland flow is taken as the sum of the load transported by sheet flow during runoff and a constant weight of soil presented to the flow at the stationary ground surface. The con-

Table I. Determinations of K_d for ^{90}Sr and ^{137}Cs

Storm				K_d	
Date	*Time*	m, *grams*	w, *liters*	^{90}Sr	^{137}Cs
12/28/65	1300	19.1	10.90	306 ± 45	13,200 ± 6,000
12/28/65	1600	59.7	11.27	310 ± 45	19,500 ± 10,000
2/1/66	0640	9.5	12.16	300 ± 50	25,300 ± 12,000
2/1/66	0710	8.8	11.65	242 ± 45	23,500 ± 12,000
11/28/66	1800	3.5	11.95	324 ± 52	31,600 ± 15,000
11/28/66	2100	3.6	12.20	333 ± 55	38,600 ± 15,000
Average value for K_d				302 ± 30	25,300 ± 10,000

stant weight of soil exposed at the land surface has been taken as the ratio of surface area to the average specific area for the soil.

The weight of soil carried in the surface runoff has been estimated by relating the sediment load to the rate of energy dissipation at the land surface by the rainfall and flowing water. The resistance of the soil to eroding forces has also been considered (*4*), and a method has been developed to estimate the net effect of erosion on radioaerosol transport. The volume of the liquid phase is estimated on a continuous basis by the Stanford watershed model, through consideration of a water budget. This feature has been retained in the HTM-1.

The effect of infiltrating water is a downward migration of radioactive aerosols from the surface into the soil profile. As infiltrating water percolates downward, ion exchange occurs between the soil and water phases, and gradually the radioactive aerosols are left behind in the soil phase. The migration process removes some of the deposited aerosol from the soil surface, altering the aerosol transport rate out of the watershed.

A number of methods have been proposed for predicting the migration of radionuclides through the soil. Most methods have used a concept of layers of soil, one upon another, with the radionuclide migrating from the top layer downward.

Thornthwaite (*14*) proposed the equation:

$$X_n = \frac{t!}{(t-n)!n!} k^n (1-k)^{(t-n)} X_o \qquad (7)$$

where X_n = concentration of nuclide on the nth layer
n = receiving layer
t = cycle of leaching
k = fractional loss per cycle
X_o = initial concentration of strontium in the source layer

to relate the concentration of ^{90}Sr in any layer to the initial concentration of ^{90}Sr in the source layer. Spitsyn, Balekova *et al.* (*13*) report a similar

equation for migration of ^{90}Sr through soil by a solution of constant composition:

$$q_n = q_o \frac{(k)^n}{V/m + k} \tag{8}$$

where q_o = quantity of ^{90}Sr on sorbent prior to desorption
q_n = quantity of ^{90}Sr on sorbent after desorption
n = number of desorption events
k = constant
v = volume of solution used in each desorption cycle
m = weight of sorbent

Both equations consider the migration of a single input source of ^{90}Sr in the top layer. Under natural conditions however, additional input of radioactive aerosol to the "source layer" is furnished by the incoming precipitation.

The quantitative description of the migration process and resulting soil contamination profile, including the effect of a continuous and variable aerosol input, may be adopted from ion exchange plate theory as presented by Mayer and Tompkins (9).

The soil profile is considered to be composed of a number of theoretical plates of finite thickness in which ion exchange equilibrium is achieved. Each plate has an equivalent mass of exchanger m, and volume of solution v. During infiltration, a plate volume of solution is defined as progressing downward into the soil from plate to plate slowly enough that exchange equilibrium is achieved in each plate. The general equations used to describe the migration process and the resulting radionuclide profile may be written as:

$$A_{L_{n,p}} + A_{S_{n,p}} = A_{L_{n,p-1}} + A_{S_{n-1,p}} \tag{9}$$

$$\frac{A_{S_{n,p}}}{A_{L_{n,p}}} = C \tag{10}$$

where A = amount of nuclide present in d.p.m.
L = liquid phase
S = soil phase
n = number of plate volumes of water that have entered into a plate up to any given time
p = the number of the theoretical plate
C = constant related to the distribution coefficient.

It may be shown that in general, for any plate p and any n,

$$A_{L_{n,p}} = (A_{L_{n,p-1}} + A_{S_{n-1,p}}) \cdot \frac{1}{(1 + C)} \tag{11}$$

$$A_{S_{n,p}} = C \cdot A_{L_{n,p}} \tag{12}$$

Table II. Aerosol Input Parameters
Basin Inventory

Program Parameter	*Parameter Definition*	*Input Values, d.p.m./ft.²*	
		^{90}Sr	*^{137}Cs*
AZERO	Quantity of aerosol contained on vegetal surfaces which is available for hydrologic transport	400	600
ANOT	Quantity of aerosol contained on the land surface which is available for hydrologic transport	20	30
SDPM	Quantity of aerosol contained in top 2-inch layer of soil	16,100	24,915
SONE STWO STRE SFOR	Quantity of aerosol contained in the four theoretical exchange plates	80	578

Table III. Radioaerosol Discharge Saratoga Creek Watershed
December 28, 1965

Time	*Q, c.f.s.*		*^{90}Sr Discharge*[a]		*^{137}Cs Discharge*[a]	
	Observed	*Simulated*	*Observed*	*Simulated*	*Observed*	*Simulated*
1230	33	40	1620	1120	5100	3579
1300	30	43	1070	1189	2530	3754
1400	52	42	2660	1122	4890	4318
1500	75	38	4480	967	16300	2831
1600	85	47	4790	1149	22600	3294
1700	99	64	6140	1848	21300	4799
1745	118	72	7660	2235	27700	5350

[a] Discharge units are d.p.m./sec. corresponding to the hydrograph discharge units of ft.³/sec. Errors on observed values are estimated to be ±5% based upon repeated analysis of ^{90}Sr and ^{137}Cs standards in water samples.

Model computations begin with an estimate of the radioactive aerosol content of the infiltrating solution. This may be based on either direct input from vegetal storage in the absence of overland flow or the sheet flow aerosol concentration computed on the basis of exchange reactions during overland runoff. The known value of the surface soil content prior to infiltration is also used to determine the total content of the

Table IV. Radioaerosol Discharge Saratoga Creek Watershed
February 1, 1966

	Q, *c.f.s.*		*^{90}Sr Discharge*[a]		*^{137}Cs Discharge*[a]	
Time	*Observed*	*Simulated*	*Observed*	*Simulated*	*Observed*	*Simulated*
2115[b]	8.4	10.5	143	121	31	2
0115	10.8	10	206	108	162	2
0300	14.5	12	246	142	103	108
0411	14.8	14	259	170	84	202
0508	21.6	25	441	715	415	894
0607	33.5	44	892	967	2300	2364
0640	37.3	45	832	1000	2480	2366
0710	36.0	41	846	904	1510	2034
0740	33.5	36	841	771	2080	1589
1040	20.5	22	514	367	1180	230
1140	19.0	21	493	337	970	129

[a] Discharge units are d.p.m./sec. corresponding to the hydrograph discharge units of ft.^{3}/sec. Errors on observed values are estimated to be ±5% based upon repeated analysis of ^{90}Sr and ^{137}Cs standards in water samples.
[b] Jan. 31, 1966.

Table V. Radioaerosol Discharge Saratoga Creek Watershed
November 28, 1966

	Q, *c.f.s.*		*^{90}Sr Discharge*[a]		*^{137}Cs Discharge*[a]	
Time	*Observed*	*Simulated*	*Observed.*	*Simulated*	*Observed*	*Simulated*
1617	7.4	15.5	178	235	140	700
1700	8.8	18	204	265	170	803
1800	9.2	23	187	352	270	1090
1900	9.6	23	304	353	350	1105
2000	12.0	19	308	279	320	866
2100	12.0	14	292	198	500	595
2200	11.6	11	285	142	380	405
2300	10.4	8	267	105	250	276
2400	10.4	7	277	81	210	191

[a] Discharge units are d.p.m./sec. corresponding to the hydrograph discharge units of ft.^{3}/sec. Errors on observed values are estimated to be ±5% based upon repeated analysis of ^{90}Sr and ^{137}Cs standards in water samples.

theoretical plate. Each infiltrating volume migrates through four plate thicknesses, and the resulting outflow is added to the subsurface soil inventory. A four-theoretical plate model was chosen arbitrarily. The goal of the computation is not a complete depth-concentration profile; instead it is to provide a smooth transition between the surface layer and the subsurface (interflow) layer radioaerosol content.

The numerical values assigned to the constants in the migration equations may be obtained by experimentally ascertaining the thickness

of the theoretical plates, their effective mass, their liquid capacity v, and the constant C. The effective soil mass is the density of the undisturbed soil multiplied by the volume of one plate. The liquid capacity v, is the porosity multiplied by the plate volume, and the value of C may be computed as:

$$C = \frac{m}{v} \cdot K_d \tag{13}$$

The beginning radionuclide concentration values for individual plates are initial conditions determined by the soil concentration profiles. Thus, a continuous tabulation of the concentration profiles is maintained during simulation. This is of primary importance during rain periods when no overland flow occurs since it will tend to alter the surface soil concentration. Decreases in the surface layer radioaerosol concentration arising from infiltration will cause a corresponding decrease in subsequent surface runoff aerosol transport.

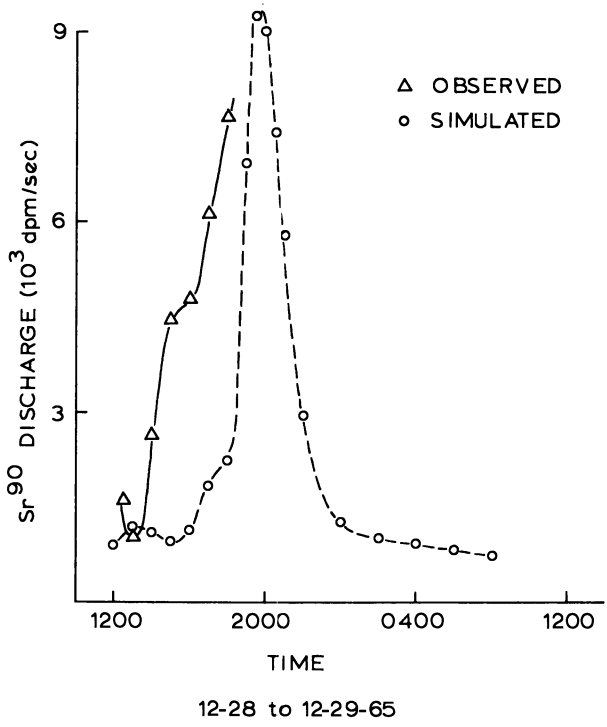

Figure 2. Saratoga Creek ^{90}Sr radioaerosol discharge (Dec. 28, 1965)

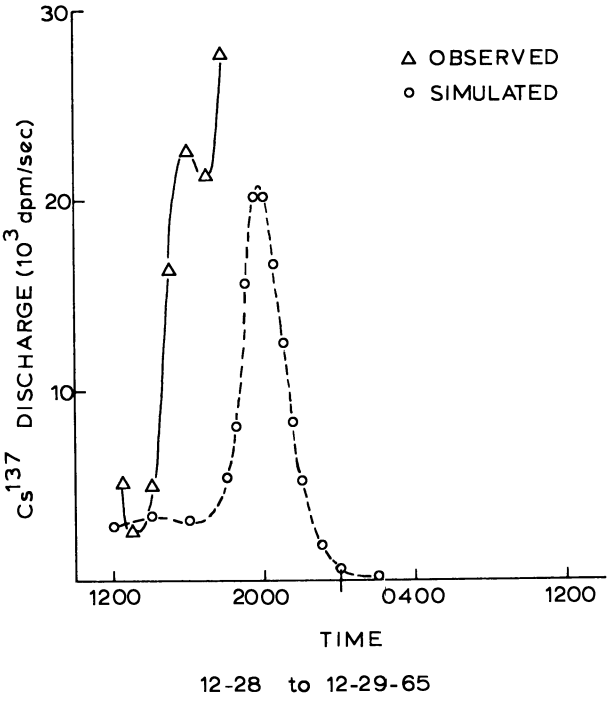

Figure 3. Saratoga Creek ^{137}Cs radioaerosol discharge (Dec. 28, 1965)

The effects of interflow on radioactive aerosol transport must also be considered, especially for the more readily exchanged elements. It has been assumed for the model, that interflow input to the channel will remain in the top layer of the soil long enough before reaching the stream channel system for the distribution of the radioactive aerosols to reach equilibrium between solid and liquid phases. The aerosol content of the interflow water may be computed using Equation 5 with the distribution coefficient, the estimated soil content, and the content of incoming water for surface infiltration. A continuous balance between incoming aerosol from infiltration and aerosol loss from the interflow generating layer, through channel inflow and deep percolation, is maintained during all storms. All radioaerosols lost by deep percolation are assumed to remain within the watershed until they decay to stable isotopes. The groundwater input of radioaerosols to the stream channel is assumed to be negligible. Measured values of ^{90}Sr and ^{137}Cs both in groundwater from wells within the experimental watershed and in base (groundwater) flow in the stream channel indicate this is a valid assumption.

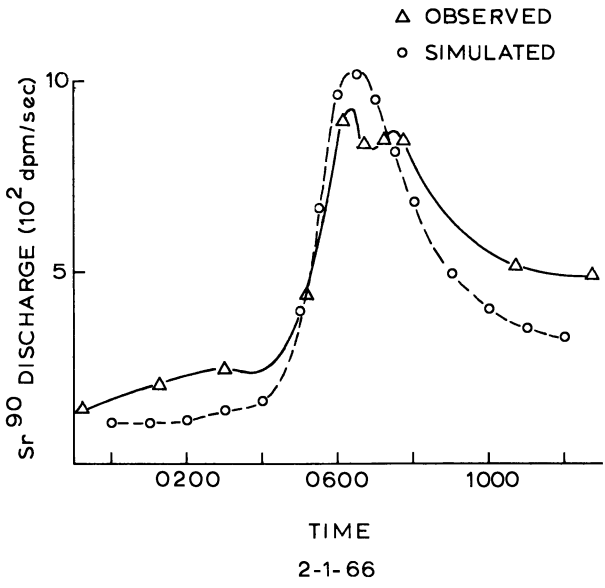

Figure 4. Saratoga Creek ^{90}Sr radioaerosol discharge (Feb. 1, 1966)

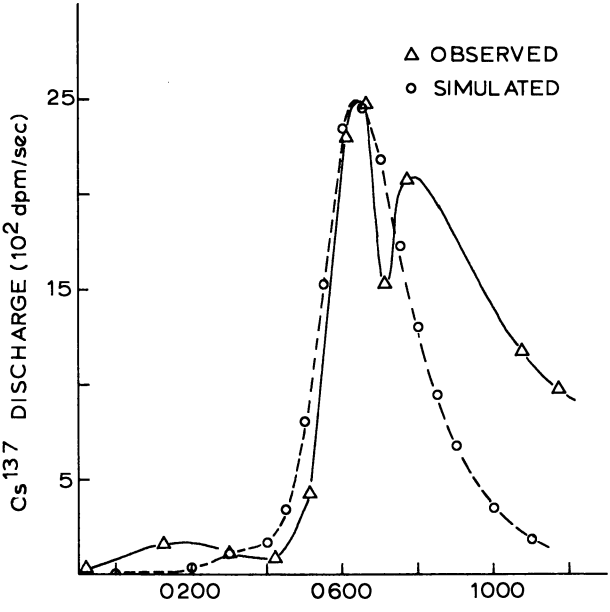

Figure 5. Saratoga Creek ^{137}Cs radioaerosol discharge (Feb. 1, 1966)

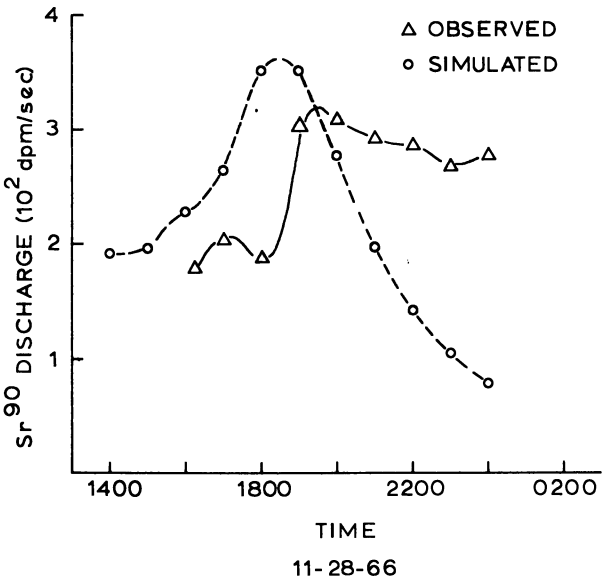

Figure 6. Saratoga Creek ^{90}Sr radioaerosol discharge (Nov. 28, 1966)

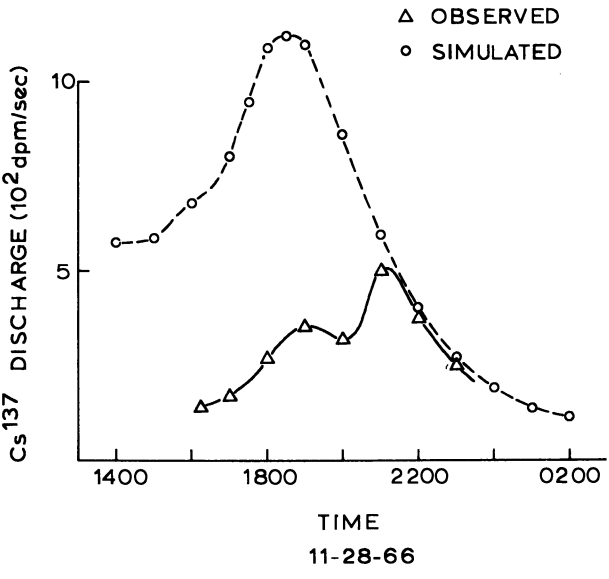

Figure 7. Saratoga Creek ^{137}Cs radioaerosol discharge (Nov. 28, 1966)

Channel System Transport

The final step in the hydrologic transport of radioactive aerosols through a watershed is transmission through the channel system to the basin outlet. Aerosol input to the main channels in the basin from land surface runoff and interflow must pass through the channel system in a manner governed by the laws of hydraulics. Simulation of the timing of radioaerosol outflow from the basin must therefore include a consideration of channel transport.

Shih and Gloyna (*12*) studied the transport of ^{137}Cs and ^{85}Sr in a model river containing sediments, typical rooted plants, and suspended plankton. A single release of radionuclides into a sluggish stream system was made, and it was found that most of the ^{137}Cs and ^{85}Sr remained in the water phase. A significant amount of both nuclides was temporarily removed from solution by plants and sediments, however, and subsequent release ranged from a few days for the plants to several months for the bottom sediments. In other work related to channel transport of radioaerosols Kornegay *et al.* (*5*) reviewed studies in determining movement of nuclides in stream channels and the uptake and release of these nuclides by sediments within the stream. Most of the investigations reviewed were concerned with channel transport of nuclides in solution discharged into streams over long periods. The results generally show that considerable uptake by sediments can occur and that radioaerosol accumulation points may be found within the channel system. Release from these areas may constitute an important long term source of stream contamination. However, during natural transport of aerosols carried through the channel system by storm runoff, conditions are likely to be considerably different from those encountered during quiescent conditions. The size of the channel system and the physical and hydraulic characteristics are of considerable importance. Removal of aerosol nuclides from the flow by bottom sediments may occur during storm flow, but subsequent channel scour may still act to carry the sorbed nuclides out of the basin. For the model, it has been assumed that the radioactive aerosols carried into the stream channel remain in solution or sorbed on suspended material. Soluble radionuclides in the stream water may exchange with suspended sediments during flow, but it is most likely that sorption will take place on the fine grained clay minerals; thus the probability of deposition in the stream channel is small. Based on these considerations, the radioactive aerosol is assumed to be quantitatively carried by the transporting water.

Results of Field Studies. Standard radiochemical analyses were performed on selected soil and vegetation samples taken from the experi-

mental catchment. Representative values from these assays served as primary input to the HTM-1 computations. These data are given in Table II.

Radioaerosol discharge is computed as the product of observed concentration $\left(\frac{\text{d.p.m.}}{\text{ft.}^3}\right)$ and observed discharge $\left(\frac{\text{ft.}^3}{\text{sec.}}\right)$. Thus the radioaerosol discharge represents the total mass flow of the specified nuclide out of the basin. The computed values of radioaerosol discharge in streamflow and the corresponding measured values for the three storms examined are listed in Tables III, IV, and V. Comparisons of these data are shown in Figures 2 through 7. These data are considered insufficient for meaningful quantitative evaluation of the model operation, but they suggest that the HTM-1 simulation model does give a reasonable representation of the processes causing hydrologic transport of radioaerosols.

One major difficulty in assessing the accuracy of any transport simulation method is the inaccuracy in runoff estimations. The basin selected for the study described was of minimum size for application of the Stanford watershed model. This is reflected in the corresponding uncertainties in all computations. However, it is worth noting that the measured and simulated concentrations of ^{90}Sr and ^{137}Cs seldom differed by more than a factor of two. This observation suggests that increasing the accuracy of simulated runoff processes will result in an increased accuracy in radioaerosol transport estimates as well.

Sediment load and radioaerosol discharge are highly correlated for the three storms investigated in the field study. This is expected for cesium, owing to its strong tendency to sorb on soil particles. It is also expected to a lesser degree for strontium. Some indication of the strength of the relationship between sediment load and radioaerosol discharge may be derived from experimental observations. If a weight-concentration of radioaerosol is empirically determined from radioassay of a single sediment sample, and the product of the measured weight concentration and sediment load at various times throughout a storm event are computed, the results compare well with corresponding observed radioaerosol discharge values. This observation suggests that frequent sediment load measurements, in combination with a few radioassays to determine ^{90}Sr and ^{137}Cs weight-concentrations in the sediment load, could be used to estimate continuous radioaerosol discharge. Such a procedure would substantially reduce the time, effort, and cost expended in determining the time graph of radioaerosol discharge for a basin. The advantages of such a reduction are clearly evident.

The strong correlation between sediment load in a stream and corresponding radioaerosol discharge emphasizes the importance of interactions between soils and radioaerosols in contact. The results to date

indicate that several aspects of soil-radioaerosol interactions could be studied fruitfully in the future. The most important of these aspects are the equilibrium rates between soil and radioaerosols in solution during overland flow, migration of radioaerosols into the soil profile through the leaching action of infiltrating water, and a more detailed consideration of suspended sediment movement in a channel system during storm events. Inclusion of the results of such studies in later versions of the HTM should lead to improved performance of the model in the future.

Acknowledgments

The authors acknowledge with appreciation the assistance of N. H. Crawford and R. K. Linsley in the use of the Stanford watershed model computer program. Assistance and data for this study were also provided by the Santa Clara County Flood Control and Water District, the San Jose Water Works, and the U. S. Geological Survey in Menlo Park.

Literature Cited

(1) Crawford, N. H., Linsley, R. K., Stanford University, Department of Civil Engineering, *Tech. Rept.* 12 (1962).
(2) Huff, D. D., Kruger, P., *Am. Geophys. Union Monograph* 11 (1967).
(3) Huff, D. D., Kruger, P., *Intern. Hydrology Symp., Fort Collins, Colo., Sept. 1967.*
(4) Huff, D. D., Ph.D. Dissertation, Stanford University (Jan. 1968).
(5) Kornegay, B. H., Vaughan, W. A., Jamison, D. K., Morgan, Jr., J. M., Eds., *U. S. At. Energy Comm. Rept.* **TID 7664** (1963).
(6) Kunin, R., "Ion Exchange Resins," Wiley, New York, 1958.
(7) Lockhart, Jr., L. B., Patterson, Jr., R. L., Saunders, Jr., A. W., U. S. Naval Research Laboratory, *Rept.* **6164** (1964).
(8) Martell, E. A., *Science* **129,** 1197-1206 (1959).
(9) Mayer, S. W., Thompkins, E. R., *J. Am. Chem. Soc.* **69,** 2866-2873 (1947).
(10) Menzel, R. G., Frere, M. H., Larson, K. H., Overstreet, R., Reitemeier, R. F., *Natl. Acad. Sci.—Natl. Res. Council Publ.* **1092** (1963).
(11) Reynolds, T. D., Gloyna, E. F., *Intern. Conf. Water Pollution Res., 2nd,* Section 1, Paper 8, 1-14 (1964).
(12) Shih, Chia-Shun, Gloyna, E. F., University of Texas, Environmental Health Engineering Research Laboratory, **CRWR-10** (1966).
(13) Spitsyn, V. I., Balekova, V. D., Naumova, A. F., Gromov, V. V., Spiridonov, F. M., Vetror, E. M., Grafov, G. I., *Proc. U. N. Intern. Conf. Peaceful Uses Atomic Energy, Geneva, 2nd,* **18,** 439-448 (1958).
(14) Thornthwaite, C. W., Mather, J. R., Nakamura, J. K., C. CW Thornthwaite Associates Laboratory of Glimatology, *Tech. Rept.* 1 (1961).

RECEIVED November 13, 1968. Work supported in part by the U. S. Public Health Service Grant ES-00047 and by a Federal Water Pollution Control Administration Fellowship Grant.

28

Short Lived Cosmic Ray-Produced Radionuclides as Tracers of Atmospheric Processes

JAMES A. YOUNG, NED A. WOGMAN, CHARLES W. THOMAS, and RICHARD W. PERKINS

Battelle Memorial Institute, Pacific Northwest Laboratories, Richland, Wash. 99352

Radionuclides are produced in the atmosphere by cosmic rays at a relatively constant rate. This paper reports the measured atmospheric disintegration rates of the cosmogenic radionuclides ^{7}Be (53 days) and ^{24}Na (15 hours) at 46°N from ground level to 63,000 feet. The activity of ^{7}Be changes with time owing to atmospheric motions and deposition at the earth's surface; however, the shorter lived radionuclide ^{24}Na remains nearly at equilibrium with its production rate. The disintegration rates of the cosmogenic radionuclides ^{39}Cl (55 min.), ^{38}Cl (37 min.), and ^{7}Be (53 days) in rainwater are also reported, and their use in studying the efficiencies and time scales of the precipitation scavenging of atmospheric aerosols is discussed.

Radionuclides are produced continuously in the atmosphere by cosmic rays. Their production rates vary considerably with altitude and latitude but remain relatively constant with time. Following formation, these radionuclides quickly become attached to atmospheric aerosols and thus can trace the subsequent behavior of these aerosols. Some of the cosmic-ray produced radionuclides with half-lives of months to years have been used in studying atmospheric mixing processes, while the longer lived radionuclides have served as tracers of geophysical processes and in dating biological and geological phenomena.

Radionuclides with half-lives of minutes to hours would be useful in studying atmospheric precipitation scavenging mechanisms since their half-lives are of the same order of magnitude as the time scale on which

precipitation processes occur (*1, 4*). The natural atmospheric aerosols are vital to rain and snow formation since water droplets or ice particles are formed by the condensation of water vapor on aerosol particles. Aerosol particles are also picked up by a water droplet or ice particle after nucleation while it is still in the cloud or falling below the cloud. Not much is known about the relative efficiencies of nucleation and post-nucleation scavenging of the aerosol particles. The problem is difficult to study in the laboratory or by introducing artificial aerosols such as silver iodide into the atmosphere since scavenging mechanisms are very sensitive to the properties, including electrical charge, of the aerosol particle. It is difficult, if not impossible, to duplicate the natural atmospheric aerosol distribution in the laboratory.

The concentrations and concentration ratios of the short lived cosmic ray-produced radionuclides in precipitation can be used to study the efficiencies and time scales of nucleation and post-nucleation scavenging. As shown below, the $^{39}Cl/^{38}Cl$ ratios in precipitation provide information on the time between the incorporation of aerosol particles in the raindrop or snowflake and the arrival of the precipitation at ground level if the atmospheric ^{38}Cl (37 min.) and ^{39}Cl (55 min.) concentrations are known. If the altitude of rain formation can be determined using radar or some other method, the aerosol scavenging efficiency of the precipitation can be determined from the concentrations of the short lived cosmic ray radionuclides in the atmosphere and in the precipitation.

Table I. Half-Lives and Decay Characteristics of the Cosmic Ray-Produced Radionuclides

Radionuclide	*Half-Life*	
^{10}Be	2.7×10^6 years	β^- 555 k.e.v.
^{36}Cl	3.1×10^5 years	β^- 714 k.e.v.
^{14}C	5568 years	β^- 156 k.e.v.
^{32}Si	~700 years	β^- 100 k.e.v.
^{3}H	12.3 years	β^- 18 k.e.v.
^{22}Na	2.6 years	β^+, γ 1.28 M.e.v.
^{35}S	88 days	β^- 167 k.e.v.
^{7}Be	53 days	β^-, γ 480 k.e.v.
^{33}P	25 days	β^- 246 k.e.v.
^{32}P	14.3 days	β^- 1.724 M.e.v.
^{28}Mg	21.3 hours	β^-, γ 1.35 + 0.031 M.e.v.
^{24}Na	15.0 hours	β^-, γ 1.38 + 2.76 M.e.v.
^{38}S	2.9 hours	β^-, γ[a] 1.6 + 2.16 M.e.v.
^{31}Si	2.62 hours	β^-, γ 1.27 M.e.v.
^{39}Cl	55 min.	β^-, γ 0.246 + 1.266 M.e.v.
^{38}Cl	37 min.	β^-, γ 1.6 + 2.16 M.e.v.
^{34m}Cl	32 min.	β^+, γ 1.16 + 2.13 M.e.v.

[a] Radiation caused by the ^{38}Cl daughter.

Since the production rates of the cosmic ray radionuclides increase rapidly with increasing altitude in the lower atmosphere, the atmospheric concentrations and ratios of short lived cosmic ray radionuclides can be used to study rapid vertical air motions if the equilibrium concentrations of the radionuclides are known. For example, the concentrations of the short lived cosmic ray radionuclides in air which has moved upward recently from a lower altitude will be less than the equilibrium concentrations. The concentrations of the radionuclides will therefore increase with time until equilibrium is reached. However, the concentration of the shorter lived of two short lived radionuclides will increase more rapidly initially, causing the ratio of the two radionuclides of different half-lives to change with time until equilibrium is reached. Therefore, the time since the air moved from a lower altitude, the speed of the upward motion, and the altitude from which the air originated could be calculated from the concentrations and concentration ratios of cosmic ray radionuclides of different half-lives. Vertical motions of different speeds could be studied since several cosmic ray radionuclides of different half-lives are present in the atmosphere (Table I). Many other radionuclides are produced by cosmic rays in the atmosphere, but they have not yet been detected. Some of these with half-lives of a few minutes could serve as tracers of very short term processes such as post-nucleation scavenging.

The use of short lived cosmic ray produced radionuclides for studying air motions and precipitation scavenging has been limited by a lack of knowledge of their production rates as a function of latitude and altitude. Estimates have been extrapolated from mass yield and charge distribution curves for spallation reactions. However, most of these extrapolations are good only to within a factor of about four. Before short term air motions and precipitation scavenging can be studied quantitatively by this technique, the atmospheric disintegration rates of the short lived radionuclides must be determined. The atmospheric ^{24}Na disintegration rates from ground level to 63,000 feet reported herein provide the first atmospheric measurement of the production rate of ^{24}Na as a function of altitude. This paper also includes measurements of ^{24}Na, ^{38}Cl, and ^{39}Cl in rainwater and discusses their use in the study of atmospheric mixing and precipitation processes.

Production and Distribution of Cosmic Ray-Produced Radionuclides

The high energy primary cosmic rays produce many secondary neutrons and protons which in turn are responsible for most of the spallation reactions resulting in radionuclide production in the atmosphere. The formation of these radionuclides occurs at reaction thresholds of 10–40 M.e.v. Because of local ionization losses the secondary protons lose their

energy quickly; hence, neutrons are responsible for most of the nuclear reactions resulting in radionuclide production. As a first approximation, the ratios of the production rates of the various radionuclides are independent of latitude and time. The relative atmospheric radionuclide production rate has been calculated as a function of altitude and latitude by Lal (3). The radionuclide production rate per gram of air increases approximately exponentially with increasing altitude, increasing by almost three orders of magnitude between ground level and about 70,000 feet at 46°N. Above 70,000 feet the production rate at 46°N decreases slowly with increasing altitude owing to the escape of neutrons from the top of the atmosphere. The production rate increases by almost an order of magnitude in moving from the equator to the geomagnetic poles.

High Altitude Air-Sampling Program

Sample Collection and Analysis. In March 1967 we began obtaining air filter samples from RB-57 aircraft flights. Approximately once a month, samples were collected at 5000- or 10,000-foot intervals between 10,000 and 63,000 feet. Most of the initial samples were collected over

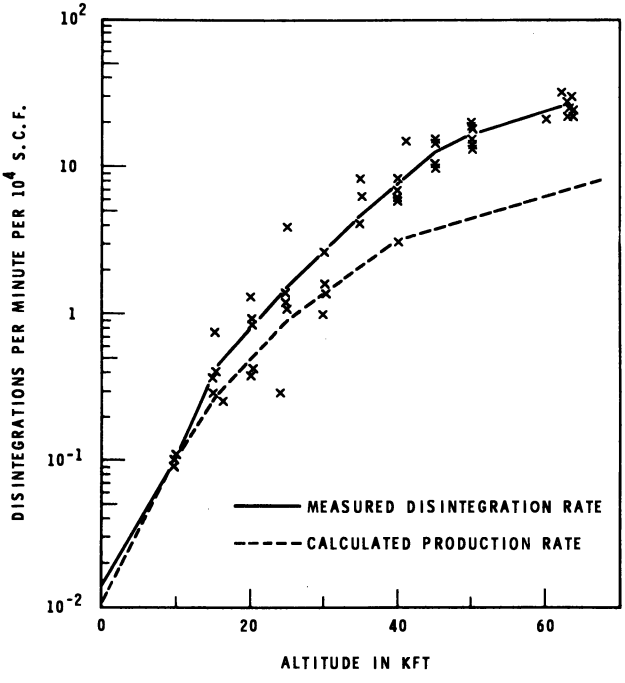

Figure 1. ^{24}Na disintegration rate as a function of altitude at 46°N

an area just south of Spokane, Wash. at 46°N and 117°W. On some flights a complete profile of samples over this altitude range was obtained. Immediately after the filters were removed from the RB-57 at Spokane, Wash., they were rushed to the Pacific Northwest Laboratory near Richland, Wash. and counted directly for 1000 minutes using multidimensional γ-ray spectrometers (5) to determine the concentration of the short lived cosmic ray produced radionuclide ^{24}Na (15 hours) and to look for shorter lived ^{38}Cl (37 min.) and ^{39}Cl (55 min.). The concentrations of the longer lived cosmic ray produced ^{7}Be (53 days) and ^{22}Na (2.6 years) and the nuclear bomb produced radionuclides ^{54}Mn, ^{60}Co, ^{65}Zn, ^{95}Zr–Nb, ^{103}Ru, ^{106}Ru, ^{110m}Ag, ^{125}Sb, ^{134}Cs, ^{137}Cs, ^{140}Ba, ^{144}Ce, and the radon daughters ^{208}Tl and ^{214}Bi were also determined from this or a subsequent count.

Results. ^{24}Na. The measured ^{24}Na disintegration rates at 46°N are plotted as a function of altitude in Figure 1. The ground level disintegration rate used was measured on an air sample collected in early 1967 on the Hoh River in the Olympic Peninsula, Wash. This point is about 600 feet above sea level. In the high altitude measurements there appears to be no systematic variation in activity with time. The activity increased approximately exponentially with increasing altitude by a factor of about 2000 between ground level and 62,000 feet. The ^{24}Na activities in the atmosphere are low, and the measured disintegration rates had fairly large statistical counting errors. The scatter of the points from the line in Figure 1 is about equal to the counting error standard deviations of the individual points. Since the variation in the measured disintegration rates were within the expected statistical limits, the ^{24}Na activity at each altitude appears to be fairly constant and is probably in near equilibrium with its production rate by cosmic rays.

The calculated production rate of ^{24}Na as a function of altitude at 46°N is also shown in Figure 1. Below about 20,000 feet the calculated production rates agree fairly well with the measured disintegration rates. With increasing altitude, however, the observed disintegration rates become progressively higher than the calculated production rates. There does not seem to be any mechanism by which disintegration rates in the stratosphere at the above latitude could be continuously maintained significantly above the production rates. Vertical and meridional air movement are relatively slow in the stratosphere. The calculated production rate increases little above 62,000 feet, reaching a maximum at about 70,000 feet. Also the production rate increases little with increasing latitude north of 46°N. Therefore, the measured disintegration rate should provide a very good estimate of the true production rate, and thus the observed disintegration rate curve in Figure 1 can serve as a production rate curve.

^{38}Cl AND ^{39}Cl. Recently we put into operation a portable counting laboratory containing a chemical laboratory and two multidimensional

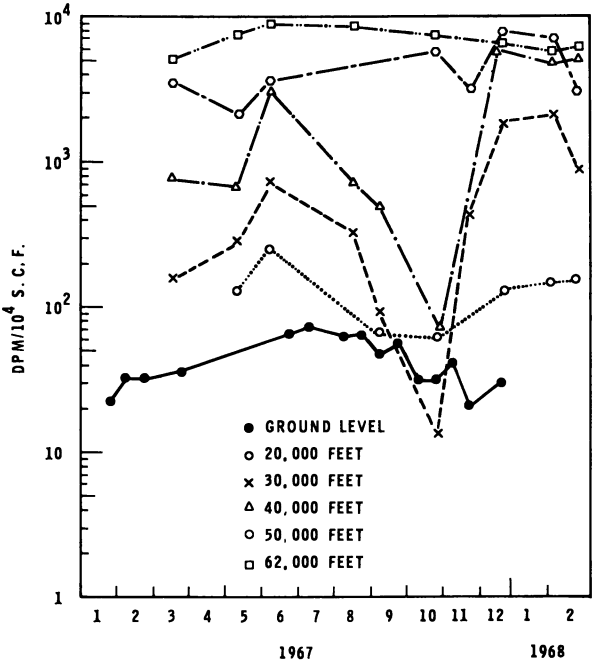

Figure 2. ^{7}Be disintegration rate as a function of time and altitude at 46°N, 117°W

γ-ray spectrometers. With this mobile laboratory we have determined the ^{38}Cl (37.3 min.) and ^{39}Cl (55 min.) disintegration rates in air filter samples by counting them immediately after the RB-57 sampling aircraft landed at Spokane. The ^{38}Cl and ^{39}Cl disintegration rates were about equal and were about 10 times the ^{24}Na disintegration rate. The measured ^{38}Cl and ^{39}Cl disintegration rates will be published later (7).

^{7}Be. The half-life of the cosmic ray-produced radionuclide ^{7}Be (53 days) is long enough so that its atmospheric activities are affected considerably by air motions and wet and dry deposition at the earth's surface. In Figure 2 the ^{7}Be disintegration rate is plotted as a function of time for several altitudes from ground level to 62,000 feet. The disintegration rate increased by a factor of approximately 100 between ground level and 62,000 feet. This increase is only about one-tenth as great as the increase in ^{24}Na activity between ground level and 62,000 feet.

At 50,000 and 62,000 feet ^{7}Be showed little change with time. However, below 40,000 feet ^{7}Be showed a marked seasonal variation. In 1967 the ^{7}Be activity increased in the spring, reaching a maximum in the June 5 sample. The activity then decreased again, reaching a minimum in the October 23 sample. By December 18 the ^{7}Be activity had increased

by a factor of 100 at 30,000 and 40,000 feet. At this time there was little difference between the ^{7}Be activities at 40,000 and 62,000 feet. The increase in ^{7}Be activity after October 23 was much smaller at 20,000 feet.

The variation in ^{7}Be with altitude and time at 46°N was very similar to the variations in the activities of the bomb-produced radionuclides, except in the case of short lived fission products whose seasonal variations were obscured largely by debris from recent nuclear tests. Figure 3 shows the ^{137}Cs disintegration rate plotted as function of time for several altitudes. As for ^{7}Be, ^{137}Cs reached a maximum at 40,000 feet and below on June 5, 1967 and then decreased. The activities of ^{137}Cs and the other bomb-produced radionuclides increased sharply again from 20,000 to 40,000 feet after October 23.

Because of the similarity in the seasonal variations of ^{7}Be and the bomb-produced radionuclides it seems likely that the variations can be attributed primarily to the same cause. Probably radionuclides are transported down into the low polar stratosphere in the winter when the polar stratosphere is least stable and, therefore, vertical mixing is most intense (*2*). The radionuclides then diffuse quasihorizontally through the tropopause gap into the troposphere and eventually to ground level. This

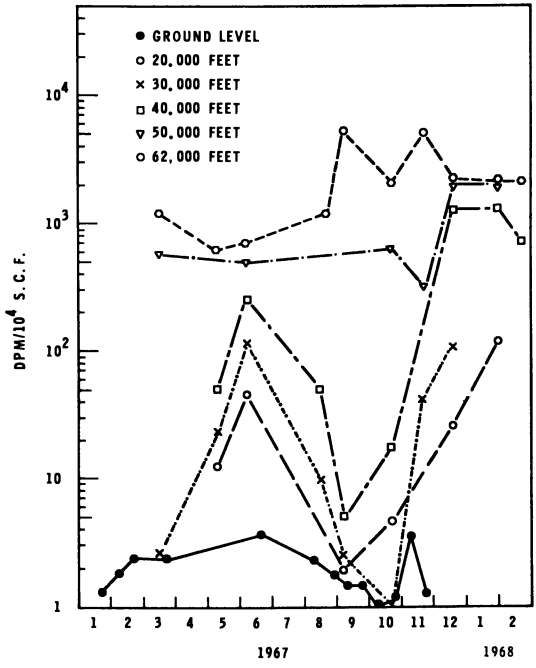

Figure 3. Disintegration rate of ^{137}Cs as a function of time and altitude at 46°N, 117°W

would explain why radionuclide disintegration rates reached a maximum in the lower stratosphere some time before maximums are generally observed at ground level. In the troposphere, of course, the seasonal variations are also affected considerably by seasonal variations in the rainfall rate and the rates of vertical and meridional mixing.

^{7}Be should be a useful tracer in detailed studies of atmospheric transport and washout. It is not produced in significant quantities by nuclear tests, and therefore variations in its activity from year to year should reflect variations in atmospheric processes. Several investigators have measured ^{7}Be at different altitudes and latitudes. As the latitude, altitude, and time variations become better known, it should be possible to calculate precisely the rates of vertical and meridional transport and the rates of deposition at the earth's surface.

Cosmic Ray-Produced Radionuclides in Rainwater

In 1966 and 1967 several rain and snow samples were collected at our laboratory (*6*). The analysis of these samples for the short lived cosmogenic radionuclides has provided new insight into precipitation mechanisms. However, the rainfall rate at Richland is only about 7 inches a year, and it was therefore difficult to obtain sufficient samples for detailed precipitation scavenging studies. In January 1968 our portable laboratory was moved to Quillayute air base near Forks, Wash. on the western side of the Olympic Peninsula, where the average yearly rainfall is about 120 inches. During a five-day period 37 rain samples, one snow sample, and one mixed snow and hail sample were collected. The atmospheric precipitation samples were collected on plastic sheets with surface areas of approximately 1000 square feet. These samples, having volumes of up to 110 liters, were transferred immediately to the laboratory where the radionuclides ^{34m}Cl, ^{38}Cl, and ^{39}Cl were separated by a rapid silver chloride precipitation and immediately counted, using multidimensional γ-ray spectrometers. The filtrate, which contained the remaining airborne radionuclides, was later evaporated to dryness, and the radionuclide disintegration rates were determined by direct counting, using multidimensional γ-ray spectrometers.

Results. The observed ^{38}Cl and ^{39}Cl disintegration rates in the rain and snow samples are plotted as a function of precipitation rate in Figures 4 and 5. The observed activities varied inversely with the precipitation rate, with ^{39}Cl and ^{38}Cl decreasing by more than an order of magnitude when the rainfall rate increased from 0.015 to about 0.15 inch/hour. The activities did not appear to decrease significantly with increasing rainfall at rates greater than 0.15 inch/hour. Most of the order of magnitude change in ^{38}Cl and ^{39}Cl results from the higher activities measured in a few rain samples collected at very low rainfall rates near Richland. If only the Forks samples are considered, the decrease in activity with increasing rainfall rate is not nearly as great. It is possible that the high ^{38}Cl and

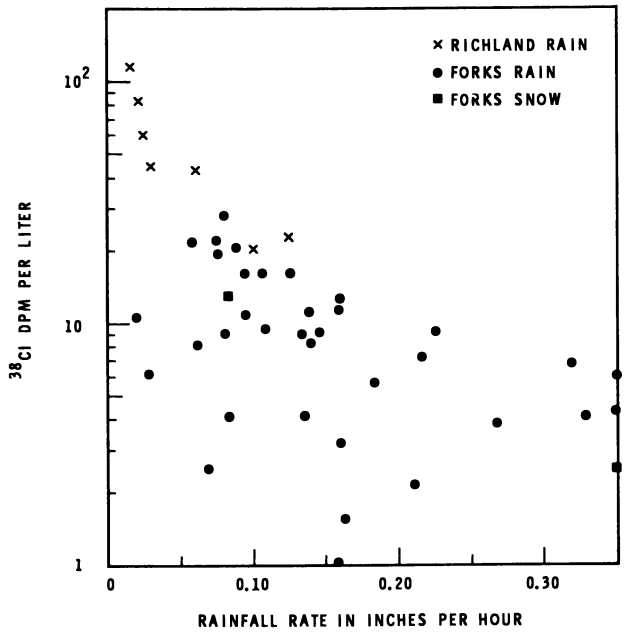

Figure 4. ^{38}Cl disintegration rate per liter of water in rain and snow as a function of rainfall rate

^{39}Cl activities measured near Richland resulted from some other cause than a low rainfall rate, such as a higher rain formation altitude.

When a cloud forms, water vapor condenses on aerosol particles present in the atmosphere. Regardless of the size of a cloud droplet, at least one aerosol particle is required for its formation. A major portion of the radionuclides present in the initial raindrop is caused by this aerosol particle. Although increases in the drop size owing to coalescence would tend to keep the radionuclide concentration constant, increases in size owing to the condensation of moisture on drops already present would tend to decrease the radionuclide concentrations. Therefore, one would expect a maximum in radionuclide concentrations in small drops. Raindrops tend to be larger in heavier rains. Therefore, the decrease in the ^{38}Cl and ^{39}Cl activities with an increase in rainfall rate could be caused by an increase in the drop size.

If the above explanation is correct, the rainwater disintegration rates of other airborne radionuclides should also decrease with increasing rainfall rate. However, the atmospheric activities of the longer lived radionuclides change with time, making it difficult to compare the activities in different rainwater samples. The ^{7}Be activity in rainwater ap-

peared to decrease with increasing rainfall rate, although the scatter of the points makes it difficult to be certain.

The decrease in the ^{38}Cl and ^{39}Cl disintegration rates in rain with increasing rainfall rate could also be caused by the depletion in the atmospheric activities at high rainfall rates. In view of their short half-lives and continuous production, however, it seems unlikely that the atmospheric ^{38}Cl and ^{39}Cl activities could decrease by a factor as great as 10 by an increased rainfall rate. If atmospheric ^{38}Cl and ^{39}Cl were depleted by heavy rainfall, the ^{38}Cl would initially grow back faster owing to its shorter half-life. This would make the $^{39}Cl/^{38}Cl$ ratio decrease with increasing rainfall rate. There appeared to be no general correlation between the rainfall rate and the $^{39}Cl/^{38}Cl$ ratio.

Two rainwater samples were collected consecutively during each of five rain showers at Forks, Wash. and one rain shower at Richland. The ^{38}Cl ^{39}Cl, and ^{7}Be disintegration rates and the $^{39}Cl/^{38}Cl$ ratios for the two consecutive samples in two of the rain showers are shown in Figure 6. In five of the six showers the ^{39}Cl activity was considerably higher in the second sample than in the first. In one shower, the ^{39}Cl activity was nearly 10 times as high in the second sample as in the first. The ^{38}Cl

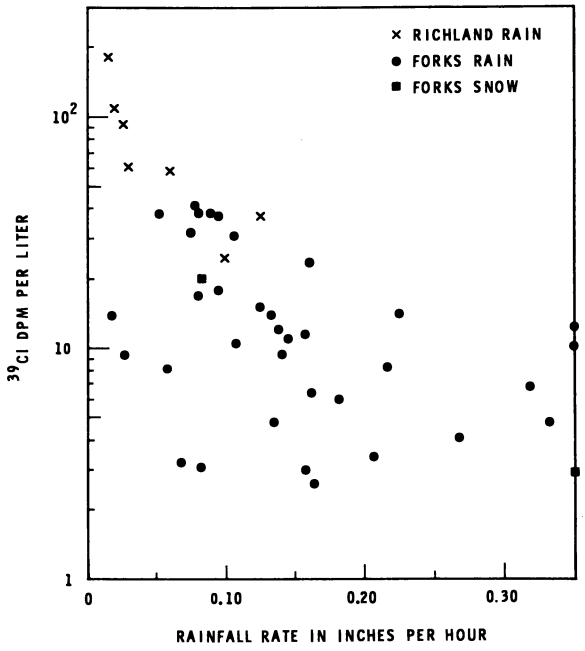

Figure 5. ^{39}Cl disintegration rate per liter of water in rain and snow as a function of rainfall rate

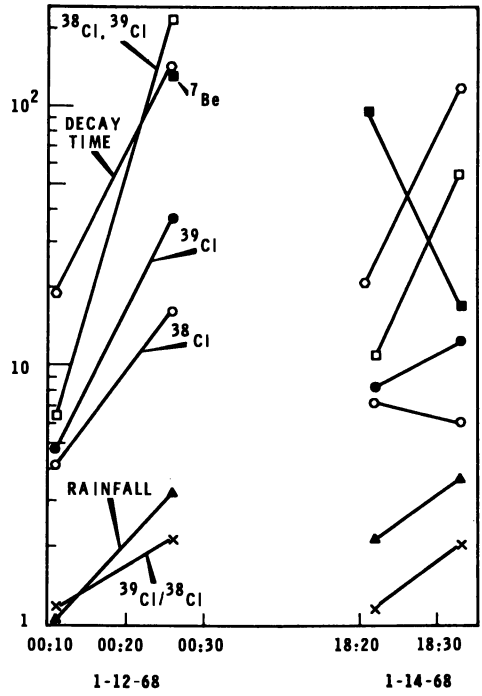

Figure 6. Cosmic ray radionuclide disintegration rates in rainwater from two rain showers at Forks, Wash.

● *d.p.m. ^{39}Cl/liter at time of collection*
○ *d.p.m. ^{38}Cl/liter at time of collection*
■ *d.p.m. ^{7}Be/liter at time of collection*
▲ *Rainfall rate in 0.01 inch/hour*
× *^{39}Cl/^{38}Cl*
□ *d.p.m. ^{38}Cl and ^{39}Cl at time when ^{39}Cl/^{38}Cl = 1*
⬡ *Calculated time in minutes between nucleation and collection*

activity, on the other hand, was higher in the second sample in only three of the six showers. In every shower the ^{39}Cl/^{38}Cl ratio was higher in the second sample than in the first. Since chlorine-39 has a longer half-life than does ^{38}Cl, the ^{39}Cl/^{38} ratio will increase continuously between the time the ^{38}Cl and ^{39}Cl are incorporated in the raindrop and the time the raindrop is collected. Therefore, the high ^{39}Cl/^{38}Cl ratio of the second sample in each shower may imply that the drops in the second sample spent a longer time in the cloud before falling as rain.

If one assumes that all ^{38}Cl and ^{39}Cl in the raindrop is incorporated during nucleation, the time between nucleation and raindrop collection can be calculated from the ^{39}Cl/^{38}Cl ratios at nucleation and at the time

of sample collection. The $^{39}Cl/^{38}Cl$ ratio at nucleation should be nearly equal to the ratio of the ^{38}Cl and ^{39}Cl production rates since ^{38}Cl and ^{39}Cl should be nearly at equilibrium in the atmosphere. Since the atmospheric ^{38}Cl and ^{39}Cl disintegration rates are about equal (7), the time between nucleation and rain collection was calculated using a value of one for the $^{39}Cl/^{38}Cl$ ratio at nucleation. The results are entered in Figure 6. If significant amounts of ^{38}Cl and ^{39}Cl were incorporated after nucleation, the calculated times would represent the average time spent by the ^{38}Cl and ^{39}Cl in the drop before rain collection, rather than the time since nucleation. In each of the six showers the calculated time between nucleation and collection was appreciably longer for the second sample. In one shower the time was two hours longer for the second sample than the first. Using the times between nucleation and collection the ^{38}Cl and ^{39}Cl disintegration rates in the rainwater at the time of collection were

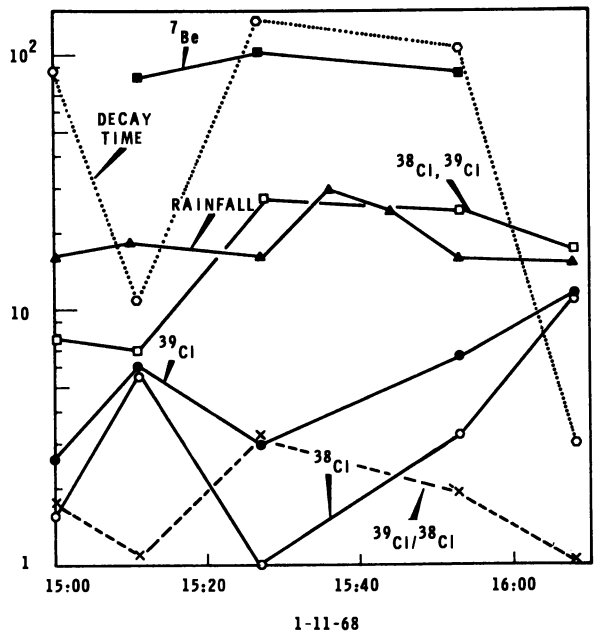

Figure 7. Cosmic ray radionuclide disintegration rates in rainwater from a rain storm at Forks, Wash.

- ● *d.p.m. ^{39}Cl/liter*
- ○ *d.p.m. ^{38}Cl/liter*
- ■ *d.p.m. ^{7}Be/liter*
- ▲ *Rainfall rate in 0.01 inch/hour*
- × *$^{39}Cl/^{38}Cl$*
- ⬡ *Calculated time in minutes between nucleation and collection*
- □ *d.p.m. ^{38}Cl and ^{39}Cl at time when $^{39}Cl/^{38}Cl = 1$*

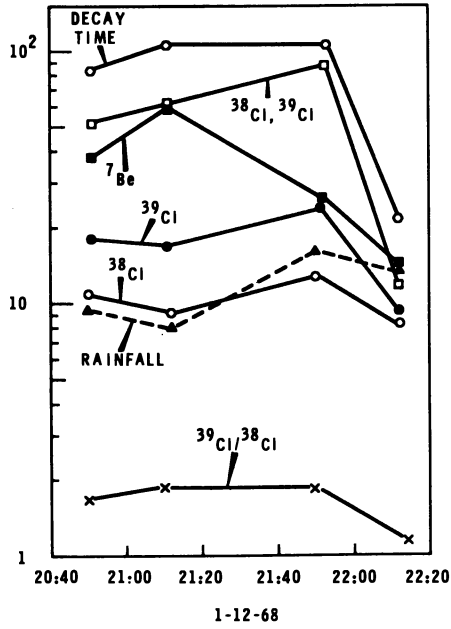

Figure 8. Cosmic ray radionuclide disintegration rates in rainwater from a rain storm at Forks, Wash.

● *d.p.m. ^{39}Cl/ liter*
○ *d.p.m. ^{38}Cl/liter*
■ *d.p.m. ^{7}Be/liter*
▲ *Rainfall rate in 0.01 inch/hour*
× *^{39}Cl/^{38}Cl*
⬡ *Calculated time (min.) between nucleation and collection*
□ *d.p.m. ^{38}Cl and ^{39}Cl at time when ^{39}Cl/^{38}Cl = 1*

decay-corrected back to the time of nucleation. When this was done, the decay-corrected ^{38}Cl and ^{39}Cl activities in all six showers were considerably higher in the second sample than in the first.

At Forks, Wash. several samples were collected consecutively during each of two rainstorms of about 2 hours duration. The ^{38}Cl, ^{39}Cl, and ^{7}Be disintegration rates, the ^{39}Cl/^{38}Cl ratios, and the rainfall rate are plotted as a function of time in Figures 7 and 8. In the first storm the ^{38}Cl and ^{39}Cl activities fluctuated somewhat but showed an over-all increase as the storm passed through. In the second storm the ^{38}Cl and ^{39}Cl activities at first showed relatively little change, reaching a small maximum late in the rain, then decreased considerably at the end of the rainfall. In each storm the ^{39}Cl/^{38}Cl ratio reached a maximum around the middle of the storm and then decreased toward the trailing edge of

the storm, indicating that the time between nucleation and rain collection was at a maximum near the middle of the storm. If the ^{38}Cl and ^{39}Cl activities are decay-corrected to the calculated time of nucleation, the ^{38}Cl and ^{39}Cl activities reached a maximum late in each storm and then decreased rapidly at the trailing edge of the storm. In the second storm the decay-corrected ^{38}Cl and ^{39}Cl activities reached a maximum at the same time as the maximum in the rainfall rate. In the first storm the ^{38}Cl activity was so low in the sample collected at 1527 that only a less than value for the ^{38}Cl could be determined. In the first storm two of the samples at the middle of the storm were not analyzed for the chlorine isotopes, owing to lack of time. Therefore, it was impossible to tell if the activity maximum corresponded to the rainfall maximum.

The ^{7}Be disintegration rate also reached a maximum in the middle of the storms. In the second storm the ^{7}Be maximum preceded the rainfall maximum. The ^{7}Be activity began to decrease before the decay-corrected ^{38}Cl and ^{39}Cl activities.

The main difference between the variation with time of the ^{38}Cl and ^{39}Cl in the two longer storms and the time variation in the six rain showers was the decrease in the disintegration rate at the trailing edge of the longer storms. Since each sample was collected over a 4 to 60-min. period, it is possible that at the end of the showers the activities decreased, but that the second sample in the shower contained enough rain from earlier in the sampling period to give it high average ^{38}Cl and ^{39}Cl activities. ^{7}Be, which tended to reach a maximum earlier in the longer storms than did ^{38}Cl and ^{39}Cl, had a lower activity in the second sample than in the first for one of the showers.

The maximum in the ^{39}Cl generally occurred at about the same time as the maximum in the $^{39}Cl/^{38}Cl$ ratio. Therefore, the maximum could not have been caused by a shorter time between the incorporation of ^{38}Cl and ^{39}Cl in the raindrop and the collection of the rain sample. The maximum in the ^{39}Cl could be attributed to an increase in the altitude of rain formation, caused by an increase in the height of the cloud base or an increase in the depth of the cloud layer. Since the rainfall should be heaviest when the cloud depth is greatest, the ^{39}Cl maximum and the rainfall maximum should occur at the same time. The tendency of ^{7}Be in rainwater to reach a small maximum before the rainfall maximum and then decrease rapidly could have resulted from a depletion in the atmospheric disintegration rate of ^{7}Be at the time of heaviest rainfall. Since the atmospheric ^{7}Be activity does not increase as much with increasing altitude as the ^{38}Cl and ^{39}Cl activities, its activity in rainwater would not increase as much as ^{39}Cl and ^{38}Cl with increasing altitude of rain formation. During these studies radiosonde balloons were released every 12 hours, or upon request, at the weather station. From the radio-

sonde data estimates cloud heights could be estimated at the release time. However, the radiosonde data did not give the continuous record of cloud heights necessary to interpret the variation in radionuclide activities during a rain. In the future, we intend to collect rain samples near a weather station which has radar capable of measuring continuously the height of rain formation.

There are other possible explanations for the variations in the radionuclide disintegration rates during a rainstorm. In an updraft, air of relatively low ^{38}Cl and ^{39}Cl activities would be transported to altitudes of greater production rate. The shorter half-life of ^{38}Cl would result initially in a faster buildup of the ^{38}Cl and a decrease in the $^{39}Cl/^{38}Cl$ ratio. A downdraft, on the other hand, would transport air of relatively high ^{38}Cl and ^{39}Cl activities to altitudes of lower production rate. The ^{38}Cl would decay faster, resulting in an initial increase in the $^{39}Cl/^{38}Cl$ ratio. Therefore, the relatively higher $^{39}Cl/^{38}Cl$ ratios toward the end of the rain showers could be caused either by updrafts at the leading edge of the rain cloud or by downdrafts at the trailing edge of the cloud. Either mechanism would lead to higher ^{39}Cl activities at the end of the rain. It seems unlikely that either updrafts or downdrafts would be rapid enough to produce tenfold increases in the ^{39}Cl activity. The much longer lived cosmic ray radionuclide ^{24}Na (15 hours) has not shown nearly this large a variation in atmospheric disintegration rate in the air filters collected during RB-57 flights.

Summary

The short-lived cosmic ray-produced radionuclides can be extremely useful atmospheric tracers because their atmospheric disintegration rates vary little with time, being affected only by very rapid processes. To be most useful their equilibrium disintegration rates in the atmosphere must be known as a function of latitude and altitude. The ^{24}Na disintegration rates reported here provide the first measurement of its production rates as a function of altitude, and this gives a firm basis for its use as an atmospheric tracer. We plan to extend our measurements of ^{24}Na to define the vertical profiles at other latitudes and thereby to obtain the dependence of the production rate upon latitude. In addition, we are determining the ^{38}Cl and ^{39}Cl activities as a function of latitude and altitude. Since the ratios of the production rates of the cosmic ray radionuclides vary little with altitude and latitude, it will then be possible to calculate production rates of other cosmic ray radionuclides as a function of altitude and latitude from the ^{24}Na, ^{38}Cl, and ^{39}Cl measurements.

The ^{38}Cl and ^{39}Cl activities and activity ratios can be especially useful in studying the efficiencies and time scales of nucleation and post-nucleation scavenging studies. Cosmic ray radionuclides having shorter half-lives than those of ^{38}Cl and ^{39}Cl could be used to determine the relative efficiencies of nucleation and post-nucleation scavenging. For example, ^{40}Cl (1.4 min.) should be produced in the atmosphere in measurable quantities by cosmic rays, but it has not been detected as yet because of its short half-life. In the future we intend to measure ^{40}Cl in rainwater under steady-state conditions. This may be possible by passing the rainwater directly through an absorption bed which is located between the detectors of a multidimensional γ-ray spectrometer. Owing to its short half-life any ^{40}Cl present in the rainwater would have been picked up by post-nucleation scavenging. From the ratios of ^{38}Cl, ^{39}Cl, and ^{40}Cl in the atmosphere and in the rainwater the relative efficiencies of nucleation and post-nucleation scavenging could be calculated.

Literature Cited

(1) Bhandari, N., Bhat, S. G., Karkar, D. P., Lal, D., Tamhane, A. S., *Tellus* **18**, 504 (1966).
(2) Friend, James P., Feely, Herbert W., Krey, Philip W., Spar, Jerome, Walton, Alan, *DASA 1300*, **3**, 201-305 (1961).
(3) Lal, D., *Progr. Elementary Particle Cosmic Ray Phys.*, VI (1962).
(4) Perkins, R. W., Thomas, C. W., Hill, M. W., Nielsen, J. M., *Nature* **205**, 790-791 (1965).
(5) Wogman, N. A., Robertson, D. E., Perkins, R. W., *Nucl. Instr. Methods* **50**, 1-10 (1967).
(6) Wogman, N. A., Thomas, C. W., Cooper, J. A., Engelmann, R. J., Perkins, R. W., **BNWL-SA-1146** (1967).
(7) Young, J. A., Thomas, C. W., Wogman, N. A., Perkins, R. W., *J. Geophys. Res.* (in press).

RECEIVED July 5, 1968. Based on work performed under the U. S. Atomic Energy Commission Contract AT(45-1)-1830.

INDEX

R

S

T

U

V

W

X

Y

Z